Transactions of the ASME

EDITORIAL STAFF
Editor, J. J. JAKLITSCH, JR.
Production Editor, CORNELIA MONAHAN
Editorial Production Assistant, BETH DARCHI

FLUIDS ENGINEERING DIVISION
Technical Editor
FRANK M. WHITE (1981)
Executive Secretary
L. T. NELSON (1981)
Calendar Editor
M. F. ACKERSON

Associate Editors
Fluid Machinery
H. JAMES HERRING (1981)
BUDUGUR LAKSHMINARAYANA (1982)
Fluid Measurements
BHARATAN R. PATEL (1982)
Fluid Mechanics
CHARLES DALTON (1983)
OWEN M. GRIFFIN (1981)
BRIAN E. LAUNDER (1981)
WILLIAM G. TIEDERMAN (1981)
Fluid Transients
M. HANIF CHAUDHRY (1983)
Polyphase Flow
PAUL H. ROTHE (1983)
ROBERT L. STREET (1981)
Review Articles
KENNETH E. HICKMAN (1981)

FOREIGN CORRESPONDENTS
Europe and Russia
JACQUES CHAUVIN
Europe and Russia
JOHN H. HORLOCK
India and Middle East
ARUN PRASAD
Japan and China
YASUTOSHI SENOO

POLICY BOARD, COMMUNICATIONS
Chairman and Vice-President
I. BERMAN

Members-at-Large
W. J. WARREN
J. E. ORTLOFF
M. J. RABINS
J. W. LOCKE

Policy Board Representiatives
Basic Engineering, FRED LANDIS
General Engineering, C. F. PHILLIPS
Industry, J. E. ORTLOFF
Power, R. E. REDER
Research, G. P. COOPER
Codes and Stds., L. L. ELDER
Nom. Com. Rep., J. W. LOCKE

Business Staff
345 East 47th St.
New York, N. Y. 10017
(212) 644-7789
Mng. Dir., Publ., J. J. FREY

OFFICERS OF THE ASME
President, CHARLES E. JONES
Deputy Exec. Dir. & Asst. Sec'y, PETER CHIARULLI
Secretary and Treasurer, ROBERT A. BENNETT

The Journal of FLUIDS ENGINEERING (USPS 278-480) is edited and published quarterly at the offices of The American Society of Mechanical Engineers, United Engineering Center, 345 E. 47th St., New York, N. Y. 10017. Cable Address, "Mechaneer," New York. Second-class postage paid at New York, CHANGES OF ADDRESS must be received at Society headquarters seven weeks before they are to be effective. Please send old label and new address. PRICES: To members, $30.00, annually; to nonmembers, $60.00. Single copies, $20.00 each. Add $5.00 for postage to countries outside the United States and Canada. STATEMENT from By-Laws. The Society shall not be responsible for statements or opinions advanced in papers or ... printed in its publications (B7.1, Par. 3).

INDEXED ... Engineering Index, Inc.

Journal of Fluids Engineering

Published Quarterly by The American Society of Mechanical Engineers

VOLUME 103 • NUMBER 2 • JUNE 1981

(Contents Continued on p. 334)

CONTENTS
(Continued)

Journal of Fluids Engineering

Correspondent Report

The first of two meetings of the 1980-1981 AFOSR-HTTM-Stanford Conference on Complex Turbulent Flows: Comparison of Computation and Experiment is described. The Conference is a cooperative research effort involving a major fraction of research workers in turbulent flow. It has three objectives: (i) establishment of trustworthy data sets that can be used as the basis for modeling complex turbulent flows and as standard trial cases for checking output of computations in such flows; (ii) the creation of a data library in standardized, machine-readable form on magnetic tape of the trustworthy cases; (iii) the comparison of current computational output from many groups with the standard trial cases. The meeting on data held at Stanford University, Sept. 3-5, 1980, is described in this paper, including: a short history of the problem, difficulties in turbulence research and recordation of adequate data sets, organization and special procedures in the conference, the trial cases established for the 1981 meeting on computation, a number of other specific results from the meeting, and conclusions. It is concluded that the 1980 meeting was successful not only in meeting goals (i) and (ii) but also in clarifying many other issues that have been troubling the research community and clarifying needs for future researches. The Proceedings from the 1980 meeting will be published in spring, 1981 and may be ordered from the first author.

Correspondent Report

On the Initial Meeting, Held September 3–6, 1980, of the 1980–1981 AFOSR-HTTM-Stanford Conference on Complex Turbulent Flows: Comparison of Computation and Experiment[1]

by

S. J. Kline[2] and G. M. Lilley[3]

1 Introduction

The meeting at Stanford University from September 3–6, 1980 completed the first stage in the *1980–1981 AFOSR-HTTM-Stanford Conference on Complex Turbulent Flows: Comparison of Computation and Experiment.* The major goal of this initial meeting was to reach a consensus in the research community on trustworthy experimental data sets that can be used as inputs for modeling of turbulence in complex flows and as a basis for standard "trials" for checking outputs of computations. In order to achieve this aim with impartiality, the cooperation of scientific and engineering communities was sought and generously given, forming the foundation for the September, 1980 meeting.

The Conference as a whole is best viewed as a cooperative learning process within the research community. The second and final meeting of the Conference will be held on September 14–18, 1981. The complete, detailed goals of the Conference are given below.

At the conclusion of the September 1980 meeting it was possible to select some 50[4] trustworthy experimental data sets of complex turbulent flows which will form the standard "trial" cases for comparison with the outputs of computations from many groups of computors.[5] The output of these computations will be compared with the standard cases in the September, 1981 meeting.

An essential component of the 1980–1981 Conference has been the creation of a "Data Library" on magnetic tape. This library holds the data selected as trustworthy in a standard and normalized form. The data will be computer-readable and the tapes will be held in repositories in USA and EEC countries and will be generally accessible for a moderate fee. The establishment of the Data Library is well advanced. It is intended that the library should be an ongoing function whose contents will be periodically updated using methods for the establishment of trustworthy data sets similar to those used for the 1980 meeting. The future home for the Data Library and its funding are matters for further consideration.

The aims of the September, 1980 meeting stated above were met, as can be seen by reference to the lively and pertinent discussions which followed each presentation and which are recorded in the *Proceedings* of the 1980 Conference. The September, 1980 meeting also achieved several other useful results. The bringing together of so many experienced experimentalists in the field of fluid mechanics became an important opportunity to explore many of the problems facing anyone setting up experiments involving turbulent flows. Arising from the several discussions, many suggestions were made regarding instrumentation and calibration for specific flows. Perhaps of more importance, these needs were identified: to plan the experiment carefully; to record in detail the initial or entry flow characteristics, as well as the downstream conditions; to set up a systematic analysis of uncertainty in the proposed measurements and, from trial runs, to make explicit that these uncertainty estimates are realized, or to determine what is needed to reduce uncertainty. It was agreed that such considerations are essential to the production of trustworthy experimental turbulent flow data but regrettably have often not been fully implemented in the

[1] The financial sponsorship of the U.S. Air Force of Scientific Research and the NASA Ames Laboratory are gratefully acknowledged.

[2] Professor, Thermosciences Division, Mechanical Engineering Department, Stanford University, Stanford, Calif.

[3] Professor of Aeronautics and Astronautics, University of Southampton, U.K.

[4] The number of data sets is approximate, since it depends on how one counts "sub-cases."

[5] "Computor" is used to describe individuals using computers.

past. This deficiency made the work of the Data Evaluators for the 1980 Conference more difficult but, at the same time, more important. Further details of these suggestions and recommendations are given below.

The September, 1980 meeting was also useful in providing increased understanding between experimentalists and computors. The interaction between these two groups became important in drawing up the specifications for the "trials" which the computors will undertake. This interaction was badly needed, in that it helped data takers appreciate what information needs to be supplied about a flow in order to provide satisfactory initial and boundary information[6] needed in experiments intended as input for turbulence modeling, for checking output of computation, or both. The data needs for these purposes in Computational Fluid Dynamics differ markedly with regard to demands on recordation of initial conditions, documentation of uncertainty, and verification of experimental control from the needs for experiments intended to provide direct data for engineering design or to increase understanding of fluid motions. Both a position paper (composed through seriatim revision by a number of workers) and discussions in sessions and ad hoc committees in the 1980 Meeting thus appropriately focus on "Data Needs for Computational Fluid Dynamics."

There was general agreement that although the range of computational methods in fluid mechanics will greatly increase within the next decade and beyond, it will not replace the need for high-quality experimental results. Thus there is a continuing need for closer contact between experimentalists and computors. The two groups of workers have much to give and learn from each other. Improvements in turbulence modeling techniques will inevitably come from closer collaboration between these two groups of workers. It cannot be over-stressed that an individual computor *does not have sufficient resources to assess the reliability and accuracy of data*; the task is not only arduous, but requires considerable experience in both experimental technique and the specific flow type considered. Hence it is essential that the experimental research community furnish computors with information on which flows are trustworthy. This was the central work of the 1980 meeting and the two-year-long preparation for it.

2 History

The study and prediction of the flow of Newtonian fluids have advanced greatly in recent years with the advent of fast methods of computation. Computational methods in fluid dynamics (CFD) now provide an appropriate and reliable tool for the prediction of a wide range of fluid-flow problems in many industries. This is particularly so if the fluid flow may be regarded as inviscid or if viscous effects are confined to regions whose geometries are relatively simple, for example, thin shear layers. Even so, there remain certain classes of inviscid flows, notably those containing free vortex sheets, which continue to present formidable problems in CFD.

In the case of turbulent flow, development of CFD methods for their prediction have depended on an adequate and trustworthy experimental data base. Such a data base has not always been available. It is therefore not surprising that a wide range of turbulence models and methods has been developed, presenting a confused picture as to which method or class of methods is best suited for the accurate prediction of a given fluid-flow problem. In order to make any significant advance, it is agreed that the available prediction methods need to be critically examined and compared with trustworthy experimental data. This conclusion is fully borne out by the experiences of the 1968, 1969, and 1972 Conferences.

In 1968 the AFOSR-IFP-Stanford Conference was set up to clarify the state of the art in prediction of incompressible turbulent boundary layers.[7] Its success may be measured not only by the establishment of similar NASA Conferences in 1969 and 1972 on turbulent compressible boundary layers and free-shear layers, respectively, but even more from the fact that the three Conferences showed that, contrary to prior common wisdom, adequate programs for computing shear layers did exist.[8] The *Proceedings* of these conferences still provide important reference works governing the structure and prediction of these initial types of flows, including satisfactory calculation methods.

The "trial cases" from these three meetings still serve as the functional standards for testing computational models of thin shear layers. Thus, experience shows: (i) standard trial cases composed of data known to be trustworthy are necessary in order to clarify the state of the art; (ii) such cases tend to remain a useful basis for a considerable period of years.

The 1980-81 AFOSR-HTTM-Stanford Conference has similar objectives with respect to a wide range of internal and external, incompressible and compressible, complex turbulent flows. However, the principal problem facing the Organizing Committee, when it first met in 1977, was the lack of trustworthy experimental data sets. The data base had to be created first. The first two years' work and the 1980 meeting were accordingly devoted to exploring the reliability of available data sets.

3 Difficulties in Turbulent Flow Research Affecting the Conference

Even though excluding turbulent flow involving changes in phase, heat transfer, and chemical reactions and limiting consideration to turbulent flow of a single, pure Newtonian fluid, the 1980–1981 Conference still faced a wide variety of complex flows which occur in practice and for which the characteristics must be known. Experiments have shown that turbulence does not have a single, simple structure, and its structure is greatly influenced not only by the initial and boundary conditions, but also by a score of effects such as body forces, surface roughness, curvature, etc.[9] There are therefore many flows requiring experimental investigation. Many of these flows present severe set-up problems in conventional laboratories. In most cases the laboratory experiment needs to be idealized in order to help clarify the phenomenon to be investigated. However, the idealization can change the phenomenon to be be investigated. Thus, the practical case may only be uncovered when a sufficient range of conditions have been explored in the laboratory tests. Consequently, a large number of experiments are required in order to clarify the description of the turbulence structure and its influence on the flow fields for practical situations. The 1980–1981 Conference has considered some 40 different classes of turbulent flows. These classes were of necessity constrained by the existence of adequate data, rather than by an ideal taxonomy of constraints and effects. Thus, other

[6] The remarks of D. Humphreys and B. van den Berg on three-dimensional boundary layers are particularly detailed and thorough.

[7] The 1968 Conference was fortunate in being able to use more than a decade of insightful work by D. E. Coles of C.I.T. on the relevant data, thus providing an existing data base.

[8] Certain exceptions were noted; specifically, detachment, reattaching layers, and the near zone of free shear layers. This information has helped to focus research during the following decade, with the result that important progress on all these problems has been made and efforts on the already solved problems have greatly diminished.

[9] A list of such effects is given in the Introduction to the 1980 meeting by the first author.

flows still need detailed investigation in order to provide a basis for trial cases.

Measurements within turbulent flows have always presented difficulties in the data collection, and even with modern methods of data-taking continue to do so. The instruments used, whether hot wires or laser anemometers, need frequent calibration, and have considerable uncertainty in resulting measurements. Thus, analysis of uncertainty becomes important in judging adequacy of computation.[10] The assessment of the uncertainties in the data for the test cases presented at the 1980 meeting was a major task for the Data Evaluators. A paper by R. J. Moffat at the 1980 meeting provides two major advances beyond the existing JFE standards for uncertainty analysis.[11] In particular, Moffat provides: (i) a method for systematic incorporation of uncertainty analysis into data-collection and reduction processes; (ii) the construction of a hierarchy of levels of replication, each of which has a specific use as the basis for operational checks on the adequacy of actual experimental control.

This brief section states only some of the difficulties in turbulent flow measurement that affect the work of the conference. A more complete discussion of the difficulties is given in the Introduction to the Proceedings of the 1980 meeting by the first author. Discussion of particular problems occurs at numerous places in the reports on data evaluations, discussions, and reports of ad hoc committees.

4 Organization of the Conference

An Organizing Committee was set up in 1977 to create the workshops for the 1980 and 1981 meetings. The Organizing Committee includes: S. J. Kline (Chairman), P. Bradshaw, B. Cantwell, B. Launder, E. Reshotko, M. Rubesin, and G. Sovran.

The task before the Organizing Committee for the 1980–81 Conference was far more complex than in the previous conferences held in 1968, 1969, and 1972, for four reasons:

- The flows needed for consideration were more diverse and complex and were selected as representing examples of most of the basic turbulent flows occurring in practice.
- No sound data base existed in 1977; accordingly, one had to be created.
- Computational methods have advanced considerably since the 1968–1972 era and are now more complex, more varied, and far more expensive to run.
- Adequate review procedures for very large programs did not exist.

The plan of work created by the Organizing Committee set three goals:

(1) The creation of a data base of trustworthy experimental cases and specifications of "trials," using those cases against which computations can be tested comparatively (task of data evaluators and the 1980 meeting).

(2) The creation of a data library on magnetic tape which will hold those trustworthy cases, together with complete descriptions and data lists. The tapes will be held in repositories in USA and EEC countries and will be generally accessible, for a moderate fee (an ongoing task).

(3) Comparison of outputs of computations from many groups of computors with the standard "trial cases" of item (1) (Task of the 1981 meeting).

Work toward Goal (1) included the efforts of some 30 groups of data evaluators during 1979 and 1980. Each flow was evaluated by a leading expert (the Data Evaluator) and reviewed by several other experts. The combined evaluations and reviews were presented to the 1980 meeting in twelve sessions and were followed by evening meetings to establish a consensus on which flows met the criteria for trustworthy data adequate to be used for test cases and in the formulation of new computer models of turbulent flows.

The 1980 meeting also brought into sharper focus a number of underlying but sometimes neglected questions, including:

(*a*) The uncertainty in various classes of critical measurements, such as in hot-wire measurements.

(*b*) Procedures for improving uncertainty estimates of data.

(*c*) Discussions of appropriate means of comparison of computations and experiments in the light of uncertainties in both.

(*d*) The establishment of general rules and guidelines for future data-takers concerned with experiments intended to be the basis for turbulence modeling or comparison with computations.

(*e*) Detailing the needs for data in computational fluid dynamics as a class of experiments, and delineating flows needing improved data bases.

(*f*) An increased emphasis and understanding of the need for iterating between data and computation.

(*g*) Focusing on the need for a means to differentiate errors arising from "numerics" from those owing to deficiencies of turbulence models.

The 1980 Conference was attended by 181 invited participants from 12 countries (Australia, Canada, France, India, Japan, Norway, Sweden, Switzerland, United Kingdom, United States of America, West Germany, and Yugoslavia).

5 Test Cases for 1981

As a result of the work of the Data Evaluators and the presentations and discussions held at the 1980 meeting, approximately 50 Test Cases (30 incompressible plus 20 compressible) have been selected as broadly meeting the criteria laid down for "trustworthy experimental data sets." A detailed specification is being provided for each test case delineating computations to be done, and plotted in prespecified form for comparison. Except in a few special cases, computations are specified only where trustworthy data exist.[12]

The Test Cases have been subdivided as follows:

A. Simple Case: Shear layers or homogeneous flows (at the level of the 1968, 1969 and 1972 meetings).

B. Entry Case: A test case that is more complex than type A and thereby meets the entry requirement for presentation at the 1981 meeting.

C. Central Case: Four entry cases (two incompressible, two compressible) selected by the Organizing Committee as being sufficiently important as a test of turbulence modeling, numerics, and the current state of the art to warrant requesting as many computers as possible to submit computations in order to provide dense results to improve the learning process.

D. Predictive Case: A case for which only the initial conditions and geometry are given in the specification. Data are being taken in parallel with the computations and will be compared in the 1981 meeting. Four such cases will be used in the 1981 meeting.

The *Simple Cases* include attached, two-dimensional

[10] In the 1968 cases, the data uncertainties are generally small compared to uncertainty of computation, so that the issue of uncertainty analysis was far less important.

[11] "Analysis of Uncertainty in Single-Sample Experiments," S. J. Kline and F. A. McClintock, in *Mech. Engrg.*, Jan. 1953, or equivalent.

[12] The second author collated, integrated, and in some instances arbitrated the numerous recommendations for improvement of test cases arising during the 1980 meeting.

boundary layers with pressure gradient in incompressible flow and a considerable number of incompressible homogenous flows. (The homogeneous flows are particularly important to model formation, and computors requested extensions of the data set; this has been done.)

The *Central Cases* for incompressible flow include a curved free-shear layer and a backward-facing step, while for compressible flow they include a well-documented transonic airfoil and a compression corner at Ma = 3.

The *Entry Cases* in incompressible flow include: conical diffusers with low and high inlet turbulence; the effect of freestream turbulence on a boundary layer; separating and separated flow in a passage; boundary layers with strong convex and concave curvature; boundary layers with blowing and suction; the near-wake of a circular cylinder; a stalled two-dimensional airfoil; secondary flows in a wing-body junction, in a curved rectangular channel, and in a square duct; equilibrium, self-preserving, and three-dimensional wall jets; relaminarizing boundary layer; relaminarizing tube flow; development and asymptotic state of a mixing layer; symmetric and asymmetric two-dimensional wakes, and other cases.

The *Entry Cases* in compressible flow include: a supersonic boundary layer with blowing; boundary layers with three-dimensional and axisymmetric shock impingement; shock-separated boundary layer on transonic airfoils at zero lift and incidence; normal shock wave/boundary layer interaction; transonic flow over axisymmetric and two-dimensional bumps; cone at incidence in supersonic flow, and other cases.

The *Predictive Cases* for incompressible flow include: the developing flow in a square duct with a non-uniform velocity profile at inlet; sudden expansions in ducts of varying geometries. Unfortunately, no predictive cases for compressible flow will be completed soon enough for use in the 1981 meeting.

It is expected that about 50 computor groups will provide computations in time for the 1981 meeting. Of that number, about 16 groups have declared an intention to tackle ten test cases or more. Standard plots are being supplied for each case, so that direct comparison of results will be possible. Problems concerning difficulties in numerics, methods for disclosure of numerical codes, computing times, and computing difficulties (including methods which do not work) are all matters which will be discussed at the 1981 meeting.

The 50 Test Cases chosen for the 1981 meeting do not exhaust the data sets available which meet the criteria discussed previously. Some 20 other Test Cases are available for inclusion in the Data Library. In addition, more than a dozen other classes of flow have yet to be evaluated and remain as possible future additions to the library.

It will be noted that the 50 selected Test Cases do not include incompressible flow in three-dimensional attached boundary layers and flows with swirl. (Such flows form a vital component in the prediction of airfoil and wing performance at subsonic and supersonic speeds and in combustion systems, respectively.) These flows were studied by Data Evaluators and were presented at the 1980 meeting. They were recommended by the 1980 meeting, but regrettably were not completed soon enough to be available for selection as Test Cases for the 1981 meeting. They will be made available for later testing and discussion through the data library and will, therefore, be available as a basis for later meetings.

In addition, several important classes of flows were evaluated in which the Data Evaluators reported deficiencies in all data so severe that they did not meet the criteria laid down for possible Test Cases. These flow cases include: three-dimensional flows other than boundary layers; complex wakes, including ship wakes, wakes from buildings, and the flow around protuberances from solid surfaces: turbulence-turbulence interactions; strongly non-equilibrium flows; laminar-turbulent transition; and flows with distributed buoyancy effects. Further experimental work on each of these flows is an urgent task for the future. Experimental groups engaged in work on these flows are advised to refer to the reports of the Data Evaluators and to the Proceedings of the 1980 meeting, to ascertain the nature of the deficiencies in the existing data sets as a guide to future research. They are also urged to note the recommendations for future data-takers, with particular reference to uncertainty checks and experimental control.

6 Special Problems Discussed at the 1980 Meeting

Because of the presence of so many experienced experimentalists, the 1980 meeting provided a special opportunity to discuss and report on difficulties that frequently arise in experiments on turbulent flows. The following account includes brief remarks on several such topics and issues which arose during the course of discussion or were the subjects for the Special Committees set up during the meeting. The complete reports will appear in the Proceedings.

(*a*) *The Effect of Initial Turbulence Conditions on the Development of Free-Shear Layers and Wall Boundary Layers.* This question arose several times during the meeting and was the subject for a Special Committee under the chairmanship of Professor H. Nagib. The problem is not one of academic importance only; there have been several recent applications which rest on modification of the large-scale turbulent structure in a shear flow, with subsequent significant changes in the downstream development. The possible applications include enhanced mixing, increased heat transfer rates, and reductions in surface drag. The Committee proposed that advanced computer-prediction schemes for turbulent flow should be tested for their sensitivity to the initial conditions, specifically changes in the spectral distribution of the turbulent energy over the "inlet" flow plane.

(*b*) *Uncertainties in Hot-Wire Fluctuation Data at Low Mach Numbers.* This was the subject of a Special Committee chaired by Professor B. G. Newman. The complete report includes much important practical information for use by experimenters relating to: uncertainty analysis; drift; measurement of dissipation; integrating times; measurements in high-intensity turbulent flows; measurements in reversed flows; and the circumstances which warrant replacement of the hot wire by the laser.

(*c*) *Turbulence Measurements in Transonic and Supersonic Flows.* This was the subject of a Special Committee chaired by Professor E. Reshotko. There was general agreement that the continued use of the hot wire is recommended, even though output uncertainty is more than 15 percent in the transonic zone. The laser-doppler anemometer is found to give only limited information on temperature and density fluctuations. Some redundancy checks using both the hot wire and the LDA are badly needed at this time.

It was also agreed that turbulent flow measurements in transonic and supersonic flows require more careful preplanning than in low-speed flows; a greater number of measurements are required, although the usable data are fewer than in low-speed flows; the experiments are much more expensive to run; as a result of these factors, more attention to the uncertainty analysis is needed.[13] As a result of these factors, there is much less agreement concerning what

[13] Paradoxically, uncertainty analysis appears to have been used far less in these difficult compressible cases than in incompressible flows, apparently owing to historical rather than logical reasons.

constitutes "trustworthy data" in transonic and supersonic flows.

(*d*) *Experiments and computations on Free-Shear Layers or Mixing Layers.* This Special Committee was chaired by Professor F. Champagne. The Committee made recommendations with respect to suitable "trailing edge" geometry for both two-dimensional and axisymmetric flow where, in the latter case, the first two diameters are assumed to be a reasonable simulation of a two-dimensional (planar) mixing layer. Also discussed were levels of free-stream turbulence which are likely to have little effect on the structure of the mixing region and the initial conditions for the boundary layer at the trailing edge.

(*e*) *Shock Waves in Turbulent Flows.* In discussing transonic and supersonic flows at the 1980 meeting, the question of the location of the shock wave and its independence with respect to time was raised frequently. No clear answer was forthcoming to this question. Many experimentalists were agreed that, where the mean flow field remained steady, observations of the shock wave appeared to show it was steady also. However, others suggested some residual unsteadiness of shock waves is generally observed, and there was no evidence available to prove conclusively that a shock wave immersed in turbulent flow does not undergo oscillations owing to effects of turbulent fluctuations. This is a topic that also calls for future careful experimentation.

(*f*) *Two-Dimensional Flow.* Recurrent questions were, "What constitutes a two-dimensional flow?" and "What measurements need to be made to provide acceptable experimental confirmation that a given flow is two-dimensional?" The meeting agreed that the questions can be answered only by taking suitable control-volume measurements of rates of mass and momentum flux. There was agreement that a flow could not be certified as two-dimensional simply because the mean flow was relatively independent of the spanwise location.

7 Position Papers Presented at the 1980 Meeting

Three Position Papers were presented to the 1980 meeting and will be reported in full in the *Proceedings* of that meeting. They are:

(i) The Data Library, by B. Cantwell

(ii) Contributions to the Theory of Uncertainty Analysis for Single-Sample Experiments, by R. J. Moffat.

(iii) Experimental Data Needs for Computational Fluid Dynamics, by P. Bradshaw, B. Cantwell, J. Ferziger, S. Kline, M. Rubesin, and C. Horstman.

Some information on (i) has been given above indicating the importance of the existence of the library for the work of the 1980–81 Conference and its continuing function.

The importance of uncertainty analysis in controlling experiments, the need for wider use of such analysis, the importance of uncertainty bands in comparing computation with experiments, and the nature of the new contributions by R. Moffat have all been covered earlier in paper (ii).

Paper (iii) provides a starting point for the clear delineation of the interaction between experimental data and computational fluid dynamics which is central to the 1980–81 Conference. Study of this paper should be useful for nearly anyone involved in experimental or computational fluid dynamics at this time.

8 Conclusions

(i) The 1980 Stanford meeting is best looked on as a successful, impartial, cooperative effort of a large fraction of the experimental fluid mechanics experts in reaching a consensus concerning: "what currently available experimental data on turbulent flows are sufficiently trustworthy to be used as inputs to turbulence modeling and/or a basis for standard "trials" for checking outputs of computations?"

(ii) The central conclusion of the meeting was that about 70-100 sets of such data are suitable as Test Cases within the framework of Complex Turbulent Flows; of these sets, about 50 will be used as Test Cases for the 1981 meeting.

(iii) No adequate data exist for some complex flows nor in general for any *very* complex flows such as flow behind three-dimensional bluff bodies; collection of such data remains a task for future research. The 1980 meeting showed there is need for many more experimental investigations of high quality for some classes of turbulent flows. Recommendations regarding the planning of these experiments, the care needed in setting up the initial conditions and in continuously monitoring uncertainty analysis and deserve checks are all matters considered at the Conference. Considerable detail on these matters are reported in the *Proceedings*.

(iv) Increased interaction appears to be needed between computors and experimentalists in fluid dynamics in order to close the loop iteratively between experiment and computation and thereby speed progress.

(v) Contributors to the 1980 meeting repeatedly stressed the importance of initial and boundary conditions in many complex turbulent flows. They also emphasized the need for more careful reporting and documentation of those conditions than has usually been the case in the past.

(vi) The period involving preparations for the 1980 meeting as well as the meeting itself appears to have been a period of great stimulation and hence of accelerated learning in turbulent flow research. The full fruits of this learning will not be evident until the 1981 meeting is completed and the results digested. What the learning process has already made very clear is that turbulent flow research is of such magnitude that the resources of one laboratory are insufficient to the totality of problems in providing and assessing reliable data sets, or in evaluating the many developing methods of CFD to practical applications. Thus, cooperation among research workers on the scale associated with the 1980 meeting has many advantages and is probably essential if the opportunity to move toward adequate prediction of complex turbulent flows is to be realized in an effective manner.

(vii) It seems likely that the 1981 meeting will confirm that the progress made in CFD is such that, given time, many complex turbulent flows of the types used as Test Cases for the 1980–1981 Conference will be computable to an accuracy satisfactory for engineering and other applications, provided the initial and boundary conditions are adequately specified. Major questions remaining to be assessed by the 1981 meeting include: (i) the current extent of progress in predicting complex turbulent flows, (ii) the likelihood of constructing a single turbulence closure model that is both sufficiently accurate and computationally not-too-slow for a wide variety of flows, or on the contrary, whether a variety of closure models will be needed to fulfill the requirements of engineering prediction.

(viii) At this stage of the 1980–1981 Conference, it is important to emphasize that neither the requisite experimental data base nor CFD methods will be completed by the 1980–1981 Conference. Further work on the Data Library will be required, and development of the computational methods will be far from concluded. Despite this, if the rate of progress in the highly useful assessment of the 1980 meeting can be maintained, the 1981 meeting will conclude with a state-of-the-art in the prediction of, and a solid core of test cases for use in assessing further progress in, computation of complex turbulent flows. The authors are grateful for having had the opportunity to play a role in this challenging and important research task.

The Stability of Pumping Systems—The 1980 Freeman Scholar Lecture

E. M. Greitzer
Associate Professor,
Department of Aeronautics and Astronautics,
Massachusetts Institute of Technology,
Cambridge, Mass. 02139

A review is presented of the types of instabilities which are encountered in pumping systems of technological interest. These include axial and centrifugal compression systems, pumping systems involving cavitation, systems with two-phase flow, systems with combustion, hydraulic systems, and systems which have two or more pumping elements in parallel. All of the above will be seen to exhibit instabilities under certain operating conditions, although the mechanism of instability, as well as the particular system element that is responsible for the instability, will be quite different in the different systems. However, several basic concepts, such as the idea of negative damping which is associated with dynamic instability, will be seen to be common to the different systems.

The review is organized around the different types of systems that are discussed, and includes descriptions of the steady-state performance, the regimes in which one would expect instability, and the mechanisms of instability. An idealized pumping system is first examined to illustrate some of the basic concepts. More realistic systems are then treated in the same manner of showing steady-state performance, regimes of instability and mechanisms. In the review attention is given mainly to those areas in which there is high current engineering interest, and an attempt is made to describe those areas of research which can be most fruitfully pursued. In general, it is suggested that efforts should be directed toward obtaining an improved understanding of the transient behavior of the active (instability causing) elements within the system, since it is lack of knowledge of this aspect that currently limits the accuracy of system stability predictions.

1 Introduction

There are a large variety of pumping systems which are commonly used by fluids engineers; there are also a large variety of instabilities encountered in these systems. The consequences of these instabilities result in widely varying difficulties with the fluid mechanic performance of the systems. At one extreme the instability may lead to only a minor annoyance, such as a small decrease in efficiency or a rise in noise. At the other extreme, however (which is the more usual situation), instability may lead to a totally unacceptable flow regime or even to the catastrophic failure of the system. This review addresses those types of system instabilities which are important in technological applications of fluids engineering.

As a starting point it is useful to state what will be meant herein by the terms "stability" and "pumping system." For the first term we can use the definition given by Betchov and Criminale [1]: "Stability can be defined as the quality of being immune to small disturbances." Thus if one has a system at a given operating point and the system is subjected to a small perturbation, a critical question to be answered is whether or not the system will return to the original operating point. This does not completely encompass the scope of the material to be discussed below, however, since it only focusses on the response to small perturbations and the initiation of instability. Often of great importance is the behavior subsequent to this onset, where the perturbations of the system from steady operations are no longer small. We will therefore examine some of the (large amplitude) consequences of system instability as well.

The term "pumping system" can be defined for purposes of this review to include almost any system where one drives a fluid through a pipe, channel, etc. by means other than gravity or other source of natural circulation. In the review, the most attention will be devoted to the type of system in which the pumping element is a turbomachine of some type and where it is the performance of the turbomachine that triggers the instability; however, we will also address other situations such as instabilities in two-phase flows, instabilities in vaneless diffusers, self-excited instabilities in hydraulic systems, supersonic diffusers, etc.

A. Overall System Characteristics and Stability of a Basic Pumping System. As a focus for the overall problem, let us consider a basic pumping system, examine the performance, and describe some of the fundamental criteria that determine

Contributed by the Fluids Engineering Division for publication in the JOURNAL OF FLUIDS ENGINEERING. Manuscript received at ASME Headquarters, January 12, 1981.

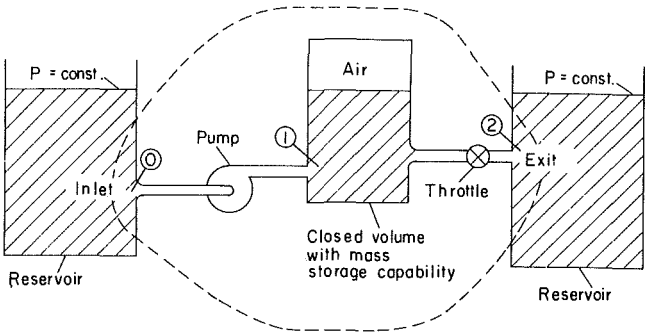

Fig. 1 A basic pumping system

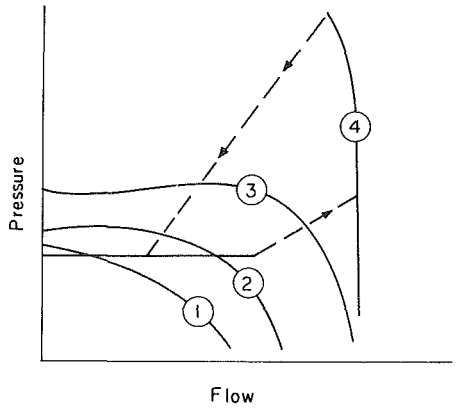

Fig. 2 Typical pumping characteristics

the system stability. This is shown in Figure 1, where we see an idealized system. An incompressible fluid is pumped from a large, constant pressure reservoir through a closed tank which contains a compressible gas (air) and then through a throttle valve into another large reservoir. The second reservoir does not necessarily have to be at the same pressure level as the first; however, in this example we *will* take the two to be at the same (constant) pressure. In addition, if we neglect end effects we can take the inlet of the pump (the "Inlet" station) and the exit of the throttle (the "Exit" station) to be at the same pressure, and thus consider for now only the parts of the system within the dotted control surface. The essential elements are therefore the pump, the compliance or mass storage capability of the closed volume, the throttle (which controls the system flow rate) and the inertance of the fluid in the pump inlet and exit and throttle lines.

We can examine briefly the overall steady-state performance of the different elements. Some typical forms of pump, fan, and compressor characteristic curves are shown in Fig. 2. The horizontal axis is flow, which is usually the independently controlled variable, and the vertical axis represents the pressure rise or pressure ratio. (The shapes of the curves are representative, but the curves are not drawn to scale.) Curves 1 and 2 would be found in centrifugal pumps, while curve 3 might be for an axial flow fan, and the discontinuous curve 4 would be for a multistage axial compressor. In our simple system the resistance that the pump has to work against is provided almost wholly by the throttle valve. In a more general system the resistance would also include the various losses in the system piping, the influence of bleeds or other subsystems, etc. However, the overall shape of the typical system flow-pressure requirement curve would look somewhat like that sketched in Fig. 3, where curves 2 and 3 correspond to decreasing throttle areas from curve 1, and where curve 4 might represent the effect of increasing throttle area or the presence of a bleed. These curves, which all have positive slope, can be taken as typical of many systems; however, it can be noted that important exceptions to this occur in two-phase flow systems, as will be discussed below. For the present we will consider only the positively sloped, single-phase situation.

The steady-state operating point of our system is set by two conditions, namely that the flow through the compressor and the flow through the throttle are the same and (since the two reservoirs are at the same pressure) that the pressure rise through the compressor is equal to the pressure drop due to the system resistance. These two conditions imply that the steady-state "match point" is at the intersection of the pumping characteristics and the throttle (or system resistance) curves shown in Figs. 2 and 3, respectively.

Let us now examine the stability of an arbitrary steady-state operating point. With reference to the left-hand side of Fig. 4, consider the effect of a small perturbation in mass flow (a

Nomenclature

a = speed of sound
A = flow-through area
A_{in} = inlet flow-through area
B = compressor stability parameter; $B = (U/2a)\sqrt{V/AL_c}$
C = fluid velocity
C_P = specific heat at constant pressure
C_v = specific heat at constant volume
C_x = axial velocity
C_x' = axial velocity nonuniformity, see Fig. 12
D = diameter (also D-factor, see footnote 7)
i = $\sqrt{-1}$
L = length of compressor or pump ducting, duct length between heated section and throttle
l = length of heated section of channel
$\dot{m}$ = mass flow
$\dot{m}\sqrt{\theta}/\delta$ = corrected flow, defined in footnote 11
N = number of compressor stages
$N/\sqrt{\theta}$ = corrected speed, defined in footnote 11
N_{pch} = phase change number; $N_{pch} = (\Omega_p l/v_{fi})$
N_{sub} = subcooling parameter; $N_{sub} = (\Delta\rho/\rho_g)\ (\Delta h_{sub}/\Delta h_{fg})$
P = pressure
P_T = total pressure
PR = pressure ratio
R = radius
SP = stability slope parameter; defined in the section on "Stage Stall in a Centrifugal Compressor"
T = temperature
T_T = total temperature
W = diffuser width (also relative velocity)
U = blade speed at mean radius of axial compressor
U_t = axial inducer tip speed
U_{tip} = impeller tip speed
V = volume
V_a = air volume
V_c = compliant volume
v_{fi} = fluid velocity at inlet to heated section
X_e = exit quality
γ = specific heat ratio
δP = pressure perturbation
$\delta\dot{m}$ = mass flow perturbation
Δh_{sub} = subcooling
Δh_{fg} = latent heat of vaporization
ΔP = pressure difference
ΔP_c = pressure difference across pump or compressor

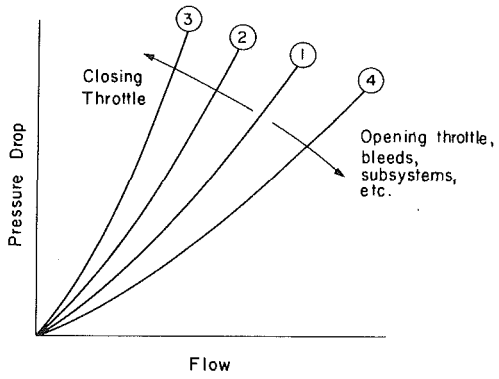

Fig. 3 Typical system pressure requirements

decrease, say) at operating point A. If this occurs, the pressure drop across the throttle is now smaller than that produced by the pump. This pressure imbalance will cause fluid accelerations that return the system to operation at the initial point, so that point A is a stable operating point. This will be true for all points to the right of point A or for points between A and B. However, consider the situation at point B, where the throttle line is tangent to the pumping characteristic. For a small decrease in mass flow the pressure forces that arise now will be such as to cause the system to depart further from the initial operating point, so that point B is an unstable operating point. We have thus derived the most basic of the stability criteria for a pumping system—the system will become unstable if the slope of the pump (or compressor) pressure rise curve is steeper than the slope of the throttle curve.

This criterion is, however, too simple to describe many of the real phenomena that are observed in pumping systems since it only considers the *static stability* of the system (static instability is associated with a pure divergence from the initial operating point). In fact, it is often the criteria for *dynamic stability* (dynamic instability leads to growing *oscillatory* motion about the initial point) which are violated first.

Static instabilities can be inferred from viewing the transient performance of the system as a sequence of (quasi-) steady states. Hence steady-state performance considerations, in particular a knowledge of the steady-state pump characteristics, throttle lines, etc., is enough to define the stability. In the prediction of dynamic instability, on the other hand, parameters such as inertances and capacitances must be included since they play an essential role in determining the transient response of the system to disturbances. These parameters are not part of the information needed to describe the steady-state system operation. Hence knowledge of steady-state performance curves alone is not sufficient for prediction of dynamic instability, and additional information about quantities such as volumes, duct lengths, etc., must also be included. As shown on the right-hand side of Fig. 4, the point to be emphasized is that a pumping system can be statically stable (according to the slope criterion described in the foregoing) and still exhibit instability.[1]

[1] The terms dynamic and static instability can be made more quantitative by the following illustration. Consider a simple second order system described by the equation

$$\frac{d^2X}{dt^2} + 2\alpha\frac{dX}{dt} + \beta X = 0$$

where α and β are constants of the system. The transient response of the system to an initial perturbation is given by

$$X = A\exp\{(-\alpha+\sqrt{\alpha^2-\beta})t\} + B\exp\{(-\alpha-\sqrt{\alpha^2-\beta})t\}$$

where the constants A and B are determined by the initial conditions. If $\beta > \alpha^2$, the condition for instability is simply $\alpha < 0$, which corresponds to oscillations of exponentially growing amplitude. Instability will also occur if $\beta < 0$, independent of the value of α; however in this case the exponential growth is nonoscillatory. It is usual to denote these two types of instability as dynamic and static respectively. Static stability ($\beta > 0$) is a necessary but not sufficient condition for dynamic stability.

The distinction between the two types of instability appears to have been made first by Maxwell [2], who wrote:

"It will be seen that the motion of a machine with its governor consists in general of a uniform motion, combined with a disturbance which may be expressed as the sum of several component motions. These components may be of four different kinds:

1. The disturbance may continually increase.
2. It may continually diminish.
3. It may be an oscillation of continually increasing amplitude.
4. It may be an oscillation of continually decreasing amplitude.

The first and third cases are evidently inconsistent with the stability of motion; and the second and fourth alone are admissible in a good governor."

The first case is the static instability, the third is the dynamic instability.

Nomenclature (cont.)

ΔP_H = pressure difference across heated section
ΔP_T = pressure difference across throttle
ΔT = temperature difference
$\Delta\rho$ = density change, liquid to vapor
λ = stall cell blockage
μ = proportionality constant defined in equation (A-36)
ρ = density
ρ_g = vapor density
σ = cavitation number (also used for solidity in definition of D-factor)
τ = time delay
ϕ = axial velocity parameter; $\phi = C_x/U$
ϕ^* = design value of axial velocity parameter
ϕ_t = axial velocity parameter based on tip speed
ϕ_d = centrifugal impeller flow rate parameter based on radial velocity at diffuser inlet divided by tip speed
ψ = pressure rise coefficient, $\psi = \Delta P / \frac{1}{2}\rho U_t^2$
ψ_{TS} = inlet total to exit static pressure rise coefficient, $\psi_{TS} = (P_{\text{out}} - P_{T_{\text{in}}})/\rho U^2$
ψ_d = centrifugal impeller/vaneless diffuser pressure rise coefficient,

$$\psi_d = \frac{(P_{\text{diffuser exit}} - P_{T_{\text{impeller inlet}}})}{\frac{1}{2}\rho U_{\text{tip}}^2}$$

ψ_t = axial inducer pressure rise coefficient, $\psi_t = \Delta P / \frac{1}{2}\rho U_t^2$
ω = frequency (or Helmholtz resonator frequency when specified)
Ω_p = reciprocal of characteristic time associated with phase change; see [147] or [152]

Subscripts and Superscripts

$(\bar{\ })$ = mean flow quantity
$\delta(\ )$ = perturbation quantity
$(\ )^*$ = design point value
P = pump
H = heated section

Numerical subscripts are defined in the text.

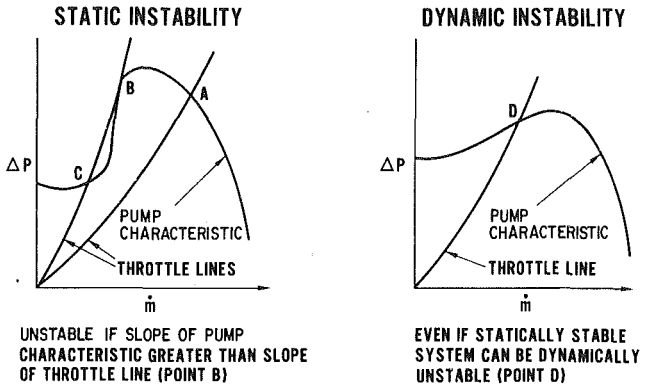

Fig. 4 Instabilities in pumping systems

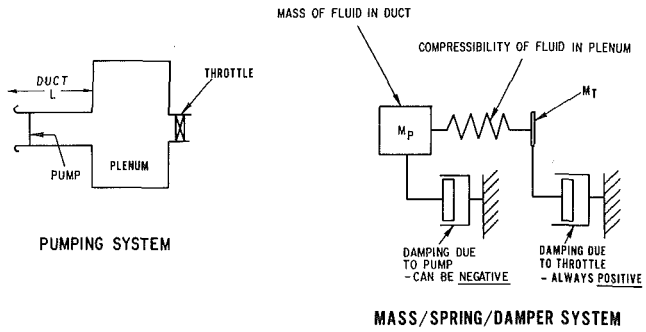

Fig. 5 Mechanical analogue of simple pumping system

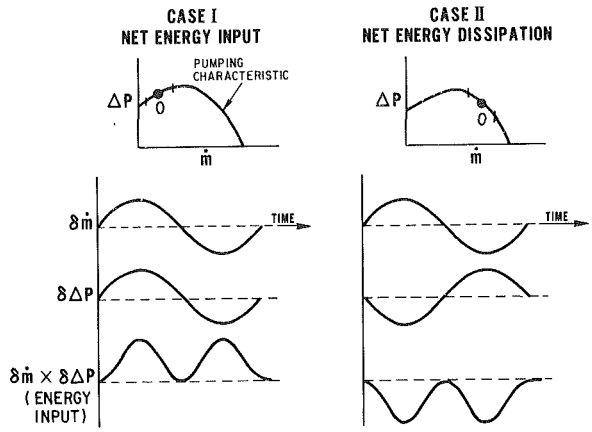

Fig. 6 Physical mechanism for dynamic instability

B. Physical Mechanism for System Dynamic Instability. To analyze the dynamic stability of our idealized system we can consider a lumped parameter system model. In this model all the kinetic energy of the unsteady flow in the system is associated with the flow in the pump and throttle lines, and all the potential energy associated with the system transients is taken to arise from the expansion and compression of the fluid in the closed storage volume. The mass-spring-damper mechanical analogue of such a lumped parameter system is illustrated schematically in Fig. 5 where the essential components of the simple pumping system are shown. As is indicated, a key feature due to the pump is the ability to provide a negative damping (i.e., a net input of mechanical energy) to the system transients, as will be described shortly. Analyses of the stability of this type of system have been carried out by Emmons et al. [3], Taylor [4], Stenning [5], and others. Although there are differences between the various analyses, the general result that emerges is that the system will be (dynamically) unstable near the peak of the pressure rise/mass flow characteristic, at some slightly positively sloped operating point, and this is usually well before the simple static stability criterion is violated. The explicit criteria are derived in the Appendix, which presents stability analyses of the system shown in Fig. 1, as well as of several of the other types of pumping systems described in this review.

The physical mechanism for this dynamic instability is quite different from that responsible for the static instability and, as stated, can be regarded as due to a negative damping of the system perturbations. In addition, in the discussion of the static stability no mention was made of the mass storage capability of the closed volume in the system. This, however, is a key part of the dynamic instability, since the restoring force generated by the expansion and compression of the gas in this volume is critical to the (growing) oscillatory behavior associated with dynamic instability. To understand the basic mechanism, as well as the requirement of a positive slope for instability, consider the system undergoing oscillations about a mean operating point. Since the flow through the throttle is dissipative, there must be energy put into the system to maintain the oscillation (or to increase its amplitude in the case of instability). The only source of this energy is the pump. Therefore let us examine the mass flow and pressure rise perturbations through the pump. These are shown in Fig. 6 which presents the *perturbations* in mass flow ($\dot{m}$) and pressure rise (Δp) through the pump, plotted versus time over a period of one cycle (assuming that the pump responds *quasi-steadily* to fluctuations in mass flow). The product of the two, $\delta\dot{m} \times \delta\Delta p$, whose integral over a cycle is equal to the net *excess* (over the steady-state value) of the rate of production of mechanical energy is also shown.

In the case of a positive slope it is found that favorable conditions for net energy input occur, since high mass flow rate and high rate of mechanical energy addition (in the form of pressure rise) go together. As shown in the figure the product of the two is positive definite over the whole cycle. Thus the net amount of mechanical energy that the pump puts into the flow will be higher than if the system were in steady operation at the mean flow rate. In a similar fashion the net dissipation due to the throttle will also be higher than if the system were in steady operation. When the net energy input over a cycle balances the dissipation, a periodic oscillation can be maintained. This corresponds to the boundary between stability and instability. In the case of an operating point on the negatively sloped region, as shown in the right-hand side of the figure, the pump actually puts in less mechanical energy over a cycle than in steady operation (since high mass flow is associated with low energy input); the perturbations will therefore decay and the operating point will be stable. To summarize, dynamic instability for our simple system can occur when the mechanical energy input from the pump is greater than during a mean (steady) flow (i.e., when there is the required amount of negative damping), and this can only occur if the pump characteristic is positively sloped so that high mass flow and high mechanical energy input per unit mass flow go together.

We have so far discussed system stability with reference to a simple pumping system, and this has served to introduce ideas such as dynamic and static stability and system modelling concepts. We will use this as a framework for discussion of some of the more complex system instabilities. It will be seen that the above discussion is useful for providing insight into the transient behavior of a number of types of pumping systems. However, there are other situations in which the instabilities will be seen to arise from quite different causes,

and we will need to extend the ideas concerning the physical mechanisms that lead to instability.

It is to be emphasized that this review examines system excursions from a steady operating point which are *self-excited*, rather than the result of a response to an external forcing function. We will therefore not consider such topics as, for example, the large pressure amplifications which can occur in hydraulic systems due to periodic opening and closing of a valve, since these are really forced response (resonance) phenomena rather than instances of system instabilities. (A general reference for these types of phenomena is the book by Wylie and Streeter [6].) In addition, the various types of aeroelastic instabilities that are encountered in pumping systems (such as flutter in axial turbomachines, flow induced vibrations of liquid lines or of cylinders in crossflow, etc.) will not be discussed, nor will the self-excited lateral vibrations, such as rotor whirl, which can occur in rotating machines. Further the review will also not address the development of (mathematical) techniques for assessing the stability of a system at a given operating point once an adequate mathematical description of the system dynamics has been formulated. The different methods for doing this (using the Routh-Hurwitz Criterion, the Nyquist Stability Criterion, etc.) are very well covered in a number of texts (e.g. [7], [8], [9]) and our emphasis here will rather be on the fluid dynamic features that are important in the generation of the instability.[2]

The structure of the review is as follows. The different sections will be organized around the different types of pumping systems and their associated instabilities. Discussion will be given of the steady-state system performance, as a way to put in perspective the parameter regions in which instability is to be expected. The instabilities that occur in the specific systems will then be described, along with the kinds of analyses and relevant criteria used to predict them. In several instances the large amplitude system transients that occur subsequent to the onset of (linear) instability will also be examined since these can have important engineering consequences. The type of system to be discussed first will be the axial compression system with a single phase fluid, since this is a system which has been extensively studied and with which the author is most familiar. Centrifugal compressor and (non-cavitating) pump systems with single phase fluids will then be described, including instabilities associated with vaneless diffuser flows. Next we will examine the instabilities that arise in turbopumps because of the presence of cavitation. Self-excited pulsations in supersonic diffusers will also be briefly mentioned. Some attention will then be given to the various types of instabilities that are associated with two-phase flow in pumping systems. Low frequency combustion oscillations and instabilities in hydraulic systems will also be briefly surveyed. The last types of instability to be considered will be those that occur in compound pumping systems (pumps in parallel), with the oscillatory flow that occurs in branched diffusers being a simple case of this type. Although there is not space to give details of all of the different analyses that are discussed, quantitative stability criteria for several different simple pumping systems are derived in an appendix. In the review the emphasis is aimed at the physical mechanisms that are of import, the ability of present methods to predict the salient features of the phenomena of interest, and the problems that should be addressed in order to provide the fluids engineer with improved guidelines for designing stable flow systems.

II Axial Compressor Pumping Systems

As a first step in the discussion of more realistic systems, let us examine a configuration in which the simple model developed above is, in fact, quite useful. These are the pumping systems (compression systems) found in gas turbine engines. To be more specific, we consider an aircraft turbine engine consisting of a multistage axial compressor (or compressors) which discharges into a relatively large volume (the combustor) with the throttling provided by the downstream turbines. It is thus reasonably similar to the basic system of Fig. 1.

A. General Types of Instabilities Encountered in Axial Compression Systems. The performance map of a multistage compressor is customarily plotted as pressure ratio versus (corrected) mass flow at different (corrected) rotational speeds.[3] A typical "compressor map" of this sort is shown in Fig. 7, taken from [13]. Contours of adiabatic efficiency are also indicated. The steepness of the low pressure ratio portion of the constant speed lines is due to the effects of compressibility. The line at which the speedlines terminate is referred to as the stall line (or surge line) and marks the limit of stability of axisymmetric flow. To the left of this line large oscillations of the mass flow rate may occur (called *surge*) or severe self-induced circumferential flow distortions may rotate around the annulus (*rotating stall*) or a combination of both phenomena may appear.

Rotating stall induces large vibratory stresses in the blading of compressors and is therefore often unacceptable for structural reasons. In addition there can be a large drop in performance associated with this flow regime (efficiencies below twenty percent can be seen in the literature) [14], so that overall gas turbine engine cycles may not be self-sustained. In an engine the greatly decreased mass flow through the system can also cause turbine overtemperatures. Surge can be intolerable from the point of view of system operation and can also lead to high blade and casing stress levels [15]. Thus, no matter which type of instability appears when the stall line is crossed, the stall line generally represents a limit to the useful operation of the machine and is therefore to be avoided.

The position of the stall line is a matter of great concern to the designer, and considerable effort is frequently expended to ensure that there is sufficient margin between the stall line and the operating line. Even if this is done, there are still certain situations under which stall will occur, such as rotor speed transients, flow distortions, and nonsteady inlet and exit flow pulsations. Given this fact, the problem of *recovery* from a stall condition, i.e., recovery from the regime that results from an initial system instability, also becomes extremely important, especially in aircraft engine applications.

Because of this, there are really two technologically im-

[2] Note that when we use the term stability (or instability) in this review, it will generally refer to the behavior of a linearized system which is undergoing small amplitude transients about a given mean operating condition. As such, whether the system is stable or unstable is unambiguous (see the definitions given by Maxwell quoted above). However, in formulating a general approach to consideration of the behavior of nonlinear systems, it becomes useful to distinguish between relative degrees of stability. Discussion of this topic is also outside the scope of this lecture; however, readable introductions to it are given in [10] and [11]. This subject is also covered in many books on modern control theory.

[3] The corrected flow is defined as $\dot{m}\sqrt{\theta}/\delta$, where $\dot{m}$ is the actual mass flow, θ is the ratio of inlet total temperature to a reference temperature ($\theta = T_{\text{Tin}}/T_{\text{ref}}$), and δ is the ratio of inlet total pressure to a reference pressure ($\delta = P_{\text{Tin}}/P_{\text{ref}}$). For a specific machine compressing a given (perfect) gas this quantity is a function only of the inlet flow Mach number. The corrected speed is defined as $N/\sqrt{\theta}$, where N is the rotational speed, and can be regarded as a form of blade Mach number. Use of these parameters ensures that the results of tests are applicable to operation at levels of temperature and pressure different from the original test conditions. Discussion of the use of these parameters for representation of compressor performance is given in many texts on turbomachinery, for example that of Horlock [12].

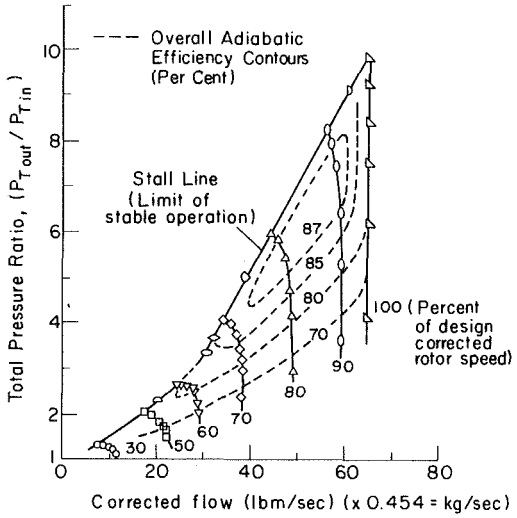

Fig. 7 Multistage axial compressor performance (eight stage compressor) [13]

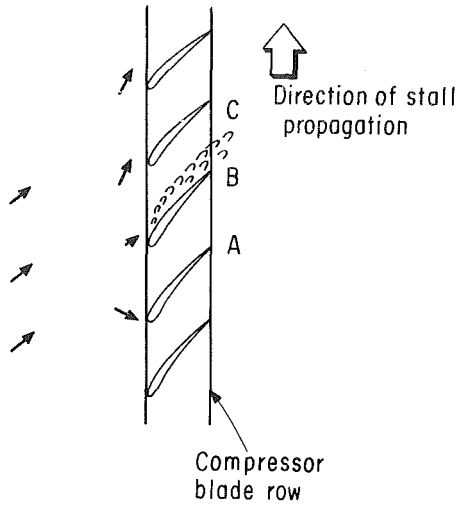

Fig. 8 Physical mechanism for inception of rotating stall [3]

portant aspects of axial compressor pumping system instability that must be addressed. These are: (1) examination of the basic fluid mechanics associated with the *onset* of the instabilities that lead to rotating stall and/or surge, and (2) behavior subsequent to the onset of the initial instability, including large amplitude system transients. In discussing these, the author has, of necessity, made use of parts of a recent review on the topic of axial compressor stall phenomena [16]; the reader is referred to that article for a more detailed exposition of points that are not covered here in depth.

The instabilities in the type of pumping system under consideration arise in general due to the presence of stall. Looked at from the point of view of the individual diffusing passages in the compressor, stall generally implies separation of the flow from one or more of the passage walls. However, compressor blade rows consist of many of these diffusing passages in parallel, so that phenomena can occur which do not happen with a single airfoil or diffusing passage. One of the most striking of these is rotating stall. This is a flow regime in which one or more "stall cells" propagate around the circumference of the compressor with a constant rotational speed, which is usually between twenty and seventy percent of the rotor speed. In the cells the blades are very severely stalled. Typically there is negligible net through-flow, with areas of local reverse flow, in these regions. The cells can range from covering only part of the span (either at the root or at the tip) and being only a few blades in angular width, to covering the full-span and extending over more than 180 degrees of the compressor annulus. It is this latter situation which most commonly occurs in multistage compressors at speeds near design and which is most serious. The part-span stall of the first stages of multistage compressors at low speed attracted a large amount of interest in earlier years, but this has generally much less severe consequences and is hence not of primary concern.

The basic explanation of the mechanism associated with the onset of stall propagation was first given by Emmons et al. [3] and can be summarized as follows. Consider a row of axial compressor blades operating at a high angle of attack, such as is shown in Fig. 8. Suppose that there is a non-uniformity in the inlet flow such that a locally higher angle of attack is produced on blade B which is enough to stall it. If this happens, the flow can separate from the suction surface of the blade so that a substantial flow blockage occurs in the channel between B and C. This blockage causes a diversion of the inlet flow away from blade B and towards C and A to occur (as shown by the arrows), resulting in an increased angle of attack on C and a reduced angle of attack on A. Since C was on the verge of stall before, it will now tend to stall, whereas the reduced angle of attack on A will inhibit its tendencies to stall. The stall will thus propagate along the blade row in the direction shown, and under suitable conditions it can grow to a fully developed cell covering half the flow annulus or more. In this fully developed regime, the flow at any local position is quite unsteady; however, the annulus averaged mass flow is steady, with the stall cells serving only to redistribute this flow.

The onset of rotating stall is thus associated with an instability which arises due to the stall of the compressor blade passages.[4] As far as the overall system is concerned, this can be regarded as a localized instability. However, there is also a more global *system* instability that can occur, which leads to surge. In contrast to the behavior during rotating stall, the annulus averaged mass flow and the system pressure rise during surge undergo large amplitude oscillations. The frequencies of these oscillations are generally at least an order of magnitude below those associated with passage of a rotating stall cell and depend on the parameters of the entire system. In addition, during the surge cycles the instantaneous mass flow through the compressor changes from values at which (in steady state operation) the compressor would be free from stall, to values at which one would find rotating stall or totally reversed flow. Because of the low frequency of the oscillations, the compressor can pass in and out of these flow regimes in an approximately quasi-steady manner.[5]

The two types of instability are indicated schematically in Fig. 9. A sketch of the transient signatures that would be given by typical high response instrumentation, such as a hot wire at the compressor inlet for the rotating stall situation and a pressure probe in the combustor (or other volume downstream of the compressor) for the surge cycles, are also indicated in the figure. Rough magnitudes of the time scales associated with the different phenomena in an aircraft gas turbine context are shown as well. It is to be emphasized that

[4] The point of stall can, however, be affected by other closely coupled components in the system as described below.

[5] In view of this behavior E. S. Taylor [17] has paraphrased P. T. Barnum to describe the distinction between surge and rotating stall respectively: "you can operate a compressor to stall all of the blades some of the time, or to stall some of the blades all of the time."

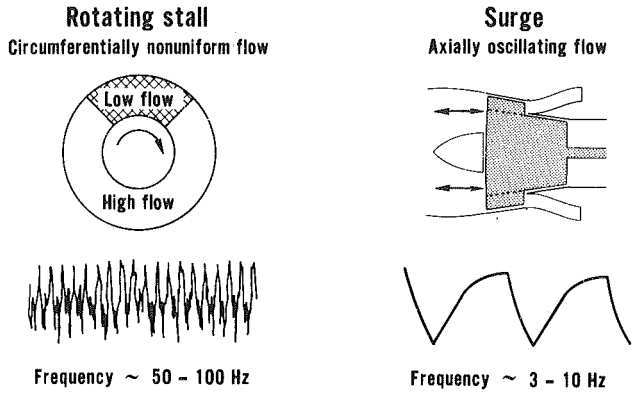

Fig. 9 Modes of system response due to stall

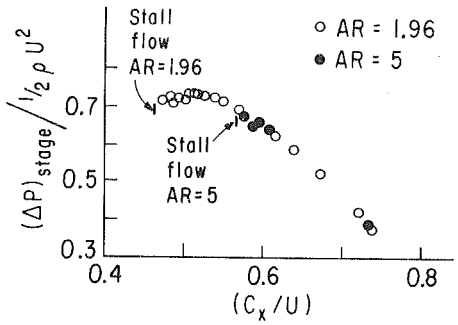

Fig. 10 Performance of high and low aspect ratio compressors (data of Smith [21])

although the illustration indicates the phenomena only in this particular context, these instabilities are inherent in pumping systems involving all types of turbomachines.

The two phenomena (surge and rotating stall) can be seen to be quite distinct. However, they are not unrelated, since often the occurrence of the local instability (associated with the onset of rotating stall) can trigger the more global type of system instability (leading to surge). It is therefore necessary to consider the possibility for *both* types of instability and develop methods for their prediction. We will examine the techniques for predicting rotating stall first.

B. Prediction of the Onset of Rotating Stall in Axial Compressors; Correlations for Stall Inception. As noted earlier, a key problem is the prediction of the point at which stall occurs. This problem has been attacked by many investigators at several quite different levels of approach. The most empirical are the correlations that have been developed for stall onset. The basic concept is to find a parameter (or parameters) which correlates the "stall point"[6] for a number of different blade geometries, compressor designs, etc. In a design procedure for a low hub-tip ratio fan, for example, the parameter could be applied at different span locations along the blading, using the local flow conditions generated by use of one of the many axisymmetric compressor flow field calculations, to see whether any section would be operating under too adverse a condition, while for a multistage compressor the parameter might be applied only on a meanline or averaged basis. Several of the early correlations of this sort are described by Horlock [12], but one of the well-known examples of this type of approach, which is still much in use, is the work of Leiblein [18]. He developed a parameter which he called the diffusion factor (or D-factor),[7] which was related to the adverse pressure gradient which the boundary layer on the suction surface of the airfoil was subjected to.

It was found that the total pressure loss correlates quite well with D, and, based on Leiblein's cascade results, one can see a rather sharp rise in loss occur as D is increased past a value of roughly 0.6. This can therefore be taken as a very *approximate* criterion for the onset of stall in a cascade (see also [19] for further work using this approach). Although much of the work done by Leiblein was based on two-dimensional cascades,the use of the D-factor has been carried over to axial as well as to centrifugal compressors (Rogers [20]). Features such as the differences between the flows in a cascade and the flows at the tips of axial compressor rotors, for example, are "recognized" by noting that different limiting values of the D-factor are used for the rotor tips than for other sections.

The correlations based on D-factor, as well as other improved correlations for the stall point, have been extensively investigated by the aircraft engine companies. Virtually all of this information, however, is held as proprietary and there is little in the open literature, particularly as regards multistage compressors and transonic fans. Several features that are significant, however, are that the "limiting" D-factor, or other loading parameter (i.e., the value at onset of stall), tends to increase as the aspect ratio and/or the nondimensional tip clearance[8] decreases. An example of the first of these trends, as presented by Smith [21], is given in Fig. 10, which shows non-dimensional stage pressure rise versus flow coefficient from two compressors with aspect ratios of 1.96 and 5. The two compressors each have four stages and the same nondimensional tip clearance.[8] It can be seen that the lower aspect ratio compressor has a higher pressure rise per stage at the stall point, and stalls at a lower flow rate. Similar results have been found by Fligg [22]. Effects of tip clearance are also illustrated in the above-mentioned paper by Smith, as well as in [23] and [24]. There are several other factors such as Reynolds number, tolerances and deterioration, etc., that can also have an effect on the stall point. These are also accounted for in practice by using correlations, and they will not be discussed here save for the remark that there can be a substantial loss in stall margin as the blade Reynolds number drops below *roughly* 100,000 [25].

Although the use of correlations such as D-factor may appear to be an overly simple approach, it is one that is at present in common usage for multistage axial compressors, since the more theoretical approaches have not yet led to the definition of the stall point with any additional precision. However, although it is important to mention these correlations, and to give several relevant references, the main emphasis in this review is on the fluid dynamics associated with the instability phenomena, and the correlative procedures do not really provide insight into this aspect. Therefore let us now consider analyses which are tied more closely to the flow instabilities occurring in the compressor. These can be divided into two types: linearized (small disturbance) stability analyses for predicting the *onset* of rotating stall, and nonlinear treatments which follow the growth of small perturbations to a fully developed, finite amplitude state.

C. Linearized Stability Analyses for Rotating Stall Onset. The first of the linearized stability analyses was by Emmons et al. [3], who investigated the conditions under

[6] Defined here as the condition at which the steady axisymmetric flow becomes unstable.

[7] The D-factor was defined by Leiblein as: $D = 1 - C_2/C_1 + \Delta C_\theta/2\sigma C_1$, where C_1 is the inlet relative velocity, C_2 is the exit relative velocity, ΔC_θ is the change in the circumferential velocity component, and σ is the solidity.

[8] Tip clearance/staggered spacing; "staggered spacing" = blade pitch × cos α_{CH} where α_{CH} is the stagger angle, measured from the axial direction.

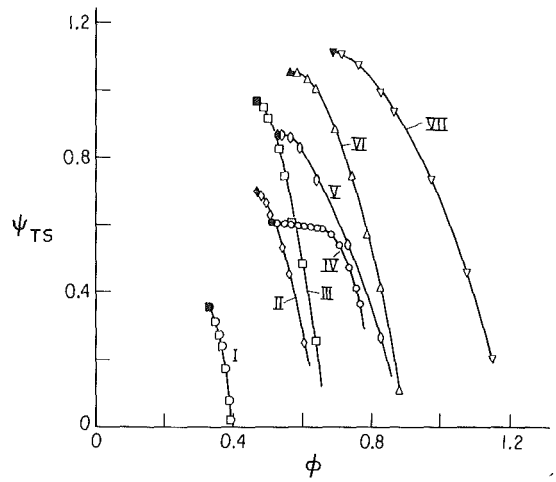

Fig. 11 Multistage compressor performance (low speed rigs): Curves I, II, V, VII from [31]; IV from [32]; VI from [33]; III from [34]

which a small amplitude, circumferentially nonuniform, two-dimensional flow perturbation in a cascade would grow. Since then there have been many extensions of this investigation, of which two recent examples are the papers by Nenni and Ludwig [26] and by Fabri [27]. An excellent summary of the earlier work is given by Emmons, Rockett, and Kronauer [28] and a comprehensive bibliography up to 1967 has been compiled by Fabri [29]. A useful overall introduction to the topic is given by Stenning [5].

In these analyses a small amplitude perturbation is superimposed on a given mean operating condition of the compressor or cascade. The linearized equations of motion are solved to yield the forms of the flow perturbations in regions upstream and downstream of the compressor blade row (cascade). The wavelength of the flow non-uniformities is taken to be much larger than the blade pitch (as is experimentally found to be the case) so that an actuator disk[9] model of the cascade can be used. Suitable matching conditions are then applied across the cascade to link the flow quantities upstream and downstream. In general the conditions used (for the two-dimensional case) have been continuity of mass across the cascade, an inlet/exit flow angle relation, and an inlet angle/total pressure loss relation, although some investigators have found it more convenient to work in terms of circulation and shed vorticity [26] rather than total pressure. From this procedure one can then determine the eigenvalues of the system of equations, which define the stability of the flow field, or one can examine the growth in time of an initially prescribed small perturbation (for times until the disturbances become too large for the linearized theory to apply).

These calculations yield results in terms of the critical *slope* of a function such as the mean compressor performance curve, or cascade loss curve, etc., at which the axisymmetric flow becomes unstable. However, these slopes are extremely difficult to obtain accurately, especially for the cases of greatest interest—multistage compressors or transonic fans. This is a major reason for the relatively little usage of these methods by designers. In other words, if one wishes to use one of the instability calculations as a predictive tool, one must be able to predict the *slopes* of the compressor constant speed characteristic at off-design conditions, and, at present, this cannot be done with an adequate degree of precision.

Putting aside this difficulty, however, there is still the question of how well existing stability criteria describe the onset of rotating stall. As an example let us consider one of the best known of the (two-dimensional) criteria, due initially to Dunham [30], which states that rotating stall inception will occur at the peak (zero slope point) of the exit static pressure minus inlet total pressure compressor characteristic. This criterion, which has also been derived by other investigators, has been applied with some success and does appear to furnish a rough "rule of thumb." However, counter examples in which it does not hold can also readily be found. An illustration of this, Fig. 11, shows data from a sample of low-speed multistage compressors.[10] In this figure the horizontal axis is axial velocity parameter, ϕ, $[=(C_x/U)]$ and the vertical axis is non-dimensional pressure rise,

$$\psi_{TS}\left(=\frac{[P_{\text{exit}}-P_{T_{\text{inlet}}}]}{\rho U^2}\right),^{11}$$

Curves V, VI, and VII do appear to show approximately zero slope (within the accuracy of the data), but curves I-IV have a negative (i.e., stable) slope right up to the stall points. This situation, where there does not appear to be a zero slope region of the compressor characteristic, is even more apparent in high-speed multistage compressor data. (The author has not seen any multistage data in which the converse is true—i.e., in which operation significantly on the positive slope part of the characteristic is found.)

Having said this, however, it should be emphasized that in the opinion of this author these types of stability calculations can still be useful. This is true on several counts, not the least of which is that they provide an overall physical understanding of the breakdown of the axisymmetric flow in axial pumps or compressors. Also, an important advantage of the stability analyses is that they can be used to show effects that correlations would not predict. One of these is the coupling, or interaction, between blade rows, between different compressor spools, or between a compressor and components downstream in the compression system. Such coupling is much stronger with asymmetric flows than in the axisymmetric situation. This feature, which is central to the understanding of non-axisymmetric flows in compressors, occurs because of the much larger length scales of the flow non-uniformities than in the axisymmetric situation. Specifically, it is the "single lobed" (i.e., one per circumference) flow perturbation which appears to be of most practical interest in multistage compressors. For disturbances of this type the relevant length over which adjoining rows can be considered to interact is on the order of the radius of the machine. Thus, adjacent blade rows, or even the two spools of a gas turbine engine, can be considered to be closely coupled as far as circumferentially nonuniform flow is concerned, and, as emphasized by Dunham, it is not correct to analyze the stability of one row in a compressor without considering the influence of the other rows. This coupling can be taken into account by the stability analyses and although, as stated, they may not be quantitatively precise, they can still give valuable guidance as to when row-row, spool-spool, etc. interactions will be important (see section H, below).

D. Nonlinear Investigations of Rotating Stall Inception and Growth. Although the linearized analyses have in the past

[9] Defined as a representation of a blade row as a plane across which the mass flow is continuous but the total pressure, circumferential velocity, pressure, etc. can be discontinuous.

[10] Three-stage compressors: I, II, V, VII [31]; IV [32]; VI [33]; Four-stage compressor: III [34].

[11] These are appropriate parameters for representation of compressor (or pump) performance in regimes in which compressibility is not important. This can be seen directly from dimensional analysis, or it can be shown formally that the more general representation of pressure ratio as a function of corrected flow and corrected speed will reduce to the ψ versus ϕ representation when the influence of compressibility can be neglected.

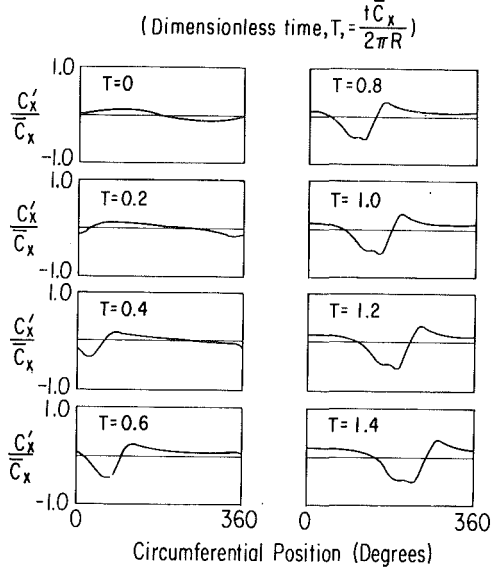

Fig. 12 Growth of small disturbance (dimensionless time, $T = t\bar{C}_x/2\pi R$) [35]

been used to try to predict some of the features of fully developed rotating stall, it has become clear that in this flow regime the stall cells are definitely not small perturbations and linear analysis is inapplicable. Thus this type of investigation is only useful for the problem of stall inception, and to follow the subsequent development of the rotating stall, one must use a nonlinear model. This has been done by Takata and Nagano [35], as well as by Orner [36]. (It should also be mentioned that extension of these calculation procedures to the case of circumferentially distorted inlet flow has been carried out by Adamczyk [37] and Pandolfi and Colasurdo [38].) These models use time marching techniques to determine whether a small disturbance will grow or decay by calculating the development of the flow to some eventual steady-state solution. This could consist of a flow with a large amplitude disturbance propagating around the compressor, which is taken to be indicative of compressor operation in rotating stall.

An example of the results of this type of calculation for an isolated rotor is given in Figure 12 taken from Takata [35]. The figures show the normalized axial velocity nonuniformity $C_x'/\bar{C}_x$ versus circumferential position at different non-dimensional times, T, = (time • $\bar{C}_x$)/$2\pi R$. It can be seen that the initial sinusoidal perturbation grows into a large amplitude disturbance which propagates round the circumference.

Calculations of this type can show some of the features of rotating stall such as the hysteresis in the stall/unstall process. Other aspects, however, do not appear to be modeled very well, and a general comment on these nonlinear models is that, in spite of their complexity, many of the central features of the fully developed stalled flow may not yet be represented. For example, the present calculation procedures are either two-dimensional, assume that the flow occurs along axisymmetric stream surfaces so that flows perpendicular to these surfaces are supposed zero, or only include three-dimensionality in a potential flow representation. Experiments, however, indicate that strong radial flows can in fact occur. In addition the models of unsteady blade row performance that are used are quite rudimentary. They are essentially one-dimensional and rely heavily on extrapolation of the loss and turning characteristics (to the negative flow regime according to experimental measurements). Further, the calculations are carried out with a constant mass flow, whereas in the actual situation the mass flow will change (along a throttle line) as the flow develops from unstalled to fully developed rotating stall. In addition, the steepness of the downstream throttle characteristics can have a significant effect [39]. In view of the path dependent behavior shown by some features of rotating stall (i.e., the hysteresis) it may be that these latter aspects should also be taken into account.

Because of the above, the author feels that while it is useful to pursue calculations of this type, they should be closely compared with available experimental data to assess the effects of the assumptions. For example, one result of these calculations which is not satisfactorily explained is that for an isolated rotor the number of cells that appears from the calculation is equal to the number of lobes in the initial perturbation, whereas tests with isolated rotors have shown that the number of cells is rather a function of the overall mass flow through the stage [40].

E. Overall Compression System Instability. We have so far discussed the prediction procedures for the inception of rotating stall in a compressor with a uniform inlet flow, and we can now turn to an examination of the criteria for the onset of the more global type of instability leading to surge. This is a system phenomenon and one in which, in contrast to rotating stall, the compressor appears to participate in an essentially one-dimensional manner. Although the calculation of this system stability point can readily be carried out using analyses of the type described in the introduction, once again we encounter a situation where the critical parameters are the slopes of the steady-state (uniform flow) compressor speed lines at the stall point, and, as stated, there is difficulty in predicting these.

It is useful, at this point, to again mention the relation between the two types of instability. The global (system) instability is a basically one-dimensional phenomenon, involving an overall, annulus averaged (in some sense) compressor performance curve. For typical volumes, lengths, and throttle characteristics this must generally be slightly positively sloped for system instability to occur. We have also seen that the axisymmetric flow through a compressor can be unstable to two- or three-dimensional infinitesimal disturbances and that this local instability marks the inception of rotating stall. However, the onset of this rotating stall is very often associated with a precipitous drop in the overall ("one-dimensional") pressure rise mass flow curve of compressor performance. In other words, the inception of rotating stall can lead to a situation where the instantaneous compressor operating point is on a steeply positively sloped part of the characteristic, with a consequent violation of the dynamic and/or the static instability criteria. In this sense, the onset of the local compressor instability can trigger the more global compression system instability.

F. Multi-element Stability Models. Up to now the discussion of compression system stability has been based on viewing the compressor as a single element. However, under some circumstances this can be too simple, since there can be differences between the mass flow perturbations at the front of the compressor and those at the rear, due to compressibility. Thus, different investigators have extended the overall lumped parameter analysis and modeled the compressor with a stage by stage (or even row by row) method, using separate volumes and actuator disks for each stage. Mass, momentum, and energy balances are written for each of the stages. Examples of such investigations are references [41]-[45], and a discussion and comparison of some of the basic models can be found in [42].

The determination of the instability point for these models can be found either by solving for the eigenvalues or by (digital) simulation of the system transients. In addition these models can explore the effects of pulsations that are imposed

on the compression system. However, as with the simpler models, "the compressor stability boundary is strongly influenced by the stage characteristics. The overall results are thus dependent on the accuracy of the stage characteristics. . ." [45]. Hence the ability to predict the *slopes* of the steady-state (uniform-flow) compressor speed lines *at the stall point* is a key item in the successful use of these techniques.

G. Inlet Distortion Effects on Compressor Stability. In the above discussion we have regarded the stall point of the turbomachine as being essentially set by the geometrical parameters of the machine. However, in practice there are other factors that can significantly affect the point at which the onset of instability occurs. One of the most important of these is inlet distortion, which is a term used to describe a situation in which substantial total pressure, velocity, and/or flow angle variations exist at the compressor inlet face. Aircraft gas turbine engines are particularly prone to inlet distortion problems due to changes in aircraft attitude and the effect of the airframe on the inlet flow conditions. However, industrial installations can also suffer from inlet distortion in cases where poorly designed bends have been installed upstream of the compressor. In these situations, some portion of the blading is likely to be operating under more unfavorable conditions than would occur with a uniform flow at the same mass flow rate, leading to a decrease in the useful range of operation of the machine.

An illustration of the effect of inlet distortion on compressor stability and performance is given in Fig. 13, which shows data from a nine-stage axial flow compressor [46]. The horizontal axis shows corrected mass flow, and the vertical axis is the total pressure ratio. The dashed lines indicate the measured performance with a uniform inlet, while the solid curves give the measured performance with a circumferential distortion, i.e., a circumferentially nonuniform inlet flow. It can be seen that there is a substantial degradation in performance and, far more importantly, a large drop in the position of the stall line (the stability boundary) due to the distortion. While the consequence may not be this severe with all compressors, there is generally a reduction in the stability of the compression system associated with the presence of an inlet distortion.

Because of the widespread occurrence of inlet distortions, and their adverse effects on system stability, there has been a large amount of work on the problem of predicting compressor response to flow distortion. These again range from correlations to more basic analyses. The review mentioned previously ([16]) has discussed these in some detail, and we will therefore only summarize some of the main conclusions. Although a detailed bibliography is given in [16], several useful references on this topic are [47]-[52].

Perhaps the most important point that emerges from these investigations is that there is a strong interaction between the compressor and the distorted flow field. Put another way, the compressor does not passively accept the distortion, but plays an active role in determining the velocity distribution that will occur at the compressor face, which is what the individual compressor airfoils actually respond to.

In the investigations that have been carried out on the effect of inlet distortions, the flow non-uniformities are commonly divided into radially varying steady-state, circumferentially varying steady-state, and unsteady distortions. In reality the distortions encountered are combinations of two or possibly all three of these types, but significant progress has been made using the above simplifications since, in many situations, the principal loss in stall margin can be regarded as due to one of the three. For example, during changes of aircraft attitude the inlet distortion may vary significantly with time over a time scale of the order of tenths of seconds or longer, which is

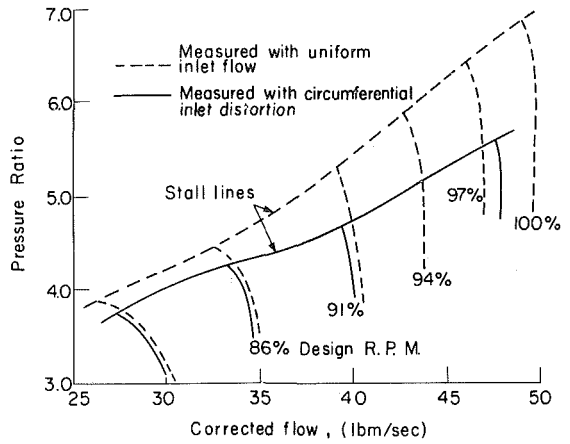

Fig. 13 Effect of inlet distortion on axial compressor stability (nine-stage compressor) [46]

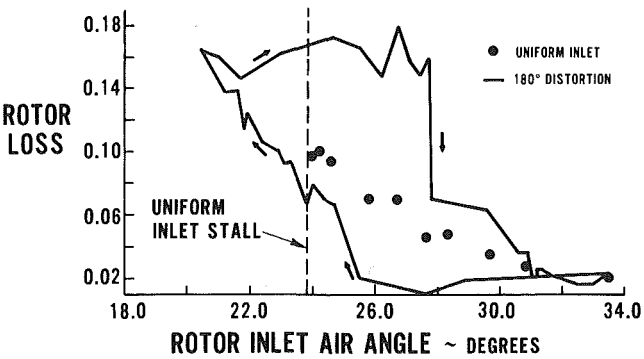

Fig. 14 Unsteady rotor response [52]

many times longer than the time for a fluid particle to move through the compressor. These distortions can therefore be considered as if they were steady.

For transient distortions, or for a steady circumferentially nonuniform flow (which the moving compressor rotor sees as an unsteady flow) the effect of unsteady blade row response is to mitigate the degradation of stall point by the distortion. This effect increases as the reduced frequency (based on blade length, through-flow velocity, and a frequency which characterizes the time scale of the distortion) increases. Hence, for the circumferential distortions, it is the distortions with low harmonic content, i.e., a small number of "lobes" around the circumference that are most serious. In addition, in connection with the unsteady effects, it is found that the local transient performance of a blade row can be considerably different than the quasi-steady situation, especially near the stall point. As one example of this, Fig. 14 shows the (relative) total pressure loss coefficient for a rotor operating in a 180 degree distortion [52]. The horizontal axis is the relative inlet air angle (measured from the tangential direction, so that decreasing inlet angle means increasing angle of attack on the blades) and the vertical axis is the rotor total pressure loss coefficient. It can be seen that the loss coefficient exhibits an unsteady "loop" as a function of inlet angle as the rotor moves through the distortion. The values obtained in a uniform flow test of the rotor are also shown, and it can be seen that there are substantial differences between the steady and unsteady performance.

A further very important point illustrated in this figure is that with distortion the rotor is operating transiently at flow angles below those associated with the uniform flow stall

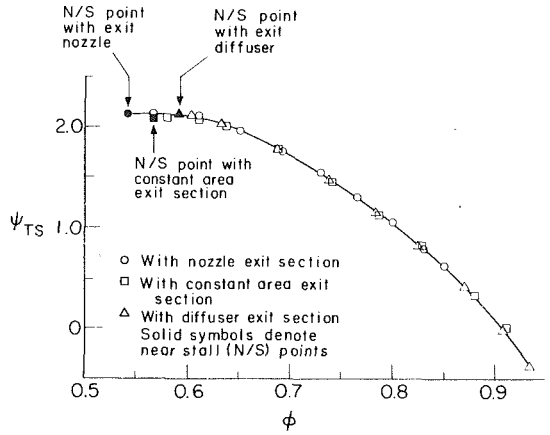

Fig. 15 Effect of exit conditions on compressor stability boundary [54]

point. That is, excursions to higher angles of attack (i.e., lower flow rates) than could be tolerated with a uniform flow can be tolerated locally (transiently) in the distorted case. Thus the unsteady response is an important feature to include in developing predictive methods for circumferential inlet distortion.

Another conclusion is related to the relevant length scale over which two compression system components interact in the presence of inlet distortion. This length scale is basically set by the wavelength of the flow non-uniformity. For example, for the one-lobed type of pattern with a strong first Fourier component, the axial length needed before two components can be considered not to interact is roughly a diameter. Gas turbine engine components are generally spaced much closer than this. Hence, for the type of flow non-uniformities that have the greatest effect on stability, the compressor must be viewed as closely coupled to downstream components, and the distorted flow performance of the compressor can thus be quite dependent on the downstream component.

H. Effect of Downstream Components on Compressor Stability. The above discussion of the coupling between a compressor and a downstream component furnishes a useful introduction to another aspect of the onset of instability in pumping systems. We have said that the response of a compressor to a circumferentially nonuniform flow can be altered by the presence of a downstream component in the system. However, consider the stability boundary for nominally *uniform inlet flow* conditions, i.e., the inception point of rotating stall. This occurs when conditions are such that a *circumferentially nonuniform* flow perturbation in the compressor annulus can grow. Based on the previous paragraphs, it might be expected that this point could be affected by components downstream of the compressor, since the downstream boundary condition on the flow perturbation is altered. The extent of any change in stability boundary is of course dependent not only on the nature of the downstream component, but on the circumferential length scale of the flow perturbation, since this determines how close the coupling is between compressor and downstream component [53]. However, for many situations of practical interest the predominant mode of instability occurs with a one-lobed type of disturbance, so that the relevant axial distance within which there can be a strong interaction is on the order of the machine diameter. This generally means that in terms of the stability boundary the compressor is *not* isolated from the influence of downstream components. More detailed analytical and experimental studies of this phenomenon bear out this general conclusion. The analysis predicts that, relative to the situation with a constant area exit annulus, an exit (annular) diffuser should be destabilizing (i.e., the onset of rotating stall should occur at a higher flow rate), whereas an exit (annular) nozzle should be stabilizing (rotating stall onset occurring at a lower flow rate) [54]. The theory predicts the slopes of the compressor pumping curve at which instability will occur and these are difficult to measure precisely; however, the experiments bear out the predicted trends. As an example, Fig. 15 shows data from a three-stage compressor run with three different downstream components. The tests were carried out with a uniform inlet flow. The stability limits are marked for the three conditions. It can be seen that even with these relatively passive devices a shift in the stall point of roughly ten percent in flow occurs. It should be noted that the diffuser used was of quite conservative design so that no diffuser stall occurred, and that the diffuser and nozzle were spaced more than a passage height downstream of the compressor so that (as can be seen from basic flow scaling arguments) no upstream influence of an *axisymmetric* sort would occur. This type of interaction between the pumping element and downstream components can be even more strongly manifested in centrifugal compressors, as will be discussed below. In these situations the diffusers (vaned or vaneless) can be not only the cause of premature compressor stall, but can *themselves* exhibit rotating stall, as will be discussed in subsequent sections.

This stabilizing effect of a downstream component on rotating stall inception has also been noted in a test of a flow configuration designed to simulate a movable door in the outer casing of the fan duct of a turbofan engine [55]. The actual geometry employed resulted in essentially coupling an axisymmetric nozzle close i.e., downstream of the outer portion of a fan rotor. The rotor had previously exhibited rotating stall without this downstream flow modification. However, with the "door" in place, the inception of rotating stall was suppressed down to the lowest flow that could be achieved with the facility; this occurred at a flow roughly one-half the flow at the previously observed stall limit. Measurements indicated that at these lower flows there was an axisymmetric type of recirculating flow near the rotor tip. (There was also a significant efficiency penalty associated with the presence of the downstream door.)

I. Stability Enhancement With "Casing Treatment." We have described some of the various types of instability, commented on the criteria for determining their onset, and discussed the adverse effects on stall of inlet distortion on stall inception. However, another area which is of interest concerns techniques for enhancing the stability margin of a turbomachine. The most obvious of these is to achieve the needed stability margin by matching the compression system below its peak efficiency point (in effect setting the match point so that the compressor blading has incidences and pressure rises far below the maximum). Although this provides an increase in airfoil incidence range between the operating line and the stability limit, it would lead to decreased efficiency on the (down-rated) operating line, and this is generally unacceptable.

One of the solutions to this problem that has been applied is the use of so-called "rotor casing treatment" to improve the stability of compressors. This casing treatment consists of grooves or perforations, over the tips of the rotors in an axial compressor, or located on the (outer) shroud in a centrifugal machine. Numerous investigations of these types of configuration have been carried out under widely varying flow conditions, and these have demonstrated that the range of usefulness of these casing configurations extends from compressor operation in basically incompressible flow (relative Mach numbers of roughly 0.15) to the supersonic flow regime (relative Mach numbers of 1.5) ([56]-[60] and see

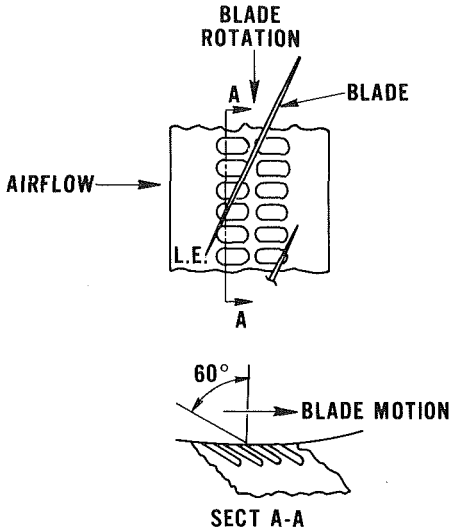

Fig. 16 Axial skewed groove casing treatment [51]

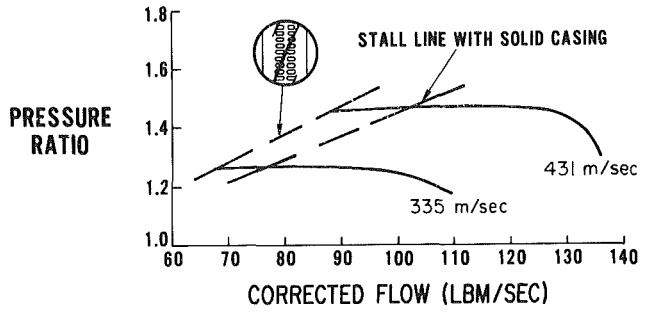

Fig. 17 Axial compressor stall margin increase due to casing treatment [51]

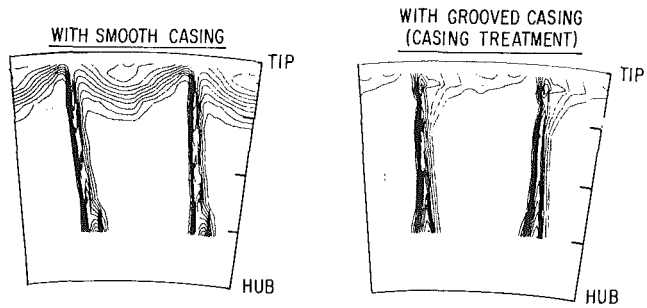

Fig. 18 Rotor exit total pressure loss contours near stall [61]

[16] for additional references and discussion of this topic). A sketch of one of the more successful of these casing configurations is shown in Fig. 16. These grooves are known as axial skewed grooves. A typical improvement in stall line brought about by use of these grooves is shown in Fig. 17 for a transonic axial fan. It is to be noted that far larger improvements have been seen, and that casing treatment has also been used to inhibit instability in centrifugal compressors, as will be discussed in a subsequent section.

Although the basic mechanism of operation of the casing treatment has not yet been fully elucidated, some important points have emerged. If we refer back to the description of the onset of rotating stall, it is apparent that for this type of instability to occur, the blade passages must be operating at a condition such that they have the capacity to generate large blockages for small changes in inlet condition. What is found, however, is that the level of blockage in the rotor passages is greatly decreased due to the presence of these grooves. As an example of this, Fig. 18 shows data taken just downstream of an axial compressor rotor [61]. The measured quantity is the nondimensional relative frame total pressure loss across the rotor, i.e., the total pressure loss measured (by a probe rotating with the rotor) in a coordinate system fixed to the rotating blades. Data are shown for both solid wall and casing treatment, at a mass flow rate near the stall limit of the solid wall configuration. In this instance the onset of rotating stall was associated with a large blockage created near the end wall of the blade passage. The contours are increments of 0.05 in relative total pressure loss across the rotor divided by inlet dynamic pressure. It can be seen that with the casing treatment there is a much smaller region of low total pressure fluid and hence a greatly decreased blockage in the blade passage. Thus one would expect that the tendency towards rotating stall would also be greatly suppressed, and the stable flow range of the machine extended, with the grooved casing. This indeed was the case, as can be seen in [61], where it is shown that a substantial increase in stability margin has been achieved.

Casing treatment is a potent remedy in increasing stall range. However, it is *not* a panacea, since there is generally some penalty in efficiency for those treatments which have the most success in improving stall range. Thus, it is important to understand the basic principles of its operation if one wishes to optimize the treatment in a rational manner.

J. System Transients Subsequent to Instability Initiation. We have, until this point, been concerned primarily with the phenomena associated with the onset of instability. As mentioned previously, another very important problem is associated with the behavior subsequent to the onset of instability. As was illustrated in Fig. 9, there are two modes of system behavior that can result—surge and rotating stall. The former consists of large amplitude oscillations in pressure rise and flow during which the compressor undergoes periodic excursion from a stalled to an unstalled condition. Operation in rotating stall is characterized by a situation in which, after an initial transient, the overall (annulus averaged) mass flow and pressure ratio are steady and can be greatly reduced from the values that existed prior to the onset of instability.

For an aircraft gas turbine engine, a key requirement is recovery from stalled conditions once instability occurs. In this connection, therefore, it is important to note that even though surge may be associated with severe transient stresses due to the large amplitude flow variations, the engine does operate in an unstalled condition over part of the surge cycle. Because of this, one is able to open bleed valves or make other changes that will have an effect on bringing the system out of surge. In contrast to this, rotating stall, and in particular the full-span, large extent, rotating stall which is characteristic of a multistage compressor, can be very difficult to recover from, as will be discussed in detail below. Therefore, it is the surge mode that is much more favorable for recovery in systems such as aircraft gas turbine engines and is hence the more desirable one. On the other hand, for an industrial centrifugal compressor or pump, it may be that operation in rotating stall can be tolerated, and that throttle movement is wide enough so that recovery is readily achieved. In this situation it may be that the often violent oscillations that occur during surge make this the less desirable of the two modes.

Whatever the situation, however, it is apparent that an important question is whether a given pumping system will exhibit large amplitude oscillations of mass flow and pressure ratio (surge), or whether the system will operate in rotating stall where the annulus average mass flow and pressure ratio

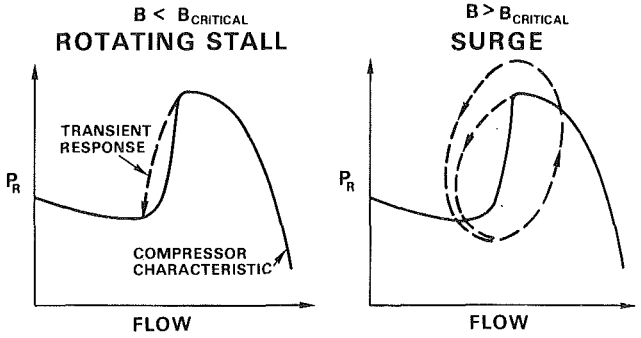

Fig. 19 Transient system response subsequent to initial instability

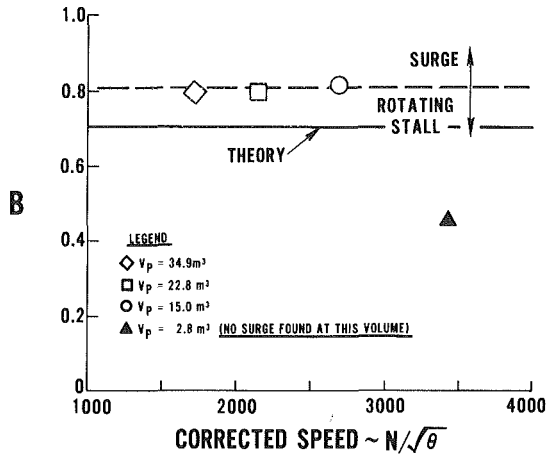

Fig. 20 Surge/rotating stall boundary for different plenum volumes [32]

are essentially steady, but are greatly reduced from the pre-stall values.

To answer this, one must analyze the nonlinear system behavior. This was done by Greitzer [62] using the Helmholtz resonator type of compression system model introduced by Emmons [3] (for the linear case). The analysis shows that for a given compression system, i.e., *specified compressor characteristic*, plenum volume, compressor length, etc., there is an important non-dimensional parameter on which the system response depends. This parameter is denoted as B:

$$B = \frac{U}{2\omega L_c}$$

where ω is the Helmholtz resonator frequency of the system, L_c is an "effective length" of the compressor duct, and U is the rotor speed. If we insert the definition of ω we can define B in terms of geometric and physical system parameters as

$$B = \frac{U}{2a}\sqrt{\frac{V}{A_c L_c}}$$

where a is the speed of sound, A_c is the compressor flow-through area and V is the plenum volume.[12] For a given compressor characteristic there is a critical value of B which determines whether the mode of instability will be surge or rotating stall. Thus if we examine the system transient response as represented on a compressor map format (pressure rise versus flow) we find the following situation, as indicated in Fig. 19. The steady-state pumping characteristic is shown for reference. Systems with B above the critical value, as shown on the right (e.g. speeds above a critical value) will exhibit surge oscillations, while those having B lower than the critical (speeds below the critical value) will undergo an initial transient to the (annulus averaged) steady flow and pressure rise associated with operation in rotating stall.

Experimental evaluation of this concept is shown in Fig. 20, in which data is presented for a three-stage compressor that was run with several different downstream volumes [32]. The horizontal axis is corrected speed and the vertical axis is the B parameter. The open symbols mark the experimental values of B at which the changeover from rotating stall to surge occurred for the different volumes tested. (The solid point indicates the highest value of B that could be obtained with the smallest volume used.) The regions in which one encounters surge (B above the critical value) or rotating stall (B below critical) as the mode of instability are also indicated. It can be seen that the prediction of a constant B as the boundary between surge and rotating stall is well borne out, although the value at which the change occurs is somewhat above that predicted by the theory. (It should again be emphasized that the value of 0.8 is for this particular compressor.)

Although it is necessary to carry out the calculations for any specific case, some motivation for this general result may be gained by the following qualitative physical arguments. Notice that we can write B as

$$B = \frac{(\rho U^2/2)A_c}{\rho U \omega L_c A_c}.$$

For a given compressor, the numerator, which is proportioned to the magnitude of the pressure difference across the duct ($P_{\text{plenum}} - P_{\text{atmospheric}}$), represents the driving force for the acceleration of the fluid in the duct. If we consider oscillations that are essentially sinusoidal in character, the order of magnitude of the inertial forces that arise because of these local fluid accelerations will be given by the product of the fluid density, ρ, the frequency of the oscillations, ω, the amplitude of the axial velocity fluctuation, and the volume of the fluid in the duct, $L_c A_c$. Hence, if we assume that the axial velocity fluctuation is a specified fraction of the mean wheel speed, the magnitude of these inertial forces will be proportional to the denominator. The ratio of the two forces (pressure to inertial) is therefore proportional to B. Thus as B is increased, for example by increasing the rotor speed, a fixed percent amplitude of the compressor axial velocity oscillations will result in inertial forces that are relatively smaller and smaller compared to the driving force due to the pressure differential. The capability to accelerate the fluid in the duct is thus increased as B increases. Hence, as B becomes larger one would expect greater excursions in axial velocity and thus a general trend towards surge rather than rotating stall, and this is in accord with the experimental results.

The B parameter is useful not only in defining the boundary between surge and rotating stall, but also as a guide to the scaling of the overall transient behavior of a compression system. In other words, for the same value of B, a compression system should exhibit the same transient behavior regardless of whether this value has been obtained using a large volume and a low speed or a small volume and a high speed. Figure 21 shows a comparison of the measured transient response for two systems at approximately the same value of B, one with a large volume and low speed and one with a small volume and high speed, with the value of B high enough such that surge occurred [32]. The figures show the instantaneous annulus averaged axial flow parameter (C_x/U) versus nondimensional system pressure rise, i.e., the instantaneous system operating point. As described in [32] the instantaneous mass flow was obtained using a continuity

[12] For the system of Fig. 1, V should be the volume of the compressible gas in the closed volume.

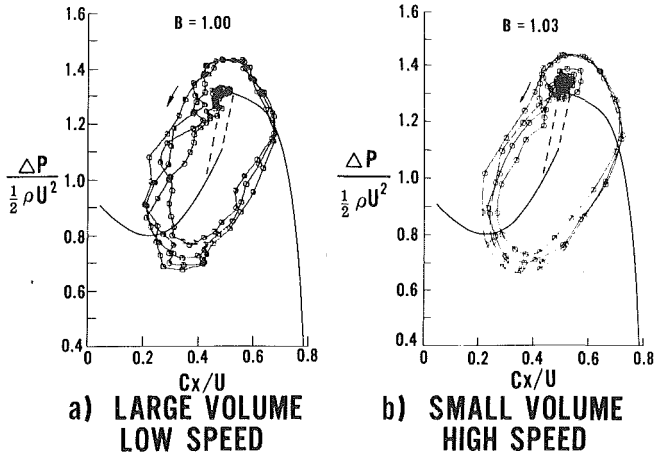

Fig. 21 Dependence of system response on B [32]

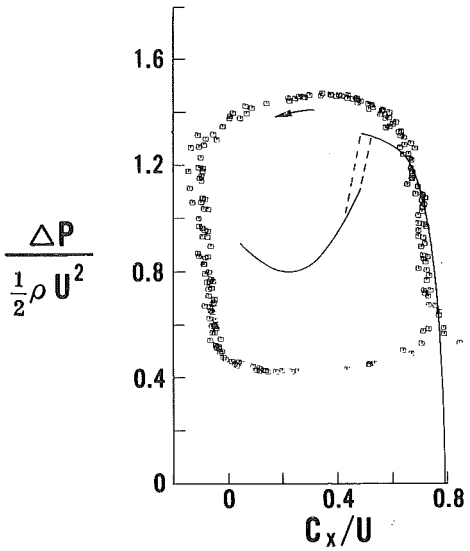

Fig. 22 Relaxation type of surge cycle oscillation showing reverse flow through compressor [32]

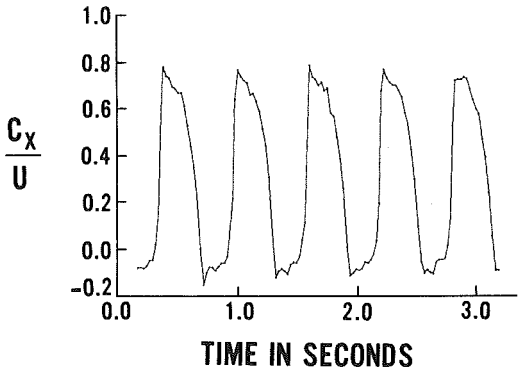

Fig. 23 Oscillations of compressor axial velocity parameter during surge cycles [32]

balance; reasons for doing this and difficulties of alternative ways of measuring this quantity are also discussed. The steady-state compressor curves are also shown for reference. As can be seen, the two surge cycles show extremely similar behavior, emphasizing the influence of B as the relevant nondimensional parameter for the phenomena under study.

The surge cycles of Fig. 21 do not show periods of overall flow reversal. However, with high pressure ratio multistage compressors, surge cycles having periods of reversed flow are, in fact, the more common situation. In addition, although the mass flow and pressure rise oscillations associated with surge cycles of the type shown in Fig. 21 are relatively sinusoidal (as a function of time), the variations in mass flow and pressure rise that occur in compressors of high pressure ratio are quite non-sinusoidal and are more nearly a relaxation type of oscillation. The two types of oscillation were referred to as classic surge and deep surge, respectively, in [32], where it was shown that this deep surge mode could also be seen with a low speed compressor as one reduced the throttle area somewhat from that value associated with the initial instability. Since this deep surge behavior, which includes overall reversed flow periods, is the type that is often encountered in practical situations with multistage axial compressors, it is useful to spend some time discussing it.

An illustration of the form of this type of oscillation is presented in Figs. 22 and 23, which show data taken during deep surge of a compressor. Note that these two figures show several seconds of data from the middle of a record of approximately one half minute of surging at this operating point, so that the surge cycle is basically a steady-state event, and there is thus no initial transient indicated in the figures. Figure 22 gives a plot of the same variables as in Fig. 21, i.e., the abcissa is the axial velocity parameter, C_x/U, (essentially nondimensional compressor mass flow) and the ordinate is the nondimensional pressure rise. For reference the measured steady-state compressor characteristic is again indicated by the solid line. It can be seen that there is a substantial portion of the cycle during which the overall flow is reversed and that the general form of the cycle is roughly "square" with two sections of approximately constant pressure and two of roughly constant flow.

The time history of the axial velocity parameter is shown in Fig. 23. For this type of oscillation, most of the time during the surge cycle can be seen to be taken up in either emptying the downstream volume (this is the period at small reversed flow) or in filling it (the period at the high values of compressor mass flow). Between these two relatively long time periods there are quite rapid increases or decreases in compressor mass flow. There are thus two widely different time scales that characterize the oscillation. The first is that associated with the emptying or filling, and is basically set by a balance between the system resistances (the compressor and throttle characteristics) and capacitances (the mass storage capability of the plenum). During this period changes in mass flow are small and effects associated with system inertances are not important. In addition, since there is a significant mass flow through the throttle, the filling period is generally somewhat longer than the emptying period. The second time scale is that which characterizes the rapid changes in mass flow that occur between the emptying and filling portions of the cycle. The magnitude of this much shorter time scale is dependent on the system inertances, which become important during this part of the cycle. This type of strongly nonlinear oscillation thus falls into the category of a relaxation oscillation, as described for example in [63]. Calculations showing this type of behavior for a compression system are presented in [62]. Further examples can be seen in the subsequent sections of this review.

We have said that the question of whether surge or rotating stall will occur is not only dependent on B, but upon the compressor characteristic. A basic attempt to take into account one aspect of this, the number of stages (N), leads to the use of NB as the relevant parameter for scaling rather than B. The motivation for this is that for N identical stages and a given value of B the pressure rise will be approximately

proportional to N, so that the ratio of pressure to inertia forces will increase as the number of stages. There is thus a strong trend toward lower values of B needed to encounter surge, rather than rotating stall, as the number of stages and overall pressure rise of the machine is increased.

We have described the necessity for certain system parameters to be of a specified magnitude in order to encounter surge. A further aspect of the problem concerns the physical mechanism for maintaining the surge cycles. These are large amplitude, nonlinear limit cycle phenomena; however, the overall mechanism is similar to that described in the introduction when the concept of dynamic stability was discussed. This is an increased mechanical energy input from the compressor during the cycles compared to during a mean steady flow (which results from a positively sloped compressor characteristic), although it should be emphasized that it is not just a local value of the slope that matters, but rather the instantaneous values over a finite range of flows.

We have mentioned that surge frequencies are commonly an order of magnitude or more lower than those associated with the passage of a rotating stall cell. In this context we can also note that, for a given compressor, the rotating stall frequencies (i.e., the speed or propagation of the rotating stall cell) will be proportional to rotor speed and independent of the system parameters. In contrast the surge frequencies are set by the overall system dynamics and do not scale with rotor speed. However, changes in surge frequency with speed can result from changes in either the shape of the compressor characteristic or changes in the system response as B (which is proportional to speed) is varied. As an example, [62] gives an illustration of the calculated large alteration in the frequency and in the form of the surge cycles, from roughly sinusoidal with relatively small fluctuations in mass flow to a relaxation type of oscillation, with much larger mass flow variations, as B is varied by a factor of six. (Experimental confirmation of this trend can also be seen in Figs. 8-12 of [32].) In the first instance the period of the oscillations is basically set by the natural frequency of the system viewed as a Helmholtz resonator, that is to say, by a balance between the system inertance and capacitance whereas in the second it is set by the emptying and filling times of the downstream plenum, i.e., by a balance between the system capacitance and resistance. However, for many practical situations the changes in values of B encountered over the operating range are not as extreme as this, and the alterations in the shape of the compressor characteristic are not very severe. Thus, as a first approximation, one can assume that the surge frequency of a given compression system will remain roughly constant as the speed is changed.

Other aspects of the overall influence of the shape of the compressor characteristic on system dynamics can readily be evaluated using models such as that described above. One important facet of this topic concerns the effect of stall/unstall hysteresis; that is, differences in the values of the axial velocity parameter (and throttle area) associated with the onset and cessation of rotating stall as one reduces and then increases the mass flow during steady-state operation. As will be discussed later, this type of hysteresis is commonly encountered in multistage compressors at speeds near design. Several authors have postulated that it is the presence of the hysteresis "loop" in the compressor pumping characteristic that is responsible for the occurrence of surge. It is to be emphasized that this is not correct and, in fact, hysteresis is detrimental to the formation of a surge cycle.

The reason for this can be seen in Fig. 24 which shows the calculated transient system response with a compressor that has no hysteresis as well as with one that has a reasonable amount of hysteresis. The value of B is the same in both these figures (0.8) so that the systems can be regarded as identical

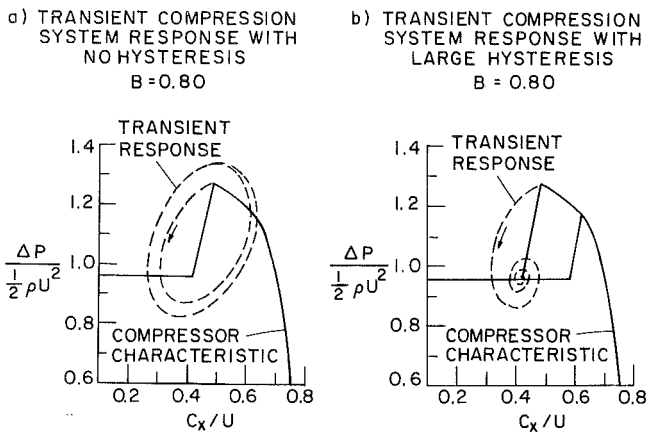

Fig. 24 Effect of stall/unstall hysteresis on compression system dynamics

except for the difference in compressor hysteresis. The steady-state pumping characteristics used in the calculations are shown by the solid curves. The initial motion of the operating point is the same in both cases, as the axial velocity parameter decreases to 0.31 and then starts to increase. However, in Fig. 24(*a*) (no hysteresis), as the compressor flow increases, a range of compressor operation is encountered where the characteristic has a strongly positive slope—a situation in which energy can be fed into the system oscillations to increase their amplitude, resulting in surge. In contrast, in Fig. 24(*b*) as the compressor flow increases after the initial decrease, the region of positive slope is never seen. The swings in compressor mass flow are not enough to get off the stalled branch of the characteristic and the system exhibits damped oscillations about the equilibrium point as shown, ending up in rotating stall. It can therefore be seen that the presence of appreciable stall/unstall hysteresis in the compressor characteristic strongly inhibits the occurrence of surge oscillations in compression systems, making it more likely that the result of an initial instability of the uniform flow will be operation at the decreased flow and pressure rise that is associated with rotating stall.

We can also note that the equilibrium point, i.e., the intersection of the compressor and throttle curves, for this transient is on the horizontal (zero slope) part of the compressor characteristic. A linear analysis would predict that this point would be a stable one for any finite B, since a positive slope is needed for instability. The fact that this point is actually meta-stable, in that surge oscillations can occur as a result of the finite amplitude system transients that are encountered, is another illustration of the qualitative difference between linear and nonlinear systems.

The strongly nonlinear system dynamics are also manifested in another type of hysteresis (path dependent behavior). This exists between surge and rotating stall when changing the operating point, either by changing the rotor speed or altering the throttle area. For example, for the system studied in [32] there was a sizeable regime in which two different behaviors could be obtained at a given operating point (given rotor speed and throttle setting) depending on whether one approached the point from a lower speed, where the compressor was operating stably in rotating stall, or from a higher speed in which large amplitude "deep surge," with periods of overall reverse flow, existed. In the first case the behavior at the specified point would be rotating stall, whereas it would be surge in the second. In addition, in this regime, surge could occur even for points where the local compressor characteristic had a negative slope (*in the stalled region*), for example at a $C_x/U \sim 0.15$ in the characteristics

shown in Figs. 21 and 22. This behavior is described in detail in [32], where a heuristic model is developed for its occurrence based on calculations carried out with the nonlinear system model; however, the main point to be noted here is the large influence of effects that are inherently nonlinear in character on the overall features of the system transients.

As a further comment on the fluid mechanics that determines whether a given compression system will exhibit surge or rotating stall, we can mention that for more complex configurations than have been described above, there can be other features of the problem that must be considered. In particular for a turbofan engine (which has two separate air streams), it appears that there can be other phenomena that will drive the system into rotating stall. This is a question of considerable importance in connection with the general topic of "Stall Stagnation," but is one in which there is much less known.

Finally, although not of direct practical import, it is interesting to relate the result on nonlinear surge cycles discussed above to previous work on nonlinear oscillations. It can be shown that for certain special cases, the equations describing the compressor system transients reduce to the form of nonlinear equations that have been studied extensively in connection with oscillations in electrical systems. In particular for the case of a compressor characteristic curve that can be described by a cubic function of mass flow, taking the compressor response to be quasi-steady and the throttle curve to be linear, one obtains an equation which can be regarded as a combined Van der Pol-Duffing equation. In fact, for the case of a vertical throttle line the equation reduces to the well known Van der Pol equation. With these restrictions, the limit cycle behavior for the case of small nonlinearity has been found in [64] using a perturbation approach. Other results for this particular set of circumstances have been computed numerically by Horvath [65], some of whose results have also been reported in [66].

K. Rotating Stall in Axial Compressors. The other consequence of compression system instability is rotating stall. We can describe the flow regimes encountered during compressor operation in rotating stall by considering a hypothetical compressor of, say, three stages. We examine the performance curves plotted in the form ψ_{TS} versus ϕ, where ψ_{TS} = (exit static pressure - inlet total pressure)/ρU^2, and $\phi = C_x/U$. Two possibilities are shown in Figs. 25(*a*) and 25(*b*), which can be regarded as being representative of data from a number of actual compressor tests. Figure 25(*a*) shows a compressor whose performance curve is either continuous or has only a small discontinuity in pressure rise (a few percent) at a stall point, A. This behavior, where there is a very gradual drop in delivery pressure (or often no drop) at the inception of stall, is associated with the compressor operating with one or more stall cells that do not cover the total height of the annulus. This is known as part-span stall, and an indication of a typical configuration is shown in the figure where we see two regions of severely retarded flow, i.e., two stall cells, at the tip. It is of course not always true that the cells appear at the tip; they can also be found at the hub, and the picture should just be regarded as giving one typical possibility.

Part-span stalls are also often seen during low-speed operation of multistage high pressure ratio compressors. Under these conditions, which can occur to the right of (i.e., below) the stall line shown in Fig. 7, there can be severe mismatching between the front and rear of the compressor, and the overall characteristic may thus still be quite negatively sloped.

As the throttle is closed from the stall point and the mass flow through the compressor illustrated in Fig. 25(*a*) is further

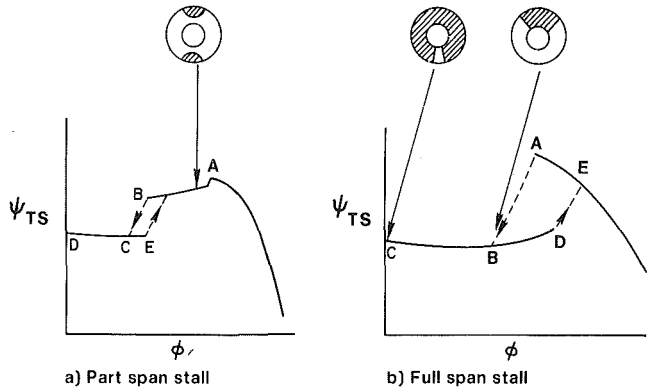

Fig. 25 Compressor characteristics showing stalled performance

decreased, the performance curve can exhibit a large discontinuity where the pressure rise and mass flow jump to significantly reduced values; this occurs from point B to C on the figure. This jump is associated with a change in the type of stall. At point C there is one single cell, occupying a sizeable fraction of the annulus and extending over the full annulus height. This regime is known as full-span stall. Further throttling causes this cell to increase in size with the delivery pressure remaining relatively constant from point C to D. As the mass flow approaches zero, the stall cell can grow to fill the annulus so that the flow can become basically axisymmetric with the pressure rise often dropping off slightly. If we were to once again open the throttle, we would find that the mass flow at which the compressor left the *full-span* stall regime, point E, was different from that at which it entered. However, this hysteresis is usually negligible for the onset and cessation of *part-span* stall.

If we examine Fig. 25(*b*) we see a somewhat different picture. The large discontinuity in pressure rise and flow now occurs right at the stall limit (point A). The sharp drop in both these quantities as the operating point jumps from point A to point B in this figure is associated with the compressor going directly into single-cell, full-span stall, as indicated schematically. Further throttling causes the stall cell area to grow, although it may not reach 100 percent of the annulus area even at zero mass flow through the compressor, with the pressure rise being relatively constant from point B to "shut off" at point C. If one opens the throttle, it is found that there is a substantial hysteresis between the onset and the cessation of stall, in that the throttle area has to be increased to a significantly larger value than that associated with stall onset, in order for the machine to unstall. The large hysteresis is therefore responsible for the difficulty in recovering from a stalled condition.

Just as in the theoretical treatments of stall and stall inception, much of the detailed experimental work on the structure of the stall cell flow field considers isolated rotors and [29] can be consulted for a bibliography on the subject. However, it has become apparent that the constraints on the flow field in a multistage machine are quite different from those in an isolated rotor, and we will therefore concentrate on one of the few investigations of rotating stall in a multistage environment, by Day and Cumpsty [31]. They used an ensemble averaging technique which was triggered on each passage of the stall cell so that they could average the results of many revolutions of the cell to provide detailed definition of stall cell properties. Their investigations were carried out on several different three-stage compressors having quite different design values of axial velocity parameter, ϕ^*, i.e., $(C_x/U)_{design}$, so the effect of this important parameter could be clearly seen.

Their paper, which addressed the full-span stall problem,

shows that in most cases the flow in the compressor can be divided into distinct areas of stalled and unstalled flow. To a reasonable approximation the flow in the unstalled area behaved as it would if there were no stall cell at all. In the stall cells the fluid velocities ahead of the rotors were near blade speed and in the direction of rotation, while behind the rotor the velocities were much lower. The axial velocities in the cells were small compared with either blade speed or the unstalled axial velocity; their precise magnitude and direction, however, varied from compressor to compressor. In addition it was emphasized that the full span stall cell extends axially through the compressor. The basic reason for this is that the axial spacing between blades is quite small compared to the width of the stall cell. Since a mass flow defect (which is what a stall cell is) in the front of the compressor can only be "filled in" by circumferential cross flows between the blade rows, the close spacing means that this defect will extend basically straight through the compressor.[13]

Day and Cumpsty emphasize that the stall cell is very different from the wake of a bluff body, the model used by many previous investigators. If this were the case, then in a coordinate system fixed to the cell the edges of the cell would coincide with the steady streamlines in the unstalled flow surrounding the wake. Such a description had been proposed by Rannie [67], for example, and has also been used as a model by Fabri (for an isolated rotor) [29]. The measurements, however, show clearly that this is not in accord with the actual picture of an essentially axial cell propagating at the observed rates. The concept that emerges therefore, of the instantaneous streamlines as viewed in an absolute coordinate system, is shown in Fig. 26. There is in fact mass transport *across* the cell boundaries so that fluid that was in the unstalled region (with a high axial velocity) is violently decelerated as it enters the cell, whereas particles which were in the cell are accelerated at the cell edges as they enter the unstalled flow. It should therefore be emphasized that the "wake" models of stall cell flow cannot be applied to the single or multistage compressor situation.

L. Prediction of Compressor Performance in Rotating Stall. The prediction of the compressor flow regimes in rotating stall is important for several reasons. One consideration can be that the speed and number of stall cells determine the forcing frequency for blade vibration, and it is desirable to design the blades such that no resonance occurs. However, a very much more pressing consideration is that of *stall recovery*, i.e., the prediction of overall performance including the hysteresis loop.

In an approach to this problem, Day, Greitzer, and Cumpsty [39] developed a correlation to predict stalled flow performance. The correlation is based on a heuristic fluid dynamic model of the compressor flow field in rotating stall, which is derived from the abovementioned measurements. Essentially the compressor is divided into a stalled and unstalled zone analogous to the concept developed for inlet distortion. The stall cell is modeled by a zone of zero flow, and in the unstalled part of the flow the compressor is assumed to operate at a point on the unstalled performance curve. The situation is thus shown in Fig. 27 where we see the stalled "zone" of the compressor working at S and the unstalled zone, at the same pressure rise, at *U*, with the mean

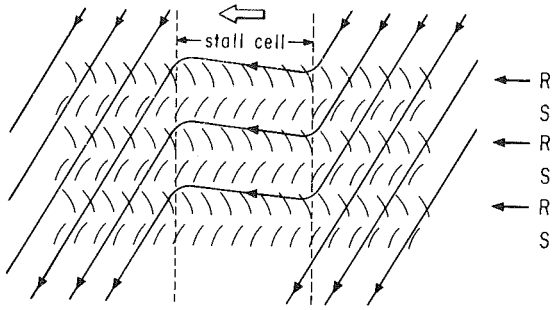

Fig. 26 Sketch of stall cell structure (drawn in absolute reference frame) [31]

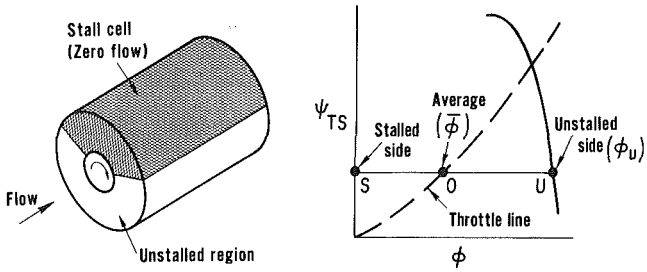

Fig. 27 Compressor performance in rotating stall

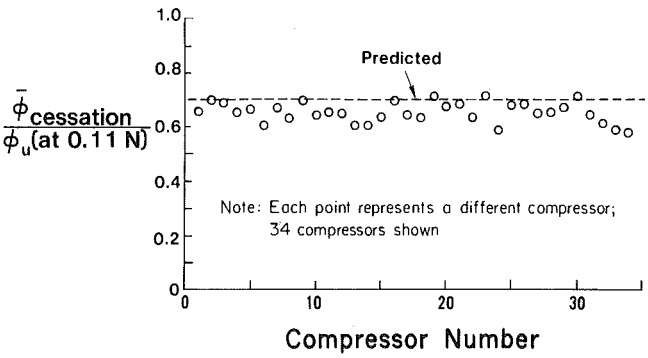

Fig. 28 Correlation for $\bar{\phi}$ at cessation of full-span stall [39], [69]

operating point defined by the intersection of the horizontal line from S to U and the throttle curve at 0. This model is applied in conjunction with two experimental observations. The first is that, following an observation originally due to McKenzie [68], the nondimensional inlet total to exit static pressure rise per stage in rotating stall is constant *independent of the unstalled performance* ($\psi_{TS} = 0.11\,N$ in stall, where N is the number of stages). The second is that there is a critical value of stall cell blockage, λ, (i.e., extent of annulus covered by the cell) below which *full-span* stall cannot exist, ($\lambda_{crit} = 0.3$). Using these, one can make predictions about whether a given compressor will exhibit full-span or part-span stall as well as about the extent of the hysteresis loop.

In particular a correlation has been derived for the flow coefficient at stall cessation.

$$\frac{\bar{\phi}_{cessation}}{\phi_{unstalled\ at\ 0.11\ N}} = 0.7$$

where $\phi_{unstalled}$ is the value of ϕ on the unstalled characteristic at a level of ψ_{TS} equal to $0.11\,N$. This correlation is shown in Fig. 28.

[13] This can be readily seen by considering the limiting case of incompressible flow with infinitesimal axial gaps between the blade rows and with rotor and stator having equal chord and stagger angle. In this situation there is essentially no net mass transfer between the stalled and unstalled regions, and the stall cell must extend axially through the compressor. In the actual situation, the effects of compressibility, nonzero axial gap, and nonsimilar rotor and stator geometry will mitigate this argument; however the basic concept (and the conclusion) are still very useful approximations.

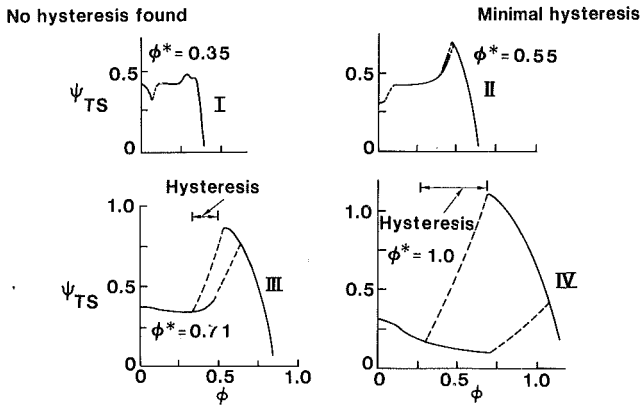

Fig. 29 Effect of ϕ^* (design C_X/U) on stall/unstall hysteresis (three-stage compressors) [39]

The vertical axis in the figure is the ratio $\phi_{\text{cessation}}/\phi_{\text{unstalled}}$ at $0.11N$, and the horizontal axis represents the different compressor builds (i.e., each point represents a different compressor). Data are presented from thirty-four different single and (mostly) multistage low speed compressors [39], [69]. It can be seen that the correlation furnishes a very useful method for predicting stall cessation.

Using this basic procedure, parametric studies can be carried out to determine the effect of different design parameters on stall performance. As shown in [39], two important parameters are ϕ^* (design value of axial velocity parameter) and number of stages. For a given design value of C_x/U, the larger the number of stages the larger the size of the stall/unstall hysteresis. However, a more potent driver is the value of ϕ^*; the higher the value for a given number of stages the larger the size of the stall/unstall hysteresis loop. Experimental evidence to support this idea is shown in Fig. 29, which presents data for four different three-stage compressors with different values of ϕ^*. At the lowest value of ϕ^* (curve I) no hysteresis could be found. As we examine curves II, III, and IV, which have increasing values of ϕ^*, we find an increase in the extent of hysteresis.

M. Research Needs and Suggestions for Future Work. There are many areas in which research is needed as regards the axial compression system. To start, it should be emphasized that at present we still do not know how to predict the stall onset point with the desired degree of precision. Thus further work in this general area is needed, although there seems to be little more to be gained from purely two-dimensional linearized treatments. Approaches which include the three-dimensional aspects of stall inception, however, appear useful to pursue. As one example, questions such as the impact of wall stall versus blade stall on compressor stability, have not been resolved. Approaches that are based on treating the blade row or rows as a "black box," however, will still have to contend with the capability of present axisymmetric flow calculation procedures to predict the slopes of the uniform flow speedlines or loss characteristics near stall. Because of this it may well be that a numerical treatment of the flow *in* the blade passage region would be of considerable use here in clarifying how the blockage changes with small changes in incidence angle near the stall point.

There is also a need to develop better stability criteria in the case of compressors operating with inlet distortion. When one examines present approaches to this, it seems that a disproportionate effort has gone into the relatively straightforward task of solving the inviscid flow equations outside of the blade row, while the simple models that are in use for the fluid dynamics *in* the blade row are essentially the same one-dimensional treatments that were presented over twenty-five years ago. Thus, the author feels that more effort should be spent concentrating on the more difficult problem of understanding the unsteady rotor response in the heavily loaded (near stall) regime. Probably both experiment and numerical investigations will be needed for this. It might also be useful to attempt to formulate the linearized stability problem for a situation where the "mean flow" has a steady finite amplitude circumferential inlet distortion. Such an analysis might give some additional insight into the basic fluid mechanics of the onset of instability with the inlet distortion.

Although not discussed herein, it should be noted that there are distortions that are characterized by large variations in inlet flow angles rather than by non-uniformities in total pressure. The inlet vortex (or ground vortex) is an important example of this type of distortion, which can have a significant effect on stability [70]. At present no theory exists to adequately describe this type of inlet non-uniformity.

From the point of view of stall stability enhancement using casing treatment, there is considerable scope for useful work. As stated, the mechanism by which the treatment decreases the passage blockage is still unclear and there is a need for both theoretical and experimental work on this topic.

There are also important areas which are associated with the behavior subsequent to the onset of the initial instability. More accurate models are needed to predict the local details of the surge phenomenon in multistage compressors. This is important from an aeroelastic standpoint as well as from a purely aerodynamic one.

The transient behavior of compression systems with separate air streams, e.g. turbofan engines, is also an area for further work. As mentioned previously the basic single stream compression system models do not appear adequate to describe all of the relevant dynamics in this situation. Identification of the different mechanisms which cause the compression system to undergo a transient that results in rotating stall is an important problem as regards aircraft gas turbine engines.

Prediction of the features of rotating stall in multistage compressors is also needed. We can first discuss the overall performance characteristic. In particular the data reported in [39] and the subsequent discussion by Harman [69] seem to bear out the hypothesis that the inlet total to exit static pressure rise in rotating stall is roughly constant per stage independent of unstalled performance, but there is no understanding of why this occurs. Further, even though the pressure rise is independent of the unstalled performance, the torque does depend strongly on details of stall behavior related to compressor design parameters, and this is not understood. Investigation of these "global" properties should be pursued since they directly affect the hysteresis phenomenon and hence the recoverability of the compressor. A further facet of this topic is that from the point of view of aircraft engines which have two or more spools, it is extremely important to understand the interactions between the high and low pressure compressors and their effect on stalled flow performance.

The central features of the stall cell structure are also not well modeled at present. Work is being carried out on this topic, but, as stated in the text, present models are still rudimentary, compared to the aspects of the flow determined experimentally. Here again an important facet seems to be the complex three-dimensional, separated unsteady flow in the blade passages. The blade row models in use for the calculation procedures are essentially the same as those used for the inlet distortion problem; however, they are now being extrapolated even further (to the negative flow regime). Again, the author feels that more attention should be paid to the blade row characteristics, particularly in view of Takata's

comment that the nonlinearities in the equations of motion do not seem to have an important role in determining the wave shape, disturbance amplitude, etc., but rather that these aspects are believed to be determined chiefly through the nonlinear effects due to the blade row characteristic [35].

Work is also needed in the area of overall system modeling of compression systems, particularly high pressure ratio multistage compressors. In this context, it is important to note that some of the transients associated with surge in modern gas turbine compressors can be on the same time scale as rotor rotation, or particle flow-through time. Under such conditions the compressor response can be far from a quasi-steady one. This is true for transients both from unstalled to negative flow as well as from negative flow to unstalled. Thus (again) if one wants to do significantly better than present models, the effort should be in trying to understand the overall unsteady performance of the blading.

III Centrifugal Compressor Pumping Systems

We have dwelt in detail on the instabilities in axial compressor pumping systems because they have received a great deal of study. As a result, although there are still many problems that remain, there are certain areas in which a reasonable amount of understanding has been achieved. This is generally less true for centrifugal compressors. Thus, as will be seen, the discussion of centrifugal compressor stability cannot be presented at a comparably detailed level (as that for axial compressors). There are several reasons for this. One is that there has been considerably less engineering effort applied to studies of flow instability in centrifugal compressors, but perhaps also important is that the flow fields in centrifugal (radial) compressors may be inherently more resistant to analysis than in axial compressors. Although the distinction made in this review based on the difference in level of understanding may seem at first sight to be somewhat artificial, there is another reason for separating the two types of machines. This can perhaps be summed up by saying that although many of the same phenomena do occur with both types of turbomachines (especially when viewed on an overall system basis) there seem to be, especially in high pressure ratio centrifugal compressors, differences in the fluid mechanic features associated with the onset of instability. We will start in this section by describing those facets of instability in systems using centrifugal compressors or pumps that *are* similar to those already seen with axial compressors, and then turn to those areas in which there seem to be differences.

A. General System Characteristics. The basic pumping system to be considered is again that shown in Fig. 1. However the type of curve that we would find for a pump or low pressure ratio centrifugal compressor might be similar to curve 1 or curve 2 in Fig. 2. For a high pressure ratio centrifugal compressor stage, on the other hand, the constant speed lines are quite steep, due to compressibility, and they would look quite different. For example, Fig. 30 presents data from a high pressure ratio centrifugal compressor stage [71]. Pressure ratio is plotted versus corrected flow, with several contours of constant efficiency also indicated. It can be seen that as the speed and pressure ratio increase, the flow margin from choke (maximum flow) to stall becomes increasingly narrow. Thus the problem of ensuring adequate stable flow range can become especially acute at the high pressure ratios that might be used in aircraft engine applications, for example.

A pumping system configuration (using a centrifugal pump) which very closely resembles the picture in Fig. 1 has, in fact, been tested by Rothe and Runstadler (the only minor difference being that their facility was closed loop rather than

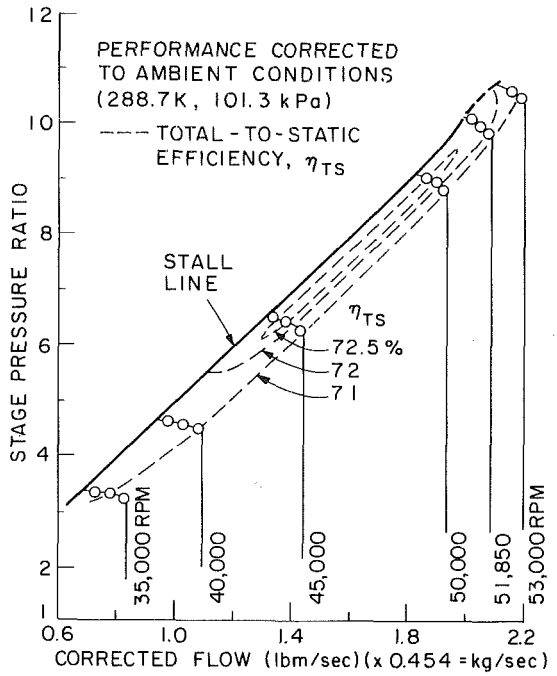

Fig. 30 High pressure ratio single stage centrifugal compressor performance [71]

open loop) [72]. The mass storage capability of their system could be varied by changing the amount of liquid in the closed volume, so that experiments to determine the influence of the system compliance could be run (similar to those carried out in [32], [62] for the axial compressor). The pump that was used was designed with forward leaning blades, in order to create a pumping curve with a substantial region of positive slope. The experimental results were complemented by numerical studies using a nonlinear lumped parameter model for the transient system behavior.

In general the analytical results concerning the system oscillations appeared to be in reasonable agreement with experiment, similar to the situation found with axial compressors where this type of modeling does show many of the important features of the surge cycles [62]. Much of the physical interpretation given previously (for the axial compressor) can be taken over to these centrifugal pumping systems. For example, with reference to previous remarks on the physical significance of the B parameter, it is to be expected that the amplitude of the limit cycle system oscillation should increase as the compliant volume is increased, and this is seen in the data shown in [72]. Thus the overall conclusion is that the same type of lumped parameter compression system analysis that has been described with regard to axial compressor systems is also applicable to transients with centrifugal pumps. (Note that in this section we are limiting the systems under consideration to those with single phase flow, and that situations in which cavitation is important or in which the pump is operating in a two-phase flow will be examined in subsequent sections.)

The similarity with the general behavior of axial compressors is not only manifested in pumps, but also has been seen in the flow instabilities encountered in (low pressure ratio) centrifugal compression systems. For example, one of the first discussions of rotating stall and surge was by Emmons, Pearson, and Grant [3], who tested a centrifugal compressor with a vaneless diffuser. It was found that the system exhibited two types of surge—a mild surge and a deep surge. During the mild surge the compressor went in and out of rotating stall as the mass flow changed, while during the deep surge there was no coherent stall cell pattern to be seen.

Between the two regimes, on a constant speed line, there was a region in which the compressor characteristic was negatively sloped and stable (i.e., non-oscillatory on a system basis) flow was found, although the compressor was in rotating stall. As the speed increased the two regions tended to merge. (Similar behavior has also been reported in [73].) This behavior is quite similar to that found with an axial compressor (for example see the description on pages 208–211 of [32]) and it again emphasizes that many of the overall system modelling concepts apply to both centrifugal and axial systems.

At least at the present level of understanding, therefore, one would tend to expect that the basic ideas concerning the overall system behavior would apply to the centrifugal as well as axial compression systems. When one examines the specifics of the local phenomena that can "trigger" this overall instability, however, there do appear to be differences between the two types of machine. Because of this, it is useful to discuss the phenomena that are associated with the stall of the centrifugal compressor *stage*, since this lies at the root of the system instability.

B. Stage Stall in a Centrifugal Compressor. Centrifugal compressor stages consist of an impeller and a diffuser, with the latter of either vaned or vaneless design. The type of diffuser used can have a considerable effect on the stable flow range of the stage. As an illustration of this, Table 1, taken from [74], divides diffusers into two types according to whether the principal objective is a high efficiency or a wide flow range, with the choice of design depending strongly on the application. Process compressors, which can require very broad range, may use vaneless diffusers—centrifugal compressor stages in aircraft gas turbine engines, where efficiency is very important, will tend to have vaned diffusers.

Table 1 Diffuser types (from [74])

Wide range	High efficiency
Dump collector	Vaneless plus cascade (1-3 row)
Vaneless diffuser with:	Thin vane:
dump collector or	single row
scroll or	multiple row
scroll plus discharge diffuser	Contoured vane:
	single row
	multiple row
	Vane-island with:
	curved
	straight centerline passages
	"Pipe" diffuser (UACL patent) with:
	circular
	non-circular "pipe" cross section
	Rotating-wall vaneless plus vaned diffuser

As with axial compressors, there are several levels of approach to finding the most important contributor to stage stall. The most empirical are based on correlations of impeller or diffuser flow range as functions of various flow parameters. One example of this is given in the papers by Rogers [20], [75], which describe the use of a modified diffusion factor, based on the relative velocity diffusion, to correlate the onset of impeller stall. For the vaned diffuser there are also a number of correlations that exist. One of these is by Kenny [76], who used the criteria that the non-dimensional static pressure rise coefficient from impeller tip to diffuser throat = 0.45 as an indication of stage stall. Another method is given in [77], in which correlations are developed to predict the flow range as functions of impeller exit conditions and diffuser geometries. This paper also reports tests of stages in which diffusers designed according to the ideas of the correlation resulted in improved stall margin. A further method, developed from tests on a vortex nozzle swirl facility, is also reported in [78]. A very recent study of this sort is reported in [79], where the non-dimensional semi-vaneless space (diffuser inlet to throat) static pressure rise coefficient has been used. In this last paper, a distinction is drawn between the stall points of stages having annular dump collectors of snail-shell form and those which have the diffuser discharging into a radial to axial bend followed by axial cascade vanes, since it was found that the pressure rise coefficient at the surge point could be considerably less with the latter geometrical configuration than with the former. As one might expect from seeing the diversity of the correlative procedures, none of them provides a criterion that applies in all cases of interest and, in general, designers appear to rely heavily on data correlations from similar geometries that have been run previously.

A somewhat different approach has been taken by Dean [74] and other investigators at Creare. This is based on the idea that (as discussed in connection with the basic pumping system and the axial compressor) the slope of the overall total-to-static stage pressure ratio is an indication of the onset of instability. Dean breaks up this overall ratio into the product of separate ratios for inlet, impeller, impeller exit to vaned diffuser throat and channel diffuser to diffuser exit. The first of these is a total-to-static and the rest are all static-to-static pressure ratios. Writing this overall ratio as a product and logarithmically differentiating, an expression can be obtained for the normalized slope of the overall stage pressure ratio $PR_{overall}$, in terms of the different element pressure ratios:

$$\left(\frac{1}{PR_{overall}}\right)\frac{\partial PR_{overall}}{\partial \dot{m}} = \sum_i \frac{1}{(PR)_i}\frac{\partial PR_i}{\partial \dot{m}}$$

where the sum over i indicates the different elements of the stage. This normalized slope may be regarded as a type of stability parameter, which we can call the stability slope parameter. An illustration of the behavior of this stability parameter is plotted in Fig. 31, taken from [74]. The values of the stability slope parameter (referred to as SP in the original report) are presented for the individual elements as well as for the overall stage, plotted as functions of the mass flow rate. Positive values indicate a tendency toward instability (positive slopes); negative values indicate stability. It can be seen that, in this example at least, the channel diffuser appears to be the element that has the largest destabilizing effect and that as the flow is reduced the counteracting influence of other elements decreases so that the overall value moves towards positive. Another example of the breakup of the stage performance into the elements is given in [80] in which the performance curves of each component are presented.

The conclusion from [71], [74], and [80] appears to be that in medium to high pressure ratio centrifugal compressors, it is very often the vaned diffuser that sets the stall point, although this is not true in all cases. For example, Young [81] points out that a variable geometry diffuser, which could be set close to choke over a wide flow range, could well be used as the stabilizing element in some stages. (An illustration of this type of effect is reported in [82], where the addition of a *rotating* vaned diffuser had a stabilizing influence, so that flow range was increased substantially over the situation with a stationary vaneless diffuser.) It should also be emphasized that although some evidence is presented in [74] concerning the usefulness of the overall total to static pressure ratio as a guide to the initiation of stage stall, the author of this review tends to regard its direct quantitative application with the same amount of caution as in the axial compressor case (see Figure 11 and the relevant discussion).

The picture that emerges, then, is of a situation where the stalling element cannot *always* be regarded as being the diffuser, but should be found from examination of the aerodynamics of each component. (An additional comment

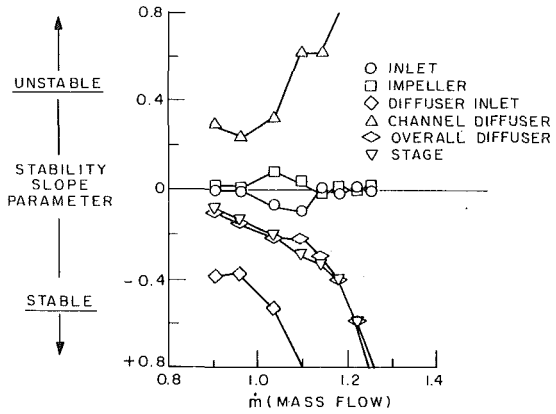

Fig. 31 Influence of stage elements on centrifugal compressor stage stability [74]

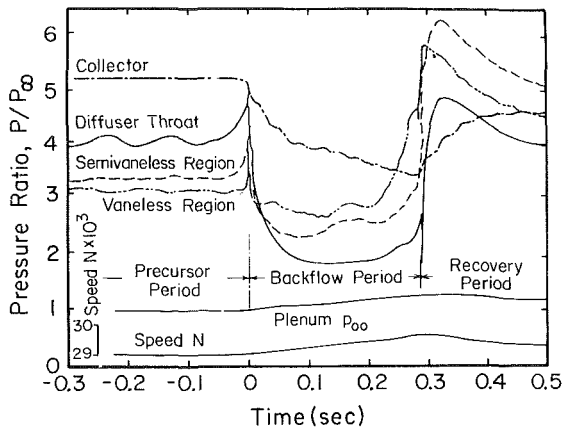

Fig. 32 Pressure variations during centrifugal compressor surge [71]

on this point is given in the next section.) In addition the choice of parameters to correlate the onset of stall is still under considerable debate, as are the unsteady physical phenomena that characterize the stage stall process. For an axial compressor, the sequence of events seems to be that as one approaches stall the flow becomes more and more unsteady ("rough"), although there do not appear to be large amplitude fluctuations in mass flow or pressure ratio. The onset of system instability is then associated with the onset of a rotating stall pattern, as described previously (although the rotating stall may not have time to grow to a fully developed state before the overall compression system flow instability occurs). For a high pressure ratio centrifugal compressor, a different behavior has been reported [71]. This consists of large amplitude fluctuations in mass flow which are encountered even in the supposedly stable (as measured with steady-state instrumentation) region of the compressor speedline. During these oscillations (which are of low frequency compared to the flow-through time of a fluid particle) the conditions in the compressor and the diffuser also fluctuate. The view expressed in [80] is that during one of these fluctuations the conditions necessary for surge initiations are exceeded and system instability occurs. In this connection, it is of interest to note that it is reported in [80] that the instantaneous value of the impeller exit to throat static pressure rise coefficient just prior to surge did appear to be in accord with Kenny's criteria. The time averaged value at this condition could, however, be considerably less than this. This is just a small amount of data, and one cannot generalize on the universality of this situation, but the main point is that even *if* there is some type of criterion based on the instantaneous flow conditions, in order to use it one has to be able to predict the unsteady behavior of the stage. Means for doing this do not exist at present.

An illustration of this unsteady behavior of a centrifugal stage is presented in Fig. 32, from [71], which shows the transient pressure measurements in the collector, the diffuser throat, the semivaneless region, and the vaneless region, plotted versus time. It can be seen that before the severe flow breakdown and reverse flow that the authors term surge, there is oscillatory behavior occurring in the diffuser throat static pressure. The characteristic frequency of this is on the order of 10 Hz, which is close to that calculated using a lumped parameter (Helmholtz resonator) type of system analysis. (In fact, in the terminology used in this review, these oscillations in the "precursor period" would be classified as a mild surge.)

Although the frequencies of these precursor oscillations are generally in some accord with those given by the system models, attempts to predict the quantitative behavior as far as oscillation amplitude (using a nonlinear model) have not been very successful. In particular it was found that the measured slopes are far too large (i.e., too positive) to give the required limit cycle behavior, if one assumes that the compressor stays on its steady-state characteristic during these transients. This tends to imply that the stage departs from quasi-steady behavior, and in fact such behavior has been observed (but not well understood) with axial compressors. If this departure is modeled with a first order lag, then calculations show that the effect of unsteadiness would be to yield an instantaneous slope that is less positive than the measured steady-state one. Although this does proceed in the general direction of reconciling experiment and theory, the whole question of unsteady pump or compressor response near stall is an area in which little is known. (For a discussion on the unsteady response of a compressor as regards stall inception see [16].) Thus, a basic limitation to the use of any lumped parameter analysis in modeling the instability process in high pressure ratio centrifugal compressors is the proper simulation of the transient behavior of the pumping elements, and their unsteady behavior is an area in which further research is needed.

A further point made in [71] is that before the onset of surge there was no indication of rotating stall. Again this is different than the situation in axial compressors, although there is no fundamental bar to the positively sloped characteristic necessary for system instability occurring without rotating stall appearing. A recent report of a test of a small 8:1 pressure ratio centrifugal stage also shows large unsteady pressure variations in the diffuser throat as the stage flow approaches surge [83]. In this test, however, the possibility of rotating stall in the diffuser was not ruled out and indeed the frequency of oscillations is within the range one might expect for vaned diffuser rotating stall. A further pertinent piece of information on this point is provided in [84]. In this set of experiments, time-wise analysis of the unsteady pressure measurements at the leading edge of centrifugal impeller blades showed no discernable rotating stall before the surge point. However, the frequency-analyzed results did exhibit an emerging peak at a frequency that is not inconsistent with the occurrence of rotating stall. At present, therefore, we can say only that stage stall in a moderate to high pressure ratio centrifugal compressor with vaned diffuser is very often but not always set by the diffuser at speeds near design, that there can be substantial fluctuations in mass flow rate and pressure before the onset of surge (reverse flow), and that the presence of rotating stall in the diffuser may not be necessary for the initiation of overall system instability.

It may appear that this reviewer has not been able to discourse with as much confidence on the causes of, and mechanisms associated with, the onset of instability in cen-

trifugal compressor pumping systems as he has in the case of axial machines. This is the impression that is meant to be created since many of the issues under discussion are still not well understood. (As a means of giving some perspective to the situation, one can refer to the March 1977 issue of the JOURNAL OF FLUIDS ENGINEERING, which includes several papers from the ASME Symposium on Centrifugal Compressor and Pump Stability, Stall, and Surge, as well as to [78] on vaned diffuser stability. As can be seen from the extended discussion on many of the papers (as an example, the "Discussion" and "Author's Closure" to [78] are roughly twice as long as the paper itself!) there is, at present, no unanimity of opinion on many of the relevant issues.)

C. Stability Enhancement in Centrifugal Compressors. There are many applications of centrifugal compressors in which considerable flow range is required. Thus, one topic of interest has been approaches to extending the stable flow range of the compression system, even at some small cost in efficiency. As with the axial compressor, there are several techniques that have been developed. One of these is to use inlet guide vanes to impart a "prewhirl" to the inducer, shifting the pumping characteristics on the map and altering the flow rate at which one encounters instability. The effects of using this technique are well documented in the literature, and a discussion of this method, with references, can be found in [74]. Other well known means for increasing stability are the use of backward impeller leaning blades to create a negatively sloped pumping curve, and/or the use of vaneless diffusers (as mentioned above) rather than vaned.

Apart from these well known methods, however, there are other approaches that have been less discussed, and to which we will give more attention. In particular we will examine three other methods. The first to be discussed will be the use of closely coupled system resistances to extend the stable operating range, since this is an example of some of the principles that we have developed in connection with the axial compressor, and which hold true for turbomachines in general. Second we will look at the use of casing treatment, since this is a relatively unexplored area, and last the use of thick bladed impellers for flow range increase.

The requirements for centrifugal compressor operating range can vary widely according to usage. In particular, in process operations there is often a necessity for wide (stable) flow range even if this range has to be achieved at a slight cost in efficiency. One approach to this problem is presented in [85]. The basic idea can be illustrated with respect to Fig. 33. This is simply that if operation on the positively sloped characteristic leads to instability, we can change the characteristic slope by *closely coupling* another element to the stage to make the combined slope negative. Thus in Fig. 33 curve C is the pumping characteristic and curves A and B are two examples of resistance curves (exit pressure dropping as flow is increased). If operation at a low flow rate such as A' is needed, then we can closely couple resistance A to the pump; if further reduction to point B′ is needed, then we can use resistance B. The combined curves in the two cases are shown as having basically zero slope at the desired operating points; negative slopes could be obtained with larger resistances.

In [85], this idea was subjected to experimental scrutiny, using a compressor that had exhibited large amplitude surge cycles (including severe reverse flow) as a result of system instabilities. In the experiments the closely coupled downstream throttling was achieved by means of overlapping plates with slots cut in them so that the open area, i.e., the downstream resistance curve, could be varied. The results of doing this are shown in Fig. 34, which gives the measured compressor characteristics for one configuration tested. The data shown are from the baseline (no downstream resistance) run and from several other runs with varying resistance. Several

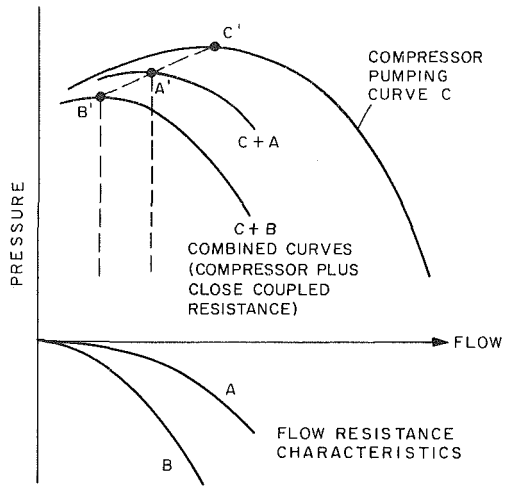

Fig. 33 Surge control concept using close coupled resistances [85]

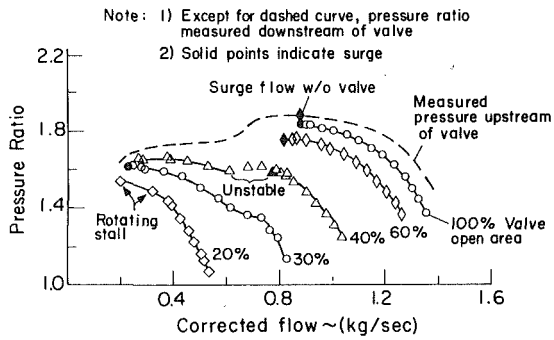

Fig. 34 Centrifugal compressor performance with close-coupled surge control valve [85]

trends can be seen. First, the possibility of extending the flow range is definitely exhibited. Second, the trend towards instability as the slope becomes positive is again notable. In particular the region of steep positively sloped curve was not stabilized with the more open configurations, although the instability was much less severe than with no resistance. However, even this instability was suppressed with the more closed (higher resistance) configurations. Third, the downstream resistance did not completely inhibit the onset of rotating stall. However, here the stall was associated with a gradual decrease in performance so that the overall "stage" curve was still rising and the system behavior was stable. Further details of the geometry and considerations aimed at multistage centrifugal compressor usage are given in the cited reference.

Another example illustrating the idea of using a closely coupled resistance to stabilize a pumping system is reported in [86], which describes large pressure pulsations encountered in a boiler feedwater system. The pulsations, which caused "heavy pipework vibration," occurred when the (multistage centrifugal) feed pumps were operated at flows much lower than design. A solution was the insertion of an orifice (i.e., a flow restriction) in the pump delivery line close to the pump. This reduced the amplitude of the pulsations significantly and stopped the vibration over the whole boiler flow range.

The second approach we discuss is the use of casing treatment. There have been several reports of its use with centrifugal compressors. Amman, Nordenson and Skellenger [73] tested a centrifugal compressor whose range was limited by stalling in the vaned diffuser. They put a circumferential groove in the shroud at the impeller tip, with a chamber

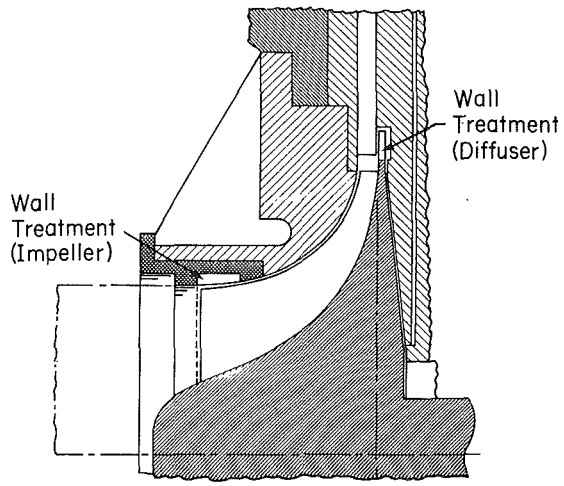

Fig. 35 Casing treatment locations in centrifugal compressor stage [84]

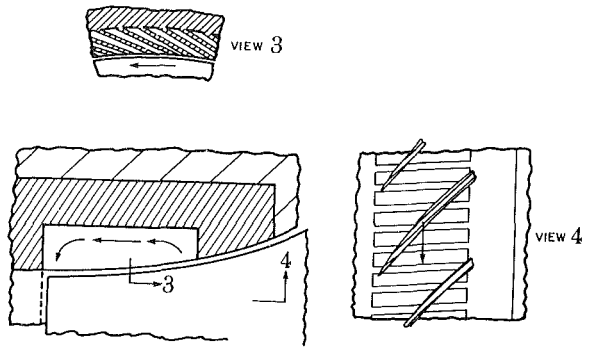

Fig. 36 Centrifugal compressor impeller casing treatment geometry [84]

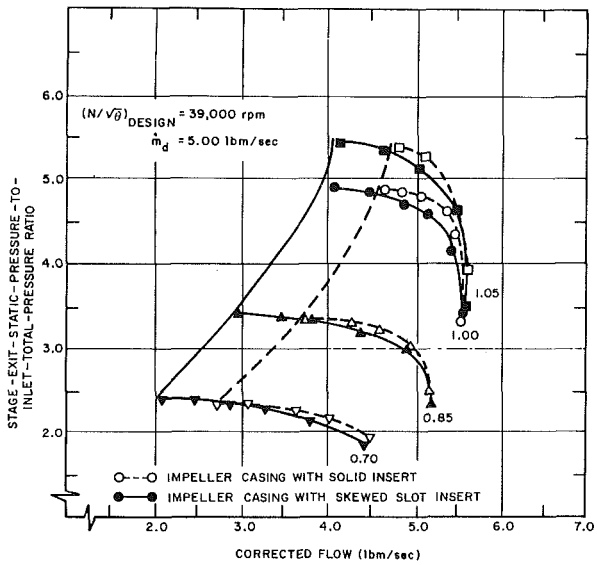

Fig. 37 Effect of casing treatment on centrifugal impeller flow range [84]

behind it, and found an improvement in range. Another study has recently been reported by Jansen, Carter, and Swarden [84]. The view expressed there is that if the stall line is controlled by the inducer (impeller) at low speed and by the vaned diffuser at high speed, one can improve performance over a considerable speed range by the use of treatment on both the impeller and the diffuser. Thus, an essentially axial, skewed groove treatment was put over the tip of the impeller at inlet. In addition tests were also run with the impeller hub wall extended under the inlet of the vaned diffuser so that a treated (grooved) wall moved under the diffuser inlet. The locations of the casing treatment are indicated in Figure 35, and a sketch of the casing treatment used in the impeller is given in Figure 36. The treatment used under the diffuser inlet was a radial skewed groove.

Tests were carried out with two impeller/vaneless diffuser combinations (in which case it was the impeller that set the stall) as well as with the impeller and vaned diffuser complete stage. It was found that a significant improvement in stall range was obtained with the grooves at the impeller inlet for speeds from 0.70 to 1.05 of design speed, with some small loss in efficiency. This is shown in Fig. 37. In addition the "hub treatment" under the vaned diffuser gave an improvement in stall flow margin, as well as an increase in choke flow. (This latter is perhaps not surprising in view of the comments made previously regarding the effect of the grooved treatment on decreasing the blockage.)

Finally there is another means of extending the flow range that should also be mentioned. This is the use of an impeller in which the impeller blades are thickened. This has been used in centrifugal compressors which have application as turbochargers. The procedure followed was to thicken the radial portion of the impeller blades, the tip width being increased so as to have the same exit area as with the original (thin) blades. A substantial increase in stable operating range resulted. A description of the actual modifications, as well as pictures of the wheels, is given in [87], which also presents supporting arguments against the idea that this range increase is due solely to backward lean.

D. Suggested Research Needs. It should be evident from the previous two sections that the problem of developing accurate and general methods for prediction of centrifugal compressor stability boundaries is far from solved, as well as that the relevant phenomena do appear to be less well understood than with axial compressors. Even for low-speed centrifugal compressors or pumps, the basic stability (rotating stall onset) calculations, analogous to those carried out for the axial compressor, are not available. With high pressure ratio centrifugal stages the unsteady fluid dynamic processes that result (eventually) in system instability have not been resolved.

At the most empirical level, a large number of correlative procedures exist which use a variety of different parameters as an indication of the stability limit of the machine. Studies are needed to determine which of these are the most useful as a means of defining the stall point in terms of the steady-state flow quantities that the designer has at his disposal, as well as the limits of applicability of the present procedures.

At a more basic level, there are also important questions to be answered. It would seem to be most appropriate to focus attention on the so-called stage stall process, since it is the breakdown of the pressure rise in the stage that is viewed herein as being the (local) event that "triggers" the overall system instability. The causal relationships in this process are also not clear. For example, even if the channel diffuser is a destabilizing "element," is this merely an *effect* of increased blockage in the throat *caused* by the flow in the diffuser inlet section? There is also conflicting data concerning the part played by rotating stall in the flow breakdown of the stage. If this breakdown is not necessarily associated with the onset of rotating stall, then one may be able to regard the process in terms of the individual diffusers, whereas if a rotating stall is inherent in this phenomenon then one must include the strong

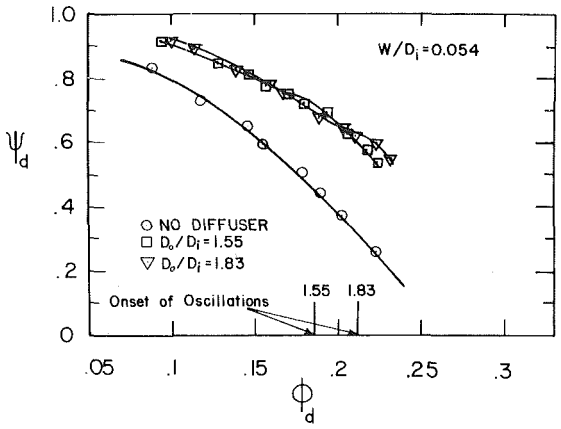

Fig. 38 Onset of oscillations in radial vaneless diffuser [89]

flow field coupling that exists between the different passages. The influence of the observed mass flow fluctuations on stall initiation including the connection between the steady-state (time mean) and the instantaneous flow conditions imposed upon the various elements of the stage, as well as the possible effects of the coupling between the diffuser and impeller (as reported for example in [82]) is also not resolved. In general, in fact, one might say that the question of "what stalls?" in the sense of what does one fix first to increase stall range (and *how* does one do this) cannot be answered with adequate precision in many cases, since much of the data can be interpreted as giving only the manifestations of stall rather than allowing one to formulate the cause and effect relationships that are needed to unravel the relevant physical mechanisms.

As with the axial compressor, therefore, it appears to be the unsteady behavior of the turbomachinery in a condition of high aerodynamic loading which is the least understood facet of the overall system response, and which thus appears to be the key area for further research. It seems clear that much of the investigations that are called for will be experimental, involving time-resolved measurements of the type presented in [71] for example. However, it may be that there is also scope here for use of numerical calculations of some of these unsteady, viscous and three-dimensional flows.

A further area of basic fluid dynamic interest, and one in which it appears that progress can be made, is that of casing treatment. The treatments used have demonstrated significant range increases, but at some penalty in efficiency, and the problem is to find casing treatments that provide good stall margin, yet are efficient, and preferably easily manufactured. The geometries that have been used were taken from tests done with axial compressors, and it is natural to ask whether their geometric configuration, as well as their placement within the stage, can be tailored to better fit their present environment.

E. Instability in Radial Vaneless Diffusers. It was not a very large stretch to extend our ideas on the onset of rotating stall from the axial flow compressor (or cascade) to the vaned radial diffuser. Indeed some of the basic work on rotating stall was done on a cascade of radial outflow blades. (This is still one of the most impressive sources of flow visualization of rotating stall [88].) It may be more surprising, however, that *vaneless* diffusers also exhibit a type of propagating disturbance. This has also come to be called "rotating stall" although there does not appear to be as direct a connection with stall as there is in the case of the bladed cascades.

To see the context in which these oscillations arise let us examine a performance curve for a (low speed) centrifugal compressor/vaneless diffuser combination as shown in Fig. 38 [89]. The parameter ψ_d is the overall pressure rise (compressor inlet total to diffuser exit static) divided by $\rho U_{tip}^2/2$, and ϕ_d is a nondimensional flow coefficient based on a mean radial velocity at diffuser inlet divided by U_{tip}. Pressure rise characteristics are shown for the impeller alone as well as the impeller plus diffuser, for parallel walled vaneless diffusers of two ratios of outlet to inlet diameter (1.55 and 1.83). The diffusers tested had a ratio of axial width to inlet diameter (W/D_i) of 0.054. Indicated on the figure are the points at which the axisymmetric flow would cease and "rotating stall" was seen. It can be seen that the onset of oscillation is well on the negatively sloped portion of the impeller pressure rise curve (and the overall stage pressure rise curve, as well). No oscillations were found in this regime when the impeller alone was operated, and it is the vaneless diffuser that is responsible for their presence.

This phenomenon was first described by Jansen [90]. He tested parallel walled vaneless diffusers, creating the swirl at the diffuser inlet by means of a rotating screen. He found that a pattern with a small number of lobes (two was a usual number) would propagate at a speed less than ten percent of the inlet tangential velocity. An approximate analysis was also developed to explain the breakdown of the steady axisymmetric flow.

Since then there have been several other investigations of this topic. Experiments have shown that there can be (at least) two different types of oscillatory behavior, one occuring at a speed of roughly one-fourth to one-thrid of the impeller velocity and one which occurs at less than ten percent [89]. It should be noted that these oscillations are local, in the sense that they merely redistribute the flow round the diffuser and that the overall mass flow is *not* affected. Thus they are not truly system phenomena, since the *system* behavior is *stable* [91], and we will not discuss them at length.

Aside from the experimental investigations there have also been analytical studies of the phenomenon, proceeding along two avenues. Senoo and his co-workers have attempted to explain the onset of vaneless diffuser rotating stall by using an axisymmetric boundary layer analysis [92], [93], [94]. They base their criterion on the extent of the (calculated) reverse flow that exists on the diffuser walls. The other approach to predicting the onset of non-axisymmetric flow is to analyze the stability of the steady axisymmetric flow pattern. This is carried out in [95] and [96]. It is to be noted that the analysis must be carried out incorporating a description of the flow in the impeller as well, since this sets the diffuser inlet boundary conditions. Thus some assumptions have been made in carrying out the calculations, which do show several of the features of the observed oscillations. In particular the difference between the "high" and "low" speed types of propagation is well brought out [95]. (It may be remarked that this type of description treats the flow in the diffuser as inviscid, with no mechanism analogous to the compressor cascade total pressure loss to generate a stall. To call the oscillations "rotating stall" may therefore be somewhat of a misnomer.)

An additional piece of information is furnished in [97]. In this study, the use of a flow resistance at the *diffuser exit* was able to suppress the onset of diffuser rotating stall. It was also found in these tests that rotating stall onset occurred when the regions of back flow on the diffuser walls were larger in (radial) extent than without the resistance. The first result tends to indicate that analyses of stall inception must include effects of exit conditions (exit impedances), as might be done in a stability analysis, rather than just local details of boundary layer behavior. However, the occurrence of regions of reverse flow does seem to be a precursor to the rotating stall—whether the relationship is a casual one is difficult to say at present.

It would appear then that neither of the present approaches

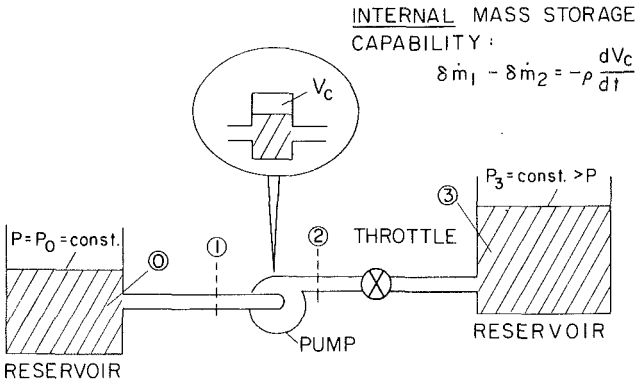

Fig. 39 Idealized pumping system with cavitating turbopump

is totally satisfactory, although a (nonaxisymmetric) stability analysis would seem to be the most fundamental type of approach for predicting these instabilities. It is also not evident that a purely two-dimensional inviscid treatment will suffice for quantitative predictions. Thus further work on this topic should be directed at assessing how critical are the assumptions that have been as far as impeller performance on the overall conclusions, and how sensitive are the results to non-two-dimensional and viscous effects.

IV Oscillations in Systems with Cavitating Turbopumps

The instabilities occurring in the pumping systems discussed above have been almost entirely associated with stall. However there are other classes of instabilities in pumping systems in which stall is not the primary cause, and these can occur even when the turbomachine is operating at its design flow rate. Such a type of instability occurs in systems with cavitating turbopumps. This type of behavior has been reported by many investigators, and has been associated, for example, with severe oscillations in the flow systems of liquid fuel rocket engines (the POGO Instability) [98], [99], [100].

An idealized system for this type of instability can be described with reference to Fig. 39. Here we have a tank of liquid at one pressure being pumped to another tank at a different pressure, with a throttle to regulate the flow. There is now not necessarily any compliant volume *external* to the pump, as in the case of a single phase fluid. However, we now have the possibility of cavitation which can cause an *internal* compliance (capacitance), as is indicated schematically. This will be seen to be an important feature of the system dynamics.

The instabilities associated with cavitating turbopumps appear to fall into two general categories. One mode is associated with the local flow in the inducer and the inlet flow field. This is known as rotating cavitation, and it manifests itself as an unsteady cavitation pattern at the inducer inlet that rotates with respect to the inducer blades. This has been described by Kamijyo [101]. Although not being dependent on stall per se for its occurrence, this rotating cavitation is somewhat similar to rotating stall in at least one respect, which is that it does not appear to involve fluctuations in the overall (annulus averaged) mass flow rate through the pump.

The other type of instability encountered with cavitating pumps (or inducers), is associated with overall mass flow oscillations through the entire hydraulic system and is known as auto-oscillation or surge. It can result in severe fluctuations in inlet and discharge pressures and mass flows [102], [103], [104], [105]. It is this type of system instability which is the more important and which we will focus on in this section. As background to the discussion of the dynamic performance of

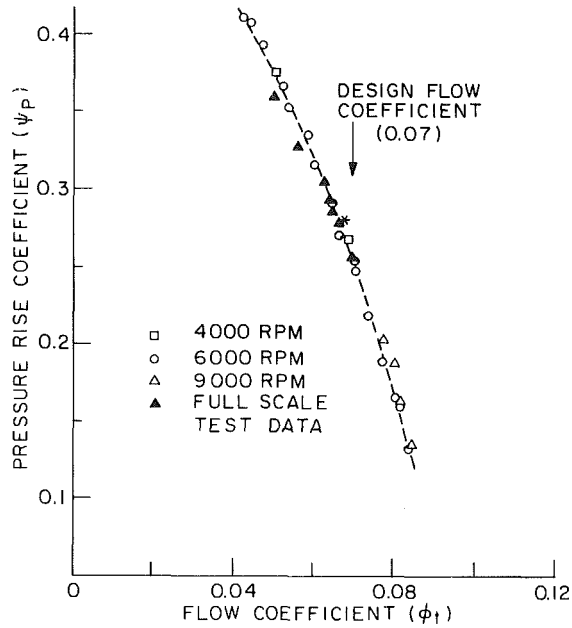

Fig. 40 Noncavitating impeller performance [108]

pumps with cavitation, however, we will first examine the steady-state performance of these devices.

A. General Performance Features of Cavitating Pumps. Since auto-oscillations have often occurred in the flow systems of liquid-fueled rockets, let us consider specifically the performance of a typical rocket pump impeller, with a three- or four-bladed helical inducer. (Details of configurations of this sort are presented, for example, in references [106] and [107].) In the single-phase systems we have studied up until now, the pressure rise capability of the pump or compressor, running at a constant rotor speed, was viewed as essentially a function of a single parameter, the nondimensional mass flow. However, if we examine situations in which there is the possibility of cavitation, we will need an additional parameter to indicate the influence of cavitation on steady-state performance. A suitable nondimensional parameter which is often used is the cavitation number, defined by

$$\sigma = \frac{P_1 - P_v}{\frac{1}{2}\rho U_t^2}$$

where P_1 = pump inlet pressure, P_v = vapor pressure of the liquid, ρ = liquid density, and U_t = the rotor tip speed. This parameter indicates, for a given geometry, the extent of the cavitation which will occur, a decrease in cavitation number being associated with an increase in cavitation extent.

The performance of the pump can therefore be expressed as

$$\psi_P = f(\phi_t, \sigma)$$

where ψ_P is a pressure rise coefficient ($\psi_P = P_2 - P_1 / \frac{1}{2}\rho U_t^2$, where P_2 is the pump discharge pressure), ϕ_t is a flow coefficient or nondimensional mass flow ($\phi_t = C_x / U_t$ where C_x is based on the volumetric flow rate and the inlet area). Under noncavitating conditions the performance can be described by only one variable, ϕ_t as shown in Fig. 40, which gives the pressure rise versus flow characteristic (at constant speed) of an impeller for a situation in which the cavitation number is high enough so that there was negligible cavitation [108].

As cavitation becomes important, the pressure rise becomes

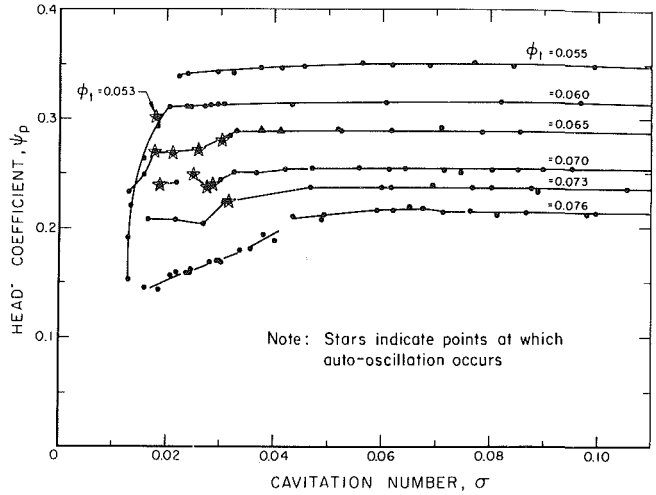

Fig. 41 Cavitation performance of impeller [108]; stars indicate points at which auto-oscillation occurs

a function of cavitation number as well. Representative performance curves for the type of pump described are given in Fig. 41 for a range of cavitation numbers [108]. In this figure the horizontal axis is cavitation number and the vertical axis is the pressure rise coefficient, ψ_P, with the different curves corresponding to different non-dimensional mass flows. The design value of ϕ_t is 0.07. Also indicated on the figure by the stars are the points at which the instability known as auto-oscillation was encountered with this system.

It can be seen clearly that this instability occurred even at design and higher flows, well within the negatively sloped part of the performance curve. This is in direct contrast to the behavior we observed in the single phase systems, and it is evident that stall is not involved in this instance. It is apparent, however, that the cavitation is in some way connected with the onset of instability. Thus any attempt to analyze the instability observed in this system must deal with the problem of devising a model for the unsteady performance of cavitating turbopumps, which is a central feature of the overall problem.

Initial attempts to model pump transients occurring at very low frequencies assumed simply that the pump traversed the steady-state performance curves. However, it was soon recognized that this was too simple an assumption to adequately describe the dynamic performance for the range of frequencies that are associated with auto-oscillations. Thus attempts were also made to account for unsteady effects by including the effects of the inertance and the internal compliance (mass storage), using models which lead to expressions for the quantities which are linearly proportional to the frequency. With these modifications one can in fact show some of the features of the instabilities, although a further degree of sophistication is required for accurate quantitative descriptions as will be discussed subsequently.

B. Qualitative Considerations of System Stability. To see in a qualitative manner the mechanism associated with the instability, we can consider the idealized system shown in Fig. 39. (A derivation of the quantitative stability criteria for this system is given in the Appendix.) The essential components are the inlet line (from 0 to 1) which has inertance only, the pump, and a downstream throttle, as shown, which is just a resistance. We adopt a simple model of transient pump performance in which we take the pump pressure rise and the difference between inlet and exit mass flow to be functions of the inlet mass flow and the absolute inlet pressure based on the quasi-steady pump performance curves.[14] Note that the model adopted does not imply that the pump inlet and exit mass flows are the same, since as the inlet conditions change, the volume of vapor associated with the cavitation in the pump will also change. If the vapor and the liquid are assumed to be incompressible, it follows from continuity that the difference in mass flow between inlet and exit will be proportional to the rate of change of the volume of vapor in the pump. For small amplitude transients about a mean operating point, we therefore can write the linearized equations for the perturbations in pressure rise and mass flow as [104]:

$$\delta\Delta P_P = \delta P_2 - \delta P_1 = \left(\frac{\partial\overline{\Delta P}_P}{\partial P_1}\right)\delta P_1 + \left(\frac{\partial\overline{\Delta P}_P}{\partial \dot{m}}\right)\delta\dot{m}_1,$$

$$\delta\dot{m}_2 - \delta\dot{m}_1 = \rho\left\{\left(\frac{\partial\overline{V}_c}{\partial P_1}\right)\frac{d\delta P_1}{dt} + \left(\frac{\partial\overline{V}_c}{\partial \dot{m}}\right)\frac{d\delta\dot{m}_1}{dt}\right\}$$

where we have adopted dimensional variables here so as to introduce a minimum of new notation. In these relations ΔP_P is the pump pressure rise, $\dot{m}$ is the mass flow, V_c is the volume occupied by the cavitation, the subscripts 1 and 2 denote pump inlet and outlet (as indicated in Fig. 39), ($\bar{}$) denotes a mean flow condition, and δ denotes a perturbation. In writing the second relation, the continuity equation has been invoked, as described just previously.

Using this representation of the transient pump behavior, one can readily carry out a calculation to determine the stability of the system shown in Fig. 39. It is found that for pumps operating near the design value of ϕ (mass flow), the system will become unstable when $(\partial\overline{V}_c/\partial\dot{m})$, which is referred to here as the mass flow gain factor [109], [110], becomes sufficiently negative (the explicit criterion is shown in the Appendix).

Although the physical arguments leading to this are less apparent than those for the simple pumping system treated in the introduction, a qualitative explanation for this trend can be given as follows. Consider the pump in the system shown in Fig. 39 undergoing oscillatory flow perturbations of small amplitude. Let us examine the behavior of the system as the absolute inlet pressure is reduced, while the mean mass flow and the speed are kept constant. Specifically we again adopt the approach that was used in the Introduction and examine the changes, due to the flow perturbations, in the flux of mechanical energy out of a control volume that encloses the pump. The net difference in this energy flux from that which occurs in a steady flow is given by the integral of the quantity $\{\delta P_2 \cdot \delta\dot{m}_2 - \delta P_1 \cdot \delta\dot{m}_1\}$ over a cycle, where $\delta\dot{m}_1$ and $\delta\dot{m}_2$ are now not necessarily the same. In the system under study the mass flow and pressure perturbations at the pump inlet differ in phase by $\pi/2$, since the pressure perturbations at station 1 are due only to the inertance of the inlet line. Thus if we consider the system over a full cycle, their product is zero and we need only look at the first term.

In the non-cavitating regime (high cavitation number) this term is negative and the situation is similar to that shown on the right hand side of Fig. 6. However, as the pressure is decreased and cavitation becomes more extensive, the inlet and exit mass flows can become different. Conditions favorable for instability will occur as the exit pressure and mass flow fluctuations become closer in phase so that their product (integrated over a cycle) becomes larger.

Within the context of the simple model described above,

[14] We could also include the possibility of pressure change across the pump due to inertance *within* the pump. However, as shown in the derivation given in the Appendix, this does not change the qualitative features of the phenomenon. Since we wish to keep this introductory discussion on as basic a level as possible, it is omitted here.

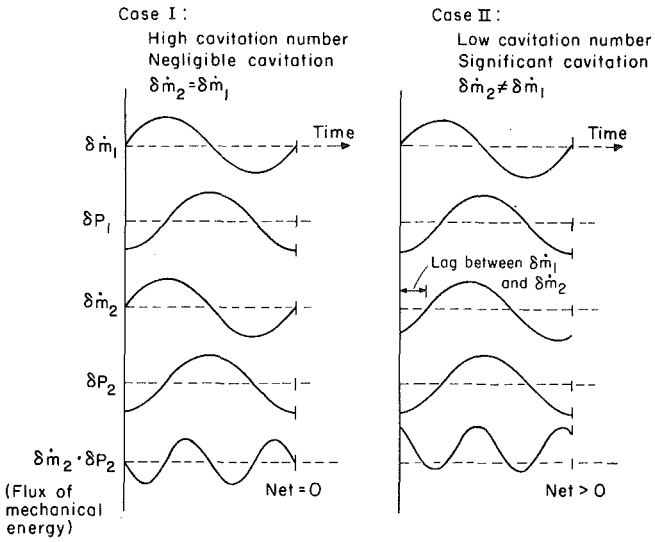

Fig. 42 Mechanical energy flux due to mass flow gain in cavitating inducer

changes in exit pressure are due to two effects, one associated with the change in pump pressure rise as inlet mass flow is changed and one due to the changes in the inlet pressure. However, within the context of the simple model described here, the flux of energy associated with the first part is negative, i.e., this effect is stabilizing. It is thus the pressure changes due to changes in inlet pressure that are associated with the destabilizing mechanism. Let us therefore focus *only* on the change in exit pressure due to a change in inlet pressure. For conditions above the so-called head breakdown (the point where the steady-state curve of pressure rise versus cavitation number becomes steeply positively sloped), which is in the region of interest for auto-oscillation, variations in the inlet pressure will be fairly closely reflected in variations in the exit pressure since $(\partial\overline{\Delta P}_p/\partial P_1)$ is small. Thus if the exit mass flow fluctuations start to lag those of the inlet, due to an increase in the magnitude of the mass flow gain factor as the inlet pressure level drops, they will be more and more in phase with the exit pressure fluctuations.

This situation is shown schematically in Fig. 42, where the pump inlet and exit mass flow and pressure perturbations ($\delta\dot{m}_1$, $\delta\dot{m}_2$, δP_1, δP_2) and the product $\delta P_2 \cdot \delta\dot{m}_2$ have been plotted versus time. It should be stressed that the figure represents only that part of the pressure perturbation due to variations in inlet pressure, and effects of the quasi-steady pump pressure rise and of pump inertance are not included. The figure at the left shows the situation at high cavitation number where the mass flow gain factor is negligible. There is no net flux of energy over a cycle. In contrast, the figure at the right shows the situation at low cavitation number (but above head fall-off) where there is an appreciable mass flow gain factor. It is seen that the exit mass flow now lags the inlet mass flow and the product of $\delta P_2 \cdot \delta\dot{m}_2$ over a cycle is positive. The situation that is needed for instability is thus a large enough lag between inlet and exit mass flows so that the outflux of mechanical energy due to this effect is great enough to offset the net decrease in mechanical energy due to the pump operating in the negatively sloped region of its characteristic as well as the dissipation occurring in the throttle. (It should be noted that the figure pertains to the net flux of mechanical energy associated with the *pump only* and not with the overall system.) From these arguments it therefore appears that the role of the mass flow gain factor which sets this lag, is a key one in determining the instability of the system.

One further result can also be extracted from the stability analysis based on this simple model. This is the determination of the natural frequency of the system. It is found that for a given cavitation number the square of the natural frequency is proportional to $1/[\partial\bar{V}_c/\partial P_1]$ (the actual expression is given in the Appendix). If we write this in terms of cavitation number and pump rotor speed, we find that the square of the frequency scales as $\omega^2 \propto [U_t^2/(\partial\bar{V}_c/\partial\sigma)]$; in other words, for a given system at a given mean value of ϕ_t and cavitation number, the natural frequency for small oscillations scales linearly with speed. This is in direct contrast to the behavior in the single phase system studied previously, where the natural frequency of small amplitude oscillations was independent of rotor speed, being set only by the physical *system* parameters. The reason for this is that the pressure "compliance" of the system $(\partial\bar{V}_c/\partial P_1)$, which plays a role analogous to the spring constant, decreases as the blade speed increases, since a fixed increment in inlet absolute pressure changes the cavitation number less and less as the speed increases.

The simple model has been used to demonstrate the idea of mass flow gain factor and the strong effect it can have on stability. However it should be again emphasized that this shows only one type of destabilizing mechanism and that there are other effects not accounted for by this treatment. In particular we can anticipate the experimental results on transient pump performance to be described subsequently, and note that the data shows that the mass flow gain factor has an imaginary part as well. If this occurs, then the expression for $\delta\dot{m}_2$ would have a term that was 180 degrees out of phase with $\delta\dot{m}_1$. Hence the net flux of mechanical energy out of the pump which is associated with the pressure rise/mass flow characteristic of the pump could be positive, or at least less negative (even though the quantity $(\partial\overline{\Delta P}_p/\partial\dot{m})$ is negative), and may also contribute to the destabilization of the system.

C. Dynamic Performance of Cavitating Pumps. Using the simple idealized system as a model we have been able to discuss *qualitatively* some of the relevant features of the basic fluid mechanics of the instabilities that occur in cavitating turbopumps. However, for more quantitative prediction of these oscillations one must use a more precise description of the pump dynamic performance. A useful approach to developing such a description has been taken by Brennen and Acosta and their co-workers [109], [110], [111], [112]. This approach makes use of the idea of a transfer matrix representation of the pump performance to relate the quantities at the inlet and exit of the pump. Although the approach assumes that the system transients are small enough in amplitude so that a linearized description of the motion can be adopted, it has proved of value in clarifying the nature of dynamic performance of cavitating pumps.

The concept of transfer matrix has been used for some time in the analysis of linear electrical and mechanical four-pole networks [113], [114]. Although this technique provides no new information compared to writing down the dynamic equations which describe the system behavior, it does provide a compact and convenient manner in which to approach dealing with complicated networks. To understand this approach, let us consider a system undergoing small amplitude oscillations at a given frequency. Let us also assume, as is often the case, that for the transients of interest the relevant nondimensional perturbations in mass flow and pressure are much larger than the rotor speed changes. We can represent the *perturbations* in flow variables by the real parts of quantities of the form $\delta P = \hat{P}\, e^{i\omega t}$, where ω is the frequency and $\hat{P}$ is possibly complex.

The relation between inlet and outlet pressure and mass flow perturbations δP_1 and $\delta\dot{m}_1$, δP_2 and $\delta\dot{m}_2$, can be expressed as

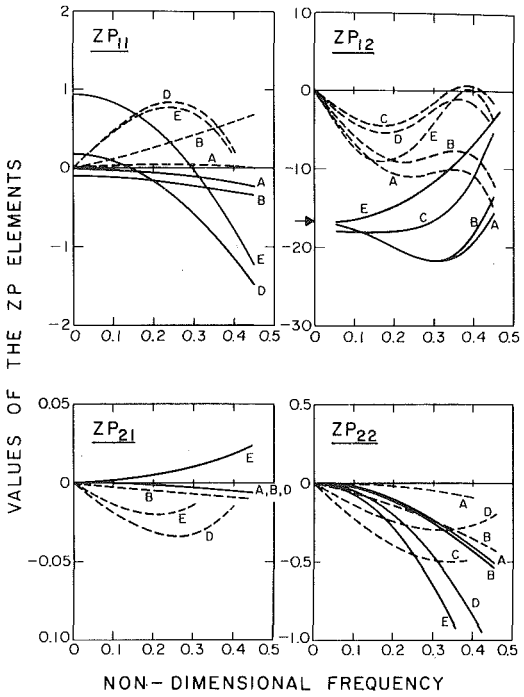

Fig. 43 Curve fits to experimental transfer matrix for pump impeller showing effect of cavitation; ϕ = 0.07, σ = 0.51(A), 0.11(B), 0.046(C), 0.040(D) and 0.023(E). The solid lines indicate the real part and the dashed lines the imaginary part. The quasi-static resistance is indicated by the arrow [108], [111].

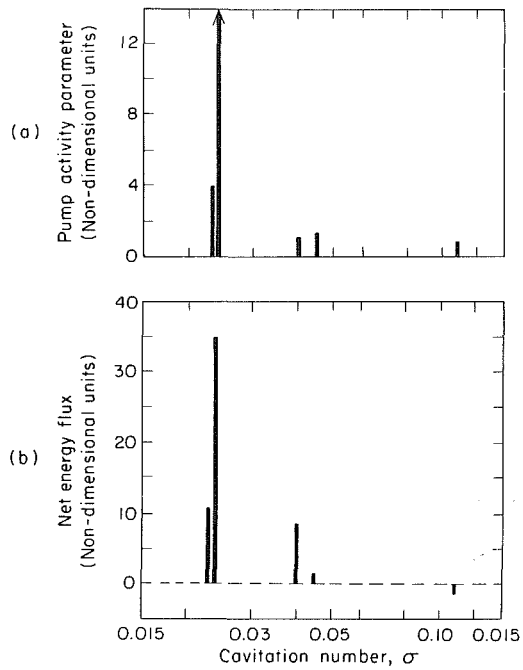

Fig. 44 Effect of cavitation number on pump activity parameter and net system energy flux [108]

$$\begin{bmatrix} \delta P_2 \\ \delta \dot{m}_2 \end{bmatrix} = \begin{bmatrix} M_{11} & M_{12} \\ M_{21} & M_{22} \end{bmatrix} \begin{bmatrix} \delta P_1 \\ \delta \dot{m}_1 \end{bmatrix}$$

where the M_{ij} are the transfer matrix elements.

Such a representation can be carried out for each element of a pumping system. As an example, if we were to examine quasi-steady transients in a regime where cavitation was not important, we could represent the pump performance as

$$\delta P_2 = \delta P_1 + \left(\frac{\overline{d\Delta P_P}}{d\dot{m}}\right)\delta \dot{m}_1$$

(where $[\overline{d\Delta P_P/d\dot{m}}]$ is evaluated at the mean flow conditions) to first order in the perturbation amplitudes. The transfer matrix corresponding to this situation would therefore have $M_{11} = 1, M_{12} = (d\Delta P_P/d\dot{m}), M_{21} = 0, M_{22} = 1$. Note that even for this simple situation, the elements in the transfer matrix depend on the mean operating point of the system, and that, in general there will also be a dependence on the frequency of oscillation.

The forms of these transfer matrices have been examined theoretically and experimentally for a cavitating pump (a rocket pump impeller) in references [106], [109 - 112]. The results are typified by Fig. 43 which shows polynomial curve fits[15] to the measured pump transfer matrix for a particular impeller [108], [111] (the one whose performance is shown in Figs. 40 and 41). The four sets of curves are for the four elements of the transfer matrix. Within each set, the curves are plotted as functions of nondimensional frequency. The different lettered curves correspond to different cavitation numbers, as given in the figure caption, and the solid and dashed lines indicate the real and imaginary parts of the elements. All data are taken at a mean value of ϕ_t = 0.07, corresponding to the pump design flow. In examining this figure, it should be noted that the definition of the matrix elements is different than that given previously, since the pressure and mass flow differences across the pump, not the absolute output pressure and mass flow, have been taken as the output variables, and the variables have all been nondimensionalized. In addition it should be remembered that these are fits to the original dynamic data and hence subject to experimental uncertainty. The magnitude of the "error bars" can be seen in [110]; these have not been plotted on Fig. 43 for reasons of clarity.

The important point is that there are large differences in the forms of the curves as the cavitation number is reduced (curve A corresponds to a condition of negligible cavitation, while curve E corresponds to extensive cavitation, with the other curves being representative of conditions between these limits). In particular the element ZP_{22}, which represents the mass flow gain factor becomes increasingly nonzero as the cavitation number decreases. (It can also be seen that it can have an imaginary component, which was not accounted for in the simple model described above and presented in the Appendix.)

D. Transfer Matrix Approach to System Stability. In describing the transfer matrix approach to the stability of systems with cavitating turbopumps, it is useful to briefly discuss some further aspects of its general application to linear systems. In the application of transfer matrices to analysis of linear electrical or mechanical systems, it is common to classify the systems as active or passive, depending on the value of the determinant of the system transfer matrix. Passive systems have transfer matrices with determinant unity (by definition), active systems do not. This concept, however, is not as useful when applied to pumping systems since it does not give an adequate indication of situations in which there are elements in the system which can feed energy into system oscillations, i.e., of situations in which an instability will occur. A primary reason for this is that it is possible to have an unstable pumping system even with an overall transfer matrix having a unity determinant,

[15] In powers of the nondimensional frequency

since one can have an element with negative damping, such as a stalled compressor.[16]

A more useful way to classify whether a system will actually be dynamically active, i.e., capable of supplying energy to small oscillations, is to examine the net energy flux through the various elements and the overall system. This is similar to the approach that we have used in a qualitative manner to introduce the mechanism of instability for the basic pumping system (compressor), as well as in this section for the cavitating turbopump, and which we will refer to again in connection with pressure drop instabilities in two phase flow. It focuses on the net flux of mechanical energy out of the various elements. Brennen and Braisted [115] have used this approach to define several levels of activity for elements in a pumping system, and have described the response of a particular element in terms of a dynamic activity parameter, which is a measure of this net flux of mechanical energy. This can be found for the pump by using the experimentally measured transfer matrices, and [108] and [115] present curves of the dynamic activity as a function of frequency for different cavitation numbers. Figure 44a presents a crossplot of a typical result where we have presented a graph of the activity parameter as a function of cavitation number. The vertical scale in this figure indicates the nondimensional value of the net flux of kinetic energy. All the bars are for a pump mass flow corresponding to $\phi_t = 0.07$, the design point, and are for the same impeller that data were shown for in Figs. 41-43.[17] The convention used is that a positive value indicates a dynamically active element, i.e., one that is feeding energy into the oscillations. It should be noted that the activity parameter is strongly dependent on frequency as well as cavitation number and mass flow, and that the quantity shown in the figure is the maximum occurring at a particular cavitation number. This would be the frequency that characterizes the largest outflux of mechanical energy.

A positive value of the dynamic activity of the pump is a necessary, but not sufficient, condition for system instability, since there can be dissipation occurring in the rest of the system to offset the pump behavior. Thus, to find the overall stability of the system, one must couple the dynamic pump behavior to the rest of the system dynamics, and this can readily be done using the transfer matrix techniques. This was carried out in [116] (see also [108]) where the system that was analyzed is shown in Fig. 45. In this figure, I denotes a nondimensional inertance, C a nondimensional compliance, and Ω the nondimensional frequency. The system is a closed one, but by breaking it at an arbitrary control point and tracing through the various elements, one can evaluate the net

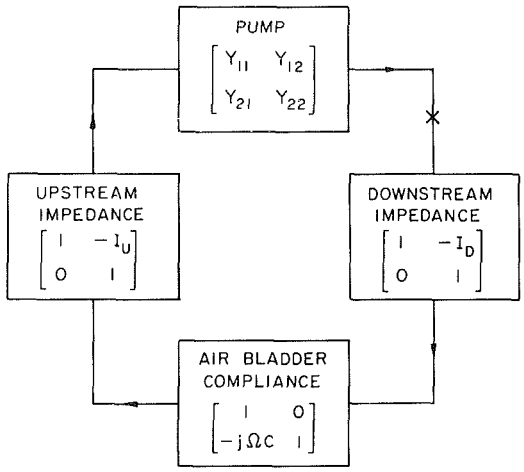

Fig. 45 Transfer matrix representation of overall pumping system [108, 116]

mechanical energy output over a cycle.[18] (In fact, the system studied had a very large compliance supplied by an air bag, so that it could be regarded as an open system to a good approximation). Figure 44(*b*) shows the results of this overall energy analysis, and is again a crossplot of information presented in [116]. It shows the net flux of mechanical energy through the control point as a function of cavitation number. As before, the convention used here is that a positive number indicates a trend toward instability (this is opposite to the convention adopted in [116]), whereas negative values indicate stability. The bars are for the same conditions as described in connection with Fig. 44(*a*), with the vertical axis now being the overall system nondimensional energy flux. Note that it is the value of this quantity, rather than that shown in Fig. 44(*a*), that is directly tied to whether the system is unstable or not, and it is again pointed out that the bars indicate the maximum value (as a function of frequency) for the particular cavitation numbers shown.

It can be seen that the cavitation number plays an important role in determining whether a given operating point will be stable. In addition, the calculations in [108] point to the mass flow gain factor as being the element that most affects the stability of the system, as was suggested by the qualitative arguments presented earlier.

Discussion of the comparison of the stability calculations with the experimentally measured features of the auto-

[16] The dimensional transfer matrix representation of the basic pumping system shown in Figure 1 (inertance, pump, compliance, and throttle) is given by

$$\begin{bmatrix} \delta P_{\text{exit}} \\ \delta \dot{m}_{\text{exit}} \end{bmatrix} = \begin{bmatrix} 1 & -\dfrac{d\overline{\Delta P}_T}{d\dot{m}} \\ 0 & 1 \end{bmatrix} \begin{bmatrix} 1 & 0 \\ -i\omega \dfrac{\rho V_a}{\gamma P} & 1 \end{bmatrix} \begin{bmatrix} 1 + \dfrac{d\Delta P_P}{d\dot{m}} - i\omega \dfrac{L}{A} & \\ 0 & 1 \end{bmatrix} \begin{bmatrix} \delta P_{\text{inlet}} \\ \delta \dot{m}_{\text{inlet}} \end{bmatrix}$$

In this, δP and $\delta \dot{m}$ are the perturbations in pressure and mass flow, ω is the oscillation frequency, $d\overline{\Delta P}_T/d\dot{m}$ and $d\Delta P_p/d\dot{m}$ are the slopes of the throttle and pump characteristic curves, V_a is the compliant volume, L is the effective pump duct length, and A is the through-flow area. The overall transfer matrix is the product of the three above matrices. As can be seen, since the three individual matrices have determinants of unity, the overall matrix will also—whether the pumping system is stable or unstable.

[17] Again, although both 44*a* and 44*b* show calculated quantities, these are based on the experimentally determined pump transfer matrices, and hence have an uncertainty associated with them. This is given in [110].

oscillation is given in [116]. The frequency of the oscillation and especially its dependence on various parameters were predicted reasonably well. The frequency was found to scale with pump speed for fixed value of ϕ_t and σ, as is also

[18] Alternatively, one could use the fact that if one traces *completely* around the *closed* loop from a given point, the "input" and "output" quantities of the *overall* loop transfer matrix are (identically) the same. Application of this condition leads to an eigenvalue problem for the determination of the growth rates of the system perturbations [105].

suggested by the simple model developed in the Appendix. The predictions also were in reasonable agreement with the experimental results as far as the range over which the oscillations are encountered. Measurements of the phase and amplitude of the mass flow and pressure perturbations are presented, and it can be seen that during auto-oscillation there is indeed a lag between the upstream and downstream mass flows. Although other aspects, such as the dynamics of the inlet flow field, are not described as well, the transfer matrix approach appears to be an important contribution to the subject of auto-oscillations in systems with cavitating turbopumps. (As a further note on this technique, it should be mentioned that it has been applied to other types of flow systems as well [117]. As an example, it has been applied to the dynamic behavior of phase changes in such hydraulic systems as the pressure suppression systems in boiling water reactors [118].)

E. Cavitation Induced Instabilities at Off-Design Conditions in Axial and Centrifugal Pumps. The discussion of instabilities associated with cavitating pumps has been so far focussed on flow regimes near design. However (as one might expect) instability is also seen in systems of this sort during "throttled," i.e., low flow, operation. Such phenomena have been described in [119] and [120]. In fact, in many instances it appears that system oscillations can become more severe as the flow is reduced from the design. For example, [120] shows a substantial increase in the oscillation amplitude and in the extent of instability as a function of NPSH[19], as the flow through a combined inducer-impeller was reduced.

In addition, although we have described cavitation induced instability with reference to a specific pump (an axial flow helical inducer) it should be stressed that the occurrence of severe system oscillations due to cavitation are by no means limited to this geometry. They can also occur with centrifugal pumps, and [105] and [121] address the problem of large amplitude, low frequency pulsations in boiler feed pumps, which are associated with the occurrence of cavitation.

Observations of the flow fields in both types of pumps (axial and centrifugal) reveal that during operation at low flows there is a strong backflow in the tip region of the pump [122], [105], [108]. This can give rise to a substantial tangential velocity component in the fluid upstream of the inducer. The inlet flow can also contain a significant cavitation volume *upstream* of the pump and is in general quite different from a simple one-dimensional unsteady slug flow. For example, flow visualization shows that the extent of the upstream prerotation region and the cavitation volume can vary substantially during the surge cycle [105]. Further it has also been found that augmentation of the "prewhirl" upstream of the pump, by injecting high pressure fluid from the pump discharge in a tangential duration has a significant stabilizing effect [105], [119].

The stability of systems in which the pumps are operating at these low flow conditions has also been investigated with a transfer matrix approach, although only basic models of the dynamic pump performance (similar to that presented in the Appendix) have been used [105], [122]. In particular, based on their visual observations of oscillations in a model pump loop, Hobson and Marshall [105] assumed simply that all the cavitation occurred in the inlet region ahead of the pump. They computed stability boundaries and frequencies of oscillation for a representative range of values of pressure compliance and mass flow gain factor; the analytical results again showed the latter to be a strong destabilizing influence.

[19]NPSH (Net positive suction head) is defined as the sum of the total head of the fluid at the location of interest, plus the atmospheric head, minus the vapor head corresponding to the local temperature of the fluid.

Although instability at off design conditions appears to be quite important, the information in the open literature is not very complete, and no real quantitative understanding of this behavior seems to exist.

F. Suggestions for Future Work. The results of studies such as [115] and [116] are very encouraging but there are still aspects of the phenomenon that are in need of further work. One of these topics concerns the dynamics of the flow field in the duct upstream of the pump inlet. As stated this is not a uniform non-dimensional "slug flow" but a region in which high swirl velocities (associated with the backflow through the impeller tip) and cavitation can occur. This is particularly true at low flow coefficients, where the pressure differences across the impeller blades are large. The dynamics of this inlet flow field are suggested to play "a major role in the inducer dynamics and the auto-oscillation phenomenon" [116] and this appears to be an area that should be addressed.

Further understanding is needed of the unsteady behavior of these flows and, in fact, of pumps in the cavitating regime in general. In this connection it is to be noted that the obtaining of detailed experimental data on transfer matrices for a range of cavitation numbers requires considerable effort, and the investigations reported in [116] were therefore limited to the design flow rate. These should also be extended to examine behavior during throttled operation in order to clarify the dynamic response at other conditions than design. Again, as in the discussions of the two previous types of pumping systems, it appears that the calculations of system stability boundaries are very much dependent upon accurate models of the behavior of the active element in the system, and the primary problem at present is in the resolution of the transient performance of these elements.

Another possible avenue of research concerns the nonlinear effects associated with auto-oscillation. The transfer matrix approach is limited to small amplitude transients and is inherently unable to treat these. One result of these effects, with an axial inducer, is the hysteresis behavior in the curve of head coefficient versus cavitation number, in that the performance drops off sharply as one reduces the cavitation number and enters auto-oscillation, and stays at this reduced level until the cavitation number is increased significantly beyond the value at which the drop initially occurred. The area of nonlinear effects is thus another topic for investigation.

V Instabilities in Systems with "No Moving Parts"

The oscillatory flows described so far have involved systems which have turbomachines as the primary pumping element. There are, however, instabilities which can occur in situations not associated with the turbomachinery, and in which the geometry of the essential elements has "no moving parts." One example of these are the oscillations that are encountered in supersonic intake diffusers—in particular the low frequency pulsations which are termed buzz. This occurs in the subcritical (low mass flow) regime, where the steady flow can break down and the terminal shock wave exhibit amplitude excursions in position, from well ahead of the cowl to far down in the subsonic part of the diffuser. These excursions are accompanied by severe fluctuations in mass flow and pressure recovery [123], [124], [125], [126].

These instabilities were of serious concern in some of the early gas turbine engine and ramjet intakes. Many of the difficulties have now been overcome as experience with this phenomenon built up, but experimental investigations of proposed inlet configurations are still required in order to provide accurate definition of the buzz onset point. In particular, considerable development time can be spent to ensure that the buzz regime does not intersect the engine operating

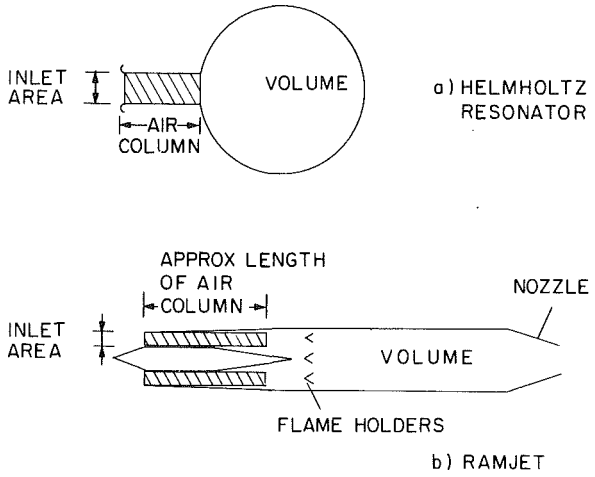

Fig. 46 Helmholtz resonator model of ram jet [126]

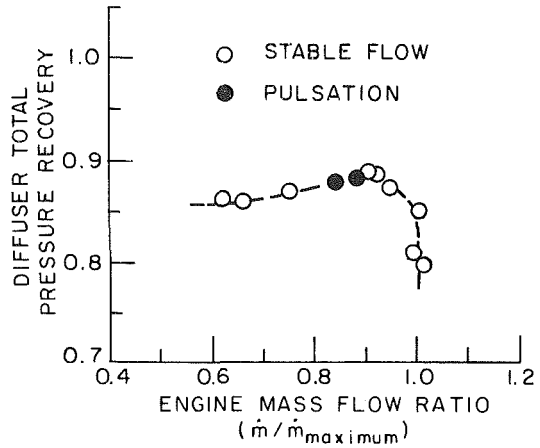

Fig. 47 Flow pulsation regimes in ramjet supersonic diffuser [126]

envelope. In spite of this, the current situation appears to be that enough knowlege has been obtained concerning this problem so as not to warrant a substantial further research effort at present. For this reason we will discuss it only briefly.

Buzz has been studied by several different investigators. One experimental and theoretical investigation was conducted by Sterbentz and Evvard [126], with application to ramjet intakes. They viewed the system of intake/diffuser, burner volume, and nozzle as analogous to a Helmholtz resonator (similar to the approach used to describe surge oscillations in axial and centrifugal compression systems). This concept is pictured in Figure 46, which is taken from [126], and shows the basic model. The relevant "pumping curve" now, however, is the curve of diffuser pressure recovery versus mass flow.

The analysis predicted that in regions where this curve had a negative slope the system would be stable; however, if the curve had a positive slope greater than some critical value, instability would result. These predictions appeared to be in reasonable agreement with the experimental results for the onset of oscillations. As an illustration of this, Figure 47 shows the regimes of flow pulsation (buzz) in a supersonic inlet diffuser on a ramjet model. The curve is of pressure recovery versus mass flow (given as a fraction of the maximum mass flow rate) at a flight Mach number of 1.77. Details of the diffuser geometry are given in the reference. The open symbols show the stable operating conditions and the solid symbols indicate the points at which buzz was observed. It can be seen that, as predicted, no instability occurred on the negatively sloped part of the curve, but that, as the mass flow is decreased, instability does occur at places where the positive slope of the curve is greatest. As the flow is reduced still further, the slope decreases and, in accord with the trends of the theory, the instability disappears.

This basic Helmholtz resonator type of model has also been used by Leynart to describe these inlet oscillations [127]. However, a recent approach to analyzing the phenomenon on a more detailed level has been presented in [128].

Although buzz is the self-excited supersonic flow phenomenon that perhaps most closely fits with the scope of the title of this review, there are a number of other types of self-induced supersonic flow oscillations which occur in a system with non-moving geometry. Many of these are discussed in the review paper by Jungowski [129]. In addition Ref. [130] presents an analysis of the instabilities which occur with supersonic flow past an open cavity. (This last-mentioned instability, in fact, belongs to a wider class of flows both supersonic and subsonic which are susceptible to self-excited oscillations. These are the flows in and near cavity-type geometries, not only in aircraft components as discussed in [130], but also in applications such as slotted wall wind and water tunnels, high head gates, etc. These are reviewed by Rockwell and Naudascher [131], who also survey the closely related problem of oscillations in impinging shear layers [132].)

As a final note on this topic, we can also mention that there are more complex types of systems with "no moving parts," which can exhibit instabilities. We will discuss one example of such a situation, the branched diffuser system, in the section dealing with compound pumping systems.

VI Two-Phase Flow Instabilities

Many of the systems discussed in this review are subject to instabilities that are associated with the pumping element, or at least with a component which raises the pressure of the fluid flowing through it. However, there is also a large class of fluid systems which have instabilities associated with components that are not of this type. Important examples of these are the system instabilities that occur with two-phase flow, especially those in heated pipes or channels. Such instabilities are found not only in forced convection pumping systems, but in natural convection loops as well, and they are of particular importance in, for example, water cooled and water moderated nuclear reactors.

Although not all specifically related to the pumping characteristics, these instabilities deserve mention because of their significance in fluids engineering applications. We cannot discuss all the various types of instabilities that occur in two-phase flow.[20] A listing of some of these is given in Table 2, which is excerpted from that in the review by Boure, Bergles, and Tong [133]. (Note that in [133] and in the later article by Boure [134] these groupings are in fact subdivided even further.) It can be seen that there are a considerable number of phenomena that come under the general heading of two-phase flow system instabilities, and indeed, one of the difficulties in many cases seems to be the identification of the particular mechanism which is at the root cause of the instability. We shall attempt to discuss the fluid- and thermodynamics involved in several of the most basic of these instabilities, concentrating on those which depend on the pumping system characteristics, i.e., pressure drop requirements; it should be noted, however, that two-phase

[20] In this context it can be pointed out that one can compile a fair-sized reference list even if he includes only the review and survey papers on the subject of two-phase flow instability.

Table 2 Types of two-phase flow instability (from [133])

Type	Mechanism	Characteristics
Static instabilities		
1. Flow excursion or Ledinegg instability	Slope of pressure drop curve more steeply negative than pumping (supply) characteristic	Flow undergoes sudden large amplitude excursion to a new, stable operating condition
2. Boiling crisis	Ineffective removal of heat from heated surface	Wall temperature excursion and flow oscillation
3. Flow pattern transition (relaxation instability)	Bubbly flow has less void but higher ΔP than that of annular flow	Cyclic flow pattern transitions and flow rate variations
4. Bumping, geysering, or chugging (relaxation instability)	Periodic adjustment of metastable condition, usually due to lack of nucleation sites	Period process of super-heat and violent evaporation with possible expulsion and refilling
Dynamic Instabilities		
1. Pressure drop oscillations	Flow excursion initiates dynamic interaction between channel and compressible volume	Very low frequency periodic process
2. Acoustic oscillations	Resonance of pressure waves	High frequencies (10-100 Hz) related to time required for pressure wave propagation in system
3. Density wave oscillations	Delay and feedback effects in relationship between flow rate, density, and pressure drop	Low frequencies (1 Hz) related to transit time of a continuity wave
4. Thermal oscillations	Interaction of variable heat transfer coefficient with flow dynamics	Occurs in film boiling
5. BWR instability	Interaction of void reactivity coupling with flow dynamics and heat transfer	Strong only for a small fuel time constant and under low pressures
6. Parallel channel instability	Interaction among small number of parallel channels	Various modes of flow redistribution

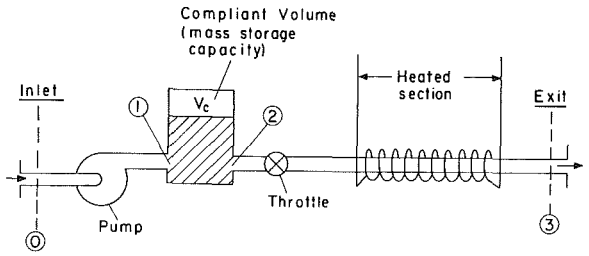

Fig. 48 Two-phase flow pumping system

flow instabilities are an area of considerable research and many problems are still unresolved.

For definiteness consider a simplified open-loop system consisting of a pump and a heated section with a possibility for mass storage due to a compliant volume. Such a system is shown in Fig. 48. The heat transfer portion of this system will typically consist of an electrically or nuclear heated tube (or tubes) with a throttling element (or elements) connected in series with it. The general engineering question that can be addressed is, under what conditions will a nominally steady flow through this configuration change to another flow regime in which conditions are such that there can be an adverse effect on overall performance and/or system life?

A. Flow Transition Due to Boiling Crisis. Perhaps the best known of the flow regime transitions that can occur in a system of this type is the so-called boiling crisis (sometimes referred to as departure from nucleate boiling). The basic situation can be discussed with reference to a typical heat transfer curve for a fluid flowing past a heated surface, as indicated in Fig. 49 [135]. The horizontal axis is the temperature difference between the surface and the bulk fluid and the vertical axis is the heat transfer per unit area. One can divide the different flow regimes that occur into those in which the heat transfer is by convective processes, i.e., nonboiling regimes, and those in which boiling becomes the primary agent. Although the factors of liquid subcooling and fluid velocity affect the absolute value of the heat transfer, the general shape of the curve will be similar whatever the values of the parameters. The region between A and B is that in which nucleate boiling occurs. In this process, the evaporation takes place at nucleation sites on the surface. Heat is transferred directly to the bulk liquid, and the conversion of liquid to vapor is responsible for only a small part of the total heat transferred. As the temperature difference is increased, the heat flux and vapor production increase until (at temperatures corresponding to point B) the vapor which forms next to the surface starts to significantly interfere with the heat transfer to the liquid. Further increase in the temperature difference causes the production of a greater concentration of vapor near the surface with the consequent *decrease* of the heat flux. At point C the surface is essentially blanketed by a vapor film (thus the name "film boiling") and heat transfer takes place through this film rather than by direct liquid-solid contact. Because of the insulating effect of the vapor film, the heat transfer coefficients that occur during film boiling are generally much lower than those found in nucleate boiling. As the temperature difference is increased from $\Delta T(C)$, the heat transfer once again rises, with radiation becoming more important as higher temperatures are reached.

It can be seen that the heat transfer curve passes through a local maximum at point B. If one is operating at this point and a small perturbation (increase) in heat flux occurs, the result will be that the heat which cannot be transferred away at that wall temperature goes into increasing the wall temperature. However, this permits even less heat transfer and the system undergoes a rapid transient until a new stable operating point is reached, at point D. Unfortunately in many situations, especially those using water as the cooling liquid, this temperature is above the heat transfer surface melting temperature and the system fails. Thus this type of instability is often known as burnout. The occurrence of this phenomenon is a matter of great interest to designers of boiling heat transfer systems, and there is a great deal of literature on the prediction of this point. Two recent survey references are [136] and [137].

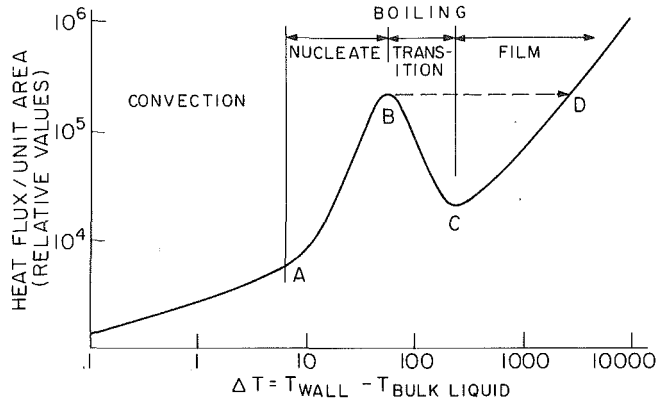

Fig. 49 Representative boiling heat transfer curve

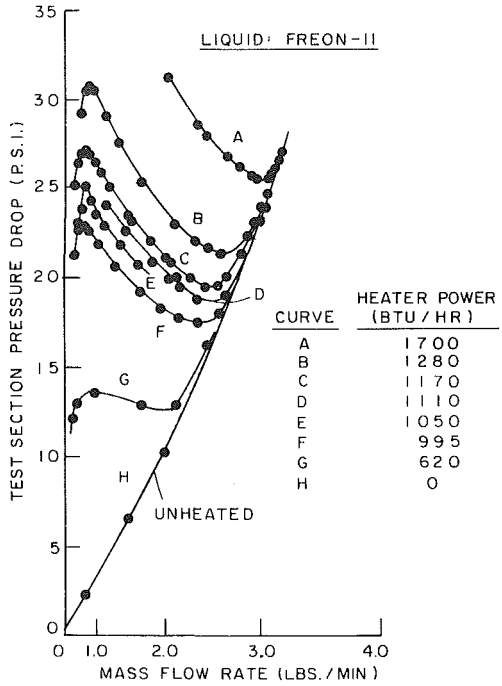

Fig. 50 Pressure drop - flow rate curves for two-phase flow in heated tube (steady-state measurements) [139]

This static instability has been mentioned because of its technological import, but it is not really directly connected with the overall pumping system characteristics and we will therefore not discuss it in any greater depth. There are, however, other types of instabilities which occur with two-phase flow systems which are also of major importance and which are closely related to the system characteristics. These are pressure drop instabilities.

B. Pressure Drop Instabilities.

1. Negatively Sloped System Resistance Curves in Two-Phase Flow. As will be seen in the next section, pressure drop instabilities occur due to negatively sloped pressure drop versus mass flow (system resistances) curves. Before considering the instabilities themselves, it is thus useful to examine the situations which give rise to this type of system characteristics. Following the presentation given by Griffith [138], we consider gas-liquid two-phase flow in a tube. The overall static pressure difference between two stations can be viewed as being composed of three different components—friction, momentum, and gravity.

$$\Delta P_{\text{overall}} = \Delta P_{\text{friction}} + \Delta P_{\text{mom.}} + \Delta P_{\text{gravity}}$$

In certain physical situations, it is possible for each of these terms to increase with decreasing flow. We can examine examples of each of these.

In most cases, the frictional component of the pressure drop increases with increasing flow. One significant exception is that of subcooled boiling at relatively high heat fluxes. Consider flow in a heated tube with heat flux, exit pressure, and inlet temperature held constant. At very high flow rates, no surface boiling will be required to transfer the heat, and the pressure drop may be calculated from single phase correlations. As the flow rate is reduced, local boiling begins at the downstream end and then moves upstream with further flow reduction. A considerable fraction of the tube length can be boiling with large bulk exit subcoolings. At these conditions, the void fraction is quite small as is any momentum pressure drop.The rapid growth and collapse of bubbles near the heated surface, however, will increase the wall shear stress so that a decrease in the flow results in the pressure drop curve passing through a minimum with a consequent negatively sloped region.

A negatively sloped region can also be due to the momentum pressure drop. In a steady flow, with constant mass flow rate down the tube, an increase in void fraction will lead to an increased momentum flux and an associated momentum pressure drop. This may come about because of heat addition or because of decreasing pressure level in an adiabatic situation. Again, considering flow in a tube with constant heat flux, a reduction in the flow rate will result in a higher exit quality (vapor mass flow fraction). If the operating point is in a region where small quality changes lead to a large change in the void fraction, an increased momentum pressure drop may result.

Other situations in which the pressure drop can increase with reduced flow occur because of the pressure gradient due to gravitational effects. For a flow in a vertical tube, say, the overall pressure drop between two stations will depend on the gravitational head difference (as well as the effects discussed in the previous paragraph, which are associated with the motion of the fluid). In the case of an upward flow this head difference represents a pressure drop. For an air/water flow, an increase in air flow at constant water flow would give a higher void fraction and a reduced gravitational pressure drop. For a downward flow situation (i.e., a downcomer) the hydrostatic head difference represents a pressure rise in the flow direction. In a downcomer with heating, a flow reduction at constant heat input will result in a higher average quality (lower density) and hence a decreased hydrostatic head. The possibility thus exists here also for an increase in the overall pressure drop as the flow rate is reduced.

A not uncomonly encountered situation in two-phase flow, therefore, is a pressure drop versus flow curve that has a minimum and hence a negatively sloped region. An illustration of this is seen in the data of Figure 50, which shows pressure drop versus flow at different heat flux levels for a heated tube (plus valves) [139]. The different lettered curves correspond to different heat flux levels, and it can be seen that as the heat flux is increased there can be a substantial region in which the curves have a negative slope.

2. Qualitative System Stability Considerations. Let us now examine the consequences of the type of pressure drop versus flow curve shown in Fig. 50 on system stability.[21] As a first step let us superimpose this type of system pressure requirement (based on constant heat flux) on some typical

[21] It is to be emphasized that although we use the heated system of Fig. 50 as our primary example, the occurrence of pressure drop instability is not restricted to this situation only, as will be discussed below.

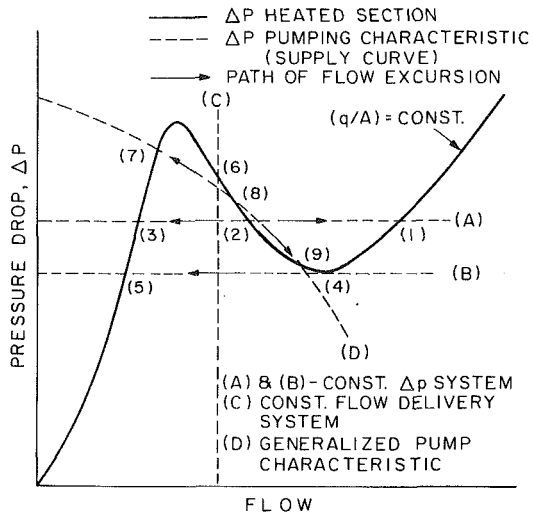

Fig. 51 Pressure drop static instability in forced convection flow with subcooled boiling [140]

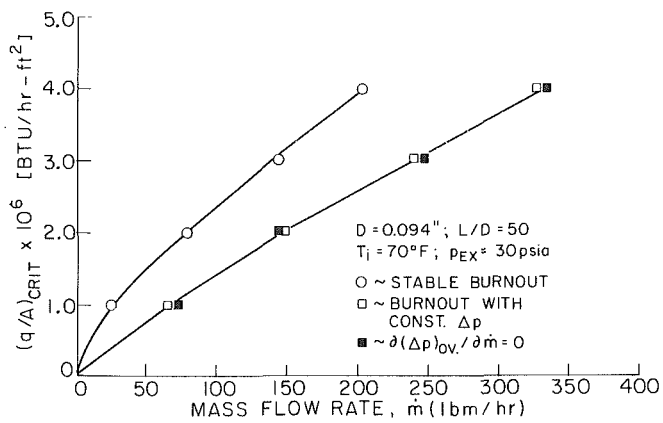

Fig. 52 Critical heat flux versus mass flow rate for constant pressure drop system [140]

pumping curves. These are presented in Fig. 51, from [140], which shows a representative pump curve (D), two lines corresponding to constant pressure delivery systems, (A) and (B), and a curve for a constant flow system (C). The constant pressure situation could occur if the tube were one of a large number of tubes, connected at inlet and outlet to headers. It is evident that point 2 is statically unstable since a slight increase (or decrease) in flow leads to circumstances in which pressure imbalances tend to magnify the initial perturbation, leading to operation at point 1 (or 3) respectively. If one in fact examines the stability of an arbitrary intersection of pump and heating section characteristics (points 8 or 9), it can be seen that the criterion which describes the static stability is that the pump characteristic must be steeper than the system pressure drop requirement for stable operation. Thus although point 8 would not be a stable point, point 9, which is on a less steeply sloped portion of the negatively sloped part of the curve, would be statically stable. For a system with a constant imposed pressure drop, this implies that the onset of static instability is right at the minimum point (4), whereas for a system in which the flow rate is maintained constant (by a displacement pump, say) there are no regions of static instability on the curve.

A serious consequence of this instability can be that the flow rate at point 3, say, occurs at a condition such that the heated section is at an excessive temperature so that the system fails. An illustration of this is given in Fig. 52. This shows the critical heat flux (burnout point) versus mass flow rate for heated tubes in two types of systems [140]. One system had a constant flow delivery while the other maintained an essentially constant pressure drop across the section. The burnout points obtained with the first (which can be referred to as stable burnout) are indicated by the open circles. The points obtained with the second are shown by the open squares, with the solid squares indicating the predicted point of excursive instability (the minimum of the pressure drop/flow rate curve). It can be seen that in this instance the excursive instability leads to a practical burnout limit which occurs at heat fluxes that are approximately one-half those obtained in a stable system.

This static instability is well known and is referred to as the Ledinegg, or excursive instability. However, there is also another type of pressure drop instability, which is a dynamic instability and leads to an oscillatory situation. (Note that the static instability pictured in Figure 51 cannot by itself lead to an oscillation.) To analyze this, Maulbetsch and Griffith [140] considered a lumped parameter model of the heated channel, which included the mass storage capability inherent in such heating sections. Using this model they derived a criterion for the onset of dynamic pressure drop instability and they were able to experimentally verify their predictions. Their system had a large mass storage capability in it, so that the point of dynamic instability occurred very near the minimum of the pressure drop versus flow curve. In their system the onset of instability led to failure of the heated section. Hence for a system of this type the dynamic instability point would also be the practical burnout limit, which could occur considerably below the heat fluxes that could be achieved if the system were stable up to the true burnout (boiling crisis) point.

A simple analysis of pressure drop instability is presented in the Appendix. However, the physical mechanism associated with this type of dynamic instability can be understood by examining the transient behavior of the system from an energy standpoint, in a manner similar to the approach used in the Introduction to describe the dynamic instability of the basic pumping system. Therefore let us suppose that the system shown in Fig. 48 is undergoing small amplitude oscillations about a given operating point 0. For definiteness, we take the system inlet and outlet pressures and the heated section heat input to be constant.

Let us now examine the overall production of mechanical energy associated with each of the system elements for a complete cycle of the oscillations. As with the pumping system the inertances and capacitances will not give rise to any production of mechanical energy. In addition, since we can consider the pump to be operating near design, i.e., on the negatively sloped part of its characteristic, the unsteady flow through both the pump and the throttle will result in an increased level of dissipation (or decreased energy addition) compared to the situation with steady flow through the system. The only element that is capable of feeding energy *into* the oscillations is thus the heated section.

Therefore consider now the oscillating flow in this section in two cases, namely a situation where the operating point 0 is on the negatively sloped part of the pressure drop versus flow curve, Case I, and a situation where it is on the positively sloped part of the curve, Case II, as shown in Fig. 53. In the figure the *perturbations* in heated section mass flow, $\delta\dot{m}$, and in heated section pressure drop, $\delta\Delta P$, are plotted versus time as is their product, $\delta\Delta P \times \delta\dot{m}$. The integral of this product over a cycle is just the excess of dissipation of mechanical energy in the heated section compared to the steady-state situation. The plots show one complete period. It can be seen that, with the positive slope (Case II, on the right-hand side) the heated section is just another resistance, and increased dissipation occurs. However, with operation in the negatively

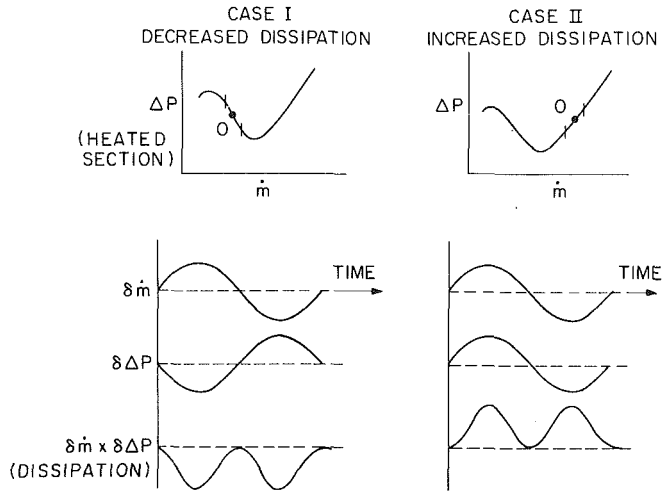

Fig. 53 Physical mechanism for pressure drop dynamic instability

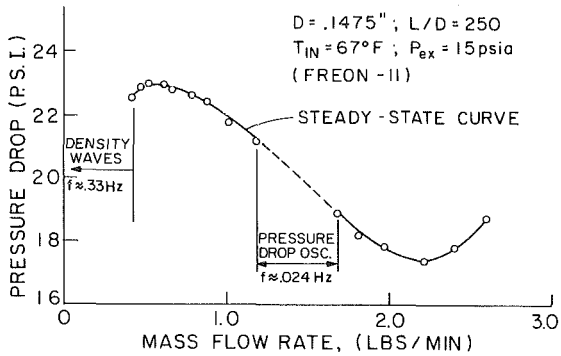

Fig. 54 Regimes of instability in two-phase flow [131]

sloped part of the curve (Case I) there is a lower value of dissipation than in the steady case. This deficit in dissipation is equivalent to a net production of mechanical energy. Put another way, one could think of the dissipation occurring in Case I as analogous to that associated with the product of *negative* damping force and velocity in a mass/spring/damper system.

Since the pressure is constant at the inlet and outlet of the system there is no net outflow of mechanical energy. Hence the *net* amount "produced" by the oscillatory flow in the heated section minus that dissipated in the pump and throttle will appear as either an increase or a decrease in the mechanical energy of the oscillations. (Note that the role of the heat transfer itself is only to create the conditions needed for a positive negatively sloped curve—it does not enter into the system mechanical energy balances described here.) Paraphrasing the summary of the mechanism of dynamic pump instability given in the Introduction, we can therefore state that dynamic instability can occur in the system pictured in Fig. 50, when the dissipation of mechanical energy in the heated section is less during the oscillatory flow than during a mean (steady flow) and this can only occur if the pressure rise versus flow characteristic is negatively sloped so that high mass flow and low mechanical energy dissipation per unit mass flow go together.

It should be stressed that the preceding has served only to describe qualitatively the basic fluid mechanics which lead to those conditions necessary for the onset of dynamic instability. To find the conditions which are also sufficient, i.e., to find the specific system operating point at which the increased dissipation in the pump and throttle will just balance the decreased dissipation in the heated section (this situation marks the boundary between stability and instability) one must carry out a quantitative calculation of the transient response of the system. A calculation of this sort for an idealized system is given in the Appendix. The results of the stability analysis show that for a given system with specified inertances, capacitances, etc., there is a critical value of slope of the pressure drop versus flow curve that is necessary for instability. Thus, as one decreases the mean flow through the system and moves toward the (local) maximum of pressure drop, it might be anticipated that the system would once again become stable. This was also found by Stenning and Veziroglu [141], as shown in Fig. 54, where the regions of different types of instability are indicated. It can be seen that there is a finite region in which the pressure drop oscillation persisted; however, at lower (or higher) flows the system was stable. Decreasing the flow past the local maximum brought with it another type of instability known as density waves, which will be discussed in a subsequent section. Although the frequencies shown are specific to the system studied, the trend (of the pressure drop oscillations having a much longer period than the density oscillations) is a general result.

Whether the pressure drop instability is static or dynamic, one remedy can be to increase the system pressure drop. For the static instability, the additional throttling can be anywhere within the system (i.e., anywhere between stations 0 and 3 in Fig. 48). On the other hand, for the dynamic instability, the throttling should be such as to increase the pressure drop in the "heated section," i.e., should be between stations 2 and 3 in the figure. Throttling at the location indicated in Fig. 48, for example, would thus be useful for suppressing dynamic instability in the system illustrated. However, if the internal mass storage capability of the system is due mainly to the inherent compressibility of the vapor phase, as it might be in a long heated section where there can be significant capacitance *within* the section, this remedy may not be effective. In addition, for the dynamic instability, changes in parameters that tend to decrease the system compressibility (compliance) are also a stabilizing influence. There is not scope in this review to discuss this topic further, but additional information, including numerical studies of the instability, can be found in [142], [143]. Other useful (review) articles on the general topic of two-phase flow instability are [144], [145], [146], [147].

3. Limit Cycle Oscillations due to Pressure Drop Instabilty. The experimental system used by Maulbetsch and Griffith [140] made use of water as the heat transfer fluid. Consequently, data could not be obtained on the behavior of the large amplitude oscillations that occur subsequent to this initial instability. Stenning, Veziroglu, and Callahan [139] also investigated this phenomenon using Freon 11. The considerably lower heat transfer rates and temperatures encountered with this liquid meant that they could study the nonlinear system behavior as well. Their investigation showed several main points, among which was that the dynamic instability can lead to the occurrence of nonlinear, limit cycle oscillations in the pressure rise and mass flow through the heated tube. An illustration of these is shown in Figure 55. The axes are mass flow rate and pressure drop, and the times (in seconds) during the cycle are indicated. A typical period for the apparatus used was on the order of a minute. These cycles are analogous to the surge cycles found with compressors in that their features are determined by global system properties rather than by the properties at one point. Analysis of this nonlinear behavior was also carried out in [139] and qualitative agreement was obtained between the predicted trends and those found in the experiments.

Investigations of the nonlinear limit cycle oscillations that occur as a result of pressure drop instability have also been described in [148] and [149]. The first of these used a heated

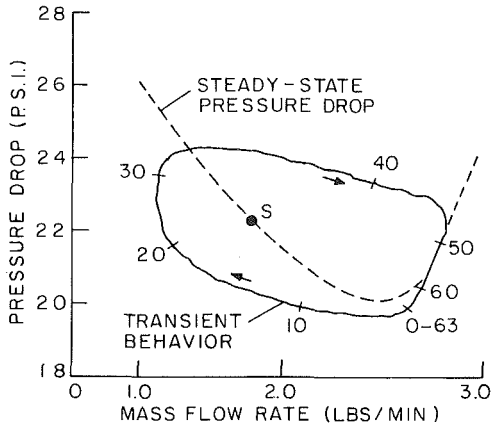

Fig. 55 Limit cycle oscillation due to pressure drop dynamic instability [141]

test section apparatus along the lines of those in [139] or [140]. However, in the second, the two-phase flow was composed of a mixture of air and water (i.e., there was no heated section), with the flow rates of each being independently controlled. By varying the relative rates of the two components it was possible to obtain a pressure drop curve with a negatively sloped region. The oscillations obtained in this facility were similar to those obtained with the heated section experiment.

The experimental facility as described in [138] had a compliant volume in the system whose size could be varied, and a set of experiments were carried out to assess the effect of volume size on system behavior. It was found that as the volume was increased the limit cycles would have substantially larger swings in flow rate, directly analogous to the situation that occurs with limit cycles in compression systems. (Compare Fig. 7 or 8 of [149] with Figs. 8-12 of [32], for example.)

Theoretical studies of the transient system behavior were also carried out in [148] and [149] using nonlinear lumped parameter models. The curves of pressure drop versus flow were approximated by cubics. This led to an equation for the system flow rate which was somewhat similar to the van der Pol equation, and in fact reduced to the van der Pol equation for the important case of the (unstable) system equilibrium point being situated symmetrically with respect to the local maximum and minimum of the pressure drop curve. This is of interest in view of the previous discussions of some of the work carried out on compression system limit cycles (references [63]-[65]) and can be taken as yet another indication of the strong similarities that exist between the dynamical behavior of many of the systems that are considered in this review. The results of the analysis were found to be in reasonable agreement with the experiments.

There is one further point that can be remarked upon in connection with [149]. In the equations developed to model the system behavior, a non-dimensional parameter occurs which is similar in form to the B parameter previously discussed in the section on compressor stability. Increases in volume correspond to increases in this parameter. It should not therefore be surprising that the swings in flow rate during the limit cycles become larger as this parameter is increased.

C. Density Wave Oscillations. Pressure drop instability is related directly to the system resistance characteristics, and thus has been described in some detail. There is, however, another class of instability which is common in two-phase flow systems and which should also be mentioned. This is the so-called density wave oscillation (sometimes referred to as "flow-void feedback instability" or "time delay instability").

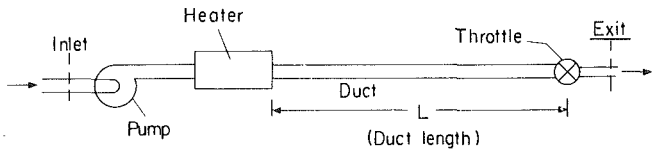

Fig. 56 Idealized two-phase flow pumping system model for illustration of density wave oscillations

A presentation of the salient features of density waves has been given by Stenning and Griffith [150] and the following description is based on that reference. Consider the system shown in Fig. 56, consisting of a short heated section followed by a duct, at the end of which is a flow restriction (throttle). Assume that the heat input is constant, that fluid enters the heated section as a liquid and leaves as a saturated or superheated vapor, and that all of the system pressure drop occurs across the throttle.

If the pressure drop across the throttle is small compared to the absolute pressure level in the system, then the volume flow rate in the exit duct is proportional to $A_r \sqrt{\Delta P_r/\rho_r}$, where A_r is the area of the restriction, ΔP_r is the pressure drop across the restriction, and ρ_r is the density of the fluid at the restriction. If the system is operating at a steady state and the throttle area is decreased slightly, there will be a reduction in system flow rate.[22] With constant heat input, the enthalpy of the fluid leaving the heated section will increase and the density ρ_e leaving the heated section will decrease. Hence after a time L/C equal to the transport time of a particle from the evaporator to the restriction (L is the duct length between heater and throttle, C is the fluid velocity), the density ρ_r at the restriction will drop. When this occurs, the volume flow rate through the system will rise, the density ρ_e of the fluid leaving the heated section will increase, and after another time interval L/C the density ρ_r will change again at the restriction. Depending on the characteristics of the system, the transient may damp out or amplify to a finite amplitude oscillation and the resulting (density wave) oscillations will have a period which is roughly equal to twice the residence time of a particle in the system.

The particular arrangement of the system used in the simplified discussion given above is not essential for the existence of density-wave instability. The flow resistance may be distributed throughout the heater, an exit duct is not essential, the fluid may leave the heater as a mixture of liquid and vapor, and the heat transfer into the fluid may be a complex function of the fluid properties and the mass flow rate. In each case, there will be some critical power level above which density-wave oscillations will appear. The essential ingredients which combine to produce density-wave instability are (*a*) a density distribution throughout the system which depends on flow rate, (*b*) a time delay between flow rate change and density response and, (*c*) a relationship between heater pressure drop, flow rate and density distribution. Density-wave oscillations can occur when a gas is bubbled into a flowing liquid, or even when a very light liquid is injected into a heavy liquid. Note that the above requirements can be satisfied by a single-phase as well as by a two-phase system, and density-wave oscillations have been observed in fluids at supercritical pressures. They may also occur in heating of gases at subcritical pressures if the volume change is sufficient. It should be emphasized that the simple mechanism for the initiation of oscillations, which is described in the foregoing, does not depend on the compressibility of the vapor or on inertial effects. The waves are

[22] One could make analogous arguments based on small flow perturbations due to other causes as well as the one mentioned.

thus examples of continuity (or kinematic) waves. (An introductory discussion of this type of wave is given in [151].)

This type of oscillation is a quite commonly encountered instability in systems with two phase flow. As a consequence it has been widely studied, and various models have been developed to analyze the phenomenon. These range from simple, lumped parameter, homogeneous flow models, which treat the mixture of liquid and vapor downstream of the heater as a homogeneous fluid with some average density, to models which treat the two phases separately, allow a slip between them, allow nonuniform and/or non-constant heat input, as well as account for a non-equilibrium situation existing between the liquid and vapor. A detailed description of the latter type of model is given in [147]. Other good descriptions of this work, as well as useful bibliographies, are given in the reviews cited previously [133, 134, 145]. These mention many of the specific computer codes that have been developed to analyze the onset of density waves.

Although we will not enter into a discussion of the assumptions used in the various models, it is useful to present a summary of some of the main conclusions that have emerged out of the work on density waves. In particular what we can describe are the overall effects on stability of changes in the parameters that characterize system operation. As a start, it should be noted that a large number of non-dimensional parameters are needed to define the operating conditions of a given system. For example, for a basic system of given geometry, which is a heated tube with throttles at either end, Ishii [136] derives six non-dimensional parameters, in addition to the inlet and outlet throttle pressure drop coefficients, that are needed to characterize the system operation.

For constant system pressure and inlet velocity with fixed geometry four of these parameters are fixed and the stability boundary can be plotted in a plane involving the two remaining parameters. The two parameters used by Ishii (an alternative set of parameters has been developed by Boure [133]) are the subcooling number N_{sub}, which is proportional to the inlet subcooling, and the phase change number N_{pch} which scales the phase change of the system. The first of these parameters is essentially a measure of the "time lag" effects (between entrance and the inception of bulk boiling) due to subcooling of the fluid entering the heated section of the duct. The second is related to the time to vaporize a unit amount of the fluid compared to the through-flow transit time. (The two parameters are defined explicitly in the Nomenclature section.)

Ishii carried out stability analyses of this type of system for various conditions and presented the results in an N_{sub}, N_{pch} plane [147]. (One interesting point is that the equations describing the system response have time delays in them, and are similar to the equations that one finds when analyzing combustion instability in liquid rocket motors, as discussed in the next section.) Figure 57 shows a schematic of the stability results. The horizontal axis is the phase change parameter, N_{pch}, and the vertical axis is the subcooling parameter, N_{sub}. The region of interest is as indicated since the amount of subcooling is bounded by the freezing point, and the exit quality is between 0 and 1. On this plane a constant exit quality line is a straight line parallel to the $X_e = 0$ line. A typical region of instability is also indicated on the map. For detailed quantitative results, and for calculations of the effects of the other nondimensional parameters the reader is referred to [147] or [152]. However, general trends that are associated with the stability boundary are:

1) Increasing N_{pch}, i.e., increasing heat flux at constant inlet velocity is destabilizing.

2) Increasing N_{sub}, i.e., increasing inlet subcooling is stabilizing for N_{sub} greater than some critical N_{sub} and destabilizing for N_{sub} less than this critical value.

3) The effect of inlet throttling is strongly stabilizing whereas the exit throttling is destabilizing.

4) Increasing the system pressure level increases the vapor density and reduces the density effect. For given values of power, subcooling and flow rate it has a stabilizing effect. Note that the ratio of vapor to fluid densities appears in the parameters N_{pch} and N_{sub}, and the calculations of Ishii, which are carried out at several pressure levels, appear to show that the effect of system pressure on the stability boundary is essentially all taken into account through the influence of N_{sub} and N_{pch}.

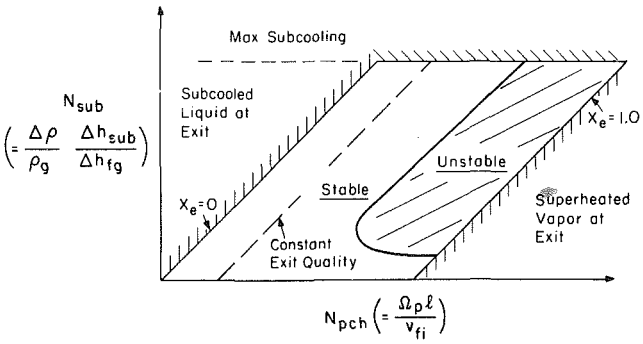

Fig. 57 Representative stability boundaries for density wave oscillations [147]

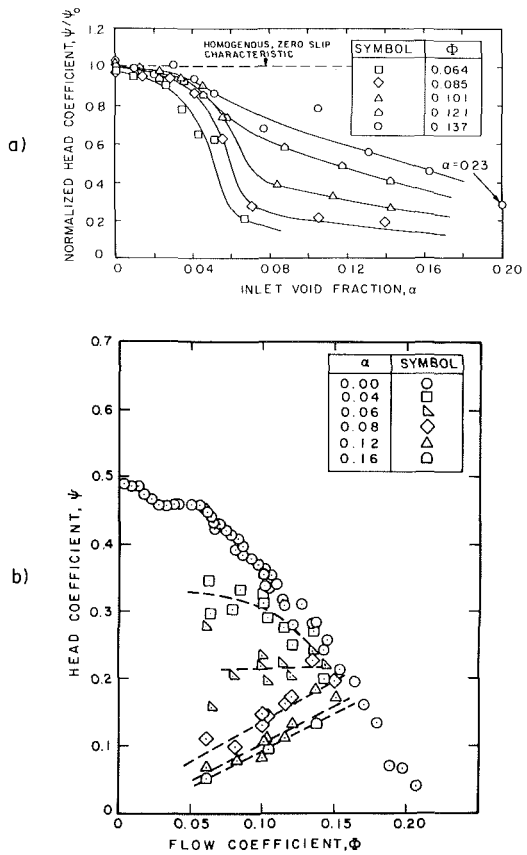

Fig. 58 Steady state pump performance in two-phase flow
***(a)* Pressure rise coefficient versus inlet void fraction for different flows [153]**
***(b)* Pressure rise coefficient versus flow for different inlet void fraction (crossplot of *a*) [154]**

D. Pump Surge Due to Two-Phase Flow. Another type of instability that is encountered in two-phase flow systems has

been associated directly with the pumping element. This has been termed pump surge by Rothe, Runstadler, and Dolan [153] in view of the apparent similarity to the types of instability observed with single phase flow in pumps and compressors. They found large amplitude oscillations in a two-phase flow system which used a centrifugal pump.

Although no quantitative analysis of this phenomenon has been carried out, some qualitative observations relating to the system stability have been made in [153]. These have to do with the two-phase performance of the pump. In particular we can examine the steady-state behavior of the headrise (pressure rise) coefficient for a centrifugal pump in a two-phase flow as the inlet void fraction (the volumetric concentration of the gas phase) is increased. Data of this type are shown in Fig. 58(*a*), which is taken from [154]. The vertical axis is the actual head coefficient (pump head rise divided by impeller tip wheel speed squared), normalized by the head coefficient for single phase flow, and the horizontal axis is the inlet void fraction. The different symbols represent different total flow coefficients (defined as total volumetric flow at inlet divided by the product of impeller tip wheel speed and impeller discharge area). It can be seen that as the void fraction is increased there is a significant falloff in head coefficient, as well as that at constant void fraction the falloff in head coefficient increases as the flow coefficient is decreased.

With this as background, it is more pertinent to plot this data in the usual headrise versus flow coefficient format, as is done in Fig. 58(*b*) from [153]. It can be seen directly that whereas the single phase curve (the circles) is negatively sloped except for a small region at quite low flow rates, the curves for higher inlet void fractions have a considerable positive slope over much of the range shown. Thus, if one considered small perturbations which occurred in a system with a pumping characteristic of this type, there would be a definite possibility for the promotion of an instability as has been described in detail previously.

For the general case of an arbitrary perturbation in system operating point there is no need for the inlet void fraction to remain constant and even *if* we consider the pump transient performance to be approximately quasi-steady, the head rise will then be a function of both the instantaneous inlet void fraction and the flow coefficient. The pump operating point could thus traverse a path that cut across the curves in Fig. 58(*b*) and the effective slope could be more or less steeply sloped than shown. Nevertheless, it does appear that the falloff in head coefficient as the result of a two-phase inlet flow could be a potentially important factor in promoting instability.

Although a similar type of phenomenon has been noted in [155], where it is reported that increasing the inlet void fraction for a centrifugal pump resulted in an oscillation of the whole piping system, there appears to be little other data on this type of instability. In addition, no quantitative analysis has been done, and the basic unsteady flow characteristics of the pump remain unclear. This is therefore another area which is of engineering importance and in which much further work needs to be carried out before adequate understanding is achieved.

E. Other Types of Two-Phase Flow System Instability. There are, as seen from Table 2, many types of two-phase flow instability which can plague fluid systems and there is a considerable amount of literature on these other types also. As they are less frequently observed, and are less related to the overall system pumping or throttling characteristics, they are not really within the scope of this review, and for discussions of them one is referred to the review articles on two-phase flow cited previously.

F. Multiple Channel Instabilities in Two-Phase Flow. The foregoing discussion of two-phase flow instabilities has been limited to single channel flow. However, many practical two-phase flow systems occur with several or more channels in parallel. These channels can exhibit coupled oscillations in which the flow in a given channel can even be reversed. The subject of parallel channel instability is therefore also one in which work has been done. Reference [156] reports investigations of boiling oscillations in a four parallel channel up-flow system. Both density and pressure drop oscillations were observed. The influence of cross sections on the system behavior has also been studied. Other references on this topic are [157], [133], [134], Chapter 9 of [136], [145]. Of the many conclusions that have emerged from this work we will mention here only two. First, a parallel channel configuration having a large number of channels is essentially a constant pressure drop situation as far as any one channel is concerned. Hence pressure drop instability can occur right at the minimum of the pressure drop versus flow curve. Second, the use of cross channels is likely to stabilize density wave oscillations since the pressures in different channels are out of phase and the connections tend to attenuate the pressure nonuniformities.

VII Combustion Associated Instability in Pumping Systems

There are many types of pumping systems in which combustion takes place, and there are a number of instabilities that can occur which are associated with the presence of the combustion. A useful distinction between the different types is made in [158] in which the instabilities have been defined as falling into three main classes:

1) Instabilities that are specific to the chamber (combustion chamber instabilities)
2) Instabilities involving the entire system (system instabilities)
3) Instabilities involving only the reactants (intrinsic instabilities)

It is the second group only which falls within the scope of this review. Prime examples of this type are the oscillations that can occur in liquid propellant rocket motors and which are commonly referred to as "chugging," and the low frequency oscillations that can be encountered in oil- and gas-fired boilers.

The first of these, low frequency instabilities in liquid propellant rockets, received substantial attention in the past. The early work on this topic is described in the monograph by Crocco and Cheng [159], as well as in [160]. A key element in the stability analyses is the idealization of the combustion process by using the concept of a combustion time lag, or time delay, between the instant the propellant is introduced into the combustion chamber and the time at which the burnt gas (the products of combustion) is generated. Although we will not reproduce the analysis presented in the reference, some motivation for the destabilizing effect of such lags (in a different context, to be sure) can be given following the presentation in [1]. Thus consider a single degree of freedom oscillation where the restoring force is considered to be delayed (has a lag) by some time constant τ. The equation for this system can be written

$$\frac{d^2X(t)}{dt^2} + X(t-\tau) = 0.$$

If we expand the restoring force term in a Taylor series in powers of τ, and retain only the first term, we find:

$$\frac{d^2X(t)}{dt^2} - \tau\frac{dX(t)}{dt} + X(t) = 0$$

This is the equation for a system with a negative damping, in other words a system that will exhibit dynamic instability. The argument thus gives some motivation for the effect of a time delay on system stability, although it is by no means intended to be a rigorous demonstration of the influence of time lags in the more complex cases under consideration.

One of the important conclusions that emerged from the stability analyses that were carried out for liquid propellant rocket engines was that the oscillations could be suppressed by various changes in the feed system, in particular by having a large enough flow resistance in the propellant inlet line. In addition, Tsien [160], among others, has shown that feedback control techniques can also be used to increase stability. It therefore appears that there are now useful techniques available to help control the low frequency oscillations in these systems, and that there is now less research on this particular topic than there has been in the past. Summaries of some of the later developments in this field (as well as of other combustion instabilities) are given in the review articles by Crocco [161], [162], and a very detailed survey of the specific topic of liquid propellant rocket combustion instabilities (with almost 800 references) is given in the volume edited by Harrje [163].

Somewhat related to this instability are the oscillations that can occur in industrial furnaces. These are also low frequency oscillations, in which the energy for the oscillations comes from the combustion. There have been several treatments of this type of instability, which model the system as a Helmholtz resonator, and in which criteria for the onset of oscillations are derived. (The fundamental investigation of the problem in this fashion is due to Rayleigh [164], who stated the following criterion for the maintenance of oscillations by an unsteady heat input: "If heat be given to the air at the moment of greatest condensation, or taken from it at the moment of greatest rarefaction, the vibration is encouraged." A derivation of this criterion for a simple system is presented in the Appendix.) Examples of investigations of this problem for systems of practical concern are [165]-[169], and a review of some of these approaches is given in [158]. The analyses are based on various hypotheses about the combustion phenomena which are responsible for the fluctuating heat release during the oscillation, since once this is specified the system dynamics can be determined. While the analyses are able to predict some of the experimentally observed oscillations, it appears that the basic mechanism that determines the quantitative nature of the relation between the pressure/flow rate pulsations and the heat release due to combustion is still not understood, and that this is the most important question for future research in this area. In fact this might also be said of the rocket engine instabilities, where the relevant processes that determine the time lag are still not totally clarified. In this general context, a recent study which examines some of the non-steady fluid mechanic phenomena in large combustors is given in [170]. One other example of combustion associated system instability which is of technological import is the oscillations that are encountered in gas turbine engine afterburners. An introductory discussion of this phenomenon is given in [171].

VIII Self-Excited Oscillations in Hydraulic Systems and Other Types of Pumping System Instability

In this section we will discuss some of the pumping systems encountered in the general area of hydraulics and their associated instabilities. We will also mention some other types of pumping system instabilities which are of interest but in which there is less current engineering activity than in those areas which we have discussed at length. As a preamble to the discussion of the first topic, we again state that the transients to be covered will be of the self-excited type only. It should thus be noted that, for example, even though many of the oscillatory phenomena that occur in hydraulic systems, especially large scale (power station) installations, are sometimes referred to using the term "surge," they are often not really instabilities, but are rather resonant responses of a stable system to some external forcing function. In consistency with the general theme of the review, therefore, we will only discuss those transients which do arise from true instability. Even with this restriction, however, the view expressed in [6] is that: "A complete list of component parts of hydraulic systems capable of supporting a self excited oscillation. . .is practically impossible to compile." We will only mention several reported examples of these instabilities, concentrating on those which are due to the pressure versus flow system characteristics.

Self-excited oscillations of a check valve with a spring damper are described in [172]. Experimental studies of a simplified model were carried out to clarify the cause of instability which was associated with high rates of change of discharge in the last few degrees of closing. Instabilities have also been encountered with hydraulic gate seals [173]. In this case the analysis indicated that there was a dynamic instability, due to a negative damping, which was responsible for the growth of the oscillations.

Auto-oscillations due to hydraulic turbine penstock valves at a hydro-electric plant are discussed in [174]. In this paper, an explanation was given for the instability based on the ratio between the valve leakage area and the pressure. Situations in which the area decreases with increasing pressure are favorable for the growth of auto-oscillations while those in which the area increases as the pressure increases are not. We can relate the former condition to a (local) negatively sloping pressure drop versus flow characteristic for the valve, while the latter results in a positively sloping curve. We have already seen, however, (in connection with the pressure drop instabilities in two-phase flow) that a resistance with a negative slope acts as a negative damping and can result in energy being fed into the oscillatory motion. This type of hydraulic instability can therefore be viewed as related to the mechanism shown in Fig. 51 and described in the section on pressure drop oscillations. Other references on the general topic are [175] which gives a discussion of pulsations in the boiler feed system of a pumping station due to rotating stall in one of the pumps, [176] which presents graphic descriptions of some of the consequences of instabilities in power stations, and [177] which discusses large amplitude low frequency pulsations which occur in centrifugal pumping systems.

We conclude this section with mention of another type of system instability. This occurs in plenum-type air cushion suspensions, such as might be used in marine hovercraft, which can exhibit self-excited oscillations of the unsprung mass (cushion) in the suspension system. An experimental and theoretical investigation of this type of phenomenon is reported in [178], which also presents discussion on the assumptions made in using lumped parameter analyses to model continuous systems. Two causes of the instability were identified, resulting from dynamic lags in the response of different system components.

IX Flow Transients and Instabilities in Compound Pumping Systems (Systems with Pumps in Parallel)

Aside from brief mention of the multichannel instabilities that occur in two-phase flows, the review up till now has addressed the instabilities that occur in systems in which there is only one "pump" (although it could have many stages or even run on two or three separate shafts). There are, however,

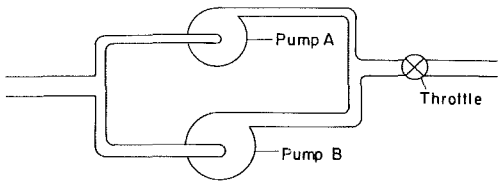

Fig. 59 Compound pumping system with pumps in parallel

many practical situations in which there are two or more pumping devices in parallel. Under these conditions not only are there possibilities for instabilities of the types that we have already discussed, but new problems, associated with the compound system, can also appear. In particular there can be severe problems associated with transients, such as startups, in these kinds of systems.

For definiteness, we can consider the very simple model pumping system pictured in Fig. 59, but it should be remembered that systems encountered in process applications, for example, can be substantially more complicated. Let us suppose that the two pumps have different pressure rise and mass flow capabilities. The steady-state operating points of such a configuration might be as given in Fig. 60 which is taken from the lucid introduction to this topic given by Emmons [179]. Curves A and B are the individual curves for each machine; the dash-dot curve C is the combined. For system pressure requirement curve 1, the two machines do better than one, while for the system resistance curve 3 the capacity of the two machines is actually smaller than that of the larger machine by itself. Note that although, as we have drawn it, the smaller machine would be operating with reverse flow, in general a not very favorable condition, the overall system operation is stable in that the pump performance changes smoothly and continuously as the throttle area is decreased.

Often, however, the situation is such that one or the other of the pumps has been shut off and is brought on line. To be specific, let us suppose that we are operating pump A with pump B off, and B is now brought on line. If the throttle curve is considered fixed at 3, A's operating point would undergo a large transient from a to a′, with operation of B at point b′. If the demand (flow volume) is considered to be fixed, then the transient would be to a″. In either case the result could be that a pump that was running near peak efficiency undergoes a transient to a region of much less benign operation.

The difficulties can be compounded if the pump curves have regions with positive slope, as one can see using the basically quasi-steady arguments similar to those presented before. In general it is therefore found that for pumps to operate satisfactorily in parallel they should have negatively sloped pressure rise versus flow curves, and they should have roughly the same percentage reduction in capacity over the operating range.

The transients just described can be large and can lead to considerable difficulty. In addition to this excursive behavior, however, there are also situations in which compound systems give rise to an oscillatory type of transient.[23] An example of this is described by Ehrich [180], who examined the basic compound system associated with a branched diffuser configuration. This is a situation encountered in gas turbine annular combustors. *Each* branch of the system has a diffuser, a volume with a mass storage capability, and a downstream resistance similar to the configuration shown in

[23] In this context it may be of interest to note that one of the first instabilities that we discussed, rotating stall, has also been viewed as an instability of (blade channel) diffusers in parallel [179].

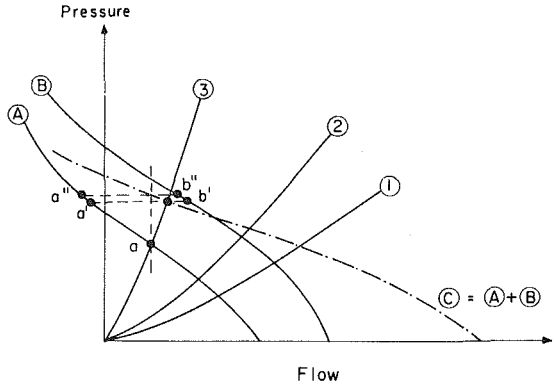

Fig. 60 Pressure-flow characteristics of pumps in parallel [179]

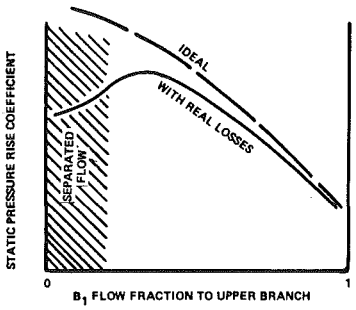

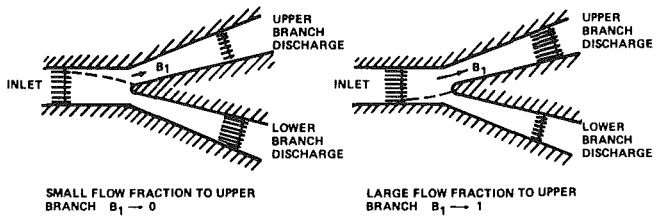

Fig. 61 Static pressure recovery characteristic of a branched diffuser [180]

Fig. 1 for the simple system. The "pumping characteristics" of one branch of the system are shown in Fig. 61. A key feature is that the static pressure recovery in either diffuser branch is a function of the flow fraction entering that branch. A small flow fraction will result in low velocity at the branch discharge and, ideally, high static pressure recovery. However, this would imply a high diffusion which may not actually be possible, so that separation could occur. If so, the pressure recovery characteristic will have its peak at some intermediate flow fraction as shown by the curve marked "with real losses" in the figure.

The analysis of the branched diffuser system showed that operation to the left of the maximum is unstable and that, for the conditions studied, a relaxation type of oscillation would be set up. For symmetric diffusers this results in the flow through the combustor shells, i.e., the downstream resistance varying periodically in an approximately triangular fashion while the system pressure drop will vary periodically (approximately as a sawtooth wave) with twice the frequency of the other parameters. Results of the analysis are shown in Fig. 62 which presents the oscillations in branch inlet and exit flow and in overall system pressure drop. One point that should be noted in interpreting these results as well as others in [180] is that there are no inertial effects considered. These will: (1)

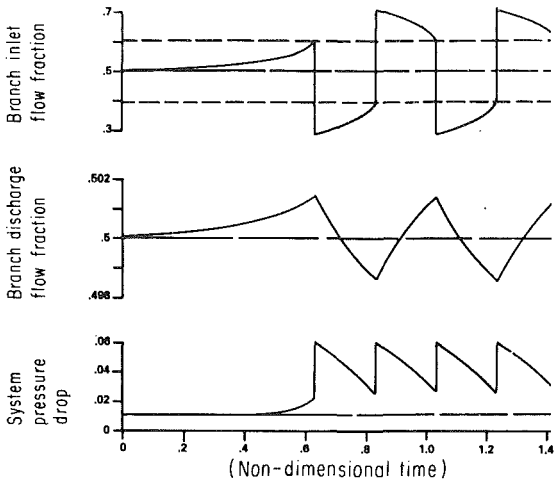

Fig. 62 Calculated flow oscillations in branched diffuser system [180]

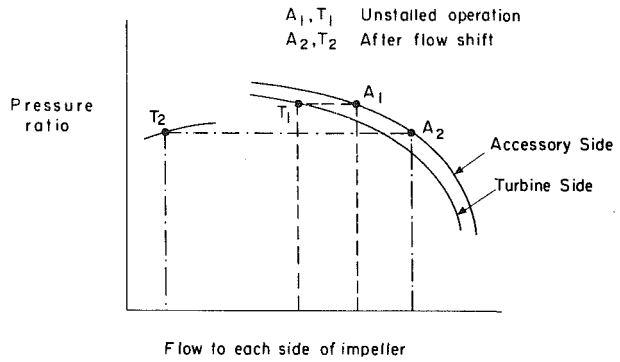

Fig. 63 Flow transient in dual entry impeller [181]

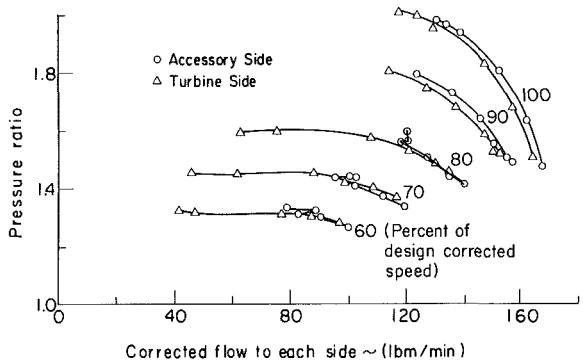

Fig. 64 Measured pressure-flow characteristics of each side of a dual entry impeller [181]

modify the stability criterion somewhat, moving the point of instability to the left of the peak, and (2) change the shape of the oscillations shown for the nonlinear calculations, with the tendency being to make the waveforms less like the relaxation oscillation situation.

A further example of flow transients that can arise in pumping systems in parallel has been documented in [181]. This was a phenomenon that occurred in a dual entry centrifugal compressor, where a large amplitude, sudden flow shift occurred, accompanied by a substantial pressure change. The phenomenon is illustrated schematically in Fig. 63, where the two sides of the impeller, having slightly different characteristics, are shown. In position A_1 and T_1 (for Accessory and Turbine sides, respectively) stable operation exists, although with some asymmetry. As the *overall* flow is reduced, the flow in the turbine side of the impeller (point T_1) reaches the stall line first and ends up at point T_2. The operating point of the accessory side then falls back to A_2, with an attendant change in flow and pressure rise. The machine is thus operating in rotating stall on the turbine side and at a high flow rate on the accessory side. Reference [181] also cites instances in which the flow at T_2 might not be stable, in which case this side encounters mild surging.

As an illustration of the actual performance of the individual sides of the impellers, Fig. 64 shows the curves of pressure ratio versus flow at different speeds for each side of the machine. The circles are the accessory (A) side and the triangles the turbine (T) side. It can be seen that in the lower speed ranges there is the possibility for a large "flow shift" even when the accessory side is operating far from stall. One cure for this type of instability is to reduce the pressure rise in the stronger side by using an inlet screen until the two sides are matched. This was tried successfully, although one must be careful to tailor the screens properly since too much blockage can cause a mismatch of the two sides in the opposite direction, with the accessory side now being the stalling element. In general, however, the best remedy is to match the two inlets carefully.

Instability in dual entry centrifugal compressors was apparently noted first by Chesire [182] and it still appears to be a problem in many installations. A recent example of this is in [183]. In this instance a double entry centrifugal fan, operating near the peak efficiency point, exhibited pulsations of approximately thirteen percent of the overall fan pressure rise.

Although there does not appear to be a large amount of literature covering specific instabilities that occur in complex pumping systems with parallel pumping elements, it is clear that there are many instances in which these can be important. Piping systems in the process industries, for example, can use several compressors in parallel. The boiler feed systems described in [181] and [86] (in which large amplitude pulsations were encountered) had three multistage centrifugal pumps in parallel, and exhaust gas systems for power plants can also have several fans operating in parallel.

To carry out an analysis of such systems one must dynamically couple the various components. For small oscillatory perturbations, one method of doing this is to use the transfer matrix approach that was described in the section on cavitating inducer stability. This technique has been used to analyze hydraulic transients in complex piping systems and a good treatment of the subject is given in Chapters 12 and 13 of [6]. For predicting large amplitude transients, one must integrate the equations of motion for the flow in the system numerically; however, if the stability boundary is what is desired a linear analysis will suffice. As far as overall results are concerned, the author cannot make a general statement about the stability of the complicated pumping systems that exist in practice, except to note that a very conservative criterion would be that if none of the components in the system are dynamically active, i.e., if none of them have a net outflux of mechanical energy over a complete period, then the system will be dynamically stable.

X General Comments on the Modeling of Pumping System Dynamic Behavior

There are several points that should be addressed concerning the type of stability analyses that we have been discussing. One of these is that in the main we have referred to these as if they were lumped parameter treatments of the system dynamics. However this is not necessarily so, and one could well use a distributed parameter approach if the

situation warranted it. This is the first point, and one that should be evident.

A much more serious comment concerns the modeling of the different active elements in the systems, or, more precisely, the transient behavior of the active elements that are responsible for the instability. This seems to be the area of greatest uncertainty in developing useful prediction models for stability onset. We can examine several illustrations of this, starting with the axial compression system. Consider a compressor which is undergoing perturbations in mass flow. For a given compressor, it appears that the behavior of the individual blade rows (i.e., the instantaneous loss and turning characteristics) departs more and more from a quasi-steady performance as one nears the stall line. At present there is no way to predict this unsteady response. Thus, models of axial compressor stability, which break the flow domain into very small (axial) elements with the hope of obtaining accurate predictions of high frequency response are not really appropriate since one is actually limited by the knowledge of the unsteady blade row performance.

Another facet of this unsteady response concerns the departure from quasi-steady behavior that is associated with the onset of rotating stall. The time scale that one would associate with the unsteady response of an individual blade row is on the order of b/W, where b is the blade chord and W is the relative velocity. However, there is a much larger time scale that characterizes the transformation of an axisymmetric flow into a severely non-uniform rotating stall pattern. A representative time scale might now be the disturbance wavelength (the mean circumference of the machine) divided by the through flow velocity. Some qualitative support for this scaling can be given by noting that the change from unstalled to stalled flow involves the shedding of blade circulation of the same sign over a significant circumferential extent of the flow annulus. The flow will thus only approach a "fully developed" state when this shed vorticity has been convected downstream a distance which is on the order of the disturbance wavelength. These considerations imply that for a given machine the stall cell growth time might scale with axial velocity (or, since C_x/U is roughly constant at stall, with rotor speed) and circumference. In one of the few instances in which data is available this has been found to be the case, as shown in [16]. The important point is that the response of the overall flow field is likely to occur on a time scale an order of magnitude or more longer than the time associated with the individual blade row response, and the compressor performance (pressure rise, torque) during a transient past the stall line may therefore be substantially different from the steady-state or quasi-steady performance. This is a facet of unsteady response which may be quite important in the application of one-dimensional compression system stability models, but is one that is at present not well understood and on which there is little data.

This situation is also true in regard to centrifugal compressor systems. We have mentioned in the review that there is even more uncertainty about the unsteady performance of a centrifugal stage near the stall line, and that questions of the relation of instantaneous operating point excursions compared to steady-state characteristics are not resolved. Thus here again there is a need for more understanding of the active element performance.

This basic criticism is true for the majority of the systems that have been mentioned in the review. In some instances (the area of cavitating turbopumps for example) work has started on a systematic attack on this problem. However that is only a beginning, since the work so far is limited to the design flow condition and to small perturbations, and in many of the systems of interest one cannot restrict oneself to only these situations. Even in instances in which one might suspect that the response could be truly quasi-steady since the frequencies are very low, as for example in the case of pressue drop oscillations during two-phase flow, it is to be emphasized that the conclusions of the stability analysis will be dependent on the *slopes* of the steady-state performance curves and these can be extremely difficult to predict with the desired accuracy. For the combustion associated instability also, the principal difficulties appear to be in obtaining a priori knowledge of such global aspects of the process as the time constant, or the relation between heat input and chamber pressure, etc.

The overall comment then is that the problem to be attacked is not ever more refined calculations of pumping system instability using models of the active elements that are the same as or minor variations of those that have been used previously, but rather that the efforts should be on more detailed understanding of the unsteady performance of these elements. As stated previously, the models used for unsteady response of axial compressor blade rows are essentially those proposed by Emmons et al. [3] and Stenning and Kriebel [88] twenty-five years ago, and it appears inconsistent to concentrate on merely developing better and better models of the flow field outside the blade rows. Put another way one might say that present computational capability is such that one could calculate the dynamic behavior of many complex systems of interest *provided* the performance of the different active elements of the system were known (i.e., compressors, combustion chambers, sections with two-phase flow). Whether the techniques used to obtain this information are numerical or experimental, it seems that future work should address this general area.

XI Summary and Concluding Remarks

In this survey we have attempted to review the fluid mechanic phenomena which are associated with instabilities in different types of pumping sytems. In several of these systems, such as axial and centrifugal compression systems in gas turbine engines, the instabilities occur at flow rates which are less than design, and a key feature of the onset of instability is the occurrence of stall in the compressor. In other turbomachinery applications, such as cavitating flows in axial inducers, the instability can occur at the design flow rate of the pump, and stall is not involved. In still others, such as two-phase flow pumping systems, the system element that is responsible for the instability can actually have a pressure drop across it.

In spite of these diverse circumstances, there are several basic concepts that are applicable in the analysis and understanding of the systems that have been described. The first of these is the distinction between dynamic and static stability. Information about the former can be obtained from knowledge of the steady-state pumping and pressure drop characteristics of the system. Information about dynamic stability requires, at the least, additional knowledge about other parameters, such as inertances and capacitances, which affect the transient system behavior, and it may well necessitate obtaining knowledge about the dynamic behavior of the active (instability causing) elements in the system. The distinction is important since even though, in some instances, a static stability analysis may be enough to point up potential difficulties of operation, it is often the dynamic instability that it is more critical to predict. The physical mechanism associated with dynamic instability has been seen to be a "negative damping" in the system, so that one (or more) of the components are able to feed energy into the oscillatory flow which characterizes the instability. Further, it has also been seen that there are similarities between the overall transient response of various systems. An important aspect in several of the systems was the differentiation between the

local (or component) instability, and the more global system instability, as exemplified by rotating stall and surge, respectively, in an axial compression system. In some cases, however, it was pointed out that the occurrence of the former can trigger the latter, so that adequate prediction of the system instability can also involve prediction of the component instability.

Last, but by no means least, we can mention the areas in which future work has been suggested. Specific topics have been pointed out in the text, in the various parts of this review which relate to the different systems. However, as discussed at length in the preceding section, a strong recommendation has been made that, in general, future efforts should be focussed on understanding the dynamic behavior of the active elements within the various systems. It is the lack of knowledge of this aspect that often appears to be the limiting feature in developing improved methods for prediction of system stability boundaries.

Acknowledgments

This review was made possible by the Freeman Scholar Program in Fluids Engineering of the ASME. The author is grateful to the Program and to the Standing Committee of the Program, Professor A. H. Shapiro, Dr. A. M. O. Smith, and Professor J. Robertson, for giving him this opportunity, as well as for their suggestions. He is also indebted to Professor H. W. Emmons, former Chairman of the Standing Committee, for his encouragement.

In the preparation of this review the author has had assistance from a number of individuals. In particular, Dr. N. A. Cumpsty of Cambridge University, Mr. R. S. Mazzawy of Pratt & Whitney Aircraft, and Dr. C. S. Tan of MIT have all contributed their expertise. In addition the critiques and comments of Profs. E. E. Covert and J. L. Kerrebrock of MIT, Prof. C. E. Brennen of Cal Tech, Prof. J. H. Horlock of Salford University, Prof. L. S. Langston of U. Conn., Mr. J. P. Nikkanen of Pratt & Whitney Aircraft, and Mr. W. Swift of Creare have also been quite helpful. F. Ehrich, W. Jansen, B. Clem, M. El-Masri, D. Hobson, and A. Morris have kindly provided references and/or originals of some of the figures used in the review. The (many) drafts of the manuscript were rapidly and accurately typed by Miss E. Mandigo. This work was partially supported by the Air Force Office of Scientific Research under Contract F49620-78-C-0084, Dr. J. D. Wilson, Program Manager.

References

1 Betchov, R., and Criminale, W., *Stability of Parallel Flows*, Academic Press, New York, 1967, p. 1.

2 Maxwell, J.C., "On Governors," *Proc. Roy. Soc.* No. 100, 1868, reprinted in *Collected Works*, Vol. II, Dover Publications, New York 1965, pp. 104–120.

3 Emmons, H.W., Pearson, C.E., and Grant, H.P., "Compressor Surge and Stall Propagation," TRANS. ASME, Vol. 79, Apr. 1955, pp. 455–469.

4 Taylor, E.S., "The Centrifugal Compressor," Part J in *Aerodynamics of Compressors and Turbines*, W.R. Hawthorne, editor, Princeton University press, Princeton, N.J., 1964.

5 Stenning, A.H., "Rotating Stall and Surge," Chapter 14 in *Fluid Dynamics of Turbomachinery*, ASME Lecture Series, Iowa State University, 1973, reprinted in ASME JOURNAL OF FLUIDS ENGINEERING, Vol. 102, Mar. 1980, pp. 14–21.

6 Wylie, E.B., and Streeter, V.L., *Fluid Transients*, McGraw-Hill, New York, 1978.

7 Porter, B., *Stability Criteria for Linear Dynamical Systems*, Oliver and Boyd, 1967.

8 Dorf, R.C., *Modern Control Systems*, Second Ed., Chapter 5-8, Addison-Wesley Publishing Co., 1974.

9 Den Hartog, J.P., *Mechanical Vibrations*, Fourth Ed., McGraw-Hill, 1956.

10 Hale, J.K., and LaSalle, J.P., "Differential Equations: Linearity vs Nonlinearity," *SIAM Review*, Vol. 5, No. 3, July 1963, pp. 249–272.

11 LaSalle, J.P., and Lefschetz, S., *Stability by Liapunov's Direct Method*, Academic Press, New York, 1961.

12 Horlock, J.H., *Axial Flow Compressors*, Krieger Publishers, 1973.

13 Serovy, G.K., "Axial Flow Compressor Aerodynamics," Chapter 17 in *The Aerothermodynamics of Aircraft Gas Turbine Engines*, G. Oates, editor, AFAPL-TR-78-52, Air Force Aero Propulsion Laboratory, 1978.

14 Iura, T., and Rannie, W.D., "Experimental Investigations of Propagating Stall in Axial-Flow Compressors," TRANS. ASME, Apr. 1954, pp. 463–471.

15 Mazzawy, R.S. "Surge Induced Structural Loads in Gas Turbines," ASME *Journal of Engineering for Power*, Vol. 102, Jan. 1980, pp. 162–168.

16 Greitzer, E.M., "Review—Axial Compressor Stall Phenomena," ASME JOURNAL OF FLUIDS ENGINEERING, Vol. 102, June 1980, pp. 134–151.

17 Taylor, E.S., "Evolution of the Jet Engine," *Astronautics and Aeronautics*, Vol. 8, 1970, pp. 64–72.

18 Leiblein, S., "Experimental Flow in Two Dimensional Cascades," Chapter VI in *Aerodynamic Design of Axial Flow Compressors*, NASA SP-36, 1965.

19 Leiblein, S., "Loss and Stall Analysis of Compressor Cascades," ASME *Journal of Basic Engineering*, Vol. 81, Sept. 1959, pp. 387–400.

20 Rodgers, C., "A Diffussion Factor Correlation for Centrifugal Impeller Stalling," ASME *Journal of Engineering Power*, Vol. 100, Oct. 1978, pp. 592–603.

21 Smith, L.H., Jr., "Casing Boundary Layers in Multistage Axial Flow Compressors," in *Flow Research on Blading*, edited by L.S. Dzung, Elsevier Publishing Co., 1970.

22 Fligg, J.A., "Tests of a Low Speed Three-Stage Axial Flow Compressor at Aspect Ratios of One, Two and Four," AIAA Paper 66-613, AIAA 2nd Propulsion Joint Specialist Conference, 1966.

23 Smith, L.H., "The Effect of Tip Clearance on the Peak Pressure Rise of Axial Flow Fans and Compressors," ASME Symposium on Stall, 1958.

24 McNair, R.E., "Tip Clearance Effects on Stalling Pressure Rise in Axial Flow Compressors," ASME Symposium on Stall, Surge, and System Response, 1960.

25 Lakhwani, C., and Marsh, H., "Rotating Stall in an Isolated Rotor Row and a Single Stage Compressor," Conference Publication 3, Institution of Mechanical Engineering, 1973.

26 Nenni, J.P., and Ludwig, G.R., "A Theory to Predict the Inception of Rotating Stall in Axial Flow Compressors," AIAA Paper 74-528. AIAA 7th Fluid and Plasma Dynamics Conference, 1974.

27 Fabri, J., "Growth of a Perturbation in an Axial Flow Compressor," ASME paper 78-GT-30, 1978.

28 Emmons, H.W., Kronauer, R.E., and Rockett, J.A., "A Survey of Stall Propagation - Experiment and Theory," ASME *Journal of Basic Engineering*, Vol. 81, Sept. 1959, pp. 409–416.

29 Fabri, J., "Rotating Stall in Axial Flow Compressors," *Internal Aerodynamics (Turbomachinery)*, Inst. of Mechanical Engineers, 1967.

30 Dunham, J., "Non Axisymmetric Flows in Axial Flow Compressors," Mechanical Engineering Sciences Monograph No. 3, Inst. of Mechanical Engineers, 1963.

31 Day, I.J., and Cumpsty, N.A., "The Measurement and Interpretation of Flow within Rotating Stall Cells in Axial Compressors," *J. Mech. Eng. Sciences*, Vol. 20, 1978, pp. 101–114.

32 Greitzer, E.M., "Surge and Rotating Stall in Axial Flow Compressors. Part II: Experimental Results and Comparisons with Theory," ASME *Journal of Engineering Power*, Vol. 98, Apr. 1976, pp. 199–217.

33 Greitzer, E.M., Mazzawy, R.S., and Fulkerson, D.A., "Flow Field Coupling between Compression System Components in Asymmetric Flow," ASME *Journal of Engineering Power*, Vol. 100, Jan. 1978, pp. 66–72.

34 Day, I.J., "Axial Compressor Stall," PhD thesis, Cambridge University Engineering Department, 1976.

35 Takata, H., and S. Nagano, "Nonlinear Analysis of Rotating Stall," ASME paper 72-GT-3, 1972.

36 Orner, N., Rotating Stall in Axial Flow Compressors, Von Karman Institute Lecture Series, "Unsteady Flow in Turbomachines," Brussels, Belgium, 1979.

37 Adamczyk, J.J., "Unsteady Fluid Dynamic Response of an Isolated Rotor with Distorted Inflow," AIAA paper 74-49, 1974.

38 Pandolfi, M. and Colasurdo, "Numerical Investigations on the Generation and Development of Rotating Stalls," ASME paper 78-WA/GT-5, 1978.

39 Day, I.J., Greitzer, E.M., and Cumpsty, N.A., "Prediction of Compressor Performance in Rotating Stall," ASME *Journal of Engineering Power*, Vol. 100, Jan. 1978, pp. 1–14.

40 Montgomery, S.R., and Braun, J.J., "Investigation of Rotating Stall in a Single Stage Axial Compressor," NACA Technical Note TN3823, 1955.

41 Tesch, W.A. and Steenken, W.G., "J85 Clean Inlet Flow and Parallel Compressor Models," NASA Contractor Report CR-134978, Mar. 1976.

42 Corbett, A.G., and Elder, R.L., "Stability of an Axial Flow Compressor with Steady Inlet Conditions," *J. Mech. Eng. Science*, Vol. 16, No. 6, 1975.

43 Corbett, A.G., and Elder, R.L., "Mathematical Modelling of Compressor Stability in Steady and Unsteady Flow Conditions," in *Unsteady Phenomena in Turbomachinery*, AGARD CP-177, 1976.

44 Chamblee, C.E., Davis, M.W., and Kimzey, W.F., "A Multistage Axial Flow Compressor Mathematical Modelling Technique with Application to Two Current Turbofan Compression Systems," AIAA paper AIAA-80-0054, 1980.

45 Willoh, R.G., and Seldner, K., "Multistage Compressor Simulation Applied to the Prediction of Axial Flow Instabilities," NASA TMX-1880, 1960.

46 Reid, C., "The Response of Axial Flow Compressors to Intake Flow Distortion," ASME paper 69-GT-29, Gas Turbine Conference, 1969.

47 Plourde, G.A., and Stenning, A.H., "Attenuation of Circumferential Inlet Distortion in Multistage Axial Compressors," *Journal of Aircraft*, Vol 5, No. 3, 1968.

48 Stenning, A.H., "Inlet Distortion Effects in Axial Compressors," Chapter 14 in *Fluid Dynamics of Turbomachinery*, ASME Lecture Course, Iowa State University 1973. reprinted in ASME JOURNAL OF FLUIDS ENGINEERING, Vol. 102, Mar. 1980, pp. 7–14.

49 Herrcock, R.G. and Williams, D.D., "Aerodynamic Response," in *Distortion Induced Engine Instability*, AGARD Lecture Series, No. 72, 1974.

50 Mokelke, H., "Prediction Methods," in *Distortion Induced Engine Instability*, AGARD Lecture Series, No. 72, 1974.

51 Mikolajczak, A.A., and Pfeffer, A.M., "Methods to Increase Engine Stability and Tolerance to Distortion" in *Distortion Induced Engine Instability*, AGARD Lecture Series, No. 72, 1974.

52 Mazzawy, R.S., "Multiple Segment Parallel Compressor Model," ASME *Journal of Engineering Power*, Vol. 99, Apr. 1977, pp. 288–296.

53 Greitzer, E.M., and Griswold, H.R., "Compressor Diffuser Interaction with Circumferential Flow Distortion," *J. Mech. Eng. Sci.*, Vol. 18, Feb. 1976, pp. 25–43.

54 Greitzer, E.M., "Coupled Compressor-Diffuser Flow Instability," *J. Aircraft*, Vol. 14, Mar. 1977, pp. 233–238.

55 Osborn, W.M., and Wagner, J.M., "Effect of Simulated Downstream Flow Blockage Doors on the Performance of an Axial-Flow Fan Rotor," NASA TND-6071, 1970.

56 Takata, H., and Tsukuda, Y., "Study on the Mechanism of Stall Margin Improvement of Casing Treatment," ASME paper 75-GT-13, Gas Turbine Conf., Houston, Texas, Mar. 1975.

57 Prince, D.C., Jr., Wisler, D.C., and Hilvers, D.E., "Study of Casing Treatment Stall Margin Improvement Phenomena," NASA CR-134552, Mar. 1974.

58 Osborn, W.M., Lewis, G.W., Jr., and Heidelberg,L.J., "Effect of Several Porous Casing Treatments on Stall Limit and on Overall Performance of an Axial-Flow Compressor Rotor," NASA TND-6537, Nov. 1971.

59 Moore, R.D., Kovich, G., and Blade, R.J., "Effect of Casing Treatment on Overall and Blade-Element Performance of a Compressor Rotor," NASA TND-6538, Nov. 1971.

60 Tesch, W.A., "Evaluation of Range and Distortion Tolerance for High Mach Number Transonic Fan Stages, Task IV Stage Data and Performance Report for Casing Treatment Investigations, Vol. I," NASA-CR-72862, May 1971.

61 Greitzer, E.M., Nikkanen, J.P., Haddad, D.E., Mazzawy, R.S., and Joslyn, H.D., "A Fundamental Criterion for the Application of Rotor Casing Treatment," ASME JOURNAL OF FLUIDS ENGINEERING, Vol. 101, June 1979, pp. 237–244.

62 Greitzer, E.M., "Surge and Rotating Stall in Axial Flow Compressors, Part I: Theoretical Compression System Model," ASME *Journal of Engineering for Power*, Vol. 98, Apr. 1976, pp. 190–198.

63 Stoker, J.J., *Nonlinear Vibrations*, Interscience Publishers, Inc., New York, 1950.

64 Greitzer, E.M. and Blaisdell, J.A., "Further Investigations of Compressor Surge," Internal Pratt & Whitney Report, 1972.

65 Horvath, A.J.T., "Periodic Solutions of a Combined VanDerPol-Duffing Differential Equation," *Int. J. Mech. Eng. Sc.*, Vol. 17, 1975, pp. 677–680.

66 Gyarmathy, G., "Nonlinear Analysis of Surge Cycles," ASME J. FLUIDS ENG., Vol. 99, Mar. 1977, pp. 258–259.

67 Rannie, W.D., "The Axial Compressor Stage," Part F in *Aerodynamics of Turbines and Compressors*, edited by W.R. Hawthorne, Princeton University Press, 1964.

68 McKenzie, A., Private Communication.

69 Harman, J.W., "Discussion (on the paper "Prediction of Compres Performance in Rotating Stall"), ASME *J. Eng. Power*, Vol. 100, Jan. 19 pp. 11–14.

70 Motycka, D.L., "Ground Vortex - Limit to Engine/Reverser Operation," ASME *J. Eng. Power*, Vol. 98, Apr. 1976, pp. 258–264.

71 Toyama, K., Runstadler, P.W., Jr. and Dean, R.C. Jr., "An Experimental Study of Surge in Centrifugal Compressors," ASME JOURNAL OF FLUIDS ENGINEERING, Vol. 99, 1977, pp. 115–131.

72 Rothe, P.H., and Runstadler, P.W., Jr., "First-Order Pump Surge Behavior," ASME JOURNAL OF FLUIDS ENGINEERING, Vol. 100, Dec. 1978, pp. 459–466.

73 Amann, C.A., Nordensen, G.E., and Skellenger, G.D., "Casing Modification for Increasing the Surge Margin of a Centrifugal Compressor in an Automotive Turbine Engine," ASME *Journal of Engineering for Power*, Vol. 97, July 1975, pp. 329–336.

74 Dean, R.C., Jr., "The Fluid Dynamic Design of Advanced Centrifugal Compressors," Creare Technical Note TN-185, July 1974.

75 Rodgers, C., "Impeller Stalling as Influenced by Diffusion Limitations," ASME JOURNAL OF FLUIDS ENGINEERING, Vol. 99, 1977, pp. 76–84.

76 Kenny, D.P., "A Comparison of the Predicted and Measured Performance of High Pressure Ratio Centrifugal Compressor Diffusers," ASME paper 72-GT-54, 1972.

77 Reeves, G.B., "Estimation of Centrifugal Compressor Stability with Diffuser Loss-Range System," ASME JOURNAL OF FLUIDS ENGINEERING, Vol. 99, 1977, pp. 76–84.

78 Baghdadi, S., and McDonald, A.T., "Performance of Three Vaned Radial Diffusers with Swirling Transonic Flow," ASME JOURNAL OF FLUIDS ENGINEERING, Vol. 97, 1975, pp. 155–160.

79 Came, P.M., and Herbert, M.V., "Design and Experimental Performance of Some High Pressure Ratio Centrifugal Compressors," presented at AGARD Specialists' Meeting "Centrifugal Compressors, Flow Performance and Phenomena," Brussels, Belgium, May 1980.

80 Dean, R.C., Jr., and Young, L.R., "The Time Domain of Centrifugal Compressor and Pump Stability and Surge," ASME JOURNAL OF FLUIDS ENGINEERING, Vol. 99, 1977, pp. 53–63.

81 Young, L.R., Discussion of [75], ASME JOURNAL OF FLUIDS ENGINEERING, Vol. 99, 1977, pp. 94–95.

82 Rogers, C., "Design and Test of an Experimental Rotating Diffuser Centrifugal Compressor Test Rig," SAE Paper 760927, Soc. of Automotive Engineers, 1976.

83 Dolan, F.X., and Rundstadler, P.W., Jr., "Design, Development, and Test of a Laser Velocimeter for a Small 8:1 Pressure Ratio Centrifugal Compressor," NASA CR-134781, NASA Lewis Research Center, 1979.

84 Jansen, W.,Carter, A.F., Swarden, M.C., "Improvements in Surge Margin for Centrifugal Compressors," presented at AGARD 55th Specialists' Mtg, "Centrifugal Compressors, Flow Phenomena and Performance," Brussels, Belgium, 1980.

85 Dussourd, J.L., Pfannebecker, G.W., and Singhania, S.K., "An Experimental Investigation of the Control of Surge in Radial Compressors Using Close Coupled Resistances," ASME J. FL. ENG., Vol. 99, 1977, pp. 64–76.

86 Erskine, J.B., and Henaman, N., "Vibration Induced by Pump Instability and Surging," *I. Mech. E. Conf. on "Vibrations and Noise in Pump*, Fan and Compressor Installations," University of Southampton, 1975.

87 Flynn, P.F., and Weber, H.G., "Design and Test of an Extremely Wide Flow Range Compressor," ASME paper 79-GT-80, 1979

88 Stenning, A.H., and Kriebel, A.R., "Stall Propagation in a Cascade of Airfoils," TRANS. ASME, Vol 80, May 1958, pp. 777–790.

89 Abdelhamid, A.N. and Bertrand, J., "Distinctions Between Two Types of Self-Excited Gas Oscillations in Vaneless Radial Diffusers," ASME paper 79-GT-58, 1979.

90 Jansen, W., "Rotating Stall in a Radial Vaneless Diffuser," ASME *Journal of Basic Engineering*, Dec. 1964, pp. 750–758.

91 Abdelhamid, A.N., Colwill, W.H., and Barrows, J.F., "Experimental Investigation of Unsteady Phenomena in Vaneless Radial Diffusers," ASME paper 78-GT-23, 1978.

92 Senoo, Y., Kinoshita, Y., and Ishida, M., "Asymmetric Flow in Vaneless Diffusers of Centrifugal Blowers," ASME JOURNAL OF FLUIDS ENGINEERING, Vol. 99, Mar. 1977, pp. 104–114.

93 Senoo, Y., and Kinoshita, Y., "Influence of Inlet Flow Conditions and Geometries of Centrifugal Vaneless Diffusers on Critical Angle for Reverse Flow," ASME JOURNAL OF FLUIDS ENGINEERING, Vol. 99, Mar. 1977, pp. 98–103.

94 Senoo, Y., and Kinoshita, Y., "Limits of Rotating Stall and Stall in Vaneless Diffuser of Centrifugal Compressors," ASME paper 78-GT-19, 1978.

95 Abdelhamid, A.N., "Analysis of Rotating Stall in Vaneless Diffusers of Centrifugal Compressors," ASME paper 80-GT-184, 1980.

96 Van Den Braembussche, R.A., Figue, P. and Roustan, M., "Rotating Non-Uniform Flow in Radial Compressors," presented at AGARD 55th Specialists Meeting. "Centrifugal Compressors, Flow Phenomena and Performance," Brussels, Belgium, 1980.

97 Imachi, K. and Tsurusaki, H., "Rotating Stall in a Vaneless Diffuser of a Centrifugal Fan," in *Flows in Primary and Non-Rotating Turbomachinery Passages*, ASME Winter Annual Meeting, 1979.

98 Rubin, S., "Longitudinal Instability of Liquid Rockets Due to Propulsion Feedback (POGO)," *J. Spacecraft and Rockets*, Vol. 3, No. 8, Aug. 1966, pp. 1188–1195.

99 NASA SP-8055, "Prevention of Coupled Structure Propulsion Instability (POGO)," Oct. 1970.

100 Zielke, W., Wylie, E.B., and Keller, R.B., "Forced and Self-Excited Oscillations in Propellant Lines," ASME *Journal of Basic Engineering*, Vol. 91, Dec. 1969, pp. 671–677.

101 Kamijo, K., Shimura, T., and Watanabe, M., "Experimental Investigation of Cavitating Inducer Instability," ASME paper 77/WA-FE-14, 1977.

102 Natazon, M.S., Bal'tsev, N.I., Bazhanov, V.V. and Leydervarger, M.R., "Experimental Investigation of Cavitation-Induced Oscillations of Helical Inducers," *Fluid Mechanics-Soviet Research*, Vol. 3, No. 1, pp. 38–45.

103 Sack, L.E., and Nottage, H.B., "System Oscillations Associated With Cavitating Inducders," ASME *Journal of Basic Engineering*, Vol. 87, Dec. 1965, pp. 917–924.

104 Young, W.E., Murphy, R., and Reddecliff, J.M., "Study of Cavitating Inducer Instabilities," Pratt & Whitney report PWA FR-5131, 1972.

105 Hobson, D.E., and Marshall, A., "Surge in Centrifugal Pumps," in *Proc. of the Sixth Conference on Fluid Machinery*, Vol. I, Hungarian Academy of Sciences, Budapest, 1979.

106 Ng, S.L., "Dynamic Response of Cavitating Turbomachines," Cal. Inst. of Tech. Report No. E.183.1, Div. Eng. and Appl. Sc., 1976.

107 Lakshminarayana, B., Britsch,W.R., and Gearhart, W.S. editors, Fluid Mechanics, Acqustics and Design of Turbomachinery, Session VI, "Pumping Machinery for Aerospace Applications," M.J. Hartmann, Chairman, NASA SP-304, 1974, pp. 629–759.

108 Braisted, D.M., "Cavitation Induced Instabilities Associated With Turbomachines," Report No. E184.2, Div. Eng. and Appl. Sc., Cal. Inst. of Tech., 1979.

109 Brennen, C.E., and Acosta, A., "The Dynamic Transfer Function for a Cavitating Inducer," ASME JOURNAL OF FLUIDS ENGINEERING, Vol. 98, 1976, pp. 182–191.

110 Ng, S.L. and Brennen, C.E., "Experiments on the Dynamic Behavior of Cavitating Pumps," ASME JOURNAL OF FLUIDS ENGINEERING, Vol. 100, June 1978, pp. 166–176.

111 Brennen, C.E., "Bubbly Flow Model for the Dynamic Characteristics of Cavitating Pumps," *Journal of Fluid Mechanics*, Vol. 89, 1978, pp. 223–240.

112 Brennen, C.E. et al., "Scale Effects in the Dynamic Transfer Functions for Cavitating Inducers," 1979 (unpublished).

113 Malloy, C.T., "Use of Four-Pole Parameters in Vibration Calculation," *J. Acoustic Soc. America*, Vol. 29, No. 7, pp. 842–853.

114 Pipes, L.A., and Hovanessian, S.A., "Electrical Application of Matrices," Chapter 5 in *Matrix Computer Methods in Engineering*, Wiley, 1969.

115 Brennen, C.E., and Braisted, D.M., "Stability of Hydraulic Systems with Focus on Cavitating Pumps," *Proc. of IAHR Conference*, Tokyo, Japan, 1980.

116 Braisted, D.M., and Brennen, C.E., "Auto-Oscillation of Cavitating Inducers," *Proc. of Conference on Polyphase Flows*, ASME, July 1980.

117 Brennen, C.E., "On Unsteady Dynamic Response of Phase Changes in Hydraulic Systems," in *Proc. of 1978 Int. Seminar of Int. Center for Heat and Mass Transfer in Two-Phase and Chemical Systems*, Dubrovnik, Yugoslavia, 1978, Hemisphere Publishing Corp.

118 Brennen, C.E., "A Linear Dynamic Analysis of Vent Condensation Stability," submitted to ASME JOURNAL OF FLUIDS ENGINEERING, 1979.

119 Wong, G.S., MacGregor, C.A., and Hoshide, R., "Suppression of Cavitation and Unstable Flow in Throttled Turbopumps," *J. Spacecraft and Rockets*, Vol. 2, Jan.-Feb. 1965, pp. 73–80.

120 Nagengast, P., "Cavitation Patterns and System Instabilities of a Shrouded Inducer," 1967 ASME Cavitation Forum, pp. 28–31.

121 Black, H.F., and Dos Santos, L., "Stability of Oscillations in Boiler Feed Pump Pipe-Line Systems," I. Mech. E. Conference on "Vibrations and Noise in Pump, Fan, and Compressor Installations," University of Southampton, 1975.

122 Badowski, H.R., "An Explanation for Instability in Cavitating Inducers," 1973 ASME Cavitation and Polyphase Flow Forum, pp. 38–40.

123 Paul, D.L., and Younghans, J.L., "Inlets and Inlet Engine Integration," Chapter 13 in *The Aerothermodynamics of Aircraft and Gas Turbine Engines*, G.C. Oates, Editor, Air Force Aero Propulsion Laboratory, AFAPL-TR-78-52, 1978.

124 Wyatt, D.D., "A Review of Supersonic Air Intake Problems," in *Air Intake Problems in Supersonic Propulsion*, edited by J. Fabri, Pergamon Press, 1958.

125 Chang, C.C., and Han, C-T, "Aerodynamic Instability of Supersonic Inlet Diffusers," *Am. Rocket Society Journal*, May 1960, pp. 468–475.

126 Sterbentz, W.H., and Evvard, J.C., "Criterion for Prediction and Control of Ram-Jet Flow Pulsations," NACA TN 3506, 1955.

127 Leynaert, J., "Pompage Dans Les Entrees d'Air Supersoniques," *L'Aeronautique et l'Astronautique*, No. 22, 1970-1976, pp. 47–62.

128 Hankey, W.L., Jr., Hunter, L.G., Jr., and Harney, D., "Self-Sustained Oscillations (Buzz) on Spiked Tipped Bodies at Mach 3," Air Force Flight Dynamics Laboratory, Wright-Patterson Air Force Base, AFFDL-TM-99-23-FXM

129 Jungowski, W.M., "Some Self Induced Supersonic Flow Oscillations," *Progress in Aerospace Sciences*, Vol. 18, 1978, pp. 151–175.

130 Hankey, W.L. and Shang, J.S., "The Numerical Solution to Pressure Oscillations in an Open Cavity," AIAA paper 79-0136, 17th Aerospace Sciences Meeting, Jan. 1979.

131 Rockwell, D., and Nuadascher, E., "Review—Self Sustaining Oscillations of Flow Past Cavities," ASME JOURNAL OF FLUIDS ENGINEERING, Vol. 100, June 1978, pp. 152–165.

132 Rockwell, D., and Naudascher, E., "Self-Sustained Oscillations of Impinging Free Shear Layers," *Annual Review of Fluid Mechanics*, Vol. 11, 1979, pp. 67–94.

133 Boure, J.A., Bergles, A.E., and Tong, L.S., "Review of Two Phase Flow Instability," *Nuclear Engineering and Design*, Vol. 25, 1973, pp. 165–192, (Revised and expanded version of ASME paper 71-HT-42)

134 Boure, J.A., "Oscillatory Two Phase Flows," Chapter 11 in *Two-Phase Flows and Heat Transfer With Application to Nuclear Reactor Design Problems*, J.J. Ginoux, editor, Hemisphere Publishing Corp., 1978.

135 Greitzer, E.M., "Film Boiling on Vertical Surfaces," Technical Report No. 1, Div. of Eng. and Appl. Physics, Harvard University, June 1969.

136 Hsu, Y-Y. and Graham, R.W., *Transport Processes in Boiling and Two-Phase Systems*, Hemisphere Publishing Corp., 1976.

137 Hewitt, G.F., "Burnout," Chapter 8 in *Two-Phase Flows and Heat Transfer with Applications to Nuclear Reactor Design Problems*, Hemisphere Publishing Corp. 1978.

138 Griffith, P., "Pressure Drop Flow Rate Instabilities in Two Phase Systems," MIT notes (unpublished).

139 Stenning, A.H., Veziroglu, T.N., and Callahan, G.M., "Pressure Drop Oscillations in Forced Convection Flow with Boiling," *Proc. of Symposium on Two Phase Flow Dynamics*, Eindhoven, 1967.

140 Maulbetsch, J.S., and Griffith, P., "A Study of System Induced Instabilities in Forced-Convection Flows with Subcooled Boiling," MIT report No. 5382-35, Dept. of Mechanical Engineering, Apr. 1965.

141 Stenning, A.H., and Veziroglu, T.N., "Flow Oscillation Modes in Forced Convection Boiling," *Proc. of Heat Transfer and Fluid Mechanics Institute*, 1965, pp. 301–316.

142 Akyuzlu, K., Veziroglu, T.N., Kakac, S., and Dogan, T., "Finite Difference Analysis of Two-Phase Flow Pressure Drop and Density Wave Oscillations," Heat Transfer Laboratory Report, Univ. of Miami, Apr. 1979.

143 Dogan, T., Veziroglu, T.N., Kakac, S., Akyuzlu, K., "A Numerical Approach for the Analysis of Boiling Flow Instabilities," 1979.

144 Bergles, A.E., "Review of Instabilities in Two Phase Flow," in *Proceedings of the NATO Advanced Study Institute*, Istanbul, Turkey, Aug. 1976, edited by S. Kakac and F. Mayinger, Hemisphere Publishing Corp. 1977.

145 Yadigaroglu, G., "Two Phase Flow Instabilities and Propagation Phenomena" in VonKarman Lecture Series 1978-5, Two Phase Flows in Nuclear Reactors, VonKarman Institute, Brussels, Belgium, 1978.

146 El-Masri, M., "A Review of Two-Phase Flow Instability" (unpublished).

147 Ishii, M., "Study on Flow Instabilities in Two-Phase Mixtures," Report ANL-76-23, Argonne National Laboratory, 1976.

148 Ozawa, M. et al, "Oscillatory Flow Instabilities in Air-Water Two-Phase Flow Systems," *Bulletin of the JSME*, Vol. 22, No. 174, 1979, pp. 1763–1770.

149 Nakanishi, S. et al., *Trans JSME* 44-388 (1978-12) 1978 (in Japanese), pp. 4245–4249.

150 Stenning, A.H., and Griffith, P., "Density Wave Oscillations," MIT notes (unpublished).

151 Wallis, G.B., "One Dimensional Waves," Chapter 6 in *One Dimensional Two Phase Flow*, McGraw-Hill, 1969.

152 Saha, P., Ishii, M., and Zuber, N., "An Experimental Investigation of the Thermally Induced Flow Oscillations in Two-Phase Systems," ASME paper 75-WA-HT6, 1975.

153 Patel, B.R., and Runstadler, P.W., Jr., "Investigations into the Two-Phase Behavior of Centrifugal Pumps," in *Polyphase Flow in Turbomachinery*, ASME Winter Annual Meeting, 1978, Published by ASME.

154 Rothe, P.H., Runstadler, P.W., Jr. and Dolan, F.X., "Pump Surge Due to Two-Phase Flow," in *Polyphase Flow in Turbomachinery*, ASME Winter Annual Meeting, 1978, Published by ASME.

155 Murakami, M., and Minemura, K., "Effects of Entrained Air on the Performance of a Centrifugal Pump," *Bulletin of the JSME*, Vol. 17, No. 110, 1974, pp. 1047–1055.

156 Kakac, S., Ozboya, N. Veziroglu, T.N., and Lee, S.S., "Transient Boiling Flow Instabilities in a Multi-Channel Upflow System," in *Two Phase Transport and Reactor Safety*, Vol. II, *Proceedings of the Two-Phase Flow and Heat Transfer Symposium*, Fort Lauderdale, Fla., 1976, ed. by T.N. Veziroglu and S. Kakac.

157 Fukuda, D.K., and Kobori, T., "Two-Phase Flow Instability in Parallel Channels," Sixth Int. Heat Transfer Conference, Toronto, Canada, Vol. I, 1978, pp. 369–375.

158 Barrere, M., and Williams, F.A., "Comparison of Combustion Instabilities Found in Various Types of Combustion Chambers," Twelfth Symposium (International) on Combustion, The Combustion Institute, 1968, pp. 169–181.

159 Crocco, L., and Cheng, S.I., *Theory of Combustion Instability in Liquid Propellant Rocket Motors*, AGARDograph 8, Butterworths, 1956.

160 Tsien, H.S., *Engineering Cybernetics*, Chapter 8, McGraw-Hill, 1954.

161 Crocco, L., "Theoretical Studies on Liquid-Propellant Rocket Instability," Tenth Symposium (International) on Combustion, The Combustion Institute, 1965, pp. 1101–1127.

162 Crocco, L., "Research on Combustion Instability in Liquid Rockets," Twelfth Symposium (International) on Combustion, The Combustion Institute, 1969.

163 *Liquid Propellant Rocket Combustion Instability*, D.T. Harrje, Editor. NASA SP-194, 1972.

164 Rayleigh, Lord, "The Explanation of Certain Acoustical Phenomena," Friday Evening Lecture at the Royal Institute, March 15, 1878; see also *The Theory of Sound*, Vol. II, Dover Pub. Co., 1945, pp. 226–230.

165 Thring, W., "Combustion Oscillations in Industrial Combustion Chambers," Twelfth Symposium (International) on Combustion, 1968, pp. 163–168.

166 Kydd, P.H., "Analysis and Experiments on Unsteady Flows in Gas Turbine Main Combustors," Twelfth Symposium (International) on Combustion, pp 183–192., The Combustion Institute, 1968.

167 Mauss, F., Perthuss, E., and Sale, B., "A Contribution to the Study of Low Frequency Oscillations in Fuel Oil Boilers," Tenth Symposium (International) on Combustion, The Combustion Institute, 1965, pp. 1241–1249.

168 Pariel, J.M., and De Saint Martin, L., "Contribution to the Study of Nonsteady-State Combustion in Industrial Hearths," Twelfth Symposium (International) on Combustion, The Combustion Institute, 1968, pp. 193–201.

169 Thring, M.W., "A Non-Acoustic Theory of Oscillations in Pressure Jet Oil-Fired Combustion Chambers," Seventh Symposium (International) on Combustion, Butterworths, 1959, pp. 659–663.

170 Marble, F.E., and Candel, S.M., "An Analytical Study of the Non-

Steady Behavior of Large Combustors," Seventeenth Symposium (International) on Combustion, The Combustion Institute, 1978, pp. 761–769.

171 Zukoski, E.E., "Afterburners," Chapter 21 in *The Aerodynamics of Gas Turbine Engines*, G. Oates, editor, AFAPL-TR-78-52, Air Force Aero Propulsion Laboratory, 1978.

172 Weavers, D.S., Adubi, F.A., and Kouwen, N., "Flow Induced Vibrations of a Hydraulic Valve and Their Elimination," ASME JOURNAL OF FLUIDS ENGINEERING, Vol. 100, June 1978, pp. 239–245.

173 Lyssenko, P.E., and Chepajkin, G.A., "On Self-Excited Oscillations of Seals Concerning the Gates of Hydro-Technical Structures," *Proceedings IUTAM-IAHR Symposium on Flow Induced Structural Vibrations*, Karlsrhue 1972, Springer-Verlag, 1974.

174 Abbott, H.F., Gibson, W.L., and McCaig, "Measurements of Auto-Oscillation in a Hydroelectric Supply Tunnel and Penstock System," ASME *Journal of Basic Engineering*, Vol. 85, Dec. 1963, pp. 625–630.

175 Dussourd, J.L., "An Investigation of Pulsations in the Boiler Feed System of a Central Power Station," ASME *Journal of Basic Engineering*, Vol. 90, Dec. 1968, pp. 607–619.

176 Dartnell, L., "Hydraulic and Thermal Hydraulic Instability in Condensate Feed Systems for Large Thermal Power Stations," *Proc. Inst. Mech. Engineers*, Vol. 186, 1972, pp. 585–593.

177 Sparks, C.R., and Wachel, J.C., "Pulsations in Liquid Pumps and Piping Systems," in *Proceedings of the Fifth Turbomachinery Symposium*, Texas A & M University, edited by M.P. Boyce, 1976.

178 Sweet, L.M., Richardson, H.H., and Wormley, D.N., "Plenum Air Cushion/Compressor-Duct Dynamic Interactions," ASME paper 75-WA/Aug-23, 1975.

179 Emmons, H.W., "Introduction," in *Symposium on Compressor Stall, Surge, and System Response*, ASME, 1960.

180 Ehrich, F.E., "Aerodynamic Stability of Branched Diffusers," ASME *Journal of Engineering for Power*, Vol. 92, July 1970, pp. 330–334.

181 Dussourd, J.L., and Putman, W.C., "Instability and Surge in Dual Entry Centrifugal Compressors," in *Symposium on Compressor Stall, Surge and System Response*, ASME, 1960.

182 Chesire, L.J., "The Design and Development of Centrifugal Compressors for Aircraft Gas Turbines," *Proc. Inst. Mech. Eng.*, Vol. 153, 1945, p. 426–440.

183 Goldschmeid, F.R., and Wormley, D.N., "Frequency Response of Blower/Duct/Plenum Fluid Systems," *Journal of Hydronautics*, Vol. 11, Jan. 1977, pp. 18–27.

APPENDIX

Elementary Stability Analyses of Several Pumping Systems

In this appendix we present analyses describing four of the system instabilities that have been discussed in the paper. The systems examined are: 1) the "Basic Pumping System" shown in Fig. 1, 2) the "Idealized Pumping System with a Cavitating Turbopump" shown in Fig. 39, 3) the "Two-Phase Flow Pumping System" shown in Fig. 48, and 4) a Pumping System with Unsteady Heat Addition.

The analyses have been carried out to show, with a minimum of algebraic complexity, the basic parameters that enter into the determination of the system dynamics, as well as to illustrate in a simple fashion the trends that occur as these parameters are varied. It is therefore strongly emphasized that they should only be regarded (as the title of the Appendix indicates) as *elementary* approaches to these phenomena. More accurate (and more complex) models have indeed been developed, and these can be found in the references that are cited in the appropriate sections. It is felt, however, that the basic analyses presented below are a useful introductory adjunct to the material presented in the main body of the text, and that they demonstrate the central physical concepts that are common to the diverse systems that have been described.

1) The Basic Pumping System (Compression System) Shown in Fig. 1. Consider the "Basic Pumping System" represented in Fig. 1 which consists of a pump, a volume with capacity for transient mass storage, and a throttle. The liquid that is pumped is taken to be incompressible and the mass of gas (air) in the volume to behave isentropically. The transient pump performance is also taken to be quasi-steady. More elaborate allowances for unsteady behavior can be found [16], but this approximation will suffice here. Assuming that the pump output is significantly larger than the dynamic pressure based on the through-flow velocity (as is generally true in a centrifugal pump), the first integral of the momentum equation between station 0 and station 1 can be written

$$P_0 - P_1 = \int_0^1 \rho \frac{\partial C_x}{\partial t}\, dx - \Delta P_P \tag{A-1}$$

where C_x is the axial velocity, ΔP_P is the *pump pressure rise* and is a function of pump mass flow, $\dot{m}_1$, and x is in the streamwise direction. Using continuity we can define a length L such that

$$L = A_{in} \int_0^1 \frac{dx}{A(x)} \tag{A-2}$$

where $A(x)$ is the area at different values of x, and A_{in} is a convenient reference area. Thus

$$P_0 - P_1 = \frac{L}{A_{in}} \frac{d\dot{m}_1}{dt} - \Delta P_P \tag{A-3}$$

since the mass flow is the same at all stations from 0 to 1.

A similar equation could be written for the throttle. However, it is found in practice that, in many throttling elements, by far the largest part of the pressure drop occurs due to the quasi-steady throttling characteristics of the device, i.e., the inertance in the throttle can be neglected. Thus we can write

$$P_1 - P_2 = \Delta P_T \tag{A-4}$$

where ΔP_T is the *throttle pressure drop* and is a function of throttle mass flow $\dot{m}_2$, which is not necessarily the same as $\dot{m}_1$.

In the volume we assume that fluid accelerations are negligible and the pressure is spatially uniform, although varying in time. The mass conservation equation for the volume is

$$\dot{m}_1 - \dot{m}_2 = -\rho \frac{dV_a}{dt} \tag{A-5}$$

where V_a is the volume of the air in the plenum. Mass conservation for the air in the volume is:

$$\frac{d}{dt}(\rho_a V_a) = 0 \tag{A-6}$$

These equations, plus the isentropic relation ($\ln P_a + \gamma \ln V_a$ = constant) for the gas in the plenum, describe the system behavior.

To find whether the system is stable or unstable we examine the response to small perturbations for a system operating at a given mean operating condition. To do this we will represent the flow quantities as being composed of a mean (time-independent) part, denoted by an overbar ( ), and a small perturbation, denoted by δ, and only retain quantities of the first order in δ. Under these conditions we can write the mass flow as

$$\dot{m} = \bar{\dot{m}} + \delta\dot{m}$$

the pump performance as

$$\Delta P_P = \overline{\Delta P_P} + \delta \Delta P_P = \overline{\Delta P} + \left(\overline{\frac{d\Delta P_P}{d\dot{m}}}\right) \delta\dot{m} \tag{A-7}$$

etc. In equation (A-7) we have used a Taylor series expansion about the mean operating point, $\overline{\Delta P_P}$. The (steady-state) slope

of the pump characteristic, $(\overline{d\Delta P_P/d\dot{m}})$, is taken to be a known quantity.

If we apply this linearization to the above equations, and subtract off the mean flow quantities ($\dot{m}_1 = \dot{m}_2 = \dot{m}$; $\overline{\Delta P_P} = \overline{\Delta P_T}$) we arrive at equations for the perturbation quantities, $\delta\dot{m}_1$, $\delta\dot{m}_2$, δP_1:

$$\left(\frac{d\bar{\Delta}P_P}{d\dot{m}}\right)\delta\dot{m}_1 - \frac{L}{A_{in}}\frac{d}{dt}\delta\dot{m}_1 - \delta P_1 = 0 \tag{A-8}$$

$$\left(\frac{d\bar{\Delta}P_T}{d\dot{m}}\right)\delta\dot{m}_2 - \delta P_1 = 0 \tag{A-9}$$

$$\delta\dot{m}_1 - \delta\dot{m}_2 - \frac{\rho}{\gamma P_1} V_a \frac{d}{dt}(\delta P_1) = 0 \tag{A-10}$$

where we have used the conditions that P_0 and P_2 are constant.

Equations (A-8) to (A-10) are all linear with constant coefficients. Hence the solutions are of the form e^{st}. For stability the real part of s must be negative.

Substituting expressions of the form e^{st} for the perturbations we find that if there are to be non-trivial solutions to the resulting system of linear algebraic equations, the growth rate, s, must satisfy the equation:

$$s^2 + s\left\{\left[\frac{\gamma P_1}{\rho V_a}\frac{L}{A_{in}}\frac{1}{\left(\overline{\frac{d\Delta P_T}{d\dot{m}}}\right)} - \left(\frac{d\bar{\Delta}P_P}{d\dot{m}}\right)\right]\frac{A_{in}}{L}\right\}$$

(a)

$$+\left\{1 - \frac{\left(\overline{\frac{d\Delta P_P}{d\dot{m}}}\right)}{\left(\overline{\frac{d\Delta P_T}{d\dot{m}}}\right)}\right\}\frac{A_{in}}{LV_a}\frac{\gamma P_1}{\rho} = 0. \tag{A-11}$$

(b)

For *instability* either quantity in brackets can be negative. Condition (b) is the static stability criterion, while condition (a) is that for dynamic stability. These imply restrictions on the slope of the pump characteristic. In general the condition for dynamic stability, bracket (a), is the more critical, and since throttle slopes are often steep and volumes large, this may occur very near the peak of the pump characteristic curve. Bracket (b) represents the static stability criterion discussed in the Introduction.

Note that we have based this derivation on the liquid pumping system shown in Figure 1. We can also consider a compressor (whose pressure rise is small compared to the ambient level) operating in a gas. In this case the capacity for mass flow storage in the volume is due to the compressibility of the flowing medium. The analysis is not changed materially. The only change in equation (A-11) is that the density that appears is the air density, so that $\gamma P/\rho$ is now the square of the sound speed. We can thus write the equation for s as

$$s^2 + s\left\{\left[\frac{a^2}{V_a}\frac{L}{A_{in}}\frac{1}{\left(\overline{\frac{d\Delta P_T}{d\dot{m}}}\right)} - \left(\overline{\frac{d\Delta P_P}{d\dot{m}}}\right)\right]\frac{A_{in}}{L}\right\}$$

$$+\omega^2\left\{1 - \frac{\left(\overline{\frac{d\Delta P_P}{d\dot{m}}}\right)}{\left(\overline{\frac{d\Delta P_T}{d\dot{m}}}\right)}\right\} = 0 \tag{A-12}$$

where $\omega = a\sqrt{A/LV_a}$, the Helmholtz resonator frequency for the system. This is the natural frequency of the system and can be seen to be independent of compressor speed.

Finally note that if one carries out the analysis using non-dimensional quantities [denoted by tildes (~)] which are defined by

$$\phi = \frac{\dot{m}}{\rho A_{in} U},$$

$$\delta\tilde{P}, \Delta\tilde{P}_P, \Delta\tilde{P}_T = \frac{\delta P}{\frac{1}{2}\rho U^2}, \frac{\Delta P_P}{\frac{1}{2}\rho U^2}, \frac{\Delta P_T}{\frac{1}{2}\rho U^2},$$

$$\tilde{t} = \omega t$$

it is found that equation (A-12) can be written as

$$\tilde{s}^2 + \tilde{s}\left\{\frac{1}{B\left(\overline{\frac{d\bar{\Delta}P_T}{d\phi}}\right)} - B\left(\overline{\frac{d\bar{\Delta}P_P}{d\phi}}\right)\right\} + \left\{1 - \frac{\left(\overline{\frac{d\bar{\Delta}P_P}{d\phi}}\right)}{\left(\overline{\frac{d\bar{\Delta}P_T}{d\phi}}\right)}\right\} = 0 \tag{A-13}$$

where B is the parameter

$$B = \frac{U}{2\omega L} \tag{A-14}$$

defined in the section on axial compressor stability. It can be seen clearly from this that for given compressor (or pump) and throttle characteristics, changing the value of B can considerably alter the damping and hence the system dynamic response.

2) The Cavitating Turbopump System Shown in Fig. 39. The station numbers are given in the figure. The equations that describe the system response can be written as follows:

$$P_0 - P_1 = \frac{L_1}{A_1}\frac{d\dot{m}_1}{dt} \tag{A-15}$$

where L_1 is an effective length of the inlet duct defined as in 1). Since we are again concerned with the behavior of small perturbations about a mean operating point, we linearize as before, so that equation (A-15) becomes

$$-\delta P_1 = \frac{L_1}{A_1}\frac{d\delta\dot{m}_1}{dt} \tag{A-16}$$

The pump performance is now a function of two variables, the inlet mass flow ($\dot{m}_1$) and the absolute pressure level at inlet, P_1. In addition we include the possibility for pressure changes due to inertance within the pump, i.e., pressure changes associated with local accelerations within the pump. Therefore for small perturbations about the given mean, (constant speed) operating point, the perturbations in pump performance are given by

$$\delta P_2 - \delta P_1 = \left(\overline{\frac{\partial\Delta P_P}{\partial P_1}}\right)\delta P_1 + \left(\overline{\frac{\partial\Delta P_P}{\partial\dot{m}}}\right)\delta\dot{m}_1 - \frac{L_P}{A_1}\frac{d\delta\dot{m}_1}{dt} \tag{A-17}$$

The quantities $(\partial\bar{\Delta}P_P/\partial P_1)$ and $(\partial\bar{\Delta}P_P/\partial\dot{m})$ are the (known) slopes of the steady-state, pump performance curves and L_P is the effective length within the pump (i.e., from stations 1 to 2).

The volume of vapor contained within the pump due to cavitation, V_c, is also a function of inlet mass flow and pressure. Thus the perturbation in this volume is

$$\delta V_c = \left(\overline{\frac{\partial V_c}{\partial P_1}}\right)\delta P_1 + \left(\overline{\frac{\Delta V_c}{\partial\dot{m}}}\right)\delta\dot{m}_1 \tag{A-18}$$

Assuming the vapor and liquid can be taken as incompressible, with $\rho_g/\rho << 1$, the linearized mass con-

servation equation between stations 1 and 2 is:

$$\delta\dot{m}_2 - \delta\dot{m}_1 = \rho \frac{d\delta V_c}{dt} \tag{A-19}$$

Finally, as in 1), the linearized throttle pressure drop can be expressed by

$$\delta P_2 = \left(\frac{\overline{d\Delta P_T}}{d\dot{m}}\right)\delta\dot{m}_2 \tag{A-20}$$

As before we can assume that all the perturbations are of the form e^{st} and substitute into equations (A-16) through (A-20). The condition that the resulting system of equations has a non-trivial solution then results in the following equation for the growth rate, s:

$$s^2 - s\left\{\frac{\frac{L_1}{\rho A_1}\left[\frac{1+\left(\frac{\overline{\partial\Delta P_P}}{\partial P_1}\right)+\frac{L_P}{L_1}}{\left(\frac{\overline{d\Delta P_T}}{d\dot{m}}\right)}\right]+\left(\frac{\overline{\partial V_c}}{\partial\dot{m}}\right)}{\frac{L_1}{A}\left(\frac{\overline{\partial V_c}}{\partial P_1}\right)}\right\} - \left\{\frac{1-\frac{\left(\frac{\overline{\partial\Delta P_P}}{\partial\dot{m}}\right)}{\left(\frac{\overline{d\Delta P_T}}{d\dot{m}}\right)}}{\rho\frac{L_1}{A_1}\left(\frac{\overline{\partial V_c}}{\partial P_1}\right)}\right\} = 0 \tag{A-21}$$

The quantity $(\overline{\partial V_c}/\partial P_1)$, the rate of change of vapor volume with inlet pressure (due to cavitation), is a negative number. The pump pressure-flow characteristic is also negatively sloped at the conditions of interest. Therefore the condition for *instability* is that the quantity in the first bracket is negative. This means that for instability

$$\left(\frac{\overline{\partial V_c}}{\partial\dot{m}}\right) < -\left\{\frac{\frac{L_1}{\rho A_1}\left[1+\left(\frac{\overline{\partial\Delta P_P}}{\partial P_1}\right)+\frac{L_P}{L_1}\right]}{\left(\frac{\overline{d\Delta P_T}}{d\dot{m}}\right)}\right\} \tag{A-22}$$

Thus if $(-\overline{\partial V_c}/\partial m)$, which represents the mass flow gain factor, is large enough the system will be unstable. Although this analysis is perhaps overly simple, we can note that the experimental results (as well as more elaborate dynamic pump models [111]) do show values for mass flow gain factor which have qualitatively similar behavior, at low frequency, to the basic description given here. The occurrence of a significant negative value of $(\partial\bar{V}_c/\partial\dot{m})$ in the region of interest is thus in accord with the actual physical situation.

We can readily see some further implications of this analysis if we cast the results in nondimensional form. Therefore let us define the variables

$$\phi_t = \dot{m}/\rho U_t A_1$$

$$\tilde{\Delta P}_P, \tilde{P}, \tilde{\Delta P}_T = \frac{\Delta P_P}{\frac{1}{2}\rho U_t^2}, \frac{P}{\frac{1}{2}\rho U_t^2}, \frac{\Delta P_T}{\frac{1}{2}\rho U_t^2}$$

$$\tilde{V}_c = V_c/A_1 L_P$$

$$\tilde{s} = \frac{sL_p}{U_t}$$

Substituting into equation (A-21), and using $\partial(\ )/\partial\sigma = 1/2\,\rho U_t^2\,\partial(\ )/\partial P$ we find an equation for the nondimensional growth rate $\tilde{s}$.[24]

$$\tilde{s}^2 - \tilde{s}\left\{\frac{\left[1+\left(\frac{\overline{\partial\tilde{\Delta}P_P}}{\partial\sigma}\right)+\frac{L_P}{L_1}\right]}{\left(\frac{\overline{d\tilde{\Delta}P_T}}{d\phi_t}\right)\left(\frac{\overline{\partial\tilde{V}_c}}{\partial\sigma}\right)} = \frac{\frac{L_P}{2L_1}\left(\frac{\overline{\partial\tilde{V}_c}}{\partial\phi_t}\right)}{\left(\frac{\overline{\partial\tilde{V}_c}}{\partial\sigma}\right)}\right\} - \left\{\frac{1-\left(\frac{\overline{\partial\tilde{\Delta}P_P}}{\partial\phi_t}\right)\Big/\left(\frac{\overline{d\Delta\tilde{P}_T}}{d\phi_t}\right)}{\left(\frac{\overline{\partial\tilde{V}_c}}{\partial\sigma}\right)}\right\}\left(\frac{L_P}{2L_1}\right) = 0 \tag{A-23}$$

As the speed is changed, none of the coefficients in the equation will change. Hence the dimensional natural frequency should scale as the speed and the stability point should be independent of speed, in contrast to the results for the pumping system analyzed in part 1.

Several comments can be made about the conclusions of this simple stability analysis. First as discussed in the body of the paper, the frequency scales directly with pump speed for fixed values of mean flow and cavitation number, and this appears to be in accord with the experimental results shown in [108]. Second, it is found that if the curve of pump pressure rise versus inlet pressure (i.e., cavitation number) has a steep positive slope, as it will in the region of "head breakdown," this will tend to stabilize the system. This can perhaps be seen most directly from equation (A-22), and is again in general accord with the experimental data.

It is also important, however, to note the features of the phenomenon that are not described adequately within the scope of this simple model. One of these is the dependence on frequency of the pump activity parameter and the net energy flux, as shown in [108] and [116]. Another is seen in the quantitative prediction of auto-oscillation frequency in [116] (where the experimental configuration has a pump inertance much larger than the upstream line inertance). In addition the fluid mechanics of the inlet line appears to be more complex than can be described by a simple one-dimensional model. In summary, it is again to be remarked that the analysis here is deliberately simplified to focus on the central features of the phenomenon and to show the overall trends, and should not therefore be expected to model all the aspects of auto-oscillation in a quantitative manner.

3) Pressure Drop Instabilities in Two-Phase Flows. We consider the system shown in Fig. 48 in which a liquid is pumped through a heated section, of constant heat flux. The station locations are also given in the figure. The liquid is subcooled at inlet, but can be of significant quality at exit. The steady-state pressure drop across the heated section plus the throttle, $P_2 - P_3$, is denoted by ΔP_H, and is a function of the mass flow to this section. Again we assume that the transient pressure drop characteristic can be modeled by a quasi-steady part plus a term which accounts for the inertia of the fluid in the section between 2 and 3. Thus

$$P_2 - P_3 = \Delta P_H + \frac{L_H}{A}\frac{d\dot{m}_2}{dt} \tag{A-24}$$

where the subscript H refers to the overall element between 2 and 3 and A is a reference area, say the area at inlet to the heated section. As in 1) and 2) we consider small perturbations about a mean operating point, linearize, and

[24] σ is the cavitation number, $\sigma = (P_1 - P_v)/(1/2\,\rho U_t^2)$

subtract out the mean quantities to obtain an expression in terms of the perturbation quantities:

$$\delta P_2 = \left(\frac{\overline{d\Delta P_H}}{d\dot{m}}\right)\delta\dot{m}_2 + \frac{L_H}{A}\frac{d\delta\dot{m}_2}{dt}. \qquad \text{(A-25)}$$

In deriving this we have taken station 3 to refer to a downstream reservoir at constant pressure so that $\delta P_3 = 0$.

In a similar manner we can write the linearized equation for the pressure perturbation at station 1 in terms of the pump pressure rise curve, which represents the "external" pressure difference imposed on the heated section. Neglecting the inertia of the fluid in the pump lines we have:

$$\delta P_2 = \left(\frac{\overline{d\Delta P_P}}{d\dot{m}}\right)\delta\dot{m}_1, \qquad \text{(A-26)}$$

where we have used the condition that there are negligible fluid accelerations within the compliant volume chamber to set $P_1 = P_2$.

The difference between the mass flows at station 1 and 2 is related to the rate of change of mass in the volume. If V_c is the compliant volume we have (with $\rho_g/\rho << 1$)

$$\delta\dot{m}_1 - \delta\dot{m}_2 = -\rho\frac{dV_c}{dt} \qquad \text{(A-27)}$$

where ρ is the density of the liquid. The perturbations in volume can be related to those in pressure by

$$\delta V_c = \left(\frac{dV}{dP}\right)_c \delta P_2 \qquad \text{(A-28)}$$

where we will not at this point specify the precise nature of the relationship between P and V in the compliant volume. (The subscript c is used to denote conditions at the state of the gas in V_c.) This relation can be substituted into equation (A-27) to yield:

$$\delta\dot{m}_1 - \delta\dot{m}_2 = -\rho\left(\frac{\overline{dV}}{dP}\right)_c \frac{d\delta P_2}{dt} \qquad \text{(A-29)}$$

There are now three equations in three unknowns, and we can again take the perturbations to be of the form e^{st}, substitute into (A-25), (A-26), and (A-29), and use the condition for a nontrivial solution to exist to derive an expression for the growth rate, s. This is:

$$s^2 + s\left[\left(\frac{d\bar{\Delta}P_H}{d\dot{m}}\right)\frac{A}{L_H} + \frac{1}{\rho\left(\frac{d\bar{\Delta}P_P}{d\dot{m}}\right)\left(\frac{dV}{dP}\right)_c}\right] \qquad \text{(a)}$$

$$+\left\{\frac{A}{\rho L_H}\frac{1}{\left(\frac{dV}{dP}\right)_c}\left[\frac{\left(\frac{\overline{d\Delta P_H}}{d\dot{m}}\right)}{\left(\frac{d\bar{\Delta}P_P}{d\dot{m}}\right)} - 1\right]\right\} = 0 \qquad \text{(A-30)}$$

(b)

It is again useful to look at the individual bracketed terms. The condition for the system to be *unstable* is that either of the two square bracketed terms is negative. (In examining this, however, it is to be noted that $(\overline{dV/dP})_c$ will be negative.) Bracket (b) represents static instability. This is just the Ledinegg criterion of having the heated section pressure drop characteristic more steeply sloped negatively than the external (pump) pressure rise characteristic. It is not dependent on system volumes, lengths, etc. The other term (a) represents the dynamic instability mechanism discussed with reference to Fig. 50. It can be seen that for given heated section and external (pump) characteristic curves there is now an influence of other system parameters. In particular, if we make the (somewhat sweeping) approximation that the behavior of the compliant volume can be represented by an isentropic process so that $\ln P + \gamma \ln V = \text{const.}$, we can write the equation for s as:

$$s^2 + s\left[\left(\frac{d\Delta P_H}{d\dot{m}}\right)\frac{A}{L_H} - \frac{\gamma\bar{P}_c}{\rho\bar{V}_c}\frac{1}{\left(\frac{d\Delta P_P}{d\dot{m}}\right)}\right]$$

$$+\frac{A}{\rho L_H}\frac{\gamma\bar{P}_c}{\bar{V}_c}\left[1 - \frac{\left(\frac{d\Delta P_H}{d\dot{m}}\right)}{\left(\frac{d\Delta P_P}{d\dot{m}}\right)}\right] = 0 \qquad \text{(A-31)}$$

It can be seen from (A-31) that an increase in the compliant volume will be destabilizing whereas an increase in the overall pressure, or more precisely a decrease in the system compressibility, will be stabilizing. It can also be seen that increasing the throttling will be stabilizing, although, as stated in the paper, if the actual system has a compliant volume downstream of the throttle, this will be ineffective. (In addition, although one might tend to infer that increasing L_H is stabilizing, as emphasized above the conclusions reached with this simple model should not be pushed too far. As discussed in [124], an increased length in the actual situation can also result in an increased system compressibility as well and this can have the opposite effect.)

Two limiting cases can be mentioned with regard to equation (A-31). A constant flow system, with $(d\Delta P_P/d\dot{m}) = \infty$, is always statically stable but will be dynamically unstable at the minimum of the pressure drop versus flow curve, whereas a constant pressure drop system, with $(d\Delta P_P/d\dot{m}) = 0$, cannot exhibit dynamic instability, although it will be statically unstable at the minimum.

4) Effect of Unsteady Heat Input on Pumping System Stability. We consider a system somewhat similar to that shown in Fig. 1. However we now have a gas, rather than a liquid, as the working fluid. There is a compressor, a plenum in which heat is added to the fluid in a time varying manner, and a downstream throttle. In modeling the effect of this unsteady heat transfer on system stability, we will, for simplicity, restrict attention to the case where the heat transfer can be regarded as a perturbation only, denoted by δQ. We also limit the situations examined to cases where the compressor pressure and temperature rises are small compared to the ambient values, and where we have low Mach number in the compressor and throttle ducts and low frequency oscillations. Under these conditions the first integral of the momentum equation which relates *perturbations* in compressor duct mass flow and plenum pressure is

$$-\delta P_1 = \frac{L}{A}\frac{d\delta\dot{m}_1}{dt} - \left(\frac{d\Delta P_c}{d\dot{m}}\right)\delta\dot{m}_1 \qquad \text{(A-32)}$$

The equation for the pressure drop across the throttle similarly becomes

$$\delta P_1 = \left(\frac{d\Delta P_T}{d\dot{m}}\right)\delta\dot{m}_2 \qquad \text{(A-33)}$$

To link these we use the First Law applied to a control volume coincident with the plenum. The perturbation form of this is

$$-[C_p\delta\dot{m}_1\bar{T}_{T_1} + C_p\bar{\dot{m}}_1\delta T_{T_1}] + C_p\delta\dot{m}_2\bar{T}_{T_2}$$

$$+ C_p\bar{\dot{m}}_2\delta T_{T_2} = -V\frac{d}{dt}(\rho_1 C_v T_1) + \delta Q \qquad \text{(A-34)}$$

Under the conditions described above this can be approximated as

$$\delta\dot{m}_2 - \delta\dot{m}_1 = \frac{\delta Q'}{C_p \bar{T}} - \frac{V}{a^2}\frac{dP_1}{dt} \quad [25] \qquad \text{(A-35)}$$

Since we are interested in showing the effect of an unsteady heat input which is in phase with the pressure perturbations, we now take the perturbations in heat input to be of the form

$$\delta Q' = \mu \delta P_1 \qquad \text{(A-36)}$$

where μ is a (dimensional) positive constant.

Substituting in equation (A-35) we obtain

$$\delta\dot{m}_2 - \delta\dot{m}_1 = \frac{\mu \delta P_1}{C_p \bar{T}} - \frac{V}{\gamma R T}\frac{dP_1}{dt} \qquad \text{(A-37)}$$

Equations (A-33), (A-35) and (A-37) are the equations describing the dynamic behavior of the system. To investigate stability we again take the perturbations to be of the form e^{st} and substitute in these three equations to obtain one equation for the growth rate, s. This is

$$s^2 + s\left[-\left(\frac{\overline{d\Delta P_c}}{d\dot{m}}\right)\frac{A}{L} + \frac{a^2}{V\left(\frac{\overline{d\Delta P_T}}{d\dot{m}}\right)} - \mu\frac{(\gamma-1)}{V}\right] + \frac{a^2 A}{LV}\left[1 - \frac{\left(\frac{\overline{d\Delta P_c}}{d\dot{m}}\right)}{\left(\frac{\overline{d\Delta P_T}}{d\dot{m}}\right)} + \mu\frac{\left(\frac{\overline{d\Delta P_c}}{d\dot{m}}\right)}{C_p T}\right] = 0 \qquad \text{(A-38)}$$

It can be seen that the conditions for instability are altered from the case for no heat input. In particular, if the heat addition is intense enough, i.e., if μ is large enough, there is the possibility for instability.

Note that if we had restricted attention to the situation in which the system were a closed resonator such that $\dot{m}_2 = 0$, and there were no compressor in the duct connecting the plenum with the atmosphere $[(d\Delta P_c/d\dot{m}) = 0]$, the equation for s would reduce to

$$s^2 - \frac{(\gamma-1)\mu}{V} + \frac{a^2 A}{LV} = 0 \qquad \text{(A-39)}$$

This shows immediately that, in this simpler case, an unsteady heat input in phase with the pressure perturbation will lead to instability, as stated in the criterion due to Rayleigh.

[25] $\overline{\delta Q'} = \delta Q - \bar{\dot{m}} C_P \delta T_{T_2}$

REVIEW: Turbulent Developing Pipe Flow

A. Klein
Motoren- und Turbinen-Union, München GmbH, D8000 München, Germany

Experimental results on turbulent developing pipe flow are reviewed. Upstream conditions are shown to have a large effect, in particular on the development of the velocity profile. It is demonstrated also that the blockage factor, when plotted against the Reynolds number defined with flow distance, is the parameter best suited to indicate the onset and termination of transition.

Introduction

Until recently, flow development in pipes was believed to be solely determined by a flat-plate like growth of the wall-boundary layers. Therefore, the peakiness of the velocity profile, defined as the ratio between the maximum value and the spatial mean, was thought to increase gradually until the boundary layers meet at the pipe centerline. According to measurements quoted by Schlichting [1] this appeared to occur in turbulent flow after 25 to 100 pipe diameters, the exact length depending on the Reynolds number. Thereafter the flow was considered fully developed, that is, the flow properties were thought to have become independent of inlet conditions and to remain unchanged as the flow proceeded further down the pipe. In fact, however, developing pipe flow is much more complex. Bradley (quoted in [2]) appears to be the first who discovered that velocity profile peakiness may reach a maximum, which he found at about 40 pipe diameters, and then decrease again. Weir, Priest, and Shárán [3] also obtained a maximum core velocity at 40 pipe diameters, while gradual velocity increases along the pipe were measured by Deissler [4] and Sale [5]. The latter type of velocity distribution was produced in [3] also, when a trip ring was inserted at the pipe entrance (see also Shárán [6]). Thus it was shown that a change of inlet conditions may create substantial differences in flow development. To investigate this observation further, all the experimental results on turbulent velocity-profile development in pipes known to the author are reviewed. Since the performance of diffusers depends on the flow conditions at the ends of their entrance pipes, the present work is a necessary first step towards the comparison of diffuser data presented in the same issue of this Journal [7].

Turbulent Pipe Flow

The measure of flow development used in this review is Sovran and Klomp's [8] blockage factor which is defined by the ratio of the axisymmetric displacement thickness δ_{lax} to pipe radius R or of the ratio of the centerline velocity u_c to the spatial mean velocity $\bar{u}$ (the bulk velocity)

$$B = \frac{2\delta_{lax}}{R} = 1 - \frac{\bar{u}}{u_c}, \tag{1}$$

where

$$\frac{\delta_{lax}}{R} = \int_0^1 \left(1 - \frac{u}{u_c}\right) \frac{r}{R} d\left(\frac{r}{R}\right). \tag{2}$$

Some researchers used a two-dimensionally defined displacement thickness

$$\frac{\delta_{1two}}{R} = \int_0^1 \left(1 - \frac{u}{u_c}\right) d\left(\frac{r}{R}\right). \tag{3}$$

In these cases the blockage factor was calculated from

$$B = \frac{2\delta_{1two}}{R} - \left(\frac{\delta_{1two}}{R}\right)^2. \tag{4}$$

In Fig. 1 the blockage factor has been plotted against normalized pipe length for all those cases where these distributions exhibit a maximum. The entry conditions of the various experiments, as far as they are known, also are given. In addition to Reynolds number $Re_D = \bar{u} D/\nu$ and centerline turbulence intensity Tu_c, the caption to the figure includes such details as the area ratio of the contraction upstream.

It can be seen immediately that all the maxima of the distributions are located at $x/D = 35$ to 40. The results of Bradley (see [2]) and Miller [9] (for the lower of the two Reynolds numbers) very well confirm those of Barbin and Jones [10], which are usually considered "classic", since a false datum (nonzero displacement thickness at inlet) and disturbances in the wall region were avoided by a boundary-layer bleed, while laminar-turbulent transition phenomena were excluded by use of a small contraction ratio and a sand-grain trip. Larger Reynolds numbers are seen to produce lower peak values and smaller Reynolds numbers higher peak values: $B_{max} = 0.155$ for $Re_D = 13 \cdot 10^5$ (Miller [9]) and 0.215 for $Re_D = 1.8 \cdot 10^5$ (Cockrell and Markland [11]). Beyond their maxima the curves show different amounts and locations of "undershoot" compared with the fully developed values. This waviness is due to the adjustment of the shear stress in the central region, an extremely complicated process since shear stresses of any direction exist (see Bradshaw [12]). Nevertheless, there is good agreement between the $Re_D = 4 \cdot 10^5$ curve from [3] (full triangles in Fig. 1) and the single data points due to Bradley and Cockrell [13] and to Patel [14].

Figure 1 also contains the classical fully developed flow data of Nikuradse [15][1] for four Reynolds numbers. They are

Contributed by the Fluids Engineering Division for publication in the JOURNAL OF FLUIDS ENGINEERING. Manuscript received at ASME Headquarters February 19, 1981.

[1] Note that Schlichting's [1] power law presentation of the Nikuradse data results in somewhat higher blockage factors.

shown as asymptotic values for very long pipes, although they were obtained with $x/D = 100$ (for $Re_D = 1.0 \cdot 10^5$), $x/D = 120$ (for $Re_D = 2.0 \cdot 10^5$ and $4.0 \cdot 10^5$) and $x/D = 70.5$ (for $Re_D = 11 \cdot 10^5$). The last pipe length appears to be rather short for full flow development to occur, but Nikuradse reports that tests with $x/D = 40$, 65 and 100, conducted at $Re_D = 9.0 \cdot 10^5$, showed exactly the same velocity profile. From Fig. 1 one may deduce that his data are indeed representative of fully developed conditions.

Figure 1 exhibits one more interesting feature. It reproduces two curves from [3], obtained at approximately the same Reynolds number in the same test facility with the only distinguishing feature that the blockage factors were calculated from δ_{lax}/D in one case (full triangles) and from

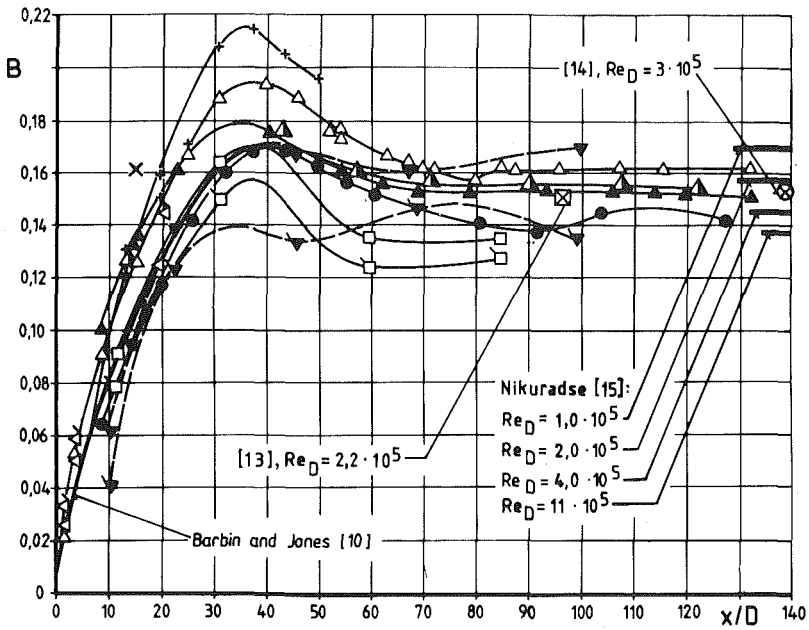

Fig. 1 Development of the velocity profile with nondimensional distance from inlet: cases where the blockage-factor distribution has a maximum

Symbol	Ref. No.	$10^{-5} \times Re_D$	Tu_c [%] at entry	Contr. ratio	Obtained from	Remarks
▲	3	4.3	0.25	16:1	$\frac{\delta_{lax}}{D}$	natural development
◭			2 to 3			wire gauze at entry
△		4.0	0.25		$u_c/\bar{u}$	natural development
+	11	1.8	?	?		
□ ◹	9	5.5	1.0	12:1		quarter-circle nozzle entry
		13.0	1.0			
●	2	?	?	?		
▼	4	1.6	?	?	$\frac{u_c}{\bar{u}}$	
▼		5.8	?	?		square-edged entry
—	10	3.9	0.5	4:1		b.-l.-bleed plus *sand grain trip*
×	17	6.0	?	6:1		L_a/D = 15, screen ring h/D = 0.10 high
◭ ◹	16	2.5	0.4	16:1	$\frac{\delta_{lax}}{D}$	turbulent; tripping device
		5.0	0.3			
⊠	13	2.2	?	?	$u_c/\bar{u}$	
⊗	14	2.7	?	4:1	$u_c/\bar{u}$	

Nomenclature

B = blockage factor (see equation (1))
$D = 2R$ = pipe diameter
$H_{1,2}$ = boundary-layer shape factor, ratio between the axisymmetric boundary-layer displacement and momentum thickness
h = height of trip ring
k_S = height of equivalent sand roughness
Re_D, Re_x = Reynolds number, based on $\bar{u}$ and on D or x, respectively
r = coordinate in the radial direction
Tu = turbulence intensity in the axial direction, Tu_c value at pipe centerline
u = velocity, u_c value at pipe centerline
$\bar{u}$ = bulk velocity
x = coordinate along pipe axis, $x = 0$ at pipe entry
δ_{lax} = axisymmetric boundary-layer displacement thickness (see equation (2))
ν = kinematic viscosity of fluid

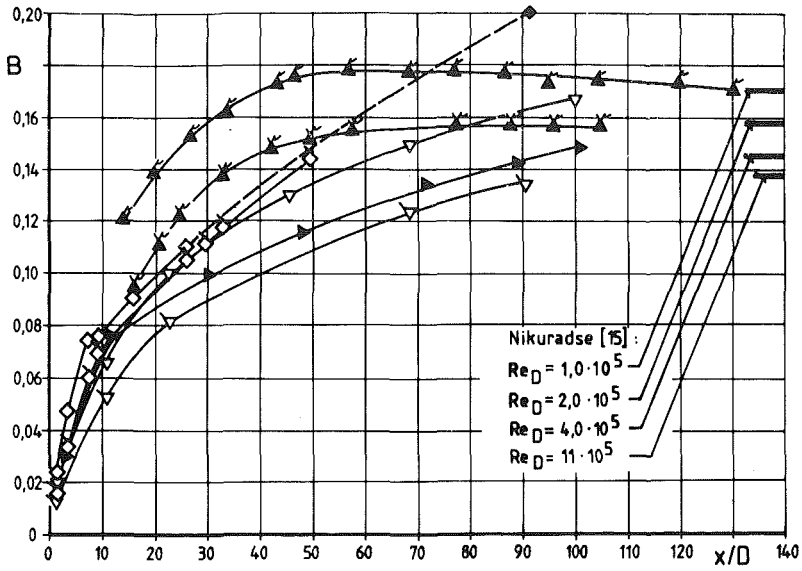

Fig. 2 Development of the velocity profile with nondimensional distance from inlet: cases where the blockage-factor distribution has no maximum

Symbol	Ref. No.	$10^{-5} \times Re_D$	Tu_c [%] at entry	Contr. ratio	Obtained from	Remarks
▲	6	1.0 4.0	0.25	16:1	$\frac{\delta_{lax}}{D}$	trip ring at entry, h/D = 0.062 high
▽	4	1.6 5.8	?	?	$\frac{u_c}{\bar{u}}$	bellmouth entry, blow-down facility
▶	5	4.0	1.0	20:1		5^o-diffuser upstr. of contraction
◆	13	2.2	?	?		rough, sand paper $k_s/D = 40 \cdot 10^{-4}$
◇	19	7.8 25.0	?	25:1		rough pipe $k_s/D = 3.8 \cdot 10^{-4}$ rough pipe $k_s/D = 2.0 \cdot 10^{-4}$

u/u_c in the other case (open triangles). The discrepancy is considerable, although both procedures should of course produce identical results. It may be due to marked asymmetries of the turbulence distribution at the inlet which were noted in these experiments, although the velocity distribution at the inlet was symmetrical (see [6]). But a more general explanation can be deduced from an investigation recently conducted by Pozzorini [16]. Air was sucked through filter mats into a chamber of square cross section, through a bellmouth, a settling length with turbulence screens, and through a carefully shaped 16:1-contraction with a trip close to its outlet optimized so that the boundary layer was completely turbulent around the entire circumference. The peripheral total-head distribution within the boundary layer of a pipe attached to the contraction exhibited the four corners of the chamber. When the chamber (whose filter mats acted as flow straighteners) was omitted, the data showed a large scatter, because damping of the entry vortex was incomplete owing to screen instabilities. The disturbances were particularly great when the screens also were removed so that the intermittent entry vortex could pass without being disturbed. All these macroscopic flow irregularities were avoided when the square chamber was replaced by an axisymmetric one into which the flow entered axially through a round filter plate. However, this gave rise to a new phenomenon, a fine transverse structure of the boundary layer (circumferential dynamic-head changes) in the contraction which was magnified by the tripping device and persisted along the entire length of pipe (20 diameters). Consequently, the boundary layer displayed a waviness at the circumference with departures of its thickness of 25 percent and of the wall shear stress of 10 percent from their mean values. The type of modulation changed when the screen configuration was altered, but it never vanished. As in the tests employing the square chamber, disturbances were confined entirely to the boundary layer.

These experiments clearly demonstrate the extreme sensitivity of developing pipe flow to upstream conditions. They also show that a truly axisymmetric pipe flow does not exist. Hence determination of the blockage from $\tilde{u}/u_c$ (where $\tilde{u}$ is derived from the flow rate) will generally be more accurate than from δ_{lax}/D, especially if the latter is calculated from measurements in a single plane only.

The cases where profile peakiness does not exhibit a maximum as the flow proceeds along the pipe, depicted in Fig. 2, show the same amount of diversification as the curves in Fig. 1. Of particular interest are the measurements downstream of a trip ring, reported in [3] and [6], which differ substantially from those for natural flow development made by the same researchers. Shárán [6] attributed this to differences in turbulence structure. In the naturally developing flow, he noted, in conjunction with Barbin and Jones [10], that the turbulence energy in the boundary layer is dissipated in the axial direction rather than being convected radially outward. Contrary to this, the trip ring produced large eddies of high intensity close to the wall, which convected turbulence energy outward at a high rate. It appears to be the radial momentum transfer thus created which is responsible for the flow to develop at a much slower rate initially than an undisturbed flow and for the centerline velocity not to attain a maximum. The high development rate obtained by Liepe and Jahn [17] behind a screen ring (see the data point in Fig. 1) may be due to particularly small eddies thus produced.

The phenomenon can be also analyzed from Bradshaw's [18] explanation for the peak in naturally developing flow.

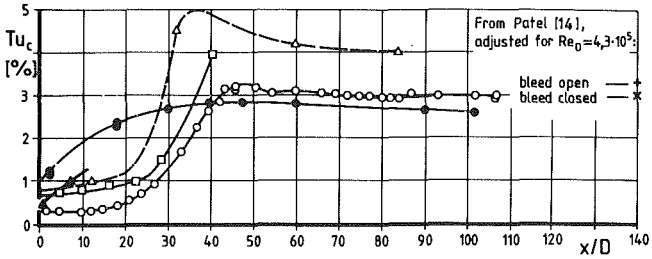

Fig. 3 Development of centerline turbulence intensity with non-dimensional distance from inlet

○	Weir, Priest and Shárán [3],	$Re_D = 4.3 \cdot 10^5$
●	Sale [5],	$Re_D = 4.0 \cdot 10^5$
△	Miller [9],	$Re_D = 5.5 \cdot 10^5$
□	Barbin and Jones [10],	$Re_D = 3.9 \cdot 10^5$
▲	Sprenger [20],	$Re_D = 3.6 \cdot 10^5$

When the wall boundary layers meet, the radial shear-stress distribution in either of them is very similar to that of a flat-plate boundary layer. Because of the type of curvature of this distribution, the shear-stress gradient over most of the central portion exceeds that of fully developed pipe flow, in which the shear stress changes linearly with the radius. As a consequence, the flow in the central region is accelerated. Thus the absence of a maximum centerline velocity in the trip-ring tests suggests that the core-shear-stress gradient at boundary-layer merger must have been smaller than in fully developed flow. According to Shárán's measurements this indeed is true, while near the wall the shear-stress gradient was greater than in fully developed flow. Although shear-stress and turbulence are related to each other, the former provides a deeper insight, because its slow adjustment in the central portion is responsible for the long distances required for velocity-profile development. In the wall region the adjustment rates of naturally developing flow are very much faster; the wall shear stress reaches its fully developed value after 8 to 15 pipe diameters (results according to [6] and [10]), the pressure gradient after about 10 diameters [10].

Apparently, roughness has a similar effect as a trip ring [19], Fig. 2, with higher blockage factors at large distances (see the value of $B = 0.20$ at $x/D = 96$, from [13]). However, this would not appear to explain Deissler's [4] measurements made downstream of a bellmouth entry and Sale's [5] behind a well designed 20:1 contraction. The curves obtained by these two researchers are surprisingly similar. Sale incorporated a long 5 deg conical diffuser upstream of the contraction, and this could be the cause of the shape of his curve. On the other hand Sale reports that his pipe had crude joints between its sections, and this roughness could also account for the lack of "overshoot." Deissler's set-up employed a settling length upstream of the bellmouth, preceded by an orifice, a filter and control valves. It is possible that the settling length was too short to fully eliminate the disturbances created upstream. It is interesting to note that the distributions obtained when the bellmouth was replaced by a square-edged entry are very similar to the curves in Fig. 1 and therefore have been included here instead of in Fig. 2.

Turbulence data for developing pipe flow would be of great help for a better understanding of the phenomena involved. Such data are scarce, however. The development of Tu_c along a pipe downstream of a 16:1 contraction was measured in [3] and compared with Sale's and Barbin and Jones's data. These and a few additional results are reproduced in Fig. 3. In three of these cases Tu_c remains fairly constant to about 15 to 25 diameters, then rises steeply, has a peak at $x/D = 40$ to 45 (at approximately the same location where the centerline velocity has a maximum), and then falls very slowly towards its fully developed value far downstream. This is in line with Barbin and Jones's observation of centerline intermittency starting at $x/D = 25$ and boundary-layer merger at about $x/D = 28$.

Sale's distribution is completely different, having its steepest gradient right at the pipe entry and having no overshoot. This could be due to the crude pipe joints, but also to the particular entry conditions: obviously the boundary layer had already joined at the diffuser exit and therefore turbulence was high in the entire cross section at this point[2]. Sprenger's [20] results, also obtained behind a contraction preceded by a diffuser, indicate the same trend as Sale's.

Laufer's [21] experiments, for a long time believed to be representative of fully developed flow, employed far too short a pipe ($x/D = 50$). Patel [14], who was the first to mention this, did not obtain fully developed turbulence conditions even after 142 pipe diameters. Tu_c increased by nearly 10 percent when a bleed upstream of the pipe was opened, probably owing to sound waves transmitted from there. In Shárán's [6] trip-ring experiments Tu at the center exceeded the values for natural flow development within the first 30 diameters, but close to the wall for only 15 diameters. On the other hand, at $x/D = 65$ Tu differed only slightly at the center, while close to the wall it was still lower than in naturally developing flow even at $x/D = 140$.

It is also worth mentioning that in the experiments without a trip ring in [3] and [6], an increase of free-stream turbulence intensity had no apparent effect on velocity-profile development at $Re_D = 4 \cdot 10^5$ (see Fig. 1), in agreement with tests reported in [14], but it did have an effect at $Re_D = 1 \cdot 10^5$, a result confirmed by Lee and Goel [22]. This is due to the transitional behavior of the boundary layer, which is also the reason for the abrupt changes in slope at small values of x/D displayed by some of the curves in Fig. 4. Some other distributions also show changes in slope at larger values of x/D where, with the high Reynolds numbers used, the flow must have been turbulent: Sprenger's [20] between $x/d \approx 11$ and 17, that of Jeng-Song-Wang and Tullis [19] between $x/D \approx 7$ and 10, Sale's [5] at $x/D \approx 12$ and Deissler's [4] at $x/D \approx 20$ (Fig. 2). The reason remains unknown, but it is interesting to note that these are the cases where no overshoot of the centerline velocity occurs in the absence of trip rings, in spite of well-rounded, large-area-ratio contractions being fitted ahead of the pipe inlets.

Laminar-turbulent Transition

Some of the differences depicted in Figs. 1 and 2 are due to laminar-turbulent transition. This can be seen more clearly in Fig. 4 with its enlarged x/D-scale where, in addition to curves from Figs. 1 and 2, results of researchers who tested only short pipes have been included. Most distributions, when extrapolated to $x/D = 0$, would have a negative value of B (for example that of Robertson and Ross [23]). Since B must remain positive, the slopes must change drastically at small values of x/D, indicating a significantly reduced development rate due to laminar flow in the initial portion of the pipes. In fact, these curves have a pronounced kink, as is verified by the results of Sprenger [20] and of Müller [24]. The extent of laminar or transitional flow portions depends primarily on the Reynolds number, but also on upstream conditions; in particular, on the contraction ratio which determines the degree of relaminarization of an initially turbulent boundary layer. Contraction shape and length are of importance as well as the presence or absence of screens which, in addition to affecting turbulence, may determine whether separation occurs in the contraction and thus affect the turbulence

[2] Note that $Tu_c = 1$ percent was measured at the pipe entrance, which is an extremely large value for a 20:1 contraction.

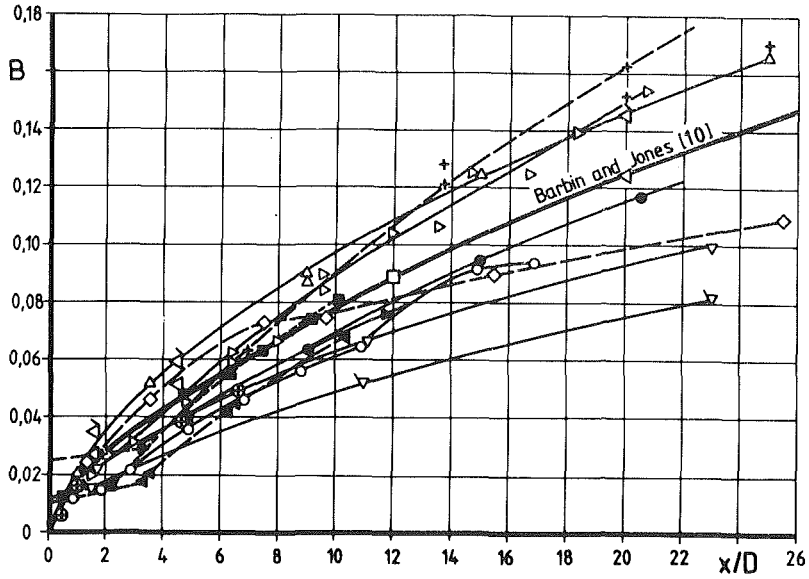

Fig. 4 Development of the velocity profile within the first 26 pipe diameters

Symbol	Ref. No.	$10^{-5} \times Re_D$	Tu_c [%] at entry	Contr. ratio	Remarks
○	20	3.5	0.45	25:1	diffuser upstream
◀	23	12	?	9:1	water tunnel
■	24	1.8	1.0	18:1	
▷	28	2.5	?	4:1	conical contr., faired
⊕	29	10	?	?	also: $Re_D \approx 20 \cdot 10^5$

All data points obtained from δ_{lax}/D.
Further symbols as in Figs. 1 and 2

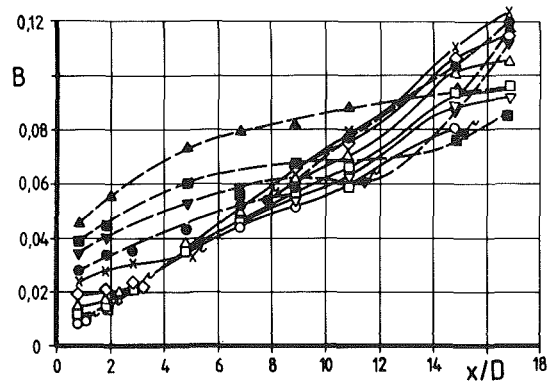

Fig. 5 Effect of Reynolds number on blockage-factor development, from Sprenger [20]

Symbol	▲	■	▼	●	×	◇	△	□	▽	○
$Re_D \cdot 10^{-5}$	0.35	0.46	0.56	0.77	1.12	1.75	2.50	3.54	5.20	6.25

Flagged symbols: onset of transition, from Fig. 7

structure at its outlet (see Klein, Ramjee and Venkataramani [25]).

A thorough experimental investigation of transitional developing pipe flow was conducted by Sprenger [20]. It appears that these results have not been sufficiently appreciated, probably because Sprenger presented them only in tables and not graphically. Therefore they have been plotted in a comprehensive form and are depicted in Figs. 5–8. While various types of trips for initiating transition were used in the investigations described so far, the discussion related to Figs. 5 to 8 pertains to natural transition without artificial means to trip the boundary layer.

As expected, the changes in slope of the curves in Fig. 4 shift towards larger distances x/D when Re_D decreases (Fig. 5). These distances are far larger than the ones at which the shape factor $H_{1,2}$ starts falling towards its turbulent value; see the arrows in Fig. 6. The beginning of this fall therefore indicates much earlier transition than the slopes of the blockage curves. To clarify this observation, B and $H_{1,2}$ were plotted in Figs. 7 and 8 against Re_x, the Reynolds number defined with distance x from pipe entry. The distributions in Fig. 7 are similar to the well-known relationship for the flat-plate friction factor[3]. In the log-log plot used, in both the laminar and turbulent flow regimes B falls linearly as Re_x rises, the slope being smaller for turbulent flow. Respective laminar- and turbulent-flow lines are joined by a curve representing the transitional flow regime, which makes a pronounced kink with the former and converges smoothly with the latter. The locations of the kinks have been included in Fig. 5 (flagged symbols) and are seen to coincide very well with the changes in slope observed there. For all pipe lengths they occur at the same value, $Re_x \approx 6 \cdot 10^5$ (Fig. 7), the lower critical Reynolds number. The upper critical Reynolds number (where the transitional curves become tangential to the turbulent-flow lines) has also one fixed value, $Re_x = 1.85 \cdot 10^6$ [4], for all the pipe lengths. In terms of pipe-Reynolds number, the beginning of the turbulent regime thus ranges from $Re_D = 1.1 \cdot 10^5$ for $x/D = 16.85$ to $Re_D = 2.2 \cdot 10^6$ for $x/D = 0.85$.

Cross reference between Fig. 7 and Fig. 8 is facilitated by numbers which mark corresponding points. It can be seen

[3] This is not surprising because this friction factor varies with the same power of Reynolds number as the displacement thickness.

[4] This value was determined from a plot on a larger scale than Fig. 7.

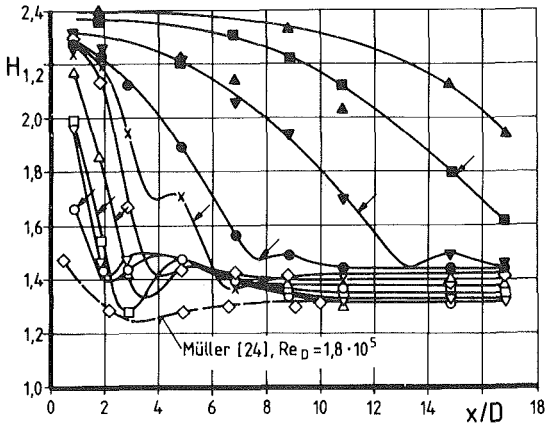

Fig. 6 Effect of Reynolds number on shape-factor development, from Sprenger [20]
Symbols as in Fig. 5.
Arrows: location of minima of the curves $B = f(Re_x)$ (Fig. 7)

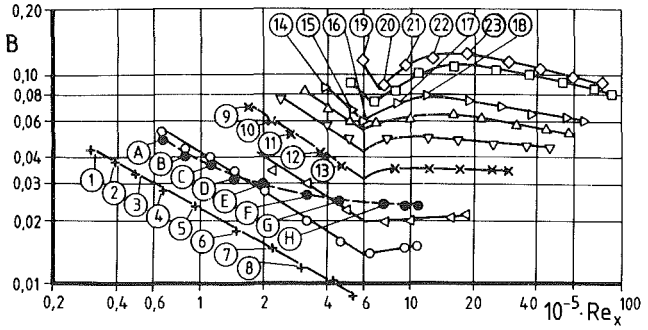

Fig. 7 Relationship between blockage factor and flow-distance Reynolds number, from Sprenger [20]

Symbol	+	○	◁	×	▽	△	▷	□	◇
x/D	0.85	1.85	2.85	4.85	6.85	8.85	10.85	14.85	16.85

• x/D = 1.85, trip ring of height h/D = 0.005 at x/D = 0.35
Encircled numbers and letters: for cross reference with Fig. 8
Arrows: termination of transitional and beginning of turbulent regime

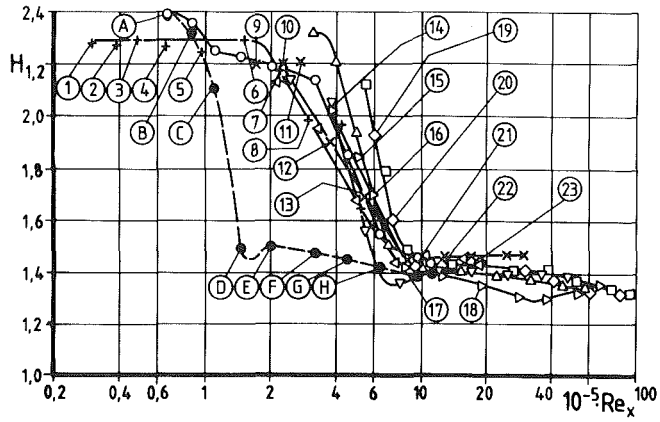

Fig. 8 Relationship between shape factor and flow-distance Reynolds number, from Sprenger [20]
Symbols as in Fig. 7
Encircled numbers and letters: for cross reference with Fig. 7

from the shape-factor distributions that neither the lower nor the upper critical Reynolds number can be deduced. One could argue that determination of the latter from Fig. 7 was inaccurate and that it must be assumed to be as low as $Re_x \approx 1.0 \cdot 10^6$, where the shape-factor curves, after their steep fall, become nearly horizontal. However, this is very unlikely for the following reason: Sprenger tested a diffuser over a range of Reynolds numbers downstream of various entrance pipes. When plotted against blockage factor, all the nondimensional pressure recoveries for turbulent approach flow formed a single curve, while recoveries for nonturbulent flow departed from this curve. Now, for conditions corresponding to points 17 and 21, which in Fig. 8 mark the end of the fall of $H_{1,2}$, the pressure recoveries still indicate a nonturbulent approach flow (see Fig. 10 of [7]), but turbulent flow for points 18 and 22, which are close to the upper critical Reynolds number, $Re_x = 1.85 \cdot 10^6$. This is even more obvious in the tests where a trip ring was fitted 1.5 diameters upstream. Here the blockage factor changes smoothly with Re_x. The lower critical Reynolds number is reduced to $Re_x \approx 1 \cdot 10^5$. The upper critical Reynolds number is not clearly determined, but according to Fig. 10 in [7] it must be $Re_x \geq 6 \cdot 10^5$, because only then does diffuser performance correspond to turbulent flow (see points G and H). A much lower limit for the termination of the transitional regime would follow from the shape factor if the end of its steep fall is regarded as a valid criterion (point D in Fig. 8).

We must deduce that with the nonequilibrium boundary layers produced by contractions upstream, the displacement thickness or blockage factor reflects the peculiarities of transitional developing pipe flow far better than the shape factor $H_{1,2}$ or the momentum thickness. The two latter parameters are obviously more affected by differences in contraction geometry and by other upstream conditions. This can be seen when comparing Sprenger's [20] and Müller's [24] results for $Re_D \approx 1.8 \cdot 10^5$: While within the first five diameters of flow development the blockage factors are nearly identical (Fig. 4), the shape factors are entirely different (Fig. 6). Consequently, for diffusers with entrance pipes, the blockage factor is a more reasonable parameter than momentum thickness for describing inlet conditions.

Lee and Goel [22] also investigated transitional developing pipe flow. They found a strong reduction of both the lower and the upper critical Reynolds number as the free-stream turbulence intensity was increased. Both these quantities had lower values, and the pipe lengths required for the occurrence of transition were much shorter, than in Sprenger's tests. With Sprenger's turbulence level $Tu_c = 0.45$ percent, their lower critical Reynolds number was $Re_x = 1 \cdot 10^5$ compared with $6 \cdot 10^5$, the critical pipe length was $x/D = 2.6$ compared with 13. These differences are due to the fact that Lee and Goel did not derive the critical values from the blockage factor, but from a plot of the friction factor against x/D^5. One must conclude that not only does turbulent flow develop more quickly, but also that the beginning and end of transition occur much earlier at the wall region than at the central region. This has an analogy in the fully developed pipe flow tests of Patel and Head [26], where the upper critical Reynolds number was about four times higher when determined from blockage than when obtained from skin friction, a result confirmed in [27]. Since, as was shown, Sprenger's diffuser data correlate very well with the critical quantities derived from the blockage factor, the definition of critical quantities by blockage is more reasonable than use of the friction factor.

Conclusions

The conclusions from this review are as follows:

1 The development of both the velocity profile and turbulence in turbulent pipe flow depends largely on upstream flow history. Undisturbed entry flow generates a maximum in

[5] Velocity-profile development was not presented in [22].

profile-peakiness at about 40 pipe-diameters, while certain types of initial disturbances produce a smooth profile development without such a maximum.

2 The distance required for full flow development may exceed 140 pipe diameters. Some of the classical measurements of fully developed pipe flow were in fact conducted at conditions when the flow was still developing.

3 The beginning and termination of laminar-turbulent transition is determined most reasonably from a plot of the blockage factor against Reynolds number defined with flow distance. For this, the momentum thickness or the shape factor are unsuitable parameters.

4 The effects of inlet conditions on flow development are not yet sufficiently understood.

Note

One of the reviewers pointed out three papers to the author which have been added to the list of references.

Walklate et al. [30] present blockage factors for $Re_D = 2.25 \cdot 10^5$ to $x/D = 30$ which nearly coincide with those according to Bradley [2], shown in Fig. 1. Turbulence intensities from [30] agree well with the values according to [3] and [10] in Fig. 3.

Reichert and Azad [31] present velocity profile development to $x/D = 67$ for two Reynolds numbers, $Re_D = 0.76 \cdot 10^5$ and $1.53 \cdot 10^5$. They used a 89:1 contraction cone and a 0.5-D long sandpaper trip at the pipe entry. Owing to this sandpaper, the initial boundary layer was extremely thick ($B = 0.08$ at $x/D = 2$). Apart from this, their blockage factor distributions are very similar to those of [3] and [11] shown in Fig. 1. They have marked peaks at $x/D = 32$ and minima at $x/D \approx 60$.

Laws et al. [32] present some evidence for an oscillatory development of pipe flow which has not been reported before.

References

1 Schlichting, H., *Boundary Layer Theory*, 6th edition, McGraw-Hill, 1968.

2 Cockrell, D.J., "Effect of Inlet and Outlet Conditions on Pipe and Duct Components," The Ninth Members Conference, Sept. 1967, Cranfield, SP 929, The British Hydromechanics Research Association.

3 Weir, J., Priest, A.J., and Shárán, V.K., "Research Note: The Effect of Inlet Disturbances on Turbulent Pipe Flow," *Journal of Mechanical Engineering Science*, Vol. 16, No. 3, 1974, pp. 211–213.

4 Deissler, R.G., "Analytical and Experimental Investigation of Adiabatic Turbulent Flow in Smooth Tubes," NACA T.N.2138, 1950.

5 Sale, D.E., "Entrance Effects in Incompressible Diffuser Flow," M.Sc. thesis, University of Manchester, 1967.

6 Shárán, V.K., "An Experimental Investigation of Naturally Developing Turbulent Flow and Flow with Fixed Transition in a Parallel Pipe," ASME-Paper 72 WA/FE-38, 1972. See Also: "The Effect of Inlet Disturbances on Turbulent Boundary Layer Development in a Parallel Pipe," *Journal of Applied Mathematics and Physics (ZAMP)*, Vol. 25, 1974, pp. 659–666.

7 Klein, A., "Review: Effects of Inlet Conditions on Conical-Diffuser Performance," ASME JOURNAL OF FLUIDS ENGINEERING, published in this issue pp. 250–257.

8 Sovran, G., and Klomp, E., "Experimentally Determined Optimum Geometries for Rectilinear Diffusers with Rectangular, Conical or Annular Cross Section," in *Fluid Mechanics of Internal Flow* (ed.: G. Sovran), Elsevier Publishing Company, Amsterdam, 1967.

9 Miller, D., "Performance of Straight Diffusers," Part II of "Internal Flow. A Guide to Losses in Pipe and Duct Systems," B.H.R.A.-Fluid Engineering, Cranfield/Bedford, 1971.

10 Barbin, A.R., and Jones, J.B., "Turbulent Flow in the Inlet Region of a Smooth Pipe," ASME *Journal of Basic Engineering*, Vol. 85, No. 1, 1963, pp. 29–34.

11 Cockrell, D.J., and Markland, E., "The Effect of Inlet Conditions on Incompressible Fluid Flow Through Conical Diffusers," *Journal of the Royal Aeronautical Society*, Vol. 66, No. 1, 1962, pp. 51–52.

12 Bradshaw, P., "Review-Complex Turbulent Flows," ASME JOURNAL OF FLUIDS ENGINEERING, Vol. 97, No. 2, 1975, pp. 146–154.

13 Bradley, I.C., and Cockrell, D.J., "The Response of Diffusers to Flow Conditions at Their Inlet," *Symposium on Internal Flows*, University of Salford, England, 1971, Paper 5.

14 Patel, R.P., "A Note on Fully Developed Turbulent Flow Down a Circular Pipe," *Aeronautical Journal*, Vol. 78, No. 2/3, 1974, pp. 93–97.

15 Nikuradse, J.,"Gesetzmässigkeiten der turbulenten Strömung in glatten Rohren," Forschungsheft 356, VDI-Verlag GmbH, Berlin, 1932.

16 Pozzorini, R., "Das turbulente Strömungsfeld in einem langen Kreiskegel-Diffusor," PhD dissertation ETH Zürich, 1976. Eduard Truninger AG Zürich, 1976.

17 Liepe, F., and Jahn, K., "Untere Wirkungsgrade von Kegeldiffusoren," *Maschinenbautechnik*, Vol. 11, No. 11, 1962, pp. 588–589.

18 Bradshaw, P., *An Introduction to Turbulence and its Measurement*, Pergamon Press, New York, 1971.

19 Jeng-Song-Wang, and Tullis, J.P., "Turbulent Flow in the Entry Region of a Rough Pipe," ASME JOURNAL OF FLUIDS ENGINEERING, Vol. 96, No. 1, 1974, pp. 62–68.

20 Sprenger, H., "Experimentelle Untersuchungen an geraden und gekrümmten Diffusoren," Mitteilung Nr. 27 aus dem Institut für Aerodynamik an der ETH Zürich, Verlag Leemann, Zürich, 1959. See also: "Experimental investigations of straight and curved diffusers," British Ministry of Aviation Translation, TIL/T. 5134, 1962.

21 Laufer, J., "The Structure of Turbulence in Fully Developed Pipe Flow," NACA T.N. 2954, 1963.

22 Lee, Y., and Goel, K.C., "Free Stream Turbulence and Transition in a Circular Duct," *Proceedings of the Second International JSME Symposium Fluid Machinery and Fluidics*, Tokyo, Sept. 1972, pp. 11–20.

23 Robertson, J.M., and Ross, D., "Effect of Entrance Conditions on Diffuser Flow," *Proceedings of the ASCE*, Vol. 78, Separate No. 141, 1952, pp. 1–24.

24 Müller, H.P., "Experimentelle Untersuchungen an Kegeldiffusoren einer mehrstutzigen Radialverdichterspirale," *Brennstoff-Wärme-Kraft*, Vol. 28, No. 3, 1976, pp. 97–101. See also: PhD dissertation of same title, Ruhr-Universität Bochum, 1974.

25 Klein, A., Ramjee, V., and Venkataramani, K.S., "An Experimental Study of the Subsonic Flow in Axisymmetric Contractions," *Zeitschrift für Flugwissenschaften*, Vol. 21, No. 9, 1973, pp. 312–320.

26 Patel, V.C., and Head, M.R., "Some Observations on Skin Friction and Velocity Profiles in Fully Developed Pipe and Channel Flows," *Journal of Fluid Mechanics*, Vol. 38, Part 1, 1969, pp. 181–201.

27 Pennell, W.T., Sparrow, E.M., and Eckert, E.R.G., "Turbulence Intensity and Time-Mean Velocity Distributions in Low Reynolds Number Turbulent Pipe Flows," *International Journal of Heat and Mass Transfer*, Vol. 15, 1972, pp. 1067–1074.

28 Winternitz, F.A.L., and Ramsay, W.J., "Effects of Inlet Boundary Layer on Pressure Recovery, Energy Conversion and Losses in Conical Diffusers," *Journal of the Royal Aeronautical Society*, Vol. 61, No. 2, 1957, pp. 116–124.

29 Little, B.H., and Wilbur, S.W., "Performance and Boundary-Layer Data From 12° and 23° Conical Diffusers at Area Ratio 2, 0 at Mach Numbers up to Choking and Reynolds Numbers up to 7, 5×10^6," NACA-Report 1201, 1954.

30 Walklate, P., Heikal, M.R.F., and Hatton, A.P., "Measurement and Prediction of Turbulence and Heat Transfer in the Entrance Region of a Pipe," *Heat and Fluid Flow*, Vol. 6, No. 2, 1976, pp. 89–95.

31 Reichert, J.K., and Azad, R.S., "Nonasymptotic Behavior of Developing Turbulent Pipe Flow," *Canadian Journal of Physics*, Vol. 54, No. 3, 1976, pp. 268–278.

32 Laws, E.M., Lim, E-H., and Livesey, J.L., "Turbulent Pipe Flows in Development and Decay," *Symposium on Turbulent Shear Flows*, London, June 1979.

REVIEW: Effects of Inlet Conditions on Conical-Diffuser Performance

A. Klein
Motoren- und Turbinen-Union München GmbH,
D 8000 München, Germany

The available experimental evidence of the effects of inlet conditions on the performance of conical diffusers with a free discharge is reviewed. The effects of inlet boundary layer thickness blockage, inlet shape parameter, turbulence, and Reynolds number are discussed. It is shown that many of the inconsistencies between different sources of data are the result of nonturbulent approach flows. Graphs are presented as guidelines for diffuser design.

Introduction

Peters [1] was probably the first to demonstrate that diffuser performance greatly depends on inlet conditions. This is particularly true of diffusers with a free discharge since the distortion of the outlet profile, and hence its excess kinetic energy, increases with that of the inlet profile. Peters' results have been qualitatively confirmed by Robertson and Ross [2], Cockrell and Markland [3, 4] and others.

Sovran and Klomp [5] showed that blockage is the main parameter representing turbulent-inlet-flow conditions (see also Reneau et al. [6]). To which extent the blockage factor, defined in [5], represents inlet conditions for approach pipes, or distortions created otherwise, remains an unsolved problem. Experiments with screen rings by Cockrell et al. [7] and by Winternitz and Ramsay [8] led to contradicting conclusions. Bradley and Cockrell [9] as well as Shárán [10] showed that artificial changes of the inlet turbulence intensity markedly affected diffuser performance, while Sajben et al. [11] concluded exactly the opposite. Bradshaw [12] demonstrated that long entrance pipes create larger pressure recoveries than shorter ones and ascribed this to changes in turbulence structure. This was confirmed by Cockrell [13], but conflicting evidence exists also.

The curves from different sources showing diffuser performance against blockage factor also reveal discrepancies: some of these curves fall continuously with increasing blockage [1], others drop sharply initially and then remain constant over a large range (for example, Miller [14]), and again others decrease at a low rate even with small blockages [2]. In addition, a comparison of results is complicated by the variety of definitions of diffuser performance used.

This review of experimental conical-diffuser research has been conducted to clarify this confusing picture. It is restricted to diffusers with a free discharge with nonswirling inlet flows where compressibility and artificially created distortions are essentially absent.

Contributed by the Fluids Engineering Division for publication in the JOURNAL OF FLUIDS ENGINEERING. Manuscript received by the Fluids Engineering Division, May 19, 1978.

General Remarks

Developing pipe flow significantly depends on upstream flow conditions (see Klein [15]). A striking example of the even higher sensitivity of diffuser flow to upstream flow history was reported by Sprenger [16]: a perfectly uniform flow was produced at the exit of a contraction, but when a diffuser was attached, lines of constant kinetic energy in its outlet plane showed an octagonal pattern due to the cross section shape of a duct far upstream. Pozzorini [17] demonstrated the impossibility of producing a genuinely axisymmetric flow in a conical diffuser. These observations show that differences may be expected when comparing diffuser results from different sources.

Another difficulty is the various forms by which diffuser performance and entry conditions (if at all) have been described. We will use the pressure-rise coefficient, which represents best the performance of diffusers with a free discharge:

$$C_p = \frac{P_{sout} - P_{sin}}{\frac{\bar{\rho}_{in}}{2}\bar{u}_{in}^2}. \tag{1}$$

Actually $C_{p\alpha_{in}}$, which includes the parameter

$$\alpha_{in} = \frac{1}{A_{in}}\int_0^{A_{in}} \left(\frac{u}{\bar{u}}\right)_{in}^3 dA_{in} \tag{2}$$

in the denominator, is a more correct definition. However, $\alpha_{in} \approx 1$ for the types of flow considered. Besides, α_{in} was not recorded by most researchers. For describing entry conditions we will use the shape factor $H_{1,2} = \delta_{1ax}/\delta_{2ax}$ and the blockage factor

$$B = 2\frac{\delta_{1ax}}{R_{in}} = 1 - \frac{\bar{u}}{u_c}, \tag{3}$$

which was introduced in [5]. The blockage factor was shown in [15] to be indeed superior to the momentum thickness (also employed by some researchers) for use as a parameter of influence.

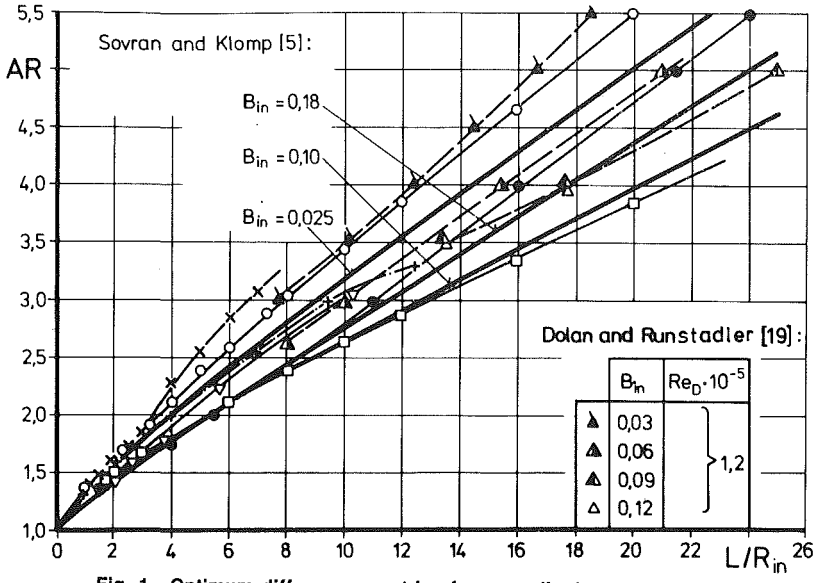

Fig. 1 Optimum diffuser geometries for prescribed nondimensional diffuser length

▽ [9], $Re_D = 2.2 \cdot 10^5$, $B_{in} = 0.15$, $L_a/D = 96$
×, + [14], $Re_D = 5.5 \cdot 10^5$, $B_{in} \approx 0.015$ and 0.16 ($L_a/D = 30$)
● [20], $Re_D = 1.3 \cdot 10^5$, $B_{in} = 0.034$
○, □ [23], $Re_D = 6.0 \cdot 10^5$, $B_{in} \approx 0.020$ and 0.16 (screen ring 15 D upstream)

The results of about thirty publications have been correlated in the preparation of this paper. In addition, the unpublished data of diffuser research conducted under the direction of the author at the Indian Institute of Technology (I.I.T.), Madras, have been included.

The following corrections and assumptions have been made:

Absolutely correct static pressures at the diffuser inlet were used only in [1, 2, 14, 18, and 19]. Since static pressures usually were recorded by wall taps and researchers wished to avoid errors due to the entrance-corner effect, the static pressures often were measured too far upstream of the entry. In such cases, the pressures have been corrected in this review to allow for frictional drop. The pressure rises given by McDonald and Fox [20] were reduced to the form of equation (1) by assuming $B_{in} = 0.034$, stated in [21].

In [1, 12 and 22] only the approach lengths are cited, and not the blockages. In the present paper, the correlations of [15] have been applied for the results of [12] and [22], whereas the correlations of [3] and [4] have been applied for Peters [1]. For the unspecified "thin-boundary-layer" arrangements of [14] and [23], respectively, $B_{in} = 0.015$ and 0.020 were chosen from the contraction tests of Klein et al. [24] and Müller [25]. Sovran and Klomp's [5] performance map, derived from [4], was assumed to apply to $B_{in} = 0.025$ (derived from cross-plotting the data of [3, 4]) rather than 0.020 (the value given in [5]).

Only results obtained at entry Mach numbers up to 0.2 have been used without change; otherwise a compressibility correction has been made. The performances measured by Rippl [26] have been discarded since Rippl's measurements were conducted at a variety of unspecified Mach numbers and the blockage is unknown.

Optimum Geometries

Various researchers derived optimum area-ratio length correlations for a given AR or L/R_{in}. The correlations with AR are insensitive to entrance conditions. Sovran and Klomp [5] found similar insensitivity for L/R_{in} also. Figure 1[1] shows, however, that these optimum geometries in fact change with blockage: the value of optimum AR for a given L/R_{in} decreases with increasing B_{in}.[2] According to Fig. 2

[1] A slash in the upper left quadrant of a symbol here and in what follows means that the entry flow is known to have been laminar.

[2] Exceptions to this rule appear to be the $B_{in} = 0.03$-curve from [19] and the $B_{in} = 0.10$- and 0.18-curves originally derived in [5]. The importance of these exceptions, however, should not be rated very high, because in the first case the entry flow was laminar and in the second the available data were scarce.

Nomenclature

A = cross-sectional area
AR = diffuser area ratio
B = blockage factor (see equation (3))
C_p = pressure-recovery coefficient (see equation (1))
D = pipe diameter
$H_{1,2}$ = boundary-layer shape factor, $H_{1,2} = \delta_{1ax}/\delta_{2ax}$
h = height of trip ring
L = diffuser length
L_a = approach length
P_s = static pressure
R_{in} = radius of diffuser at its inlet
Re_D = Reynolds number, based on $\bar{u}$ and D
Tu = turbulence intensity in the axial direction
u = velocity
$\bar{u}$ = bulk velocity
α = kinetic-energy-flux velocity profile parameter (see eq. (2))
$\delta_{1ax}, \delta_{2ax}$ = axisymmetric boundary-layer displacement or momentum thickness, respectively
ρ = fluid density ($\bar{\rho}$-mean value in cross section)

Subscripts

c = center (of pipe)
in = inlet
out = outlet
α = flow characteristics based on the dynamic pressure $\alpha\bar{\rho}\bar{u}/2$

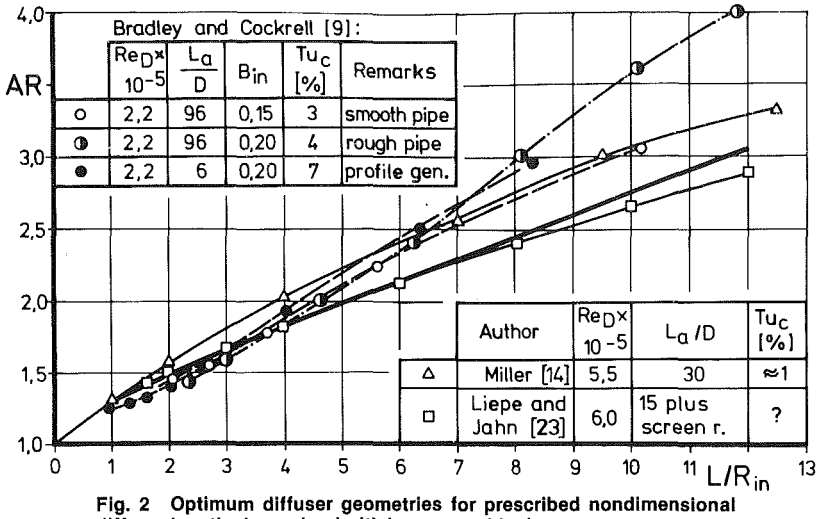

Fig. 2 Optimum diffuser geometries for prescribed nondimensional diffuser length, determined with large entry blockages. Thick line: Sovran and Klomp [5], $B_{in} = 0.18$, $Tu_c = ?$

turbulence is also of importance, the optimum value of AR increasing as Tu_{in} increases[3], at least for $L/R_{in} \geq 8$.

Figure 3, derived from [19], shows extremely peculiar correlations for nonturbulent inlet flows. In such cases both smaller and higher area ratios may be optimum for a given L/R_{in} than with turbulent flow. Two more important conclusions are drawn from Fig. 3. First, the criterion used in [19] by far underestimated the approach lengths required to produce a turbulent flow: for $Re_D = 0.6 \cdot 10^5$, laminar flow must not only have prevailed to $B_{in} = 0.06$, the largest value of B_{in} for which the entry flow was classified as laminar in [19], but at least to $B_{in} = 0.12$ (note the peculiar data). Second, only extremely long diffusers respond to a laminar approach flow as if it were turbulent ($L/R_{in} \geq 30$ for $B_{in} = 0.12$ and $L/R_{in} \geq 40$ for $B_{in} = 0.06$).

Effects of Inlet Blockage

Diffusers with AR ≈ 2.3, investigated in [1, 4 and 14], are a rare case where results obtained by different researchers can be compared over a large range of inlet blockages, although only one length ($L/R_{in} \approx 4.0$) was the same in all the three test series. Figures 4(*a*) to (*c*) compare the results with performance-map data from [19], equal symbols denoting comparable geometries. All the curves show the well-known fall of C_p as B_{in} increases, particularly steep at low values of B_{in}, smallest for diffusers longer than optimum and largest for short, stalled diffusers. However, their shapes differ widely. In Miller's tests, [14] $C_p \approx$ const for $0.06 \leq B_{in} \leq 0.16$, while Peters' [1] distributions fall continuously to $B_{in} \approx 0.18$.[4] The curves from [4] and [19] are intermediate in character with generally lower C_p values (from [4] in particular for $L_a/R_{in} = 5.7$). A further analysis will be given later.

Results from [4] and [19] for an AR = 5 diffuser compare better, Fig. 5, although the ones from [4] are again somewhat low. Excellent agreement generally exists among the performances from various sources for AR = 4 diffusers, depicted in Fig. 6. Of particular interest here is the comparison with the effects of screen rings, to be analyzed later, and with Sprenger's [16] classical data, because Kenny [28] reported that Sprenger's geometry would stall for $B_{in} \geq 0.10$.

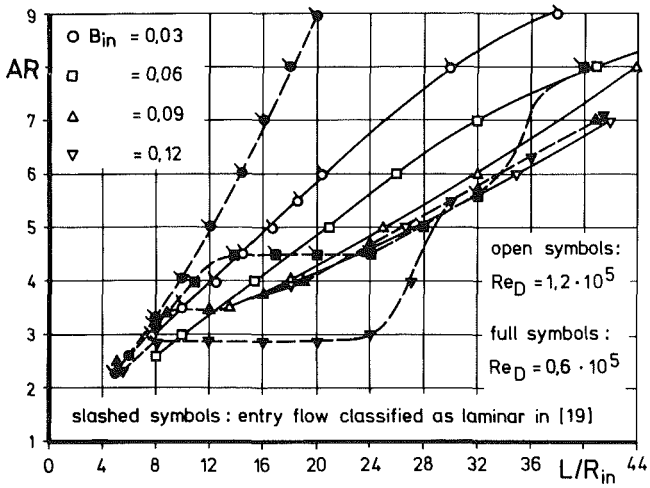

Fig. 3 Optimum diffuser geometries for prescribed nondimensional diffuser length at low Reynolds numbers (from [19])

Other measurements conducted with similar blockages [29, 30, 31] gave no such indication, and according to Fig. 6 are perfectly in line with the Sprenger data.

Effects of Turbulence and Shape Factor

With long approach pipes, diffuser performance rises as approach lengths increase. This was first noted in the Cockrell- and Markland data (Figs. 4(*b*) and 5), confirmed by Bradshaw [12], Fig. 7(*a*), and attributed by him to changes in turbulence which enhance mixing transverse to the flow direction, thus reducing distortions. Indeed, the core-turbulence intensity of developing pipe flow rises significantly from $L_a/D \approx 20$ to ≈ 45 [15] (the corresponding blockage factors depending on Re_D), and then remains nearly constant. Since generally B_{in} increases only to $L_a/D \approx 40$ and then falls to $L_a/D \approx 70$ [15], approach pipes of that length range should produce higher diffuser performance than shorter ones of equal B_{in}, if Bradshaw's explanation is correct. This is in fact the case, see Peters' curve for $L/R_{in} = 4.1$ in Fig. 4(*c*) and Miller's data for $L_a/D = 60$ in Fig. 4(*a*). (Flagged symbols[5] denote increased Tu_c here and in what follows; they more generally denote altered inlet conditions from such sources as

[3] When examining the Bradley and Cockrell data in Fig. 2, it should be noted that the rough pipe produced a higher turbulence intensity close to the walls than either the smooth pipe or the profile generator.

[4] The relationship between B_{in} and L_a/R_{in} used in [27] results in steeper slopes and hence still larger deviations from Miller.

[5] Flags always have positive slope (example: O) while slashes have negative slope (example: O).

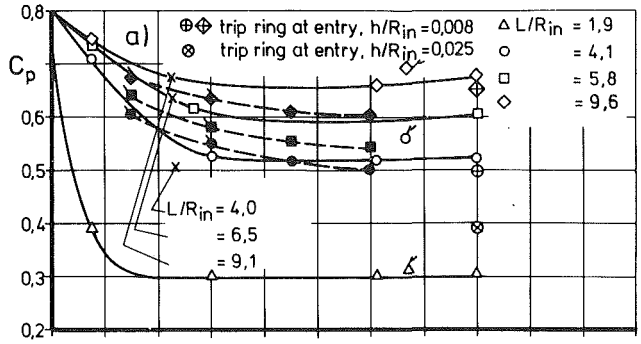

Fig. 4(*a*) Results of Miller [14], AR = 2.28, $Re_D = 5.5 \cdot 10^5$; flagged symbols: $L_a/D = 60$; full symbols: Dolan and Runstadler [19], $Re_D = 1.2 \cdot 10^5$; × I.I.T. Madras, $Re_D = 8.3 \cdot 10^5$.

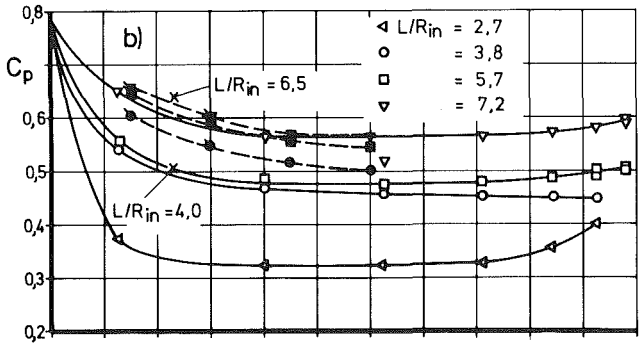

Fig. 4(*b*) Results of Cockrell and Markland [4], AR = 2.25, $Re_D = 1.8 \cdot 10^5$; full symbols: Dolan and Runstadler [19], $Re_D = 0.6 \cdot 10^5$; × I.I.T. Madras, $Re_D = 8.3 \cdot 10^5$.

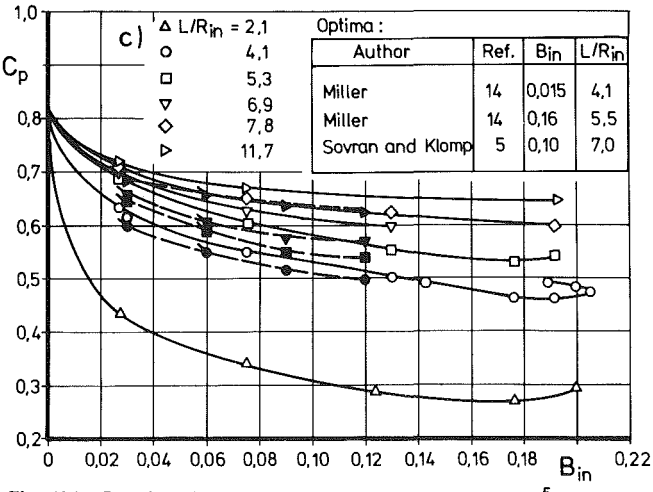

Fig. 4(*c*) Results of Peters [1], AR = 2.34, $Re_D = 2.0 \cdot 10^5$; full symbols: Dolan and Runstadler [19], $Re_D = 0.6 \cdot 10^5$

Fig. 4 Effects of inlet blockage on the performance of diffusers with an area ratio AR ≈ 2.3.
Slashed symbols denote entrance flows classified as laminar in [19]

upstream rings, trips, screens, etc., which produce increased turbulence intensity.) Hence turbulence is indeed an additional inlet parameter affecting diffuser flow. Since turbulence development in pipes depends on the entry conditions [15], this may account for some of the differences in diffuser results. Our understanding of developing pipe flow is, however, insufficient to explain all the phenomena observed: Shárán [32] demonstrated that C_p falls as L_a/D increases from 65 to 105 and then rises again to $L_a/D \approx 130$ (Fig. 7(*b*)).

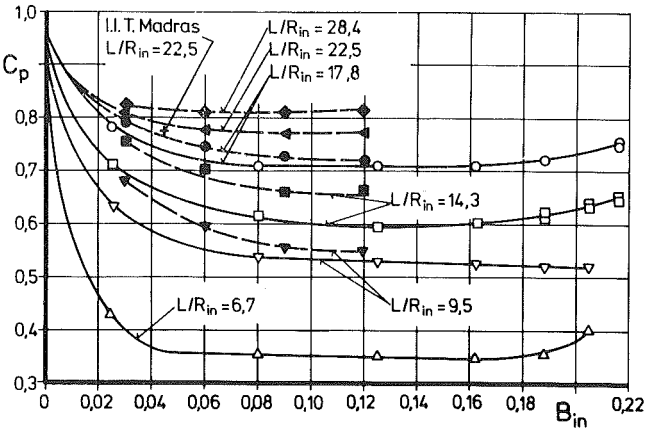

Fig. 5 Effects of inlet blockage on the performance of diffusers with an area ratio AR = 5.
Open symbols: Cockrell and Markland [4], $Re_D = 1.8 \cdot 10^5$; full symbols: Dolan and Runstadler [19], $Re_D = 1.2 \cdot 10^5$; slashed symbols: entry flow classified as laminar in [19].

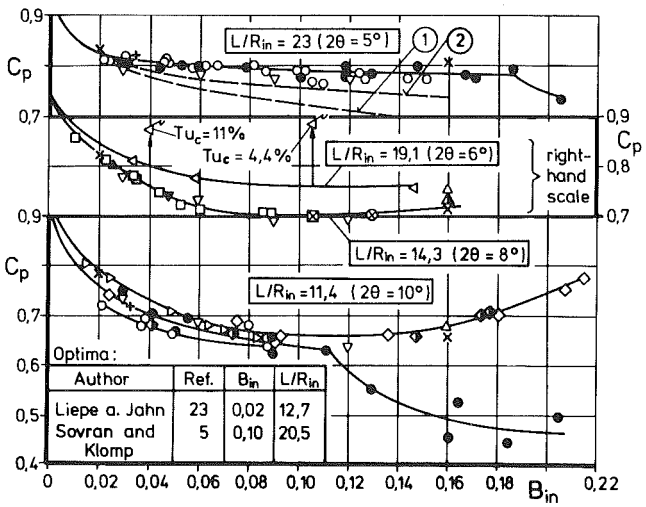

	Author	Ref. No.	$Re_D \times 10^{-5}$		Author	Ref. No.	$Re_D \times 10^{-5}$
○ ●	Winternitz and Ramsay*	8	2,5	▽	Dolan a. Runstadler	19	1,2
◁	Pozzorini**	17	2,5	⊗	Trupp et al.	30	
□	Sprenger	16	5,2	▲	Okwuobi and Azad	29	6,0
△	Miller	14	5,5	x	Liepe a. Jahn	23	6,0
◈	Cockrell	33		◇	Cockrell et al.	7	
▷	Müller	25	1,8	+	Mc Donald a. Fox	20	1,3
▽	I.I.T. Madras		8,3	▲	Senoo a. Nishi	22	3,0
				⊠	Azad a. Hummel	31	

* Full symbols: blockage produced by screen rings

** Flagged symbols: blockage produced by sudden expansion

Fig. 6 Effects of inlet blockage on the performance of diffusers with an area ratio AR = 4
Broken lines: $C_{p\alpha_{in}}$ according to Winternitz and Ramsay [8],
① for screen rings
② for approach lengths

Beneficial effects of artificially increasing Tu at entry also have been reported by several researchers. Shárán [10], using grids, measured a C_p-rise of up to 25 percent in an AR = 2.5-diffuser and of 15 percent with AR = 5.0 (see Fig. 7(*b*)). In these tests the approach flow in the absence of the grids was probably laminar (as will be explained later), but Pozzorini [17] demonstrated a similar C_p-rise relative to a genuine

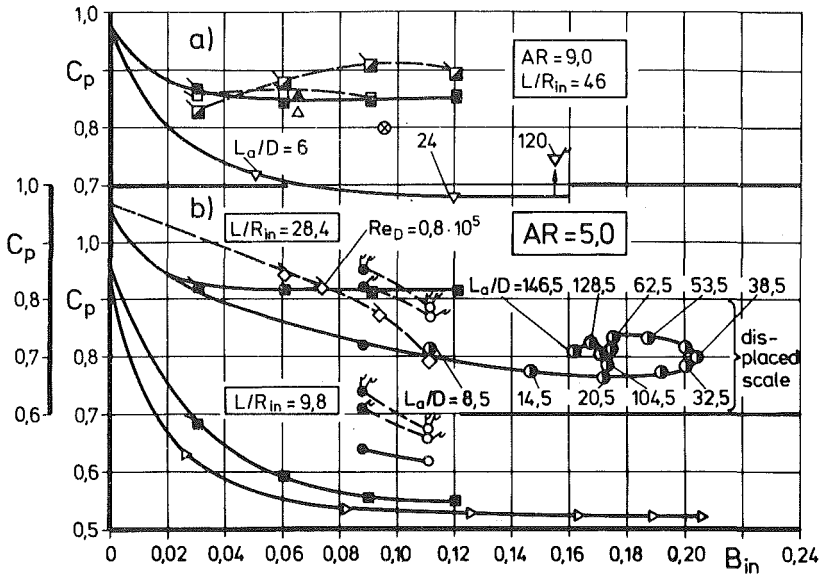

Fig. 7 Effects on performance observed in two large-area diffusers

- ▷ Cockrell and Markland [4], $Re_D = 1.8 \cdot 10^5$
- ○, ● Sháran [10], $Re_D = 1$ and $4 \cdot 10^5$, $Tu_c \approx 1$ percent; flagged symbols: $Tu_c = 4$ percent, double-flagged symbols: $Tu_c = 8$ percent
- △, ▲ Sale (from [10]), $Re_D = 1$ and $4 \cdot 10^5$
- ⊗ Hugh (from [10]), $Re_D = 2 \cdot 10^5$, B_{in} unknown
- ▽ Bradshaw [12], $Re_D = 0.8 \cdot 10^5$, trip
- ◪, □, □ Dolan and Runstadler [19], $Re_D = 0.3 \cdot 10^5$, $0.6 \cdot 10^5$ and $1.2 \cdot 10^5$, trip
- ◑ Sháran [32], $Re_D = 1 \cdot 10^5$
- ◇ Eschrich [36], $0.1 \cdot 10^5 \leq Re_D \leq 0.8 \cdot 10^5$, rounded entrance

Slashed symbols: entry flow classified as laminar

turbulent entrance-pipe flow by fitting sudden expansions 8.75 and 18.75 pipe diameters upstream of a diffuser (see Fig. 6). In this case, $H_{1,2}$, turbulence intensity, and structure all were changed. These parameters were separated in [9] by a special profile generator. When fitted 6 diameters upstream of a diffuser, it produced in its entrance plane the same velocity profile and turbulence spectrum as a $L_a/D = 96$-pipe with a similar Tu-distribution at a higher level. Some results are shown in Fig. 8. Thus, the C_p - rise (up to 14 percent) was almost certainly due to the increased turbulence intensity alone.[6]

Sajben et al. [11], instead of increasing turbulence, suppressed it in the wall region by special screens producing velocity profiles very close to developing pipe flow of equal blockage, but with Tu $\approx$ 1 percent to very small wall distances. Figure 8 compares the results with entrance-pipe performances mainly from [5, 14, 20, and 23] (the data points have been omitted for the sake of clarity): C_p is up to 20 percent lower. The importance of turbulence for diffuser performance, thus proved, was not realized by Sajben et al., owing to lack of comparable approach-length data. They wrongly concluded that the screens are an effective means of generating flows with the same properties as pipes (see also [34]).

The effects of initial turbulence and shape factor are interconnected because profile distortion depends on both. Indeed, the growth rate of $H_{1,2}$ in a diffuser is retarded and hence performance improved when Tu increases [35]. Conversely, screen rings with large values of $H_{1,2}$ produce lower recoveries than approach lengths [7]. Some confusion as to the validity of the latter observation exists since similar tests in [8] apparently had shown no such differences. Figure 6 reveals that the conclusion drawn in [8] does not hold true: in fact, the $L/R_{in} = 11.4$-diffuser obviously separated when tested with screen rings producing $B_{in} \approx 0.12$, but it did not when other researchers investigated it with equivalent entrance pipes (not employed in [8]). With $L/R_{in} = 23$, both types of approach flow gave the same C_p values in [8]. But even then the effect of an increased $H_{1,2}$ is apparent: when using the more correct coefficient $C_{p\alpha_{in}}$, the screen rings created definitely lower recoveries (Fig. 6). Three other references also clearly demonstrate a reduction of C_p owing to an increase in $H_{1,2}$, in spite of high turbulence: [11], when a screen ring enlarged the wake component of the velocity profile (data points at $B_{in} = 0.23$ in Fig. 8), [9], when a rough entrance pipe was employed (Fig. 8), and [14] when the entrance plane contained annular steps.

Laminar and Transitional Flow Phenomena

It is generally accepted that the Reynolds number does not affect diffuser performance if large enough for transition phenomena to be absent. The consequences of transition occurring in a diffuser are not very well understood. A high free-stream turbulence, tripping devices and sharp corners at the entry will enhance transition; a rounded entrance will inhibit it.

Eschrich [36] investigated a number of Venturi nozzles (diffusers with rounded entrances) in the range of $0.1 \cdot 10^5 \leq Re_D \leq 0.8 \cdot 10^5$. Examples of the results are included in Fig. 7. Recoveries at the larger Re_D values are higher than or equal to the recoveries for turbulent flow, whereas those for the

[6] It is worth mentioning that C_p rose to an upstream distance of the profile generator of 30 D, then slowly decreased again and remained unaffected only from 60 D onward (see Cockrell [33]).

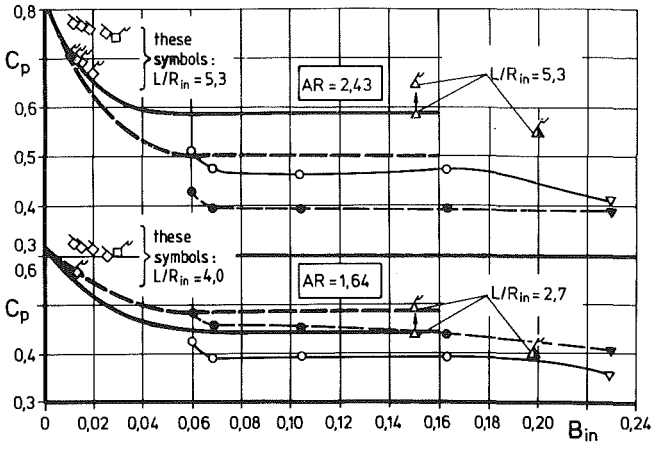

Symbol	Tu_c [percent]	$Re_D \cdot 10^{-5}$	$H_{1,2}$	Remarks
◇	0.3	1.5 - 6.0	3.0 - 2.4	laminar entry flow
□	3.0	4.3	?	uniform screen upstream
◆	0.75	7.2	?	natural transition
◇	0.3	1.5 - 6.0	1.5 - 1.4	serrated trip
○, ●	0.9	4.3	?	Tu at wall reduced
▽, ▼	0.7	4.3	?	as ○, ●, $H_{1,2}$ increased
△	2.9	2.2	?	smooth inlet pipe, $L_a/D = 96$
△	4.1	2.2	?	rough inlet pipe $L_a/D = 96$, $k_S/D = 4 \cdot 10^{-3}$
△	7.0	2.2	as △	profile generator 6 dia upstream

Results represented by symbols in the upper part of the table are from Sajben, et al. [11, 18]. Results represented by symbols in the lower part of the table (upright triangles) are from Bradley and Cockrell [9].

Fig. 8 Effects on diffuser performance of various methods of changing entry turbulence

Broken lines: $L/R_{in} = 4.0$
Solid lines: $L/R_{in} = 5.3$ for AR = 2.43 (upper part of figure), $L/R_{in} = 2.7$ for AR = 1.64 (lower part of figure)
Thin lines: Results according to Sajben, et al. [11]
Thick lines: Mean curves through data points from [5, 14, 20, and 29] (points omitted for the sake of clarity)

smaller Re_D values are considerably lower. Laminar approach flow, however, is not restricted to low Reynolds numbers. It may also result at much higher Re_D from the acceleration in large contractions. This was the case in the experiments on rounded-entrance diffusers in [18], and the recoveries lie again significantly above the curve for turbulent approach flow (Fig. 8). In these tests Tu_c was generally 0.3 percent but at $Re_D = 7.2 \cdot 10^5$ it suddenly rose to 0.75 percent (probably due to acoustic modes created in the air supply line) and C_p dropped onto the curve for turbulent flow (Fig. 8). A serrated trip (which altered $H_{1,2}$ only a little) had the same effect, (see [11]) while increase of Tu_c by a uniform screen to a value as high as 3 percent did not affect C_p even at $Re_D = 4.3 \cdot 10^5$ (Fig. 8). Extreme Re_D effects not included in Fig. 8 were noted in [18] on a diffuser shorter than optimum (AR = 2.43, $L/R_{in} = 2.7$): as Re_D increased from $2 \cdot 10^5$ to $6 \cdot 10^5$, C_p rose from 0.3 to 0.7, but at $Re_D = 7.2 \cdot 10^5$ (when Tu_c was 0.75 percent), it suddenly dropped to about 0.50, a value to be expected for turbulent entry flow. These observations confirm Eschrich's results at Re_D values nearly ten times higher.

Shárán's [32] recoveries, depicted in Fig. 7(*b*), are very low compared to [19], although in both cases $Re_D \approx 1 \cdot 10^5$. Shárán's recoveries fall continuously to $B_{in} = 0.17$ ($L_a/D \approx 20$), while those from [19] are constant beyond $B_{in} \approx 0.06$. Because of the observations made in [18] at still higher Re_D, we must conclude that the entry flow to Shárán's diffuser was laminar, due to the 16:1 contraction and the turbulence-reducing screens employed. The sharp corners of this diffuser probably failed to act as a trip because of the very small diffuser angle. By contrast, the trip in [19] was stated to have been effective when $B_{in} \geq 0.06$. Only when Shárán artificially increased Tu did C_p reach or exceed the levels recorded in [19] and in other references (Fig. 7(*b*)).

A continuous fall of C_p with increasing blockages and, hence, low pressure recoveries at intermediate and large blockages, were obtained in most tests conducted at $Re_D \leq 2 \cdot 10^5$; notably those of Peters [1] (Fig. 4(*c*)), Bradshaw [12] (Fig. 7(*a*)), and Müller [25]. This holds true even for the short configurations in [19], in spite of the trip used (Fig. 7). We must attribute this to laminar approach flow. Whenever Re_D was sufficiently high, C_p remained constant for $B_{in} \geq 0.06$ (Fig. 4(*a*)), and this is also found for the longer diffusers in [19] (Fig. 5). Transitional flow may be also responsible for the generally low performances in [4] (Figs. 4(*b*) and 5). Transitional flow probably occurred even at a Reynolds number as high as $1.2 \cdot 10^6$, in the rounded-entry-diffuser tests reported in [2], because when B_{in} increases, these recoveries again fall at a much slower rate than with turbulent flow (Fig. 9). By contrast, turbulent flow recoveries were obtained in [37, 38, 39] with the same faired inlet section as in [2] since trip wires were employed.

Sprenger [16] varied Re_D in addition to blockage. Figure 10 presents these results in a comprehensive form. Slashed data points belong to approach flows which Sprenger classified, from stethoscope investigations, as laminar. The turbulent-entry-flow recoveries form a single curve with surprising agreement, and hence indeed depend on blockage only and not on Re_D. Data points for laminar approach flow are located both above and below this curve, as was already deduced from [18] and [36]. The physical reason for this phenomenon remains unknown: cross reference by the numbers assigned to the data points with Figs. 7 and 8 in [15] in the same issue of this Journal (which specify entry conditions in more detail) does not explain it. Short approach lengths appear to produce higher recoveries than turbulent flow with comparable blockage (points 1 to 7, $L_a/D = 0.85$) and intermediate approach lengths lower recoveries (points 14 to 16, $L_a/D = 10.85$). This is in agreement with the results from other sources, already described, including the changes in optimum geometries depicted in Fig. 3. For still longer entrance pipes, however, Fig. 10 again shows higher performances than comparable turbulent flows (points 19 to 21, $L_a/D = 16.85$). Cross reference with Fig. 7 of [15] also reveals that the pressure recoveries may differ from those for turbulent inlet flow not only for laminar entry flow, but also for transitional entry conditions. In the case of the longer entrance pipes, pressure recoveries become equal to those for turbulent entry only when the Reynolds number approaches its upper critical value (point 17 compared with 18 and point 21 with 22) which, according to [15], in the Sprenger experiments was $Re_{D_{crit}} = 1.1 \cdot 10^5$ for $x/D = 16.85$. With short entrance pipes the same pressure recoveries as for turbulent entry flow are obtained already at a Reynolds number less than its lower critical value, when the entry flow is still laminar (with $L_a/D = 0.85$ at $Re_D \approx 3 \cdot 10^5$, between points 7 and 8 in Fig. 10[7]). Hence when $Re_D \geq 3 \cdot 10^5$, Sprenger's sharp-edged diffuser, with its particular upstream conditions (especially a rather high turbulence level), always performed as if the entry flow were turbulent.

Little information exists, apart from the evidence already presented, on the effects of tripping devices. Sprenger's tests indicate very low recoveries if a wire fails to trip the boundary layer (points A and B in Fig. 10; see also Figs. 7 and 8 of [15]), and even when the wire is effective, the performance is shown to be less than for turbulent entry over a wide range of

[7] For $L_a/D = 0.85$ the lower and upper critical Reynolds numbers had the values $7.0 \cdot 10^5$ and $2.2 \cdot 10^6$ respectively, as can be deduced from [15].

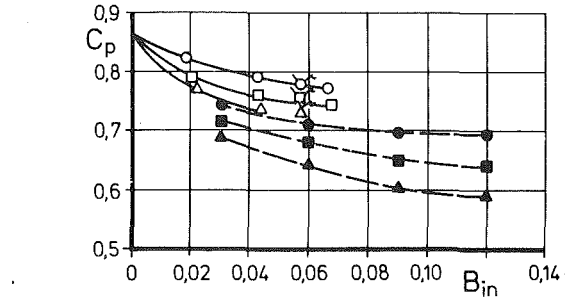

Fig. 9 Transitional-flow diffuser performance with $Re_D = 1.2 \cdot 10^6$
△, □, ○ Robertson and Ross [2], L/R_{in} = 8.4; 10.3; 15.7, $Re_D = 1.2 \cdot 10^6$
Full symbols: Dolan and Runstadler [19], $Re_D = 1.2 \cdot 10^5$, trip
Flagged symbols: Eschrich [36], $Re_D = 0.8 \cdot 10^5$, round entrance
Slashed symbols: entry flow classified as laminar

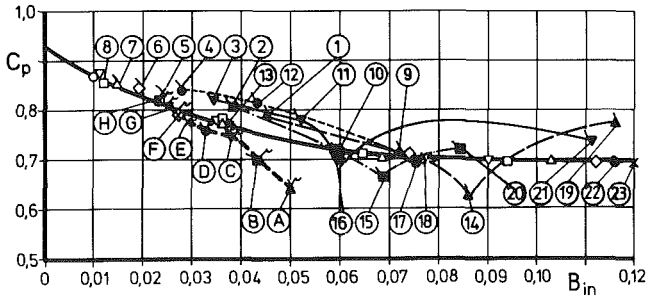

Fig. 10 Performance of a diffuser at various Reynolds numbers, according to Sprenger [16]

Symbol	▲	■	▼	●	×	◇	△	□	▽	○
$Re_D \cdot 10^{-5}$	0.35	0.46	0.56	0.77	1.12	1.75	2.50	3.54	5.20	6.25

Slashed symbols: entry flow classified as laminar by Sprenger
Flagged symbols: $L_a/D = 1.85$, trip ring $h/R_{in} = 0.02$ 1.5 D upstream
Thick solid line: connection of data points for which entry flow was classified as turbulent by Sprenger
Thick broken line: connection of data points taken at various Reynolds numbers with $L_a/D = 1.85$ and the trip ring
Thin lines: connection of data points taken at a constant Reynolds number with various values of L_a/D, namely,
—— —— ——: $Re_D = 0.35 \cdot 10^5$
- —— - —— -: $Re_D = 0.46 \cdot 10^5$
——————: $Re_D = 0.56 \cdot 10^5$
- - - - - - - -: $Re_D = 0.77 \cdot 10^5$
Encircled numbers at respective fixed vertical distances from the abscissa identify data points taken with a constant value of L_a/D at different values of Re_D, where the numbers increase as Re_D increases:
(1) to (8): $L_a/D = 0.85$, $Re_D = 0.35 \cdot 10^5$ to $3.54 \cdot 10^5$
(9) to (13): $L_a/D = 4.85$, $Re_D = 0.35 \cdot 10^5$ to $1.12 \cdot 10^5$
(14) to (18): $L_a/D = 10.85$, $Re_D = 0.35 \cdot 10^5$ to $1.12 \cdot 10^5$
(19) to (23): $L_a/D = 16.85$, $Re_D = 0.35 \cdot 10^5$ to $1.12 \cdot 10^5$
Encircled letters identify data points taken at various Reynolds numbers with $L_a/D = 1.85$ and the trip ring.

Reynolds numbers (points C to G). Only for $Re_D \geq 3 \cdot 10^5$ does C_p become equal to the respective turbulent recovery (between points G and H), and this value is no less than would be expected for the same L_a/D without a trip. Eschrich [36] correlated for $C_{p\,\text{laminar}} > C_{p\,\text{turbulent}}$ the reduction of C_p with increasing wire diameter, demonstrating that a trip makes C_p rise when $C_{p\,\text{laminar}} < C_{p\,\text{turbulent}}$ and showing that grooves are equally effective as wires.

Diffuser Design Recommendations

On the basis of this review, a guide for the design of diffusers with a free discharge is presented. It is generally valid for turbulent inlet flow, primarily with the type and intensity of turbulence produced by approach lengths. The relationship between the latter and the blockage factor is given in [15]. For $B_{in} \leq 0.02$, optimum diffusers should be selected according to the respective curve from [23], shown by open circles in Fig. 1, and for $B_{in} \geq 0.12$ Sovran and Klomp's $B_{in} = 0.18$-line is recommended (Fig. 1, which also gives some guidance for intermediate blockages). The pressure recoveries of these geometries vary with inlet blockage as depicted in Fig. 11, full lines pertaining to the second case and broken lines to the first case. Very long entrance pipes ($L_a/D \geq 40$) and flows with an increased turbulence intensity (common in practical applications) will usually create higher recoveries, and the two sets of data points included in Fig. 11 indicate the gain to be expected. Generally Fig. 11 is applicable only if $Re_D \geq 3 \cdot 10^5$, but for AR ≥ 3.5 and $L_a/D \geq 10$ this limit can be relaxed to $Re_D \approx 1 \cdot 10^5$ in cases with early transition (no large area-ratio contractions upstream, high turbulence etc.). Application to diffusers with faired entrances requires effective tripping devices even at much higher Reynolds numbers. Caution is also advised if the shape factor of a turbulent approach flow exceeds $H_{1,2} \approx 1.5$: lower performance may then result even with a high turbulence level. Note that Fig. 11 predicts higher pressure recoveries than the uncorrected McDonald and Fox data [20], and for the smaller area ratios it also predicts higher pressure recoveries than the often used performance maps of Sovran and Klomp [5] and Dolan Runstadler [19] (in the latter case the entry conditions were usually nonturbulent).

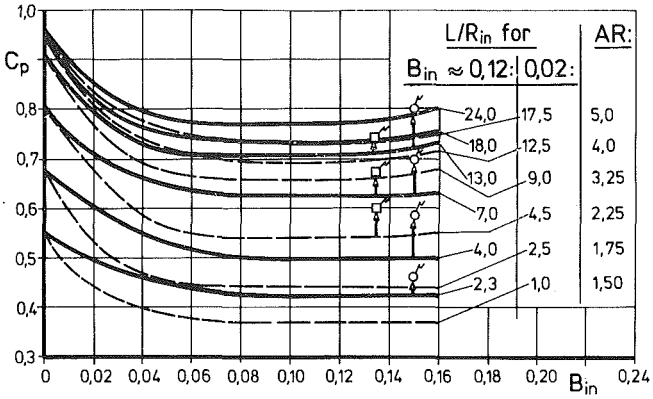

Fig. 11 Design recommendations for diffusers with turbulent-entry flow performance
Solid lines: optimum for $B_{in} \geq 0.12$
Broken lines: optimum for $B_{in} \approx 0.02$
Flagged symbols: increased turbulence intensity, $\triangle L_a/D = 60$, $\delta Tu_c = 7$ percent
Uncertainty estimate (only valid if performance corresponds to that for turbulent entry flow):

Coordinate		Uncertainty	
C_p	B_{in}	C_p	B_{in}
0.8	0.16	±0.03	±0.01
0.4	0.02	±0.02	±0.005

Conclusions

For truly turbulent entry flow the main conclusions are:

1 For approach length blockage, the effect of the entry blockage factor on diffuser performance is well defined. Hence accurate design recommendations can be given for the dependence of diffuser pressure recovery on entry blockage.

2 The effect of increasing inlet turbulence intensity is to increase pressure recovery.

3 The effect of increasing the inlet shape factor (ratio of

inlet displacement to inlet momentum thickness) is to reduce diffuser pressure recovery.

4 Optimum geometries at a fixed nondimensional length depend to some extent on the entry blockage factor.

Additional conclusions are:

5 Laminar and/or transitional entry flow may produce higher performance than turbulent entry flow, but lower performance also is found.

6 Most diffuser performance data measured at Reynolds numbers $Re_D \leq 2 \cdot 10^5$ differ from those at higher values of Re_D because of a nonturbulent entry flow, even when tripping devices were employed.

7 The nature of the inlet flow, turbulent or not, cannot be deduced from the inlet Reynolds number alone. Higher pressure recoveries than usual, due to nonturbulent entry flow, occurred up to $Re_D = 1.2 \cdot 10^6$ in diffusers with a rounded inlet when no effective tripping device was employed.

References

1 Peters, H., "Energieumsetzung in Querschnittserweiterungen bei verschiedenen Zulaufbedingungen," *Ingenieur-Archiv,* Vol. 2, 1931, pp. 92–107. See also: "Conversion of Energy in Cross-Sectional Divergences Under Different Conditions of Inflow," NACA TM 737, 1934.

2 Robertson, J.M., and Ross, D., "Effect of Entrance Conditions on Diffuser Flow," *Proceedings of the ASCE,* Vol. 78, 1952, Separate No. 141, pp. 1–24.

3 Cockrell, D.J., and Markland, E., "The Effects of Inlet Conditions on Incompressible Fluid Flow Through Conical Diffusers," *Journal of the Royal Aeronautical Society,* Vol. 66, No. 1, 1962, pp. 51–52.

4 Cockrell, D.J., and Markland, E., "A Review of Incompressible Diffuser Flow," *Aircraft Engineering,* Vol. 35, 1963, No. 10, pp. 286–292. See also: "Diffuser Behavior: A Review of Past Experimental Work Relevant Today," *Aircraft Engineering,* Vol. 46, No. 4, 1974, pp. 16–26.

5 Sovran, G., and Klomp, E., "Experimentally Determined Optimum Geometries for Rectilinear Diffusers with Rectangular, Conical or Annular Cross Section," *Fluid Mechanics of Internal Flow* (ed.: G. Sovran), Elsevier Publishing Company, Amsterdam, 1967.

6 Reneau, L.R., Johnston, J.P., and Kline, S.J., "Performance and Design of Straight, Two-Dimensional Diffusers," ASME *Journal of Basic Engineering,* Vol. 89, No. 1, 1967, pp. 141–150.

7 Cockrell, D.J., Diamond, M.J., and Jones, G.D., "The Diffuser Inlet Flow Parameter," *Journal of the Royal Aeronautical Society,* Vol. 69, No. 5, 1965, pp. 350–352.

8 Winternitz, F.A.L., and Ramsay, W.J., "Effects of Inlet Boundary Layer on Pressure Recovery, Energy Conversion and Losses in Conical Diffusers," *Journal of the Royal Aeronautical Society,* Vol. 61, No. 2, 1957, pp. 116–124.

9 Bradley, I.C., and Cockrell, D.J., "The Response of Diffusers to Flow Conditions at Their Inlet," *Symposium on Internal Flows,* University of Salford, England, Paper 5, 1971.

10 Shárán, V.K., "Improving Diffuser Performance by Artificial Means," *AIAA Journal,* Vol. 10, No. 8, 1972, pp. 1105–1106.

11 Sajben, M., et al., "Experiment on Conical Diffusers with Distorted Inflow," *AIAA Journal,* Vol. 14, No. 12, 1976, pp. 1723–1732.

12 Bradshaw, P., "Peformance of a Diffuser with Fully-Developed Pipe Flow at Entry," *Journal of the Royal Aeronautical Society,* Vol. 67, No. 11, 1963, p. 733.

13 Cockrell, D.J., "Pressure Coefficient and Diffuser Efficiency," *Journal of the Royal Aeronautical Society,* Vol. 68, No. 12, 1964, pp. 844–845.

14 Miller, D., "Performance of Straight Diffusers," Part II of "Internal Flow: A Guide to Losses in Pipe and Duct Systems," B.H.R.A.-Fluid Engineering, Cranfield/Bedford, 1971.

15 Klein, A., "Review: Turbulent Developing Pipe Flow," ASME JOURNAL OF FLUIDS ENGINEERING, published in this issue pp. 243–249.

16 Sprenger, H., "Experimentelle Untersuchungen an geraden und gekrümmten Diffusoren," Mitteilung Nr. 27 aus dem Institut für Aerodynamik an der ETH Zürich, Verlag Leemann, Zürich, 1959. See Also: "Experimental Investigations of Straight and Curved Diffusers," British Ministry of Aviation Translation, TIL/T. 5134, 1962.

17 Pozzorini, R., "Das turbulente Strömungsfeld in einem langen Kreiskegel-Diffusor," PhD dissertation ETH Zürich, 1976. Eduard Truninger AG Zürich, 1976.

18 Sajben, M., Kroutil, J.C., and Sedrick, A.V., "Forces Acting on Conical Diffusers and Their Relation to Integral Performance Parameters," AIAA Paper No. 73-686, 1973.

19 Dolan, F.X., and Runstadler, P.W., Jr., "Pressure Recovery Performance of Conical Diffusers at High Subsonic Mach Numbers," NASA CR-2299, 1973.

20 McDonald, A.T., and Fox, R.W., "An Experimental Investigation of Incompressible Flow in Conical Diffusers," *Intern. Journal of Mechanical Sciences,* Vol. 8, No. 2, 1966, pp. 125–139.

21 Van Dewoestine, R.V., and Fox, R.W., "An Experimental Investigation on the Effect of Subsonic Inlet Mach Number on the Performance of Conical Diffusers," *Intern. Journal of Mechanical Sciences,* Vol. 8, No. 12, 1966, pp. 759–769.

22 Senoo, Y., and Nishi, M., "Improvement of the Performance of Conical Diffusers by Vortex Generators," ASME JOURNAL OF FLUIDS ENGINEERING, Vol. 96, No. 4, 1974, pp. 4–10.

23 Liepe, F., and Jahn, K., "Untere Wirkungsgrade von Kegeldiffusoren," *Maschinenbautechnik,* Vol. 11, No. 11, 1962, pp. 588–589.

24 Klein, A., Ramjee, V., and Venkataramani, K.S., "An Experimental Study of the Subsonic Flow in Axisymmetric Contractions," *Zeitschrift für Flugwissenschaften,* Vol. 21, No. 9, 1973, pp. 312–320.

25 Müller, H.P., "Experimentelle Untersuchungen an Kegeldiffusoren einer mehrstutzigen Radialverdichterspirale," *Brennstoff-Wärme-Kraft,* Vol. 28, No. 3, 1976, pp. 97–101. See also: PhD dissertation of same title, Ruhr-Universität, Bochum, 1974.

26 Rippl, E., "Experimentelle Untersuchungen über Wirkungsgrade und Abreissverhalten von schlanken Kegeldiffusoren," *Maschinenbautechnik,* Vol. 5, No. 8, 1956, pp. 405–412.

27 Henry, J.R., Wood, C.C., and Wilbur, S.W., "Summary of Subsonic Diffuser Data," NACA-RM-L 56 F 05, 1956.

28 Kenny, D.P., "A Turbulent Boundary Layer Analysis of Conical Diffusers," *Transactions, Canadian Aeronautics and Space Institute,* Vol. 7, No. 2, 1974, pp. 49–59.

29 Okwuobi, P.A.C., and Azad, R.S., "Turbulence in a Conical Diffuser with Fully Developed Flow at Entry," *Journal of Fluid Mechanics,* Vol. 57, Part 3, 1973, pp. 603–622.

30 Trupp, A.C., et al., "Turbulence Characteristics in a Straight Conical Diffuser," Symposium on Internal Flows, University of Salford, England, 1971, Paper No. 9.

31 Azad, R.S., and Hummel, R.H., "Measurement of the Intermittency Factor in Diffuser-Flow," *Canadian Journal of Physics,* Vol. 49, 1971, pp. 2917–2930.

32 Shárán, V.K., "Factors Influencing the Performance of a Diffuser," *Indian Journal of Technology,* Vol. 14, No. 2, 1976, pp. 63–66.

33 Cockrell, D.J., "Effect of Inlet and Outlet Conditions on Pipe and Duct Components," The Ninth Members Conference, Sept. 1967, Cranfield, SP 929, The British Hydromechanics Research Association.

34 Sajben, M., et al., "Generation of Velocity Profiles Using Screens of Nonuniform Solidity," *AIAA Journal,* Vol. 13, No. 4, 1975, pp. 417–418.

35 Arnal, D., and Michel, R., "Effect of Free-Stream Turbulence on Turbulent Boundary Layers and on Boundary Layer Transition," Paper presented at the Euromech Colloquium 72: Boundary Layers and Turbulence in Internal Flows, University of Salford, England, Mar. 30-Apr. 1, 1976.

36 Eschrich, R., "Experimentelle Untersuchungen von Kegeldiffusoren an Venturidüsen," *Maschinenbautechnik,* Vol. 17, No. 1, 1968, pp. 27–32.

37 Uram, E.M., "The Growth of an Axisymmetric Turbulent Boundary Layer in an Adverse Pressure Gradient," *Proceedings of the Second U.S. National Congress of Applied Mechanics,* ASME, 1955, pp. 687–695.

38 Robertson, J.M., and Holl, J.W., "Effect of Adverse Pressure Gradients on Turbulent Boundary Layers in Axisymmetric Conduits," ASME *Journal of Applied Mechanics,* Vol. 23, No. 2, 1957, pp. 191–196.

39 Fraser, H.R., "The Turbulent Boundary Layer in a Conical Diffuser," *Journal of the Hydraulics Division, Proceedings of the ASCE,* Vol. 84, 1958, pp. 1684-1 - 1684-17.

Historical Review of Real-Fluid Isentropic Flow Models

D. A. Sullivan
Fern Engineering,
Bourne, Mass. 02532

The analysis of steady, one-dimensional, isentropic flow of nonideal compressible fluids is simplified greatly by the use of an approximate model for the PV or Pρ relation, this relation being called the isentrope equation. The simplest isentrope model is the perfect-gas or polytrope equation PV^n = constant. During the past 80 years, five isentrope equations have evolved: the polytrope, Walker, van der Waals, Rayleigh, and Callendar models. The historical development and limitations of each model are discussed. Only the polytrope and Rayleigh model yield simple, closed-form, analytic solutions for isentropic flow properties. A comparison with calculated data for sonic flow properties reveals the superiority of the Rayleigh model for the prediction of isentropic flow.

Introduction

The study of steady, isentropic flow is based almost exclusively on the perfect-gas and incompressible-liquid models. Nature has provided two notable examples; namely, air and water at atmospheric pressure and temperature, for which these models find wide application. The ideal-gas equation $PV=RT$ describes an ideal gas and the additional assumption of constant ideal-gas heat capacities defines a perfect gas. These models, however, are approximations that apply only to limited ranges of pressure and temperature. They cannot be applied, for example, to the isentropic flow of steam or natural gas at conditions normally encountered in industry. In applications where precision is of utmost importance such as flow metering, non-ideal or "real-gas" effects must be considered.

The compressibility factor function $Z = Z(V,T)$ where $Z = PV/RT$ and a temperature-dependent, ideal-gas heat capacity function $c_p^0 = c_p^0(T)$ represents a more general description of equilibrium fluid behavior. These two functions are the thermal and caloric equations of state which define *real-fluid behavior*. Various fluid models defined in terms of the thermal and caloric state equations are given in Table 1. Examples of thermal state equations in the form $P = P(V,T)$ are listed in Table 2.

Analytical solutions for steady and unsteady, one-dimensional isentropic flow utilizing a complex thermal state equation and a temperature-dependent heat capacity function have been derived for only a few special cases. Most often, solutions are obtained by iterative numerical calculations with computers, recent examples being the work of Johnson [21] and Talcott [44]. Analytical and numerical solutions represent "exact" solutions inasmuch as they are solutions to given thermal and caloric state equations. How well these state equations represent the thermodynamic properties of actual fluids is, of course, another matter. These solutions are typically complex and do not readily yield fundamental understanding of real-fluid flow processes. In addition, they do not permit simple engineering approximations of flow properties at conditions other than those computed and tabulated.

To fill this void, simple engineering models have been developed to approximate the thermodynamic paths of real-fluid processes. Five such isentropic models for compressible, real-fluid flow have been developed in the past 80 years: the Callendar, Rayleigh, Walker, van der Waals, and polytrope models. The following sections relate the historical development and implications of each model.

The Isentrope Equation. Gibbs' equation for steady, isentropic flow reduces to

$$h_0 - h = u^2/2 = \int_P^{P_0} V dP \tag{1}$$

where the 0 subscript refers to the stagnation state. The local sound speed is given by

$$c^2 = \frac{\partial P}{\partial \rho}\Big)_s = -V^2 \frac{\partial P}{\partial V}\Big)_s \tag{2}$$

By various combinations of equations (1) and (2), one finds the compressible-flow properties of interest; e.g., Mach number, mass flux, etc. Since temperature does not appear in either 1 or 2, one must resort to the thermal state equation to deduce the corresponding temperature. Equations (1) and (2) demonstrate that a PV or $P\rho$ description of the isentrope is sufficient to compute most isentropic flow properties. The relation $P(V)$ or $P(\rho)$ is the *isentrope equation* which is the basis for engineering models for the analysis of real-fluid isentropic flow.

The Perfect-Gas, Steady, Isentropic Flow Equations. Newton based his early attempts to predict the theoretical sound speed in a gas on Boyle's law (PV = constant) and, thus, deduced the isothermal sound speed. Laplace determined the correct relationship between sound speed c in an ideal gas and the ratio of ideal-gas specific heats, γ^0; namely, $c^2 = \gamma^0 PV$. Later, Poisson wrote the perfect-gas isentrope

Contributed by the Fluids Engineering Division and presented at the Winter Annual Meeting, New York, N.Y., December 2-7, 1979, of The American Society of Mechanical Engineers. Manuscript received by the Fluids Engineering Division, October 10, 1979. Paper No. 79-WA/FM-1.

Table 1 Equilibrium Fluid Models

	Real	Perfect	Ideal	Incompressible liquid
Thermal State Equation	$Z = Z(V,T)$	$Z = 1$	$Z = 1$	V = constant
Caloric State Equation	$c_p^0 = c_p^0(T)$	c_p^0 = constant	$c_p^0 = c_p^0(T)$	$c_p^0 = c_p^0(T)$ [a]

[a] Not relevant to isentropic flow.

Table 2 Common thermal state equations

Name	Equation
Ideal gas (ca. 1820)	$P = \rho RT$
van der Waals (1873)	$P = \dfrac{RT}{V-b} - \dfrac{a}{V^2}$
Redlich-Kwong (1949)	$P = \dfrac{RT}{V-b} - \dfrac{aT^{-0.5}}{V(V+b)}$
Beattie-Bridgeman (1927)	$P = \rho RT + (B_0RT - A_0Rc/T^2)\rho^2 + (-RTB_0b + A_0a - RB_0c/T^2)\rho^3 + (RB_0bc/T^2)\rho^4$
Benedict-Webb-Rubin (1940)	$P = RT\rho + (B_0RT - A_0 - C_0/T^2)\rho^2 + (bRT - a)\rho^3 + a\alpha\rho^6 + (c/T^2)\rho^3(1+\gamma\rho^2)\exp(-\gamma\rho^2)$

equation in the form used today, the Laplace-Poisson equation[1]:

$$PV\gamma^0 = A \tag{3}$$

where A is a function of entropy.

Saint-Venant and Wentzel [37] in 1839 applied the Laplace-Poisson equation (which they attributed to Lagrange and Poisson) to isentropic flow in nozzles and deduced the equation for the reduced velocity V_r $(=\rho u/\rho_0)$ as a function of the throat-to-stagnation pressure ratio P_t/P_0.

$$V_r = K\left(\frac{P_t}{P_0}\right)^{\frac{1}{\gamma^0}} \sqrt{2\frac{\gamma^0}{\gamma^0-1}\frac{P_0}{\rho_0}\left[1-\left(\frac{P_t}{P_0}\right)^{\frac{\gamma^0-1}{\gamma^0}}\right]} \tag{4}$$

[1] Cardwell [6] discusses the early history of this equation

where K is the discharge coefficient of the nozzle. They noted that equation (4) has a maximum corresponding to a pressure ratio of

$$\frac{P_t}{P_0} = \left(\frac{2}{\gamma^0+1}\right)^{\frac{\gamma^0}{\gamma^0-1}} \tag{5}$$

for which

$$V_r = K\left(\frac{2}{\gamma^0+1}\right)^{\frac{\gamma^0+1}{2(\gamma^0-1)}} \sqrt{\gamma^0 P_0/\rho_0} \tag{6}$$

Today we know equations (5) and (6) as the sonic or critical pressure ratio and mass flux equations.

For the case of a perfect gas flowing through a converging nozzle and discharging into a plenum (Fig. 1), one assumes the back pressure P_b equals the throat pressure P_t.

Nomenclature

A = cross-sectional area
A,B = constants in isentropic equation
b = van der Waals covolume term
c = sound speed
c_p, c_v = isobaric and isochoric heat capacities
h = enthalpy
J = dimensionless massflux, $= \rho u/\rho_0 c_0$
K = discharge coefficient
k = isentropic exponent
M = Mach number
m = polytropic exponent in PT relation; exponent in Walker equation
n = polytropic or Rayleigh exponent
P = pressure
R = gas constant
s = entropy
T = temperature
V = specific volume
V_r = reduced velocity in equations (4) and (6)
X,Y = Schultz; thermodynamic functions; equation (18)
Z = compressibility factor, $= PV/RT$
Γ = isentrope nonlinearity parameter
γ = ratio of specific heats
Δ = dimensionless pressure difference
ϕ = flow function
η = constant along polytrope
ρ = density

Subscripts

b = back pressure or downstream plenum condition
r = corresponding-states reduced property
t = throat condition
$*$ = sonic or critical flow condition

Superscripts

0 = ideal-gas state property

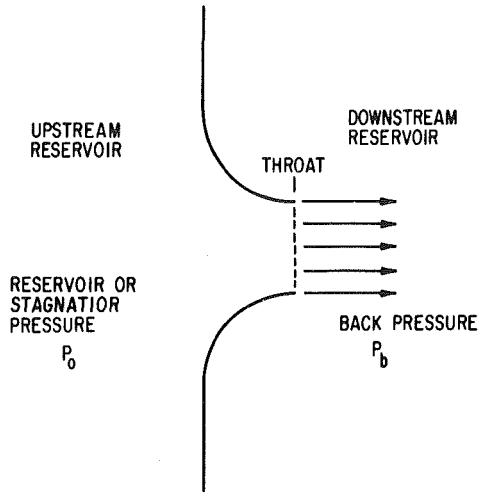

Fig. 1 The converging flow nozzle. The fluid flows from the upstream reservoir at pressure P_0 to a downstream reservoir at pressure P_b ($P_0 > P_b$).

Therefore, as the back pressure decreases, the mass flux first increases to a maximum given by equation (6) and then decreases to zero at $P_b/P_0 = 0$, according to equation (4). This gave rise to the idea for many years that a gas would not flow into a vacuum! Saint-Venant and Wentzel noted this misconception and proved with their experimental data that the mass flux remained constant as long as $P_b/P_0 < 0.4$ (approximately). From this result they correctly concluded that the equivalence of the throat pressure to the back pressure is invalid in the range $P_b/P_0 = 0$ to 0.4

Their work went unnoticed for nearly 50 years while others independently "rediscovered" these same results. For example, in 1856 Joule and Thomson [22] in England and Weisback [56] in Germany independently derived equations (4), (5), and (6). Napier [27] in 1867 experimented with the flow of steam through nozzles and found the mass flux to be independent of the nozzle back pressure as long as the nozzle back pressure ratio was less than 0.5.

Apparently, Osborne Reynolds [34] presented in 1886 the first significant contribution beyond the work of Saint-Venant and Wentzel in an exceptional article in which he was the first to recognize that under critical flow conditons, "the velocity of gas at the point of minimum area of a stream along which the pressure falls continuously is equal to the velocity of sound in the gas at that point." He also used continuity (ρuA = constant) to give a new interpretation to equation (4). Since the mass flux ρu is inversely proportional to the nozzle cross-sectional area A, equation (4) describes the area distribution in a de Laval (converging-diverging) nozzle in which the static pressure falls continuously (Fig. 2). Under these conditions, the flow is supersonic in the diverging section downstream of the throat. In fact, Fig. 6 of Reynolds' article is a diagram of a supersonic wind tunnnel, although Reynolds did not recognize it as such. Aurel Stodola provided in the early 1900's the experimental proof of the existence of supersonic flow in de Laval nozzles.

The Polytrope Model. The simplest, most common engineering model for an arbitrary, real- or perfect-gas process is the polytrope model, represented by:

$$PV^n = A \tag{7}$$

where n is the polytropic exponent and A is a constant. It is not by accident that the polytrope equation is identical in form to the Laplace-Poisson equation. Zeuner [58] in 1874 first proposed the polytrope equation as a modified form of the Laplace-Poisson equation and suggested $n < \gamma^0$ for frictional flow. In recent times the polytrope model has been

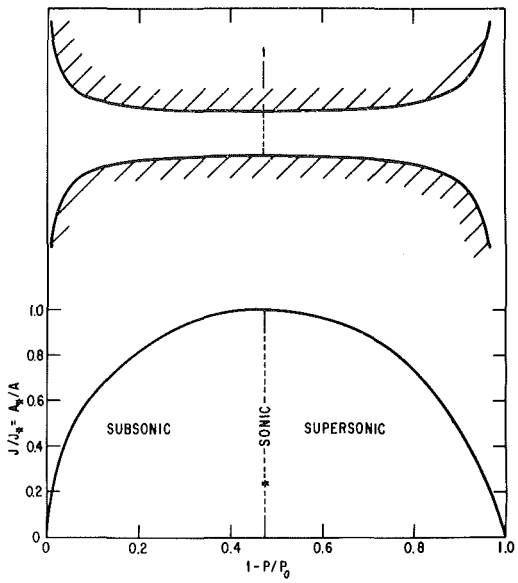

Fig. 2 Massflux as a function of static-to-stagnation ratio for a perfect gas with $\gamma^0 = 1.4$. The corresponding, one-dimensional de Laval nozzle profile is illustrated in the upper portion of the figure.

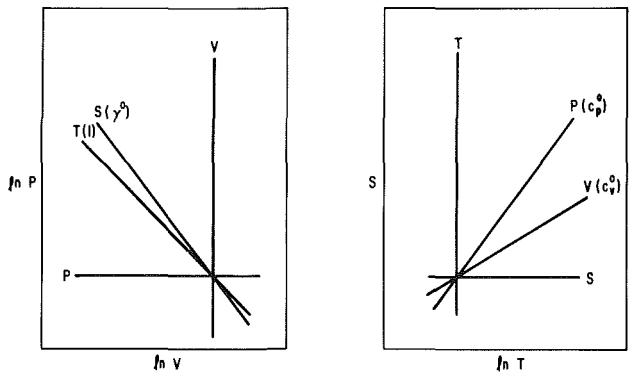

Fig. 3 Examples of perfect-gas, polytropic processes *P*, isobaric; *V*, isochoric; *T*, isothermal; *S*, isentropic. The slope of the polytrope appears in parentheses.

applied to other perfect-gas processes such as isothermal compression, adiabatic compression with losses, etc. Equation (7) and the ideal-gas equation yield the complementary equation relating pressure and temperature:

$$P^m/T = B \tag{8}$$

where B is a constant and the exponent m related to n by:

$$m = \frac{n-1}{n} \tag{9}$$

PV and *Ts* diagrams in Fig. 3 illustrate examples of four perfect-gas, polytropic processes. Here is a summary:

Process	n	m
Isentropic	γ^0	$\frac{\gamma^0-1}{\gamma^0}$
Isothermal	1	0
Isobaric	0	∞
Isochoric	∞	1

In 1948, Iberall [20] suggested the application of the polytrope to real-fluid, isentropic processes, and he noted that the ratio of specific heats is not the appropriate exponent in

equation (7). He proposed instead that the slope of the real-fluid isentrope determines the exponent, which for equation (2) is:

$$\frac{\partial P}{\partial V}\Big)_s = \gamma \frac{\partial P}{\partial V}\Big)_T \tag{10}$$

Combining equations (2) and (7), Iberall deduced the exponent n to be:

$$n = \frac{c^2}{PV} \tag{11}$$

which defines the *isentropic exponent*, denoted hereafter by the symbol k. This quantity appears in many modern tabulations of thermodynamic properties. Despite Iberall's work, the use of γ^0 or γ as the exponent n in equation (7) for real fluids has persisted.

Iberall recognized that the polytrope equation is only an approximation and suggested an effective value of n, namely, $\bar{n}$ where:

$$\bar{n} = \frac{1}{\ln(V_1/V_0)} \int_{V_0}^{V_1} \left(\frac{n}{V}\right) dV = -\frac{\ln(P_1/P_0)}{\ln(V_1/V_0)} \tag{12}$$

Edmister [15] and others have used equation [12] as part of a numerical technique for determing the sonic state in isentropic flow from tabulated thermodynamic properties. Thompson and Sullivan [50] evaluated several definitions for the effective value of n and concluded that $\bar{n}$ defined by equation (12) accurately predicts the sonic flow velocity.

Arnberg [1], in an excellent review paper on critical flow meters, recognized the importance of real-gas effects. He suggested (without verification) five methods for determining an effective value of the polytropic exponent n in evaluating the real-gas, critical flow function ϕ_* deduced from the polytrope model:

$$\phi_* = \frac{\rho_* u_* \sqrt{RT_0}}{P_0} = \sqrt{\frac{n}{Z}\left(\frac{2}{n+1}\right)^{\frac{n+1}{n-1}}} \tag{13}$$

Equation (13) is equivalent to equation (6) for $K=1$ and $Z=1$. Pate [28] seized on Arnberg's suggestions, evaluated four methods, and compared his results to Randall's calculations [29, 30] for real air. The four methods were:

(1) $n=\gamma_0$ $\quad Z=1$

(2) $n=\gamma_0$ $\quad Z=Z_0$

(3) $n=(\gamma_0+\gamma_*)/2=\bar{\gamma}$ $\quad Z=(Z_0+Z_*)/2$

The fourth method incorporated the isentropic exponent k (equation (11)), the compressibility factor Z evaluated at the sonic state, and the arithmetic mean value of the real-gas ratio of specific heats $\bar{\gamma}$:

$$\phi_* = \sqrt{\frac{k_*}{Z_*}\left(\frac{2}{\bar{\gamma}+1}\right)^{\frac{\bar{\gamma}+1}{\bar{\gamma}-1}}} \tag{14}$$

Pate concluded that the method corresponding to $n = \gamma_0$ and $Z = 1$ yields the most accurate results. All Pate's methods used the real-gas ratio of specific heats for the polytropic exponent, which, as Iberall pointed out, does not conform with thermodynamics. In fact, Sullivan and Thompson [42] showed that the use of the ideal-gas ratio of specific heats yields more accurate results in Equation 13 then does the real-gas ratio of specific heats for the critical flow of gaseous methane. Crown [7] obtained similar results for supersonic flow of real air. Reimer [33] made a direct comparison between sonic flow functions calculated with these methods to one calculated using NBS Circular 564 for real air and he found that these methods overpredict the sonic flow function at a temperature of 300 K at pressures to 20 atmospheres.

Edmister [8-10] in 1958 attacked the problem of determining the isentropic exponent for an arbitrary fluid by combining Equations 10 and 11 to yield:

$$\frac{k}{\gamma} = -\frac{V}{P}\frac{\partial P}{\partial V}\Big)_T \tag{15}$$

Since the right side of equation (15) depends only on the thermal state equation describing PVT behavior, Edmister could calculate k/γ for real fluids from the two-parameter corresponding-states correlation of Nelson and Obert. Sherwood [39] followed the same procedure in devising a method for estimating sound speed and also included data for the determination of the real-fluid heat capacities. Edmister [16] later updated his analysis for k/γ by using the three-parameter, corresponding-states correlation based on the Pitzer-Curl acentric factor.[2]

In 1952, Traupel [51] extended the use of the polytrope equation to include an arbitrary real-fluid process. First, he assumed the polytrope equation was valid and that $n = k$ for the isentropic process. He also demonstrated that the compressibility factor Z in nearly a constant long certain isentropes of super-heated steam, $Z = Z(s)$, although Z is not constant along isentropes of other fluids such as freon. Traupel then presented a graphic method for determining polytropic processes (isentropic and nonisentropic) without reevaluating the assumption Z = constant along nonisentropic paths.

Schultz [38] more rigorously extended in 1962 the polytropic model when he defined an arbitrary real-fluid process by:

$$\eta = V\frac{dP}{dh} \tag{16}$$

where h is enthalpy and η is a constant quantity along the polytrope. For adiabatic compression with losses, η is the polytropic efficiency. The thermodynamic coordinates along the polytrope were assumed to obey equations (7) and (8). Schultz used the end states of the process to define effective values of n and m, as did Iberall:

$$\bar{n} = -\frac{\ln(P/P_0)}{\ln(V/V_0)} \text{ and } \bar{m} = \frac{\ln(T/T_0)}{\ln(P/P_0)} \tag{17}$$

As an alternate method, Schultz presented equations for m and n which are functions of X, Y, and Z where:

$$X = \frac{T}{V}\left(\frac{dV}{dT}\right)_P - 1$$

$$Y = \frac{P}{V}\left(\frac{dV}{dP}\right)_T \tag{18}$$

and Z is the compressibility factor. Note that X is proportional to the Joule-Thomson coefficient. For the isentropic process, Y is equal to $-\gamma/k$ (from equation (15)). Schultz determined the thermodynamic state functions X and Y from the Nelson and Obert corresponding-states correlation for Z and investigated four special cases of the polytropic process: isentropic, isenthalpic, isochoric, and isobaric.

A final example of the polytrope model applied to real-fluid, isentropic flow is Steltz's analysis published in 1961 [40]. He investigated the choked flow of single-phase and two-phase steam using two analyses. First, he used the classical polytrope model in which the polytropic exponent is assumed

[2] See Reid, Prausnitz, and Sherwood [32] for an explanation of the Pitzer-Curl acentric factor and the corresponding-states principle.

equal to the isentropic exponent. Second, Steltz included the first-order variation in the isentropic exponent along the isentrope by deriving flow equations which included terms containing the derivative $\partial k/\partial P)_s$. This approach was a significant departure from the use of mean or effective values of n.

The Ideal-Gas Isentrope. The ideal isochoric heat capacity c_v^0 has a constant value of 1.5R for monatomic gases but is temperature-dependent for polyatomic molecules. Hence, for the general case:

$$\gamma^0(T) = \frac{c_p^0}{c_v^0} = 1 + R/c_v^0(T) \tag{19}$$

The perfect-gas isentrope equation (3) is no longer applicable since the ratio of specific heats is now a variable. One means of avoiding a variable γ^0 is to assume an appropriate mean value for γ^0 as constant.

Walker [52-55] developed an alternate approach. Assuming $PV = RT$ and a linear variation of the ideal heat capacities, $c_v^0 = B + ST$ and $c_p^0 = A + ST$ where A, B and S are constants, he derived the following equation for the isentrope:

$$PV^m \exp(\lambda T) = A \tag{20}$$

where $m = A/B$ and $\lambda = S/B$. Walker [53] also obtained the solution for the isentrope by assuming a quadratic equation for c_v^0, and deduced the corresponding isentropic flow equations. In 1924, he extended his work to include the effect of variable ideal that capacities on the sonic pressure ratio P_*/P_0.

The Callendar and van der Waals Isentropes. The development of the steam turbine near the turn of the century inspired Callendar to formulate a new isentrope model which approximates the real-gas behavior of superheated steam. Callendar [3, 4] used a modified version of the van der Waals and Rankine thermal state equations to deduce analytically the isentrope equations:

$$P(V-b)^{\gamma^0} = A \text{ and } P/T^{\left(\frac{\gamma^0}{\gamma^0-1}\right)} = B \tag{21}$$

where A and B are functions of entropy, $\gamma^0 = 1 + R/c_v^0$, and b is the van der Waals "covolume" term which accounts for the finite volume of molecules. Callendar [5] and Martin [26] used this isentrope equation in analyzing experimental data for steam flowing through nozzles to demonstrate that metastable-vapor states were attained. More recently, Bixler, et al. [2] used equation (21) to approximate thermodynamic properties of hydrogen.

The van der Waals thermal state equation:

$$P = \frac{RT}{V-b} - \frac{a}{V^2} \tag{22}$$

where a and b are constants, yields the isentropic equation for constant specific heats:

$$\left(P + \frac{a}{V^2}\right)(V-b)^{\gamma^0} = A \tag{23}$$

which is more complex than the Callendar equation. The first known derivation of equation (23) is by Thompson and Lambrakis [47] although it seems probable that earlier derivation may exist. Although both equations have a theoretical basis, they have not been used as extensively as the polytrope equation since they do not yield simple, closed-form solutions for isentropic flow properties such as mass flux and the sonic pressure ratio.

The Raleigh Adiabat

The general Adiabatic Equation. In seeking a solution for an acoustic wave of finite amplitude which exhibits invariance with time, Raleigh [31] in 1910 concluded that "the most general relationship between P and ρ consistent with the requirements is

$$P = A + B\rho^{\gamma} \tag{24}$$

where A, B, γ are constants. The relation may be regarded as a kind of generalized adiabatic law: it includes the special law under which a velocity curve is absolutely permanent in type." The permanence behavior refers to a compression wave which does not steepen into a shock wave. Although Rayleigh's general adiabatic equation has essentially gone unnoticed, the same equation has evolved via a completely separate path.

Tait-Kirkwood Equation. In 1889, Tait [43] formulated the following empirical equation to represent the compressibility of sea water:

$$\frac{V_0 - V}{V_0 P} = \frac{A}{B+P} \tag{25}$$

where V_0 is the specific volume of the liquid at zero pressure and A and B are functions of temperature. Tamann [45] and others have interpreted equation (25) as a differential equation and integrated it. For example, Tamann deduced:

$$V - V_0 = A \ln[B/(B+P)]$$

which, however, is less accurate than equation (25) in representing experimental data.

In the early 1940's, Kirkwood and co-workers [23-25] modified the Tait equation by assuming that A and B are functions of entropy rather than temperature, thereby improving the equation's accuracy, especially at high pressures. They deduced the isentrope equation to be:

$$(P+B)V^n = A \tag{26}$$

Note that equations (24) and (26) are identical with the interchange of the constants A and B. Equation (26) is known today as the Tait equation. Kirkwood and co-workers used this equation in a numerical solution for the propagation of shock waves through sea water due to underwater explosions. Richardson, Arons, and Halverson [35], co-workers of Kirkwood, determined that $n \sim 7.15$ and $B \sim 3$ kbar for sea water; then they compared equation (26) with experimental data for pressures up to 11 kbar with good results.[3]

Since the compressibility of liquids is small, values of the functions A and B must have the same sign and be relatively large compared to P and V. The sound speed for the Tait-Kirkwood fluid is:

$$c^2 = An\rho^{n-1} = n(P+B)V$$

which shows that A and B are also positive for liquids.

Constant-Γ Equations. Thompson and Arena [46] noted that the Rayleigh adiabatic or Tait fluid is one example of a constant-Γ fluid where Γ is an isentrope nonlinearity parameter related to the curvature of the isentrope in the PV plane.

$$\Gamma = -\frac{V^3}{2c^2}\frac{\partial^2 P}{\partial V^2}\Big)_s$$

From equation (26),

$$\Gamma = \frac{n+1}{2} \tag{27}$$

Recognizing that equation (26) reduces to the Laplace-Poisson equation with the substitution of $B = 0$ and $n = \gamma^0$, they suggested the application of equation (26) to both gases and liquids. Going one step further, they deduced the

[3] One can find additional historical notes on this model in Rowlinson [36] and Hirschfelder, Curtis, and Bird [19].

Table 3 Summary of isentrope models

One-parameter model	Laplace-Poisson or polytrope		
	$PV^n = A$		
Two-parameter models	Callendar isentrope	Rayleigh adiabat	Walker isentrope
	$P(V-b)^n = A$	$(P+B)V^n = A$	$PV^m \exp(\lambda T) = A$
Three-parameter models	van der Waals isentrope	???	
	$\left(P + \frac{a}{V^2}\right)(V-b)^n = A$		

Table 4 Comparison of isentropic models

Isentrope equation	Soundspeed	Isentropic exponent	Isentrope nonlinearity
Laplace-Poisson $PV^{\gamma^0} = A$	$c^2 = \gamma^0 PV$	$k = \gamma^0$	$\Gamma = \frac{(\gamma^0+1)}{2} + \frac{(\gamma^0-1)}{2\gamma^0} T \frac{d\gamma^0}{dT}$
Polytrope $PV^n = A$	$c^2 = nPV$	$k = n$	$\Gamma = \frac{n+1}{2} + \frac{n-1}{2n} T \frac{dn}{dT}$
Callendar $P(V-b)^{\gamma^0} = A$	$c^2 = \frac{\gamma^0 PV^2}{V-b}$	$k = \frac{\gamma^0 V}{V-b}$	$\Gamma = \frac{\gamma^0+1}{2} + \frac{\gamma^0-1}{2\gamma^0} \frac{PV}{R} \frac{d\gamma^0}{dT}$
Rayleigh $(P+B)V^n = A$	$c^2 = n(P+B)V$	$k = \frac{n(P+B)}{P}$	$\Gamma = \frac{n+1}{2}$
van der Waals $(P+a/V^2)(V-b)^{\gamma^0} = A$	$c^2 = \frac{\gamma^0 V^2}{V-b}\left(P + \frac{a}{V^2}\right) - \frac{2a}{V}$	$k = \frac{\gamma^0 V}{V-b}\left(1 + \frac{a}{PV^2}\right) - \frac{2a}{PV^2}$	

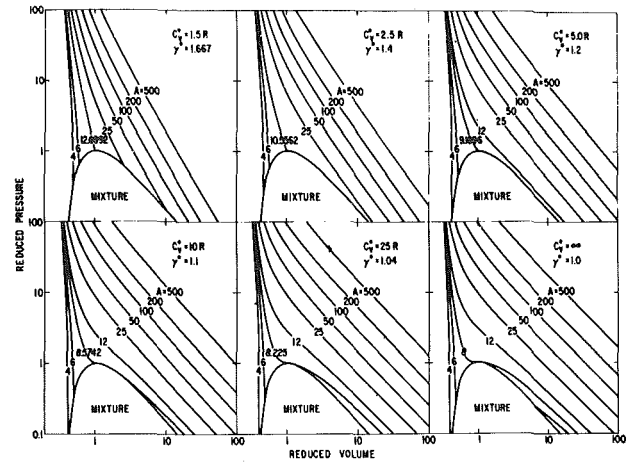

Fig. 4 Isentropes of the van der Waals fluid for various values of (constant) specific heat capacity

corresponding compressible, isentropic flow formulas which they called the constant-Γ equations. Instead of the conventional static-to-total pressure ratio P/P_0, they expressed pressure via a nondimensional pressure difference Δ:

$$\Delta = \frac{P_0 - P}{\rho_0 c_0^2}$$

which was a convenient mathematical step to eliminate the constant B in equation (26). Defining the dimensionless mass flux as:

$$J = \frac{\rho u}{\rho_0 c_0}$$

and integrating Euler's equation, they deduced:

$$J^2 = \frac{1}{\Gamma - 1}\left\{[1-(2\Gamma-1)]^{-\frac{2\Gamma-2}{2\Gamma-1}} - 1\right\}[1-(2\Gamma-1)\Delta]^{\frac{2}{2\Gamma-1}}$$

which has a maximum (sonic state) value of:

$$J_* = \Gamma^{-\frac{\Gamma}{2\Gamma-2}} \tag{28}$$

at

$$\Delta_* = \frac{1}{2\Gamma-1}\left[1-\Gamma^{-\frac{2\Gamma-1}{2\Gamma-2}}\right] \tag{29}$$

One can recast the constant-Γ equations into a form more closely resembling the familiar perfect-gas flow equations by utilizing the definitions of k, J, and Δ, which yield the identities:

$$\phi\sqrt{Z_0} = \sqrt{k_0} J$$

and

$$1 - \frac{P}{P_0} = k_0 \Delta$$

where k_0 is the isentropic exponent evaluated at the stagnation conditions. Equations (28) and (29) can now be rewritten as:

$$\phi_* = \sqrt{\frac{k_0}{Z_0}\left(\frac{2}{n+1}\right)^{\frac{n+1}{n-1}}} \tag{30}$$

and:

$$\frac{P_*}{P_0} = 1 - \frac{k_0}{n}\left[1 - \left(\frac{2}{n+1}\right)^{\frac{n}{n-1}}\right] \tag{31}$$

The appearance of both k_0 and n in place of γ^0 is reminiscent of Pate's fourth method, Equation 14. However, one must notice the equations (30) and (31) have been deduced directly from an isentrope model as opposed to Pate's unsupported assumptions. Assuming that $k_0 = n$ is equivalent to setting $B = 0$ in the Rayleigh equation which reduces it to the polytrope model, equation (7). Similarly, equation (31) reduces to:

$$\frac{P_*}{P_0} = \left(\frac{2}{n+1}\right)^{\frac{n}{n-1}} \tag{32}$$

Comparison of Isentrope Models. Table 3 summarizes the various isentrope models discussed in the previous sections. Since the Walker isentrope equation deals only with the variable heat capacity effect, it is excluded from further consideration. Each of the remaining models are "exact" solutions to some combinations of thermal and caloric state equations with, perhaps, the exception of the polytrope model since the polytropic exponent is empirically determined and not traceable to a particular state equation other than the perfect-gas model in specific cases. Table 4 summarizes the properties pertinent to the analysis of isentropic flow.

The van der Waals isentrope equation is a three-parameter model which, in corresponding-state reduced form, is:

$$\left(P_r + \frac{3}{V_r^2}\right)(3V_r - 1)^{\gamma^0} = A \tag{33}$$

Isentropes of the vdW fluid depend on the ideal heat capacities as shown by equation (33) and in Fig. 4. As the ideal-heat capacity increases, the isentropes tend toward isotherms and the two are equivalent in the limit of infinite c_v^0. Thus, the "real-gas effect" due to variable Z is more pronounced for high-c_v^0 fluids, particularly at reduced temperatures and near the critical point.

Both the Callendar and Rayleigh isentrope equations are two-parameters models which one can crudely interpret as approximations of the van der Waals models. The term $3/V_r^2$ in equation (33) accounts for the attractive force between molecules at small specific volumes as in the liquid state. If one assumes that this term can be neglected in the gaseous region, the *vdW* isentrope equation reduces to the Callendar equation. In the liquid phase, the intermolecular forces dominate and, since specific volume changes tend to be smaller than pressure changes, the term $3/V_r^2$ can be approximated as a constant, say as B in Rayleigh model.

It is important to remember that the isentropic exponent k is proportional to the local sound speed or slope of the isentrope. A constant value of k along the isentrope characterizes the Laplace-Poisson and polytrope models and such isentropes would be linear in the logarithmic coordinates of Fig. 4. A monotonic variation in k characterizes the Callendar and Rayleigh isentropic models; for example, an isentrope which curves upward in Fig. 4 corresponds to an increasing value of k for increasing pressure, i.e., $\partial k/\partial P)_s > 0$.

In Fig. 5 the ratio k/γ^0 for selected *vdW* isentropes is shown as a function of pressure. One can see that k increases and decreases in both the gaseous and liquid phases. Since the computation of k is a severe test of accuracy for any thermal equation of state, it is reasonable to question results deduced from the *vdW* equation. Figure 6 shows the variation of k along isentropes calculated by Talcott [44] using an extended Martin-Hou equation for perfluoromethane in the gaseous phase. The isentrope $s/R = 24$ intersects the saturated vapor boundary near the critical point. One sees the same qualitative behavior of k in Fig. 6 as in Fig. 5. From these figures, one can conclude that neither the Callendar nor Rayleigh model can describe adequately all real-fluid isentropes over a wide

range of pressures, particularly those with a local minimum in k. Yet, as a general rule, both models will yield results more accurate than the polytrope model for which k is a constant.

The utility of the simple isentrope equation depends on its ability to model accurately the real-fluid isentrope and to yield simple, analytical equations for the various flow properties. From this viewpoint, each model is a "curve-fit" expression and the model with more adjustable parameters will yield, in general, the most accurate results. Of the models considered, only two yield simple, closed-form equations for isentrope flow: the polytrope and Rayleigh models. Since both models yield equations similar to and, in most cases, identical with the form of perfect-gas flow equations, they are particularly attractive. Table 5 gives the isentropic flow equations corresponding to the Rayleigh model.

Sonic Flow Predictions. For the polytrope model, the sonic flow properties $\phi_* \sqrt{Z_0}$ and P_*/P_0 are functions of the polytropic exponent n from equations (13) and (32) where n is an effective value of the isentropic exponent. For the Rayleigh model $J_* = \phi_* \sqrt{Z_0/k_0}$ and $\Delta_* = (1 - P_*/P_0)/k_0$ are functions of n from equations (27), (28) and (29) where n is an effective value of $2\Gamma - 1$. Note that some value of n exists for each model which will predict exactly the sonic mass flux (or sonic pressure ratio). That is, one can use equation (13) or (30) to define the respective effective values of n. In flow metering applications, one often uses the sonic pressure ratio to determine whether choked flow has been achieved. Therefore, it is appropriate to determine if a single value of n for each model can accurately predict not only the sonic mass flux but other sonic state properties as well.

Numerical data representing "exact" solutions to the sonic flow problem have been calculated using several modified versions of the Benedict-Webb-Rubin thermal state equation with variable heat capacities. The sonic flow of Ar, Ne, N_2, O_2, CO, CO_2, and CH_4 have been calculated using the Bender and Strobridge state equations, the coefficients of which are

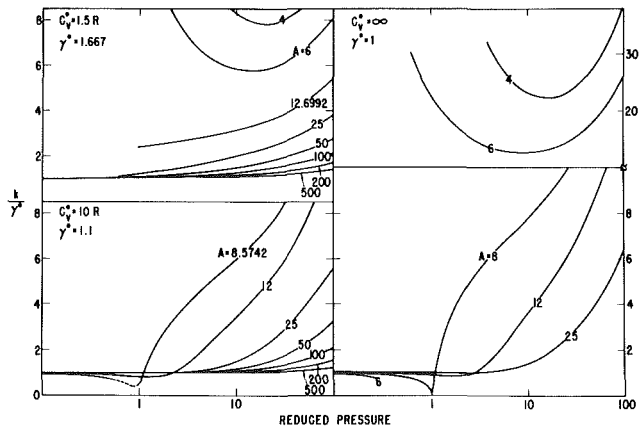

Fig. 5 The variation of the ratio k/γ^0 along isentropes of the van der Waals fluid with constant specific heat capacity

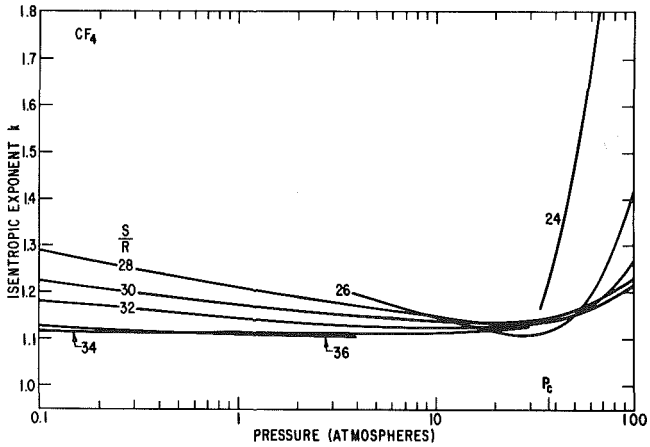

Fig. 6 The variation of the isentropic exponent along isentropes of perfluoromethane CF_4. Data taken from Talcott [44].

Table 5 The Rayleigh isentropic flow equations

	$f(M)$	$f\left(\frac{\rho}{\rho_0}\right)$	$f(\Delta)$
$\left(\frac{\rho}{\rho_0}\right)$	$\left(1+\frac{n-1}{2}M^2\right)^{\frac{-1}{n-1}}$	—	$(1-n\Delta)^{1/n}$
Δ	$\frac{1}{n}\left[1-\left(1+\frac{n-1}{2}M^2\right)^{\frac{-n}{n-1}}\right]$	$\frac{1}{n}\left[1-\left(\frac{\rho}{\rho_0}\right)^n\right]$	—
$\frac{P}{P_0}$	$1-\frac{k_0}{n}\left[1-\left(1+\frac{n-1}{2}M^2\right)^{\frac{-n}{n-1}}\right]$	$1-\frac{k_0}{n}\left[1-\left(\frac{\rho}{\rho_0}\right)^n\right]$	$1-k_0\Delta$
$\left(\frac{c}{c_0}\right)^2$	$\left(1+\frac{n-1}{2}M^2\right)^{-1}$	$\left(\frac{\rho}{\rho_0}\right)^{n-1}$	$(1-n\Delta)^{\frac{n-1}{n}}$
$\left(\frac{u}{c_0}\right)^2$	$M^2\left(1+\frac{n-1}{2}M^2\right)^{-1}$	$\frac{2}{n-1}\left[1-\left(\frac{\rho}{\rho_0}\right)^{n-1}\right]$	$\frac{2}{n-1}\left[1-(1-n\Delta)^{\frac{n-1}{n}}\right]$
J^2	$M^2\left(1+\frac{n-1}{2}M^2\right)^{-\left(\frac{n+1}{n-1}\right)}$	$\frac{2}{n-1}\left(\frac{\rho}{\rho_0}\right)^2\left[1-\left(\frac{\rho}{\rho_0}\right)^{n-1}\right]$	$\frac{2}{n-1}(1-n\Delta)^{\frac{2}{n}}\left[1-(1-n\Delta)^{\frac{n-1}{n}}\right]$

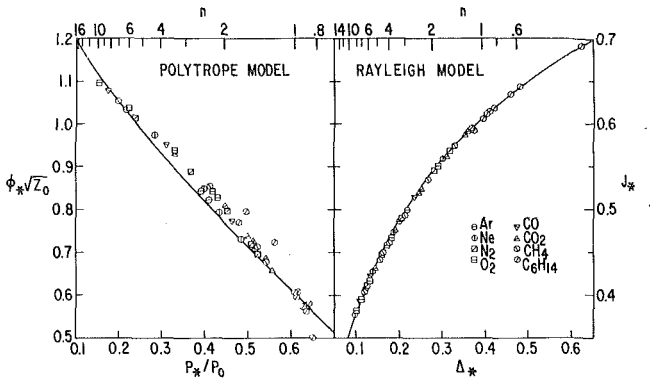

Fig. 7 A comparison of calculated sonic-state mass flux and pressure data against $\phi_*\sqrt{Z_0}$ and P_*/P_0 for the polytrope model and against J_* and Δ_* for the Rayleigh model. The solid curves represent the corresponding model predictions.

given in GASP [18]. Data for C_6H_{16} was calculated using the BWR44 equation developed by Yamada [57]. Reduced stagnation temperatures ranged from $T_r = 1.0$ to 1.6 for C_6H_{16} and from $T_r = 1.3$ to 2.5 for all other fluids, at reduced stagnation pressures up to $P_r = 10$. In Fig. 7 the same data are plotted in coordinates of $\phi_*\sqrt{Z_0}$ versus P_*/P_0 and J_* versus Δ_*. The solid curves correspond to the polytrope and Rayleigh models for values of n indicated at the top of the figure. Near ideal-gas states correspond to values of n between 1.05 (hexane) and 5/3 (argon), whereas values of n greater than roughly 5 correspond to liquid behavior. Figure 7 illustrates the Rayleigh model's superiority. One can explain this result by the additional parameter B in the Rayleigh isentrope equation, or, equivalently, by the addition of the isentropic exponent k_0 as a normalization parameter for mass flux and pressure.

It is important to note that the correlation of computed data points in Fig. 7 does not depend on any specific isentrope model but merely on the coordinates of the figure since these data are "exact" solutions to the sonic flow problem. Therefore, Fig. 7 represents an expression of two forms of a more general Similarity Principle introduced first in 1977 by Thompson and Sullivan [48] and developed further in a subsequent paper [49]. The principle can be stated as follows: The nondimensional flow properties are determined approximately by one independent flow parameter such as the Mach number and a single thermodynamic parameter; in these two cases, the polytropic and Rayleigh exponents. The degree of accuracy of the Similarity Principle depends only on the definitions of the nondimensional parameters.

The forms of the Similiarity Principle demonstrated in Fig. 7 are approximate since neither the polytropic nor the Rayleigh exponents are constant along the isentropes. However, the variation in the Rayleigh exponent along a given isentrope is typically an order of magnitude less than that of the isentropic or polytropic exponent; hence, the improved correlation. Even so, a single value of the Rayleigh exponent does not exist which will predict exactly all flow properties. Therefore, one is forced to seek appropriate effective values of the Rayleigh exponent. Thompson and Sullivan [48-50] have investigated a number of alternatives and have found that an effective value of n determined from the sonic-to-stagnation sound speed ratio, $c_*/c_0 = u_*/c_0$, which they designated $\bar{n}$, predicts adequately all the sonic flow properties. The "optimum" value of n must necessarily depend on the application and on the desired flow properties. For example, an appropriate definition of an effective Rayleigh exponent for subsonic flow metering applications where the mass flux versus pressure differential is of the utmost concern, would probably differ from $\bar{n}$, although numerical values would differ only slightly. This matter is the subject of continuing research.

Conclusions

1. Knowledge of the isentrope equation $P(V)$ is sufficient to determine most isentropic flow properties of interest, except temperature.
2. Five simple "engineering" models for the isentrope equation have been developed over the past 80 years, only two of which yield simple, closed-form isentropic flow equations; namely, the polytrope and Rayleigh equations.
3. A comparison of the polytrope and Rayleigh equations reveals that the latter is significantly more accurate with only a slight increase in the complexity of the flow equations.
4. The Rayleigh model can be expected to yield credible predictions for isentropic flow in both the gaseous and compressed liquid phases.

Acknowledgments

The present work is an outgrowth of research conducted by the author while at the Max-Planck-Institut für Strömungsforschung in Göttingen, West Germany. The author is grateful for the support and encouragement of Professor P.A. Thompson, Prof. E.A. Muller and Dr. G.E.A. Meier, and of the Max-Planck-Gesellschaft.

APPENDIX

This review has dealt exclusively with the isentrope equation $P(V)$ for specific reasons stated in the text. However, an alternate form $T(V)$ has been used to describe the adiabatic expansion of detonation product gases and nonisentropic flow processes. The model, which is analogous to the polytrope, utilizes the Gruneisen parameter G, defined as

$$G = -\frac{V}{T}\frac{\partial T}{\partial V}\Big)_s$$

Two references for the Gruneisen parameter are given below [59, 60].

References

1 Arnberg, B.T., "Review of Critical Flow Meters for Gas Flow Measurements," ASME *Journal of Basic Engineering*, Vol. 84, 1962, pp. 447-460.

2 Bixler, D.N., Piacesi, R., and Seigel, A.E., "Calculated Thermodynamic Properties of Real Hydrogen up to 30,000 Atmospheres and 3500 K," NOLTR 65-209, Ballistics Research Report 153, 1965, U.S. Naval Ordnance Laboratory, White Oak, Md.

3 Callendar, H.L., "On the Thermodynamical Properties of Gases and Vapors as Deduced from a Modified Form of the Joule-Thomson Equation, with Special Reference to the Properties of Steam," *Proceedings of the Royal Society*, Vol. A67, 1900, pp. 266-286.

5 Callendar, H.L., "Steady Flow of Steam Through a Nozzle or Throttle," *Proceedings of the Institution of Mechanical Engineers*, 1915, pp. 53-77.

6 Cardwell, D.S.L., *From Watt to Clausius: The Rise of Thermodynamics in the Early Industrial Age*, Cornell University Press, 1971.

7 Crown, J.C., "Flow of a Beattie-Bridgeman Gas with Variable Specific Heats," NAVORD Report 2148, 1951.

8 Edmister, W.C., "Applied Hydrocarbon Thermodynamics: Part 7 - Isentropic Exponents for Gases," *Petroleum Refiner*, Vol. 37, No. 7, 1958a, pp. 153-162.

9 ——, "Applied Hydrocarbon Thermodynamics: Part 8 - Polytropic Compression and Expansion," *Petroleum Refiner*, Vol. 37, No. 8, 1958b, pp. 113-122.

10 ——, "Applied Hydrocarbon Thermodynamics: Part 9 - Generalized Exponents from Entropy Balances," *Petroleum Refiner*, Vol. 37, No. 10, 1958c, pp. 111-122.

11 ——, "Applied Hydrocarbon Thermodynamics: Part 10A - Charts for Making Compressor Calculations," *Petroleum Refiner*, Vol. 38, No. 4, 1959a, pp. 161-167.

12 ——, "Applied Hydrocarbon Thermodynamics: Part 10B - Charts for Making Compressor Calculations," *Petroleum Refiner*, Vol. 38, No. 5, 1959b, pp. 195-202.

13 ——, "Applied Hydrocarbon Thermodynamics: Part II - Flow Calculations for Gases and Gas-Liquid Mixtures," *Petroleum Refiner*, Vol. 38, No. 7, 1959c, pp. 161-168.

14 ——, *Applied Hydrocarbon Thermodynamics,* 2 vols. Gulf Publishing Co., Houston, Texas, 1961.

15 ——, Discussion of Murdock and Bauman, *Journal of Basic Engineering,* Vol. 86D, No., 3, 1964, p. 517.

16 ——, "Applied Hydrocarbon Thermodynamics: Part 30 - Isentropic Exponents and Critical-Flow Metering, *Hydrocarbon Processings,* Vol. 46, No. 7, 1967, pp. 139–143.

17 ——, "Applied Hydrocarbon Thermodynamics: Part 35 - Istentropic Exponents from the Redlich-Kwong Equation of State," *Hydrocarbon Processing,* Vol. 47, No. 12, 1968, pp. 123–126.

18 Hendricks, R.C., Baron, A.K., and Peller, I.C., "GASP - A Computer Code for Calculating the Thermodynamic and Transport Properties for Ten Fluids: Parahydrogen, Helium, Neon, Methane, Nitrogen, Carbon Monoxide, Oxygen, Fluorine, Argon and Carbon Dioxide," NASA TD D-7808, 1975.

19 Hirschfelder, J.O., Curtiss, C.F., and Bird, R.B., *Molecular Theory of Gases and Liquids,* Wiley, New York, 1954, p. 261.

20 Iberall, A.S, "The Effective Gamma for Isentropic Expansions of Real Gases," *Journal of Applied Pysics,* Vol. 19, 1948, pp. 997–999.

21 Johnson, R.C., "Tables of Critical-Flow Functions and Thermodynamic Properties for Methane and Computational Procedures for Both Methane and Natural Gas," NASA SP-3074, 1972.

22 Joule, J.P., and Thomson, W., "On the Thermal Effects of Fluids in Motion," *Proceedings of the Royal Society,* Vol. 8, 1856, pp. 178–185.

23 Kirkwood, J.G., and Bethe, H., "The Pressure Wave Produced by an Underwater Explosion, Part I," OSRD Report 588 (PB32182), 1942.

24 Kirkwood, J.G., and Montrell, E., "The Pressure Wave Produced by an Underwater Explosion, Part II," OSRD Report 676 (PB32183), 1942.

25 Kirkwood, J.G., and Richardson, J.M., "The Pressure Wave Produced by an Underwater Explosion, Part III," OSRD Report 813 (PB32184), 1942.

26 Martin, H.M., "A New Theory of the Steam Turbine," *Engineering,* Vol. 106, 1918, pp. 1–3, 53–55, 107–108, errata p. 246.

27 Napier, R.D., "The Flow of Fluids Under Pressure," *Engineer,* Vol. 23, 1867.

28 Pate, S.R., "Errors in Sonic Nozzle Mass Flow Measurements at High Supply Pressures and Moderate Temperatures Due to Real Gas Effects," ASME 68-WA/FM-6, 1968.

29 Randall, R.E., "Thermodynamic Properties of Air: Tables and Graphs Derived from the Beattie-Bridgeman Equation of State Assuming Variable Specific Heats," AEDC TR 57-8 AD 135 331), 1957a.

30 Randall, R.E., "Thermodynamic Properties of Gases: Equations Derived from the Beattie-Bridgeman Equation of State Assuming Variable Specific Heats," AEDC TR 57-10 (AD 135 332), 1957b.

31 Rayleigh, Lord, "Aerial Plane Waves of Finite Amplitude," *Proceedings of the Royal Society,* Vol. A84, 1910, pp. 247–284.

32 Reid, R.C., Prausnitz, J.M., and Sherwood, T.K., *The Properties of Gases and Liquids,* 3rd ed., McGraw-Hill Book Co., New York, 1977.

33 Reimer, R.M., "Computation of the Critical Flow Function, Pressure Ratio and Temperature Ratio for Real Air," ASME *Journal of Basic Engineering,* Vol. 86, 1964, pp. 169–174.

34 Reynolds, O., "On the Flow of Gases," *Philosophical Magazine,* Series 5, Vol. 21, No. 130, 1886, pp. 185–199.

35 Richardson, J.M., Arons, A.B., and Halverson, R.R., "Hydrodynamic Properties of Sea Water at the Front of a Shock Wave," *Journal of Chemical Physics,* Vol. 15, No. 11, 1947, pp. 785–794.

36 Rowlinson, J.S., *Liquids and Liquid Mixtures,* 2nd ed., Plenum Press, New York, 1969, p. 28.

37 Saint-Venant, B., and Wantzel, L., "Memorie et experiences sur l'ecoulement de l'air, *Journal of l'Ecole Polytechnique,* Vol. 27, 1839, pp. 87–122.

38 Schultz, J.M., "The Polytropic Analysis of Centrifugal Compressors," ASME *Journal of Engineering for Power,* Vol. 84, 1962, pp. 69–82, errata p. 222.

39 Sherwood, T.K., "Velocity of Sound in Compressed Gases," *Journal of Chemical Engineering Data,* Vol. 7, No. 1, 1962, pp. 47–50.

40 Steltz, WG, "The Critical and Two-Phase Flow of Steam," ASME *Journal of Engineering for Power,* Vol. 83, No. 2, 1961, pp. 145–154.

41 Sullivan, D.A., "Annotated Bibliography on Real-Fluid Flow," General Electric TIS 78CRD264.

42 Sullivan, D.A., and Thompson, P.A., "Some General Numerical Techniques for Real-Gas Thermodynamic Calculations with Application to Isentropic Flow," Max-Planck-Institut fuer Stroemungsforschung Bericht 116/1976.

43 Tait, P.G., *The Voyage of H.M.S. Challenger,* Vol. 2, Part 2, Part 4, His Majesty's Stationary Office, London, 1888, pp. 1–73.

44 Talcott, N.A. Jr., "Thermodynamic Properties of Gaseous Fluorocarbons and Isentropic Equilibrium Expansions of Two Binary Mixtures of Fluorocarbons and Argon," NASA TN D-8405, 1977, errata issued November 1978.

45 Tamann, G., *Journal of Physical Chemistry,* Vol. 17, 1895, p. 620.

46 Thompson, P.A., and Arena, C.C., "Prediction of the Critical Mass Flux and Related Problems in the Flow of Real Gases," ASME Preprint 75-FE-12, 1975.

47 Thompson, P.A., and Lambrakis, K.C., "Negative Shock Waves," *Journal of Fluid Mechanics,* Vol. 60, 1973, pp. 187–208.

48 Thompson, P.A., and Sullivan, D.A., "Simple Predictions for the Sonic Conditions in a Real Gas," ASME JOURNAL OF FLUIDS ENGINEERING, Vol. 99, 1977, pp. 217–227.

49 Thompson, P.A. and Sullivan, D.A., "Similarity Principle for the Elementary Gas Dynamics of Real-Fluids," PHYSICS OF FLUIDS, Vol. 20, 1977, pp. 1064–1071.

50 Thompson, P.A. and Sullivan, D.A., "Exact and Approximate Equations for Real-Fluid Isentropic Flow," ASME JOURNAL OF FLUIDS ENGINEERING, Vol. 100, No. 4, 1978, pp. 413–418.

51 Traupel, W., *Zur dynamik realer Gase. Forsch. auf dem Gebiete des Ingen.-wesen,* Vol. 18, No. 1, 1952, pp. 3–9.

52 Walker, W.J., "Thermodynamic Cycles with Variable Specific Heat of Working Substances," *Philosophical Magazine,* Vol. 34, 1917, pp. 168–174.

53 Walker, W.J., "The Effect of Variable Specific Heats on the Discharge of Gases Through Orifices and Nozzles," *Philosophical Magazine,* Vol. 43, No. 6, 1922, pp. 589–592.

54 Walker, W.J., "The Critical Pressure Ratio for Gases as Affected by Variable Specific Heats," *Philosophical Magazine,* Vol. 48, No. 286, 1924, 703–707.

55 Walker, W.J., "Specific Heat Variation in Relation to the Dynamic Action of Gases and Their Equations of State," *Philosophical Magazine,* Vol. 50, No. 300, 1925, pp. 1244–1260.

56 Weisbach, J., *Der Civilingenieur,* 1856.

57 Yamada, T., "An Improved Generalized Equation of State," *Association of Industrial Chemical Engineers Journal,* Vol. 19, No. 2, 1973, pp. 286–291.

58 Zeuner, G.A. "Resultate experimentaller Untersuchungen ueber das Ausstroemen der Luft dei starkem Ueberdruck," *Der Civilingenieur,* Vol. 20, 1874, pp. 1–14.

59 Arp, V., "Thermodynamics of Single-Phase, One-Dimensional Fluid Flow," *Cryogenics,* Vol. 15, 1975, pp. 285–289.

60 Lee, E.L., and Hornig, H.C., "Equation of State of Detonation Product Gases," 12th Symp. (Int.) on Combustion, 1969, pp. 493–499.

Sen-sen Pan
Research Engineer.

Zhan-ming Yang
Research Engineer.

Pei-shuen Hsu
Research Engineer.

China Ship Scientific Research Center,
Wuxi, Jiangsu, China

Cavitation Inception Tests on Axisymmetric Headforms

Six axisymmetric headforms were tested in the 350-mm dia water tunnel at China Ship Scientific Research Center (CSSRC) for observation and measurement of cavitation inception. Among them, three of the flow patterns were displayed and analyzed by holography. Results of the tests show that cavitation inception on the headforms was closely related to the structure of the near-wall flow past the body with different flow regimes corresponding to different features of cavitation inception. By carefully fitting a trip wire of suitable height on a hemispherical headform, it was observed that under conditions of low air content, this artificial means of boundary transition may bring about a significant reduction in cavitation inception number.

Introduction

Great interest has been aroused by Prof. Acosta on the influence of viscosity on cavitation inception, by his paper [1] at the conference on cavitation at Edinburgh, 1974. Since then, there have been many immportant advances. Many workers have reported evidence of the close relationship between cavitation inception and characteristics of the flow past the body. They noted that cavitation inception does not necessarily occur in the vicinity of the lowest mean pressure on the body, but occurs in the region of laminar separated flow or in the region of natural boundary layer transition. Some experimental evidence indicates that measured cavitation numbers correspond to the negative pressure coefficients in the regions of laminar separation and natural transition. In this respect, it is interesting to note the experimental observation conducted by Arakeri and Acosta in 1976 [2]. They artificially instituted supercritical Reynolds number regimes by fitting a trip wire of suitable height on a hemispherical headform, thus obtaining a monotonically decreasing relationship of cavitation inception number with an increase in velocity, and in the extreme case they have reported complete suppression of cavitation at high speeds. This gives strong support of the view that boundary layer characteristics can directly influence cavitation inception.

We are interested in the results of their experiments and would like to find out its range of application. With this in mind and in the hope of establishing further understanding between near-wall flow characteristics and cavitation inception, we designed our present experiment, viz: to vary the air content of the flow and the height of trip wire in a systematic manner, and to observe and measure the relationship between flow characteristics and cavitation inception number for a hemispherical headform with trip wire at water speeds varying from subcritical to supercritical Reynolds numbers. Meanwhile test studies have also been made on two headforms with separated flow characteristics and one headform with natural boundary layer transition.

Contributed by the Fluids Engineering Division for publication in the JOURNAL OF FLUIDS ENGINEERING. Manuscript received by the Fluids Engineering Division, December 13, 1979.

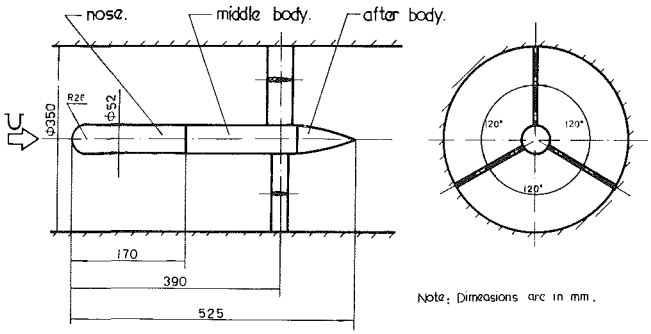

Fig. 1 Schematic representation of model installation

Description of the Experiment

Tests were conducted in the 350mm-dia cavitation tunnel of China Ship Scientific Research Center at Wuxi. Maximum water speed in the test section is 15 m/s with pressure variable continuously from 2 atm down to near vacuum. The speed and pressure are measured by U-shaped mercury manometers. Total air content at atmospheric condition is measured by a Van Slyke apparatus. There is no resorber for this tunnel, and so every observation is made only after running the tunnel at higher pressures for 3-5 minutes to ensure that the oncoming flow upstream of the model is practically free of large air bubbles.

Diameter of the model is 52 mm; it consists of three parts: the nose, the parallel middle body, and the after body, the whole being supported in the working section of the tunnel by 3 struts made of thin wing sections 120 deg apart, as shown in Fig. 1. During the experiment, only the nose is changed. The ratio of the model sectional area to the area of the working section, i.e. the blockage coefficient, is 2.2 percent. The distance between the nose stagnation point of the model and the center-line of the support strut is 7.5 times the diameter of the model. At the nose of the hemispherical headform a brass ring 0.8 mm wide with a rectangular cross-section was embedded to form the trip wire. In order to avoid data scatter

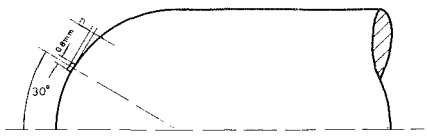

Fig. 2 Trip fitted on hemispherical headform

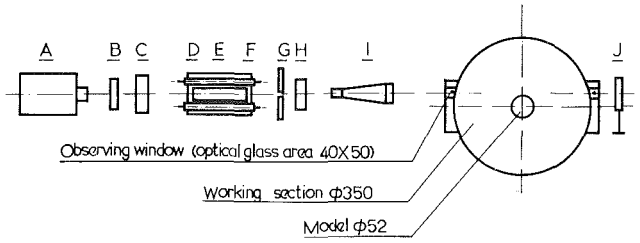

Fig. 3 Schematic drawing of holocamera: *A*-He-Ne gas laser; *B*-dielectric mirror; *C*-Q switch (chlorophyll); *D*-flashlamp; *E*-ruby rod; *F*-convergence set; *G*-light grid; *H*-dielectric mirror; *I*-collimating lens; *J*-plate.

due to machining tolerances, the same hemispherical headform was used for all the tests with the height of the trip ring adjusted to $h = 0.35, 0.25, 0.12$mm, respectively (Fig. 2). The two headforms with intentional flow separation are 45 and 25 deg cones, and the headform with intentional natural boundary layer transition was selected from a standard series due to Schiebe with $-C_{p_{\min}} = 075$ [3]. Model headforms are made of aluminum, meticulously polished and cleaned before the experiment.

The instrumentation set up for the holocamera shown in Fig. 3, was borrowed from Anhwei Sub-Academy of the National Academy of Sciences of China. It consists of a 9-mm dia ruby rod capable of emitting a laser beam of 6943 Å, pulse power ranging from a few to some tens of million watts, using chlorophyll as the Q switch, pulse width $10^{-8} \sim 10^{-9}$. For the purpose of boundary layer flow visualization a 1 percent concentration NaCl solution is injected during the experiment from a 1.2-mm dia hole located at the nose stagnation point of the model, and the holographic information is recorded on a 10E 75 holographic plate by a coaxial light path. The reconstruction and analysis of the holograms are made by using a He-Ne gas laser as the light source.

A stroboscope made by our research Center is used as a light source for observation and photography, the flash power is 2.25 Joules/flash with a pulse width of several tens of microseconds.

All tests were performed at water speeds in the range from 5 m/s to 14 m/s; corresponding Reynolds numbers being 3.37×10^5 - 9.20×10^5. For each test, the water speed was constant, while the pressure of the working section was gradually lowered until cavitation inception occurred when the inception number σ_i was duly recorded.

Analysis of Test Results

1. The Hemispherical Headform With Trip Wire. Figure 4 shows a plot of cavitation inception number (σ_i) with water speed (V) in m/s for tests made on the same hemispherical headform but with trip wire heights of 0.35mm, 0.20mm, and 0.12mm respectively under two different conditions of air content ratio α/α_s. α_s is the saturated air content at atmospheric pressure. The numbers within brackets show the number of repetitions in the measurements and the short vertical strokes indicate the range of scatter in the experimental data.

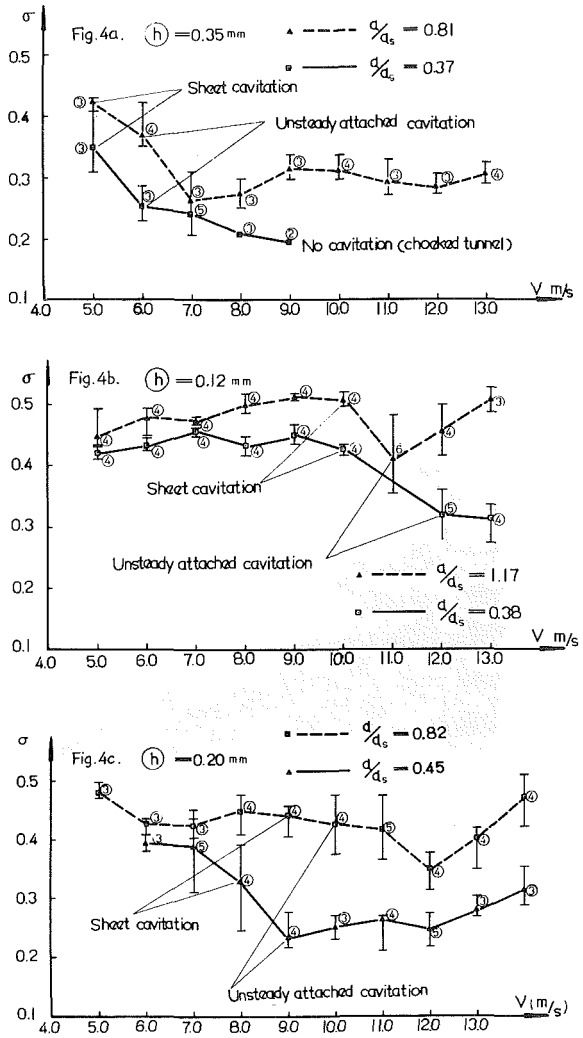

Fig. 4 Variation of hemispherical head with water speed under the condition of various air content

Analysis of cinema pictures taken during cavitation inception has shown that there are two classes of cavitation inception on the hemispherical headforms with trip wire: the first class belongs to a sheet cavitation or in other words a band cavitation, occurring at relatively low water speed, it is characterized by relative stableness and axisymmetry both as regards to shape and location, and cavitation inception is somewhat of an "explosive" occurrence, making its appearance in a sudden manner without any precursive symptoms (see Fig. 5(*a*)). The other class is of a relatively unsteady attached cavitation, occurring at relatively high water speeds, characterized by extreme unsteady or randomness both in regard to location and shape, sometimes flashing in its appearance only once after several seconds; it is generally smooth in appearance and attached to the hemispherical headform as a relatively thick convex sheet or bubble (see Fig. 5(*b*)).

Holographic recording and display were provided for the case of 0.20mm trip height. Two holographic pictures were taken for each water speed, starting from 7 m/s and increasing at 1 m/s intervals, to 11 m/s inclusive. By displaying these pictures, it was found that for speeds under 8 m/s boundary layer separated flow was always detected, whereas no laminar separation could be seen for water speeds above 9 m/s. Then another holographic picture was taken at water speed of 8.5 m/s, yet no laminar separation could be detected. So it was concluded that the critical Reynolds number for

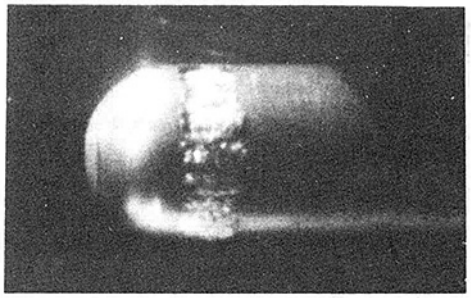

Fig. 5(a) Sheet cavitation

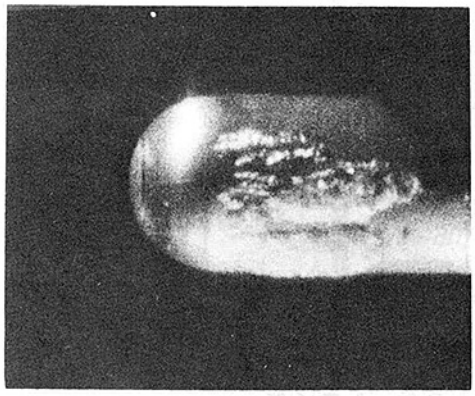

Fig. 5(b) Unstable attached cavitation

Fig. 5 Two different cavitation inception states corresponding to flow past hemispherical headform with trip wire

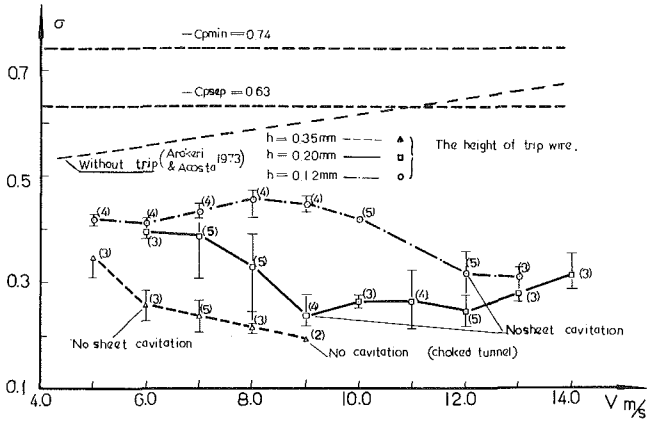

Fig. 6 Delay in cavitation for hemispherical head with different heights of trips

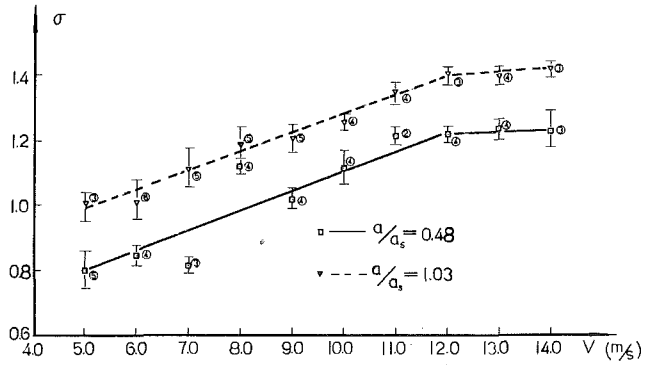

Fig. 7 Cavitation inception number as a function of speed for the 45 deg conical head

vanishing laminar separation fell in the region between Reynolds numbers 5.26×10^5 and 5.54×10^5, corresponding to water speeds of 8 m/s and 8.5 m/s respectively as shown in Fig. 4(*c*). Then it may be shown from the comparison of flow visualization measurements and cavitation inception measurements that the sheet cavitation case corresponds to the regime of laminar separated flow, while the unstable attached cavitation corresponds to the regime of induced boundary layer transition.

The influence of total air content may be seen in Fig. 4. At subcritical Reynolds numbers, the influence is relatively small and values of σ_i measured are quite close for the two different air content tests. At supercritical Reynolds numbers, tests with high air content seem to show no appreciable change in cavitation inception as long as the height of trip wire not too large as shown in Fig. 4(*b*) and (*c*). While tests with low air content show significant reduction in cavitation inception number, as compared to the values in the subcritical regime.

In order to make a comparison for the effect of the trip wire, three sets of curves with relatively low air content are plotted together in Fig. 6. It is clearly seen that by stimulating transition with a trip wire, the cavitation inception number is drastically reduced. This agrees with the results of Arakeri and Acosta [2]. Within the range of trip wire heights tested, it is seen that σ_i decreases as the height of trip wire increases.

A significant drop in σ_i for the low air content case was found at speeds slightly lower than the speed at which sheet cavitation inception was transformed into unsteady attached cavitation as shown Figs. 4 and 6. As mentioned above, the sheet cavitation case corresponds to the regime of laminar separated flow, while the disappearance of sheet cavitation corresponds to the regime of induced boundary laminar transition; so we can say that the remarkable reduction of inception index occurs, and only occurs, in the vicinity of critical Reynolds number, whereas in the ranges of subcritical and supercritical Reynolds numbers, the inception indices merely display plateau characteristics at different levels.

Figure 6 provides good evidence of the importance of the structure of the near-wall flow on cavitation inception. However, on the other hand, it also implies that the process of cavitation inception must also be influenced by other factors which cause important scale effects, since it is known that under full-scale tests values of σ_i may be relatively close to the values of $-C_{p_{\min}}$ [4].

2. Conical Heads. Figures 7 and 8 show respectively the cavitation inception number σ_i as a function of water speed V for the 45 and 25 deg conical headforms. From Fig. 7, it may be seen that the cavitation inception curve is characterized by some of the same features as that for a sharp-edged circular disc. Actually, the flow downstream from the shoulder of the 45 deg conical headform is typical of a separated flow; its cavitation inception is a kind of vortex cavitation, and rises monotonically with the Reynolds number. As comparatively richer cavitation nuclei will be provided by the case of higher air content ratio, and as these nuclei will have more than enough time to grow in the vortex core of a separated shear flow, it is natural to expect that the σ_i measured for the higher air content case will be higher than those for the lower air content case for the same water speed.

The experimental curve for the 25 deg conical head may be broken up into three regions (Fig. 8). The first region in which the cavitation inception number drops monotonically as the water speed V rises from 5 to 7 m/s; the second region, $V = 7 \sim 9$ m/s, in which the tunnel is choked and no cavitation inception is observed; and the last region, $V = 9 \sim 14$ m/s, in which the σ_i value rises monotonically with speed V. Holographic observations reveal that for all speeds the flow

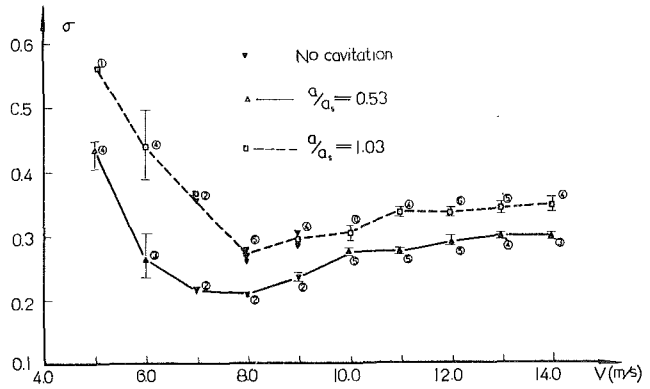

Fig. 8 Cavitation inception number as a function of speed for the 25 deg conical headform

of the boundary layer in the vicinity of the cone shoulder is turbulent, but only at comparatively lower speeds does the separated flow downstream of the shoulder have the tendency to reattach to the cylindrical surface. Thus it may be pictured that the cavitation inception in this range of speeds is controlled by two factors: the vortex in the separated flow and the pressure fluctuations at the wall of the cylinder, thereby constituting a state of unstable attached cavitation. On the other hand, at the high speed end the cavitation inception is uniquely controlled by the effect of vortex in the separated shear flow as in the case of a 45 deg cone, and therefore has similar characteristics as vortex cavitation. In the intermediate speed range, the separation is not very strong, but there is also no reattachment of separated flow, so that it is consequently featured by the lowest cavitation inception number, and so far no cavitation inception is observed in our test.

3. Schiebe Headform. For this case, $C_{p_{min}} = -0.75$. Cavitation inception is such that, for a certain constant water speed, sheet cavitation makes its appearance in an explosive manner, when the working section pressure is lowered to a certain value, without any precursive symptoms indicating cavitation inception. The smaller the amount of free bubbles in the oncoming flow, the more distinct this explosive feature becomes. As the free bubbles become more numerous, occasionally there may be observed cases of traveling bubble cavitation for relatively high water speeds before developing into sheet cavitation.

Figure 9 shows the cavitation inception number as a function of water speed for the Schiebe headform. It may be seen that cavitation inception occurs earlier as the total air content becomes higher. Even with the same air content ratio, a greater concentration of free bubbles causes a marked difference in cavitation inception as reflected in higher values of σ_i.

Analysis of a holographic display shows that with a water speed as low as 5 m/s, the natural boundary layer transition still occurs on the Schiebe headform and as the water speed increases the front edge of the turbulent boundary layer, i.e. the position of transition to turbulent flow, moves toward the point of minimum pressure. Naturally, the average static pressure in the transition region actually decreases with an increase in water speed. This is one of the reasons why the cavitation inception number rises with water speed as shown in Fig. 9 for the Schiebe headform.

The authors would like to point out that results of tests conducted in our water tunnel on the Schiebe headform agree well with those obtained by Gates and Acosta [5] in the HSWT of CIT, but are lower in values as compared to similar tests done by Van der Meulen [6] in the Ultra High Speed Water Tunnel of NSMB.

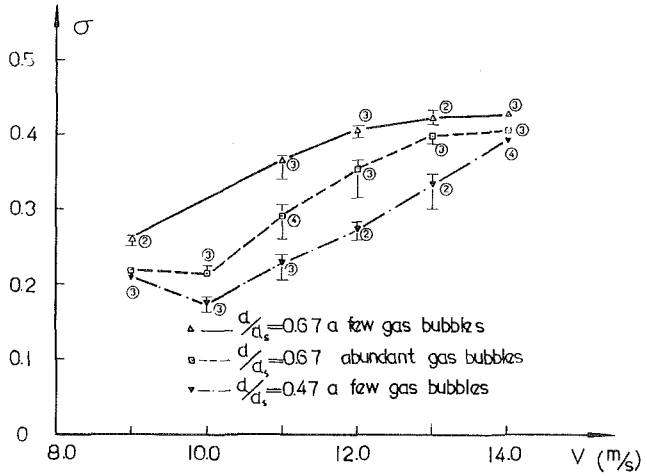

Fig. 9 Cavitation inception number as a function of speed for Schiebe headform

Fig. 10 Spot cavitation

Discussions and Conclusions

For all three types of headforms tested, we have had occasions of observing the appearance of spot cavitations as described in [2]. It occurs at fixed places in the vicinity of the minimum mean pressure, and grows into a triangular "wedge" as shown in Fig. 10. The circumstances under which spot cavitation occurs are as follows: When a model is tested in the tunnel initially, no spot cavitation is observed for any water speed, but after a certain length of time has elapsed, or when the model has been immersed in water for a certain length of time, then spot cavitation begins to appear at one or several fixed spots. After carefully examining the model surface, we found on the surface of the aluminum model certain white crystalling spots and some pits of varying depth. These spots and pits coincide approximately with the places of spot cavitation. Therefore, it is conjectured that spot cavitation is due to isolated local roughnesses on the surface, and are not due to any actions of surface nuclei. In the present experiment, no spot cavitation was recorded, and was not taken into account.

From measurements of cavitation inception and holographic analysis conducted in the present experiment, it may be concluded that cavitation inception occurring on a body is closely related to the characteristics and structures of near-wall flow:

- With laminar separation and later reattachment of the boundary layer (as for example, hemispherical headform with trip wire for subcritical Reynolds numbers flow), cavitation inception is stable, sheet-like, little affected by air content ratio, and is characterized by an explosive onset and has an axisymmetric appearance.
- With a natural transitional boundary layer (as for example, the Schiebe headform, cavitation inception is also

stable, sheet-like, "explosive" and axisymmetric. However the cavitation inception number is obviously affected by the total air content and free bubble concentration.

- With induced transitional boundary layer (as for example, the case of the hemispherical headform with trip wire for supercritical Reynolds numbers), cavitation inception is characterized by marked instability, the inception number is much lower than the case when induced transition of boundary layer has not occurred, and the number varies noticeably with air content.
- With strongly separated flow (as for example, the cases of a 45-deg conical head and a 25-deg conical head at high speeds), cavitation inception is cuased by the effect of the low pressure in the core of the vortex originated at the cone shoulder due to separated shear flow, and it is featured by instability.
- With weak separated flow (as for example, the case of a 25-deg conical head at low speed), cavitation inception becomes also unsteady and attached, but the axial position of the inception is approximately fixed.

Therefore, for cavitation inception, it may be assumed that the determining factor is the nature of local pressure P_L • P_L of four parts:

$$P_L = \bar{P} + \Delta P_R + \Delta P_F + \Delta P_V$$

where $\bar{P}$ is the average static pressure of fluid, ΔP_R is the pressure drop due to local surface roughness, ΔP_F is the pressure fluctuation as characterized by different boundary layer regimes, and ΔP_V is the pressure drop caused by eddies due to variation of flow structures. According to the local flow structures, the relative importance and effect of those components vary. For cavitation inception on a surface, generally $\bar{P}$ is the leading factor, but with the presence of vortex, $\bar{P}$ recedes to a secondary place, ΔP_R is the main cause of spot cavitation, and ΔP_F and ΔP_V are respectively closely related to sheet and unsteady cavitation.

Fitting a trip wire on a headform (with laminar separated flow) will drastically delay the inception of cavitation. As long as the height of the trip is sufficient to cause any significant change in the structure of the separated laminar boundary layer, it will have its effect in delaying the cavitation inception considerably in the region of subcritical Reynolds numbers. When the laminar separation is suppressed and the flow is transformed into an induced transitional turbulent boundary layer, the cavitation inception number will drop significantly once more, and will remain at this lower level without further decrease, even with further increase in Reynolds number. When the total air content is comparatively high, the aforementioned second decrease (or delay) may not take place, and for the entire range from subcritical to supercritical Reynolds number, the cavitation inception number does not seem to vary much. The height of trip wire has an important effect on the delay of cavitation inception. Care in mounting a suitable trip wire is of prime importance in carrying out a successful experiment.

References

1 Acosta, A.J., "Cavitation & Fluid Machinery," *Proceedings Conference on Cavitation*, Institute of Mechanical Engineers, Edinburgh, 1974, pp. 383–396.

2 Arakeri, V.H., and Acosta, A.J., "Cavitation Inception Observation on Axisymmetric Bodies at Supercritical Reynolds Numbers," *Journal of Ship Research*, Vol. 20, No. 1, pp. 40–50.

3 Schiebe, F.R., "Measurement of Cavitation of the Cavitation Susceptibility of Water Using Standard Bodies," Project Rep. No. 118, St. Anthony Falls Hydraulic Laboratory, Feb. 1972.

4 Huang, T.T., and Peterson, F.B., "Influence of Viscous Effects on Model/Full Scale Cavitation Scaling," *Journal of Ship Research*, Vol. 20, No. 4, 1976, pp. 215–223.

5 Gates, E.M., and Acosta, A.J., "Some Effects of Several Freestream Factors on Cavitation Inception of Axisymmetric Bodies," 12th Symposium on Naval Hydrodynamics, Washington, D.C., 1978, pp. 86–108.

6 Van der Meulen, J.H.J., "A Holographic Study of Cavitation on Axisymmetric Bodies and the Influence of Polymer Additives," Publication No. 509, 1976, NSMB, Wageningen, Netherlands.

Cavitation Inception Observations on Six Axisymmetric Headforms

T. T. Huang
Naval Architect,
David W. Taylor Naval Ship Research and Development Center,
Bethesda, Md.

Cavitation inception observations on a series of axisymmetric headforms were made in the DTNSRDC 36-in. water tunnel. Cavitation inception observed on headforms with natural flow transition is characterized by the growth and collapse of the individual undissolved air bubbles in the water when traveling through the low pressure regions of flow transition. Cavitation inception observed on headforms with laminar separation is characterized by an attached band or bubble-ring cavitation starting at the separation point. The traveling bubble type cavitation inception is significantly affected by the microbubble population. However, the effect of total air content and size distribution of the bubbles on attached cavitation inception is less pronounced. Attached spot or ring/band cavitation never occur at the location of minimum static pressure but are observed first in the regions of natural flow transition or laminar separation.

Introduction

Cavitation inception on the ITTC (International Towing Tank Conference) standard headform was found [1] to appear in many different physical forms when tested in different cavitation facilities around the world. Cavitation inception on this single headform occurred over the range of cavitation numbers from 0.4 to 1.1. The follow-up study by Johnsson [2] and the review by Acosta and Parkin [3] suggested that in some cases inception appeared in the form of an attached band or bubble ring cavity as the result of laminar separation and in other cases, inception appeared in the form of traveling macroscopic bubbles as a result of natural flow transition which precluded laminar separation. For a body having laminar separation, Arakeri and Acosta [4,5] designated the Reynolds number at which laminar separation disappeared as the critical Reynolds number, $R_{D_{\text{crit}}}$. Flows for which the Reynolds number is less than or more than $R_{D_{\text{crit}}}$ are called "subcritical" and "supercritical," respectively. For supercritical Reynolds numbers and for bodies without the possibility of laminar separation, there is some evidence [4,5] that cavitation inception takes place within the region of transition from laminar to turbulent flow. For subcritical Reynolds numbers, cavitation inception is found to occur in the transition region of the separated shear layer on the reattachment region following laminar separation [4,5]. Enormous pressure fluctuations on the body surface were measured by Arakeri [6] and Huang and Hannan [7] in the reattachment region following laminar separation. In addition, amplitudes of the pressure fluctuations in the natural transition region measured by Huang and Hannan [7] were found to be higher than in a fully-turbulent boundary-layer flow by a factor ranging from 2 to 3. Cavitation inception [4,5] is believed to be closely related to the high pressure fluctuations in the region following laminar separation and in the natural transition zone of an attached boundary layer. The transition process is very sensitive to the magnitude of the free-stream turbulence level and the surface condition of the body. Thus, the location of the cavitation-prone transition region and the critical Reynolds number may be different for the same body in two different facilities or, for that matter, it may be different in the same facility if the free-stream turbulence level or the surface roughness is changed. The effect of surface roughness on cavitation inception, although extremely important, falls outside the scope of the present investigation.

The growth of critical microscopic bubbles (weak spots) into the ultimately visible macroscopic cavitation in the cavitation-prone transition region depends not only upon the nature of the transition process, the presence or the absence of laminar separation, but also upon the population of the critical bubbles either within the flow or on the liquid/solid interface. Some cavitation facilities are equipped with deaeration and/or resorber systems, but others have none at all. Therefore, the concentration of critical microbubbles may vary significantly from one facility to the other so as to cause the large discrepancies between observed cavitation inception indices for the ITTC headform. The actual size range of the critical microbubbles from which cavitation grows explosively is still not known. Peterson [8] has holographically measured the particle size distribution of free microbubbles with radii varying from 25 to 200 microns in the 12-inch water tunnel. The cavitation inception indices measured by Peterson [8] and Brockett [9] on a modified ellipsoidal headform (known as the NSRDC headform [3,5] with $C_{p\min} = -0.84$) showed that the cavitation inception index decreased with decreasing air content at supercritical Reynolds numbers. The effect of gross air content on cavitation inception was also reported by Crump [10,11], by Layne [12], and by Weitendorf [13]. Recently Gates and Acosta [14] found that air content and free-stream turbulence level had a dramatic effect on cavitation inception on the NSRDC headform, but had negligible effect on a hemispheric nose. The effect of

Contributed by the Fluids Engineering Division and presented at the International Symposium on Cavitation Inception, ASME Winter Annual Meeting, New York, N.Y., December 2-9, 1979, of THE AMERICAN SOCIETY OF MECHANICAL ENGINEERS. Manuscript received by the Fluids Engineering Division, February 11, 1980.

boundary-layer development on cavitation inception on a hydrofoil was also investigated by Blake, et al. [15]. Huang and Peterson [16] evaluated the influence of viscous effects on the correlations of model and full-scale cavitation inception.

In order to gain further insight into the physics of cavitation inception and its effect on model/full-scale cavitation-inception correlation, six axisymmetric headforms were tested in the DTNSRDC 36-in water tunnel. Detailed measurements of wall-pressure fluctuations in the transition regions were made previously by Huang and Hannan [7,17]. A brief summary of this work is reported in the following.

Geometry and Flow for Six Axisymmetric Heaforms

Three axisymmetric headforms having natural flow transition and another three having laminar separation were selected for investigation. The transition resulting from the growth of Tollmein-Schlichting disturbances present in a laminar boundary layer is defined as "natural." The three headforms designated T-3, T-6, and T-8 have natural transition without any possibility of laminar separation. The other three headforms designated as S-1 (hemispheric nose), S-2, and S-10, exhibit laminar separation as a result of severe adverse pressure gradients. Detailed measurements of wall-pressure fluctuations during natural flow transition on T-3 and T-6 and following laminar separation on S-1 and S-2 had been made in a wind tunnel [7,17] using pinhole microphones.

The body contours and the distributions of potential-flow pressure coefficients of the headforms with natural transition are shown in Fig. 1. The maximum diameter D of the headforms used in the wind tunnel experiments was 0.624 meter and the models were constructed of molded fiberglass with a 0.6-micron rms surface finish. The diameters, D, of Headforms T-3 and S-2 used in the water tunnel are 9.84 cm and 7.63 cm, respectively. Both headforms were constructed of aluminum, were anodized to avoid corrosion in water, and were polished to a 0.8 micron finish. The other headforms T-6, T-8, S-1, and S-10 used in the water tunnel were constructed of plexiglass to avoid corrosion. The diameter of these four headforms was 10.2 cm and the surface finish was kept at 0.4 micron.

The calculated spatial amplification ratios [18], A, in the natural transition regions of the three headforms were found by Huang [17] to correlate well with the flow regimes measured by flush-mounted hot-films. Similar results were

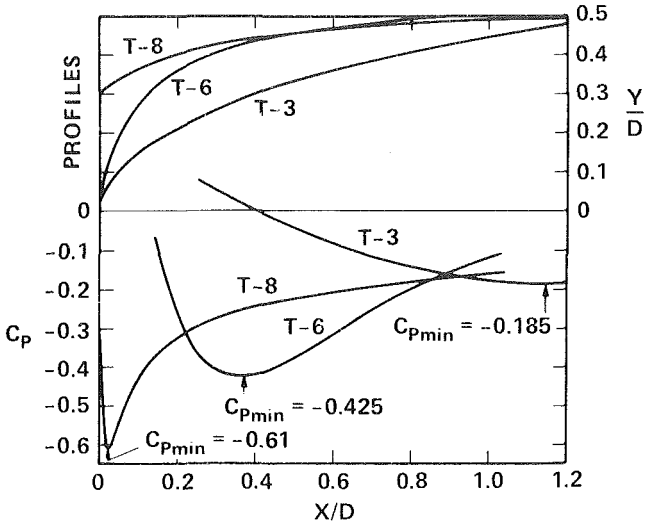

Fig. 1 Surface profiles and pressure coefficients of three headforms with natural flow transition

obtained for the headforms tested in the towing basin by Power [19]. The transition regions on T-3 and T-6 measured in the wind tunnel with low free-stream turbulence level (about 0.1 percent) correlate quite well with the computed values of $A = e^{11}$. The free-stream turbulence level of the NSRDC 36-inch water tunnel was measured by hot-film velocity probe and was found to be about 0.45%. The transition regions on T-3 and T-6 in the water tunnel are, therefore, likely to occur in a location where the computed amplification ratios are smaller than $A = e^{11}$. The measured flow regimes on T-8 (flat face) do not correlate with a particular value of the calculated amplification ratios and are less sensitive to the change of Reynolds number in comparison with the curves of constant A. The transition region of flatface Headform T-8 was found to be rather short [17]. Large measured pressure fluctuations in the transition regions of T-3 and T-6 measured by Huang [17] and the sudden transition of T-8 are likely to promote cavitation inception.

The body contours and the distributions of C_p on the three headforms having laminar separation are shown in Fig. 2. The locations and magnitudes of minimum pressure coefficient C_{pmin} and the locations of the separation points (L.S.) are given in Fig. 2. Use of fluorescent oil-film visualization in

Nomenclature

A = cumulated spatial amplification ratio of a disturbance in the boundary layer to its amplitude at point of neutral stability
A_S = A at the position of laminar boundary layer separation
C_P = pressure coefficient given by $(P - P_0)/(\frac{1}{2}\rho U_0^2)$
C_{pmin} = minimum value of C_p
C_{PS} = C_P at the position of laminar boundary layer separation
C_{ptr} = C_p at the location of transition in the laminar boundary layer
D = diameter of the axisymmetric headform
P = local static pressure on the headform
P_0 = free stream tunnel static pressure
P_v = vapor pressure of water at its bulk temperature
R_D = Reynolds number given by $U_0 D/\nu$
$R_{D_{crit}}$ = critical Reynolds number at which transition takes place at the position of laminar boundary layer separation
S = streamwise distance along the body surface from the stagnation point
S_S = S at the position of laminar boundary layer separation
U_0 = free stream tunnel velocity
X = axial distance from the stagnation point
Y = radial distance measured from the X-axis of the headform
$\sqrt{\bar{p}'^2}$ = rms wall pressure fluctuation
α/α_0 = dissolved gas content in terms of percent of saturation at 21°C water temperature and atmospheric pressure
α/α_{TS} = dissolved gas content in terms of percent of saturation at test section water temperature and pressure
ν = kinematic viscosity of water
ρ = mass density of water
σ = cavitation number given by $(P - P_v)/(\frac{1}{2}\rho U_0^2)$
σ_i = incipient cavitation number

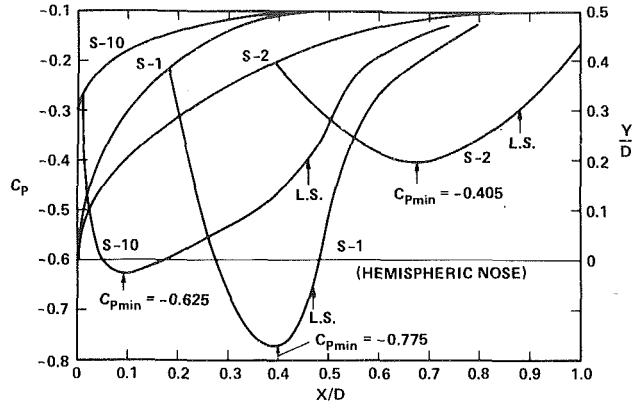

Fig. 2 Surface profiles and pressure coefficients of three headforms with laminar separation

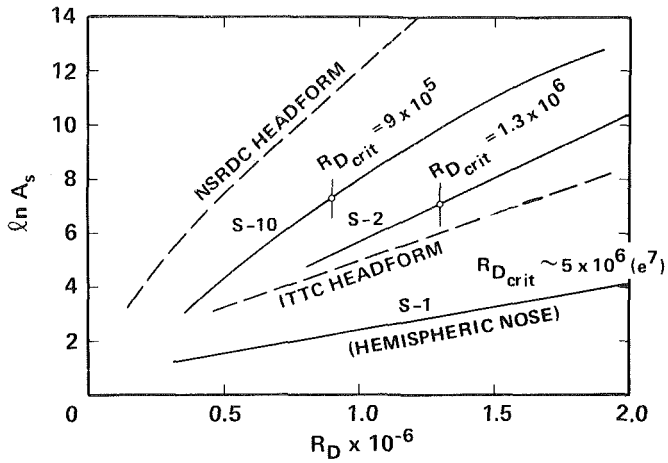

Fig. 3 Flow regions for headforms with laminar separation as estimated by amplification ratio

the wind tunnel and water tunnel verified the existence of laminar separation at the predicted locations [20]. The Reynolds number at which laminar separation disappeared as a result of the occurence of natural flow transition at separation point is designated as the critical Reynolds number, $R_{D_{crit}}$. The calculated spatial amplification ratios at the laminar separation points as a function of R_D for the three headforms, and the ITTC [1] and NSRDC [5,8,9] headforms are shown in Fig. 3. The critical Reynolds numbers of headforms S-2 and S-10 measured by fluorescent oil-film in the 36-inch water tunnel were 1.3 × 10^6 and 0.9 × 10^6, respectively. As shown in Figure 3 the two measured values of $R_{D_{crit}}$ for S-2 and S-10 correlate well with $A_{S=e^7}$. If $R_{D_{crit}}$ for S-1 is assumed to be the Reynolds number when $A_S = e^7$, then the value of $R_{D_{crit}}$ for S-1 is estimated to be 5 × 10^6, which is beyond the maximum speed capability of most existing water tunnels.

Enormous pressure fluctuations following laminar separation on Headforms S-1 and S-2 were measured in the wind tunnel [7,17]. The rms wall-pressure fluctuations, $\sqrt{p'^2}$, in the reattachment region were found to be as high as 0.15 $\rho U_0^2/2$. These extremely high pressure fluctuations have profound implications relative to cavitation inception. The computed amplification ratios on Headform S-10 for $R_D > R_{D_{crit}}$ are shown in Fig. 4 for the convenience of estimating the transition region.

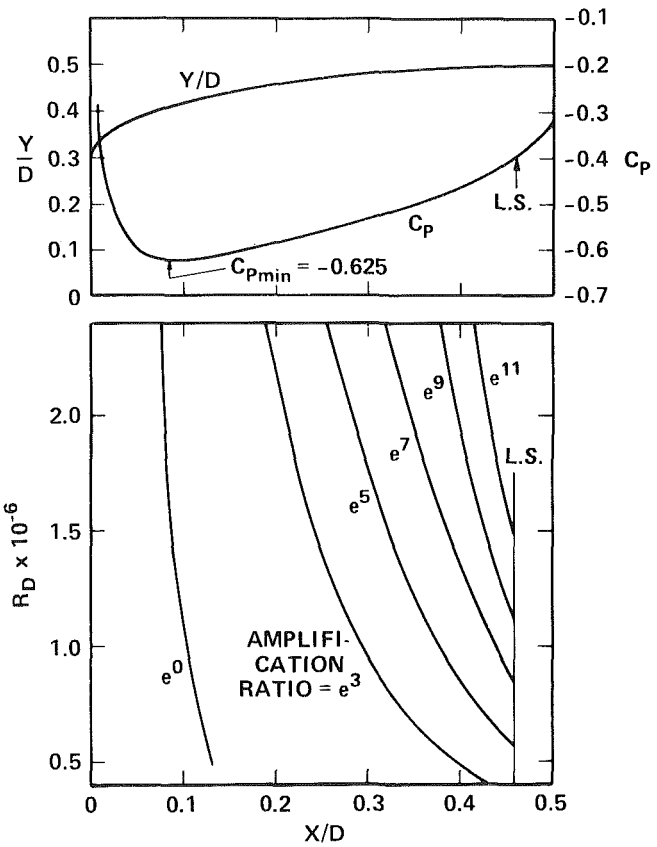

Fig. 4 Surface profile, pressure coefficients and amplification ratios on Headform S-10

Description of Cavitation Experiments

Cavitation inception measurements for the six axisymmetric headforms were carried out in the David W. Taylor Naval Ship R&D Center (DTNSRDC) 36-inch variable-pressure water tunnel with a closed-jet test section. A cylindrical resorber 7.62 metres in diameter and 21.3 metres in height is built into the circuit to permit more efficient control of the free-air content of the water. The tunnel is also equipped with a deaeration system which can be used to reduce the air content of the water. Total air content was measured by standard Van Slyke apparatus.

The headforms were attached to the housing of the propeller shaft located at the centerline of test section and were illuminated by a EG&G Xenon stroboscope (Model LS148). This system allowed the visual observation of cavitation bubbles. Cavitation inception was also independently measured by an accelerometer mounted on the inside wall of the headform. It was found that the output of the accelerometer registered the collapse of each cavitation bubble. The accelerometer output correlated well with the visual observation of cavitation under the stroboscopic lighting condition. Cavitation inception is arbitrarily defined in this report as the onset of detectable cavitation events which occur about once per second. Most of the cavitation events on the six headforms were recorded photographically by using Polaroid high-speed Type-52 film or Kodak high-speed Ektachrome 32-mm film. In addition, high-speed motion pictures (6500 frames per second) were taken by a Red Lake Hycam 16-mm camera.

Incipient cavitation numbers were determined by slowly lowering the tunnel pressure at constant tunnel velocity until cavitation events occurred about once every second. The cavitation number, σ, is given by

$$\sigma = \frac{P_0 - P_v}{\frac{1}{2}\rho U_0^2} \quad (1)$$

Table 1 Measured cavitation inception on Headform T-3

$R_D = 1.7 \times 10^6$	α/α_o	α/α_{TS}	σ_i	Type of cavitation
$C_{pmin} = -0.19$	0.80	3.1	0.17±0.02	Traveling-bubble
At x/D = 1.15		3.9	0.13±0.02	Attached spot
Estimated Transition	0.40	1.8	0.14±0.02	Traveling-bubble (once in a while)
A | x/D | $-C_{ptr}$		2.3	0.11±0.01	Attached spot
e^7 | 1.56 | 0.14				
e^9 | 1.65 | 0.12				
e^{11} | 1.72 | 0.10				

where P_v is the vapor pressure of the water, P_0 is the static pressure at the centerline of the test section, ρ is the mass density of water, and U_0 is the tunnel velocity. The incipient cavitation numbers are denoted by σ_i. Cavitation observations were made with dissolved air contents on the order of 4,9,13.5 and 18 ppmw (parts per million by weight), corresponding to 18,40,60 and 80 percent of saturation at 21°C water temperature and atmospheric pressure. No quantitative measurements of free-gas bubble distribution were made in the present experiments.

Cavitation Characteristics of Headforms With Natural Transition

Based on previous wind tunnel experiments, natural transition without any possibility of laminar separation was expected in the water tunnel for Headforms T-3, T-6, and T-8. The large pressure fluctuations measured on Headforms T-3 and T-6 in the low turbulence wind tunnel occur in the region where $e^{11} < A < e^{14}$. For a relatively high free-stream turbulence level, the transition regions on the headforms in the water tunnel are expected to occur further upstream than those obtained in the wind tunnel.

A large number of high-speed photographs and motion pictures were taken to investigate cavitation inception on the headforms at various air contents. The results are shown in Tables 1 and 2 for Headform T-3 and T-6, respectively. The dissolved air content in terms of percent of saturation at 21°C water temperature and atmospheric pressure is denoted by α/α_0 and the dissolved air content of the water referred to test pressure is denoted by α/α_{TS}. The estimated locations of flow transition for different values of amplification ratio are also given in the tables. Two types of cavitation, traveling bubble and attached spot cavitation, were observed on Headforms T-3 and T-6. Cavitation inception began with the growth of microbubbles, which became visible immediately downstream of the location of C_{pmin} and collapsed further downstream. It is important to note that the values of σ_i were smaller than $-C_{pmin}$ even though the water in the test section was supersaturated with air (Tables 1 and 2). The values of σ_i for traveling bubble cavitation decreased with decreasing air content. By careful examination of the high-speed motion pictures, the explosive growth of these traveling bubbles was found to coincide with the beginning of the estimated transition regions ($e^5 < A < e^{11}$) and the collapse to coincide with the aft end of the transition regions ($A \geq e^{11}$). The detectable bubble of growth was found to originate immediately downstream of the location of C_{pmin}. The occurrence of visible cavitation bubbles became more frequent upon further

Table 2 Measured cavitation inception on Headform T-6

$R_D = 1.28 \times 10^6$	α/α_o	α/α_{TS}	σ_i	Type of Cavitation
$C_{pmin} = -0.43$	0.6	2.3	0.34±0.04	Traveling-bubble
At x/D = 0.37		2.9	0.25±0.03	Attached spot
Estimated Transition	0.42	1.7	0.32±0.03	Traveling-bubble
A | x/D | $-C_{ptr}$		2.2	0.23±0.02	Attached spot
e^7 | 0.62 | 0.30	0.27	1.1	0.29±0.02	Traveling-bubble
e^9 | 0.68 | 0.26		1.4	0.23±0.02	Attached spot
e^{11} | 0.72 | 0.24				
$R_D = 1.6 \times 10^6$	0.6	1.4	0.36±0.03	Traveling-bubble
$C_{pmin} = -0.43$		1.9	0.25±0.02	Attached spot
Estimated Transition	0.42	1.0	0.33±0.03	Traveling-bubble
A | x/D | $-C_{ptr}$		1.8	0.23±0.02	Attached spot
e^7 | 0.60 | 0.31	0.27	0.8	0.27±0.02	Traveling-bubble
e^9 | 0.65 | 0.28		0.9	0.23±0.02	Attached spot
e^{11} | 0.69 | 0.26	0.17	0.5	0.27±0.02	Traveling-bubble
		0.6	0.23±0.02	Attached spot

Table 3 Measured cavitation inception on Headform T-8

$R_D \times 10^{-6}$	α/α_o	α/α_{TS}	σ_i	Type of cavitation
0.96	0.4	2.0	0.43±0.03	Traveling-bubble
		2.2	0.39±0.03	Attached spot
1.28	0.4	1.2	0.42±0.02	Traveling-bubble
		1.52	0.39±0.02	Attached spot
1.6	0.4	0.81	0.41±0.02	Traveling-bubble
		0.84	0.39±0.02	Attached spot

lowering of the cavitation index from its inception value. It may be noted that the actual growth process of the critical microbubbles must take place at some distance upstream of the transition region, presumably starting at the location where the local pressure first reaches the vapor pressure. This growth process may be slow in the laminar flow region. Once bubbles are in the vicinity of the transition region, the turbulence bursting process with its large pressure fluctuation enchances the rate of the bubble growth and collapse. After a short distance of explosive growth starting from the beginning of the transition region, the bubble was found to collapse at the aft end of the transition region where the turbulence and pressure fluctuations were large. The physics of this type of bubble dynamics is not yet understood.

When slowly reducing the cavitation index from the inception value for traveling bubble cavitation, attached spot cavitation was usually observed. The inception of attached spot cavitation was not found to be sensitive to the air con-

Table 4 Measured cavitation inception on Headform S-1 (*Hemispheric Nose*)

$R_D \times 10^{-6}$	α/α_o	α/α_{TS}	σ_i
0.8	0.6	3.0	0.63±0.05
	0.45	2.3	0.61±0.04
	0.25	1.3	0.60±0.04
	0.18	1.0	0.57±0.04
1.28	0.6	1.3	0.62±0.02
	0.45	0.9	0.61±0.02
	0.25	0.5	0.61±0.02
	0.18	0.4	0.58±0.02
1.6	0.6	0.8	0.61±0.02
	0.45	0.6	0.61±0.02
	0.25	0.35	0.61±0.02
	0.18	0.25	0.58±0.02

Table 5 Measured cavitation inception on Headform S-2

$R_D \times 10^{-6}$	α/α_o	α/α_{TS}	σ_i
0.96 $R_D < R_{D_{crit}}$	0.25	1.0	0.30±0.02
1.3 $R_D \sim R_{D_{crit}}$	0.8	1.8	0.30±0.02
	0.4	0.9	0.30±0.02
	0.25	0.6	0.30±0.02

tent, regardless of whether the water was super or under saturated with dissolved air in the test section.

The results shown in Tables 1 and 2 suggest that the cavitation inception index of the attached spot cavitation is very closely related to the static pressure coefficient at transition C_{ptr}, at the location where $A = e^{11}$. However, the inception indices for the traveling bubble cavitation are seen to vary between $-C_{ptr}$ and $-C_{p\min}$ depending upon the concentration of cavitatable microbubbles in the water. The use of the resorber and deaeration system in the DTNSRDC 36-inch water tunnel effectively reduces the concentration of small undissolved microbubbles. Therefore, it is understood that the cavitation inception index obtained in this water tunnel is in general smaller than other tunnels without resorbers, which have a potential plentiful supply of microbubbles.

Recall that the measured transition flow regions on flat-face Headform T-8 did not correlate well with any particular value of the computed amplification ratio; the length of the measured transition region was short, the location of transition was not too sensitive to Reynolds number, and no large pressure fluctuations in the transition region were detected. As shown in Fig. 1 this headform has a large negative pressure peak $C_{p\min} = -0.61$ and has a much larger adverse pressure gradient than exists on T-3 and T-6. The results of the cavitation inception observations are shown in Table 3. The

Table 6 Measured cavitation inception on Headform S-10

$R_D \times 10^{-6}$	α/α_o	α/α_{TS}	σ_i	Type of Cavitation
0.8 $R_D < R_{D_{crit}}$	0.5	2.6	0.60±0.05	Traveling-bubble
		3.6	0.40±0.02	Attached band at L.S.
	0.2	1.1	0.56±0.05	Traveling-bubble
		1.5	0.40±0.02	Attached band at L.S.
0.96 $R_D \sim R_{D_{crit}}$	0.5	1.9	0.57±0.05	Traveling-bubble
		2.7	0.40±0.02	Attached band
	0.2	0.8	0.55±0.03	Traveling-bubble
		1.1	0.40±0.02	Attached band
1.28 $R_D \gtrsim R_{D_{crit}}$	0.5	1.3	0.50±0.05	Traveling-bubble
		1.6	0.40±0.02	Attached band
	0.2	0.6	0.45±0.03	Traveling-bubble
		0.7	0.36±0.02	Attached band
1.6 $R_D > R_{D_{crit}}$	0.05	0.9	0.45±0.05	Traveling-bubble
		1.1	0.37±0.02	Large attached spot
	0.2	0.4	0.40±0.03	Traveling-bubble
		0.5	0.35±0.02	Large attached spot

measured inception index for the traveling bubble cavitation is about 0.4 which is much smaller than the value of $-C_{p\min} = 0.61$. The locations of collapse of the individual traveling bubbles were found to be in the range of $0.17 < x/D < 0.25$ which concides with the expected transition region on T-8; the corresponding values of C_{ptr} *are* $0.35 > -C_{ptr} > 0.30$, respectively.

The measured inception indices of the traveling bubble and attached spot cavitation are rather close. Once the attached spot cavitation originated on T-8 a band type cavitation followed immediately with its leading edge moving to about $x/D \cong 0.06$–0.07.

Cavitation Characteristics of Headforms With Laminar Separation

Recall from Fig. 3 that the measured values of critical Reynolds numbers, $R_{D_{crit}}$, for S-2 and S-10 in the 36-in water tunnel are 1.3×10^6 and 0.9×10^6, which correlate well with the computed amplification ratio at the separation point $A_S = e^7$. The value of $R_{D_{crit}}$ for S-1 is beyond the maximum speed capability of the 36-inch water tunnel. A large number of high-speed photographs and motion pictures were taken during various stages of cavitation inception and then displayed on a large screen for analysis. The results of the analyses are shown in Tables 4, 5, and 6 for Headforms S-1, S-2 and S-10 evaluated at various air contents. At a cavitation index σ of 0.61 ± 0.03, a short attached bubble ring cavity formed suddenly at the location of laminar separation on S-1, and the length of the cavity increases with decreasing cavitation index. At $\sigma = 0.3 \pm 0.02$ large attached cavitation spots (fingers) appear and disappear randomly on S-2, and these cavitation spots merge together to form a ring cavity at $\sigma = 0.25$. The effect of dissolved air content on the cavitation inception index and appearance of the attached cavitation on S-1 and S-2 is insignificant so long as $R_D < R_{D_{crit}}$ (existence of laminar separation). Traveling bubble cavitation was not observed on S-1 or S-2. The present data on attached cavitation inception index on the hemispheric headform agree

Table 7 Parameters controlling attached cavitation inception on headforms with laminar separation

	Hemispheric Nose, S-1	Headform S-2	Headform S-10
Predicted[18] $R_{D_{crit}} \times 10^{-6}$ by e^7	5.0	1.3	0.86
Predicted[18] $R_{D_{crit}} \times 10^{-6}$ by e^9	7.0	1.9	1.3
Predicted[18] $R_{D_{crit}} \times 10^{-6}$ by e^{11}	9.0	2.5	1.7
Measured $R_{D_{crit}} \times 10^{-6}$	1.8 (water tunnel) 2.5 (wind tunnel)	1.3 (water tunnel) 2.4 (wind tunnel)	0.9 (water tunnel)
$-C_{pmin}$	0.78	0.405	0.625
(x/D) at C_{pmin}	0.39	0.68	0.09
$-C_{ps}$	0.64	0.30	0.40
$(x/D)_s$	0.47	0.89	0.46
$(S/D)_s$	0.76	1.10	0.835
Measured	$= 0.61 \pm 0.02$ $0.7 < R_D \times 10^{-6} < 1.8$	$= 0.30 \pm 0.02$ $1.0 < R_D \times 10^{-6} \leqslant 1.3$	$= 0.40 \pm 0.02$ $R_D \times 10^{-6} \leqslant 0.9$
σ_i versus $-C_{ps}$	$\sigma_i = -C_{ps}$	$\sigma_i = -C_{ps}$	$\sigma_i = -C_{ps}$
Incipient Cavitation Type for R_D $R_{D_{crit}}$	Ring with Small Attached spots at L.S.	Ring with Large Attached spots at L.S.	Ring with Large Attached spots at L.S.

with lower Reynolds number data of Gates and Acosta [14] and Van der Meulen [21].

The value of $R_{D_{crit}}$ for S-10 was about 0.9×10^6. As shown in Table 6, both traveling bubble and attached band cavitation were observed on S-10. When $R_D \leq R_{D_{crit}}$, the σ_i of the attached band cavitation is 0.40 ± 0.02, which is equal to $-C_{PS}$. The cavitation ring was first observed at the location of laminar separation. When $R_D > R_{D_{crit}}$ the cavitation band is formed upstream of the location of laminar separation with σ_i about equal to $-C_{PS}$ at high values of air content and with σ_i slightly less than $-C_{PS}$ at low values of air content. The measured inception index for traveling bubble cavitation decreases with decreasing air content and Reynolds number. The values of σ_i for the traveling bubble cavitation were found to vary between $-C_{pmin}$ and $-C_{PS}$ depending upon the air content and Reynolds number. A summary of measured cavitation inception originating at the location of laminar separation on Headforms S-1, S-2 and S-10 is given in Table 7.

Conclusions

Two types of cavitation inception, traveling bubble and attached spot or ring band cavitation, were observed on six axisymmetric headforms investigated in the DTNSRDC 36-inch water tunnel. The measured cavitation inception indices of the six headforms were found to be smaller than $-C_{pmin}$ for the entire range of Reynolds numbers.

Traveling bubble cavitation was observed first on the headforms with natural flow transition without possibility of laminar separation. The observed traveling bubble cavitation indices were found to vary with air content, steady pressure distribution, and boundary-layer characteristics. With a slow reduction of the value of cavitation index from the inception value of traveling bubble cavitation, attached spot cavitation was usually observed. The locations of spot cavitation on T-3 and T-6 were found to be in the transition region and the measured cavitation inception indices of attached spot cavitation were found to be equal to the static pressure coefficient at transition and insensitive to variations of air content. Because of the steep adverse pressure gradient downstream of C_{pmin} on the flat-face Headform T-8, once attached spot cavitation originated, band type cavitation followed immediately with its leading edge moving closer to the location of C_{pmin}. The inception indices of traveling bubble cavitation on Headforms T-3 and T-6 were found to vary between $-C_{pmin}$ and $-C_{ptr}$ and to decrease with decreasing air content. The inception values of traveling bubble and attached spot cavitation on T-8 were found to be rather close to each other (0.42 versus 0.39) and to be closer to the value of $-C_{ptr}$ (0.30 to 0.35) than to the value of $-C_{pmin}$ (0.61).

A short attached cavitation bubble ring was observed on Headform S-1 at $\sigma = 0.61$. Large attached cavitation spots appeared and disappeared randomly at $\sigma = 0.30$ and merged to form a band cavity at $\sigma = 0.25$ on Headform S-2. Cavitation on both Headforms S-1 and S-2 was found to occur at the location of laminar separation. The Reynolds numbers of S-2, R_D, were about equal to $R_{D_{crit}}$, but both the values of R_D for S-1 were smaller than $R_{D_{crit}}$ in the present experiment. Large attached cavitation spots were observed at the location of laminar separation on S-10 when $R_D < R_{D_{crit}}$, and the spots suddenly moved upstream to form a large band cavity as pressure was reduced. The cavitation inception indices of attached band or spot cavitation originating at the location of the laminar separation point were found to be equal to the negative value of the static pressure coefficient at separation, $\sigma_i \cong -C_{PS}$, for all three headforms with laminar separation. The effect of air content on the inception index of cavitation originating at the location of laminar separation was not significant.

Acknowledgment

This work was funded by the David W. Taylor Naval Ship R&D Center General Hydrodynamics Research Program, Task SR 023 01 01. The author would like to thank Mr. N. Santelli and Mr. G.S. Belt for their assistance during the experiments and Mrs. N. Groves for her assistance in performing boundary-layer stability computations.

References

1. Lindgren, H., and Johnsson, C. A., "Cavitation Inception on Head Forms, ITTC Comparative Experiments," *Proceedings 11th International Towing Tank Conference,* Tokyo, 1966, pp. 219-232.

2. Johnsson, C. A., "Cavitation Inception on Head Forms, Further Tests," *Proceedings 12th International Towing Tank Conference,* Rome, 1969, pp. 381-392.

3. Acosta, A. J., and Parkin, B. R., "Cavitation Inception—A Selective Review," *Journal of Ship Research,* Vol. 19, No. 4, 1975, pp. 193-205.

4. Arakeri, V. H., and Acosta, A. J., "Viscous Effects in the Inception of Cavitation on Axisymmetric Bodies," ASME JOURNAL OF FLUIDS ENGINEERING, Vol. 95, No. 4, 1974, pp. 519-528.

5. Arakeri, V. H., and Acosta, A. J., "Cavitation Inception Observations on Axisymmetric Bodies at Supercritical Reynolds Numbers," *Journal of Ship Research,* Vol. 20, No. 1, 1976, pp. 40-50.

6. Arakeri, V. H., "A Note of Transition Observation on an Axisymmetric Body and Some Related Fluctuating Wall Pressure Measurements," ASME JOURNAL OF FLUIDS ENGINEERING, Vol. 97, No. 1, 1975, pp. 82-87.

7. Huang, T. T., and Hannan, D. E., "Pressure Fluctuations in the Regions of Flow Transition," DTNSRDC Report 4723, 1975.

8. Peterson, F. B., "Hydrodynamic Cavitation and Some Considerations of the Influence of Free-Gas Content," *9th Symposium on Naval Hydrodynamics,* Paris, (August 1972); Available in U.S. Government Printing Office, ACR-203, Vol. 2, 1972, pp. 1131-1186.

9. Brockett, T., "Some Environmental Effects on Headform Cavitation Inception," NSRDC Report 3974, 1972.

10. Crump, S. F., "Critical Pressures for the Inception of Cavitation in a Large-Scale Numachi Nozzle as Influenced by the Air Content of the Water," DTMB Report 770, 1951.

11. Crump, S. F., "Determination of Critical Pressures for the Inception of Cavitation in Fresh and Sea Water as Influenced by Air Content of Water," DTMB Report 575, 1949.

12. Layne, D. E., "Inception Cavitation Results on 16-012 and 16-(0.15) 12 Hydrofoils in 24- and 36-Inch Water Tunnels," NSRDC Report 4578, 1975.

13. Weitendorf, E. A., "Cavitation and Its Influence on Induced Hull

Pressure Amplitudes," Presented at *Symposium on Hydrodynamics of Ship and Offshore Propulsion Systems,* Hovik outside Oslo, Norway, sponsored by Det Norske Veritas, Mar 1977.

14. Gates, E. M., and Acosta, A. J., "Some Effects of Several Freestream Factors on Cavitation Inception on Axisymmetric Bodies," paper presented at the *Twelfth Symposium on Naval Hydrodynamics,* Washington, D.C., June 5–9, 1978.

15. Blake, W. K., et al, "Effect of Boundary-Layer Development on Cavitation Noise and Inception on a Hydrofoil," DTNSRDC Report 76-0051, 1976.

16. Huang, T. T. and Peterson, F. B., "Influence of Viscous Effects on Model Full-Scale Cavitation Scaling," *Journal of Ship Research,* Vol. 20, No. 4, 1976, pp. 215–223.

17. Huang, T. T., "Pressure Fluctuations in the Transition Regions of Forebodies of Revolution," *Proceedings of Low-Speed Boundary-Layer Transition Workshop II,* the Rand Corporation P-6119 (Edited by W. S. King and M. Kokota), 1978.

18. Smith, A. M. O., "Transition, Pressure Gradient, and Stability Theory," *Proceedings of the Ninth International Congress of Applied Mechanics,* Brussels, Belgium, Vol. 4, 1957, pp. 234–243.

19. Power, J. L., "Drag, Flow Transition, and Laminar Separation on Nine Bodies of Revolution Having Different Forebody Shapes," DTNSRDC Report 77-0065, 1977.

20. Curle, N. and Skan, S. W., "Approximate Methods for Predicting Separation Properties of Laminar Boundary Layers," *Aeronautical Quarterly,* Vol. 8, 1957, pp. 257–268.

21. Van der Meulen, J. H. J., "A Holographic Study of the Influence of Boundary Layer and Surface Characteristics on Inception and Developed Cavitation on Axisymmetric Bodies," paper presented at the *Twelfth Symposium on Naval Hydrodynamics,* Washington, D.C., June 5–9, 1978.

Pressure Amplitudes," Presented at *Symposium on Hydrodynamics of Ship and Offshore Propulsion Systems,* Hovik outside Oslo, Norway, sponsored by Det Norske Veritas, Mar 1977.

14. Gates, E. M., and Acosta, A. J., "Some Effects of Several Freestream Factors on Cavitation Inception on Axisymmetric Bodies," paper presented at the *Twelfth Symposium on Naval Hydrodynamics,* Washington, D.C., June 5-9, 1978.

15. Blake, W. K., et al, "Effect of Boundary-Layer Development on Cavitation Noise and Inception on a Hydrofoil," DTNSRDC Report 76-0051, 1976.

16. Huang, T. T. and Peterson, F. B., "Influence of Viscous Effects on Model Full-Scale Cavitation Scaling," *Journal of Ship Research,* Vol. 20, No. 4, 1976, pp. 215-223.

17. Huang, T. T., "Pressure Fluctuations in the Transition Regions of Forebodies of Revolution," *Proceedings of Low-Speed Boundary-Layer Transition Workshop II,* the Rand Corporation P-6119 (Edited by W. S. King and M. Kokota), 1978.

18. Smith, A. M. O., "Transition, Pressure Gradient, and Stability Theory," *Proceedings of the Ninth International Congress of Applied Mechanics,* Brussels, Belgium, Vol. 4, 1957, pp. 234-243.

19. Power, J. L., "Drag, Flow Transition, and Laminar Separation on Nine Bodies of Revolution Having Different Forebody Shapes," DTNSRDC Report 77-0065, 1977.

20. Curle, N. and Skan, S. W., "Approximate Methods for Predicting Separation Properties of Laminar Boundary Layers," *Aeronautical Quarterly,* Vol. 8, 1957, pp. 257-268.

21. Van der Meulen, J. H. J., "A Holographic Study of the Influence of Boundary Layer and Surface Characteristics on Inception and Developed Cavitation on Axisymmetric Bodies," paper presented at the *Twelfth Symposium on Naval Hydrodynamics,* Washington, D.C., June 5-9, 1978.

DISCUSSION

V. H. Arakeri[1]

The author is to be congratulated on making a most useful contribution to our existing knowledge concerning mechanism of cavitation inception on axisymmetric headforms. It is clear that several different types of cavitation at inception have been observed and the author has rightly taken the trouble to classify the inception data in an orderly manner. However, it is not clear whether the travelling bubble type of cavitation referred to by the author for headform S_{10} is of the same type as for headform T_8. From the measured values of σ_i it appears that for the headform $S_{10}(\cong 0.6 \cong -C_{pmin})$ traveling bubble cavitation may be of the type first photographed by Knapp, et al. [22] and for the headform $T_8(\sigma_i \cong 0.4 \cong -C_p)$ traveling bubble cavitation may be of the incipient spot type described by Arakeri and Acosta [5]. In this context it would have been of considerable help to readers if the author had provided actual photographs or at least a sketch of the different types of cavitation observed by him at inception.

Concerning the flow regimes on various headforms it is of interest to note that there is now overwhelming evidence that axisymmetric bodies of the type hemispherical nose, ITTC body, NSRDC body and 1.5 cal ogive which possess a discontinuity in the body curvature (ie second derivitive) at the tangent point are prone to laminar separation and in addition, the position of separation has been found to be quite close to the tangent point. Are the author's findings consistent with this in the sense that the headforms T3, T6, and T8 are free from curvature discontinuities.

Finally, it is proposed that a consistant set of definations (or descriptions) be evolved to characterize different types of cavitation at inception. The following set is suggested at least for axisymmetric headforms.

Type of cavitation	*Physical description*
1) Travelling Bubble (T-B)	Exploding bubbles in the region of theoretical minimum pressure point as first photographed by Knapp [(22)], et al.
2) Shear Layer Bubble (S-L-B)	Bubbles in the free shear layer region of flow associated with disk, jet and other large separated region.
3) Band Bubble (B-B)	A ring of bubble close to the surface typically observed in the reattachment zone of small separated regions.
4) Band Attached (B-A)	Normally associated with laminar separation and having smooth surface at leading edge.
5) Spot Bubble (S-B)	A train of growing bubbles usually from fixed spots on the surface of the test body.
6) Spot Attached (S-A)	A developed cavity from a spot on the surface of the test body typically having wedge shape.

For hydrofoil sections the (7) Vortex Bubble (V-B) and (8) Vortex Attached (V-A) may be added to complete the list. However, it must be emphasized that as Professor Holl [23] has aptly pointed out that one must always be careful of distinguishing between gaseous, pseudo, and vaporous cavitation in comparing results.

Additional References

22 Knapp, R. T., and Hollander, A., "Laboratory Investigations of the Mechanism of Cavitation," TRANS. ASME, Vol. 70, 1948, pp. 419-435.

23 Holl, J. W., "Limited Cavitation," Cavitation State of Knowledge, ASME, 1969, pp. 26-63.

Author's Closure

The author expresses his gratitude to Professor V.H. Arakeri for his valuable discussion. The observed traveling bubble cavitation in this paper (headforms T-3, T-6, T-8, and S-10) was the same type photographed by Knapp, et al. The traveling bubble cavitation was usually detected slightly earlier than the attached spot cavitation on headform T-8. These two types of cavitation were observed at about the same value of $\sigma_i = 0.4$. At $\sigma < 0.4$ the traveling bubble cavitation was still observed intermittently even though a large amount of attached cavitation spots had developed at the location of $-C_{pmin}$.

The discontinuity in the body curvature (headforms S-1 and S-10) tends to cause laminar separation. The large adverse pressure gradient on headform S-2 is sufficient to cause laminar separation even though there is no discontinuity in the body curvature. It is true that headforms T-3, T-6, and T-8 are free from curvature discontinuity.

Following definitions proposed by Professor Arakeri, the traveling bubble cavitation observed on headforms T-3, T-6, T-8 is type T-B and the attached spot cavitation is type S-A. Cavitation on S-1 is type B-B. The cavitation ring observed on S-10 is type B-A. At $\sigma_i = -C_{ps}$ large splashing cavitation with wedge leading edge appears and disappears randomly around the separation line on S-2, and these cavitation spots merge together to form a ring cavity of type B-A.

[1]Department of Mechanical Engineering, Indian Institute of Science, Bangalore, 560012, India

Viscous Effects in the Inception of Cavitation

V. H. Arakeri
Department of Mechanical Engineering,
Indian Institute of Science,
Bangalore, India

Allan Acosta
Division of Engineering and
Applied Science,
California Institute of Technology,
Pasadena, California

The inception of cavitation in the steady flow of liquids around bodies is seen to depend upon the real fluid flow around the bodies as well as the supply of nucleating cavitation sources – or nuclei – within the fluid. A primary distinction is made between bodies having a laminar separation or not having a laminar separation. The former group is relatively insensitive to the nuclei concentration whereas the latter is much more sensitive. Except for the case of fully separated wake flows and for gaseous cavitation by diffusion the cavitation inception index tends always to be less than the magnitude of the minimum pressure coefficient and only approaches that value for high Reynolds numbers in flows well supplied with nuclei.

Physical Background

One of the earliest photographic observations of cavitation bubble growth history near inception is that due to Knapp and Hollander [1]. Their findings were predicted with good accuracy by Plesset [2] employing the Rayleigh equation of bubble dynamics. One of the assumptions in this analysis was that the bubble travels at a velocity equal to that of the surrounding liquid velocity neglecting the effect of the boundary layer. However, based on a similar assumption Parkin [3] found that the predicted incipient cavitation number was in some cases an order of magnitude different from the observed one on hemispherically nosed axisymmetric bodies. He then suggested that the neglect of the role of the boundary layer or the viscous effects in the dynamics of cavitation bubbles may not be justified for the particular headform studied by him. This suggestion by Parkin was perhaps motivated from Kermeen's [4] photographic observations of a region of macroscopic and microscopic cavitation bubbles in the immediate vicinity of the surface of a hemispherically nosed test body at incipient conditions. These findings no doubt must have prompted Parkin and Kermeen [5] to conduct their now classic experiments which clearly demonstrated that there are viscous effects important for cavitation inception. Two types of cavitation are observed then on a smooth body; one, that of the traveling bubble type not apparently influenced by the viscous effects, and the other, that of the surface or an attached type of cavitation which is influenced by the viscous effects.

The work of Parkin and Kermeen though quoted extensively in later works does not seem to have been pursued further until very recently when Arakeri and Acosta [6] repeated their observations on a hemispherically-nosed body augmented, however with the schlieren technique of flow visualization. A photograph from this recent work is shown in Fig. 1. Since the schlieren technique is an optical method of flow visualization one can observe the cavitation inception process and the viscous flow past the test body simultaneously. From the first photograph of Fig. 1 the macroscopic bubbles readily visible to the naked eye are to appear in the reattachment zone of a laminar separated region. Subsequent reduction in pressure results in the separated region being filled with an attached cavity which has a glossy smooth surface at the leading edge as can be seen in the third photograph of Fig. 1. In a later study [7] similar observations on a 1.5 cal ogive showed that macroscopic cavitation bubbles occurred within the turbulent transition region of an attached boundary layer at desinent cavitation conditions. These observations shown in Fig. 2 were made

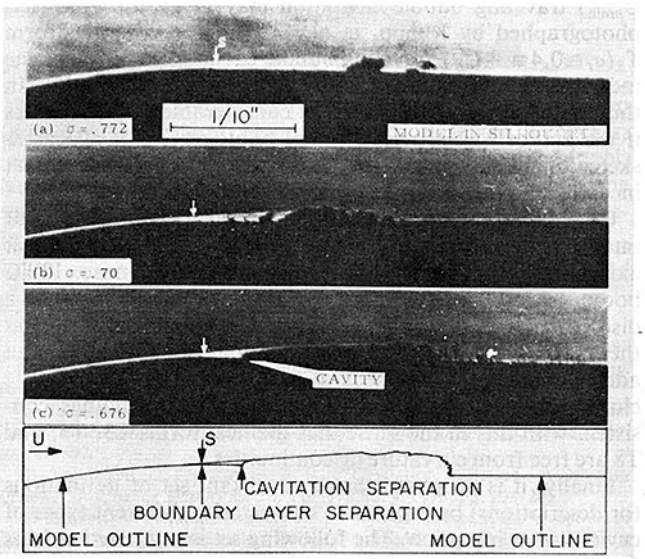

Fig. 1 Form and extent of cavitation originating within the viscous separated region of the hemispherical nose at three different levels of tunnel pressure. (U = 40 fps, $Re_D = 6.04 \times 10^5$). The dark patches above the model outline are the cavitating areas. Arrow shows the location of separation. Flow from left to right. (Arakeri and Acosta, 1973).

Contributed by the Fluids Engineering Division and presented at the International Symposium on Cavitation Symposium, ASME Winter Annual Meeting, New York, N.Y., December 2–9, 1979. Manuscript received by the Fluids Engineering Division, February 11, 1980.

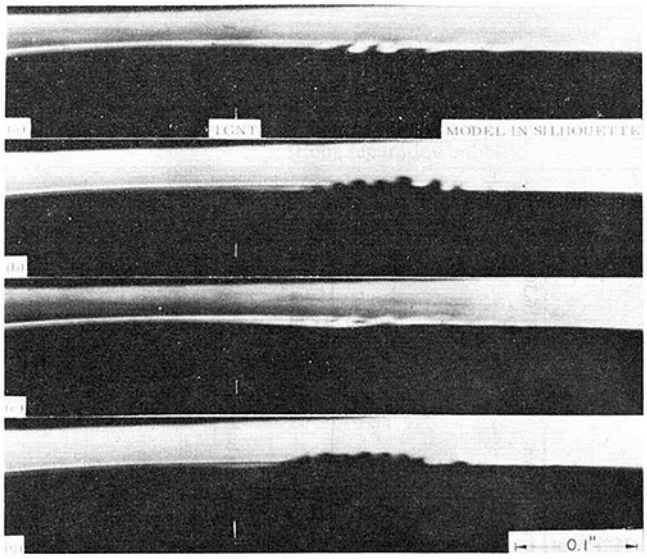

Fig. 2 Photographs showing relationship between boundary layer transition and cavitation. (*a*) and (*c*) – Schlieren photographs at 30 fps and 40 fps respectively showing transition. (*b*) and (*d*) extent of cavitation at the same velocities. The model is a two inch 1.5 cal ogive and the flow is from left to right, (Arakeri and Acosta, 1974).

under desinent conditions i.e., as the cavitation was made to disappear, since at inception the cavity appeared in an attached and developed stage. Thus, the critical zone for cavitation inception with laminar separation is found to be the reattachment region and in the absence of laminar separation it appears to be the region of turbulent transition. These findings suggest that certain special features of turbulent transition and reattachment must play a significant role in the mechanism of cavitation inception.

Features of Turbulent Transition and Reattachment

One of the special features of turbulent transition and reattachment of laminar free shear layers is the intense pressure fluctuations there [8,9]. These fluctuations are an order of magnitude greater than those existing down-stream in the fully developed turbulent flow. It is possible then that the transient pressure in the zones critical for cavitation may be lower than the minimum static pressure on the body (determined by measurements of theoretical computations). Measurements of pressure fluctuation quoted earlier indicate that this is a likely possibility for the hemispherically nosed body but not for the 1.5 cal ogive. However, even in the case of the 1.5 cal ogive limited cavitation was observed in the turbulent transition region rather than the location of minimum pressure point. This strongly suggests that additional features of turbulent transition and reattachment are involved for making these zones critical or important for cavitation inception.

There are a number of additional physical scale parameters that are normally identified with turbulence such as the magnitude and time scale of the velocity fluctuations within the boundary layer that may be important in cavitation. For example turbulent fluctuations may actually stall the local flow near the wall leading to a brief period of separation (Schlichting [10]) or a turbulent burst with reverse flow may occur (Kline and Runstadler [31]). Then it is easy to imagine that cavitation nuclei within these regions may be exposed to a low pressure longer than would otherwise be the case, thereby promoting cavitation by microscopic bubble growth. Time scales for such events are not known but as an illustration let us take the period of the most unstable Tollmein-Schlichting wave in the laminar boundary layer just prior to transition as a representative time for such a process. The frequencies of such motion on a 1.5 cal ogive in a particular water tunnel experiment were found to be about 5 KHz [8]; our reference time period for growth then would be about 0.2 ms which is about the same as that observed for a bubble lifetime on a hemisphere cavitation test (0.1 ms (5)). Thus we find it most plausible that turbulence and pressure fluctuations may definitely help the inception process. Direct experimental evidence within transition regions of microbubble growth into cavitation inception, however, still remains to be provided. Nevertheless, it seems plain that these fluctuations are the reason that the reattachment region downstream of a laminar separation is so critical. On bodies not having a laminar separation the fluctuations associated with transition are undoubtedly important but it has not been possible yet to quantify these effects.

Classification of Axisymmetric Bodies

In the preceding paragraphs we have noted that viscous effects can play a fundamental role in the mechanism of cavitation inception. Thus, for example, one may expect the cavitation characteristics of a separating class of bodies to be different from the cavitation characteristics of nonseparating class of bodies. Beyond that it seems reasonable to propose additional sub-categories as is done in Table 1. The separating class of bodies will exhibit laminar separation only for Reynolds numbers, Re, below a critical Re_{crit}. Our estimations[1] show that for the bodies of group *C* $\mathrm{Re}_{crit} \approx 5 \times 10^5$ to 10^6. Similarly, we estimate that Re_{crit} for group *B* bodies is at least 5×10^6. Guided by the shape of the pressure distribution [11] for the disk and zero (0) cal ogive, Re_{crit} for

[1] By use of e^D, *n*, 7 method and stability charts computed Wazzan et al., Rept. No. DAC 67086, McDonnell Douglas Corp., Calif. Sept. 1968. Also see appendix of reference [6].

Nomenclature

a,b,c = constants in Table 1
C_p = pressure coefficient, $(p - p_\infty)/\frac{1}{2}\rho u_\infty^2$
C_{pm} = minimum value of C_p
C_{ps} = C_p at the position of laminar separation
C_{ptr} = C_p at the position of turbulent transition
$C_{p'}$ = C_p based on magnitude of fluctuating pressure at reattachment
D = diameter of the axisymmetric headform
k = roughness height
p = local static pressure
p_m = minimum static pressure
p_v = vapor pressure of water
p_∞ = reference static pressure
Re = Reynolds number, $u_\infty D/\nu$
Re_{crit} = critical Reynolds number at which laminar separation disappears
Re_k = roughness Reynolds number, $u_k k/\nu$
u_k = velocity at roughness height in the boundary layer
u_∞ = reference velocity
ν = kinematic viscosity
ρ = density
σ = cavitation number, $(p_\infty - p_v)/\frac{1}{2}\rho u_\infty^2$
σ_i = incipient cavitation number

Table 1 Cavitation of Axisymmetric Bodies

Body Shape	$-C_{pm}$	$-C_{ps}$	Measured σ_i range	Group	Viscous Flow Characteristics	Inception Scaling Trends "Few" Nuclei	Inception Scaling Trends "Copious" Nuclei	References
Disk	0.5	0.5	1.4-2.0	*A*	Transition in the free shear layer. Formation of strong and large vortices downstream of separation.	Strong Reynolds number dependence. Scaling determined by vortices and mixing in the free shear layer. $\sigma_i \doteq a + b\,\mathrm{Re}^c$		[20,21,23,42]
0 cal ogive	0.61	0.57	1.4-1.75					
1/8 cal ogive (long separation bubble)	0.83	0.69	1.4-1.75					
1/8 cal ogive (short separation bubble)	–	–	2.05-2.2	*B*	Transition determined by reverse flow velocity profile stability. Formation and strength of vortices affected by the near wall. Measurements show strong wall pressure fluctuations near reattachment.	Weak Reynolds number effect $\sigma_i \doteq -C_{ps} + c_p'$ (equation (1)) Attached band or sheet cavities	Attached and traveling bubbles	[6,13,18,22]
1/4 cal ogive	1.1	0.96	1.15-1.35					
1/2 cal ogive	0.74	0.63	0.6-0.7					
1 1/2 cal ogive	0.4	0.24	0.2-0.25 (below Re_{crit})	*C*	Transition determined by velocity profile stability. No wall pressure fluctuation measurement exist for this class of bodies.	Reynolds number effect not well known $\sigma_i \doteq -C_{ps}$		[7,13,16,36]
ITTC Body	0.6	0.45	0.35-0.45					
NSRDC Body	0.8	0.4	0.4 (below Re_{crit})					
Blunt Body (Other bodies *of Group B,C* above Re_{crit})	0.75	no separation	0.28-0.60	*D*	Transition determined by velocity profile stability. Measurements show mild pressure fluctuations in transition region.	Potential strong Reynolds number effect $\sigma_i \doteq -c_{ptr}$ Attached cavities	$\sigma_i = -c_{pm}$ Traveling bubbles	[12,16,32,33,34]

Table 2 Similarities of Viscous Flow Regimes

Group	Examples of Axisymmetric Bodies	Likely practical situations with similar viscous flow regime
A	Disk 0 cal ogive 1/8 cal ogive (Long separation bubble)	Tip vortex flows Flow downstream of partially closed valves Flow downstream of orifices Flow downstream of hydraulic gates
B	1/8 cal ogive (Short separation bubble) 1/4 cal ogive 1/2 cal ogive	Flow on the suction side of ship propellers, blades of hydraulic machinery and strut elements at angles of attack. Flow down-stream of isolated roughness elements present in the laminar boundary layer.
C	1 1/2 cal ogive ITTC body NSRDC body	Underwater bodies and appendages
D	Blunt body Bodies in other groups for $Re > Re_{crit}$	Flow on the pressure side of ship propellers, blades of hydraulic machinery and strut elements at angles of attack. Flow past ship propellers, blades of hydraulic machinery and strut elements at zero angles of attack.

Note: One important viscous flow regime that of fully developed turbulent boundary layer flow in the region of interest is not included here. However, this regime has been covered by Arndt and Daily [23].

these two bodies in group *A* is expected to be of the order 10^7 to 10^8. Flow visualization studies [12] on a 1/8 cal ogive have indicated another relatively high critical Re judged by the marked change in the length of the region of laminar separation. This phenomenon is commonly termed "bursting" and its connection with cavitation scaling has been noted recently by Huang and Peterson [13]. The magnitude of $-c_{ps}$ noted in Table 1 was predicted with the use of Thwaites & Smith [14, 15] method for NSRDC, ITTC, 1 1/2 cal and 1/8 cal bodies and from inferences from the pressure distributions for 0 cal body and disk. The Thwaites method as well as more accurate methods do not predict laminar separation for the blunt body and this is consistent with observations of van der Muelen [16]. (Sufficiently accurate pressure distribution measurements on the 1/8 cal ogive with a short separation bubble are now not available to permit accurate boundary layer calculations.) The inception data given in Table 1 are for a nominal Re range of 10^5-10^6 and are taken from references [17-19, 35].

It may be noted from Table 1 that bodies in different groups exhibit differing viscous flow characteristics and, as suggested, these differences in turn play a role in cavitation scaling characteristics. The prominent viscous flow feature for the bodies in group *A* is the formation of strong freestream vortices downstream of a laminar separation and, at least for the disk, cavitation has been observed [20] to commence at the center of these vortices. It is worthy of note that even though the three bodies in group *A* possess differing magnitudes of $-C_{pm}$ and $-C_{ps}$, the measured σ_i values indicate a strong dependence only on Re. Thus, an empirical rule of the type proposed by Arndt [21] may work quite effectively for the class of bodies in this group. The separated shear layer is close to the wall for the class of bodies in group *B* so that its stability characteristics and formation of reattachment fluctuations are strongly influenced by the presence of the wall. These flows as discussed exhibit strong pressure fluctuations in the reattachment region. Thus, for this type of body we propose that the cavitation index should be of the form,

$$\sigma_i = -C_{ps} + C_{p'} \tag{1}$$

as has been suggested by Huang and Peterson [13]. They further indicate that $C_{p'}$ should be taken as a constant; it is most likely a function of at least the maximum height of the separated free shear layer from the wall and would seem therefore Reynolds number dependent. A laminar separation still prevails for the bodies in group *C* but with free shear layer extremely close to the surface. Thus, the normal reverse flow region in the mean and the constant pressure region commonly associated with separated flows may not even exist for these bodies. Based on experimental observations [6,22] the fluctuating pressure term of equation (1) seems not too important here and it is proposed that

$$\sigma_i = -C_{ps} \tag{2}$$

for this group.

There remains, finally, the smooth bodies of group *D* those not having a separation. It follows that under practical conditions of flow a turbulent transition is inevitable. It has been traditional to assume for this kind of shape that cavitation will occur when $p_m \leq p_v$ or that

$$\sigma_i = -C_{pm}. \tag{3(a)}$$

There is much evidence that this rule may be applicable to some flows. Silberman [32] and Schiebe [33] earlier use this idea to infer from the rate of individual traveling bubble cavitation events for $\sigma < \sigma_i$ the number density of the cavitation nuclei within the free stream. There is also evidence that in flows not so well supplied with free stream nuclei that $\sigma_i < -C_{pm}$ (without a significant number of events taking place). In this circumstance it seems plausible and it has been proposed based on experiments [7,18] that

$$\sigma_i = -C_{ptr}. \tag{3(b)}$$

This suggestion was made based on tests made on bodies for $Re > Re_{crit}$ belonging to group *C* although there is recently direct evidence based on bodies of group *D* (e.g., Huang and Santelli [34], Carrol and Holl [19] and Gates, et al. [35]). It seems clear then that inception scaling for this group of bodies may depend strongly on both Reynolds number and nuclei content.

We have suggested certain scaling rules for differing viscous flow regimes. Even though these have been derived from axisymmetric bodies, they are of practical value since these viscous flow regimes are encountered in a wide variety of applications as indicated in Table 2.

Remark on Scaling

It is clear that σ_i can be Reynolds number dependent. This dependence varies greatly within the groups of Table 1, however. It is interesting to compare the Reynolds number

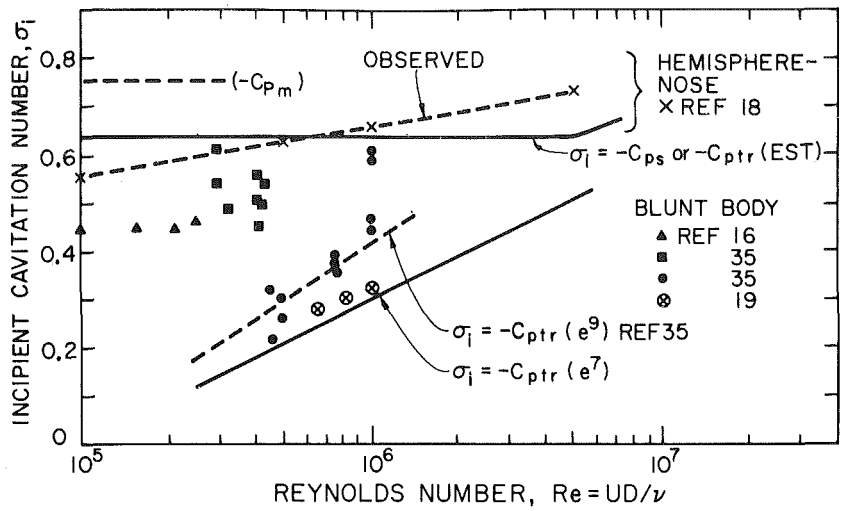

Fig. 3

effect on two bodies having nearly the same minimum pressure coefficient, $-C_{pm} = 0.75$. These are the hemisphere nose and the blunt half body. (This body formed by a source disk is described in detail in references [32,33]; the authors of reference [35] have adopted the name 'Schiebe' body for this blunt body although van Tuyl, Schiebe ibid, was the first to describe this shape). The hemisphere nose, it will be recalled, has a laminar separation to a fairly high Re of about 5×10^6; within the laboratory range, σ_i remains less than $-C_{pm}$ but does not vary more than about 30 percent. (There is a size effect or unit Reynolds number effect still not resolved (see, e.g., reference [36]). The blunt body, however, is quite a different story. Data from several sources show nearly a 3:1 change in σ_i with most of the change occurring in overlapping (lower) Reynolds numbers. Estimates have been made of the location of transition and the pressure coefficient there. Those together with experimental results are shown in Fig. 3 for both bodies. The dominant Re effect on transition of the blunt body is clear. Much of the data tend to follow this trend. Yet there are also extensive findings on the same shape showing a higher value σ_i but still rather well below $-C_{pm}$. (It should perhaps be mentioned again that the blunt body does not experience a separation and that the hemisphere body does.)

From these results we see that although there is a definite difference in σ_i levels for the hemisphere body with Re, equations (2) and (3(b)) provide a good guide over a wide range. Thus the presence of the laminar separation does not seem to lead to as large of a scale effect as on an unseparated flow. The two groups of data shown for the blunt body appear to follow different trends. The conditions under which the various tests were made are also rather different. In particular those results following equation (3(b)) ($\sigma_i \sim -C_{ptr}$) are for tunnel flows having "few" free-stream nuclei. Those data having a higher value of σ_i (but lower Re certainly) originate in flows of "generous" or "copious" nuclei. There are more basic differences, however; freestream traveling bubble cavitation is the predominant form of cavitation in nonseparating flows having many nuclei. When these nuclei become fewer, attached forms of cavitation are seen; these appear often to be associated with transition as is shown on Fig. 2. Thus, the freestream supply of nuclei is very important for cavitation inception on group D bodies and group B, C bodies too when beyond the critical Reynolds number. Thus we see that the σ_i = const. rule works considerably better for bodies which possess a laminar separation. It would be better than in model testing say at Re = 5×10^5 for prototype values Re = 10^7 to use the rule $(\sigma_i)_{\text{prototype}} = (\sigma_i)_{\text{model}}$ if a laminar separation is observed or predicted on the geometrical similar body during model testing, this despite the fact that a change in the viscous flow regime may be involved in going from model to prototype conditions (as would be the case for the 1/2 cal ogive). Even though a change in viscous flow regime is not involved for flows on bodies lacking a laminar separation a significant error is possible in predicting the prototype σ_i by using the rule $(\sigma_i)_{\text{prototype}} = (\sigma_i)_{\text{model}}$. Eventually for sufficiently large Re, $\sigma_i \rightarrow -C_{pm}$ provided sufficient nuclei are present.

Influence of Disturbances

The means (theory or experiment) employed in determining the viscous flow regimes are always based on certain ideal assumptions. These include, for example, negligible levels of freestream turbulence, surface roughness, and mechanical vibration as well as symmetry and uniformity of the flow field. "Natural" or "stimulated" disturbances lead to flow modifications, and possibly to transition and have occupied a central role in applied fluid mechanics for decades. In respect to cavitation we now categorize some of these features:

(a) Natural disturbances. These can include the free stream turbulence level, body vibrations and either distributed or isolated roughness elements. The roughness effect on cavitation inception has been studied quite extensively in the past and a comprehensive compilation of these and other related findings has been made recently by Bohn [24]. Here, we concentrate on the effects of an isolated roughness since this may have a bearing on the explanation for the commonly observed "spot" type of cavities [18] observed on bodies of group C above their critical Reynolds numbers or those of group D at higher velocities.

As pointed out by Holl [25] one can view the effect of isolated roughness as a local modification of the pressure field from which changes in σ_i can be inferred. Of course it is plain that the velocity field is modified too; Klebanoff and Tidstrom [26] have observed experimentally that a flat plate boundary layer velocity profile develops locally a separating velocity profile downstream of an isolated roughness. Furthermore, they point out that this is the mechanism by which roughness elements induce an earlier turbulent boundary layer transition. Any such region of flow offering residence time for growth of nuclei becomes a candidate for a cavitation mechanism. The important parameters determining this local flow are the relative height of the roughness with respect to the local boundary layer thickness and the roughness Reynolds number $\text{Re}_k = u_k k/\nu$, k being the roughness height,

and u_k the velocity there. Traditionally, $\mathrm{Re}_k < 25$ to forestall transition; this empirical result is however largely based on experience in flows with mild pressure gradients, not the extremely adverse one of bodies in group D, for example. We find it very plausible then as do Huang and Peterson [13] to suspect that very small isolated roughness elements, perhaps much less than $\mathrm{Re}_k = 25$ are the origin of the spot and wedge forms of cavitation seen at inception for higher values of Reynolds number. One would further imagine that the predominant form of cavitation in flows not having "many" nuclei at large Reynolds numbers would be these attached "spots".

Systematic work concerning the role of body vibrations in determining the location of turbulent transition appears to be lacking. But there has been a recent rejuvenation of interest in freestream turbulence on transition (e.g., Mack [37]). Interest in these flow characteristics of some of the bodies traditionally used for cavitation inception work is recent and we may cite the work of Gates [27] and van der Muelen [16] as examples. Gates found that the boundary layer flow of the 1/2 cal ogive (belonging to group B) was insensitive to a change in the freestream turbulence level of over an order of magnitude! A similar change in the turbulence level on the NSRDC body lowered the critical Re to 1.6×10^5 at a freestream turbulence level of 3.75 percent from the observed critical Re of 5×10^5 at a freestream turbulence level of 0.2 percent. The response of the NSRDC body was expected because the test Reynolds numbers were close to the predicted critical Re for the NSRDC body and were significantly lower than the predicted critical Re for the 1/2 cal ogive. In any case, these findings by Gates are significant since cavitation inception studies are routinely carried out in flow facilities having greatly differing levels of freestream turbulence. Gates also found another type of disturbance which may be classified as "natural" to the flow field; namely, that an existing laminar separation could be eliminated by the presence of a significant number of macroscopic air bubbles in the freestream. This change resulted in traveling bubble type cavitation at inception instead of a normally occurring "band" or attached type of cavitation at inception.

(b) Stimulated disturbances. One usually means here a boundary layer "trip" consisting either of an isolated roughness element or a distributed surface roughness. It is necessary that these disturbances be located in the high pressure regions of the flow so that they themselves do not cavitate prematurely. It may seem attractive to use these boundary layer trips to simulate a high Reynolds number as commonly done for drag measurements. This may be a misleading practice for cavitation inception studies, however. For example, the σ_i value was found to decrease with increase in Re to very low values (0.25) on a tripped 1/2 cal ogive contrary to the normal expectation (reference [18]). As noted there this behavior is attributed to drastic alteration in the location of turbulent transition by tripping and to the presumed smaller concentration of nuclei in the test facilities used. Therefore, when boundary layer stimulation used the turbulent transition location in the test model it should be carefully matched to the expected location at the higher prototype Re. In practice, this is exceedingly difficult to achieve. Thus, even though use of a boundary layer trip certainly helps to simulate high Reynolds number for normal test work cavitation inception may be delayed.

The addition of dilute polymer solutions to the test fluid has a pronounced effect on cavitation inception namely, to suppress the onset of cavitation, as does stimulation by a trip. The effect was first observed by Ellis [28] and since it has been repeated by many investigators [29,30,27]. Essentially identical effects have been found either by injecting the dilute polymer solution at the nose of the body or by dissolving the polymer solution in the tunnel water. In either case the suppression of the cavitation index has been the subject of much speculation: In particular, is the growth of the cavitation bubbles themselves inhibited by the polymer or is there another cause? It does appear that bubble growth and collapse can be affected by these non-Newtonian additives but the primary cause was later shown by van der Muelen [16] and Gates [27] to be an early boundary layer transition caused by the polymer solution. The polymer in effect stimulates the boundary layer sufficiently to remove the pre-existing laminar separation on the hemisphere nosed body used for investigation. The suppression effect on the cavitation index is due then principally to the different real fluid flow regime on the body. Bodies such as those in group D and B, C (beyond the critical Reynolds number) tend to follow the scaling laws of equation (3(b)) (depending) on nuclei content with the eventual high Reynolds number behavior of equation (3(a)).

Discussion

We see then that there is substantial experimental evidence that the characteristics of the viscous flow about a body can influence the inception of cavitation. Intuitively, we would expect this to be true for flows with gross separated regions as is the case for class of bodies in group A of Table 1. Similarily, we may expect for other types of separated flows these viscous effects to be important in the inception process when

$$-C_{ps} + C_{p'} \geq -C_{pm} \tag{4}$$

$C_{p'}$ being the amplitude of the transient pressure fluctuations. There is now a considerable amount of evidence that the nuclei content of the fluid or cavitation "susceptibility" of the fluid is not so important when the flow satisfies equation (4). When this is not so, we infer that inception will be influenced more heavily by the number of freestream nuclei. Thus we would propose that bodies of groups C, D are more "nuclei sensitive" than those of group B, say. When a copious supply of nuclei are present we would expect a preponderance of traveling-bubble cavitation, the type originally photographed by Knapp. Then, as argued by Silberman, for example, σ_i approaches $-C_{pm}$ as a limiting case. But such copious supplies of nucleating sources are not always available – even in the natural waters of the ocean – and then the suggested rules of Table 1 appear on the basis of experiment to be the appropriate guide lines. We are left then with a facility-dependent environment, one depending on the freestream nucleation content, in determining the particular inception value as has been demonstrated by the water tunnel experiments of Keller [38]. It may be possible, for cavitation indices to be smaller than even those indicated in Table 1, for example, in utterly deaerated quiescent liquids. (It is readily possible for these indices to be much greater than $-C_{pm}$, particularly for group B bodies when the liquid is supersaturated in respect to air; then air diffusion controls as Holl has shown[2] and gaseous cavitation is said to occur.)

The preceding comments have all been directed towards well-defined laboratory types of experiments. What may be said concerning cavitation inception in the more realistic flow environments of engineering applications such as large pumps and turbines? We may say as a preliminary comment, certainly for applications to pumps, that inception per se is rarely of interest. Instead, questions of erosion and performance change by cavitation are more of interest and the inception point merely marks the boundary of the application wherein these features become important. Pumps, for example, often operate with up to three percent head decrease at cavitation

[2] "Cavitation State of Knowledge," Robertson, J.M., Wislicenus, G. (Eds.), ASME, 1969.

indices, far beyond the inception value (see e.g., the discussion of Hammitt [39]). Once cavitation is developed, additional factors enter into the effect on performance; one of these effects, the subcooling of evaporating fluid, is often termed the "thermodynamic scale effect" and has been the subject of much attention over the years (e.g. references [40,41]). This is, however, beyond the present scope of concern. There is no reason to think, however, that pumps, indeed turbines, propellers, and other fluid machines are not subject to the viscous scale effects described herein for inception, although, except for propellers, there seems to have been relatively little effort devoted to this aspect of fluid machine cavitation.

In any case, it is clear from the trends of the scaling laws summarized in Table 1 and mentioned in the discussion that quantification of the nuclei concentration in all these flow environments is now of primary importance in cavitation inception and even developed cavitation phenomena.

Summary and Conclusions

The inception of cavitation is a complex physical process dependent on the concentration of nucleating sources within the flow and many features of the real fluid flow around bodies. Except for separating wake flows the inception index is almost always less than the magnitude of the minimum pressure coefficient and this latter value is only approached as a high Reynolds number limit in flows well-supplied with nuclei. It has been found useful to group the flows into those bodies having or not having a separation and the former category into those having large or small regions of laminar separation. In general, the bodies having a reattaching laminar separation are found to be less sensitive to the nuclei content of the freestream and to have cavitation indices between that of pressure coefficient magnitude at laminar separation and the minimum pressure point. Nonseparating bodies may have the inception phenomenon related to the turbulent transition pressure coefficient but in any case are sensitive to the concentration of free-stream nuclei. No single overriding factor is seen to be responsible for inception so that it does not appear likely that a single scaling law will ever suffice. Nor is there a universal kind of cavitation seen at inception so that a single physical model for cavitation onset will not be sufficient.

Acknowledgment

This work was supported in part by the General Hydromechanics Research Program of the David W. Taylor Naval Ship Research and Development Center under Contract Number N00014-75-C-0378 and the Indian Institute of Science. This support is gratefully acknowledged.

References

1 Knapp, R.T., and Hollander, A., "Laboratory Investigations of the Mechanism of Cavitation," *Trans. ASME,* Vol. 70, 1948, pp. 419-435.

2 Plesset, M.S., "The Dynamics of Cavitation Bubbles," *Journal of Applied Mechanics,* Sept. 1949, pp. 277-288.

3 Parkin, B.R., "Scale Effects in Cavitating Flow," Ph.D. dissertation, Calif. Inst. of Tech., 1952.

4 Kermeen, R.W., "Some Observations of Cavitation on Hemispherical Head Models," Calif. Inst. of Tech., Rep. No. E-35.1, June 1952.

5 Parkin, B.R., and Kermeen, R.W., "Incipient Cavitation and Boundary Layer Interaction on a Stream-lined Body," Calif. Inst. of Tech., Rep. No. E-35.2, Dec. 1953.

6 Arakeri, V.H., and Acosta, A.J., "Viscous Effects in the Inception of Cavitation on Axisymmetric Bodies," ASME JOURNAL OF FLUIDS ENGINEERING, Vol. 95, Dec. 1973, pp. 519-528.

7 Arakeri, V.H., and Acosta, A.J., "Some Transition and Cavitation Inception Observations on a 1.5 Cal ogive," *Proceedings of the 17th ATTC,* Pasadena, Calif. 1974.

8 Arakeri, V.H., "A Note on the Transition Observations on an Axisymmetric Body and Some Related Fluctuating Wall Pressure Measurements," ASME JOURNAL OF FLUIDS ENGINEERING, Vol. 97, Mar. 1975, pp. 82-87.

9 Huang, T.T., and Hannan, D.E., "Pressure Fluctuations in the Regions of Flow Transition," Nav. Ship Res. and Dev. Center, Rep. No. 4723, Dec. 1975.

10 Schlichting, H., *Boundary Layer Theory,* 6th Ed., McGraw Hill, 1968, p. 455.

11 Rouse, H., and McNown, J.S., "Cavitation and Pressure Distribution Hed Forms at Zero Angle of Yaw," State Univ. of Iowa, *Studies in Eng. Bull.,* No. 32, 1948.

12 Arakeri, V.H., Carrol, J., and Holl, J.W., "A Note on the Effect of Short and Long Laminar Separation Bubbles on Desinent Cavitation," *Measurements in Polyphase Flows,* ASME, 1978, pp. 115-120.

13 Huang, T.T., and Peterson, F.B., "Influence of Viscous Effects on Model/Full-Scale Cavitation Scaling," *Journal of Ship Resources,* Vol. 20, No. 4, Dec. 1976, pp. 215-223.

14 Thwaites, B., "Approximate Calculation of the Laminar Boundary Layer," *Aero. Quart.,* Vol. 1, 1949, pp. 245-280.

15 Smith, A.M.O., "Rapid Laminar Boundary Layer Calculations by Piecewise Application of Similar Solutions," *Journal of Aero. Sci.,* Vol. 23, No. 10, Oct. 1956, pp. 901-912.

16 Van der Muelen, J.H.J., "A Holographic Study of Cavitation on Axisymmetric Bodies and the Influence of Polymer Additives," Ph.D. dissertation, Enchede, 1976. (Also available as NSMB Rep. 509, Wageningen, The Netherlands.)

17 Robertson, J.M., McGinley, J.M., and Holl J.W., "On Several Laws of Cavitation Scaling," La Houille Blanche, No. 4, Sept. 1957, pp. 540-554.

18 Arakeri, V.H., and Acosta, A.J., "Cavitation Inception Observations on Axisymmetric Bodies at Super Critical Reynolds Numbers," *Journal of Ship Res.,* Vol. 20, No. 1, Mar. 1976, pp. 40-50.

19 Private communication, J. Carrol and J.W. Holl of the Penn. State Univ.

20 Kermeen, R.W., and Parkin, B.R., "Incipient Cavitation and Wake Flow Behind Sharp Edged Disks," Calif. Inst. of Tech. Rep. No. Eng. 85-4, Aug. 1957.

21 Arndt, R.E.A., "Semi-Empirical Analysis of Cavitation in the Wake of a Sharp Edged Disk," ASME JOURNAL OF FLUIDS ENGINEERING, Vol. 98, No. 3, 1976, pp. 560-562.

22 Casey, M.V., "Cavitation Inception on Hydrofoils," Dept. of Eng. Sci. Rep. 1071/73, Oxford, U.K., 1973.

23 Arndt, R.E.A., and Daily, J.W., "Cavitation in Turbulent Boundary Layers," Cavitation State of Knowledge, ASME, 1969, pp. 64-86.

24 Bohn, J.C., "The Influence of Surface Irregularities on Cavitation: A Collation and Analysis of New and Existing Data with Application to Design Problems," ARL TM 72-223, The Penn. State Univ., Sept. 1972.

25 Holl, J.W., "The Inception of Cavitation of Isolated Surface Irregularities," ASME *Journal of Basic Engineering,* Vol. 82, 1960, pp. 169-183.

26 Klebanoff, P.S., and Tidstrom, K.D., "Mechanism by which a Two-Dimensional Roughness Element Induces Boundary Layer Transition," *The Physics of Fluids,* Vol. 15, No. 7, July 1972, pp. 1173-1188.

27 Gates, E.M., "The Influence of Free Stream Turbulence Free Stream Nuclei Populations and a Drag-Reducing Polymer on Cavitation Inception on Two Axisymmetric Bodies," Calif. Inst. of Tech. Rep. No. 183-2, Apr. 1977.

28 Ellis, A.T., "Some Effects of Macromolecules on Cavitation Inception and Noise," Calif. Inst. of Tech. Rep. under Contract N.60530-12164.

29 Van der Muelen, J.H.J., "The Influence of Polymer Injection on Cavitation," Conf. on Cavitation, Paper No. C 149/74, Edinburgh, Scotland, Sept. 1974.

30 Arndt, R.E.A., "Cavitation Inception: The Influence of Roughness Turbulence and Polymer Additives," ORL TM 71-195, The Penn. State Univ., Aug. 1971.

31 Kline, S.J., and Runstadler, P.W. "Some Preliminary Results of Visual Studies of the Flow Model of the Wall Layers of Turbulent Boundary Layer," *Trans. ASME* Vol. 26, 1959, p. 166.

32 Silberman, E., "The Use of Equivalent Gas Bubble Nuclei to Measure the Cavitation Susceptibility of Water," 14th Intl. Towing Tank Conf., Ottawa, Vol. 2, 1975, pp. 248-251.

33 Schiebe, R., "The Measurement of Cavitation Susceptibility of Water Using Standard Bodies," St. Anthony Falls Hydraulic Lab., Rep. 118, Univ. of Minn., 1972.

34 Huang, T.T. and Santelli, N., "Cavitation Inception Observations on Two Axisymmetric Headforms," DTNSRDC Rep. SPP-807-01, 1977.

35 Gates, E.M., and Acosta, A.J., "Some Effects of Several Freestream Factors on Cavitation Inception on Axisymmetric Bodies," 12th Symp. on Nav. Hydro., Washington, D.C., 1978.

36 Parkin, B.R., Holl, J.W., "Incipient Cavitation Scaling Experiments for Hemispherical and 1.5 Cal Ogive Nosed Bodies," Joint CIT/Penn State Ord. Res. Lab. Rep. NORD 7958-264, 1953.

37 Mack, L.M., "Transition Prediction and Linear Stability Theory," Paper No. 1, AGARD Proc. 224, *Laminar Turbulent Transition,* 1978.

38 Keller, A., "Experimentalle und Theoretische Unter suchungen Fum Problem Der Modellmassigen Behandlum von Stromungskavitation," Bericht

UK 26 Miller Inst. U. Munich, 1973; see also ASME *Journal of Basic Engineering*, Vol. 94, No. 4, 1972, pp. 917–924.

39 Hammitt, F.G., "Cavitation Threshhold and Superheat in Various Fluids," Inst. Mech. Eng. Conf. on Cavitation, 1974, pp. 341–347.

40 Hutton, S.P., and Furness, R.A., "Thermodynamic Scale Effects in Cavitating Flows and Pumps," Inst. Mech. Eng. Conf. on Cavitation, 1974, pp. 341–355.

41 Billet, M.L., Holl, J.W., and Weir, D.S., "Correlations of Thermodynamic Effects for Developed Cavitation," *Polyphase Flow in Turbomachinery*, ASME, 1978, pp. 271–291.

42 Arndt, R.E.A., "Investigation of the Effects of Dissolved Gas and Free Nuclei on Cavitation and Noise in the Wake of a Sharp-Edged Disk," ASCE-IAHR-ASME Joint Symp. on Fluid Machinery, Ft. Collins, Colo. Vol. II, 1978, pp. 543–554.

V.H. Arakeri

V. Ramarajan[1]

Department of Mechanical Engineering,
Indian Institute of Science,
Bangalore, India

Inception of Cavitation From a Backward Facing Step

Cavitation inception measurements are reported for flow past a downstream facing step with the height of the step varying from about 0.4 to 5 percent of the forebody diameter. The forebody was a 49 mm hemispherical nose and σ_i values were found to be very strong function of the height of the step. In addition, σ_i values were found to depend on whether the boundary layer approaching the step was laminar or turbulent. Generally σ_i values for turbulent case were lower.

Introduction

It has now been firmly established that the inception characteristics of axisymmetric bodies are influenced by viscous effects. For example, existence of boundary layer separation was found to play a crucial role in the inception of cavitation on two axisymmetric bodies studied by Arakeri and Acosta [1]. Since then several additional investigations [2–5] have been carried out on axisymmetric bodies which possess laminar separated regions. This is in addition to the studies of Gaster [6] on separated regions created on a flat plate. Figure 1 shows a correlation of (H/θ_s) and Re_{θ_s} for data obtained from various investigations. The magnitude of H, in most cases, was obtained by flow visualization studies. For Gaster's results the definition of H was taken to be the maximum height at which $(u/U_\infty) = 0.1$ as shown in Fig. 2. The magnitude of θ_s was estimated based on Thwaites' method with the help of existing pressure distribution measurements. For axisymmetric bodies it was found that

$$\mathrm{Re}_{\theta_s} = C_1\sqrt{\mathrm{Re}_D}$$

where Re_D is the Reynolds number based on body diameter and C_1 is a constant depending on the forebody shape. Magnitude of C_1 estimated for different bodies is shown in Table 1.

The magnitude of θ_s in Gaster's experiments was measured. It is clear from Fig. 1 that (H/θ_s) correlates well with Re_{θ_s} and in a limited range of Re_{θ_s} behaves linearly. It is expected that for $\mathrm{Re}_{\theta_s} < 100$ separation bubble will be "long" as per description of Gaster [6] and for Re_{θ_s} near 400 or greater, laminar separation will most likely be eliminated. Another interestng point to note from Fig. 1 is that the observed values of (H/θ_s) for the experiments of Arakeri, et al. [1], and Gates, et al. [4] vary significantly for two different hemisperhically nosed bodies of essentially the same diameter. From the observed values of σ_i for the same two investigations and shown in Fig. 3 it is tempting to conclude that σ_i is dependent on the height of the free shear layer from the wall for separated flows. Therefore, it was felt that a systematic investigation could be made on this aspect by studying the inception characteristics of various sized downward facing step. The forebody upstream of the step was chosen such that the observed σ_i values would be reasonably high so that the nuclei characteristics of the facility and gaseous effects may not play a significant role in determining the magnitude of σ_i values. In view of this, the forebody chosen in the present experiments was a hemispherical nose rather than a flat plate. Additional motivation for the present study was that a downward facing step can be considered as a type of surface irregularity and this particular shaped irregularity has not been investigated from the point of view of cavitation inception characteristics, even though several other shapes have been studied by Holl [7] and Bohn [8].

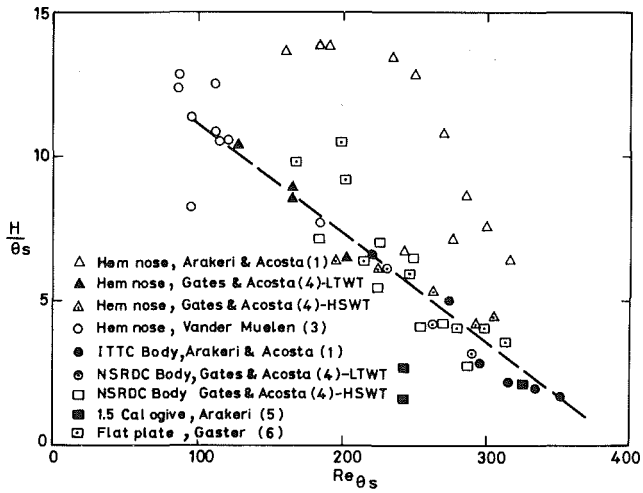

Fig. 1 Correlation of (H/θ_s) versus Re_{θ_s}

Test Facility

The experiments to be reported were carried out in the axisymmetric test section of the Indian Institute of Science high-speed water tunnel. A description of the facility is contained in an early publication by Seetharamaiah and Nanjundaswamy [9] and also in a more recent report by Arakeri and Govinda Ram [10]. A schematic diagram of the

[1] Mr. Ramarajan is currently with BHEL R and D Centre, Hyderabad, India.

Contributed by the Fluids and Engineering Division and presented at the International Symposium on Cavitation Inception, ASME Winter Annual Meeting, New York, N.Y., December 2–9, 1979, Manuscript received by the Fluids Engineering Division, February 11, 1980.

Table 1 Magnitude of C_1 for various axisymmetric bodies

Body Shape	C_1
Hem Nose	0.32
ITTC Body	0.41
NSRDC Body	0.45
1.5 Cal ogive	0.56

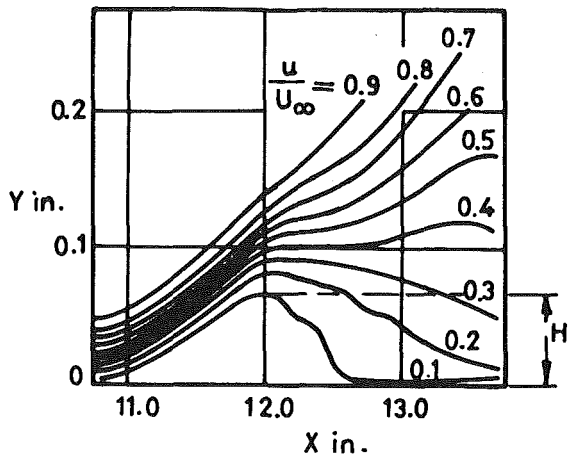

Fig. 2 Definition of H for Gaster's studies

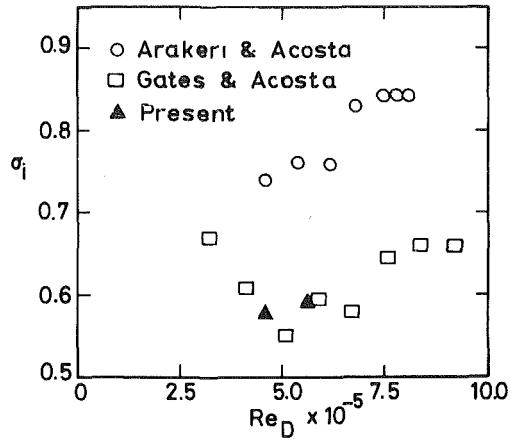

Fig. 3 σ_i versus Re_D for hem-nosed bodies

test facility is shown in Fig. 4. The axisymmetric test section is 381 mm in diameter and has an overall length of 1520 mm. The four sides of the test section are provided with 914 mm × 254 mm clear plexiglass windows for photographic and observational purposes. The top window can be replaced with a metallic hatch cover from which test bodies can be mounted. The test section is followed by a small transition section and then a diffuser. The inner profile of the transition section is such that its slope at the beginning is zero and then gradually increases to a value which matches with the slope at the entrance of the diffuser. To avoid the possibility of flow separations the overall diffuser angle has been kept to a small value of 6 deg. The diffuser is followed by two 90 deg bends to facilitate the mounting of a vertically driven propeller type of pump impeller with a diameter of 1320 mm. The flow at the exit of the impeller is led to a resorber tank through a 90 deg bend.

The resorber consists of a horizontal tank with a diameter of 3660 mm and a length of 7360 mm. Internally, baffles are provided to increase the residence time of the air bubble water mixture. The location and the geometry of the baffles in the resorber tank is shown in Fig. 4 by dotted lines. The resorber tank is followed by two 90 deg bends, a vertical constant diameter leg and an unusually long settling chamber. The diameter of the vertical leg and the settling chamber is 1524 mm. Finally, the settling chamber and the test section are connected via a carefully designed contraction cone with an overall contraction ratio of sixteen. All the 90 deg bends in the present facility are equipped with guiding vanes. A honeycomb having square cells measuring 25.4 mm by 25.4 mm with an aspect ratio of 5 is also provided in the settling chamber. Therefore, in view of these flow corrective devices and in addition to the high contraction ratio it is not surprising that preliminary velocity profile measurements indicate that it is uniform within one percent of the center-line velocity. The free stream turbulence level has not yet been measured; however, it is expected that it should be lower than many other similar facilities having smaller contraction ratios.

In the other aspects the design capabilities of the present facility compare quite favorably with other major similar facilities existing elsewhere. The maximum design speed in the present test section is 30 m/s. Speed control is possible by varying the resistance of the rotor winding of a 600 hp a-c induction motor. Due to high power dissipation involved, the resistance of the rotor winding is changed by movement of two electrodes immersed in a liquid bath. In addition to speed control, the pressure can be changed independently. This is accomplished by varying the pressure in a partially filled dome located at the top of the settling chamber. By this method the pressure at the settling section has been varied from about 0.36 to 2.6 bars absolute. It is proposed to increase this range by incorporating a modified pressure control system located at the top of the resorber tank. Experience

Nomenclature

a,b,C = constants in the power law
C_1 = constant in Table 1
C_p = pressure coefficient, $(p - p_\infty)/\frac{1}{2}\rho U_\infty^2$
C_{ps} = pressure coefficient at separation or isolated irregularity
$C_{p'}$ = pressure coefficient based on fluctuating pressure
D = diameter of the body
H = maximum height of the separated free shear layer
h = height of the downstream facing step
p = local static pressure
P_∞ = free-stream tunnel static pressure
P_v = vapor pressure of water
Re_{θ_s} = Reynolds number based on momentum thickness, $U_\infty \theta_s/\nu$
Re_D = Reynolds number based on body diameter, $U_\infty (D/\nu)$
U_e = local velocity at the edge of the boundary layer
U_∞ = free-stream tunnel velocity
δ = boundary layer thickness
ν = kinematic viscosity of water
ρ = density of water
σ = cavitation number or index, $(P_\infty - P_v)/\frac{1}{2}\rho U_\infty^2$
σ_i = incipient cavitation number
σ_{ir} = incipient cavitation number with surface irregularity in the power law
σ_d = desinent cavitation number
θ_s = boundary layer momentum thickness at separation

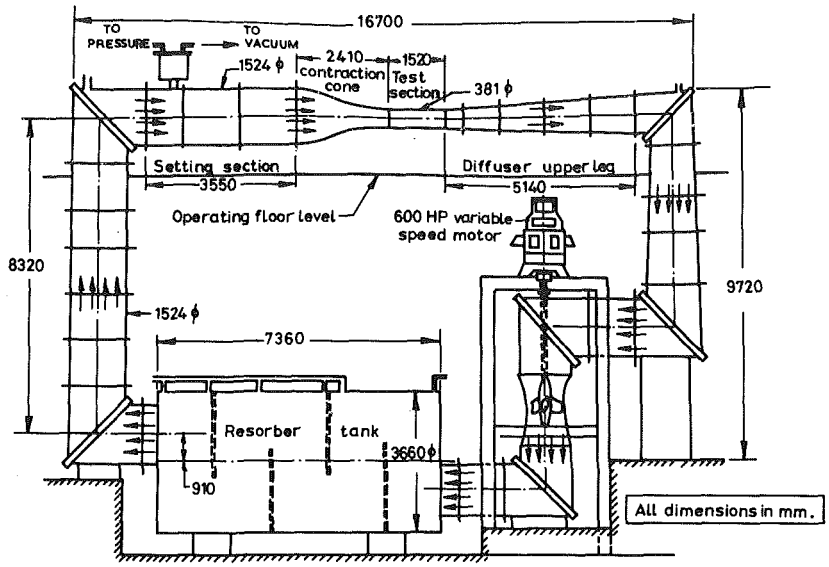

Fig. 4 Schematic diagram of the I.I.Sc. high-speed water tunnel

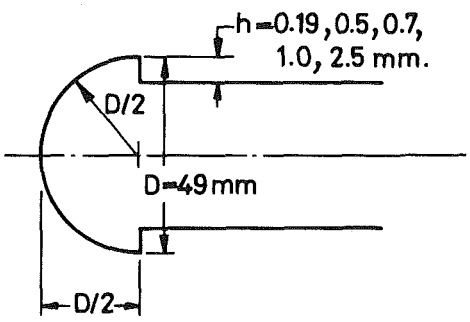

Fig. 5 Geometrical details of model with a step

from recent inception studies [10] indicates that the facility is quite suitable for cavitation studies. In particular, the resorber was found to function quite adequately and very few free-stream macroscopic air bubbles were observed with cavitation numbers as low as 0.3 in the test section. However, it must be pointed out that the present resorber design is a compromise between no resorber at all and a resorber of the type existing at the California Institute of Technology high-speed water tunnel facility.

Experimental Methods

The test model used in present experiments was a 49-mm dia hemisperhical nosed body made of stainless steel. The model occupied only 1.67 percent of the throughflow area and hence blockage effects are expected to be negligible. The accuracy of the contour at 10X magnification was found to be within 0.05 mm of the theoretical shape. Various sized downstream facing steps were cut at the tangent point and the geometrical details of the model with a step are shown in Fig. 5. The step size, h values were 0.19 mm, 0.5 mm, 0.7 mm, 1.0 mm, and 2.5 mm giving (h/D) values of 0.0039, 0.0102, 0.0143, 0.0204, and 0.0510, respectively. It may be noted that on a hemispherical nose laminar separation has been observed [1] to take place at about 87 deg or slightly upstream of the tangent point. Observations with the inception of the band type of cavitation which is now known to be closely associated with laminar separation indicated that, with the introduction of a step at the tangent point, the location of separation was not significantly different from 87 deg. However, the magnitude of boundary layer thickness at separation and the stabilty properties of the free shear layer are not expected to be greatly influenced by a slight shift in the location of separation due to the introduction of a step.

Inception of cavitation was detected visually under stroboscopic lighting. Inception observations were made with and without boundary layer tripping at two Reynolds numbers, Re_D of 4.54×10^5 and 5.7×10^5. The boundary layer trip utilized in the present experiments had a width of 1 mm, a height of 0.5 mm, and it was located at 30 deg from the stagnation point. From earlier observations [2] with the boundary layer tripping on a hemispherical nosed body it is expected that the presently employed method of boundary layer tripping would be effective in eliminating the existence of laminar separation at both the test Reynolds numbers with or without a step. Nominally, the air content of the tunnel water for present tests was 12 ppm. This air content, which is slightly below the saturation value, was achieved by heavily cavitating the body strut system for a prolonged period. Since the present facility has a horizontal resorber, free air coming out of the solution due to heavy cavitation in the test section accumulated at the top of the resorber in large quantities and this was bled off periodically. The method was effective but time consuming since a large volume ($\sim$ 135 cubic meter) of water was involved.

The velocity in the test section was calculated by using the measured value of pressure drop across the contraction cone with a mercury manometer. Similarly, a U-tube mercury manometer was used to measure the static pressure. The magnitude of the atmospheric pressure was noted down on each day of the testing from a barometer located at the test section level. Nominal temperature of the tunnel water during the present tests was 25°C and its value did not change appreciably during the tests even without arrangements for external cooling, this again being a consequence of the large volume of water involved.

To ensure that the present experimental methods of determining the cavitation inception index σ_i were consistent, inception observations were made on a hemispherical nosed body and the results were compared with the measurements reported by Parkin and Holl [11]. The comparative study detailed in reference [10] showed that the agreement between our measurements and those of Parkin and Holl was good within a Reynolds number range of 4.8×10^5 to 8.6×10^5.

Table 2 Inception measurements at $Re_D = 4.54 \times 10^5$

(h/D)	(h/δ)	σ_i (without trip)	σ_i (with trip)
0.0000	0.00	0.57	0.45*
0.0039	0.94	0.93	0.50
0.0102	2.45	1.20	0.80
0.0143	3.44	1.25	–
0.0204	4.91	1.30	–
0.0510	12.27	1.25	1.22

Table 3 Inception measurements at $Re_D = 5.7 \times 10^5$

(h/D)	(h/δ)	σ_i (without trip)	σ_i (with trip)
0.0000	0.00	0.59	0.35*
0.0039	1.05	0.98	0.53
0.0102	2.75	1.31	0.64
0.0143	3.85	1.34	–
0.0204	5.50	1.35	–
0.0510	13.75	1.36	0.98

*unsteady patchy cavitation

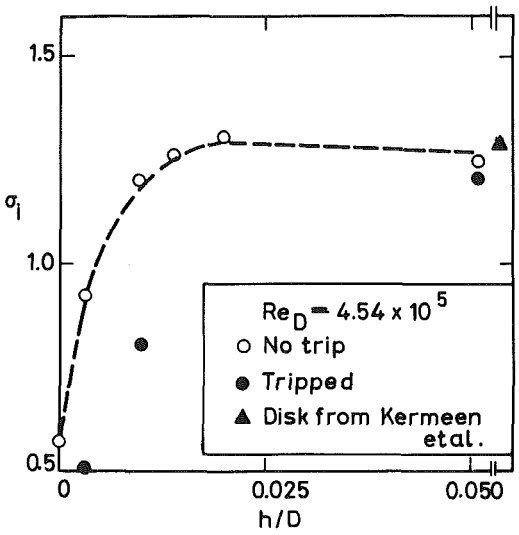

Fig. 6 σ_i versus (h/D) at $Re_D = 4.5 \times 10^5$

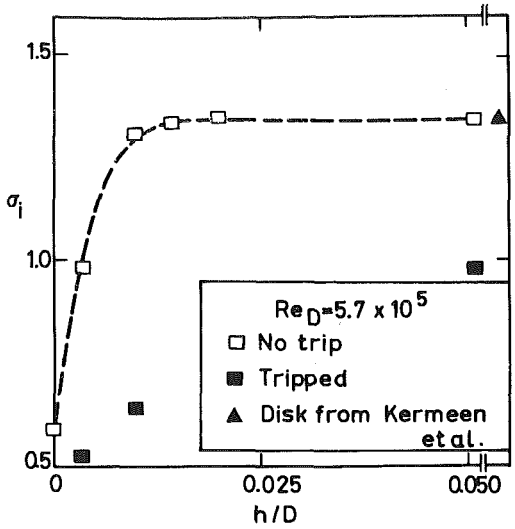

Fig. 7 σ_i versus (h/D) at $Re_D = 5.7 \times 10^5$

Experimental Results

The physical appearance of cavitation at inception without a step was in the form of a ring of bubbles quite close to the body surface slightly downstream of the tangent point. This continued to be the case even with a step however, only when the step size was small being of the order of 0.5 mm. For larger step sizes cavitation was still in the form of bubbles, but they appeared in the free shear layer away from the solid surface. These latter observations are similar to those of Kermeen and Parkin [12] for a disk. Therefore, in all cases cavitation at inception took place predominantly slightly downstream of the step. Inception was also accompanied with a clearly audible hissing sound.

The situation was somewhat different with boundary layer tripping. Since the inception indices were generally lower in some cases prior to appearance of bubble cavitation downstream of the step, traveling bubble types of cavitation associated with large free stream nuclei were observed simultaneously. In particular, in the absence of a step, an unsteady patchy type of cavitation was observed at inception; however, steady attached cavitation could not be sustained even if σ was lowered further below σ_i associated with unsteady patchy cavitation. These findings are generally in agreement with the previous findings of Arakeri and Acosta [2]. The differences are primarily due to the fact that the present resorber was not affective in complete resorption of air bubbles with the low test section σ values. Thus, even with the boundary layer, tripping inception measurements correspond to the appearance of cavitation bubbles slightly downstream of the step. With large step sizes this was the dominant type of cavitation at inception; whereas, with smaller step sizes, simultaneously traveling bubble types of cavitation were occasionally observed upstream of the step. The inception measurements carried out during the present work are presented in Tables 2 and 3 and are shown graphically in Figs. 6 and 7.

The magnitude of the boundary layer thickness approaching the step was estimated by calculating the boundary layer momentum thickness, θ_s at separation by Thwaites' method and using the relationship between θ_s and δ for Karman-Pohlhausen separating the boundary layer velocity profile. In addition to the inception measurements shown in Tables 1 and 2 a few desinent[2] measurements were also made; however, it was found that the difference between σ_i and σ_d was generally very small, on the order of 0.05.

Discussion of Results

The results shown in Figs. 6 and 7 for the cases without boundary layer tripping are replotted in Fig. 8 with (h/θ_s) replacing (h/D). It is clear from Fig. 8 that σ_i is a very strong function of (h/θ_s) up to an (h/θ_s) value of about 30. Beyond that, σ_i increases slowly with an increase in (h/θ_s) and seems to reach a constant asymptotic value for large values of (h/θ_s), this being particularly evident for the larger value of the Reynolds number, Re_D. On the basis of previous observations [1] σ_i for separated flows may be written as

$$\sigma_i = -C_{ps} + C_{p'}$$

where C_{ps} is the magnitude of the static pressure coefficient at separation and $C_{p'}$ accounts for large pressure fluctuations in the transition region. From the measurements of Tani, et al. [13] we do not expect C_{ps} to be a strong function of (h/D) or (h/θ_s). This, to a certain extent, was confirmed by our own measurements of static pressure slightly downstream of the step for different values of (h/D). Therefore, the behavior shown in Fig. 8 strongly suggests that $C_{p'}$ does vary strongly

[2] This is observed by holding the velocity fixed and slowly increasing the pressure until established cavitation just disappears. The corresponding σ at desinence is designated by σ_d.

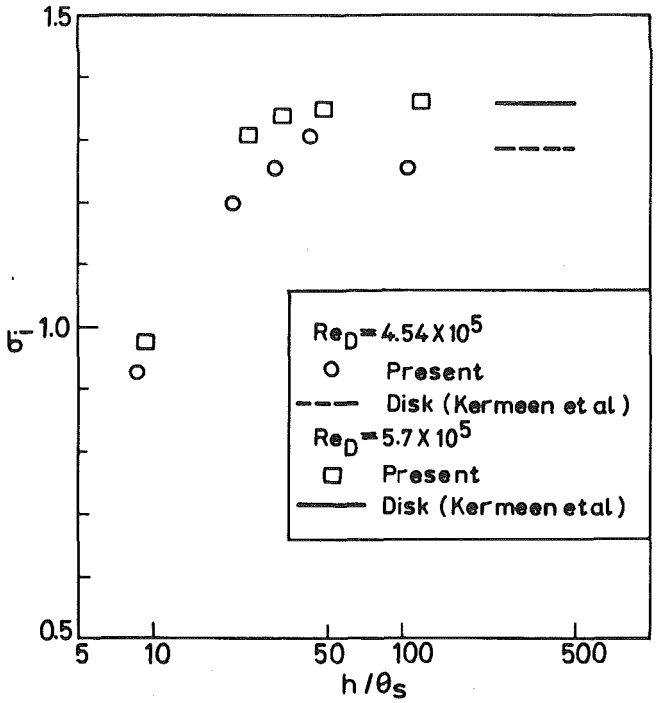

Fig. 8 σ_i versus (H/θ_s) for hem nose with step

with (h/θ_s) up to an (h/θ_s) value of about 30. In other words the magnitude of fluctuating pressure in the transition region of separated flow is a strong function of the height of the separated free shear layer from the wall unless it is sufficiently far away. Flow past a disk naturally represents one end of the spectrum where the height of the free shear layer is significantly far away from the neighboring wall. Therefore, it is of interest to note that σ_i measured in present experiments with a large value of (h/θ_s) agrees very well with the average of σ_d for various sized disks measured by Kermeen and Parkin [12] at least at one of the Reynolds numbers. This tends to confirm that flow downstream of disk is a limiting case of flow past a downstream facing step. Present observations, coupled with those of Kermeen and Parkin [12], strongly suggest that σ_i is a function of Re_D only if the height of the separted free shear layer is sufficiently far away from the solid surface irrespective of the forebody shape upstream of separation. Strictly speaking, to account for the possible variation of $-C_{ps}$ with forebody shape, we should state that $(\sigma_i + C_{ps})$[3] is only a function of Re_D, subject to the aforementioned condition. Quantitatively, then

$$(\sigma_i + C_{ps}) = f(\mathrm{Re}_D)$$

only if

$$(h/\theta_s) > 50 \text{ or } (h/\delta) > 5,$$

the latter condition being applicable to flows past a backward facing step. For disks the above criterion is easily satisfied irrespective of the size of a disk since θ_s or δ will be quite small at separation in veiw of highly accelerated flow upstream of it. The criterion is certainly established for all the disk sizes used by Kermeen, et al. [12].

It must be emphasized here that the above discussion is restricted to the flow remaining laminar up to separation. With the boundary layer tripped upstream of the backward facing step the behavior of σ_i with (h/D) is quite different as compared to the case without tripping, evident from Figs. 6 and 7. The only evidence in the present experiments to indicate that the boundary layer was tripped was based on static pressure measurements downstream of the step. At a Re_D of 5.7×10^5 the $-C_{ps}$ value was measured to be 0.5 in the tripped case as compared to its value of about 0.63 for the case of without tripping. At the lower Reynolds number of 4.54×10^5 the $-C_{ps}$ value measured to be about 0.55 in the tripped case indicating that the trip was not as effective as at the higher Reynolds number. Thus fundamentally there is no difference in the flow at the two test Reynolds numbers except that the effectiveness of the trip is likely to be different and this may partly explain the differing trend of σ_i with (h/D) in the tripped case for the two Re_D values shown in Figs. 6 and 7. In addition, whether the tripped flow truly simulates a naturally occurring turbulent flow upstream of the step is still open to question. However, the observations with tripped flow are quite interesting. First of all, σ_i does not show an asymptotic behavior within the range of (h/D) presently used; and secondly, σ_i values are considerably lower as compared to σ_i values without boundary layer tripping. The difference can partly be explained by noting that $-C_{ps}$ value was lower in the tripped case as noted earlier. In addition, the fact that (h/δ) will be smaller in the case of the tripped boundary layer may account for σ_i being lower. This is at least the trend predicted for the example by Holl [7] and Bohn [8] for various size and shaped isolated irregularities.

Therefore, a downstream facing step can be considered as an isolated surface irregularity. In general, Holl [7] and Bohn [8] have indicated that inception characteristics of surface irregularities if the boundary layer is turbulent at the location of irregularity can be correlated by a simple power law given by

$$\sigma_{\mathrm{ir}} = -C_{ps} + C\left(\frac{h}{\delta}\right)^a \left(\frac{U_{e\delta}}{\upsilon}\right)^b (1 - C_{ps})$$

if $(h/\delta) < 6$. We may note that C, a, and b are constants depending on the shape of the irregularity. Present findings with tripped boundary layer seem to suggest that the aforementioned law may be applicable at least as far as (h/δ) dependence is concerned. Quantitative confirmation of this could not be made since it would be difficult to estimate δ in the tripped case and would have to be measured. The dependence on $(U_e\delta/\upsilon)$ seems to be contradictory to the power law; however, the boundary layer may be in the transitional stage approaching the trip at the lower Reynolds number. Therefore, it is felt that that undue significance should not be attached to the trend observed for σ_i with $(U_e\delta/\upsilon)$ in the present experiments with tripping.

However, it is of significance to point out that in the case of *without* boundary layer tripping σ_{ir} does not follow the simple power law noted earlier even for (h/δ) values restricted to less than 6. The range of $(U_e\delta/\upsilon)$ covered in present experiments was not significant; but, the range of (h/δ) covered was sufficiently large. A plot of σ_{ir} versus (h/δ) on a log-log graph did not show a linear behavior and this may be expected from the asymptotic behavior of σ_{ir} versus (h/D) shown in Figs. 6 and 7. Whether the present observation is restricted to the downward facing step irregularity or is more general remains to be investigated. However, it is clear that scaling of inception characteristics of surface irregularity is different depending on whether the boundary layer approaching the irregularity is turbulent or laminar.

Scaling Implications

For separated flows past a backward facing step with flow remaining laminar up to the step, present observations suggest

[3] This quantity was not utilized in the present analysis since the magnitude of $-C_{ps}$ for flow past a disk is unknown. Present observation suggests that $-C_{ps}$ for the disk is about the same as $-C_{ps}$ for a hemispherical nose which was measured to be about 0.63. It is of significance to point out that $-C_{ps}$ for zero Cal ogive has also been measured to about 0.6 by Rouse, et al. [14].

the following scaling law:

$$(\sigma_i + C_{ps}) = f(\mathrm{Re}_D, h/\theta_s)$$

and as indicated, if $h/\theta_s > 50$ then the simplified scaling law is

$$(\sigma_i + C_{ps}) = f(\mathrm{Re}_D).$$

There is evidence that the simplified law is applicable in general to the backward facing step geometry irrespective of the forebody shape provided that the boundary layer remains laminar. It is tempting to generalize the above rules for naturally separating flows by replacing (h/θ_s) with (H/θ_s) in the above equations, with H being the maximum separated height from the wall. However, sufficient support for this still does not exist. On the basis of present observations the measured discrepancy for σ_i values (see Fig. 3) by Arakeri and Acosta [1] and Gates and Acosta [2] for two different hemispherical nosed bodies can now be directly traced to the fact that (H/θ_s) were different at a fixed value of Re_D. The reasons for the differing values of (H/θ_s) shown in Fig. 1 are not known. It may be possible that the body contours were slightly different in particular near the region of laminar separation. Therefore, if a family of axisymmetric bodies of a given forebody shape is strictly geometrically similar then we expect σ_i to be the same if the Reynolds number Re_D is the same. Hence, the observed size effect on σ_i at a fixed Re_D by Kermeen [15] for geometrically similar hemispherically nosed bodies still remains unexplained. If headforms of different forebody shapes are considered then we expect σ_i to be different even if Re_D is the same. This follows from the fact that Re θ_s has a varying magnitude for different forebody shapes at a given Re_D which in turn from Fig. 1 means that the magnitude of (H/θ_s) which influences σ_i can be different.

The Phenomenon of Singing

In the present experiments with downward facing step, if σ was lowered sufficiently below σ_i then clearly audible "singing" was heard. Again the phenomenon disappeared if σ was lowered significantly such that an attached cavity was formed. Therefore, singing persisted for σ range when change over from bubble type of cavitation to attached type of cavitation was taking place. Typical values of σ at which singing commenced at different values of (h/D) are shown in Table 4.

Table 4 Values at inception of singing

(Re_D)	(h/D)	σ
5.7×10^5	0.0102	0.87
5.7×10^5	0.0143	0.87-0.9
5.7×10^5	0.0510	0.71

The phenomenon of singing was not observed under boundary layer tripped conditions for any of the downward facing step sizes.

Conclusions

σ_i was found to increase rapidly with increase in the height of downward facing step until the height was approximately 2 percent of the diameter. Subsequently σ_i seems to reach a constant asymptotic value with step height about 5 percent of the diameter. The asymptotic value of σ_i agrees well with the measured value of σ_d for disks at the corresponding Reynolds number Re_D, the implication being that if the height of the separated free shear layer is sufficiently far away from a solid surface, then σ_i is only a function of Re_D. Under these same conditions there is evidence that $-C_{ps}$ value has about the same magnitude. The measured values of σ_i do not seem to fit a simple power law first proposed by Holl for surface irregularities. This may be attributed to the fact that the boundary layer remained laminar up to the location of irregularity or the step in the present experiments, whereas Holl's observations were for turbulent boundary layer.

Acknowledgments

The assistance of the staff of the Hydraulics Laboratory and in particular that of Mr. H. S. Govindaram in conducting part of the experiments is gratefully acknowledged.

References

1 Arakeri, V.H., and Acosta, A.J., "Viscous Effects in the Inception of Cavitation on Axisymmetric Bodies," ASME JOURNAL OF FLUIDS ENGINEERING, Vol. 95, No. 4, Dec. 1973, pp. 519-527.

2 Arakeri, V.H., and Acosta, A.J., "Cavitation Inception Observation on Two Bodies at Supercritical Reynolds Numbers," *Journal of Ship Research*, Vol. 20, No. 1, Mar. 1976, pp. 40-50.

3 Vander Muelen, J.H.J., "A Holographic Study of Cavitation on Axisymmetric Bodies and the Influence of Polymer Additives," Ph.D. thesis, University of Enschede, 1976, (Also available as Netherlands Ship Model Basin report.)

4 Gates, E.M., and Acosta, A.J., "Some Effects of Several Freestream Factors on Cavitation Inception on Axisymmetric Bodies," Twelfth Symposium on Naval Hydrodynamics, Washington D.C., June 1978.

5 Arakeri, V.H., "Experimental Investigation of Laminar Boundary Layer Stability with Surface Heating and Cooling," Report No. 01054-2-CT, June 1977, Netherlands Ship Model Basin, Holland.

6 Gaster, M., "The Structure and Behaviour of Separation Bubbles," Revised Aero Report 1181, March 1967, NPL, England (Also available as Britain R and M Report No. 3595).

7 Holl, J.W., "The Inception of Cavitation on Isolated Surface Irregularities," *Journal of Basic Engineering*, Vol. 82, 1960, pp. 169-183.

8 Bohn, J.C., "The Influence of Surface Irregularities on Cavitation: A Collation and Analysis of New and Existing Data with Application to Design Problems," M.Sc. thesis, Pennsylvania State University, 1972.

9 Seetharamaiah, K., and Nanjundaswamy, Y.S., "Design of 12 Cavitation Tunnel," Presented at the Annual Research Committee Meeting of CBIP, Simla, India, 1963. (Also see report of Civil and Hydraulic Engg. Rept. 1963, IISc., Bangalore.)

10 Arakeri, V.H., and Govindaram, H.S., "Comparative Cavitation Inception Studies on Hemispherically Nosed Body," WTL Report No. 78-1, Feb. 1978, Indian Institute of Science, Bangalore, India.

11 Parkin, B.R., and Holl, J.W., "Incipient Cavitation Scaling Experiments for Hemisperhical and 1.5 Calibre Ogive-Nosed Bodies," Report No. Nord 7958-264, Feb. 1956, Ordinance Research Laboratory, Pennsylvania State University, State College.

12 Kermeen, R.W., and Parkin, B.R., "Incipient Cavitation and Wake Flow Behind Sharp-Edged Disks," Rept. No. Engg 85-4, 1957, California Institute of Technology, Pasadena.

13 Tani, I., Fuchi, M., and Komoda, H., "Experimental Investigation of Flow Separation with a Step or a Groove," Report No. 364, April 1961, Aeronautical Research Institute, University of Tokyo.

14 Rouse, H., and McNown, J.S., "Cavitation and Pressure Distribution Head Forms at Zero Angles of Yaw," *Studies in Engineering Bulletin*, No. 32, 1948, State University of Iowa.

15 Kermeen, R.W., "Some Observations of Cavitation on Hemispherical Head Models," Report No. E-35, 1, June 1952, Hydrodynamics Laboratory, California Institute of Technology, Pasadena.

Y. Senoo
Professor,
Mem. ASME

N. Kawaguchi
Research Assistant.

Research Institute of Industrial Science,
Kyushu University,
Fukuoka, Japan

T. Kojima
Kawasaki Heavy Industries Company,
Akashi, Japan

M. Nishi
Associate Professor,
Kyushu Institute of Technology,
Kitakyushu, Japan

Optimum Strut-Configuration for Downstream Annular Diffusers With Variable Swirling Inlet Flow

Using three conical wall annular diffusers, geometries of struts mounted at the inlet tube were studied which were suitable for both the swirling inlet flow and the nonswirling inlet flow. Struts with an airfoil section which were installed at a small stagger angle served as a decelerating cascade for the swirling inlet flow, and a pressure rise was achieved across the struts. Furthermore, the residual weak swirl behind the struts improved the performance of downstream diffusers. For nonswirling inlet flow the struts induced a weak swirl which improved the performance of the diffuser. That is, if struts are designed properly, the performance of annular diffusers is improved by struts for a wide variation of swirl angle of inlet flow.

Introduction

As an element of internal flow systems an annular diffuser is popular, where the hub is sometimes supported by struts. In cases where swirl angle of the diffuser inlet flow varies during operation, special care should be taken for design of struts so that the wake of struts does not deteriorate the pressure recovery of the diffuser at all operating conditions.

The performance charts of annular diffusers have been presented in references [1, 2, 3] for nonswirling inlet flow and in references [4, 5, 6] for swirling inlet flow, but no report is available concerning the influence of wake of struts on the pressure recovery of annular diffusers. In the present experimental study, various kinds of struts were installed at the inlet of three annular diffusers, and the influences of strut geometry and stagger angle on the pressure recovery coefficient were examined for swirling inlet flow and nonswirling inlet flow. Then, the optimum strut configuration was experimentally determined for the inlet flow which changed the swirl angle between the two test conditions.

Experimental Apparatus and Procedures

Apparatus. The experimental apparatus is shown schematically in Fig. 1. Air was supplied to the plenum chamber through a venturi flow-meter. Swirl was generated while air passed inward through the swirl vanes. Then, in the annular tube the air was turned toward the axial direction keeping the swirl as it entered the test annular diffuser.

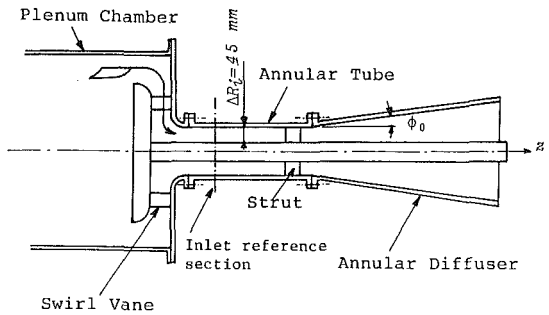

Fig. 1 Experimental apparatus. Four static pressure taps are equally spaced at the inlet reference section.

The annular diffusers tested were made up as combinations of one of three outer cones, the half-cone angles of which were 4, 6, and 8 deg, and a cylindrical hub. They were identified by a number which indicated the half-cone angles. For example, the 6-0 diffuser means a diffuser which consists of the 6 deg outer cone and the cylindrical hub. The area ratio of each annular diffuser was 4.72. The inlet and exit radii of the three outer cones were 154 mm and 310 mm respectively. The inner/outer radius ratio at the inlet section was 0.416. The annular tube was 400 mm long, about 9 times the inlet annulus height ΔR_i.

The five struts shown in Fig. 2 were tested. Four of them had the same maximum thickness of 10 mm. The C′-strut is geometrically similar to C-strut, but it was one half the scale of C-strut. The two-dimensional performance curves of NACA airfoils used as struts are reproduced in Fig. 3 [7]. It is

Contributed by the Fluids Engineering Division and presented at the Joint Applied Mechanics, Fluids Engineering, and Bioengineering Conference, Boulder, Colo., June 22-24, 1981, of THE AMERICAN SOCIETY OF MECHANICAL ENGINEERS. Manuscript received by the Fluids Engineering Division, March 17, 1979. Paper No. 81-FE-2.

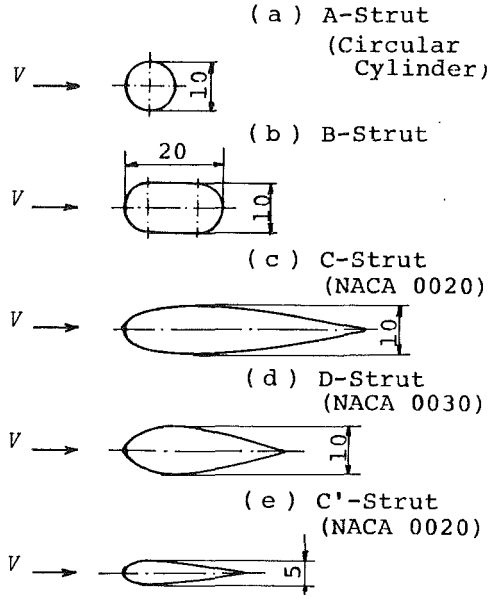

Fig. 2 Geometries of test struts (dimensions in mm)

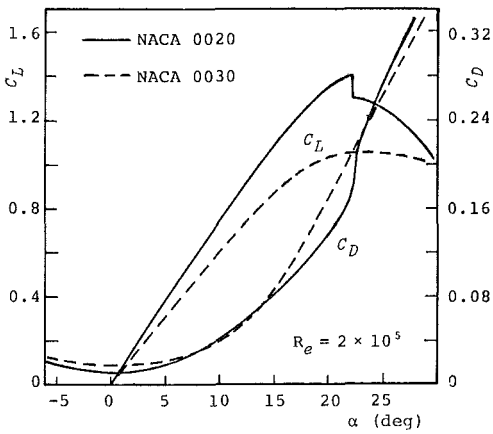

Fig. 3 Two-dimensional performance of airfoils [7]

seen that the stall angle of attack is about 22 deg. Either four or two struts were installed in the annular tube so that they were equally spaced and the center of each strut was located $1.4\Delta R_i$ upstream of the diffuser inlet. In the cases of struts with airfoil section, the stagger angle γ, shown in Fig. 4, was varied in the range between 0 and 20 deg.

Evaluation of Diffuser Performance. For evaluation of the influence of struts on the diffuser performance, the pressure recovery coefficient C_p defined by equation (1) is used.

$$C_p = \frac{p_e - p_i}{\rho \bar{V}_z^2/2} \tag{1}$$

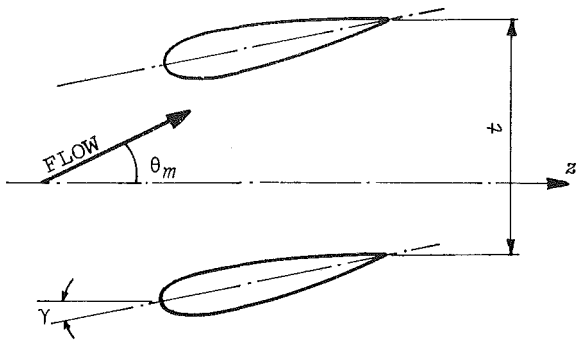

Fig. 4 Arrangement of struts

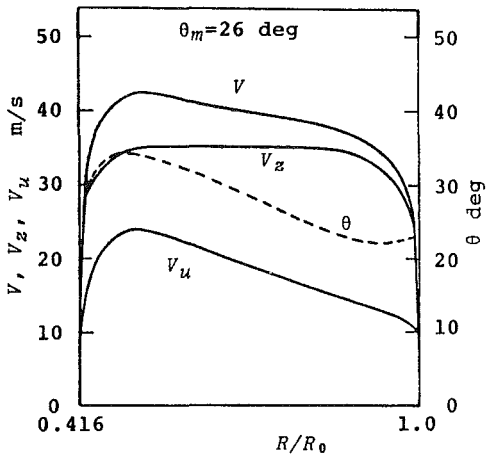

Fig. 5 Velocity distribution for the swirling inlet flow

where the mass-averaged inlet velocity $\bar{V}_z$ was calculated from the flow rate which was measured with a venturi flow-meter upstream of the plenum chamber. Subscript e indicates the diffuser exit, and subscript i indicates the reference inlet section which was chosen at $7\Delta R_i$ upstream of the diffuser inlet so that the influence of local pressure field caused by the struts was not involved. Thus, the pressure recovery of diffusers based on the pressure at this section includes the friction loss of the annular tube[1] and the loss of the struts. The uncertainty of C_p is less than 2 percent of the individual value of C_p including the effect of circumferential variation in pressure (odds of 20 to 1).

Results and Discussion

The experiments were performed at a Reynolds number based on ΔR_i and $\bar{V}_z$ approximately 10^5.

[1] Pressure loss of the inlet annular tube due to the wall friction was estimated $0.055\rho\bar{V}_z^2/2$ for the nonswirling inlet flow and it was $0.062\rho\bar{V}_z^2/2$ for the swirling inlet flow [8].

Nomenclature

AR = area ratio
B = blocked-area fraction at inlet section, $= 2\delta^*/\Delta R_i$
C_D = drag coefficient
C_L = lift coefficient
C_p = pressure recovery coefficient of diffuser, equation (1)
l = chord length of strut
p = wall pressure on outer wall
R = radial distance
R_0 = radius of outer-wall diffuser inlet
ΔR_i = annulus height at inlet section
t = pitch of struts at root mean square radius
V = velocity
V_u = circumferential component of velocity
V_z = axial component of velocity
$\bar{V}_z$ = mass-averaged inlet velocity
α = angle of attack
γ = stagger angle
δ^* = displacement thickness of boundary layer
θ = swirl flow angle from axial direction
θ_m = swirl flow angle at root mean square radius
ρ = density
ϕ_0 = half-cone angle of outer wall

Table 1 Variation of pressure recovery coefficients of annular diffusers C_p with strut-geometry. $\gamma = 0$ deg. $B = 0.05$ for $\theta_m = 0$ deg and $B = 0.06$ for $\theta_m = 26$ deg. Uncertainty of C_p is 1.6 percent of the individual value of C_p (odds of 20 to 1).

swirl angle θ_m(deg)	4-0 diffuser without struts	4-0 diffuser with struts			
		A-strut	B-strut	C-strut	D-strut
0	0.79	0.65	0.72	0.77	0.77
26	0.75	0.54	0.54	0.67	0.60

The inlet velocity profile was measured with a cobra probe at the section where the struts should be installed. Figure 5 shows the radial distributions of velocity and direction of flow for the swirling flow. It was noted that the flow at the measured section was hardly affected by the downstream diffuser geometries. The axial velocity component was uniform except near the walls, and the radial distribution of the circumferential velocity component was close to a free vortex pattern. The swirl angle θ_m, which was defined as the angle at the root mean square radius, was 26 deg from the axial direction.

Effect of Strut Geometry. The effects of the strut cross-section on diffuser performance were tested using the 4-0 diffuser. Four equally spaced struts were oriented in the annular tube so that the major axis was parallel to the diffuser axis. Variation of experimental pressure recovery coefficients with respect to strut geometry is presented in Table 1. In the case of nonswirling inlet flow, the pressure recovery coefficient for the diffuser with struts agreed fairly well with the simple difference between the pressure recovery coefficient for the diffuser without struts and the pressure loss coefficient based on the two-dimensional resistance of the struts in the literature [7, 9]. Thus obviously the airfoil section was the best among the strut geometries.

According to the results for the swirling inlet flow $\theta_m = 26$ deg, the decrease of pressure recovery coefficient due to struts is considerably larger than that observed in the case of nonswirling inlet flow. The largest decrease of pressure recovery coefficient is observed when circular cylinders were used as struts. It is suspected that the wake of struts was forced to accumulate near the hub due to the radial equilibrium condition in swirling flow and the accumulated low energy fluid was susceptible to separating the flow from the hub wall. Since the struts worked as a cascade, C-struts with airfoil section achieved the best result in spite of the largest frontal area against the inlet flow with swirl. Considering that the lift and the drag of an airfoil section depend upon the angle of attack, it is expected that a better performance may be achieved with the C-strut if the stagger angle is properly selected.

Consequently, using C-struts with airfoil section, effects of various geometrical parameters of struts on the diffuser performance were examined experimentally.

Influence of Stagger Angle. Four C-struts were mounted in the annular tube, and the influence of stagger angle on the pressure recovery coefficient of the downstream annular diffuser was examined. The results for non-swirling inlet flow ($\theta_m = 0$ deg) and for swirling inlet flow ($\theta_m = 26$ deg) are presented as circles connected with full lines in Fig. 6. For comparison, pressure recovery coefficients of the diffusers without struts are presented as circles at the left ends. The upper half of the graph corresponds to the nonswirling inlet flow, and the lower half corresponds to the swirling inlet flow. In all cases the pressure recovery coefficient became smaller as the cone angle of outer wall was increased.

Firstly, the results for non-swirling inlet flow are discussed. Although the drag of struts reduces the pressure recovery in general, for the 4-0 diffuser with struts C_p is almost as high as

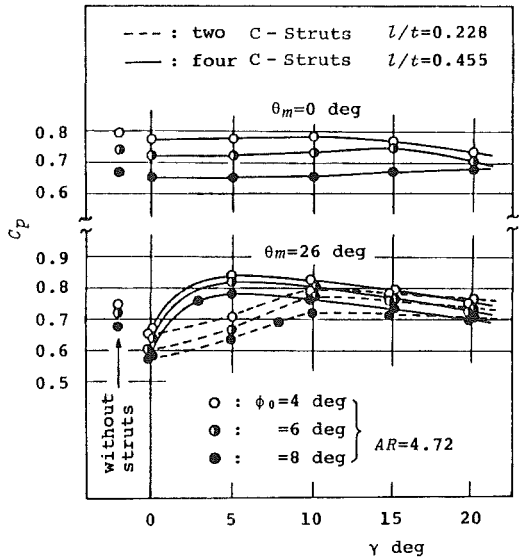

Fig. 6 Variation of pressure recovery coefficient of annular diffusers C_p with stagger angle of struts. $B = 0.05$ for $\theta_m = 0$ deg and $B = 0.06$ for $\theta_m = 26$ deg. Uncertainty of C_p is 1.6 percent of the individual value of C_p (odds of 20 to 1).

that without struts when the stagger angle γ is 10 deg, and C_p decreases as γ increases further. Similar trends are observed for the 6-0 diffuser and for the 8-0 diffuser, C_p is as high as that without struts when struts are at $\gamma = 15$ deg in the former case and $\gamma = 20$ deg in the latter case. Adding weak swirl to the flow in an annular diffuser is effective to improve the pressure recovery of flow close to a separating condition, as in conical diffusers [10, 11], because the turbulence is intensified by the curvature of streamlines and the boundary layer along the outer wall is kept thin. The larger the cone angle of a diffuser, the stronger the swirl required to prevent the flow along the outer wall from separating; hence the improvement of pressure recovery is more than the kinetic energy of swirl which is left over. If the swirl is too strong, flow separation may occur along the hub wall, as the boundary layer along the hub becomes thick due to the steep pressure gradient in the axial direction and due to the stabilizing effect of turbulence in the boundary layer along the convex surface.

In the case of the swirling inlet flow, the struts worked as a decelerating cascade which contributed to the pressure rise providing that the struts were not stalled. According to the experiments with an oil-film technique, the struts were stalled when they were set at $\gamma = 0$ deg. Stalling of the struts is understandable because the angle of attack was larger than the critical value for stall as seen in Fig. 3. If the struts are not stalled, the smaller the stagger angle, the larger the pressure rise would be, but a weak residual swirl behind the struts is desirable in these geometries because it aids the downstream diffuser to achieve higher pressure recovery coefficient. In the present experiment the best results were obtained at $\gamma = 5$ deg.

Consequently, the struts with stagger angle of 5 deg are suitable for the swirling inlet flow $\theta_m = 26$ deg as well as for the non-swirling inlet flow. Furthermore, it is expected that they may work well for the swirl flow $\theta_m = -15$ deg.

Table 2 Lift coefficient C_L of struts and downstream flow angle θ_{m2} based on two-dimensional performance curves in Fig. 3. Swirl flow angle upstream of struts is $\theta_{m1} = 26$ deg. Cross section of struts is NACA 0020.

stagger angle of struts (γ deg)		0	5	10	15	20
two struts $l/t = 0.228$	θ_{m2}(deg)	17.3	18.5	20.6	22.0	23.8
	C_L	1.40	1.24	0.97	0.68	0.38
four struts $l/t = 0.455$	θ_{m2}(deg)	9.8	12.7	15.9	19.1	22.1
	C_L	1.28	1.07	0.82	0.58	0.33

Number of Struts. Every other strut was removed, reducing the solidity to one half, and pressure recoveries for diffusers were measured. The results are also plotted in Fig. 6 as circles connected with dotted lines. In the case of the swirling inlet flow, a large reduction of pressure recovery coefficient was observed at the stagger angle $\gamma = 5$ deg. It is presumed that for a given incidence angle the blade loading increases as the solidity is reduced[2] and finally blades (struts) are stalled. Assuming that the flow is two-dimensional, the lift coefficient C_L of the airfoil section and the angle of swirl flow downstream of the cascade θ_{m2} at the root mean square radius are estimated using the performance curves in Fig. 3 for various conditions indicated in Fig. 6, and the calculated results are listed in Table 2. Judging from the curves in Fig. 6, it is suspected that the struts are stalled when $\gamma \leqq 0$ deg for $l/t = 0.455$ and $\gamma \leqq 5$ deg for $l/t = 0.228$. According to Table 2, the lift coefficient at these critical conditions is about 1.24. This value is a little less than the critical lift coefficient in two-dimensional flow in Fig. 3. The difference is probably due to the cascade effect and the three-dimensional effect.

Chord Length. The influence of chord length was examined keeping the solidity constant, and results are presented in Fig. 7. The dotted lines in Fig. 6 is reproduced to indicate the pressure recovery coefficients for diffusers where two C-struts were installed, while the full lines indicate those where four C′-struts were installed. That is, they have identical solidity, but the Reynolds number and the aspect ratio of struts are different. Comparing the two cases an appreciable difference in pressure recovery coefficient is observed where stagger angle is 10 deg. It is not likely that higher aspect ratio of the C′-struts is the cause of larger loss, and it is presumed that the difference of pressure recovery is caused by the difference in Reynolds number of the struts.

By varying the inlet velocity, Reynolds number effect was examined for the diffuser with two C-struts. Open circles in Fig. 8 show the relationship between pressure recovery coefficient and Reynolds number of struts. The three curves connecting the open circles respectively lie on the closed circle which was obtained with four C′-struts. In general the drag coefficient of a two-dimensional airfoil varies considerably [9] in the range of Reynolds number between 10^4 and 10^5. Fig. 8 indicates that the influence of Reynolds number becomes significant as the angle of incidence $(\theta_m - \gamma)$ increases. Considering these facts, it is believed that the difference between the dotted lines and full lines in Fig. 7 is attributable to the difference of Reynolds number rather than the difference of aspect ratio of struts.

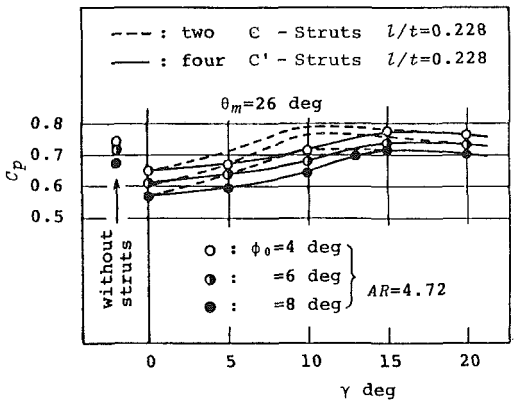

Fig. 7 Variation of C_p with chord length of struts. Solidity $l/t = 0.228$. Uncertainty of C_p is 1.6 percent of the individual value of C_p (odds of 20 to 1).

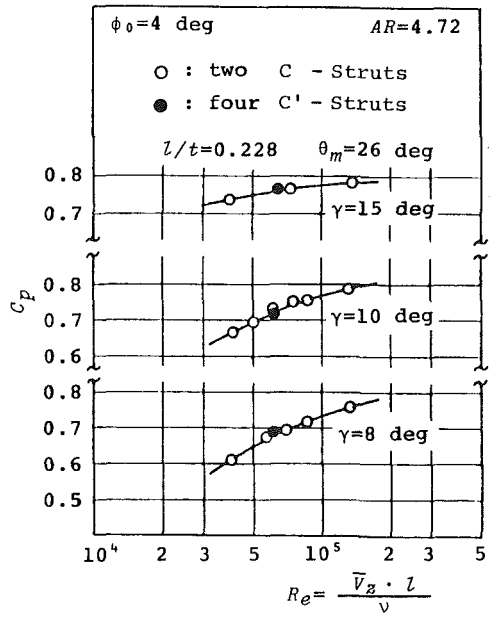

Fig. 8 Variation of C_p with Reynolds number of strut. Uncertainty of C_p is 1.6 percent of the individual value of C_p (odds of 20 to 1).

Conclusion

Varying the cross sectional geometries of struts, which were installed upstream of three annular diffusers, the best strut configuration including the stagger angle of airfoils were experimentally examined for a few diffusers with swirling inlet flow as well as non-swirling inlet flow. The major results are as follows.

1) It is possible to install struts which do not aggravate the diffuser performance for a wide range of swirl angle of inlet flow.

2) If airfoil shape is adopted for struts and they are installed as a decelerating cascade for a swirling inlet flow a pressure rise is expected across the struts. Furthermore, the pressure recovery coefficient of the annular diffuser itself

[2] As the solidity l/t increases, the angle of swirl flow downstream of struts θ_{m2} decreases, and the angle of attack of the blade relative to the vector mean velocity decreases since θ_{m1} $(= \theta_m) > \gamma$. Consequently, the blade loading decreases for a given upstream flow angle θ_{m1} or a given incidence angle $(\theta_{m1} - \gamma)$.

may sometimes be improved by the residual weak swirl which is left behind the struts. Adding these two effects together, considerable improvement in pressure recovery coefficient can be realized for swirling inlet flow. For non-swirling inlet flow the struts induce a weak swirl which improves the performance of annular diffusers with expanding outer cases.

It is noticed that the pressure recovery coefficient of an annular diffuser with struts is sensitive to the stagger angle and the Reynolds number of struts in the range of the present experiments.

References

1 Sovran, G., and Klomp, E.D., "Experimentally Determined Optimum Geometries for Rectilinear Diffusers with Rectangular, Conical or Annular Cross Section," *Fluid Mechanics of Internal Flow,* Elsevier, New York, 1967, pp. 270–310.

2 Takehira, A., Tanaka, M., Kawashima, T., and Hanabusa, H., "An Experimental Study of the Annular Diffusers in Axial-Flow Compressors and Turbines," *Proceedings of the 1977 Tokyo Joint Gas Turbine Congress,* 1977, pp. 319–328.

3 Howard, J.H.G., Henseler, H.J., and Thornton-Trump, A.B., "Performance and Flow Regimes for Annular Diffusers," ASME Paper 67-WA/FE-21, 1967.

4 Srinath, T., "An Investigation of the Effects of Swirl on the Flow Regimes and Performance of Annular Diffusers with Equal Inner and Outer Cone Angles," Msc thesis, Mech. Engineering Dept., University of Waterloo, 1968.

5 Thornton-Trump, A.B., "An Investigation of the Effects of Unequal Cone Angles and of Swirl in Annular Diffusers," MS thesis, University of Waterloo, 1967.

6 Adenubi, S.O., "Effects of Axial Turbomachine Type Discharge Condition on Performance of Annular Diffusers," Rep. PD-16, Thermosciences Div. Mech. Engineering Dept., Stanford University, 1972.

7 Jacobs, E.N., and Abbott, I.H., "Airfoil Section Data Obtained in the NACA Variable-Density Tunnel as Affected by Support Interference and Other Corrections," NACA Rep. 669, 1939.

8 Senoo, Y., and Nagata, T., "Swirl Flow in Long Pipes with Different Roughness," *Bulletin of the Japan Society of Mechanical Engineers,* Vol. 15, No. 90, 1972 pp. 1514–1521.

9 Goldstein, S., *Modern Developments in Fluid Dynamics,* Vol. 2, Dover, New York, 1965, pp. 401–490.

10 Senoo, Y., Kawaguchi, N., and Nagata, T., "Swirl Flow in Conical Diffusers," *Bulletin of the Japan Society of Mechanical Engineers,* Vol. 21, No. 151, 1978, pp. 112–119.

11 McDonald, A.T., and Fox, R.W., "Effects of Swirling Inlet Flow on Pressure Recovery in Conical Diffusers," *AIAA Journal,* Vol. 9, No. 10, 1971, pp. 2014–2018.

Forces on Staggered Airfoil Cascades in Unsteady In-Phase Motion

H. Shoji

H. Ohashi
University of Tokyo,
Tokyo, Japan

N. H. Kemp
Physical Sciences Inc.,
Woburn, Mass.

We consider incompressible potential flow through a cascade of staggered thin airfoils in general, unsteady, in-phase motion. With the assumptions of the Kutta condition and linearized wakes, exact analytical expressions are derived for pressure distribution, lift, and moment, using conformal mapping applied to the velocity field. The results are then specialized to harmonic motion, and applied to plunging, pitching, and sinusoidal gusts. All the results are expressed in closed-form as quadratures, and reduce to the well-known relations for thin airfoil theory, as the solidity decreases to zero. They agree with the unstaggered results of Kemp and Ohashi when the stagger angle is zero. Typical numerical results are given in the figures. They should serve as a measure of the accuracy of numerical or approximate solutions, as well as representing in a simple way the effects of stagger and solidity on unsteady cascade aerodynamics.

Introduction

Flow around a cascade of airfoils becomes unsteady when either the inlet or exit condition of the cascade is unsteady, or the airfoils in the cascade vibrate. Many analyses of unsteady cascade flow have been made, especially in such fields as cascade flutter, aerodynamic interference between stationary and moving blade rows, influence of circumferential inlet distortion on the following moving blade row, and dynamic performance of turbomachinery under unsteady operating conditions.

These analyses are divided broadly into two classes. One gives closed form analytical solutions, and the other gives numerical solutions of the integral equations for the vortices relating to the velocity field, or the pressure doublets relating to the pressure field.

Among many examples of the latter, the study by Whitehead [1] is well-known. His method is a purely numerical inversion of the integral equation relating vorticity to the velocities it induces. He gave the tabulation of lift and moment of staggered cascades for harmonic motion with arbitrary phase differences between blades. Nishiyama, et al. [2] solved the integral equations relating to the pressure doublets. Their method has the virtue that the wake need not be taken into consideration.

Examples of the analytical class of solutions are not so numerous, and most of them are restricted to the in-phase oscillation of an unstaggered cascade in the framework of thin airfoil theory. Among them, the papers by Mendelson and Caroll [3] and Chang and Chu [4] are well-known. Recently Murata, et al. [5, 6] gave the solutions in the case of a staggered cascade by applying conformal transformation to the acceleration potential field; however they did not give the general expressions of lift and moment, so that they had to analyze each case individually. Furthermore, their results are expressed in a mathematical form which does not lend itself readily to physical interpretation.

On the other hand, Kemp and Ohashi [7] have recently attacked the aerodynamics of unsteady in-phase motion of an unstaggered cascade of flat plates (with zero mean attack angle). They used the familiar methods of thin airfoil theory with shed vorticity, and were able to obtain analytical expressions for loading, lift and moment. These results were cast into the same form as the von Karman-Sears theory of unsteady isolated airfoils [8], divided into quasi-steady, wake, and apparent mass terms. Therefore, the physical meaning of the solution is easily perceived. Application was made to harmonic motion for plunging, pitching, and sinusoidal gusts.

The purpose of this paper is to extend the theory of Kemp and Ohashi to staggered cascades, without losing the essential feature that all the results are expressed in terms with a close affinity to isolated unsteady airfoil theory.

The analysis is developed under the same assumptions used in [7] that is, the Kutta condition is satisfied at the trailing edge, and the vorticity shed from the airfoil moves downstream with the through-flow velocity, unaffected by the additional flow generated by the airfoils.

In spite of the geometrical complications brought on by the inclusion of stagger, it proves possible to carry through a similar analysis, leading to expressions for pressure distribution, lift and moment for general unsteady motion. These are then specialized to harmonic motion, and applied to plunging, pitching and sinusoidal gusts. The results for these applications are given entirely in terms of quadratures depending on stagger angle, solidity, and reduced frequency.

Some typical numerical results are presented graphically and others can be obtained from the authors.

The virtue of the present work, as with [7], is not only the

Contributed by the Fluids Engineering Division for publication in the JOURNAL OF FLUIDS ENGINEERING. Manuscript received by the Fluids Engineering Division, April 25, 1980.

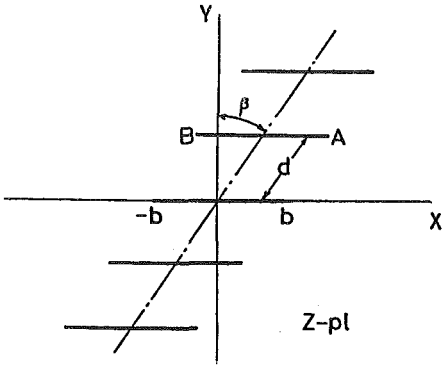

Fig. 1 Cascade geometry in the physical plane

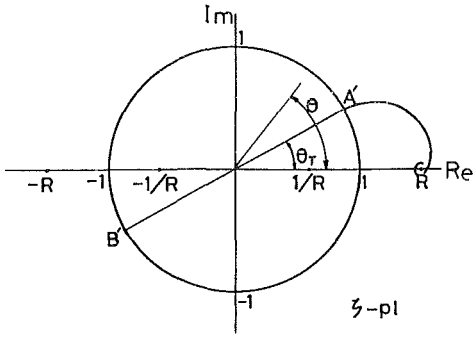

Fig. 2 Unit circle in the mapping plane

particular numerical results, which could be obtained by numerical solution, and indeed are partly contained in Whitehead [1]. It is also the analytical expression of the aerodynamic forces in a simple and physically understandable form, with close analogy to the familiar isolated airfoil results. Calculations can be made rather easily, and the effects of the various parameters can be clearly seen.

We hope these results will be interesting both for their own sake, and for testing the correctness and accuracy of approximate theories and purely numerical procedures.

Analysis

The analysis of the staggered cascade is considerably more complex than that of the unstaggered case [7]. We start with the staggered cascade of flat plates representing the airfoil chord lines, as shown by Fig. 1, in the physical $z=x+iy$ plane. They are transformed conformally into a circle of radius unity in the $\zeta=\xi+i\eta$ plane, shown in Fig. 2, with the leading edge at B' and the trailing edge at A'. The line joining A' and B' makes an angle θ_T with respect to the ξ axis. The transformation is the well-known logarithmic one:

$$z=\frac{d}{2\pi}\left[e^{-i\beta}\ln\frac{R+\zeta}{R-\zeta}+e^{i\beta}\ln\frac{\zeta+R^{-1}}{\zeta-R^{-1}}\right] \tag{1}$$

The points $-R$ and R are singularities of the transformation which represent in the ζ plane the regions at $x=\pm\infty$ in the z plane. The points at $\pm R^{-1}$ are also singularities, but they are inside the circle, and therefore not in the flow field, which is the region outside the circle.

The vortex wakes shed from the airfoils trail back from the trailing edges A parallel to the x axis in the physical plane. These wakes transform into a curve emanating from A' in the circle plane, which spirals toward the point $\zeta=R$, as indicated in Fig. 2. In the unstaggered case, $\theta_T=0$ and the image of the wake in the circle plane is simply the ξ axis, from $\xi=1$ to the end of the wake, $\xi\leq R$. Furthermore, the top and bottom surfaces of the chord line are symmetrically transformed to the top and bottom of the circle. With stagger, this symmetry disappears and the whole circle must be considered, rather than just the top half. This presents one complication, and a second is the calculation of integrals along the wake, which must be performed along the spiral shown in Fig. 2, rather than just the segment $1\leq\xi\leq R$ of the ξ axis.

These geometrical difficulties can be overcome to a large extent, and it still proves possible to obtain rather general formulas for the pressure distribution, lift, and moment on the cascade airfoils, for general unsteady motion, within the limitations of thin-airfoil theory. However, the pressure distribution contains an undetermined additive function of time, though its spatial distribution on the airfoil is determined. This function of time does not affect the loading on the airfoil, since it is the same on the top and bottom. Thus the lift and moment are completely determined.

It is, of course, possible to find the lift and moment without finding the pressure distribution explicitly. This is the approach taken by von Karman and Sears in their classical paper on unsteady motion of isolated airfoils [8]. We think that the airfoil loading may be of some interest, so we first find the pressure distribution, and then find the lift and moment by integration.

Our method is similar to that of [8], which also uses the circle plane. We find the effect of wake vorticity on the bound vorticity of the cascade. This leads to an integral equation for the wake vorticity distribution in terms of the quasi-steady circulation around the cascade, which is that circulation the cascade would have if the wake were ignored. We then find the velocity distribution on the airfoils, and integrate that to find the pressure distribution.

The complete analysis is rather lengthy and is not presented

Nomenclature

d = spacing
b = semichord length
β = stagger angle
ν = angular velocity of oscillation
$\omega=\nu b/U$ = reduced frequency
$\sigma=2b/d$ = solidity
ρ = fluid density
U = free stream velocity
u, v = component of velocity perturbation in x and y direction
t = time
i = unit of imaginary number with respect to space
j = unit of imaginary number with respect to time
$z=x+iy$ = complex coordinate in physical plane
$\zeta=\xi+i\eta$ = complex coordinate in mapped plane
R, K, K^*, J = parameters of mapping function
θ_T = angle of trailing edge in the ζ-plane
p = pressure fluctuation
L = lift fluctuation
M = moment fluctuation (positive nose-up)
Γ = circulation around the airfoil
ϵ = shed vorticity distribution in the wake

Suffix

0 = quasi-steady term
w = wake term

here. The interested reader will find the details in [9], which may be obtained from any of the authors. Here we will present an outline of the analysis, give the formulas which result, and show some numerical examples.

Geometrical Relations. The angle θ in the circle plane, measured counterclockwise from the ξ axis, denotes points on the unit circle which correspond to points x on the central airfoil (for which $y=0$) in the cascade. The relation between x and θ is found from the transformation (1) to be

$$X(\theta)=\frac{x(\theta)}{b}=\frac{d}{\pi b}\left[\cos\ \beta\ \operatorname{arctanh}\left(\frac{\cos\ \theta}{K}\right)\right.$$
$$\left.+\sin\ \beta\ \arctan\left(\frac{\sin\ \theta}{K^*}\right)\right] \tag{2}$$

where K and K^* are related to the transformation parameter R by

$$K=\frac{R+R^{-1}}{2}\qquad K^*=\frac{R-R^{-1}}{2} \tag{3}$$

The leading and trailing edges correspond to the angles θ_L and θ_T in the circle plane. The physical geometrical parameters chord $2b$, spacing along the cascade axis d, and stagger angle β (see Fig. 1) determine the parameters R, K, K^*, θ_L and θ_T. These relations follow from (1) and its derivative, since θ_T is a singular point of the transformation on the circle. It is shown in [10] that

$$\theta_L=\theta_T+\pi\qquad \tan\ \theta_T=\frac{K^*}{K}\tan\ \beta$$
$$\cos\ \theta_T=\frac{K\cos\ \beta}{J}\qquad \sin\ \theta_T=\frac{K^*\sin\ \beta}{J} \tag{4}$$
$$J=\sqrt{K^2-\sin^2\ \beta}\qquad K^*=\sqrt{K^2-1}$$

The parameter K is related to b/d by (2) at $\theta=\theta_T$, which can be written, with the help of (4), as

$$b=\frac{d}{\pi}\left[\cos\ \beta\ \operatorname{arctanh}\left(\frac{\cos\ \beta}{J}\right)+\sin\ \beta\ \arctan\left(\frac{\sin\ \beta}{J}\right)\right] \tag{5}$$

With J as defined in (4), this is a transcendental equation for K, from which all the other geometric parameters can be determined in terms of b/d and β, using (3) and (4).

A complex variable along the wake spiral in the circle plane is also useful. Let ζ_w be any point on the wake. We then introduce the complex variable s as

$$s=\frac{\zeta_w e^{-i\theta_T}+\zeta_w^{-1}e^{i\theta_T}}{2},\quad \zeta_w e^{-i\theta_T}=s+\sqrt{s^2-1} \tag{6}$$

For zero stagger, s reduces to the real variable defined in equation (13) of [7]. At the trailing edge, where the wake starts, $\zeta_w=e^{i\theta_T}$ so $s=1$.

Quasi-Steady Flow. As in unsteady isolated airfoil theory, an important component of the flow is the quasi-steady part. This is found from the instantaneous motion of the cascade, without regard to wake effects, which is to say, from steady flow theory.

The steady flow through a staggered cascade of thin airfoils was analyzed in [10]. The relation between the x and y perturbation velocities u_0 and v_0 was found to be

$$u_0(\theta)=-\frac{1}{2\pi}\frac{K^2-\cos^2\theta}{\sin\ (\theta-\theta_T)}\int_0^{2\pi}\frac{\sin\ (\phi-\theta_T)}{K^2-\cos^2\phi}v_0(\phi)\ \cot\frac{\theta-\phi}{2}\,d\phi$$
$$+\frac{\Gamma_0}{2Jd}\frac{KK^*}{\sin\ (\theta-\theta_T)} \tag{7}$$

v_0 may be interpreted as the upwash on the cascade airfoils associated with the surface velocity distribution u_0. The quasi-steady circulation is given by

$$\frac{\Gamma_0}{b}=-\frac{KK^*}{J}\frac{d}{\pi b}\int_0^{2\pi}\frac{1+\cos\ (\phi-\theta_T)}{K^2-\cos^2\phi}v_0(\phi)\,d\phi \tag{8}$$

When the motion of the airfoil is known v_0 is chosen to cancel that motion, giving the quasi-steady velocity distribution u_0 and circulation Γ_0. The quasi-steady lift is given by the Kutta-Joukowski formula $L=\rho U\Gamma_0$. The quasi-steady moment (positive nose-up) comes from integrating the perturbation pressure $-\rho U u_0$ times x around the airfoil. By transforming to the circle plane and using (7) for u_0, it can be written as

$$\frac{M_0}{\rho Ub^2}=\frac{Jd}{\pi b}\int_0^{2\pi}\frac{\sin\ (\phi-\theta_T)}{K^2-\cos^2\phi}X^*(\phi)v_0(\phi)\,d\phi \tag{9}$$

The function X^* is defined as

$$X^*(\theta)=\frac{d}{\pi b}\left[\sin\ \beta\ \operatorname{arctanh}\left(\frac{\cos\ \theta}{K}\right)\right.$$
$$\left.-\cos\ \beta\ \arctan\left(\frac{\sin\ \theta}{K^*}\right)\right] \tag{10}$$

Wake-Induced Circulation. The unsteady motion of the cascade sheds wake vorticity parallel to the x axis from the trailing edges of the cascade airfoils. Let the distribution along the x axis from the center airfoil be $\epsilon(x)$. If we consider an element of this wake ϵdx at its image point ζ_w in the circle plane, we can make the circle a streamline by putting $-\epsilon dx$ at the image point inside the circle. The Kutta condition is then satisfied by putting equal vortices at the singular points $\zeta=\pm R^{-1}$ and $\zeta=\pm R$, the latter two of negative sign, and choosing their strength to provide zero velocity at θ_T. If we now integrate along the wake from $x=b$ to D, the extent of the wake, we find the circulation the wake induces around the center airfoil to be

$$\Gamma_w=\int_b^D\epsilon(x)\left[\frac{KK^*}{J^2}\operatorname{Re}\left(\frac{s+1}{s-1}\right)^{1/2}-1\right]dx \tag{11}$$

Since the sum of Γ_0 and Γ_w is the negative integral of ϵ along the wake, by Kelvin's Theorem, we find

$$\Gamma_0=-\int_b^D\epsilon(x)\frac{KK^*}{J^2}\operatorname{Re}\left(\frac{s+1}{s-1}\right)^{1/2}dx \tag{12}$$

This is an integral equation for the wake vorticity $\epsilon(x)$, in terms of the quasi-steady circulation, which is defined once the cascade motion is known. For an unstaggered cascade it reduces to equation (18) of [7]. Its solution is the main task of unsteady airfoil theory.

For harmonic motion, the method of solution of (12) is well-known, and the result will be given later. For other types of motion (12) provides a basis for use of other methods of solution.

Pressure Distribution. In unsteady flow the pressure perturbation p can be expressed in terms of the velocity perturbation u by

$$p(x,y,t)=-\rho Uu-\rho\frac{\partial}{\partial t}\int_{-b}^{x}u'dx'-\rho\frac{\partial}{\partial t}\int_{-\infty}^{-b}u'dx' \tag{13}$$

The last term of this expression may depend on t, but it is independent of x, and therefore makes no contribution to the loading, lift, or moment. In the present analysis we obtain formulas for p which do not evaluate this last term, so p is determined only up to an additive function of time. However, in the lift and moment formulas obtained by integrating p, this function disappears, so the lift and moment are completely determined.

The pressure is found from (13) by breaking the velocity u into two parts: a quasi-steady part u_0 and a wake part u_w. The former comes from (7), and the latter is calculated from the wake vorticity and image system used to find Γ_w in (11).

When these two parts of u are substituted into (13), the second term on the right can be evaluated by a rather lengthy reduction whose details are given in [9]. The result is that p can be written as the sum of four terms:

$$\frac{p}{\rho U} = -u_0 - \frac{KK^*}{2dJ} u_{1_{FP}} \int_b^D \epsilon(x)\,\mathrm{Re}\left(\frac{1}{\sqrt{s^2-1}}\right)dx - \frac{1}{U}\frac{\partial}{\partial t}F_{AM}(\theta, t) + P(t) \tag{14}$$

The first term is the quasi-steady pressure. The second term is the wake contribution, and is proportional to $u_{1_{FP}}$, which is the velocity distribution on a staggered cascade of flat plates for unit upwash velocity (see [10] for example):

$$u_{1_{FP}} = \frac{KK^*}{J^2}\left[\frac{1-\cos(\theta-\theta_T)}{\sin(\theta-\theta_T)} - \frac{\sin\beta\,\cos\beta}{KK^*}\right] \tag{15}$$

This relation between the wake contribution to the pressure and $u_{1_{FP}}$ is the same as that found for an isolated airfoil in [8] and the unstaggered cascade in [7]. The fourth term in (14) is the undetermined function of t. Finally, the third term is the apparent mass term, containing a time derivative. The function $F_{AM}(\theta,t)$ is the integral of the noncirculatory part of the quasi-steady velocity, U_{0NC}, and can be written as

$$F_{AM}(\theta,t) = \int_{\theta_T+\pi}^{\theta} u_{0NC}(\theta')\frac{dx}{d\theta'}d\theta'$$

$$u_{0NC}(\theta)\frac{dx}{d\theta} = \frac{dJ}{2\pi^2}\int_0^{2\pi}\frac{\sin(\phi-\theta_T)}{K^2-\cos^2\phi}v(\phi)\cot\frac{\theta-\phi}{2}d\phi \tag{16a}$$

A useful alternative form, obtained by integration by parts and the use of $dx/d\theta$ from (2), is

$$F_{AM}(\theta,t) = -\frac{1}{2\pi}\int_0^{2\pi}\cot\frac{\theta-\phi}{2}d\phi\left(\int_0^{\phi} v\frac{dx}{d\phi'}d\phi'\right) \tag{16b}$$

The pressure has thus been expressed in the form familiar from isolated airfoil theory [8] as the sum of quasi-steady, wake, and apparent mass terms, with the addition of the undetermined function of t. Integration will now yield general formulas for lift and moment.

Lift and Moment. The lift is obtained by integrating the pressure difference $(p_{\text{bot}} - p_{\text{top}})$ over x:

$$L = \int_{-b}^{b}(p_{\text{bot}} - p_{\text{top}})dx = \left(\int_{\theta_T+\pi}^{\theta_T+2\pi} - \int_{\theta_T+\pi}^{\theta_T}\right)p\frac{dx}{d\theta}d\theta = \int_0^{2\pi} p\frac{dx}{d\theta}d\theta \tag{17}$$

When (14) is used, the integral of $P(t)$ vanishes. The first term integrates to the quasi-steady lift $U\Gamma_0$. The second term integrates to the flat plate cascade lift $2d\rho U/J$ (see [10] below equation (4.28) for example). The integral of the apparent mass term can be shown to be proportional to the quasi-steady moment

$$M_0 = \rho U\int_0^{2\pi} xu_0\frac{dx}{d\theta}d\theta \tag{18}$$

whose expression in terms of v_0 has been given in (9). The lift is then

$$\frac{L}{\rho Ub} = \frac{\Gamma_0}{b} + \frac{KK^*}{J^2}\int_b^B \epsilon(x)\,\mathrm{Re}\left(\frac{1}{\sqrt{s^2-1}}\right)dx + \frac{b}{U}\frac{d}{dt}\left(\frac{M_0}{\rho Ub^2}\right) \tag{19}$$

This form is closely analogous to the isolated airfoil result given in [8], and, in fact, the first and last terms are exactly the same, although the expressions for Γ_0 and M_0 are different here from the isolated ones. Only the wake term shows explicitly the cascade effect through the parameters K, K^*, J, and the definition of the wake variable s.

The moment (positive nose-up) about the airfoil center is

$$M = -\int_{-b}^{b} x(p_{\text{bot}} - p_{\text{top}})dx = -\int_0^{2\pi} xp\frac{dx}{d\theta}d\theta \tag{20}$$

Use of (14) leads to the quasi-steady moment already given in (18), a wake term proportional to the flat plate cascade quasi-steady moment $2\pi\rho U(d/\pi b)^2\ln(K/K^*)$ (see [10], below equation (4.48) for example), and an apparent mass term. The latter can be integrated by parts, so that finally

$$\frac{M}{\rho Ub^2} = \frac{M_0}{\rho Ub^2} + \frac{KK^*}{bJ}\frac{d}{\pi b}\ln\frac{K}{K^*}\int_b^B \epsilon(x)\,\mathrm{Re}\left(\frac{1}{\sqrt{s^2-1}}\right)dx - \frac{1}{U}\frac{d}{dt}\int_0^{2\pi}\frac{1}{2}\frac{x^2}{b^2}U_{0NC}\frac{dx}{d\theta}d\theta \tag{21}$$

These formulas for the lift and moment reduce to the results of the unstaggered case [7] when $\beta = 0$, and approach the results for the isolated airfoil [8] when $d \to \infty$.

Stationary Gust. A type of unsteady motion of frequent interest is a stationary gust, defined as an upwash of the form

$$v_0 = f(t - x/V)$$

where V is the velocity of passage of the gust over the airfoil. If a v_0 of this form is used in the pressure apparent mass term (16b), the time derivative of the second integral becomes $-Vv_0$. Then the apparent mass term can be combined with u, as given in (7), and the pressure from (14) can be written as

$$\frac{p}{\rho U} = -u_{1FP}F_G(t) + \frac{1}{2\pi}\left(1-\frac{V}{U}\right)\int_0^{2\pi}\cot\frac{\theta-\phi}{2}v_0 d\phi + P_G(t) \tag{22}$$

$$F_G(t) = \frac{KK^*}{2dJ}\int_b^B \epsilon(x)\,\mathrm{Re}\left(\frac{1}{\sqrt{s^2-1}}\right)dx - \frac{KK^*}{2\pi}\int_0^{2\pi}\frac{v_0 d\phi}{K^2-\cos^2\phi}$$

This shows that when the gust convects with the stream speed, so that $V = U$, the pressure distribution has the same x dependence as that for a flat plate cascade in steady flow, because F_G is independent of x. This is exactly analogous to the result for an isolated airfoil passing through this sort of gust. For such a gust, then, the lift and moment are simply

$$\frac{L}{\rho Ub} = \frac{2\pi}{J}\frac{d}{\pi b}F_G, \frac{M}{\rho Ub^2} = 2\pi\left(\frac{d}{\pi b}\right)^2\ln\frac{K}{K^*}F_G \tag{23}$$

Harmonic Motion

We now consider harmonic in-phase oscillations of the cascade, in which the upwash velocity induced by the cascade motion is harmonic in time, with frequency ν, so all time-dependent quantities have a factor $\exp(j\nu t)$. The wake extends to $x \to \infty$.

In this harmonic case, the integral equation (12) for the wake strength is easily solved, because the form of the wake dependence on x is known. The wake convects with the stream speed U so ϵ is proportional to $\exp(j\nu t - j\nu x/U)$. The constant of proportionality is found, as in the isolated case [8] by using the fact that the rate of change of total circulation is equal, but of opposite sign, to the vorticity shed from the trailing edge per unit time. Combining this with the derivative of (12) enables the wake strength to be found as

$$\epsilon(x,t) = -\frac{\Gamma_0}{b}\frac{e^{-j\omega X}}{KC_0 + KC_1} \tag{24}$$

where ω is the reduced frequency $\nu b/U$, and

$$KC_0 = \int_1^{\infty} e^{-j\omega X}\left[\frac{KK^*}{J^2}\mathrm{Re}\left(\frac{1}{\sqrt{s^2-1}}\right) - \frac{\cos\beta}{J}\right]dX + \frac{\cos\beta\; e^{-j\omega}}{j\omega J} \tag{25a}$$

$$KC_1 = \int_1^\infty e^{-j\omega X}\left[\frac{KK^*}{J^2}\,\mathrm{Re}\left(\frac{s}{\sqrt{s^2-1}}\right)-1\right]dX+\frac{e^{-j\omega}}{j\omega} \tag{25b}$$

These expressions generalize equations (34a, b) of [7]. They are the staggered cascade equivalents of the modified Bessel functions of the second kind $K_0(j\omega)$ and $K_1(j\omega)$ which appear in isolated unsteady airfoil theory, to which they reduce in the limit $d\to\infty$.

From (24), the total circulation can be found by integration to be

$$\Gamma=\frac{\Gamma_0}{j\omega}\frac{e^{-j\omega}}{KC_0+KC_1} \tag{26}$$

If we put the wake strength (24) into the wake integral term of the pressure (14), the result is proportional to $CC-1$, where CC is a cascade analogy to the Theodorsen function, defined as

$$CC=KC_1/(KC_0+KC_1) \tag{27}$$

With this, the pressure expression becomes

$$\frac{p}{\rho U}=-u_0-u_{1_{FP}}\frac{J}{2d}\Gamma_0(CC-1)-j\omega F_{AM}(\theta,t)+P(t) \tag{28}$$

Similarly, the lift is found from (19) as

$$\frac{L}{\rho Ub}=\frac{\Gamma_0}{b}+\frac{\Gamma_0}{b}(CC-1)+j\omega\left(\frac{M_0}{\rho Ub^2}\right) \tag{29}$$

and the moment is found from (21) as

$$\frac{M}{\rho Ub^2}=\frac{M_0}{\rho Ub^2}+\frac{Jd}{\pi b}\ln\frac{K}{K^*}\frac{\Gamma_0}{b}(CC-1)$$
$$-j\omega\int_0^{2\pi}d\theta\frac{1}{2}X^2u_{0_{NC}}\frac{dX}{d\theta} \tag{30}$$

For a stationary gust, the pressure, lift, and moment are given by (22) and (23), with

$$F_G(t)=\frac{J}{2d}\Gamma_0(CC-1)-\frac{KK^*}{2\pi}\int_0^{2\pi}\frac{v_0d\phi}{K^2-\cos^2\phi} \tag{31}$$

These expressions provide general formulas for the unsteady pressure distribution, lift and moment for harmonic in-phase motion of staggered cascades. They generalize the results of [7] to include stagger, and reduce to them for $\beta=0(J=K,\ \theta_T=0)$. In the limit of $d\to\infty$, they reduce to the well-known results for the isolated airfoil case. In the low frequency limit, $\omega\to0$, the cascade Theodorsen function CC tends to $J/(J+\cos\beta)$, so the lift tends to $\rho U\Gamma_0 J/(J+\cos\beta)$, not to $\rho U\Gamma_0$. This somewhat surprising result is discussed in [7], below equation (42). It arises because the far wake has a finite effect on the cascade, unlike in isolated airfoil theory, and this effect is included in the present unsteady theory.

Applications of the Harmonic Motion Theory

We will give the application of the formulas for general harmonic in-phase motion to the three most interesting cases. In each case we will specify the upwash on the center airfoil due to the relative motion of the airfoil in the stream. The velocity v_0 appearing in our formulas will be set to the negative of the specified upwash, since it is the velocity induced by the airfoil vorticity which cancels the specified upwash.

Plunging Motion: $v_0^{(0)}=-W\exp(j\nu t)$. The quasi-steady circulation and moment can be obtained from (8) and (9), of from known flat plate results ([10], below equation (4.28) for example):

$$\frac{\Gamma_0^{(0)}}{b}=2\pi\frac{d}{\pi b}\frac{W\,e^{j\nu t}}{J},$$

$$\frac{M_0^{(0)}}{\rho Ub^2}=2\pi\left(\frac{d}{\pi b}\right)^2\ln\frac{K}{K^*}W\,e^{j\nu t} \tag{32}$$

The pressure, from (28) and (16b) is, with u_0 proportional to $u_{1_{FP}}$ of (15),

$$\frac{p^{(0)}}{\rho U}=-W\,e^{j\nu t}\left[u_{1FP}CC-j\omega X^*\right]+P^{(0)}(t) \tag{33}$$

The lift follows from (29) and (32) as

$$\frac{L^{(0)}}{\rho Ub}=W\,e^{j\nu t}\frac{2\pi}{J}\frac{d}{\pi b}\left[CC+j\omega\frac{Jd}{\pi b}\ln\frac{K}{K^*}\right] \tag{34}$$

The moment is easiest to obtain by integrating the pressure. The integral of the X^* term vanishes, so the result is

$$\frac{M^{(0)}}{\rho Ub^2}=W\,e^{j\nu t}2\pi\left(\frac{d}{\pi b}\right)^2\ln\frac{K}{K^*}CC \tag{35}$$

Pitching Motion: $v_0^{(1)}=-W\,X\exp(j\nu t)$. The quasi-steady expressions for u_0, Γ_0, and M_0 are given in [10], below equation (4.33d), or can be found by integrating the present (7), (8), and (9). The results are

$$u_0^{(1)}=-W\,e^{j\nu t}X^*,\quad M_0^{(1)}=0 \tag{36}$$

$$\frac{\Gamma_0^{(1)}}{b}=2\pi\left(\frac{d}{\pi b}\right)^2\ln\frac{K}{K^*}W\,e^{j\nu t}=\frac{M_0^{(0)}}{\rho Ub^2} \tag{37}$$

The pressure, from (28), is

$$\frac{p^{(1)}}{\rho U}=W\,e^{j\nu t}\left[X^*-u_{1FP}\frac{Jd}{\pi b}\ln\frac{K}{K^*}(CC-1)\right.$$
$$-j\omega\left(\frac{d}{\pi b}\right)^2\ln\frac{K}{K^*}\arctan\left(\frac{K\tan\theta}{K^*}\right)$$
$$\left.+j\omega\int_{\theta_T+\pi}^{\theta}X^*dX\right]+P^{(1)}(t) \tag{38}$$

The lift, from (29), (36), and (35), is

$$\frac{L^{(1)}}{\rho Ub}=2\pi\left(\frac{d}{\pi b}\right)^2\ln\frac{K}{K^*}CC\;W\,e^{j\nu t}=\frac{M^{(0)}}{\rho Ub^2} \tag{39}$$

The moment is obtained by using (36) and (37) in (30). The apparent mass term is not integrable, but yields two definite integrals.

$$\frac{M^{(1)}}{\rho Ub^2}=W\,e^{j\nu t}\left[2\pi\left(\frac{d}{\pi b}\right)^3J\ln^2\frac{K}{K^*}(CC-1)+j\omega I\right] \tag{40a}$$

$$I=\frac{KK^*}{J}\frac{d}{\pi b}\left[\frac{1}{3}\int_0^\pi X^3\frac{\cos(\theta-\theta_T)}{K^2-\cos^2\theta}d\theta\right.$$
$$\left.-J\frac{d}{\pi b}\ln\frac{K}{K^*}\int_0^\pi X^2\frac{d\theta}{K^2-\cos^2\theta}\right] \tag{40b}$$

Sinusoidal Gust: $v_0^{(s)}=-W\exp(j\nu t-j\omega X)$. The quasi-steady circulation is found from (8) as

$$\frac{\Gamma_0^{(s)}}{b}=2\pi\frac{d}{\pi bJ}(JC_0^*-jJC_1^*)W\,e^{j\nu t} \tag{41}$$

where

$$JC_0^*(\omega)=\frac{KK^*}{\pi}\int_0^\pi\frac{\cos\omega X}{K^2-\cos^2\phi}d\phi \tag{42a}$$

$$JC_1^*(\omega)=\frac{KK^*}{\pi}\int_0^\pi\frac{\sin\omega X\,\cos(\phi-\theta_T)}{K^2-\cos^2\phi}d\phi \tag{42b}$$

These two integrals are the staggered cascade equivalents of the Bessel functions J_0 and J_1 to which they reduce as $d\to\infty$. (Notice that the definitions in (42) are slightly different from the JC_0 and JC_1 defined in [7].)

The pressure, lift and moment from (22) and (23) are easily

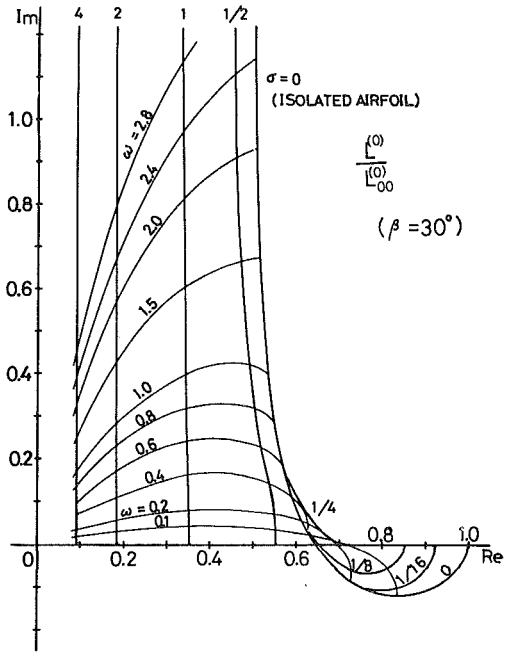

Fig. 3 The normalized lift due to plunging for $\beta = 30$ deg

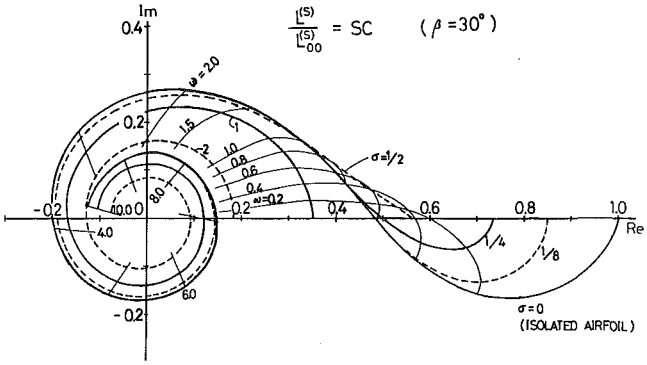

Fig. 4 The normalized lift due to sinusoidal gust for $\beta = 30$ deg

found once F_G is evaluated from (31). We find that $F_G = (\pi bJ/d)SC$, where

$$SC = \frac{d}{\pi bJ}[(JC_0^* - jJC_1^*)CC + jJC_1^*] \tag{43}$$

Then we find

$$\frac{p^{(s)}}{\rho U} = -\frac{\pi bJ}{d} u_{1_{FP}} SC\ W\ e^{j\nu t} + P^{(s)}\ (t) \tag{44}$$

$$\frac{L^{(s)}}{\rho Ub} = 2\pi\ SC\ W\ e^{j\nu t} \tag{45}$$

$$\frac{M^{(s)}}{\rho Ub^2} = 2\pi\ J\frac{d}{\pi b}\ln\frac{K}{K^*} SC\ W\ e^{j\nu t} \tag{46}$$

The function SC is the staggered cascade equivalent of the Sears gust function for an isolated airfoil. It reduces to the function introduced in equation (49*e*) of [7] when the difference in the definitions of JC there and JC^* here is considered, and the equality of J and K for zero stagger is used. It should be pointed out that Murata, et al., in [5] and [6], solved the sinusoidal gust problem by applying conformal mapping to the acceleration potential. Their result can be compared with ours and rearranged to yield the relation

$$SC = \frac{d}{\pi bJ}\frac{1}{j\omega}\frac{1}{KC_0 + KC_1} \tag{47}$$

which expresses SC in a simpler form than (43). The unstaggered version of this relation has been proved directly by the authors of [7].

All these results for plunging and pitching motion, and for the sinusoidal gust, reduce to the unstaggered results of [7] when $\beta = 0$, $J = K$, $\theta_T = 0$, and to the known isolated airfoil results when $d \to \infty$.

Numerical Results

To obtain numerical results for the lift and moment derived in this paper, only numerical quadratures are needed. There are two geometric parameters: the stagger angle β and the solidity $\sigma = 2b/d$. In addition, the reduced frequency $\omega = \nu b/U$ enters. The only numerical complication is the calculation of the integrals KC_0 and KC_1, because of the complicated relation between $s(\zeta_w)$ of (6) and x. The relation between x and ζ_w on the wake ($b \le x < \infty$) follows from the transformation (1) as

$$x = \frac{d}{2\pi}\left[e^{-i\beta}\ \ln\frac{R+\zeta_w}{R-\zeta_w} + e^{i\beta}\ \ln\frac{\zeta_w + R^{-1}}{\zeta_w - R^{-1}}\right]\ (b < x < \infty) \tag{48}$$

This relation, in the form $\zeta_w(x)$ is found numerically by a method described in the Appendix of [9], and then the quadratures for the KC functions can be performed.

To present the numerical results, we normalize the lift and moment by their low frequency, isolated airfoil values, which will be denoted by a double zero subscript.

$$L_{00}^{(0)} = L_{00}^{(s)} = 2\pi\ \rho Ub\ W\ e^{j\nu t},\quad M_{00}^{(0)} = M_{00}^{(s)} = \pi\ \rho Ub^2\ W\ e^{j\nu t} \tag{49}$$

$$L_{00}^{(1)} = \pi\ \rho Ub\ W\ e^{j\nu t},\quad M_{00}^{(1)} = \frac{\pi}{2}\ \rho Ub^2\ W\ e^{j\nu t} \tag{50}$$

The normalized lifts and moments are then

$$\frac{L^{(0)}}{L_{00}{}^{(0)}} = \frac{d}{\pi bJ}\left[CC + j\omega\frac{Jd}{\pi b}\ln\frac{K}{K^*}\right] \tag{51}$$

$$\frac{M^{(0)}}{M_{00}{}^{(0)}} = 2\left(\frac{d}{\pi b}\right)^2 \ln\frac{K}{K^*}\ CC = \frac{L^{(1)}}{L_{00}{}^{(1)}} \tag{52}$$

$$\frac{M^{(1)}}{M_{00}{}^{(1)}} = \frac{2}{\pi}\left[2\pi\left(\frac{d}{\pi b}\right)^3 J\ \ln^2\frac{K}{K^*}\ (CC - 1) + j\omega I\right] \tag{53}$$

$$\frac{L^{(s)}}{L_{00}{}^{(s)}} = SC,\quad \frac{M^{(s)}}{M_{00}{}^{(s)}} = 2\ J\frac{d}{\pi b}\ln\frac{K}{K^*}\ SC \tag{54}$$

The integral I in (53) has been defined in (40*b*).

Calculations have been made over a range of β, σ, and ω. Tabulated results for any combination of $\beta = 30$, 45, 60 deg, $\sigma = 1/32$, 1/16, 1/8, 1/4, 1/2, 1, 2 and $\omega = 0$, 0.01, 0.03, 0.05, 0.1(0.1)2(0.2)3(0.5)10 are available from any of the authors.

As examples we show the results for $\beta = 30$ deg in the figures as plots with the real part on the abscissa and the imaginary part on the ordinate.

Figure 3 shows the lift due to plunging, from (51). The higher solidity cascades have a real part which is nearly independent of reduced frequency, and an imaginary part which increases approximately proportional to ω. Figure 4 gives the sinusoidal gust lift, from (54), and shows the familiar spiral into the origin as ω increases. For $\sigma \ge 1/2$, the low frequency lift has no negative imaginary part, as it does at low solidity. Figure 5 presents the pitching lift from (52), which is the same as the plunging moment. All the imaginary parts are negative, and as the solidity increases, they become very small, while

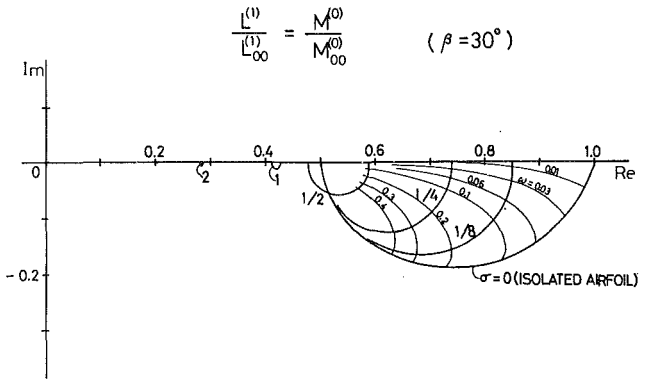

Fig. 5 The normalized lift due to pitching and moment due to plunging for $\beta = 30$ deg

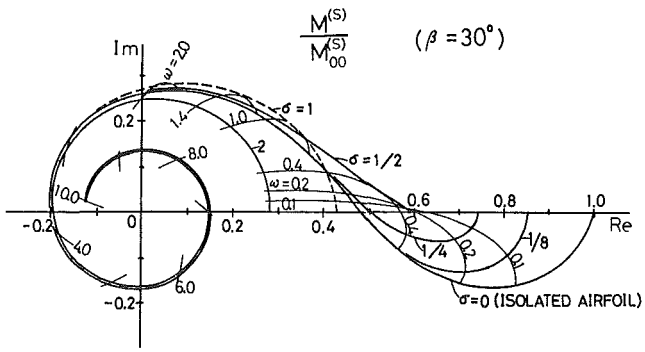

Fig. 6 The normalized moment due to sinusoidal gust for $\beta = 30$ deg

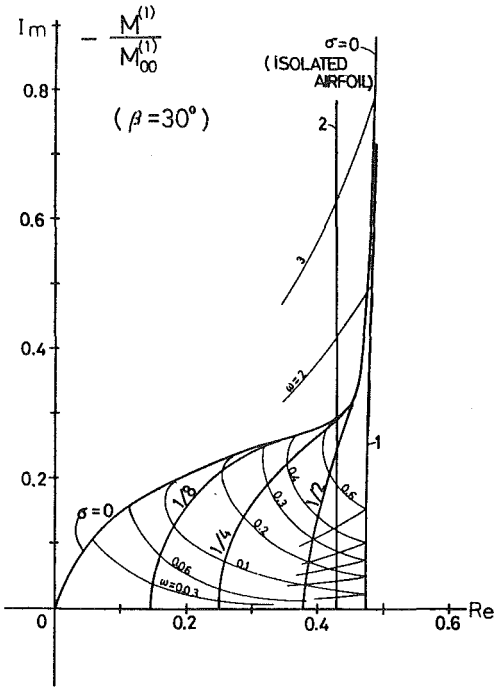

Fig. 7 The normalized moment due to pitching for $\beta = 30$ deg

the real part becomes nearly constant, independent of ω. The sinusoidal gust moment (54) in Fig. 6 shows much the same spiral character as the corresponding lift. Finally, the negative of the moment due to pitching (53) is displayed in Fig. 7. Its real part also becomes independent of reduced frequency at the higher solidities. At the lower solidities, it is nearly independent of reduced frequency and solidity for $\omega > 1$.

Conclusions

The incompressible flow through a staggered cascade of thin airfoils in unsteady in-phase motion has been solved analytically by conformal mapping. This is the extension of the work of Kemp and Ohashi [7] to staggered cascades.

First we considered general unsteady motion, and presented expressions for pressure distribution (up to an unknown additive function of time), lift and moment. They each appear in the form familiar from isolated unsteady airfoil theory, having a quasi-steady part, an apparent mass part, and a wake part. The first two parts depend only on the instantaneous motion of the cascade, while the third part depends on the shed vorticity distribution in the wake. This latter must be determined by the solution of an integral equation which has been formulated here.

For harmonic motion, this integral equation has been solved in the same manner as for isolated airfoils, and general formulas have been given for pressure distribution, lift, and moment. A staggered cascade Theodorsen function *CC* appears, defined by two integrals which depend on reduced frequency, solidity and stagger angle, and which reduce to the K Bessel functions in the isolated airfoil case.

Application of the harmonic results is made to the three important cases of plunging motion (constant upwash), pitching motion (linearly varying upwash), and a sinusoidal gust (sinusoidal upwash). Pressure distributions, lift, and moment are presented for all three cases. The moment due to pitching involves two definite integrals which depend on stagger angle and solidity. The sinusoidal gust lift introduces staggered cascade equivalents of the J_0 and J_1 Bessel functions, but they can be combined with the cascade Theodorsen function to give a staggered cascade gust function *SC*, which is the analogy of the Sears gust function for the isolated airfoil. It involves only the same two integrals as the cascade Theodorsen function. To evaluate the lift and moment for all three types of harmonic motion then required the numerical integration of four definite integrals.

The extensive results calculated show the dependence of lift and moment on the three parameters reduced frequency, solidity and stagger angle. Typical results for a stagger angle of 30 deg have been presented here, and tables of all the results are available from any of the authors. A comparison with the results of Whitehead [1] is given in the Appendix, and shows good agreement, which represents a mutual check on the present work and that of [1].

Although in-phase oscillation is not usually of much physical interest, it makes possible the analytical solution (up to quadratures) of the three parameter staggered oscillating cascade problem, and provides numerical results with a minimum of numerical computation. These results should prove useful as check cases for numerical and approximate solutions of more complex unsteady cascade problems. They also help to elucidate the dependence of lift and moment on the three parameters of this type of flow.

APPENDIX

Whitehead [1] has solved the cascade integral equation by collocation for several stagger angles β, solidities σ and reduced frequencies ω (which he calls ξ, c/s and $\lambda/2$, respectively). He also varies the blade-to-blade phase angle (called β) from 0 to 1.8π. His blade coordinate system has its origin at the leading edge, instead of the mid-chord, and his

Table A-1 Comparison of present results with those of Whitehead [1]

ω	$L^{(0)}/L_{00}^{(0)}$	$M^{(0)}/M_{00}^{(0)}$	$L^{(1)}/L_{00}^{(1)}$	$-M^{(1)}/M_{00}^{(1)}$	$L^{(s)}/L_{00}^{(s)}$	$M^{(s)}/M_{00}^{(s)}$
			$\beta = 30^\circ \quad \sigma = 1$			
0.1	.3504, .0400	.4277,-.0011	.4277,-.0011	.4759, .0261	.3494, .0186	.4265, .0227
	.3504, .0400	.4277,-.0012	.4272,-.0020	.4712, .0336	.3494, .0186	.4265, .0227
1.0	.3467, .4021	.4232,-.0082	.4232,-.0082	.4814, .2576	.2527, .1686	.3085, .2058
	.3467, .4021	.4230,-.0082	.4232,-.0082	.4808, .2604	.2527, .1686	.3086, .2059
			$\beta = 30^\circ \quad \sigma = 1/2$			
0.1	.5564, .0349	.5874,-.0132	.5874,-.0132	.3816, .0388	.5545, .0056	.5852, .0059
	.5564 .0349	.5876,-.0134	.5872,-.0118	.3672, .0316	.5543, .0056	.5853, .0061
1.0	.4938, .4195	.5214,-.0580	.5214,-.0580	.4514, .3101	.3492, .1464	.3687, .1546
	.4938, .4195	.5212,-.0582	.5214,-.0580	.4588, .3112	.3493, .1464	.3688, .1546
			$\beta = 45^\circ \quad \sigma = 1$			
0.1	.4271, .0453	.4864,-.0011	.4864,-.0011	.5001, .0268	.4259, .0210	.4850, .0239
	.4271, .0453	.4862,-.0010	.4858,-.0806	.5004, .0260	.4259, .0209	.4850, .0239
1.0	.4234, .4546	.4821,-.0092	.4821,-.0092	.5049, .2657	.3148, .1891	.3585, .2153
	.4234, .4547	.4820,-.0090	.4821,-.0094	.4976, .2612	.3147, .1892	.3584, .2155
			$\beta = 45^\circ \quad \sigma = 1/2$			
0.1	.6338, .0341	.6416,-.0158	.6416,-.0158	.3565, .0409	.6315, .0021	.6392, .0021
	.6338, .0341	.6416,-.0158	.6404,-.0162	.3552, .0404	.6314, .0020	.6392, .0022
1.0	.5528, .4195	.5596,-.0784	.5596,-.0784	.4395, .3288	.3878, .1321	.3926, .1338
	.5528, .4193	.5596,-.0786	.5596,-.0786	.4392, .3300	.3879, .1318	.3928, .1335
			$\beta = 60^\circ \quad \sigma = 1$			
0.1	.5993, .0552	.5963,-.0011	.5963,-.0011	.5277, .0272	.5979, .0260	.5950, .0258
	.5993, .0552	.5962,-.0012	.5954,-.0004	.5244, .0256	.5978, .0253	.5946, .0253
1.0	.5959, .5527	.5930,-.0106	.5930,-.0106	.5310, .2719	.4603, .2240	.4580, .2228
	.5958, .5529	.5928,-.0102	.5930,-.0104	.5308, .2752	.4568, .2274	.4545, .2263
			$\beta = 60^\circ \quad \sigma = 1/2$			
0.1	.7652, .0315	.7325,-.0201	.7325,-.0201	.3037, .0442	.7627,-.0045	.7300,-.0043
	.7648, .0308	.7320,-.0028	.7324,-.0216	.3000, .0464	.7619,-.0058	.7292,-.0056
1.0	.6462, .3985	.6186,-.1210	.6186,-.1210	.4127, .3655	.4409, .0928	.4220, .0888
	.6488, .3961	.6212,-.1234	.6210,-.1234	.4108, .3684	.4456, .0894	.4264, .0856

moment is measured about the leading edge, nose-down, rather than about the mid-chord, nose-up, as we take it. When these differences, as well as his definitions of upwash velocity, are taken into account, his lift and moment coefficients can be converted to the present normalized values defined in equations (49-54).

A comparison is then possible between his results and the present ones for the case of in-phase oscillation (his $\beta = 0$). Such a comparison is given in Table A-1 for the lift and moment due to plunging, pitching, and a sinusoidal gust. We show the real and imaginary parts of each quantity (in the form R, I) for $\omega = 0.1$ and 1.0, and for the six cases $\beta = 30$, 45, 60 deg, and $\sigma = 1$ and 1/2. The top complex number is the present value, and the bottom complex number is the one calculated from the tables of [1].

The agreement is, on the whole, very good. The differences are mostly only a few percent, except in a few cases where the imaginary parts are small, and the conversion of Whitehead's tabulated values to our definitions could be affected by round-off in his fourth figure. The only notable exception is for $\beta = 45$ deg, $\sigma = 1$, $\omega = 0.1$, where the imaginary part of $L^{(1)}/L_{00}{}^{(1)}$ calculated from Whitehead's values appears much too large in magnitude. The imaginary part of $M^{(0)}/M_{00}{}^{(0)}$ from Whitehead, on the other hand, is in good agreement with the present value. Since these two quantities should be exactly equal, there is some doubt about Whitehead's value of $C_{F\alpha}$ for this case.

This good agreement between the present calculations and those of [1] supplies a mutual confirmation of the correctness of both sets of calculations. Since the present results are found by quadrature from analytical formulas, and those of [1] were obtained by numerical solution of an integral equation using six collocation points, the agreement is particularly satisfying.

One can use this agreement for the in-phase case to infer the equal accuracy of Whitehead's results for his out-of-phase calculations. It is not likely that analytical results of the present kind can ever be obtained for out-of-phase oscillations of staggered cascades, although for unstaggered cascades the 180 and 90 deg phase angle cases are solvable analytically, as is well-known.

References

1 Whitehead, D. S., "Force and Moment Coefficients for Vibrating Aerofoils in Cascade," Aeronautical Research Council R & M 3254, Feb. 1960.

2 Nishiyama, T., and Matsudaira, Y., "Unsteady Response of the Aerofoils in Cascade in Periodically Varying Gust," Technology Reports, Tohoku University, Vol. 38, 1973, pp. 599-613.

3 Mendelson, A., and Carroll, R. W., "Lift and Moment Equations for Oscillating Airfoils in an Infinite Unstaggered Cascade," NACA TN 3263, 1954.

4 Chang, C-C, and Chu, W-H, "Aerodynamic Interference of Cascade Blades in Synchronized Oscillation," ASME *Journal of Applied Mechanics*, Vol. 22, 1955, pp. 503-507, and Discussion, *Journal of Applied Mechanics*, Vol. 23, 1956, pp. 652-653.

5 Murata, S., and Tsujimoto, T., "The Unsteady Forces on Flat-Plate-Airfoils in Cascade Moving through Sinusoidal Gusts," *ZAMM*, Vol. 56, 1976, pp. 205-216.

6 Murata, S., Tsujimoto, Y., and Sonoda, S., "Unsteady Flows Through Cascades," *Bulletin of the Japan Soc. Mech. Eng.*, Vol. 20, 1977, pp. 1277-1283.

7 Kemp, N. H., and Ohashi, H., "Forces on Unstaggered Airfoil Cascades in Unsteady In-Phase Motion," ASME JOURNAL OF FLUIDS ENGINEERING, Vol. 98, 1976, pp. 521-530.

8 von Karman, Th., and Sears, W. R., "Airfoil Theory for Non-Uniform Motion," *Journal of the Aeronautical Sciences*, Vol. 5, 1938, pp. 379-390.

9 Shoji, H., Ohashi, H., and Kemp, N. H., "Analytic Solution for Forces on Staggered Airfoil Cascades in Unsteady In-Phase Motion, Part I, Thin Airfoils with Zero Mean Angle of Attack," Sept. 1978. Available from any of the authors.

10 Fanti, R. A., Kemp, N. H., and Nilson, E. N., "A Theory of Thin Airfoils, Isolated and in Cascade, Yielding Finite Pressures at Smooth Leading Edges," *Journal of the Aeronautical Sciences*, Vol. 25, 1958, pp. 409-424.

Two-Dimensional Performance Analysis and Design of MHD Channels[1]

E. Doss
H. Geyer
R. K. Ahluwalia
K. Im

Engineering Division,
Argonne National Laboratory,
Argonne, Ill. 60439

A two-dimensional model for MHD channel design and analysis has been developed for three different modes of operation: velocity, Mach number, and pressure. Given the distribution of any of these three parameters along the channel, the channel aspect ratio, and the channel operating conditions, the MHD channel geometry can be predicted. The developed two-dimensional design model avoids unnecessary assumptions for surface losses and boundary layer voltage drops that are required in one-dimensional calculations and, thus, can yield a better prediction of MHD channel geometry and performance. The subject model includes a simplified treatment for possible arcing near the electrode walls. A one-dimensional model for slag flow along the channel walls is also incorporated. The effects of wall temperature and slag carry-over on channel performance are discussed.

Introduction

Generally, for convenience, magnetohydrodynamic (MHD) channels are analyzed by using one-dimensional models. Although several approaches [1,2,3] can be used to solve the MHD channel flow equations by a one-dimensional model, they can be broadly classified in two categories: 1) one-dimensional averaging and 2) calculation of one-dimensional inviscid core flow-plus-boundary layer development along the walls, using the integral procedures. There are two serious limitations in the use of one-dimensional models for analyzing the performance of MHD channels. First, the flow in any channel of practical interest is turbulent. This usually necessitates employment of empirical relationships to input the heat flux and shear stress at the walls to the models. However, the heat flux and shear stress are modified by the MHD induced phenomena, namely, the Joule heating and the Lorentz force. These two MHD terms are neither known beforehand, nor can their quantitative effects on heat flux and shear stress be confidently prescribed. Second, the integral boundary layer method is intrinsically incapable of accurately calculating the profiles of flow and electrical variables across the boundary layer, especially with volumic MHD effects present. Boundary layer voltage drop, a very important parameter in determining the performance level of an MHD channel, is very sensitive to the temperature profile in the boundary layer [4]. In view of the second limitation, therefore, the accuracy of the one-dimensional models is limited.

Some investigators [5–9] have used two-dimensional models for analyzing the performance of MHD channels. In references [5,6], the two-dimensional compressible turbulent MHD flow equations are solved between the electrode walls for gas dynamic profiles inside the channel. This procedure obviates the need to consider separately the core flow and the boundary layer region and should, in principle, yield more accurate results. This technique also accounts for the asymmetrical distributions of flow variables that might arise because of the component of the $\mathbf{J} \times \mathbf{B}$ force across the channel. All the past investigations of this kind have focussed on analyzing the operating characteristics of *existing channels* (area mode of operation). However, when it comes to designing a particular MHD channel, the one-dimensional model is almost always used because of the lack of a two-dimensional MHD channel design mode.

This paper describes a two-dimensional channel design model in which the *channel geometry is predicted.* Three design modes of operation are included: 1) pressure mode, 2) velocity mode, and 3) Mach number mode. Given the distribution of any one of these variables along the channel in the core, the channel aspect ratio, and the operating conditions, the channel dimensions can be determined. This capability is a great asset when conducting an investigation for optimum channel configuration. Another advantage of this model is its ability to predict boundary layer separation [5,10], which can drastically impair the performance of an MHD channel.

The walls of an open-cycle, coal-fired MHD generator will become coated with a thin layer of slag. To evaluate its effect on channel design, a conventional hydrodynamic model for slag flow is included, in which the intertia forces and convective terms are justifiably neglected. This model needs an independent calculation of the rate of slag deposition from the core to the generator walls. To this end, the formulation of reference [11] is employed, in which an expression for the slag deposition rate is obtained by solving a set of diffusion equations for the slag vapor and slag particles.

[1] Work supported by DOE/MHD Division.

Contributed by the Fluids Engineering Division for publication in the JOURNAL OF FLUIDS ENGINEERING. Manuscript received by the Fluids Engineering Division, June 13, 1979.

Wall temperature can have significant influence on the boundary layer voltage drop, heat flux to the walls, and, hence, on the channel performance. Moreover, it determines the mechanism by which the current is transported to the electrodes; that is, whether it is through an arc mode or a diffuse mode. In the case of channels operating with cold walls ($T_w \simeq$ 600-800 K) or semi-hot walls ($T_w <$ 1800 K), depending on the current density level and the type of material, arcs can be the principal means of current transport [12]. A simplified treatment for arcing near the electrode walls is included in the present work, to aid in adequately designing MHD channels with cold or semi-hot walls.

The complete model is used to predict the geometry and performance of the U.S. channel design for the U-25 facility [13], in Moscow (as part of the U.S./U.S.S.R. Cooperative Program in MHD) for the three design modes of operation. The results of these modes are compared with the results obtained with the original design, where the area is specified. The channel is designed to operate with clean fuel (no slag) and with cold walls. However, in this work the model is applied to predict the channel performance for a wide range of wall temperatures (800-2100 K) and for different amounts of assumed slag carryover.

Analysis

The two-dimensional compressible turbulent MHD flow equations are numerically solved for the gas dynamic profiles inside the channel. The numerical scheme is essentially a modified version of the Patankar and Spalding [14] method for handling internal flows.

Governing Equations. The two-dimensional flow equations in the Cartesian coordinates, with the usual boundary layer assumptions and the eddy viscosity used to relate the turbulent fluctuating quantities to the mean flow variables are:

Continuity

$$\frac{\partial}{\partial x}(\rho u a) + \frac{\partial}{\partial y}(\rho v a) = 0,$$

where the control volume considered is $\Delta x \cdot \Delta y \cdot a$, and $a(x)$ is the effective width of the channel in the z-direction (i.e., after accounting for the boundary layers on the sidewalls of the channel).

X-momentum

$$\rho u \frac{\partial u}{\partial x} + \rho v \frac{\partial u}{\partial y} = -\frac{\partial p}{\partial x} + J_y B_z + \frac{\partial}{\partial y}\left[\left(\mu + \epsilon\right)\frac{\partial u}{\partial y}\right].$$

Y-momentum

$$\frac{\partial p}{\partial y} = -J_x B_z.$$

Energy

$$\rho u \frac{\partial h}{\partial x} + \rho v \frac{\partial h}{\partial y} = u\frac{\partial p}{\partial x} + v\frac{\partial p}{\partial y} + (\mu+\epsilon)\left(\frac{\partial u}{\partial y}\right)^2 + \frac{J^2}{\sigma} + \frac{\partial}{\partial y}\left[\left(\frac{\mu}{P} + \frac{\epsilon}{P_t}\right)\frac{\partial h}{\partial y}\right].$$

Thermodynamic relationships are required for expression of gas density, temperature, electrical conductivity and Hall parameter as functions of pressure and enthalpy. These relationships are obtained by assuming the gas to be in chemical equilibrium [15], and the dependent variables (ρ, T, σ, and β) are curve fitted by fourth order polynomials.

Prandtl's mixing length theory is employed to relate the eddy viscosity to mean flow quantities. The electron energy and electron species equations can also be included if considerable nonequilibrium exists between the plasma temperature and the electron temperature [5].

It should be emphasized here that these equations, describing the two-dimensional flow along the MHD channel, correspond to the boundary layer equations. However, away from the walls, turbulence effects disappear and the equations automatically describe an inviscid flow in the core where the normal diffusion terms become negligible.

Initial and Boundary Conditions. The initial conditions on u and h ($h = \tilde{h} - 1/2\ u^2$) must be provided to start the integration procedure. For the initial turbulent profile of the mean velocity u, a $1/n$ power law variation is assumed: $n = 7$ for smooth walls and $n =$ 4-6 for rough walls [16]. For the initial temperature profile, the relationship

$$\frac{\tilde{h} - h_w}{h_\infty - h_w} = \left(\frac{u}{u_\infty}\right)^m$$

is used with an assigned input value for the exponent m ($m =$ 1.0).

The wall boundary conditions are imposed on u and h. At the two walls $u = 0$ and $v/u =$ slope at the wall. The condition on h at the wall is determined from the prescribed wall temperature (T_w) and the local value of the pressure, p.

Electrical Fields. The electric field **E** and the current density **J** can be obtained by solving Maxwell's equations:

$$\mathbf{E} + \mathbf{U}\times\mathbf{B} = \frac{\mathbf{J}}{\sigma} + \frac{\beta}{\sigma}\frac{\mathbf{J}\times\mathbf{B}}{\mathrm{B}}, \text{ (ohm's law)}$$

$$\nabla\times\mathbf{E} = 0$$

$$\nabla\cdot\mathbf{J} = 0.$$

By defining a stream function for the current or a potential function for the electric field, Maxwell's equations can be reduced to an elliptic second order boundary value problem. The solution of this problem is lengthy and can substantially slow the computation of the overall flow fields. To alleviate

Nomenclature

a = effective channel width $a = W - 2\delta^*$
$\mathbf{B}$ = magnetic field (0, 0, B)
$\mathbf{E}$ = electric field
h = static enthalpy
$\tilde{h}$ = total enthalpy, $\tilde{h} = h + u^2/2$
H = geometrical channel height
I_L = load current
$\mathbf{J}$ = current density
k = thermal conductivity
$\dot{m}$ = mass flow rate
$\dot{m}_s$ = slag deposition rate per unit area
p = static pressure
P = Prandtl number
P_t = turbulent Prandtl number
s = slag thickness
T = static temperature
u = x-velocity component
v = y-velocity component
x,y,z = Cartesian coordinates
W = geometrical channel width
β = Hall parameter
δ^* = displacement thickness
ϵ = eddy viscosity
ρ = mass density
θ = diagonalization angle
μ = molecular viscosity
σ = electrical conductivity
ω = nondimensional normal coordinate ($\psi/\dot{m}$)
ψ = stream function per unit channel width

Subscripts

H = y-direction (electrode walls)
W = z-direction (sidewalls)
x,y,z = Cartesian coordinates
∞ = free stream
$<>$ = average, in the y-direction

this problem, the approximation of "infinitely fine segmentation" is implemented. This approximation is based on the notion that, because of very fine segmentation of the electrode walls, the variation of the fields **E** and **J** will be very small in the flow direction ($\partial/\partial x << \partial/\partial y$). This situation is satisfied, at least in the main part of the channel, away from the inlet and exit and not very close to the electrode walls, and implies that

$$\frac{\partial}{\partial x}\mathbf{E} \simeq \frac{\partial}{\partial x}\mathbf{J} \simeq 0$$

Applying these relations to Maxwell's equations, it follows readily that E_x and J_y vary only with x, so that their profiles on the electrode walls reduce to constants. It then becomes possible to determine the constants $E_x(x)$ and $J_y(x)$ and the profiles $J_x(x,y)$ and $E_y(x,y)$ at every x-location along the channel from the Ohm's law, without solving the differential equations [17].

For Faraday generators, by definition $<J_x> = 0$; therefore, only one extra condition is required to determine **J** and **E**. This condition can be supplied by specifying a load factor, $K = E_y/uB$, which may be based on the centerline or average values along the channel, the Faraday potential, or the load resistance.

For diagonally connected generators, the relationship $\oint \mathbf{E} \cdot d\mathbf{s} = 0$, holds along any path connecting two points on the diagonal connection. Consequently, the diagonal configuration is characterized by the relation, $\tan\theta = -<E_y>/E_x$, where θ is the diagonalization angle, measured from the y-axis. Two conditions are required to specify **J** and **E** completely. These can include the diagonalization angle θ, the load current, the load factor, the load potential, or the load resistance. Reference [18] gives a detailed description of different options for the Faraday and diagonal generators.

Method of Solution. Solution of the equations of motion is obtained by an implicit finite difference scheme. The numerical procedure contains the desirable features of the method suggested by Patanker and Spalding [14], particularly the treatment of the Couette-flow region, which eliminates the need to use a large number of grid points near the walls.

The form of the equations is considerably simplified by the use of the von Mises stream function coordinates (x, ω) of the form:

$$x = x, \qquad \omega = \frac{\psi(x,y)}{\dot{m}}$$

$$\frac{\partial\psi}{\partial x} = -\rho v a, \qquad \frac{\partial\psi}{\partial y} = \rho u a.$$

This tranformation results in a coordinate system that adjusts itself automatically to the height of the channel (distance between the electrode walls) with the continuity equation implicitly satisfied. The dependent varaiables u and h are assumed to have stepwise variation in the downstream direction and to vary linearly between grid points in the cross direction. By evaluating the coefficients in the finite difference equations at the upstream x-values, algebraic equations are obtained that are linear in the unknowns.

Iteration Procedure. For the area mode of operation, the solution of the equations proceed as follows [5, 10]. Starting from the initial distribution of u and h across the channel and an initial guess of $\partial p/\partial x$, the finite difference equations are solved for the first integration step. The new values of u, h, and p are used to calculate the mass flow rate. If the computed mass rate of flow is equal to the initial mass flow rate (within a given tolerance), these new distributions of u, h, and p are accepted as the initial distributions for the next integration step. If not, a new $\partial p/\partial x$ is chosen and the procedure is repeated. The conservation of mass is checked by the following integral form:

$$\dot{m} = (W - 2\delta_w^*)\int_0^H \rho u dy,$$

where $(W(x) - 2\delta_w^*)$ is the effective width of the channel after accounting for the sidewall displacement thickness, δ_w^*.

For the velocity and Mach number modes of operation, conservation of mass is used, along with a prescribed aspect ratio, to determine the channel height and width. The iteration procedure over the assumed pressure gradient ($\partial p/\partial x$) is applied to satisfy, within an allowable tolerance, the prescribed velocity or Mach number distribution along the channel. For the pressure mode of operation, no interation is needed, except to update the transport and thermodynamic properties of the plasma and the MHD terms, as in the other modes of operation.

Treatment of Sidewalls. The effects of finite channel width and, in particular, the boundary layer development on the sidewalls are taken into account by considering the previously mentioned integral form of mass conservation, where the sidewall displacement thickness (δ_w^*) appears explicity.

If the temperatures of the four walls are the same, and the difference in MHD effects on electrodes and sidewalls can be neglected, the sidewall displacement thickness may be taken as the arithmetic average of the computed displacement thickness on the two electrode walls, δ_w^*, up to the point where the sidewall boundary layers merge. This situation is likely to happen in medium and large MHD channels, particularly when the height/width aspect ratio is greater than 1. In such as case, beyond the point of fully developed flow over the sidewalls, the dimensionless velocity and temperature profiles are assumed the same for the sidewalls as for the electrode walls. Then the displacement thickness over the sidewall can be evaluated as follows:

$$\delta_w^* = \delta_H^* \frac{W/2}{\delta_H}.$$

This means a similarity in the ratio of the boundary layer thickness, δ, and the displacement thickness, δ^*, is assumed over different walls.

If, however, the sidewalls temperature is different from the electrode walls temperature, or if the MHD effects are substantially different between the electrode and sidewalls, which is quite likely to be the case [19,20], the calculations of the sidewall boundary layer should be performed separately in conjunction with the two-dimensional model being described. This can be achieved by a simplified procedure, as discussed in reference [19]. Otherwise, the full three-dimensional equations must be solved. For MHD channels operating with a low magnetic field (low magnetic interaction), as the one considered later, the sidewalls boundary layers will not be much different form the electrode walls boundary layers along most of the channel.

Treatment of Arcs. The two-dimensional model being discussed has been extended to MHD channel flows with cold walls where current is transported to the electrode surface through arcs. At the present time, there exists no satisfactory analytical model for constricted current (arcs) transport phenomenon. The present analysis employs the simplified lumped-parameter arcing model suggested by Solbes [3]. In this model, the electrical fields are computed across the boundary layer assuming diffuse current transport and the integration is arbitrarily cut-off were the electric field E_y exceeds a prescribed value (10-30 kV/m) for which it is judged that the diffuse-current model becomes invalid.

The total voltage drop in MHD channels is composed of the voltage drops in the thermal boundary layer and in the arc-

plus-sheath region. The major fraction of the voltage drop occurs in the boundary layer. For example, the boundary layer voltage drop in the present application is around 400-800 V. This may be compared to 30-40 V arc voltage drop that was experimentally estimated by Solbes [3]. In the arcing model adopted in the present study, the results are not very sensitive to the assumed value of the electric field in the range of 10-30 kV/m. A more recent work by Demetriades, et al [21], discusses a more accurate method of estimating the critical cut-off value for the electric field, the voltage drop and the plasma conductivity in the arc region.

Treatment of Slag Flow. In the presence of slag, the slag flow is described by a one-dimensional flow model [11] that neglects the convective terms, but retains terms to account for MHD forces and Joule heating in the slag layer. The equations solved are:

Continuity:

$$\frac{d}{dx}\left(\int_0^s \rho u dy\right) = \dot{m}_s(x)$$

where $\dot{m}_s(x)$ is the slag deposition rate and s is the slag thickness.

Momentum:

$$0 = -\frac{dp}{dx} + (\mathbf{J}\times\mathbf{B}) + \frac{d}{dy}\left(\mu\frac{du}{dy}\right).$$

Energy:

$$0 = (\mathbf{J}\cdot\mathbf{E}) + \frac{d}{dy}\left(k\frac{dT}{dy}\right).$$

Temperature-dependent slag properties are used in the analysis.

These equations can be directly integrated once the heat flux and shear stress at the slag surface are computed from the two-dimensional flow model. The slag surface temperature, in turn, serves as a boundary condition to the gas flow energy equation. The two-dimensional model also has been modified to include the effect of leakage current along the slag and slag resistance over the channel walls.

Slag Deposition Rate. In coal-fired MHD generators, the slag comes into the generator in both gaseous and liquid forms. The high temperatures prevalent in the coal combustor, about 2800 K or more, will cause a fraction of slag in the coal to vaporize. The slag vaporizes precipitously at 2500 K or so. The actual amount of slag vaporized in the combustor is a function of combustor design (1-stage or 2-stage) and of flow configuration (plug flow or swirl flow). As the slag vapor flows into the channel, it encounters lower temperature regions wherein the slag vapor content is higher than that corresponding to the saturation condition. The slag vapor (supersaturated) in excess of the saturation content begins to nucleate and to form many submicron-sized liquid particles through the process of homogeneous nucleation. Furthermore, the condensed liquid particles grow by acting as a site for vapor condensation (heterogeneous nucleation). Slag deposition at the wall occurs both by vapor diffusion and by particle migration to the wall. Typically, most of the particles in the channel are submicron in size; their mechanism of desposition to the wall is thermophoresis, a thermal force generated by the temperature gradient at the wall. The mathematical details of these physical processes are found in reference [11]. For the purpose of the present study, it is sufficient to curve-fit the results of reference [11], that were obtained for the particular applications considered here by a simple expression for the slag deposition rate as a function of the axial distance along the channel and the difference between the plasma core and the surface temperature.

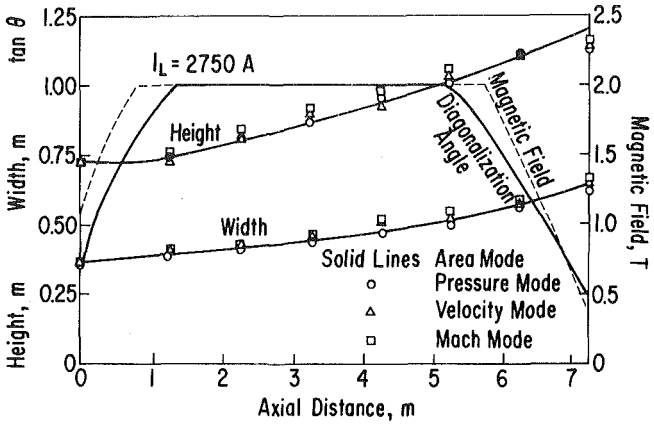

Fig. 1 U-25 channel specification

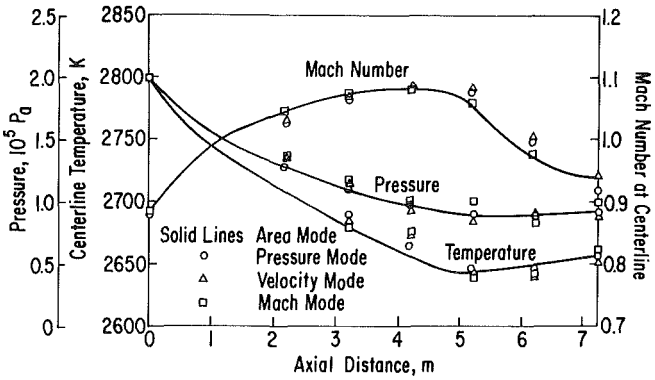

Fig. 2 Validation of two-dimensional code

Results and Discussion

Validation of the Analytical Model for the Design Modes. The two-dimensional numerical model has been tested using the design conditions of the American U-25 channel, Revision 7-E [13]. The channel geometry, applied magnetic field and the electrode diagonalization angle are given in Fig. 1. The working fluid is the stoichiometric combustion products of natural gas and N_2/O_2 mixture in the ratio of 1.72 by volume, preheated to 1473 K. Seed in the form of K_2CO_3 aqueous solution is added in the combustor. The design mass flow rate is 50 kg/s; the conducting plasma enters the channel at approximately 0.3 MPa stagnation pressure. With the channel geometry and inlet operating conditons specified, the analytical model is run in the area mode to obtain the channel performance (Fig. 2). Then, the calculated distribution of the pressure or velocity or Mach number along the channel is used as input, together with the channel aspect ratio, to predict the channel geometry and performance. The results of the four modes of operation are presented in Table 1. The close agreement between the results of the four modes of operation serves as a check on the internal consistency of the numerical analysis. Also the analytical results from the model compare favorably with the experimental data for the U-25 Bypass channel [22]. (The U-25 Bypass channel is a part of the U.S.S.R. U-25 facility where joint U.S./U.S.S.R. tests are performed under a cooperative program in MHD). Therefore, the developed two-dimensional model can be used as a design tool for MHD channels.

Differences in the results given in Table 1 can be further reduced by tightening the tolerance in the numerical interation procedure. The actual distributions of the variables along the channel, shown in Figs. 1 and 2, are the same for the different modes within the prescribed input tolerance.

Table 1 Results of the two-dimensional design model for the four modes of operation (T_w = 2100 K, I_L = 2750 A)

Inlet conditions	Area mode	Pressure mode	Mach mode	Velocity mode
Area, m^2	0.73 × 0.351	0.73 × 0.351	0.73 × 0.351	0.73 × 0.351
Pressure, atm (10^5 Pa)	2.0	2.0	2.0	2.0
Temperature, K	2798	2798	2798	2798
Mach Number	0.787	0.787	0.787	0.787
Outlet Conditions				
Area, m^2	1.178 × 0.641	1.13 × 0.617	1.21 × 0.659	1.15 × 0.626
Pressure, atm (10^5 Pa)	0.909	0.909	0.897	0.897
Temperature, K	2655.6	2658	2656.3	2654.2
Mach number	0.937	0.921	0.922	0.935
Power output, MW	13.56	13.75	13.86	13.85
Total heat loss, MW	18	17.74	17.77	18.2

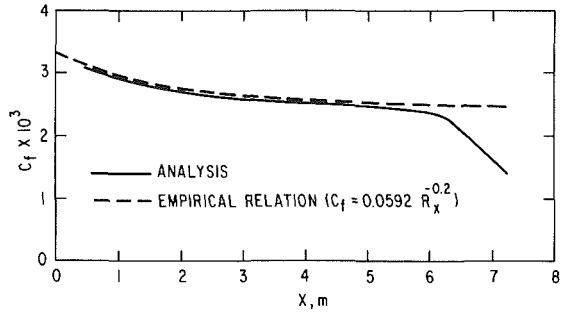

Fig. 3 Variation of the skin friction coefficient along the channel

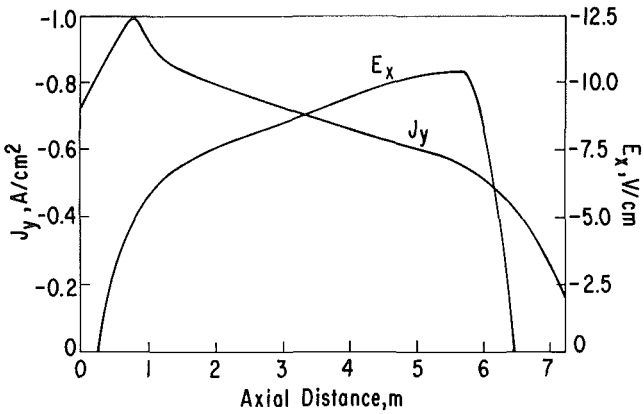

Fig. 4 Axial distribution of transverse current density and electric field

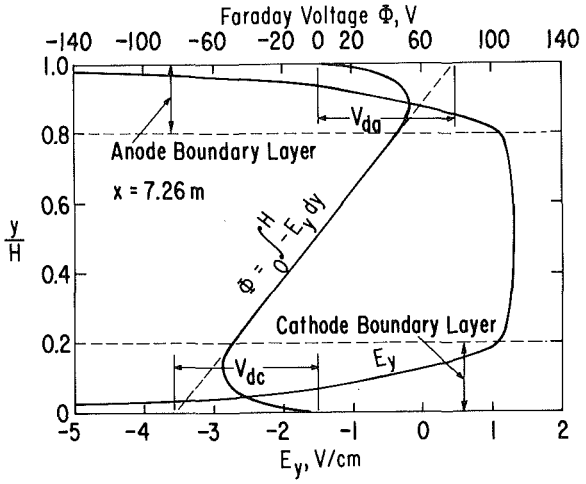

Fig. 5 Cathode and anode boundary layer voltage drops (V_{dc}, V_{da}) at the channel exit

Figure 3 present the variation of the skin friction coefficient along the electrode walls of the channel for smooth walls. The dashed curve is obtained from the empirical relationship for smooth walls [16], for flow over a flat plate. The solid curve, as obtained from the analysis, indicates that the skin friction decreases slightly along the channel, with a substantial drop in the last 1.5 meter. This is due to flow deceleration in the last portion of the channel where a pressure recovery takes place and the MHD channel behaves like a diffuser.

It should be mentioned here that the U-25 channel is a single-load, diagonally-connected generator. In the two power takeoff regions, at the beginning and end of the channel, the Hall field may become positive, unnecessarily impairing the channel performance by absorbing power at those locations. In such a case, it is prudent to use diodes to prevent electric field reversal in these regions [13]. Therefore, in the analytical model, if the Hall field becomes positive in any region, it is assigned a zero value there; this helps to explain the Hall field distribution sketched in Fig. 4.

Effect of Wall Temperature on Channel Performance. The wall temperature affects channel performance primarily because of its influence on the voltage drop in the boundary layer, and it also determines the mechanism of current transport to the electrodes. In general, the lower the wall temperature, the higher the ohmic voltage drop that results from the lowering of the electrical conductivity of the plasma. The exact definition of boundary layer voltage drop is given in Fig. 5. In this particular illustration, the net Faraday voltage Φ at the channel exit is zero. The influence of wall temperature on the boundary layer voltage drop is depicted in Fig. 6, where it is shown that the voltage drop increases as the wall temperature is decreased to 800 K from 2100 K. Of course, for the case of cold walls, 800 K, for example, arcs set in and locally rise the electrical conductivity in the arc region; however, the rest of the boundary layer is still colder than the 2100 K wall temperature case. As the flow proceeds downstream along the channel, the boundary layer grows and voltage drop increases. The voltage drop decreases in the last meter of the channel because of the tapering of the magnetic field there. In these calculations, the static inlet temperature was kept constant.

The heat flux to the wall is an inverse function of wall temperature. This implies that a lower wall temperature is accompanied by reduced core temperature, and this, together with higher boundary layer voltage drops, leads to lower

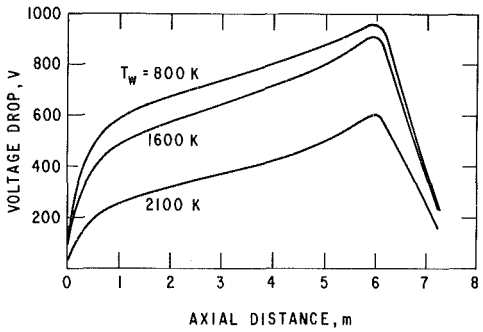

Fig. 6 Variation of voltage drop with wall temperature

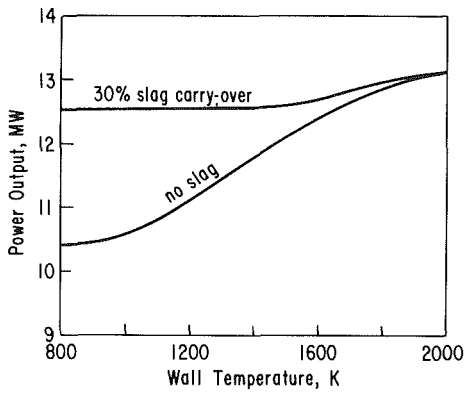

Fig. 7 Effect of wall temperature on channel performance

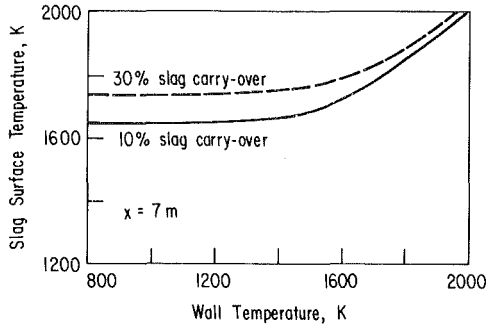

Fig. 8 Apparent wall temperature of slagging U-25 channel

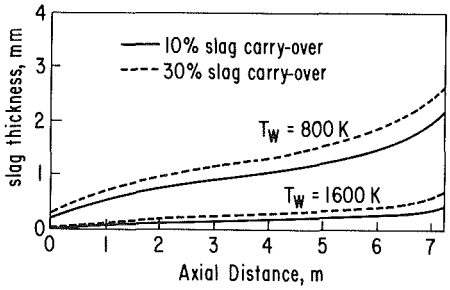

Fig. 9 Dynamics of slag thickness

power output. Figure 7 shows a 30 percent power reduction as wall temperature is reduced to 800 K from 20000 K (no slag case).

Effect of Slag on a U-25-Type Channel. To estimate the effects of the pressence of slag on channel performance, a U-25 type channel also was analyzed for 10 and 30 percent slag carryover from Montana coal. The following slag properties were used in all computations:

slag viscosity: $\mu = 5500 \exp[-0.00703(T-800)]$ kg/(m•s)

slag electrical conductivity: $\sigma = 0.3 \exp[0.00374(T-800)]$ S/m, $T < 1600$ K

$= 6.0 \exp[0.00229(T-1600)]$ S/m, $T \geq 1600$ K

slag thermal conductivity: $k = 1.0$ W/(m•K)

slag mass density: $\rho = 2700$ kg/m^3

The results of slag desposition model described in reference [11] were curve-fitted for this application over a wide range of surface temperatures to obtain the following expression for the slag deposition rate:

10 percent slag carry-over

$\dot{m}_s(x)/(T_{\text{core}} - T_s) = 10^{-7}(8.245 - 0.2592x - 0.00953x^2)$kg/(m^2•s•K),

30 percent slag carry-over

$\dot{m}_s(x)/(T_{\text{core}} - T_s) = 10^{-6}(2.514 - 0.06354x - 0.003739x^2)$ kg/(m^2•s•K), where x is the distance along the channel, T_{core} is the plasma core temperature, and T_s is the slag surface temperature.

Figure 7 presents the performance of a slagging U-25 channel with 30 percent slag carry-over. In the presence of slag, the slag-plasma interface temperature acts as the apparent wall temperature. Therefore, the heat flux to the wall is reduced, as is the electrical resistance of the plasma. Consequently, the power output of the MHD channel with slagging walls increases, particularly for cold walls. It is also shown that the power output in the presence of slag is almost constant and is independent of the wall temperature for T_w less than 1500 K. This suggests that the slag surface temperature for T_w less than 1500 K is also independent of the wall temperature, which is confirmed in Fig. 8. For 10 percent slag carry-over, the slag surface temperature (in most of the channel) is approximately 1650 K for T_w less than 1500 K, increases linearly until it becomes the same as the wall temperature at levels where no slag deposition can occur. For 30 percent carryover, the curve shifts upward; the surface temperature is approximately 1750 K for $T_w < 1400$ K and then increases with wall temperature in the manner described above. These results agree well with a Stanford University experiment in which a slag surface temperature of 1750 K was measured [12].

Typical values of slag thickness are shown in Fig. 9. The reason for the rapid increase of slag thickness near the channel exit is the reduction of shear stress because of the slight adverse pressure gradient near the exit of this particular channel. Figure 9 shows that, for 30 percent slag carry-over, the slag thickness at the channel exit is approximately 3 mm for $T_w = 800$ K.

Figures 10 and 11 show the heat flux distribution along the channel for $T_w = 800$ K and 1600 K, in that order, and for the three cases investigated (no slag, 10 percent slag carry-over, and 30 percent slag carry-over). The wall heat flux in presence of slag is reduced because of the effective thermal insulation; for $T_w = 800$ K, the surface temperature jumps to approximately 1700 K, and the heat flux is reduced by approximately 50 W/cm^2 for 30 percent slag carry-over. On the other hand, for $T_w = 1600$ K, the slag surface temperature is only 1780 K, resulting in a reduction in wall heat flux of less than 10 W/cm^2 for 30 percent slag carry-over. This explains

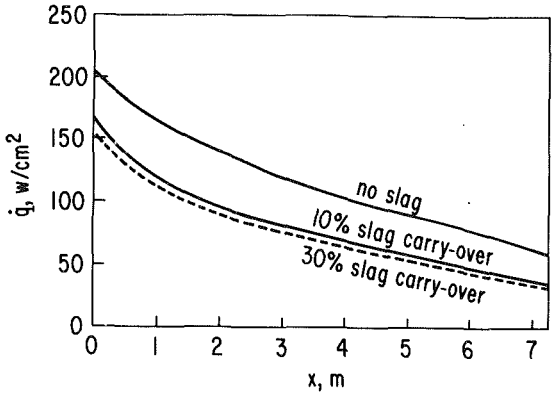

Fig. 10 Heat flux distribution (T_w = 800 K)

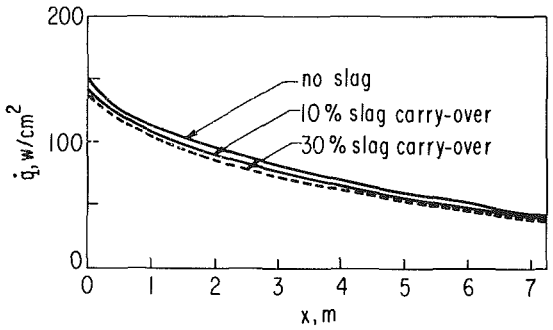

Fig. 11 Heat flux distribution (T_w = 1600 K)

the noticeable improvement in the power output seen in Fig. 7 for low temperature walls, as compared to high temperature walls.

Summary and Conclusions

A two-dimensional MHD channel *design model* has been developed for three modes of operation: the velocity, Mach number, and pressure modes. The MHD channel geometry can be predicted, given the distribution of any of these three parameters and the channel aspect ratio. The developed design model avoids unnecessary assumptions for surface losses and boundary layer voltage drops and, thus, can yield a better prediction for MHD channel geometry and performance. The results of these modes are in excellent agreement with the results obtained with an original design, where the area is specified.

An arcing model has been incorporated in the analysis, which allows MHD channels with cold walls to be rationally analyzed. In this arcing model, the location of the arc is determined by an electric field cut-off criterion. The calculations indicate substantial increase in the boundary layer voltage drop and 30% increase in wall heat flux as the wall temperature is reduced to 800 K from 2100 K; the two adverse effects combine to reduce the channel output by 30 percent.

The effect of slag on channel performance has been studied, using a conventional one-dimensional model for slag flow and a refined procedure for computing the rate of slag deposition to the channel walls; slag behavior is directly coupled to the two-dimensional flow model. The presence of slag layer elevates the apparent wall temperature, thereby improving the performance of the channel, especially at lower wall temperatures. It is found that the slag-plasma interface temperature is nearly independent of the wall temperature for cold walls, and increases almost linearly as the wall temperature is raised further; the channel output shows a similar trend.

Further work is warranted for clarification of nonhomogeneities resulting from arc formations, interaction of slag with seed, enhancement of heat transfer by radiation as a result of the presence of slag particles, and the stability of a slag layer in the arcing mode. Resolution of these equations will improve understanding of the behavior of MHD channels with cold or slagging walls.[2]

[2] Further progress has been made in extending the present analysis to a quasi-three-dimensional model that accounts for the MHD nature unique to the sidewall boundary layers [23], and in including the contribution of gas and particles radiation [24,25]. However, for the channel size considered in the present work, the gas radiation is expected to be a second-order effect.

Acknowledgments

The research activity, which formed the basis of the paper, was funded by the U.S. Department of Energy under Contract No. W-31-109-ENG-38. The participation of Dr. Z. El-Derini in the initial phase of this study is appreciated.

References

1 "Final Report on the Design of the MHD Generator Channel for the High Performance Demonstration Experiment," Rept. FE-1542-4, MEPP-SCO, Inc. Boston, Mass., Aug. 1977; also available from the National Technical Information Service.

2 Bityurin, V. A., Lubimov, G. A., Maslennikov, G. I., and Medlin, S. A., "Engineering Method of Flow Calculation in Channel of MHD Generator," First Joint Soviet-American Colloquim in the Problems of MHD-Conversion of Energy, Moscow, Feb. 1974.

3 Solbes, A., Petty, S., Sadovnik, I., and Kessler, R., "Mark VI MHD Generator Studies," Proceedings of the 16th Engineering Aspects of MHD Symposium, University of Pittsburgh, Pittsburgh, Pa., May 1977, pp. I.2.11.

4 Ahluwalia, R. K., and Doss, E. D., "Convective Heat Transfer in MHD Channels and its Influence on Channel Performance," AIAA-80-178, AIAA 18th Aerospace Sciences Meeting, Jan. 1980, Pasadena, Calif., Also, *J. Energy,* Vol. 4, No. 3, June 1980, pp. 126–134.

5 Doss, E. D., et al., "Two-Dimensional Flow in MHD Ducts with Transverse Asymmetries," *AIAA Journal,* Vol. 13, May 1975, pp. 545–546.

6 Blottner, F. G., "Flow Predictions for MHD Channels with an Approximation for Three-Dimensional Effects," AIAA Paper No. 78-1172, 11th Fluid and Plasma Dynamics Conference, July 1978.

7 Daily, J. W., et al, "Boundary-layer Profile Measurements in a Combustion Driven MHD Generator," *AIAA J.,* Vol. 14, No. 8, Aug. 1976.

8 High, M. D., and Felderman, E. J., "Turbulent MHD Boundary Layers with Electron Thermal Nonequilibrium and Finite Rate Ionization," *AIAA J.,* Vol. 10, 1972.

9 Doss, E. D., Dwyer, H. A., and Hoffman, M. A., "Influence of Segmentation and Ambipolar Diffusion on MHD Nonequilibrium Boundary Layers," *AIAA J.,* Vol. 12, No. 2, Feb. 1974, pp. 155.

10 Doss, E. D., and Geyer, H. K., "Two-Dimensional Subsonic Diffuser Code," Argonne National Laboratory Report No. ANL/MHD-77-1, Argonne, Ill., July 1977, also *Journal of Energy,* Vol. 1, No. 6, 1977.

11 Doss, E., and Im, K., "Slag Deposition and its Effect on the Performance of MHD Channels," AIAA Paper No. 79-0189, 17th Aerospace Science Meeting, Jan. 1979.

12 Rodgers, M. E., Ariessohn, P. C., and Kruger, C. H., "Comparison of Measurements and Predictions of the Fluid Mechanics and Thermal Behavior of MHD Channel Slag Layers," *Proceedings of the 16th Engineering Aspects of MHD Symposium,* University of Pittsburgh, Pittsburgh, Pa., May 1977, pp. VIII.2.26.

13 Brogan, T. R., Aframe, A. M., and Hill, J. A., "Preliminary Design of a Single Output Variable Wall Angle Windowframe MHD Channel for the U-25 Power Plant," 6th International MHD Symposium, Washington, D. C., June 1975, Vol. 1, pp. 267.

14 Patankar, S. V., and Spalding, D. B., *Heat and Mass Tranfer in Boundary Layers,* Margon-Grampian, London, 1967.

15 Sacks, R. A., et al., "Modified NASA-Lewis Chemical Equilibrium Code for MHD Applications," ANL&MHD-9-15, Argonne National Laboratory, Argonne, Ill., Dec. 79.

16 Schlichting, H., Boundary Layer Theory, Sixth Edition, McGraw-Hill, N.Y., 1968.

17 Rosa, R. J., "Physical Principles of Magnetohydrodynamic Power Generation," *Physics of Fluids,* Vol. 4, No. 2, Feb. 1961, pp. 182–194.

18 Louis, J. F., "Critical Contribution in MHD Power Generation," MIT, Report No. FE-2215-3, Mar. 1976, Mass. Also available from the National Technical Information Service.

19 Doss, E. D., and Curry, B. P., "Studies of the 3-D Coupled Flow Bet-

ween the Electrode and Side Walls of the MHD Channels," AIAA Paper No. 76-311, AIAA 9th Fluid and Plasma Dynamics Conference, July 1976.

20 Ranklin, R. R., Self, S. A., and Eustis, R. H., "A Study of MHD Insulator Wall Boundary Layer," *Proceedings of the 16th Conference on Engineering Aspects of MHD,* The University of Pittsburgh, Pittsburgh, Pa., May 1977.

21 Demetriades, S. T., Oliver, D. A., and Maxwell, C. D., "Current Transport Mechanisms in the Boundary Regions of MHD Generators," AIAA Paper No. 80-249, AIAA 18th Aerospace Sciences Meeting, Pasadena, Calif., Jan. 1980.

22 "U.S./U.S.S.R. Cooperative Program in Open Cycle MHD Electrical Power Generation, Joint Test Report No. 3," ANL-IVTAN-JT3, Argonne National Laboratory, Argonne, Ill., 1980.

23 Ahluwalia, R. K., and Doss, E. D., "Quasi-Three-Dimensional Modeling of Flow in MHD Channels," *Numerical Heat Transfer,* Vol. 3, 1980, pp. 67–87.

24 Im, K. H., and Ahluwalia, R. K., "Heat Transfer Including Radiation and Slag Particles Evaluation in MHD Channels-I," AIAA Paper No. 80-250, AIAA 18th Aerospace Sciences Meeting, Pasadena, Calif., Jan. 1980.

25 Ahluwalia, R. K., and Im, K. H., "Heat Transfer Including Particle and Gas Radiation in Subsonic MHD Diffusers-II," AIAA Paper No. 80-252, AIAA 18th Aerospace Sciences Meeting, Pasadena, Calif., Jan. 1980.

A Prediction Method for Planar Diffuser Flows

J. Bardina

A. Lyrio

S. J. Kline

J. H. Ferziger

J. P. Johnston

Heat Transfer and Turbulence Mechanics Group,
Thermosciences Division,
Department of Mechanical Engineering,
Stanford University,
Stanford, Calif. 94305

A method is presented for computation of performance of two-dimensional (planar) diffusers with steady turbulent inflow of an incompressible fluid. Previous methods can predict one regime of flow. The present method gives accurate predictions covering three flow regimes: unstalled flow, transitory stall, and fully developed stall. The method is a considerable extension of the procedure given by Ghose and Kline [5]; it also uses some ideas from the method for fully stalled flows given by Woolley and Kline [4]. The flow model is zonal and steady. It uses a one-dimensional flow model for the potential core. A momentum integral equation and an entrainment equation are employed for the boundary layer zone. Simultaneous solution is employed to model the different zones where the flow is separating or separated. Improved correlations of flow detachment and of the boundary layer flow state approaching detachment are presented as part of the work and employed in the computations. These will be reported more fully in a separate paper. This model is too simple for the full representation of the physics of transitory stall, which is not symmetric, steady, or one-dimensional in the core. Despite this, the main features of the mean flow, including wall pressure as a function of streamwise location, are accurately represented with very modest computation times, typically tenths of a second on an IBM 3033. The results again indicate that the key features in modeling separated flows are:

- *correct representation of blockage of shear layers and stalled zones,*
- *adequate modeling of the interaction of potential and viscous zones.*

1 Introduction

The systematic studies of two-dimensional, straight-walled diffusers of variable, diverging angle carried out by Moore and Kline [1] and by Fox and Kline [2] in the late 1950's led to a classification of the flow regime behavior according to the characteristics of the stalled flow pattern, as shown in Fig. 1.

In the early 1960's several authors provided methods for predicting unstalled flows well below line a-a; see summary by Cockrell and Markland [3]. The work by Woolley and Kline [4] was successful in modeling diffusers operating in the two-dimensional, fully developed stall regime. White and Kline [5] developed a method that models axisymmetric diffusers operating in the unstalled and jet flow regimes. A numerical scheme was developed by Ghose and Kline [6] which predicts diffuser performance in the unstalled and incipient stall regimes. In their work they used a unified integral method with a one-dimensional approximation for the potential core flow. They found simultaneous iteration was essential for stable convergence.

The present work is concerned with a numerical investigation which predicts two-dimensional diffuser performance of the three first flow regimes in the chart of Fox and Kline [2], i.e., unstalled flow, transitory stall, and fully stalled flow.

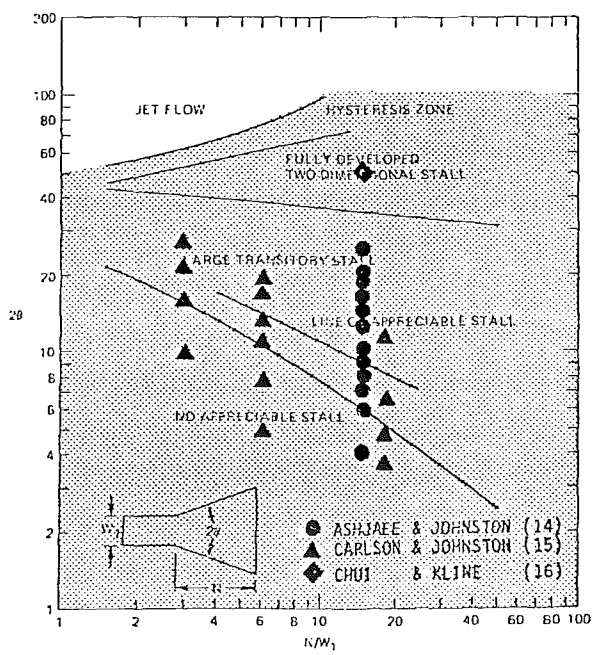

Fig. 1 Diffuser flow regime chart

Contributed by the Fluids Engineering Division and presented at the Joint Applied Mechanics, Fluids Engineering, and Bioengineering Conference, Boulder, Colo., June 22–24, 1981, of THE AMERICAN SOCIETY OF MECHANICAL ENGINEERS. Manuscript received by the Fluids Engineering Division, March 17, 1980. Paper No. 81-FE-5.

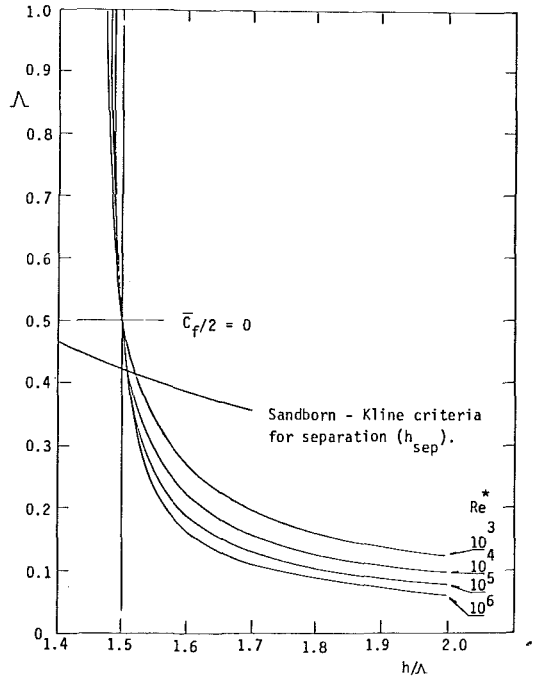

Fig. 2 h/Λ versus Λ and Re*

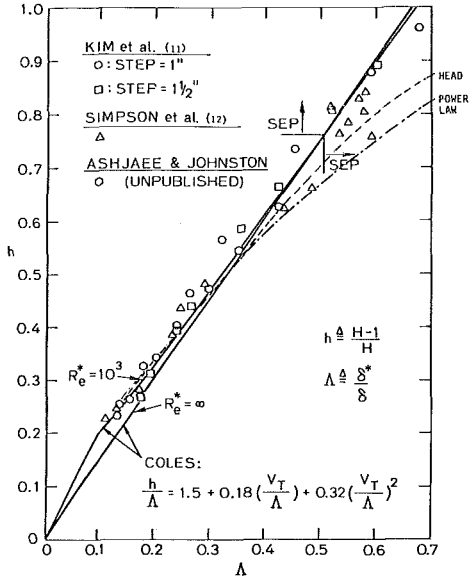

Fig. 3 h versus Λ

2 New Coordinates: Improved Correlations of Detachment and Reattachment

The model uses a new set of coordinates that provide both increased insight and simplified computations. These new nondimensional variables are defined as $\Lambda \equiv \delta^*/\delta$, and $h = (H-1)/H = (\delta^* - \delta_2)/\delta^*$. It can be observed by using Coles' velocity profile [7] that there is an approximately linear relation between these variables which is weakly dependent on the Reynolds number:

$$\frac{h}{\Lambda} = 1.5 + 0.179\frac{V_T}{\Lambda} + 0.321\left(\frac{V_T}{\Lambda}\right)^2 \tag{1}$$

where V_T/Λ is an implicit function of Re* and Λ, specifically,

$$\frac{V_T}{\Lambda} = \frac{1/\Lambda - 2}{0.05 + \ln(K\mathrm{Re}^*) - \ln|V_T/\Lambda|} \tag{2}$$

Close to separation, V_T assumes very small values. Therefore $h = 1.5\,\Lambda$ is a good simplification for $\Lambda > 0.42$, as shown in Fig. 2. At detachment (average wall shear = $\bar{C}_f = 0$) the variable Λ assumes the value 0.50 in Coles' velocity profile. As we shall show below, the value $\Lambda = 0.42$ correlates incipient detachment.[1]

When modified to allow for backflow, Coles' wall-wake profile represents detaching and detached boundary layer flows; this has been shown by Ghose and Kline [8], Kuhn and Nielsen [9], and Assassa and Papailiou [10]. For the backward-facing step reattaching flow, Kim and Kline [11] showed that the modified Coles' velocity profile also represents the separated, reattaching, and attached zones of their flows reasonably well.

Experimental data from the flows of Kim and Kline [11] and of Simpson, et al. [12] are compared to equation (1) in Fig. 3. This figure also shows the entrainment correlation of Head [13] and the equivalent result obtained using a power law velocity profile with variable exponent n instead of Coles' velocity profile. Near $\bar{C}_f = 0$, the data confirm the linear relation between h and Λ accurately. For Simpson's detaching flow, Λ and h increase in the direction of the flow. For Kim's reattaching flows, Λ and h decrease in the direction of the flow.

For the three flows, i.e., Simpson's detaching flow and

[1] In a companion paper on this new detachment and reattachment criterion, we shall also show that $\Lambda = 0.42$ correlates all known detachment results except possibly those with blowing, suction, or strong wall curvature.

Nomenclature

AR = area ratio (W_{exit}/W_{inlet})
B = blockage (δ^*/W)
$C_f/2$ = friction coefficient = $\tau_w/\rho U_\infty^2 = K^2 V_T^2 (\mathrm{sgn}\ \tau_w)$
Q = flow rate (m^3/s)
H = shape factor ($= \delta^*/\delta_2$)
h = shape factor ($= (\delta^* - \delta_2)/\delta^*$)
K = Von Kármán constant ($= 0.41$)
E = entrainment rate = $\frac{1}{U_\infty}\frac{d}{dx}[U_\infty(\delta - \delta^*)]$
Re* = displacement thickness Reynolds number = $\frac{\delta^* U_\infty}{\nu}$
U_∞ = boundary layer edge velocity (m/s)
U_τ = $U_\tau = (\mathrm{sgn}\ \tau_w)\sqrt{\frac{|\tau_w|}{\rho}}$ (m/s)
V_T = nondimensional shear velocity ($= U_\tau/KU_\infty$)
U_β = amplitude of the wake
V_B = $\frac{U_\beta}{U_\infty} = 2(\Lambda - V_T)$
W = diffuser width (m)
δ = boundary layer thickness (m)
δ^* = boundary layer displacement thickness (m)
Λ = boundary layer blockage fraction ($= \delta^*/\delta$)
η = y/δ
ρ = fluid density (kg/m^3)
δ_2 = boundary layer momentum thickness (m)
τ_{max} = maximum shear stress in the boundary layer (N/m^2)
τ_w = wall shear stress (N/m^2)
2θ = total included angle of the diffuser

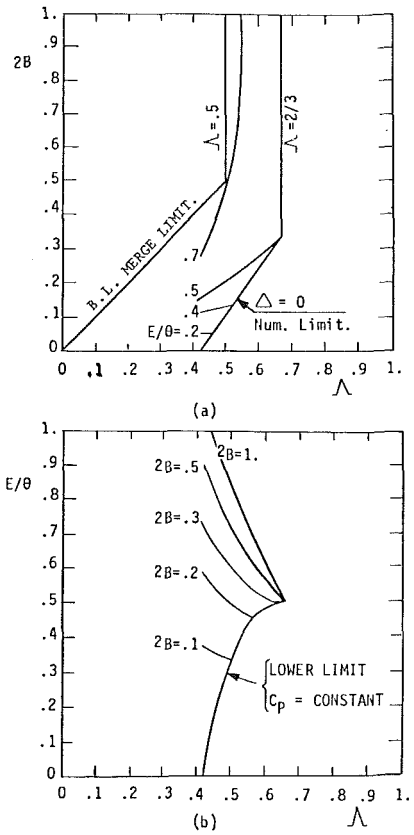

Fig. 4 Entrainment limits

Kim's reattaching flows, the point of average zero shear at the wall occurs for $\Lambda = 0.5$, in agreement with the value obtained from Coles' velocity profile.

In the region of separation (or reattachment), the wall friction velocity (V_T) is negligible, and a truly linear relation $h = 1.5\,\Lambda$ exists. This linear relation is shown by the data and is therefore not peculiar to the modified Coles' velocity profile.

The correlation in equation (1) agrees with the experimental values in the best available data not only near detachment and reattachment but also for the flows before and after the location of zero average wall shear. This is strong evidence of the power of the correlation proposed in equations (1) and (2) for a broad class of flows.

Some of the advantages of these equations for studying separating and reattaching flows are:

- the nondimensional variables h and Λ vary in the range 0-1, in contrast with other variables such as δ^* and H,
- the relation between h and Λ is approximately linear, this relation is independent of Re* near detachment and only weakly dependent on Re* far from detachment.

3 Method of Computation: General Equations

The method introduced in this paper uses a one-dimensional potential-flow approximation for the core. The method as given also assumes infinite aspect ratio (no end wall effects), and correlates the sum of δ^* for the two sidewall boundary layers in the momentum integral and entrainment equations without omitting nonlinear terms. The numerical scheme solves simultaneously the integral equations for the boundary layer and the free stream. Simultaneous interaction between the boundary layer and the potential core is used to advance the solution through detachment.

The present method solves two ordinary differential equations using B and Λ as the dependent variables. From the Von Kármán momentum integral equation, the entrainment correlation of P. Bradshaw [14], the one-dimensional continuity equation, and equations (1) and (2) obtained from Coles' velocity profile in the new coordinates, two ODE's are obtained for the two unknowns B, Λ:

$$a_{11}\frac{dB}{dx} + a_{12}\frac{d\Lambda}{dx} = b_1 \tag{3}$$

$$a_{21}\frac{dB}{dx} + a_{22}\frac{d\Lambda}{dx} = b_2 \tag{4}$$

where the coefficients a_{11}, a_{12}, a_{21}, a_{22}, b_1, and b_2 are defined in Appendix A. These coefficients depend on B, Λ, V_T, h, and the constant ξ.

For each diffuser flow, the inlet conditions are assumed to be known. The abscissa x is measured along the diffuser wall, where at the inlet section x is set equal to zero. From that station the system of equations is solved simultaneously for B and Λ by marching in x.

Once the ODE's for B and Λ are solved at a station, then the definition of blockage and continuity permit the evaluation of U_∞ and δ^*:

$$2B \equiv \frac{2\delta^*}{W} = 1 - \frac{Q}{WU_\infty} \tag{5}$$

Then, given Λ, the nondimensional shear velocity V_T and the friction coefficient are obtained from equation (2), the shape factor h from equation (1), and $H = 1/(1-h)$. The computation then provides B and Λ for the next marching step.

4 The Lag Equation

For nonequilibrium turbulent boundary layers, White [15] describes the effect of relaxing the adverse pressure gradient to zero on the outer wake region of the boundary layer.

The fluid near the wall in a turbulent boundary layer is in local equilibrium in the sense that it adjusts very rapidly to external changes, such as the pressure gradient. The outer layer, however, is dominated by large eddies that have considerable inertia and takes a finite time to adjust to new situations. A lag equation is used to model this effect.

The "lag" equation plays an important role in the present prediction method. Before detachment, it allows for a reduction of the entrainment rate, which would otherwise reach very high values.

Since the lag equation is a mathematical model originally designed as an improvement for calculation of unseparated boundary layers far from equilibrium, it contains no constraints applicable to separated flows.

From physical evidence, it was observed for separating and separated flows ($\Lambda \geq 0.42$) that as the total included angle of the diffuser increases, the rate of entrainment has upper and lower bounds. However, the lag equation is not sufficient to prevent the entrainment rate from surpassing the bounds. Hence, upper and lower bounds on entrainment rate have been introduced as constraints in the program. These limits are used in the code only when $\Lambda \geq 0.42$ and $dw/dx > 0$. We next discuss the physical bases for these bounds.

If the entrainment rate increases beyond a given upper limit in separated flows, then H would decrease and C_f would increase towards zero, approaching reattachment. If the entrainment rate lies below the lower limit, then the flow would accelerate and C_p would start decreasing. Thus exceeding either of these bounds gives results that are "nonphysical" in the sense that known data for detaching flows do not display such behavior. It is these limits that define the range of applicability of the method of Ghose and Kline [6].

These two limits provide the inequalities shown in equation (6)

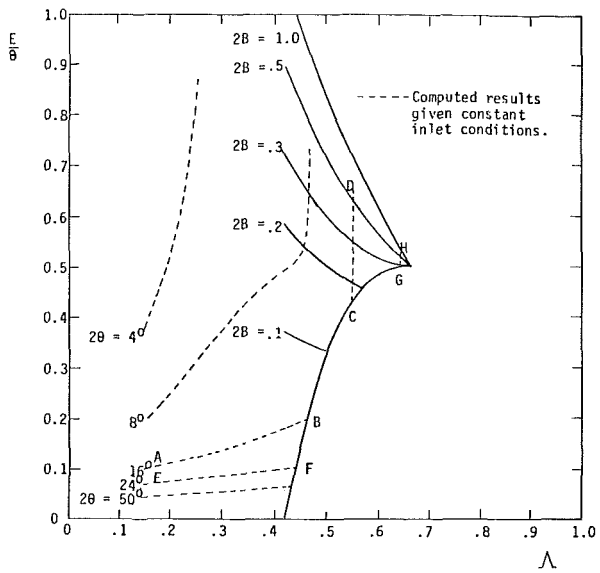

Fig. 5(a) Computational results

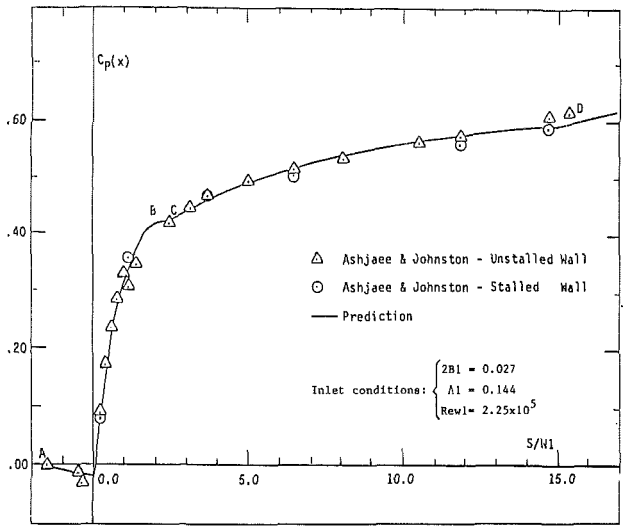

Fig. 6(a) C_p versus S/W_1 for the 16 deg diffuser

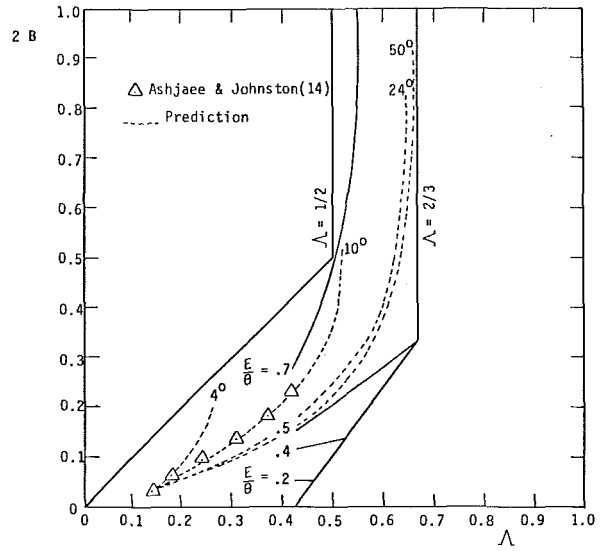

Fig. 5(b) Computational results

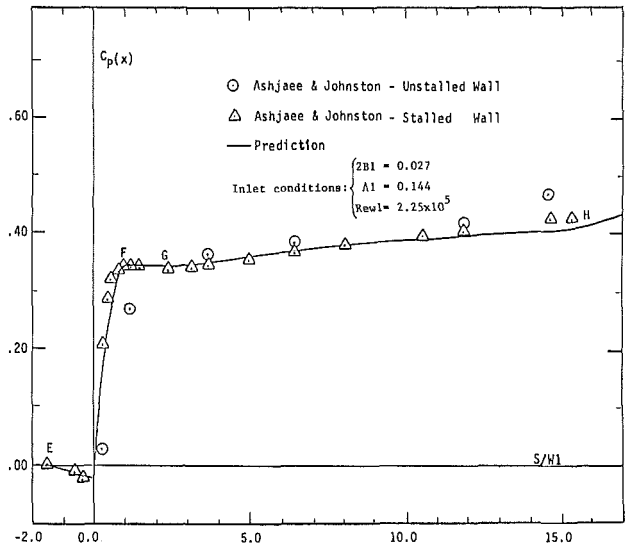

Fig. 6(b) C_p versus S/W_1 for the 24 deg diffuser

$$\frac{1}{2}\frac{dw}{dx}\left[\frac{1-\Lambda}{\Lambda}-\frac{1-h}{h\Lambda}\right] < \frac{1}{U_\infty}\frac{d}{dx}\left[U_\infty(\delta-\delta^*)\right] < \frac{1}{2}\frac{dw}{dx}2B\frac{1-\Lambda}{\Lambda}\left[\frac{4-3\Lambda}{(4-3\Lambda)(1+2B)-2}\right] \quad (6)$$

Lower limit found by requiring no acceltion of core flow, i.e., C_p = constant

Nondimensional entrainment rate

Upper limit found by requiring no decrease in H, and no increase in C_f toward zero.

When computation presses against the bounding values, the bounds are followed rather than the unmodified lag equation. If the flow develops so that the parameters move away from the bounds farther downstream, then the lag equation is again employed in the computation. These changes in the parameters predict the data for the appropriate flows in detail with surprising accuracy. In Fig. 5(*a*) the trajectory of the 16 deg diffuser is marked as ABCD, and of the 24 deg diffuser as EFGH. Figures 5(*a*) and 5(*b*) show these trajectories (which contain the limiting behavior). Figures 6(*a*) and 6(*b*) show the program output to be in excellent, detailed agreement with the recent, very accurate data of Ashjaee and Johnston [17] for the very difficult region near maximum fluctuation levels in transitory stall. Even more significant, Fig. 6(*a*) shows that the points B, C, and Fig. 6(*b*) the points, F, G when the computation encounters and leaves the limit values are the location of significant changes in the trends of the $C_p(x)$ data.

Besides these upper and lower limits, two other limits are employed. The third limit applies only to the attached part of the flow; it prevents the predicted sum of the two boundary layers from becoming wider than the diffuser width. The fourth bound is related to the numerical scheme and constitutes the limit of applicability of the system of equations (3) and (4). The fourth bound is derived by setting to zero the determinant of the coefficient matrix of the system of equations (3) and (4). It can be shown mathematically that the lower limit in equation (6) is always reached before this

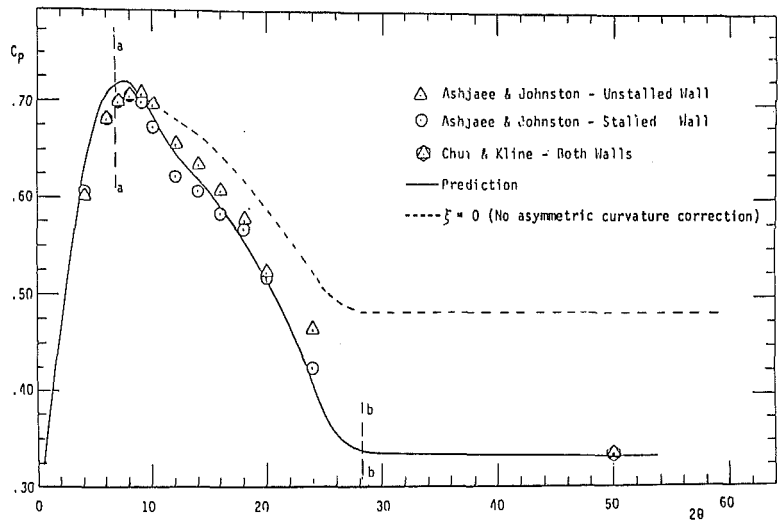

Fig. 7 C_p versus θ map for $N/W_1 = 15$ diffusers

condition is met;[2] hence no problem of numerical stability has been encountered near detachment.

Figures 4(*a*) and 4(*b*) show these limits. The line $2B = \Lambda$ represents the points for which the two opposite boundary layers start to interact. For separating external flows, or separating internal flows with $B \rightarrow 0$, the upper limit for entrainment becomes zero and the lower limit in equation (6) becomes:

$$\frac{1-\Lambda}{\Lambda} = \frac{1-h}{h\Lambda} \tag{7}$$

Equation (7) can be reduced to:

$$H = 1 + \frac{1}{1-\Lambda} \tag{8}$$

This equation was obtained in 1961 by Sandborn and Kline [16] as a correlation for incipient turbulent flow detachment. In its derivation the blockage effect was not considered. Note that equation (8) is obtained without the need for any assumption on a velocity profile form.

Inserting $h = 1.5\ \Lambda$ in equation (7) gives $\Lambda = 0.42$. The experimental results of Ashjaee and Johnston [17] show that at this value of Λ, there exists about 5 percent backflow in the diffuser wall, corresponding to the region of incipient separation.

As noted above, limits on the entrainment are introduced at $\Lambda = 0.42$, incipient detachment (not at full detachment, $\bar{C}_f = 0$, $\Lambda = 0.50$). This is consistent with the physical model of Sandborn and Kline [16] and the computations of Ghose and Kline [6], which indicate that rapid increase of δ^* begins at incipient detachment, and hence that altered modeling becomes necessary at that section. This probably explains why turbulent boundary layer procedures employing conventional coordinates and iteration schemes encounter difficulties significantly ahead of full detachment (see, for example, Kline et al. [18]).

5 Results

The diffuser flows run were those of Carlson and Johnston [19], Ashjaee and Johnston [17], and Chui and Kline [20]. These diffuser flows cover the three regimes mentioned before, as can be seen in Fig. 1. Their total included angle various from 4 to 50 degrees.

The behavior of the C_p curve for the 16 and 24 deg diffusers of Ashjaee and Johnston are shown in Figs. 6(*a*) and 6(*b*), operating in the transitory stall region. The agreement shown in Figs. 6(*a*) are typical of output for the Ashjaee and Johnston results, where the uncertainty in the data is low.[3] We chose to exhibit the most difficult flow cases.

In the present computations, one objective was to explore the range of use of a one-dimensional core model, since it is simple and extremely fast computationally. Two-dimensional core models will be explored in separate work.

Flows containing appreciable volumes of separated flow create a special problem for 1-D core model; such flows become asymmetric with different pressure gradient and boundary layers on the two walls. As explicitly shown by Chui and Kline [20], the difference in pressure gradient between the two walls in fully stalled flows agrees with the inviscid streamline curvature effect ($\partial p/\partial n = \rho V^2/R$) to within the 1 percent uncertainty of their data. In the one-dimensional model employed here, the asymmetric curvature effect is accounted for by use of a correction term in the representation of the pressure gradient in the momentum integral equation of the boundary layer. This asymmetric effect was estimated by using a simplified model of the Euler - N equation across the diffuser in the detaching region, where the momentum equation assumed the form:

$$\frac{W}{\bar{\delta}_2}\frac{d\bar{\delta}_2}{dx} + \left(2 + H + \frac{\xi H}{\Lambda}\right)\frac{W}{\bar{U}_\infty}\frac{d\bar{U}_\infty}{dx} = \frac{\bar{C}_f}{2} \times \frac{H}{B} \tag{9}$$

The extra term ($\xi H/\Lambda$) inside the parentheses, models the effects of asymmetry of the flow in a simplified way.

Comparison with several data sets showed that:

$$\xi = \begin{cases} 0 & \text{, for attached flows} \\ 0.0015 & \text{, for detached flows} \end{cases}$$

Use of this model with these values of ξ gives good representation of flows with appreciable values of stall present, without the need for an elliptic core solver (see Fig. 7). A sensitivity check on the value of ξ showed that 10 percent variation in ξ produced a 3 percent variation in C_p for fully stalled flow, the most sensitive zone. A smaller change occurs in transitory stall, and no change occurs for $2\theta \leq 10$ deg in Fig. 7. In examining Fig. 7, the physical results of Smith and Kline [23] and Layne and Smith [24] should be held

[2] This would not be true in computation using iterative rather than simultaneous solution for δ^* and dp/dx.

[3] Careful analysis of uncertainty indicates these data are significantly more accurate than prior data sets.

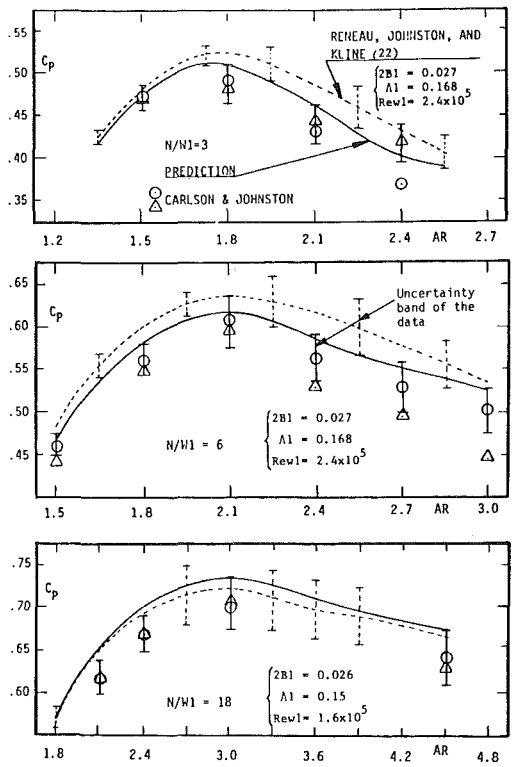

Fig. 8 C_p versus AR map for N/W_1 = 3,6 and 18 diffusers

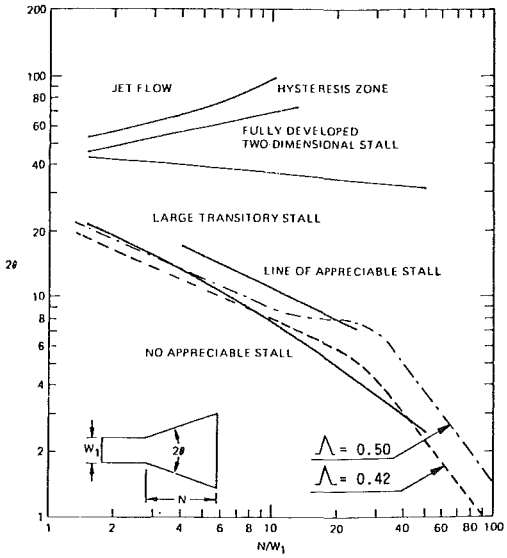

Fig. 9 Diffuser flow regime chart

in mind. The flow between a-a and b-b on Fig. 7 is grossly unsteady and three-dimensional. RMS fluctuation as high as 60 percent of U_∞ have been recorded. Despite this, computation employing steady model gives very good results for long-term average flow properties. Note also that the knee of the C_p curve should coincide with line b-b of Fox and Kline [2] if the onset at full-stall is correctly modeled. This agreement does emerge from the model as shown in Fig. 7.

The pressure recovery coefficient for the diffusers of Carlson and Johnston [19] are shown in Fig. 8. This figure also shows the recovery obtained using computer predictions, which are within the uncertainty of the data.

Finally, Fig. 9 shows the location of incipient detachment ($\Lambda = 0.42$) and full detachment ($\Lambda = 0.50$) obtained using this method to model a set of diffusers with an inlet blockage of 0.03. $\Lambda = 0.42$ should correspond to line a-a that separates the unstalled and the transitory stalled regimes, and $\Lambda = 0.50$ to the line of optimum pressure recovery C_p^* (maximum C_p at each non-dimensional length). The agreement is seen to be reasonable.

6 Conclusions

1. The computation method developed leads to a very fast code that predicts overall characteristics of three flow regimes in planar diffusers within the uncertainty in the best available data. The predictions include both regime transition and fine details of behavior in pressure recovery. The method, although very simple computationally, is built from a number of prior developments for various flow regimes coupled with several new modeling concepts.

2. An improved criterion for the detachment and reattachment using the h-Λ plane plays an essential role not only in delineating the location of detachment, but as the basis for decision criteria on changes in the model representing various flow regimes.

3. The results again show that the physics of flow detachment is not singular; the presence or absence of singular behavior at detachment is a result of the numerics employed. Using the quasi-linear relation between h and Λ in the zone of detachment and choosing dependent variables such that the interaction between the growth of the shear-layer and the outer flow is solved simultaneously in the sense of Ghose and Kline [6] provides stable calculations through detachment.

4. Separating and separated flows in diffusing sections are computed by introducing new, physically motivated limits on entrainment. These limits provide excellent results, but are not yet fully understood and are under continuing investigation. These limits apparently need to be introduced at incipient detachment for the reasons described above.

5. In the present program, the two-dimensional effect arising from asymmetry of the core flow is approximated by a simple correction factor based on the Euler N equation. This factor is introduced into the momentum-integral equation of the boundary layer. This approximation can be removed by use of a two-dimensional core flow solver. Improvement and extension of the present methods to include two-dimensional core solvers and possible extension of domain, including several other classes of problems, remain to be investigated.

APPENDIX A

Coles' velocity profile:

$$\frac{u}{u_\tau} = \frac{1}{k}\ln\left|\frac{yu_\tau}{\nu}\right| + 5 + \frac{u_\beta}{2u_\tau}\left(1-\cos\frac{\pi y}{\delta}\right)$$

$$k = .41$$

Introducing our notation,

$$\frac{U}{U_\infty} = 1 + V_T \ln\eta - 2(\Lambda - V_T)\cos^2\frac{\pi\eta}{2}$$

$$a_{11} = \frac{1}{B(1-2B)}\left[1-h+CV_T+2B\left(2-h+\frac{\xi}{\Lambda}\right)\right]$$

$$a_{12} = -1.5+.321\frac{V_T^2}{\Lambda} = C\left(\frac{V_T}{\Lambda}-2\right)$$

$$b_1 = \frac{2}{BW}\frac{C_f}{2} + \frac{2\theta}{W}\left[2-h+\frac{\xi}{\Lambda}\right]$$

$$a_{21} = \frac{1}{B(1-2B)}$$

$$a_{22} = \frac{1}{\Lambda(1-\Lambda)}$$

$$b_2 = \frac{\Lambda}{BW(1-\Lambda)} \frac{10\tau_{max}}{\rho U_\infty^2}$$

$$C + \frac{.642 + .179(2.05 + \ln(k\mathrm{Re}^*)) + (.179 - .642(.05 + \ln(k\mathrm{Re}^*))\dfrac{V_T}{\Lambda}}{(1.05 + \ln(k\mathrm{Re}^*))^2}$$

The numbers used to evaluate C are obtained in the integration of Coles profile to evaluate h/Λ.

References

1 Moore, C. A., and Kline, S. J., "Some Effects of Vanes and of Turbulence on Two-Dimensional, Wide-Angle Subsonic Diffusers," NACA TN-4080, June 1958.

2 Fox, R. W., and Kline, S. J., "Flow Regime Data and Design Method for Curved Subsonic Diffusers," ASME *Journal of Basic Engineering,* Vol. 84, 1962.

3 Cockrell, D. J., and Markland, E., "A Review of Incompressible Diffuser Flow," *Aircraft Eng.,* Vol. 35, 1963, pp. 286-292.

4 Woolley, R. L., and Kline, S. J., "A Method of Calculation for a Fully Stalled Flow," Report MD-33, Thermosciences Div., Dept. of Mech. Engrg., Stanford University, Nov. 1973.

5 White, J. W., and Kline, S. J., "A Calculation Method for Incompressible, Axisymmetric Flows, Including Unseparated, Fully Separated, and Free Surface Flows," Report MD-35, Thermosciences Div., Dept. of Mech. Engrg., Stanford University, May 1975.

6 Ghose, S., and Kline, S. J., "Prediction of Transitory Stall in Two-Dimensional Diffusers," Report MD-36, Thermosciences Div., Dept. of Mech. Engrg., Stanford University, Dec. 1976.

7 Coles, D., "The Law of the Wake in the Turbulent Boundary Layer," *Journal of Fluid Mech.,* Vol. 1, 1956, pp. 191-226.

8 Ghose, S., and Kline, S. J., "The Computation of Optimum Pressure Recovery in Two-Dimensional Diffusers," ASME JOURNAL OF FLUIDS ENGINEERING, Vol. 100, 1978.

9 Kuhn, G. D., and Nielsen, J. N., "Prediction of Turbulent Separated Boundary Layers," Paper No. 73-663, AIAA 6th Fluid and Plasma Dynamics Conference, July 1973.

10 Assassa, G. M., and Papailiou, K. D., "An Integral Method for Calculating Turbulent Boundary Layer with Separation," ASME JOURNAL OF FLUIDS ENGINEERING, Vol. 100, 1979.

11 Kim, J., and Kline, S. J., "Investigation of Separation and Rattachment of a Turbulent Shear Layer: Flow over a Backward-Facing Step," Report MD-37, Thermosciences Div., Dept. of Mech. Engrg., Stanford University, Apr. 1978.

12 Simpson, R. L., Strickland, J. H., and Barr, P. W., "Laser and Hot-Film Anemometer Measurements in a Separating Turbulent Boundary Layer," Tech. Report WT-3, Southern Methodist University, Thermal and Fluid Sciences Center, Sept. 1974.

13 Head, M. R., "Entrainment in the Turbulent Boundary Layers," ARC R & M 3152, 1958.

14 Bradshaw, P. S., Ferris, D. H., and Atwell, N. P., "Calculation of Boundary Layer Development Using the Turbulent Energy Equation," *Journal of Fluid Mech.,* Vol. 28, Part 3, 1967, pp. 593-616.

15 White, F. M., *Viscous Fluid Flow,* McGraw-Hill, 1974, pp. 512-530.

16 Sandborn, V. A., and Kline, S. J., "Flow Models in Boundary Layer Stall Inception," Paper No. 60-WA-143, ASME, Jan. 1961.

17 Ashjaee, J., and Johnston, J. P., "Transitory Stall in Diffusers," IL-9, Thermosciences Div., Dept. of Mech. Engrg., Stanford Univ., May 1979.

18 Kline, S. J., Morkovin, M. V., Sovran, G., Cockrell, D. J., (eds.), *Proceedings on Computation of Turbulent Boundary Layers — 1968,* AFOSR-IFP-Standard Conference, 1968.

19 Carlson, J. J., and Johnston, J. P., "Effects of Wall Shape on Flow Regimes and Performance in Straight, Two-Dimensional Diffusers," Report PD-11, Thermosci. Div., Dept. of Mech. Engrg., Stanford Univ., June 1965.

20 Chui, G., and Kline, S. J., "Investigation of a Fully Stalled Turbulent Flowfield," Report MD-19, Thermosciences Div., Dept. of Mech. Engrg., Stanford University, 1967.

21 Strickland, J. H., and Simpson, R. L., "The Separating Turbulent Boundary Layer: An Experimental Study of an Airfoil-Type Flow," Tech. Report WT-2, Thermal and Fluid Sciences Center, Southern Methodist University, Aug. 1973.

22 Reneau, L. R., Johnston, J. P., and Kline, S. J., "Performance and Design of Straight, Two-Dimensional Diffusers," Report PD-8, Thermosciences Div., Dept. of Mech. Engrg., Stanford University, Sept. 1974.

23 Smith, C. R., and Kline, S. J., "An Experimental Investigation of the Transitory Stall Regime in Two-Dimensional Diffusers, Including the Effects of Periodically Disturbed Inlet Conditions," Report PD-15, Thermosciences Div., Dept. of Mech. Engrg., Stanford University, Aug. 1971.

24 Layne, J. L., and Smith, C. R., "An Experimental Investigation of Inlet Flow Unsteadiness Generated by Transitory Stall in Two-Dimensional Diffusers," Reprot CFMTR 76-4, Thermosciences and Prop. Ctr., Purdue University, Aug. 1976.

G.W. Rankin
Assistant Professor.

K. Sridhar
Professor.
Mem. ASME

Department of Mechanical Engineering,
University of Windsor,
Windsor, Ontario N9B 3P4
Canada

Developing Region of Laminar Jets With Parabolic Exit Velocity Profiles

An approximate solution to the velocity distribution in a submerged axisymmetric, laminar jet which issues from a long tube is presented. The solution is a modification of that of Okabe [17] and takes into account the changes that occur in the parabolic profile downstream of the jet exit. Comparisons are made with experimental data and other approximate theories taken from the literature.

Introduction

An analytical study of the axisymmetric, submerged laminar jet with a parabolic velocity profile at the nozzle exit is likely to have a wider application than the previously considered [1] uniform case. The importance in connection with the design of fluidic control and free jet sensing devices can certainly be appreciated. The geometrical and flow conditions encountered in these devices focus our attention to the importance of the region of the jet very close to the nozzle exit.

The present investigation is also important in the study of laminar jet stability. In many cases the laminar jet becomes unstable and consequently turbulent before the theoretical similarity velocity profile is achieved [2].

The objective of this paper is to present an approximate solution for the jet which applies in the initial developing region and to compare it with experimental data and other approximate solutions that are available in the literature.

Discussion of Previous Studies

Most attempts to mathematically describe the laminar jet involve the use of Schlichting's [3] similarity solution of the boundary layer equations. This solution gives the velocity field resulting when a jet issues from an infinitesimally small nozzle. The axial velocity component is found to be

$$u = \frac{3M}{4\pi\mu}\frac{1}{x_s}\frac{1}{[1+\xi^2]^2} \tag{1}$$

where

$$\xi = \frac{1}{8\nu}\left[\frac{3M}{\pi\rho}\right]^{1/2}\frac{r}{x_s} \tag{2}$$

Andrade and Tsien [4] have shown that this solution can be made to fit experimentally determined profiles at large distances downstream of the nozzle exit if the momentum, M, in equations (1) and (2) is made equal to the momentum at the nozzle exit and if the jet issues from a virtual origin located a distance x_v inside the nozzle. They used an experimental method of determining x_v and also presented an analytical method which involved matching the kinetic energy of the jet flow to that at the tube exit. Other investigators [5,6] recognized that flow properties other than kinetic energy could also be used to estimate a theoretical value for x_v. They presented their results in the form

$$X_{cv} = \frac{x_v}{d\mathrm{Re}_c} = C \tag{3}$$

The value of C depends upon the velocity profile shape at the nozzle exit and upon the type of matching used.

Dmitriev and Kulesova [7] used the results of a finite difference solution to modify Schlichting's similarity solution for use in the developing region of the jet. Further downstream Schlichting's solution was used with a virtual origin that matched kinetic energies as suggested by Andrade and Tsien. The flow model can be summarized mathematically in a convenient form for this paper as

$$U_0 = \frac{u}{u_{m0}} = \frac{u_m/u_{m0}}{(1+BR^2)^2} = \frac{U_m}{(1+BR^2)^2} \tag{4}$$

where

$$U_m = 1 - 16X_c \text{ for } 0 \le X_c \le 0.0188 \tag{5}$$

$$= \frac{1}{32(X_c + X_{cv})} \text{ for } 0.0188 \le X_c \le \infty \tag{6}$$

also

$$X_c = \frac{x}{d\left(\frac{u_{m0}d}{\nu}\right)} = \frac{x}{d\,\mathrm{Re}_c} \tag{7}$$

$$B = 4\,U_m^2 \tag{8}$$

and

$$X_{cv} = \frac{x_v}{d\,\mathrm{Re}_c} \tag{9}$$

Contributed by the Fluids Engineering Division and presented at the Joint Applied Mechanics, Fluids Engineering, and Bioengineering Conference, Boulder, Colo., June 22-24, 1981, of THE AMERICAN SOCIETY OF MECHANICAL ENGINEERS. Manuscript received by the Fluids Engineering Division, March 17, 1980. Paper No. 81-FE-3.

In all of the models discussed above, the profile shape within the development region is that of Schlichting and hence cannot be exactly the correct form at the nozzle exit.

Chang [8] experimentally studied the flow development region of the laminar jet and determined the following empirical equation in the range $0 \leq x/d \leq 10$ for jets with $\mathrm{Re}_c = 860$ and 1200.

$$U = \frac{u}{u_m} = \frac{1 + ab\xi^2\left[\dfrac{1 - c\xi^2 - \xi^4}{1 + b\xi^6}\right]}{(1+\xi^2)^2} \tag{10}$$

where

$$a = 1 - 0.1\, x/d$$
$$b = 1.1026$$
$$c = 1.2150$$

The numerator in equation (10) is a modifying term for the Schlichting profile which gives an almost parabolic profile at $x/d = 0$. This profile is similar to that used by Sato [4] to study the plane jet. The foregoing empirical equation seems reasonable except that it does not account for the dependence of the development length on Reynolds Number. Chang also claims that the value of X_{cv}, determined by matching the centreline velocity of the Schlichting profile to the parabolic, is a reasonable one to use. This gives X_{cv} equal to 0.03125.

du Plessis, et al. [9] and Tsang [10] numerically solved the boundary layer equations for the case of a laminar jet. They compared their solution with experimental results and with Schlichting's solution. It was found that if the virtual origin was given by $X_{cv} = 0.0275$ Schlichting's profile agreed with the data in the range $X_c > 0.015$.

Pai and Hsieh [11] presented finite difference solutions of the boundary layer equations for laminar jet configurations with and without a moving free stream. The axisymmetrical case without free stream and with parabolic exit velocity profile is of particular importance here. Results are given in nondimensional terms for the centre line velocity decay and the half-width as functions of distance away from the nozzle exit. The use of the nondimensional distance, X_c, is particularly notable. Schlichting's solution altered by using a virtual origin was also compared. The value of the virtual origin used was that suggested by Andrade and Tsien, obtained by matching the kinetic energy of the exit velocity profile to that of Schlichting's. This value was $X_{cv} = 0.025$. They concluded that this value agreed reasonably well with their analytical result.

Abramovich and Solan [12, 13] obtained an experimental correlation for the centreline velocity decay as follows.

$$U_m = \frac{1}{ax^* + b} \text{ for } x^* > 0.2 \tag{11}$$

where

$$x^* = \frac{x}{d\sqrt{\mathrm{Re}}}$$

and

$$a = 1.13 \text{ with } b = 0.89.$$

In view of the fact that hot wire measurements were taken only along the jet axis, as opposed to velocity profiles, there is no check to determine whether any portion of the jet, namely, the edge of the free shear layer had become turbulent. It is felt that such a condition could drastically reduce the velocity in the laminar portion of the jet at the centre.

Vaz [14] used a hot wire anemometer to measure velocity distributions in a laminar jet of air. Due to high Reynolds number values the nondimensional axial distances were well within the development region.

Symons and Labus [15] experimentally investigated a helium into helium laminar free jet with a parabolic velocity distribution at the supply tube exit. A total pressure probe was used to obtain velocity profiles for Reynolds numbers, Re, of 437 and 1839 at axial distances up to 25 diameters from the nozzle exit. Jet centre line velocity decay and jet spread were also obtained over a range of Reynolds number, Re, from 255 to 1839. They also noticed that there was no definable potential core.

Other than the numerical method none of the above analytical methods gives exactly a parabolic velocity profile at the nozzle exit.

Thomas [16] using an integral method obtained a solution which gives the concentration and velocity profiles in a planar laminar jet which took into account the change of the parabolic velocity profile downstream of the nozzle exit. Although his solution technique is different, the method is based upon an assumed form for the velocity profile which is a modification of that used by Okabe [17] for the case of an initially uniform velocity profile.

Nomenclature

d = diameter of tube
M = momentum of the jet
r = radial coordinate
$r_{m/2}$ = radial distance to the point where U = 0.5
R = r/d
$R_{m/2}$ = value of R where $U = 0.5$
Re = Reynolds number based on average velocity at the nozzle exit, Vd/ν
Re_c = Reynolds number, based on the center line velocity at the nozzle exit, $U_{\mathrm{mo}}d/\nu$
u = $u(x,r)$ = axial velocity component
u_m = $u(x,0)$
u_{m0} = $u(0,0)$
U = u/u_m
U_0 = u/u_{m0}
U_m = u_m/u_{m0}
V = average velocity at the nozzle exit
x = axial distance measured from nozzle exit plane
x_v = axial distance from point source to the nozzle exit plane
x_s = axial distance measured from the point source
$x^* = \dfrac{x}{d\sqrt{\mathrm{Re}}}$
$X = \dfrac{x}{d\mathrm{Re}}$
$X_c = \dfrac{x}{d\mathrm{Re}_c}$
$X_{cv} = \dfrac{x_v}{d\mathrm{Re}_c}$
Δ = radial location of $U = 0$ at any x location
δ = Δ/d
ϵ = $e^{-1/\lambda}$
η = r/Δ
λ = unknown function of x
μ = absolute viscosity
ν = kinematic viscosity
ξ = similarity variable defined in equation (2)
ρ = density

In the present investigation use is made of the assumed velocity profile of Thomas and the integral technique of Okabe to solve for the velocity profiles in the development region of an axisymmetric laminar jet.

Analysis

The basic form of the velocity profile used by Thomas is given in equation (12)

$$U_0 = \frac{u}{u_{m0}} = (1-\eta^2)(1-\epsilon e^{\eta/\lambda})^3 + \alpha\eta + \beta\eta^2 + \gamma\eta^3 + \sigma\eta^4 \quad \text{for } 0<\eta<1$$
$$= 0 \quad \text{for } 1<\eta<\infty \tag{12}$$

where $\eta = r/\Delta$ and Δ is the radial distance to where the velocity is zero. Also $\epsilon = e^{-1/\lambda}$ and λ is an unknown function of x which is to be determined along with Δ. Figure 1 is an aid

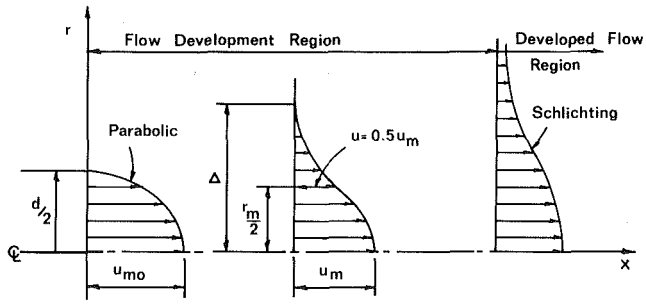

Fig. 1 Jet flow regions

in defining the variables as well as the flow development regions. α, β, γ and σ are values to be determined such that the following boundary conditions are satisfied.

$$\text{at } \eta = 0 \qquad \frac{\partial u}{\partial \eta} = 0$$
$$\text{and at } \eta = 1 \qquad u = \frac{\partial u}{\partial \eta} = \frac{\partial^2 u}{\partial \eta^2} = 0 \tag{13}$$

The condition on the second derivative is a result of applying the other conditions at $\eta = 1$ to the differential momentum equation.

By applying these conditions it can be shown that

$$3\alpha = -\beta = \gamma = -3\sigma = \frac{9\epsilon(1-\epsilon)^2}{\lambda} \tag{14}$$

Substituting these into equation (12) and simplifying yields

$$U_0 = (1-\eta^2)(1-\epsilon e^{\eta/\lambda})^3 + \frac{3\epsilon\eta(1-\epsilon)^2(1-\eta)^3}{\lambda} \tag{15}$$

This profile is used in conjunction with two physical flow equations that must be satisfied. These are the integral momentum equation over the complete jet and the momentum equation in differential form along the x axis.

The integral momentum equation, in a constant pressure region without contacting solid surfaces and subject to the boundary layer approximations is given by

$$\frac{d}{dx}\int_0^\infty r\,u^2\,dr = 0 \tag{16}$$

Accordingly, the momentum is constant and the value at the tube exit is equal to that in the jet at any axial distance, x,

1. Values of f_m in equation (19)

m	F_0	F_1	F_2	F_3	F_4	F_5	F_6
-2	0	0	$\frac{3}{280}$	$-\frac{3}{70}$	$\frac{9}{140}$	$-\frac{3}{70}$	$\frac{3}{280}$
-1	0	$\frac{1}{10}$	$-\frac{1}{5}$	$\frac{1}{10}$	0	0	0
0	1/2	0	0	0	0	0	0
1	$-2\frac{9}{20}$	0	0	0	0	0	0
2	$3\frac{2689}{3600}$	-6	$39\frac{3}{4}$	$-78\frac{13}{18}$	$46\frac{55}{144}$	$-5\frac{283}{450}$	$\frac{17}{36}$
3	0	$-101\frac{25}{36}$	$527\frac{7}{18}$	$-769\frac{17}{18}$	$365\frac{5}{6}$	$-22\frac{11}{12}$	$1\frac{1}{3}$
4	0	$838\frac{5}{27}$	$-380\frac{10}{27}$	$-1794\frac{17}{54}$	$1378\frac{7}{9}$	$-44\frac{1}{18}$	$1\frac{7}{9}$
5	0	$-2127\frac{77}{324}$	$6414\frac{77}{162}$	$-6480\frac{80}{81}$	$2228\frac{79}{162}$	$-35\frac{235}{324}$	$\frac{80}{81}$

2. Values of g_m in equation (20)

m	G_0	G_1	G_2	G_3	G_4	G_5	G_6
-1	0	$-\frac{3}{140}$	$\frac{3}{70}$	$-\frac{3}{140}$	0	0	0
0	$-\frac{1}{3}$	0	0	0	0	0	0
1	$2\frac{9}{20}$	0	0	0	0	0	0
2	$-3\frac{2689}{3600}$	0	0	0	0	0	0
3	$-37\frac{3581}{9000}$	$101\frac{25}{36}$	$-203\frac{7}{18}$	$101\frac{25}{36}$	0	0	0
4	$252\frac{125041}{270000}$	$-1604\frac{10}{27}$	$2909\frac{53}{108}$	$-795\frac{49}{54}$	$-460\frac{511}{1728}$	$14\frac{27013}{33750}$	$-\frac{65}{108}$
5	$-672\frac{60263}{720000}$	$12763\frac{23}{54}$	$-32006\frac{23}{27}$	$25824\frac{73}{108}$	$-6685\frac{75}{162}$	$107\frac{57}{324}$	$-2\frac{26}{27}$
6	$694\frac{299856520}{388800000}$	$-52162\frac{73}{81}$	$64033\frac{601}{648}$	$26617\frac{541}{972}$	$-39492\frac{13637}{13824}$	$315\frac{187573}{337500}$	$-5\frac{1795}{1944}$
7	0	$90370\frac{455}{1944}$	$-271460\frac{455}{972}$	$272164\frac{148}{243}$	$-91433\frac{3141}{8748}$	$363\frac{10377}{17496}$	$-4\frac{148}{243}$

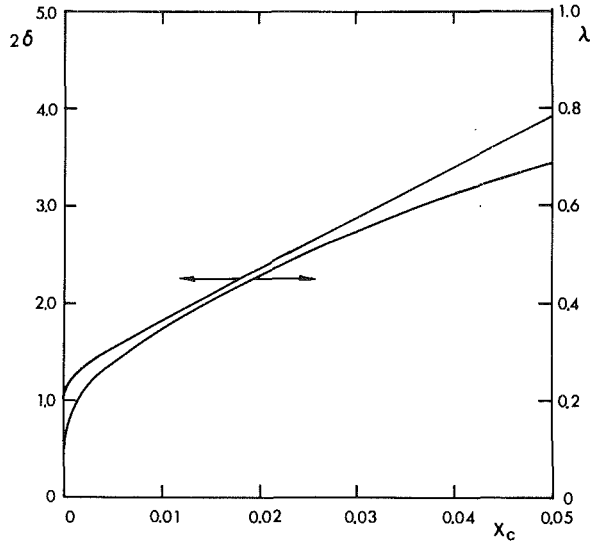

Fig. 2 Variation of profile parameters along the jet

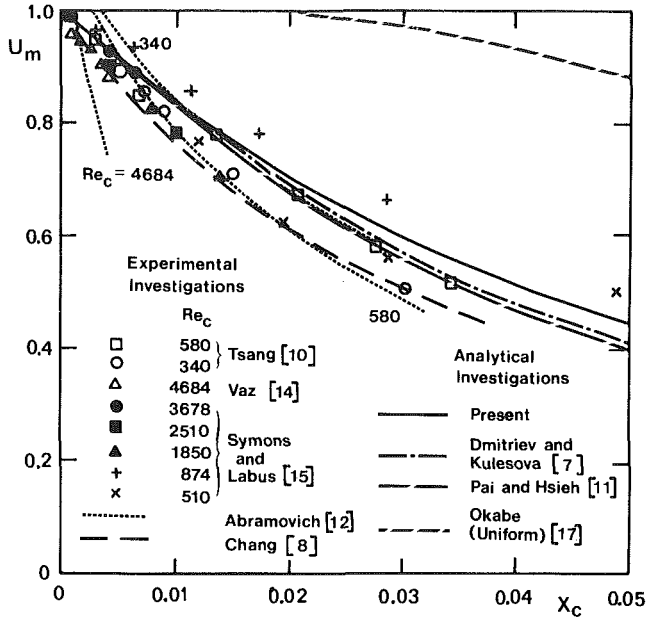

Fig. 3 Centre line velocity decay

from the nozzle. Expressing this in convenient non-dimensional terms and rearranging gives

$$\int_0^{1/2} U_0^2 R\, dR\,\Big|_{x=0} = \int_0^1 U_0^2 \delta^2 \eta\, d\eta\,\Big|_x \tag{17}$$

Using the condition that at x = 0; $U_0 = 1 - 4R^2$ and equation (15) it can be found after a lengthy procedure that

$$\delta^2 = \left[24 \sum_{n=0}^{6} (F_n + G_n)\,\epsilon^n\right]^{-1} \tag{18}$$

where

$$F_n = \sum_{m=-2}^{5} f_m \lambda^m \tag{19}$$

and

$$G_n = \sum_{m=-1}^{7} g_m \lambda^m \tag{20}$$

The coefficients of λ, f_m, and g_m are given in Tables 1 and 2 respectively.

The momentum equation in differential form including the boundary layer approximations may be written as

$$u_m \frac{du_m}{dx} = \nu\left(\frac{\partial^2 u}{\partial r^2} + \frac{1}{r}\frac{\partial u}{\partial r}\right)_{r=0} \tag{21}$$

or in convenient nondimensional terms as

$$U_m \frac{dU_m}{dX_c} = \left(\frac{\partial^2 U_0}{\partial R^2} + \frac{1}{R}\frac{\partial U_0}{\partial R}\right)_{R=0} \tag{22}$$

Making use of equation (15) and integrating both sides of equation (22) we can show that

$$X_c = \frac{1}{2}\int_0^{\lambda} \frac{\epsilon(1-\epsilon)^4 \delta^2\, d\lambda}{\left[\epsilon(1-3\epsilon) + \dfrac{2\lambda^2(1-\epsilon)^2}{3} + 6\lambda\epsilon(1-\epsilon)\right]} \tag{23}$$

The value of X_c can be determined by using equations (23) and (18) and a Simpsons rule integration scheme. The resulting values of λ and δ are shown as a function of X_c in Fig. 2.

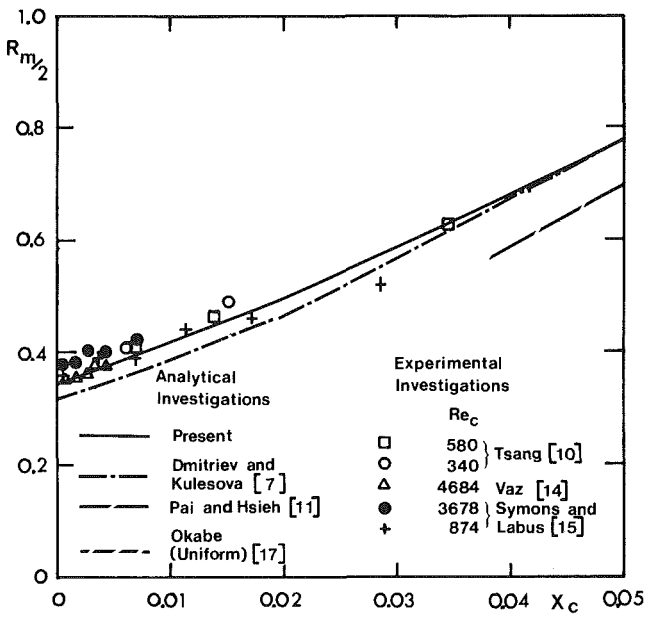

Fig. 4 Jet growth

Comparison with Experimental and Other Theoretical Results

Using equation (15) it can be shown that the center line velocity decay can be found as

$$U_m = (1-\epsilon)^3 \tag{24}$$

This is plotted versus X_c in Fig. 3 along with Okabe's solution for the uniform case as well as other theoretical and experimental results. The effect that the initial velocity profile has on centre line velocity decay can readily be seen to be significant by comparing Okabe's solution for the uniform case with the present theory. The excellent agreement of the present theory with Dmitriev and Kulesova's equation for $X_c < 0.015$ is particularly noteworthy in view of the fact that theirs was taken from a finite difference solution of the

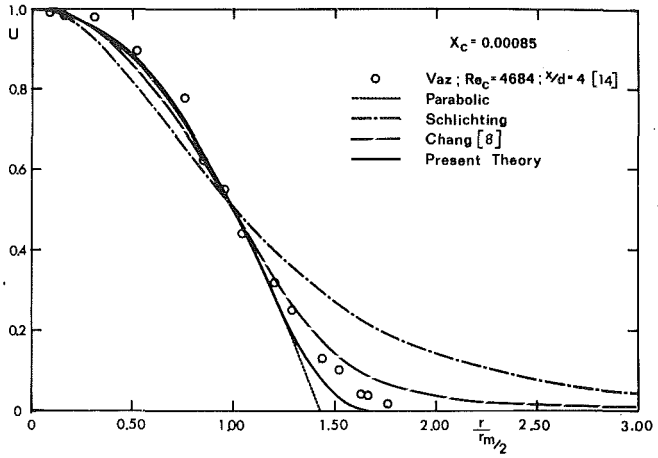

Fig. 5 Nondimensional velocity profile (X_c = 0.00085)

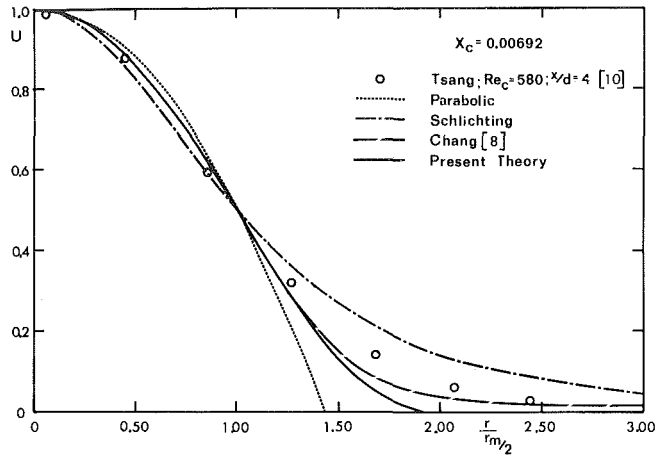

Fig. 7 Nondimensional velocity profile (X_c = 0.00692)

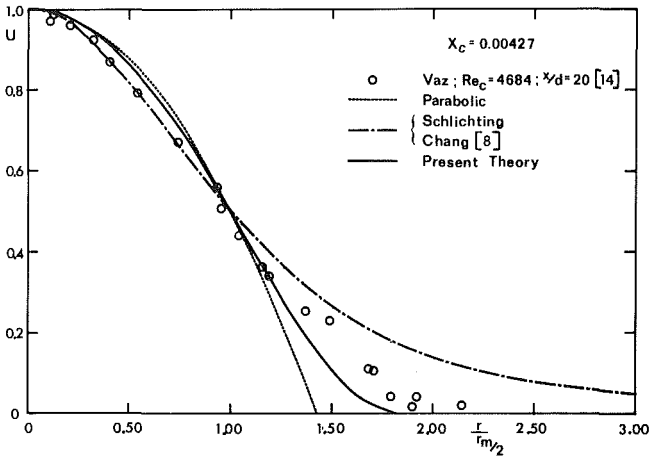

Fig. 6 Nondimensional velocity profile (X_c = 0.00427)

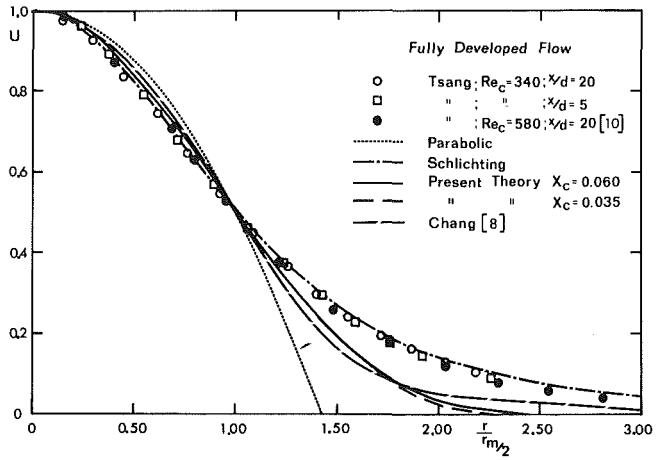

Fig. 8 Nondimensional velocity profile (fully developed)

boundary layer equations. Pai and Hsieh's numerical solution does not agree as well within this region, however, it is close to Dmitriev and Kulesova's result far downstream. The difference between Tsang's experimental results and the above two theories could possibly be due to an uncertainty in the value of the kinematic viscosity of the fluid used in their experiments [10]. Such an uncertainty could possibly shift the data points to X_c values that are 16% greater which would show a better agreement with the present theory. The data of Symons and Labus exhibit a considerable degree of scatter. This could possibly be due to uncertainties in their velocity measurements caused by the size of their pitot tube relative to the jet tube diameter. It is also possible that some of the data points may have originated from within an unstable region of the jet. The correlation of Abramovich and Solan is in reasonable agreement with the lower Reynolds number data, however, does not predict the higher Reynolds number data accurately.

It appears that although the simple centre line velocity matching scheme of Chang does not agree with either the present theory or that of Dmitriev and Kulesova, it does give a rough estimate of the centre line velocity decay.

Figure 4 shows the variation of $R_{m/2}$ along the jet. $R_{m/2}$ is the nondimensional radial coordinate of the point where the jet velocity is one half of the center line velocity. This parameter is a measure of the spread of the jet. The present theory seems to predict this parameter quite accurately. Pai and Hsieh's numerical results could not be extracted, accurately, from their graphs in the region near the jet exit. The result indicated is that the straight line obtained from their graph for large X_c. It appears to give smaller values for $R_{m/2}$ than the other methods

Figures 5, 6, 7 and 8 present velocity profile comparisons within the jet at progressively larger nondimensional distances downstream of the nozzle exit. The first three figures include profiles that are within the developing region of the jet while those in Fig. 8 are either fully developed or very close to being so.

In all of these figures the velocity is normalized with the jet centre line velocity and plotted against the radial position normalized with the radial distance to the point where the normalized velocity is 0.5. Consequently, all curves pass through the point (1.0, 0.5) in these figures. This method of plotting allows a comparison of profile shapes, independent of $R_{m/2}$ and U_m. The parabolic and fully developed similarity profile are included on each figure for comparison.

In general it can be seen that the agreement between the present assumed velocity profile shape and the experiments becomes increasingly worse as the value of X_c becomes larger.

Chang's correlation is seen to be in fair agreement in Fig. 5. In Fig. 6 it reduces to the Schlichting similarity profile since $x/d > 10$. This is found to be in relatively poor agreement with the experimental data.

Dmitriev and Kulesova's curve is coincident with the similarity profile in all of the velocity profile plots due to the fact that they only adjusted the centre line velocity and jet spread parameters and not the velocity profile shape.

The results of the present theory for X_c values of 0.035 and

0.060 are plotted on Fig. 8. This shows that the present theory almost exhibits a similarity characteristic, however, not that of the experimental data. The classical similarity solution is in good agreement with the data beyond the initial development region.

Chang's correlation is also unable to accurately predict the particular case of $Re_c = 340$ and $x/d = 5$. This again emphasizes that X_c rather than x/d is the proper nondimensional axial coordinate.

Conclusions

1) An approximate analytical solution for the axisymmetric laminar jet has been found to accurately predict the jet spread and centre line velocity decay in the initial development region. That is in the approximate range $0 \leq X_c \leq 0.015$.
2) The assumed velocity profile shape is exact at the nozzle exit for the case of fully developed pipe flow and is reasonably accurate in the region of the jet immediately downstream. However, beyond the development region, Schlichting's similarity solution should be used.
3) Although the velocity profile shape almost exhibits a similarity condition at larger axial distances downstream of the nozzle exit, this profile does not reduce to the exact boundary layer solution by Schlichting.

Acknowledgments

The authors are grateful to Professor T.W. McDonald, Head of the Mechanical Engineering Department, for his interest and continuous support. The work was financially supported through a Shell Canada Postgraduate Fellowship and a grant by the Natural Sciences and Engineering Research Council Canada (Grant Number A-2190).

References

1 Rankin, G.W., and Sridhar, K., "Developing Region of Laminar Jets with Uniform Exit Velocity Profiles," ASME JOURNAL OF FLUIDS ENGINEERING, Vol. 100, 1978, pp. 55–59.

2 Sato, H., "The Stability and Transition of a Two-Dimensional Jet," *Journal of Fluid Mechanics,* Vol. 7, 1960, pp. 53–80.

3 Schlichting, H., *Boundary Layer Theory,* 6th Ed., McGraw-Hill, New York, N.Y., 1968, pp. 218–221.

4 Andrade, E.N., and Tsien, L.C., "The Velocity Distribution in a Liquid into Liquid Jet," *Proceedings of the Physical Society,* London, Vol. 29, Part 4, 1937, pp. 381–391.

5 Foster, K., and Parker, G.A., *Fluidics: Components and Circuits,* Wiley-Interscience, London, 1970, pp. 94–96.

6 Bell, A. C., "An Analytical and Experimental Investigation of the Turbulence Amplifier," ScD thesis, Mechanical Engineering Department, Massachusetts Institute of Technology, 1969.

7 Dmitriev, V.N., and Kulesova, N.A., "The Calculation of a Laminar Jet in the Surroundings of the Supply Nozzle," *Proceedings of the "Jablonna" Fluidics Conference,* Budapest, Hungary, Nov. 1974, pp. 83–91.

8 Chang, H., "An Analytical and Experimental Investigation of a Large-Scale Model of a Turbulence Amplifier," M.Sc. thesis, State University of New York at Buffalo, 1972.

9 du Plessis, M.P., Wang, R.L., and Tsang, S., "Development of a Submerged Round Laminar Jet from an Initially Parabolic Profile," ASME *Journal of Dynamic Systems, Measurement, and Control,* Vol. 95, 1973, pp. 148–154.

10 Tsang, S., "A Study of Axisymmetric Submerged Jets Relevant to Turbulence Amplifier Design," Masters thesis, Department of Mechanical Engineering, Sir George Williams University, Montreal, Canada, Aug. 1971.

11 Pai, S.I., and Hsieh, T., "Numerical Solution of Laminar Jet Mixing with and without Free Stream," *Applied Scientific Research,* Vol. 27, No. 1, Oct. 1972, pp. 39–62.

12 Abramovich, S., and Solan, A., "The Initial Development of a Submerged Laminar Round Jet," *Journal of Fluid Mechanics,* Vol. 59, Part 4, 1973, pp. 791–801.

13 Abramovich, S., and Solan, A., "Turn-on and Turn-off Times for a Laminar Jet," ASME *Journal of Dynamic Systems, Measurement and Control,* Vol. 95, 1973, pp. 155–160.

14 Vaz, T., "An Experimental Investigation into the Response of a Turbulence-Type Amplifier, and Laminar/Turbulent Jet Study," M.A.Sc. thesis, Department of Mechanical Engineering, University of Windsor, Windsor, Ontario, Canada, 1970.

15 Symons, E.P., and Labus, T.L., "Experimental Investigation of an Axisymmetric Fully Developed Laminar Free Jet," NASA TN D-6304, 1971.

16 Thomas, A.L., "Force and Mass Balances of the Incompressible, Isothermal, Planar Laminar Jet Issuing from a Finite Source," *Chemical Engineering Science,* Vol. 8, 1958, pp. 254–264.

17 Okabe, J., "Approximate Calculations of Laminar Jets (continued)," Rep. Res. Inst. Fluid Eng., Kyushu Univ., Vol. 5, 1948, pp. 15–22.

A Comparison of Cold and Reacting Flows Around a Bluff-Body Flame Stabilizer

S. Fujii
Head, Engine Noise Group.
Mem. ASME

K. Eguchi
Senior Researcher.
Aero-Engine Div.

National Aerospace Laboratory,
Chofu, Tokyo, Japan

A confined oblique flame anchored on a bluff object was considered in a homogeneous propane/air mixture. A laser velocimeter employing a unique single-particle processor was used to quantify the turbulence velocity as well as spectrum. The results with combustion presented a striking contrast to the corresponding cold flow data. A major conclusion of the work is that the apparent suppression of turbulence observed in the separated combustion flow may be attributed to the significant dilatation effect by heat release in sheared flow regions. No vortex shedding was detected, and the negative production zone of turbulence energy was not observed. The turbulence structure was significantly distorted at the visible flame location.

Introduction

The present study was directed toward the fluid dynamic aspects of combustion processes. Flame propagation from a bluff body in a homogeneous propane/air mixture flowing in a duct of constant cross section was considered. In the bluff-body combustion system, exchange of the mass, momentum, and energy between the recirculation and the mainstream occurs through turbulent mixing. Flame stretch takes place in a flow region with high velocity gradients. The flame characteristics are largely determined by the aerodynamics of the reacting flow around the body.

Flows behind bluff bodies are complex, due to separation and recirculation, and are extremely sensitive to probe interference. Therefore, a laser Doppler velocimeter (LDV) was used to quantify the turbulence velocity as well as spectrum with a nonintrusive point measurement. An in-house single-particle processor was employed in the LDV data acquisition system to improve the signal processing reliability for use in the highly turbulent flow. The experimental results described here are an extension of the work by the present authors who made cold flow tests on the bluff object [1]. The main objective of the present paper is to report the experimental observations with combustion, and to compare or correlate the flow data in both cases with and without heat addition.

Earlier papers on bluff body stabilized flames were aimed at evolving a correlation for the flame stability limit, and a few papers dealt with the recirculation flow behavior and residence time correlations [2–15]. Despite the considerable efforts, turbulence/combustion interaction still is not well understood. Although the experimental data shown here are limited, a few of the relationships existing between fluid dynamics and combustion are discussed. The results presented are the mean flow, time-averaged turbulence velocity correlation, and turbulence spectrum. Aerodynamic considerations are emphasized rather than chemical kinetics and reaction mechanisms. Note that the flow without combustion is referred to as "cold" or "isothermal" in the paper.

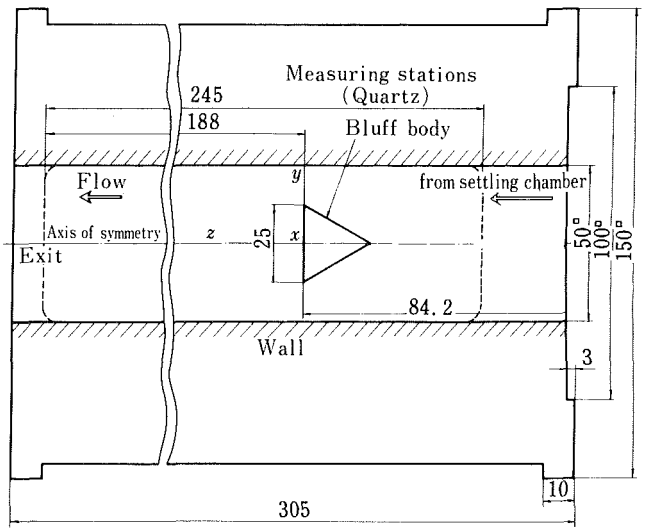

Fig. 1 Bluff body combustor (units are all in mm)

Test Hardware and Instrumentation

The test rig and flow configuration used in this experiment are the same as those reported in reference [1]. A schematic diagram of the bluff body combustor is reproduced in Fig. 1, with the x, y, and z coordinates illustrated. The side walls of the working section employed windows of laser quality quartz. A homogeneous propane/air mixture was ignited and a flame stabilized on a triangular rod, which completely spans the 50mm × 50mm duct. The flow was substantially two-dimensional, as is shown later.

Contributed by the Fluids Engineering Division for publication in the JOURNAL OF FLUIDS ENGINEERING. Manuscript received by the Fluids Engineering Division, July 21, 1980.

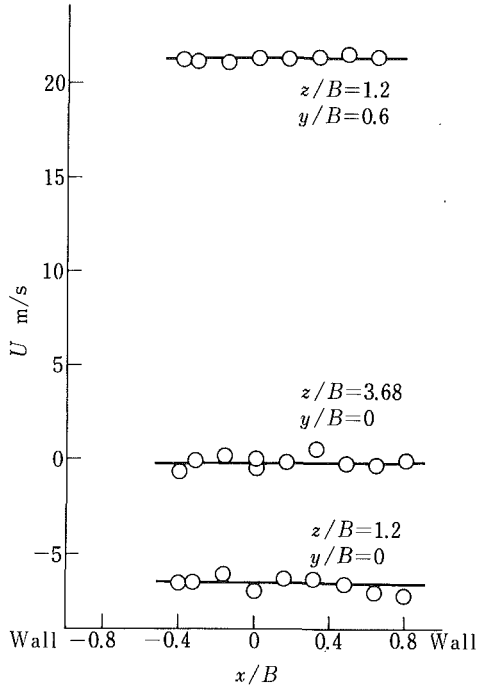

Fig. 2 Two-dimensionality assertion by the mean velocity measurement in hot gas with an equivalence ratio of ϕ_p = 0.6 (uncertainty of $x/B, y/B, z/B = \pm 0.004$ and of $U = \pm 0.2$ m/s)

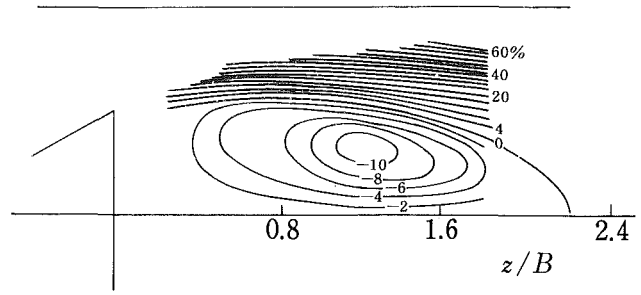

Fig. 3(a) Cold

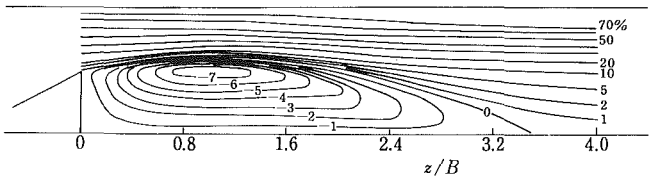

Fig. 3(b) Combustion (ϕ_p = 0.7)

Fig. 3 Time-averaged streamlines, ψ/ψ_0, given in percentage (uncertainty of $z/B = \pm 0.004$ and of $\psi/\psi_0 = \pm 2.5$ percent

The flow velocity was determined using a dual beam 15 milliwatt He-Ne laser Doppler velocimeter with a frequency off-set Bragg cell, see reference [1] for details. A single-particle processor, developed at the Japanese NAL [16], was incorporated to eliminate spurious signals due to the limit of frequency-tracking response inherent in the highly turbulent flow measurement.

Experimental Procedure, Results, and Discussion

Mean Flow Data. A velocity of 10 m/s was maintained in front of the bluff body, as done in the cold flow tests, reference [1]. With this velocity maintained, the equivalence ratio for the flammability limit was 0.52 (lean) and 1.62 (rich), respectively. The turbulence intensity level of the approach flow was about 2 percent.

Submicron particles of titanium dioxide (T_i0_2) were used as scattering centers for the LDV measurement. The test runs were sometimes interrupted due to the particle contamination on the windows. The rate of particles detected in a sensing volume was usually 10–50 s^{-1}. However, for the turbulence spectrum recovery, the particle rate was increased up to 5000 s^{-1}. Data processing and error estimation were made in a manner similar to those in the cold flow tests. Considerable care was taken to assure the spanwise two-dimensionality, as is illustrated in Fig. 2.

The effects of combustion on the mean flow behind the bluff body are illustrated in Figs. 3-6. The time averaged streamlines, Fig. 3, were calculated from $\psi = \int_0^y \bar{\rho} U dy$ and divided by the total mass flow to be expressed in terms of percentage. The density was obtained from the mean temperature and static pressure data. It is evident that combustion extended the recirculation zone further downstream in comparison with the cold flow. The maximum width of the velocity reversal zone increased with combustion; (d/B) was about 1.30 in the combustion and 1.0 in the isothermal flow. Measurements from the Na-salt color indication of Kundu, et al. [14] showed a value of $d/B = 1.35$ for the wedge recirculation boundary which coincides closely with the present result. A ratio of the reverse to the total mass flow rate, M_R/M_T which is indicative of the recirculation strength, was calculated using the streamline data and plotted in Fig. 4. The maximum reverse-flow point shifted closer to the bluff body face with combustion, and at that point, $Z/L_{RZ} = 0.3$, the visible flame was observed to commence. It is also of interest to note that the maximum value of reversed mass flow rate, because of lower density, decreased in the combustion flow. Fig. 5 allows a comparison of axial-velocity characteristics along the axis of symmetry to show how the velocity distribution was changed with different equivalence ratios that include the cold flow case. The relationship between nondimensionalized, recirculation length and equivalence ratio is summarized in Fig. 6. L_{RZ}/B showed a minimum near the stoichiometric ratio and increased when the mixture ratio

Nomenclature

B = base height of the bluff body (= 25mm)
d = transverse distance of recirculation zone from the axis of symmetry, $y = 0$
k = turbulence kinetic energy
L_{Rz} = axial length of recirculation zone
M_R = reversed mass flow rate
M_T = total mass flow rate
(x,y,z) = Cartesian coordinates, x being along the bluff body span, y the distance from the axis of symmetry and z the downstream direction
U = mean axial-velocity, aligned with the duct axis
V = mean transverse velocity
$(\bar{u}^2, \bar{v}^2, \bar{w}^2, \overline{uv})$ = time-averaged velocity correlations
$\bar{\rho}$ = time-averaged density
ψ = local stream function
ψ_0 = global stream function
ϕ_p = equivalence ratio of propane/air mixture

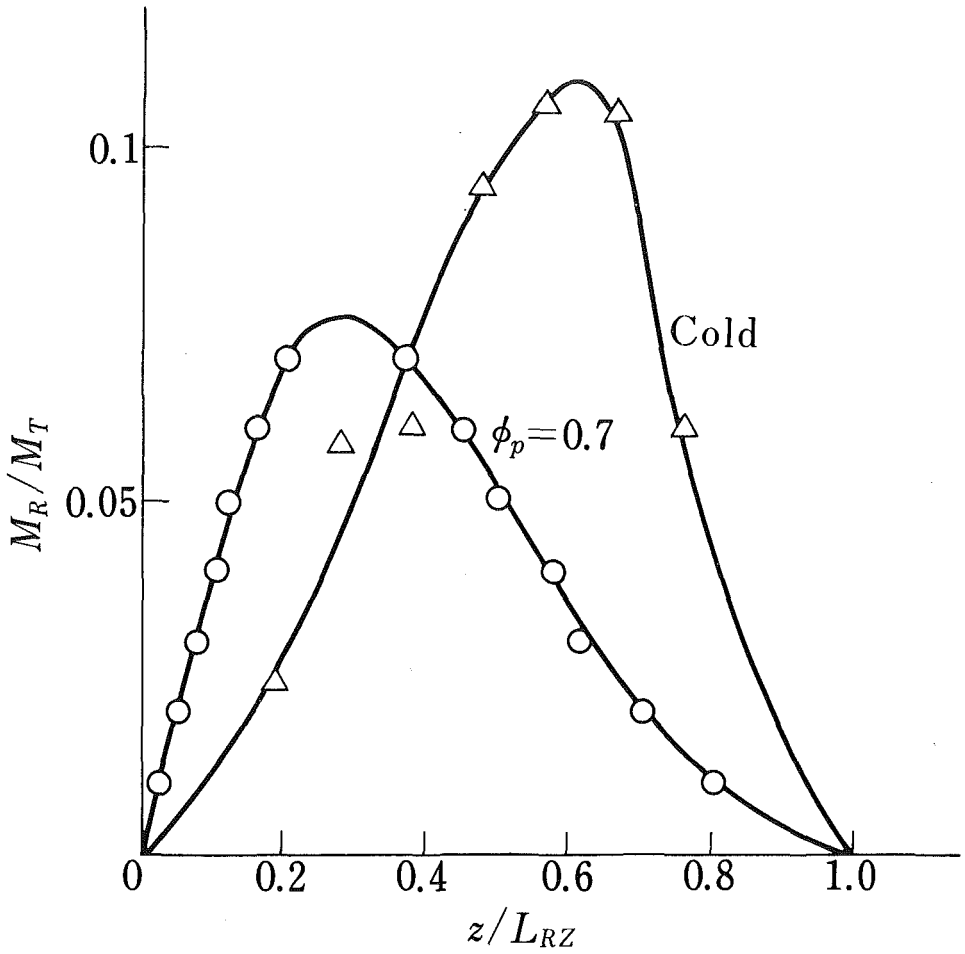

Fig. 4 Effect of combustion on reverse flow rate (z/L_{RZ} = ±0.004, and of M_R/M_T = ±0.01)

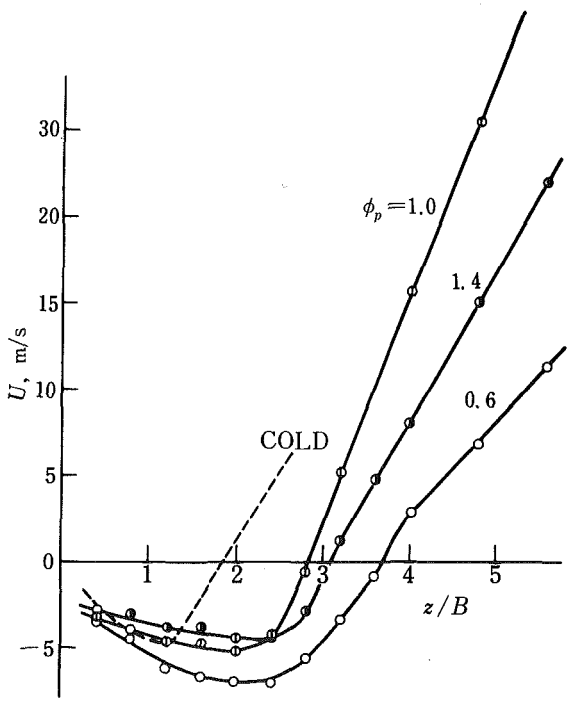

Fig. 5 Effect of equivalence ratio on axial-velocity characteristics along the axis of symmetry, y/B = 0 (uncertainty of z/B = ±0.004 and of U = ±0.2 m/s at worst)

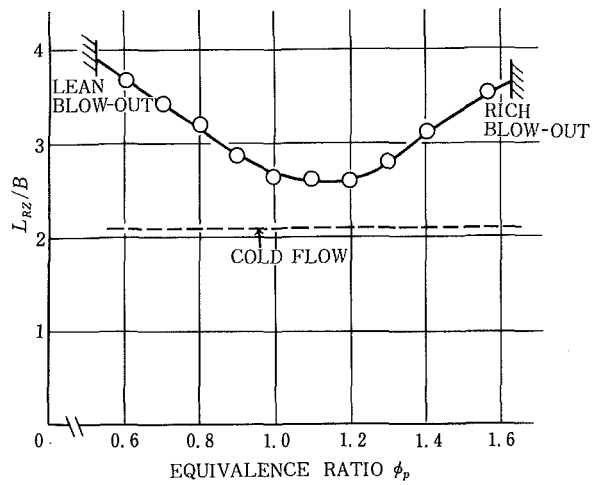

Fig. 6 Comparison of axial extents of recirculation zone (uncertainty of L_{RZ}/B = ±0.004 and of ϕ_p = ±0.01)

became richer or leaner. Winterfeld's results [9], while not exactly comparable in that he used disk flame holders, also indicated that L_{RZ}/B exhibited a minimum value of 1.5 near ϕ_p = 1.0, whereas L_{RZ}/B = 1.0 in the cold flow.

Turbulence Velocity Correlation. As is well known, there

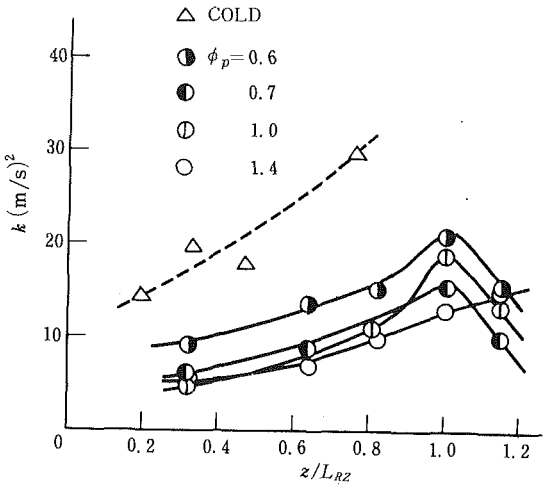

Fig. 7(a) $y/B = 0$

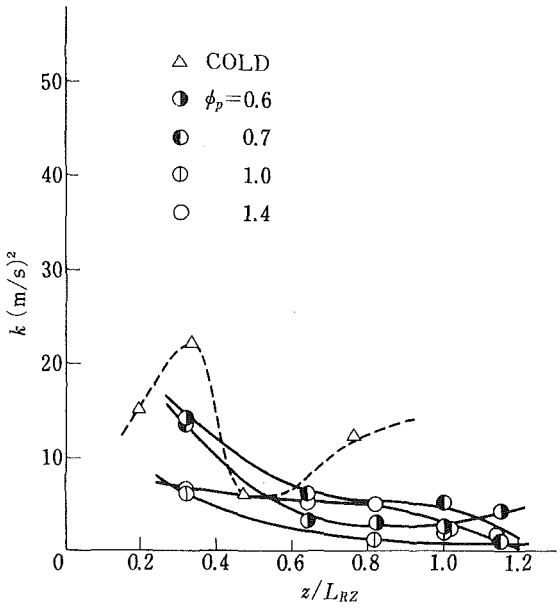

Fig. 7(c) $y/B = 0.5$

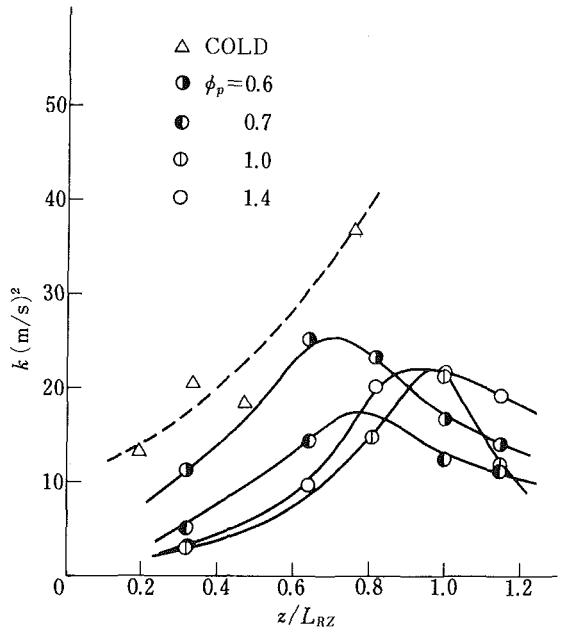

Fig. 7(b) $y/B = 0.2$

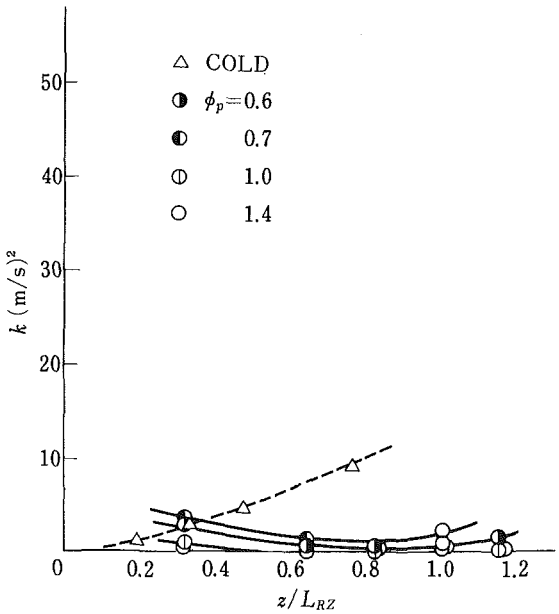

Fig. 7(d) $y/B = 0.6$

Fig. 7 Comparison of turbulence kinetic energy behind bluff body with and without combustion (uncertainty of $z/L_{RZ} = \pm 0.004$, $k = 0.2$ m^2/s^2)

exists a turbulent exchange between the recirculation and the mainstream to supply continuously the energy necessary to ignite the unburned gases. The transport of heat and mass is a consequence of the turbulent velocity fluctuations. Therefore, the turbulent flow data, presented in Figs. 7 and 8, give a better description of the turbulence/combustion interaction, which has been considered to be an important problem of combustion science.

Figure 7 displays the comparison of turbulence kinetic energy, defined as $k = (\tilde{u}^2 + \tilde{v}^2 + \tilde{w}^2)/2$ where the relation, $\tilde{w}^2 = (\tilde{u}^2 + \tilde{v}^2)/2$, was assumed. The Favre averaging or mass-weighted turbulence kinetic energy, $\tilde{k}$, is not considered in the present paper because of the inability to make time-resolved density measurements. It is of interest to note that the likely discrepancies between k and $\tilde{k}$ were evaluated to be small by the analysis of Glass and Bilger [17], made on the jet diffusion flame. A typical comparison of turbulence velocity correlations at an axial station is presented in Fig. 8. The turbulence levels in the combustion flows were much lower than those in the isothermal flow. In an oblique flame stabilized on a rod, Bray and Libby [18, 19] predicted that the production of turbulence kinetic energy would compete with or dominate the dilatation associated with heat release, which is not in agreement with the present results. It must be recalled that their analytical model was extremely simplified, and the velocity-pressure fluctuation terms were neglected. It appears

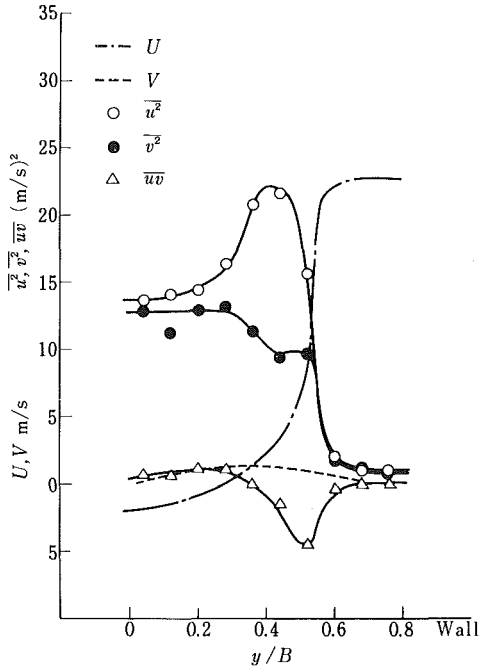

Fig. 8(a) cold flow at z/L_{RZ} = 0.33

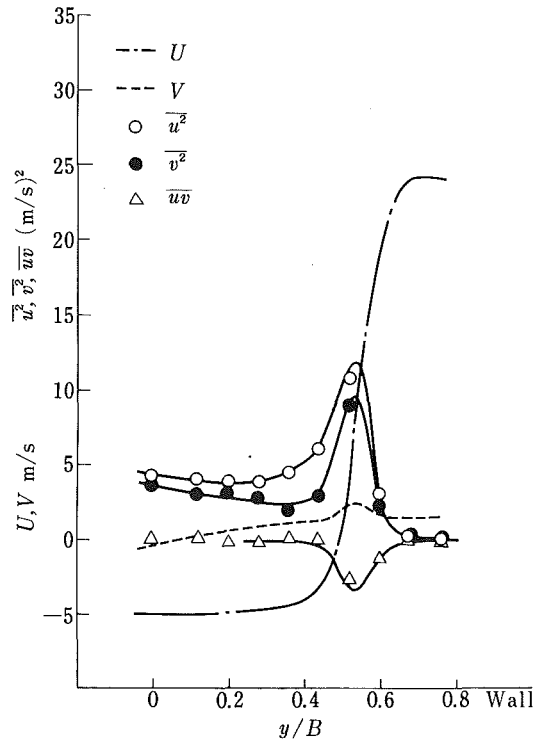

Fig. 8(b) reacting flow of ϕ_p = 0.7 at z/L_{RZ} = 0.32

Fig. 8 Comparison of selected results of mean and turbulence velocity data (uncertainty of y/B = ±0.004 and of U, V = 0.2 m/s, and of $\overline{u}^2$, $\overline{v}^2$ = 0.2 m^2/s^2)

that the dilatation or destruction of turbulence kinetic energy by chemical reaction was still significant in this experiment. The angle between the visible flame and mainstream direction, which controls the generation of turbulence energy in shear flows [19], was observed to be less than 15 degrees in all cases tested.

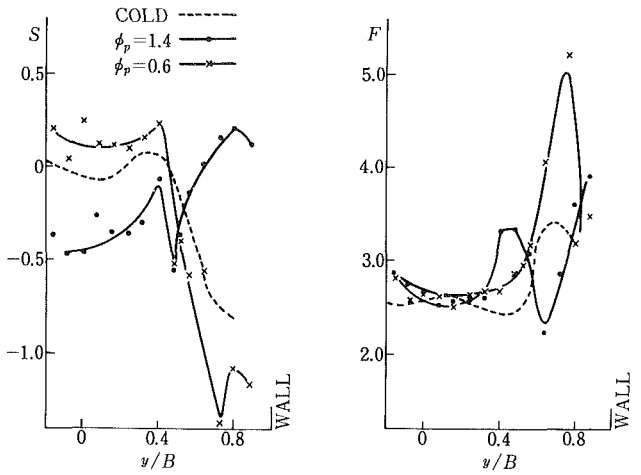

Fig. 9(a) z/L_{RZ} = 0.32

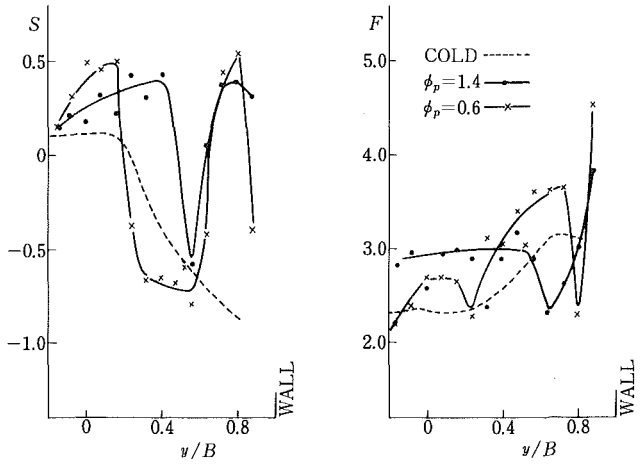

Fig. 9(b) z/L_{RZ} = 0.64

Fig. 9 Effect of combustion on turbulence structure, *S*: skewness, *F*: flatness (uncertainty of z/B = ±0.004 and of *S*, *F* = ±0.05)

Structure parameters such as skewness, $S = \bar{u}^3/(\bar{u}^2)^{3/2}$ and flatness or kurtosis, $F = \bar{u}^4/(\bar{u}^2)^2$ are shown in Fig. 9. A pronounced trough of the skewness profiles is a common feature fort he reacting flow. Considering the fact that the center of the visible flame was located in the trough, it is deduced that the turbulence structure was highly distorted and negatively skewed by heat release. The same effect was reflected in the plotted profiles of the flatness; a positive and negative deviation from a Gaussian distribution was observed for the lean and rich mixture respectively. The results obtained in this experiment differ from the experimental results of Starner and Bilger [20], whe concluded that the structure parameters were essentially the same for both the isothermal and reacting flows for a diffusion flame with axial pressure gradients.

Turbulence Spectrum and Vortex Shedding. The art of practical spectrum estimation by the LDV with finite data sets of randomly timed samples is still in its infancy. However, some knowledge has been accumulated and published on this subject [21-24]. Therefore, the time behavior information retrieval for the turbulence spectrum was recorded in the mini-computer. The velocity history data sampled at random intervals were read at every grid slot to make up the data of equal time events on the computer. The slot was placed at an

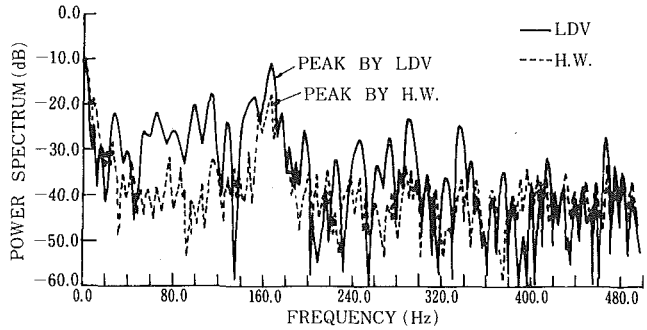

Fig. 10(*a*) cold flow data well outside of recirculation of $z/B = 1.2$ and $y/B = 0.6$

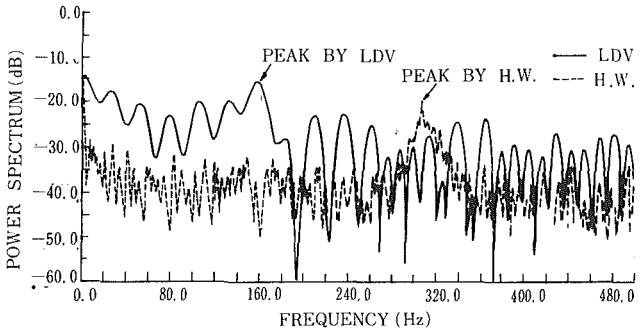

Fig. 10(*b*) cold flow data at end of recirculation

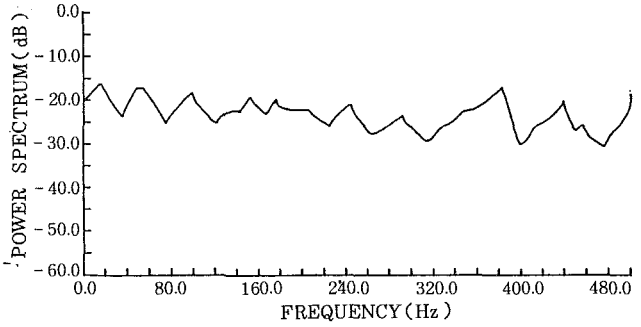

Fig. 10(*c*) reacting flow data at end of recirculation

Fig. 10 Comparison of power spectra by LDV and hot-wire measurements (uncertainty of power spectrum = ±2 *dB*)

equal time interval while its width was set to minimize errors. Those data which did not fall into any slot were discarded. An arithmetic mean of all data entered in the same slot was taken to represent the slot velocity. Having accumulated the data with an equal interval, the familiar procedure, mainly described in reference [21], was used to compute the correlation function and the power spectral density.

The results are shown in Fig. 10, in which the hot-wire data were processed with a correlator and a Fourier transformer (SAICOR-Kanomax 43A and 470). The first comparison with the hot-wire data was made well outside of the cold flow recirculation zone, in Fig. 10(*a*). Both the LDV and hot-wire measurements detected a pronounced frequency of 160 Hz and thus the corresponding Strouhal number of 0.40 for the constrained flow, which compares very closely with the data of Ramamurthy, et al. [25]. The second comparison, performed inside or at the end of recirculation, indicated that a frequency of 160 Hz was still predominant in the LDV data while the hot-wire gave a value of 320 Hz, Fig. 10(*b*). The hot-wire measurement system used did not sense a negative or positive direction of the oncoming flow, so that the frequency was falsely detected and thus doubled if both flow directions co-existed. A substantial increase of spectrum density near 2 Hz was considered to be what is called the trend effect; the cut-off frequency was about 5 Hz. In addition to the tests on the cold flow, the LDV spectra were also obtained from the reacting flow. However, any particular or pronounced frequency was not detected anywhere around the bluff object anchored by the confined oblique flame. Figure 10(*c*) shows typical results obtained at the end of hot-flow reversal zone. The absence of eddy shedding behind the bluff stabilizer during combustion was previously reported by Williams, et al. [2]. The present spectrum measured provides further evidence for the nonexistence of vortex shedding in the bluff body flow with combustion.

A thorough check of the flow data revealed that the turbulence velocity correlation, $\overline{uv}$, never became positive in the entire region investigated during combustion, while both positive and negative velocity correlation were observed in the cold flow. Another observation is that the reversal velocity gradient, $\partial U/\partial y$, was much steeper in the cold flow than that in the reacting flow, Fig. 8. The turbulence energy production terms can be estimated by, $\pi = -(\overline{u^2} - \overline{v^2})\,\partial U/\partial z - \overline{uv}\,(\partial U/\partial y + \partial V/\partial z)$ for the cold low-speed flow case. It is assumed that even with combustion this equation may be accepted with reasonable accuracy well inside the recirculation zone, where the heat release, and thus density variations may be assumed to be insignificant. With this assumption, the negative production of turbulence energy was never found in any data from the combustion flow. It is recalled that negative values of π occurred in the cold flow where signs of $\overline{uv}$ switched from negative to positive [1]. A large-scale motion of turbulence might be different in flows with and without heat addition. It is probable that the vortex shedding, observed only in the isothermal case, played an important role in producing large-scale fluctuations, which in turn resulted in an appearance of the negative production zone of turbulence energy. This conclusion is significant enough to deserve further examination in the future.

Conclusions

The measurements described here are an extension of the work by the present authors on cold flow tests with a bluff body flame stabilizer. Experimental data for the confined oblique flame, anchored on the bluff object, were compared with the corresponding cold flow data. The findings from this work are summarized as follows:

(1) *Suppression of turbulence by combustion.* The turbulence levels in the reacting flow were much lower than in the isothermal flow. It may be concluded that the dilatation by heat release competed with or dominated turbulence energy production by shear flows, notably in the vicinity of recirculation boundary.

(2) *Nonexistence of vortex shedding and of turbulence energy reversal zone during combustion.* A tentative conclusion is drawn that the absence of vortex shedding led to the fact that the sign of $\overline{uv}$ no longer switched from negative to positive in the hot-flow reversal zone; hence, the negative production of turbulence energy was not recognized. These results contrast with the observations obtained in the cold flow, where the opposing shear or turbulence energy reversal zone was apparently observed.

(3) *Other results of interest.* (*a*) The turbulence structure was significantly distorted at the visible flame location, as demonstrated by the skewness and flatness factor data. (*b*) The burning enlarged the recirculation boundary further downstream but the maximum rate of the reversed flow was decreased in magnitude, because of the low density prevailing in combustion.

Acknowledgments

The authors are indebted to M. Gomi, S. Kidawara, and A. Hagiwara for their assistance in carrying out the experimental work and in programing computer codes for the data acquisition and analysis system of the LDV reported in this paper.

References

1 Fujii, S., Gomi, M., and Eguchi, K., "Cold Flow Tests of a Bluff-Body Flame Stabilizer," ASME JOURNAL OF FLUIDS ENGINEERING, Vol. 100, Sept. 1978, p. 323.

2 Williams, G. C., Hottel, H. C., and Scurlock, A. C., "Flame Stabilization and Propagation in High Velocity Gas Streams," 3rd Symposium on Combustion and Flame, and Explosion Phenomena, 1949, p. 21.

3 Longwell, J. P., Chenevey, J. E., Clark, W. W., and Frost, E. E., "Flame Stabilization by Baffles in a High Velocity Gas Stream," ibid., p. 40.

4 Nicholson, H. M. and Field, J. P., "Some Experimental Techniques for the Investigation of the Mechanism of Flame Stabilization in the Wakes of Bluff Bodies," ibid., p. 44.

5 Spalding, D. B., "Theory of Rate of Spread of Confined Turbulent Premixed Flames," 7th Symposium (Int'l) on Combustion, Aug. 1958, p. 595.

6 Cheng, S. I., and Kovitz, A. A., "Theory of Flame Stabilization by a Bluff Body," ibid., p. 681.

7 Bovina, T. A., "Studies of Exchange Between Recirculation Zone Behind The Flame-Holder and Outer Flow," ibid., p. 692.

8 Fetting, F., Choudhury, A.P.R., and Wilhelm, R. H., "Turbulent Flame Blow-off Stability. Effect of Auxiliary Gas Addition into Separation Zone," ibid., p. 621.

9 Winterfeld, G., "On Processes of Turbulent Exchange Behind Flame Holders," 10th Symposium (Int'l) on Combustion, 1965, p. 1265.

10 Lefebvre, A. H., and Reid, R., "The Influence of Turbulence on the Structure and Propagation of Enclosed Flames," *Comb. and Flame*, Vol. 10, Dec. 1966, p. 355.

11 Kundu, K. M., Banerjee, D., and Bhaduri, D., "Theoretical Analysis on Flame Stabilization by a Bluff-Body," *Comb. Sci. and Tech.*, Vol. 17, 1977, p. 153.

12 Topps, J. C., "An Optical Technique for the Investigation of Flow in Gas Turbine Combustor," 17th Symposium (Int'l) on Combustion, Aug. 1978, p. 267.

13 Plee, S. L., and Mellor, A. M., "Characteristic Time Correlation for Lean Blowoff of Bluff-Body-Stabilized Flames," *Comb. and Flame*, Vol. 35, 1979, p. 61.

14 Kundu, K. M., Banerjee, D., and Bhaduri, D., "On Flame Stabilization by Bluff-Bodies," ASME *Journal of Engineering for Power*, Vol. 102, Jan. 1980, p. 209.

15 Kumar, R. K., "A Method of Estimating Pressure Loss Across Flame Holders in High Velocity Streams," *Comb. Sci. and Tech.*, Vol. 21, 1980, p. 199.

16 Gomi, M., Kidawara, S., and Fujii, S., "A Method of Laser Velocimeter Data Processing," Nat'l Aerospace Lab. Tech. Report TR-521, Jan. 1978.

17 Glass, M., and Bilger, R. W., "The Turbulent Jet Diffusion Flame in a Co-flowing Streams - Some Velocity Measurements," *Comb. Sci. and Tech.*, Vol. 18, 1978, p. 165.

18 Bray, K.N.C., "Kinetic Energy of Turbulence in Flames," AASU Report No. 332, Univ. of Southampton, Feb. 1974.

19 Bray, K.N.C., and Libby, P. A., "Interaction Effects in Turbulent Premixed Flames," *Physics of Fluids*, Vol. 19, No. 11, Nov. 1976, p. 1687.

20 Starner, S. H., and Bilger, R. W., "LDA Measurements in a Turbulent Diffusion Flame with Axial Pressure Gradient," *Comb. Sci. and Tech.*, Vol. 21, 1980, p. 259.

21 Smith, D. M., and Meadows, D. M., "Power Spectra from Random-Time Samples for Turbulence Measurements with a Laser Velocimeter," *Proc. 2nd Int'l Workshop on Laser Velocimetry*, Purdue Univ., Mar. 1974, p. 27.

22 Scott, P. F., "Theory and Implementation of Laser Velocimeter Turbulence Spectrum Measurements," ibid., p. 47.

23 Mayo, Jr., W. T., "A Discussion of Limitations and Extensions of Power Spectrum Estimation with Burst-Counter LDV Systems," ibid., p. 90.

24 Wang, J.C.F., "Laser Velocimeter Turbulence Spectra Measurements," *Proc. Minnesota Symposium on Laser Anemometry*, Univ. of Minn., Oct. 1975, p. 538.

25 Ramamurthy, A. S., Lee, P. M., and Ng, G. P., "Velocity Scales for Constrained Flows," *Aeronautical Jour.*, Jan. 1975, p. 38.

N.W.M. Ko
Reader.

H. Au
Graduate Student.

Department of Mechanical Engineering,
University of Hong Kong,
Hong Kong

Initial Region of Subsonic Coaxial Jets of High Mean-Velocity Ratio

This paper describes an experimental investigation of the initial region of subsonic coaxial jets of three different mean-velocity ratios λ higher than unity. Detailed measurements have found similarity of the mean velocity and turbulence intensity profiles within the three zones: initial merging, intermediate, and fully merged zone. Similarity with single jet results has been found. In the inner mixing region, however, only the similarity of the mean velocity profiles has been found.

Introduction

The initial region of homogeneous coaxial jets discharging into stationary air has been investigated [1–5]. These investigations covered coaxial jets of different exit velocity, mean-velocity ratio, nozzle diameter and area ratio. The mean-velocity ratio λ is defined as the ratio of the outer to inner nozzle exit velocity. The earlier results of the mean flow characteristics showed similarity of the mean-velocity profiles at a distance greater than six primary diameters downstream [4]. The range of mean-velocity ratio covered by the above workers varied from 0.02 to 4 and the limiting case of annular jet. The recent detailed work on coaxial jets of low mean-velocity ratios of less than unity for λ = 0.3, 0.5, 0.7 has found similarity not only of the mean velocity profiles but also of the turbulence intensity profiles [5]. Based on the similarity of the mean-velocity measurements, the initial region of coaxial jets of low mean-velocity ratios was isolated into three separate zones: the initial merging, the intermediate, and the fully merged zone. In these zones similarity was found within the two mixing regions inside the initial merging zone and within the fully merged zone. However, no similarity of the mean velocity and turbulence intensity profiles was found in the intermediate zone. The similarity of these profiles of coaxial jets agreed with that of single jet results [6, 7].

The initial region of annular jets, the limiting case of coaxial jet, has also been studied [8]. Three configurations which were the basic one, without any bullet in the centre, and those with a conical and ellipsoidal bullet, were adopted. As the cases of coaxial jets of low mean-velocity ratio, the initial region, irrespective of the type of jet, could also be divided into the initial merging, the intermediate and the fully merged zone. In these three zones, similarity of both the mean velocity and turbulence intensity profiles has been found. Again, the similarity curves agreed with those for a single jet. In view of the lack of detailed information on the flow characteristics of coaxial jets of high mean-velocity ratio, which ratio was between the limiting case of annular jet [8] and of coaxial jets of low mean-velocity ratio [5], the objective was to fill this void. Detailed measurements of both the mean velocity and turbulence intensity of coaxial jets of different velocity ratios were made and are presented.

Table 1 Length of potential core

λ^{-1}	Inner jet	Outer jet
0.4	2.1 D_0	1.8 D_0
0.6	2.9 D_0	1.5 D_0
0.8	4.1 D_0	1.7 D_0
Single Jet	4.7 D_0	

Experimental Arrangement

The experiments were carried out within coaxial air jets that mixed externally [5]. The central nozzle, which generated the inner jet has a diameter D_i of 2.0 cm. The outer jet was produced by an annular nozzle which has an outer diameter D_0 of 4.0 cm and an inner diameter D_i' of 2.2 cm. Deducting the area due to the wall thickness of the inner nozzle exit, the area ratio of the outer to inner nozzle was 2.73. The turbulence intensity was 0.5 and 1.2 percent of the mean exit velocity for the inner and outer nozzle, respectively.

The hot-wire anemometer used was a constant-temperature type with linearized output [9]. The wire had a diameter of 5 $\times 10^{-6}$ m and a length of 2 mm.

The experiments were run with the mean exit velocity $\bar{U}_0$ of the outer jet being kept constant at 50 m/s. The mean exit velocity of the inner jet was varied. The mean-velocity ratios λ (or λ^{-1}) $\bar{U}_0/\bar{U}_i$ were 2.5, 1.67, and 1.25 (or 0.4, 0.6 and 0.8), respectively.

The experimental uncertainty of the data was as follows: within the velocity range jet velocity $\bar{U}$ ± 1 percent [10] and linear dimension ± 0.1 mm. The uncertainty of the non-dimensional groups such as the local mean-velocity ratio and turbulence intensity, was about ± 2 percent and the radial distance less than ± 1 percent.

Experimental Results

The division of coaxial jets of high mean-velocity ratio into different zones follows that for annular jets [8]. The initial merging, the intermediate and the fully merged zone are shown in Fig. 1 in which the contours of the local mean velocity ratio, $\bar{U}/\bar{U}_0$ at λ^{-1} of 0.6 are also included. The

Contributed by the Fluids Engineering Division for publication in the JOURNAL OF FLUIDS ENGINEERING. Manuscript received by the Fluids Engineering Division, June 5, 1980.

initial merging zone ends roughly at the place where the outer potential core disappears. Even with the mean exit velocity of the outer jet being kept constant, the change of λ^{-1} affects the length of the outer potential core though slightly (Table 1). Thus, the termination of this zone depends slightly on the mean-velocity ratio λ^{-1}. It is also within this initial merging zone that the inner potential core exists. The disappearance of this potential core, however, depends greatly on λ^{-1} (Table 1). The length of this core varies from 2.1 D_0 for λ^{-1} of 0.4, 2.9 D_0 for 0.6 to 4.1 D_0 for 0.8. This means that the inner region of constant mean velocity is longer than the outer potential core at such velocity ratio. Immediately downstream of the initial merging zone is the intermediate zone where the mixing of the flows from the two upstream mixing regions occurs. The extent of this intermediate zone is about four to five outer diameters. It is this intermediate zone that the reattachment of the outer jet occurs (Fig. 1). This means that

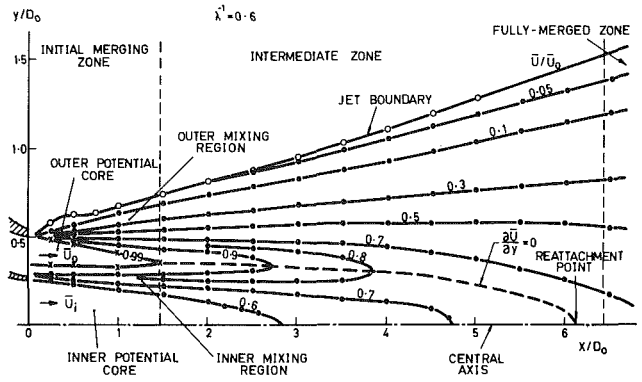

Fig. 1 Mean velocity contours of coaxial jets

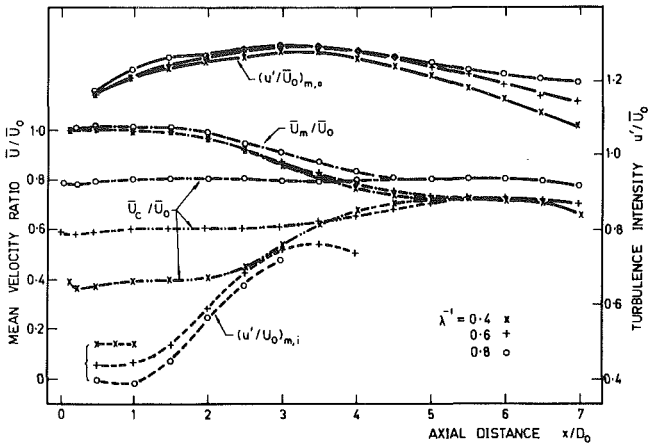

Fig. 2 Axial distribution of mean velocity ratio and turbulence intensity

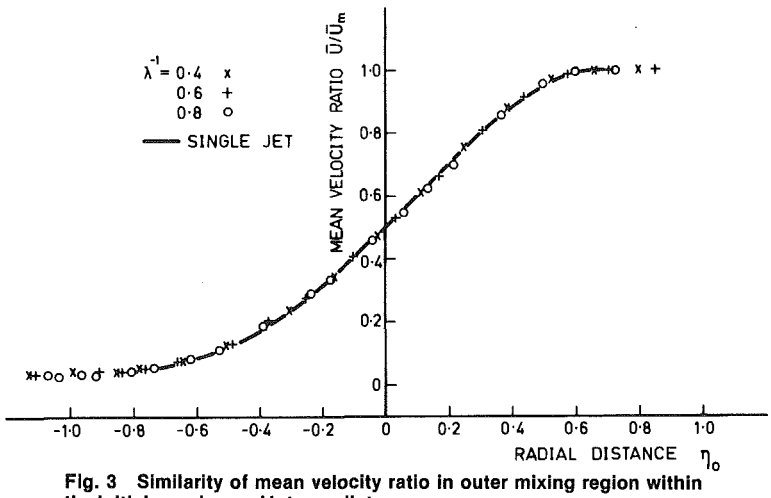

Fig. 3 Similarity of mean velocity ratio in outer mixing region within the initial merging and intermediate zone

Nomenclature

D_i = inner jet diametre
D_i' = inner diametre of outer jet
D_0 = outer jet diametre
$\bar{U}$ = local mean axial velocity
$\bar{U}_c$ = mean axial velocity at the centerline of the jet
$\bar{U}_i, \bar{U}_0$ = mean exit velocity of inner and outer jet
$\bar{U}_m$, $\bar{U}_{\min}$ = maximum and minimum mean axial velocity at any axial plane
u' = R.M.S. value of fluctuating axial velocity component
$\left(\frac{u'}{\bar{U}}\right)_{m,i}, \left(\frac{u'}{\bar{U}}\right)_{m,0}$ = maximum turbulence intensity inside and outside the locus $\partial\bar{U}/\partial y = 0$ for each axial plane
x, y = axial and radial position
$y_{0.9}, y_{0.5}, y_{0.1}$ = radial position inside the locus $\partial\bar{U}/\partial y = 0$ where $(\bar{U} - \bar{U}_{\min})$ is equal to 0.9, 0.5 and 0.1 of $(\bar{U}_m - \bar{U}_{\min})$, respectively
$y'_{0.9}, y'_{0.5}, y'_{0.1}$ = radial position outside the locus $\partial\bar{U}/\partial y = 0$ where the local mean velocity is equal to 0.9, 0.5 and 0.1 of $\bar{U}_m$, respectively
y_c = radial position in the fully merged zone where $\bar{U} = 0.5\,\bar{U}_m$
$\lambda = \frac{\bar{U}_0}{\bar{U}_i} = \frac{1}{\lambda^{-1}}$, mean-velocity ratio
$\eta_i = (y - y_{0.5})/(y_{0.9} - y_{0.1})$
$\eta_0 = (y - y'_{0.5})/(y'_{0.9} - y'_{0.1})$
$\eta_i = (y - D_i'/2)/x$

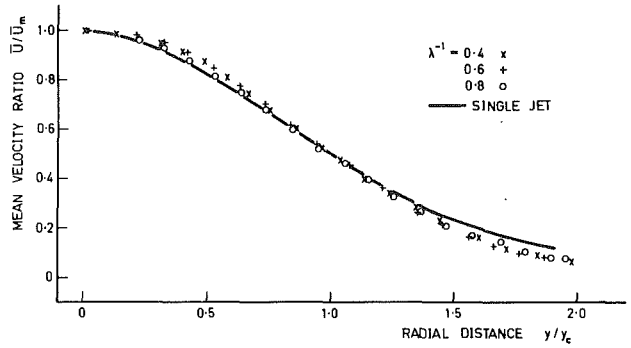

Fig. 4 Similarity of mean velocity ratio in fully merged zone

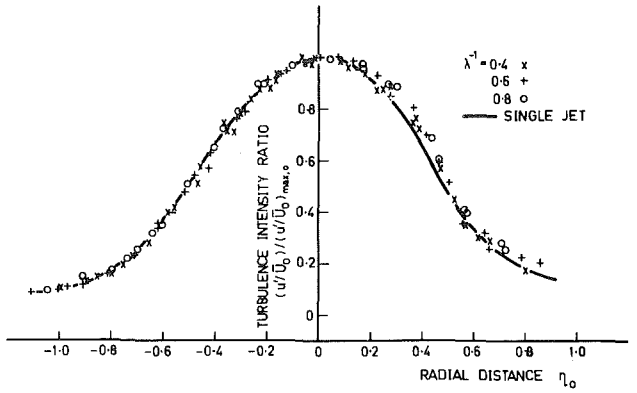

Fig. 6 Similarity of turbulence intensity ratio in outer mixing region within the initial merging zone

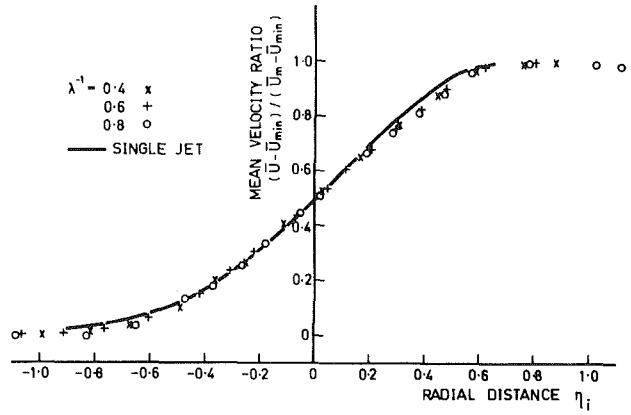

Fig. 5 Similarity of mean velocity ratio in inner mixing region. $x/D_0 \leq 4$.

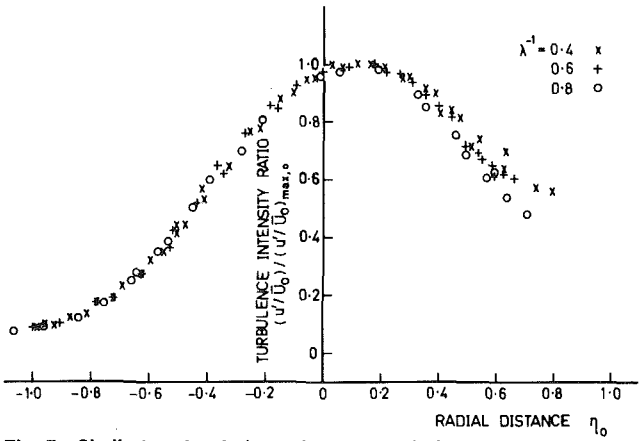

Fig. 7 Similarity of turbulence intensity ratio in outer mixing region within the intermediate zone

the high velocity flow of the outer annular flow merges at the central axis. The fully merged zone is the one downstream of the intermediate zone. Within this zone complete merging of the flow from the initial merging zone has occurred. The flow behaves like a combined jet and its characteristics are similar to those of a single jet.

The axial distribution of the maximum velocity ratio $\bar{U}_m/\bar{U}_c$ and the centerline velocity $\bar{U}_c/\bar{U}_0$ in each axial plane is shown in Fig. 2. For $x/D_0 \geq 0.5$ the value of the minimum velocity $\bar{U}_{min}/\bar{U}_0$ can be regarded as $\bar{U}_c/\bar{U}_0$. Location of the reattachment point was obtained by two methods: one was the extrapolation of the locus $\partial\bar{U}/\partial y = 0$ onto the jet axis and the other was by the determination of the location nearest to the nozzle exit where $\bar{U}_m/\bar{U}_0$ equals to $\bar{U}_c/\bar{U}_0$. Both methods gave the same result.

Similarity curves of the local mean velocity profiles of the outer mixing region in the initial merging and intermediate zone for different λ^{-1} are shown in Fig. 3. In this figure the nondimensional local mean velocity ratio $\bar{U}/\bar{U}_m$ is plotted against the nondimensional radial distance $\eta_0 = (y - y'_{0.5})/(y'_{0.9} - y'_{0.1})$. $y'_{0.9}$, $y'_{0.5}$ and $y'_{0.1}$ are the radial position outside the locus $\partial\bar{U}/\partial y = 0$, where the local mean velocity is equal to 0.9, 0.5 and 0.1 of $\bar{U}_m$, respectively (see Fig. 1 for locus $\partial\bar{U}/\partial y = 0$). For each set of results of λ^{-1} the data points cover the axial positions $1 \leq x/D_0 \leq 6$. Very good similarity of the local mean velocity profiles for the three coaxial jets is found in both the outer mixing region of the initial merging and intermediate zone. In addition, there is very good agreement of the similarity curve for the coaxial jets with that for the single jet.

Similarity curve of the local mean velocity profiles in the fully merged zone are shown in Fig. 4. The axial positions covered are $6.5 \leq x/D_0 \leq 7$. Good similarity for the coaxial jets and with that for the single jet is also found. In this zone the maximum mean velocity occurs at the central axis. It is also found that the curves $\bar{U}/\bar{U}_m$ = constant in this zone are straight lines and converge to a point which is referred as the virtual origin or pole. The axial position of the virtual origin is found to be upstream of the nozzle exit.

In the inner mixing region and in the part of intermediate region, which lies inside the locus $\partial\bar{U}/\partial y = 0$ good similarity of the local mean velocity $(\bar{U} - \bar{U}_{min})/(\bar{U}_m - \bar{U}_{min})$ with nondimensional radial distance $\eta_i = (y - y_{0.5})/(y_{0.9} - y_{0.1})$ is found. $y_{0.9}$, $y_{0.5}$, and $y_{0.1}$ are the radial position inside locus $\partial\bar{U}/\partial y = 0$ where $(\bar{U} - \bar{U}_{min})$ is equal to 0.9, 0.5 and 0.1 of $(\bar{U}_m - \bar{U}_{min})$, respectively. The similarity obtained is within $0.5 \leq x/D_0 \leq 4$ and it agrees with that of single jet.

The turbulence intensity profiles of coaxial jets of high mean velocity ratio have basically two low-intensity regions and two high-intensity regions within the initial merging and the upstream part of the intermediate zone. The two low-intensity regions correspond to the locations of the two potential cores. The two high-intensity regions correspond to the two mixing regions. In the downstream part of the intermediate zone and the fully merged zone only one high-intensity region is found.

The axial distributions of the maximum turbulence intensity inside and outside the locus $\partial\bar{U}/\partial y = 0$, that is, $(u'/\bar{U}_0)_{m,i}$ and $(u'/\bar{U}_0)_{m,0}$, respectively, are shown in Fig. 2. The value of $(u'/\bar{U}_0)_{m,i}$ decreases with λ^{-1}. This decrease may be attributed to the decrease in the local mean shear. The value of $(u'/\bar{U}_0)_{m,0}$, however, indicates a reverse trend with λ^{-1}. The reason for this is not known.

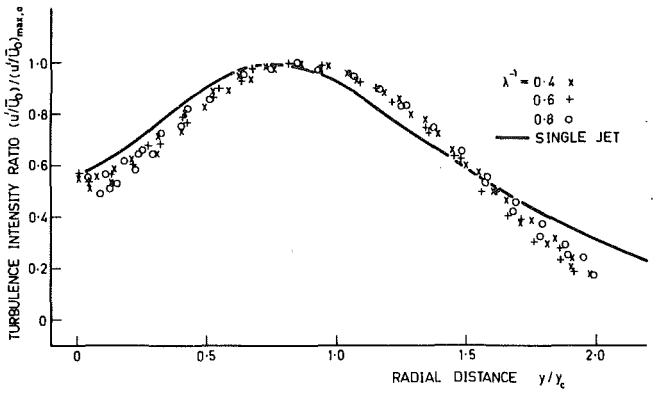

Fig. 8 Similarity of turbulence intensity ratio in fully merged zone

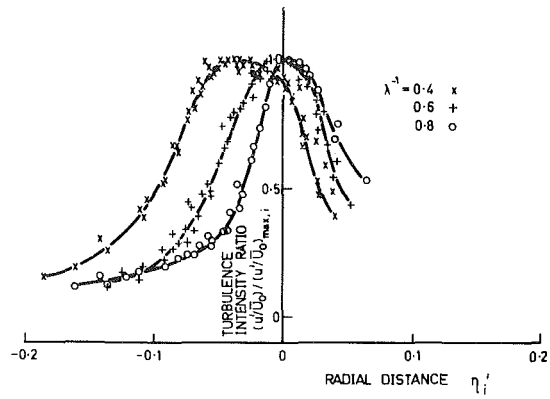

Fig. 9 Similarity of turbulence intensity ratio in inner mixing region. $x/D_0 \leq 4$.

Similarity of the turbulence intensity ratio $(u'/\bar{U}_0)/(u'/\bar{U}_0)_{max}$ to the nondimensional radial distance η_0 within the initial merging zone is shown in Fig. 6, covering the axial distance $0.5 \leq x/D_0 \leq 1.5$. Good similarity with single jet results is obtained. A similar plot in the intermediate zone is shown in Fig. 7. In view of the lack of similarity in the intermediate zone of single jet, comparison is not feasible. Though good similarity is found within these two zones, there is difference in the two similarity curves obtained. In the fully merged zone of $6.5 \leq x/D_0 \leq 7$ similarity of the turbulence intensity ratio $(u'/\bar{U}_0)/(u'/\bar{U}_0)_{max}$ with y/y_c is also found (Fig. 8). y_c is the radial location in this zone where $\bar{U} = 0.5\ \bar{U}_m$. Although there is similarity for the turbulence intensity profiles in the inner mixing region for each coaxial jet, no similarity between them is found. Though attempt with η_i and other dimensionless parameters has been tried, it was found that the best attempt was based on the nondimensional distance $\eta_i' = (y - D_i'/2)/x$ (Fig. 9). The figure shows a progressive shift of the turbulence intensity ratio towards the central axis for smaller λ^{-1}.

Conclusions

The mean velocity measurements within the initial region of coaxial jets of high mean-velocity ratio isolate three separate zones: the initial merging, the intermediate and the fully developed zone. Similarity of the mean velocity profiles is obtained in each of the three zone isolated. The similarity found applies not only in the outer mixing region but also in the inner mixing region inside the jet. The similarity obtained agrees very well with the single jet results. Except for the inner mixing region, similarity of the turbulence intensity profiles is also obtained in the whole jet. Good agreement with single jet results is also found.

References

1 Forstall, W., and Shapiro, H.H., "Momentum and Mass Transfer in Coaxial Gas Jets," ASME *Journal of Applied Mechanics,* Vol. 10, 1950, pp. 399–408.

2 Chigier, N.A., and Beer, J.M., "The Flow Region Near the Nozzle in Double Concentric Jets," ASME *Journal of Basic Engineering,* Vol. 86, 1964, pp. 797–804.

3 Gelb, G.H., and Martin, W.A., "An Experimental Investigation of the Flow Field about a Subsonic Jet Exhausting into a Quiescent and a Low Velocity Air Stream," *Canadian Aeronautics and Space Journal,* Vol. 12, 1966, pp. 333–342.

4 Williams, T.J., Ali, M.R.M.H., and Anderson, J.S., "Noise and Flow Characteristics of Coaxial Jets," *Journal of Mechanical Engineering Science,* Vol. 11, 1969, pp. 133–142.

5 Ko, N.W.M., and Kwan, A.S.H., "The Initial Region of Subsonic Coaxial Jets," *Journal of Fluid Mechanics,* Vol. 73, 1976, pp. 305–332.

6 Davies, P.O.A.L., Fisher, M.J., and Barratt, M.J., "The Characteristics of the Turbulence in the Mixing Region of a Round Jet," *Journal of Fluid Mechanics,* Vol. 15, 1963, pp. 337–367.

7 Ko, N.W.M., and Davies, P.O.A.L., "The Near Field Within the Potential Cone of Subsonic Cold Jets," *Journal of Fluid Mechanics,* Vol. 50, 1971, pp. 49–78.

8 Ko, N.W.M., and Chan, W.T., "Similarity in the Initial Region of Annular Jets: Three Configurations," *Journal of Fluid Mechanics,* Vol. 84, 1978, pp. 641–656.

9 Davies, P.O.A.L., and Davis, M.R., "Hot-Wire Anemometer," *University of Southampton, I.S.A.V. Rep. No. 155,* 1966.

10 Brunn, H.H., "Linearization and Hot Wire Anemometry," *Journal of Physics E: Scientific Instruments,* Vol. 4, 1971, pp. 815–820.

Transient Fluid Flow in Porous Media: Inertia-Dominated to Viscous-Dominated Transition[1]

R. H. Nilson
Fluid and Thermal Sciences
Department 5510,
Sandia National Laboratories,[2]
Albuquerque, N.M. 87185

A one-dimensional isothermal flow is induced by a step change in the pressure at the boundary of a semi-infinite medium. The early flow is inertia-dominated, in accordance with Ergun's equation, and is self-similar in the variable $x/\sqrt[3]{t}$. The late flow is viscous-dominated, in accordance with Darcy's law, and is self-similar in the variable $x/\sqrt{t}$. Comprehensive numerical results are presented for both of these asymptotic regimes and also for the intermediate transition period which is governed by Forchheimer's equation. The only explicit parameter is the pressure ratio, N, which is varied from $N \to \infty$ (strong gas-compression), through $N \to 1$ (constant compressibility liquid), to $N \to 0$ (strong gas-rarefaction). The solution procedure is based on a generalized separation-of-variables approach which should also be useful in other problems which possess self-similar asymptotic solutions both at early times and at late times.

I Introduction

Recent emphasis on energy-related technology provides new impetus for the study of flow through porous media, particularly in the geologic applications. Although such flows are often viscous dominated as presumed in Darcy's law, there are circumstances where the Reynolds number ($\mathrm{Re} = u\rho\delta/\mu$) is sufficiently large that inertial effects become important, as in transient flows which are induced by sudden changes in pressure. The non-Darcy inertial effects are particularly important in rubblized or fractured media where the fluid velocity u and the characteristic microscale-dimension δ are both large.

The fundamental problem considered here is that of a one-dimensional transient flow due to a step change in pressure at the boundary of a semi-infinte medium. Morrison presents one family of similarity solutions which are appropriate for low-speed Darcy flows [1] and another family of similarity solutions which are appropriate for high-speed inertia-dominated flows [2]. What has not been pointed out is that all such step-induced transient flows are inertia dominated at early times but become viscous dominated at late times, and that the transition between the asymptotics of Morrison can be described in a universal way. Although there are general porous flow codes [3,4] which are applicable to this transition problem, there has been no systematic study of the transfer between asymptotics and no attempt to formulate the problem in a minimum-parameter format.

In the present paper we first review the self-similar asymptotics of Morrison, augmenting his gas-compression results with new results (and new scaling) for gas-rarefaction and for liquid flows. Thereafter we investigate the character of the transition flow, both as it departs from the early self-similar asymptote and as it approaches the late self-similar asymptote. As summarized at the end of the paper, the results describe gas and liquid flows under all pressure ratios, compression or rarefaction, and for all time periods: early inertia domination, intermediate transition, and late viscous-domination.

The solution procedure is based on a generalized separation-of-variables approach in which the position-variable is coincident with a similarity-variable in the limits of small and large values of the time-variable. The same approach should be useful in other problems which possess self-similar asympotic solutions both at early times and at late times.

II Formulation

One-dimensional transient flow through a porous medium is governed by the conservation of mass and momentum [1–7]

$$\epsilon \frac{\partial \rho}{\partial t} + \frac{\partial}{\partial x}(\rho u) = 0 \tag{1}$$

$$-\frac{\partial P}{\partial x} = u \frac{\mu}{\kappa}\left(1 + \frac{\lambda\rho}{\mu}|u|\right) \tag{2}$$

The dependent variables (P, ρ, u) are the pressure, density, and superficial velocity of the fluid. The viscosity μ is presumed constant, as are the properties of the porous medium: porosity ϵ, permeability κ, and the Forchheimer constant λ. The force balance (2), which has the character of a constitutive law, serves as a defining equation for κ and λ. In addition there are theoretical and experimental relationships between the flow properties (κ and λ) and the more fun-

[1] This work was supported by the U.S. Department of Energy under contract DE-AC04-76-DP00789.
[2] A U.S. Department of Energy Facility.
Contributed by the Fluids Engineering Department for publication in the JOURNAL OF FLUIDS ENGINEERING. Manuscript received by the Fluids Engineering Division, November 28, 1980.

damental geometric properties (the porosity, ϵ, and the characteristic microscale dimension, δ). Two such relationships are the Kozeny equation [5] and Ergun's equation [8], respectively

$$\kappa \sim \frac{\delta^2}{180}\frac{\epsilon^3}{(1-\epsilon)^2} \qquad \lambda \sim 0.012\frac{\delta}{(1-\epsilon)} \tag{3a,b}$$

To illustrate the importance of the local Reynolds number ($\mathrm{Re} = u\rho\delta/\mu$), the force balance (2) can be combined with Ergun's equation (3*b*) to obtain the relationship

$$-\frac{\partial P}{\partial x} = u\frac{\mu}{\kappa}(1+\mathrm{Re}/C) \tag{4}$$

in which $C \sim 0.012/(1-\epsilon)$ is a constant for a uniform-porosity medium. When Re is small, the flow is viscous-dominated or Darcian ($-\partial P/\partial x \sim \mu u/\delta^2$); whereas a high-Re flow is inertia-dominated ($-\partial P/\partial x \sim \rho u\,|u|/\delta$).

The barotropic equation of state, $\rho = \rho(P)$ is appropriate in many circumstances.

(1) Ideal gas flows ($\rho = P/RT$) are often nearly isothermal, because the ambient temperature of the matrix cannot be substantially perturbed by the through-flow of a gas which has a relatively small specific heat, ρc.

(2) Liquid flows are usually characterized as having a small (and constant) compressibility, α, even in nonisothermal circumstances.

In either instance, liquid or gas, the continuity equation (1) can be written

$$\epsilon\rho\alpha\frac{\partial P}{\partial t} = \frac{\partial}{\partial x}(\rho u) \tag{5}$$

in which the product $\rho\alpha$ is essentially a constant (for the gas, $\rho\alpha = \rho/P = 1/RT$).

The fundamental problem to be solved is that of a one-dimensional flow which is induced by an abrupt change in the pressure at the boundary ($x=0$). The initial/boundary conditions are then

$$P(0,t) = P_0,\ P(x,0) = P_\infty;\ N = P_0/P_\infty \tag{6a,b}$$

The particle velocity may be either positive ($u>0$) or negative ($u<0$) depending upon whether the disturbance is a compression ($N>1$) or a rarefaction ($N<1$). Since the medium is considered to be semi-infinite during times of interest, the initial condition (6*b*) is replaced by the far-field condition, $P(x,t) \to P_\infty$ as $x \to \infty$. Under the stated initial/boundary conditions the early-time inertia-dominated flow and the late-time viscous-dominated flow are each self-similar.

III Analysis

The central theme of the present analysis is the introduction of a general transformation in which one of the independent variables is a similarity variable, θ, and the other is a dimensionless time, τ:

$$\theta = \frac{x}{l_r f(\tau)},\ \tau = \frac{t}{t_r} \tag{7}$$

The dependent variables are normalized as follows:

$$P^* = \frac{P-P_\infty}{\Delta P},\ \rho^* = \frac{\rho}{\rho_r},\ u^* = \frac{u}{u_r g(\tau)} \tag{8}$$

in which P^*, ρ^*, and u^* are considered to be functions of θ and τ. The reference scales of length, velocity, time, and density are chosen such that $P^*, \rho^*, u^* \geq 0$ ($\pm$ below for $N \gtrless 1$)

$$u_r = \pm\frac{\mu}{\rho_r\lambda} \qquad \rho_r = \frac{\rho_0+\rho_\infty}{2}$$
$$l_r = \frac{\Delta P\kappa}{u_r\mu} \qquad t_r = \frac{l_r}{u_r}\frac{2N}{N+1}\epsilon\alpha_0\Delta P \tag{9}$$

in which $\Delta P = P_0 - P_\infty$, ρ_0, and α_0 refer to the driver state (at $x=0$), and $\alpha_0 = 1/P_0$ for the ideal gas. The time-functions, $f(\tau)$ and $g(\tau)$, which presently remain arbitrary, will later be chosen such that P^*, ρ^*, and u^* depend upon θ alone in the limits $\tau \to 0$ and $\tau \to \infty$.

The problem statement (5, 2) transforms into the general format

$$\frac{f}{g}\frac{\partial P^*}{\partial\tau} - \theta\frac{f'}{g}\frac{\partial P^*}{\partial\theta} + \frac{\partial}{\partial\theta}(\rho^* u^*) = 0 \tag{10}$$

$$-\frac{\partial P^*}{\partial\theta} = fgu^*(1+g\rho^*\,|u^*|) \tag{11}$$

subject to the boundary conditions

$$P^*(0,\tau) = 1,\ P^*(\infty,\tau) = 0 \tag{12}$$

The ideal gas law is now written as

$$\rho^* = \frac{2N}{N+1}\left[P^*\left(1-\frac{1}{N}\right)+\frac{1}{N}\right] \to \begin{cases} 2(1-P^*) & \text{as } N\to 0 \\ 1 & \text{as } N\to 1 \\ 2P^* & \text{as } N\to\infty \end{cases} \tag{13}$$

In the limit $N \to 1$ this expression also happens to describe a (slightly compressible) liquid for which $\rho^* \sim 1$. So, it is only necessary to solve the system (10, 11, 12, 13), with the understanding that the liquid case is recoverable in the limit $N \to 1$. Also, note that the system becomes independent of the singular parameter, N, in the extreme cases of a strong compression ($N \to \infty$) and a strong rarefaction ($N \to 0$), which suggests that the corresponding asymptotic solutions are, likewise, independent of N.

IV Early Inertia-Dominated Flow

The early-time inertia-dominated flow is captured by the following scale functions (which are chosen such that $f'/g = 2/3$ and $fg^2 = 1$ in (10,11))

$$\hat{f} = \tau^{2/3},\ \hat{g} = \tau^{-1/3} \tag{14}$$

in which case the similarity variable is

$$\hat{\theta} = \frac{x}{l_r\tau^{2/3}} = \frac{x}{t^{2/3}}\left(\epsilon\alpha_0\left(\frac{2N}{1+N}\right)\sqrt{\frac{\Delta P\mu}{u_r\kappa}}\right)^{2/3} \tag{15}$$

and the partial differential equations (PDE's) (10,11) become

$$\tau\frac{\partial P^*}{\partial\tau} - \frac{2}{3}\hat{\theta}\frac{\partial P^*}{\partial\hat{\theta}} + \frac{\partial}{\partial\hat{\theta}}(\rho^* u^*) = 0 \tag{16}$$

Nomenclature

$N, \Delta P$ = pressure ratio, P_0/P_∞; pressure difference, $P_0 - P_\infty$
Re = Reynolds number $u\rho\delta/\mu$
$\epsilon,\kappa,\lambda,\delta$ = porosity, permeability, Forchheimer constant, characteristic pore dimension
$\mu,\alpha,(\alpha_0)$ = viscosity, isothermal compressibility, (at P_0)
x, l_r = position, reference length
t, t_r, τ = time, reference time, $\tau = t/t_r$
$\theta, \hat{\theta}, \tilde{\theta}$ = similarity variable (7, 15, 20)
$f, \hat{f}, \tilde{f}$, = time function scales θ(7, 14, 19)
$g, \hat{g}, \tilde{g}$ = time function scales u (8, 14, 19)
P, P_0, P_∞, P^* = pressure, driver, initial, $P^* = (P - P_\infty)/\Delta P$
u, u_r, u^* = velocity, reference velocity, $u^* = u/u_r g(\tau)$
ρ, ρ_r, ρ^* = density, reference density, $\rho^* = \rho/\rho_r$

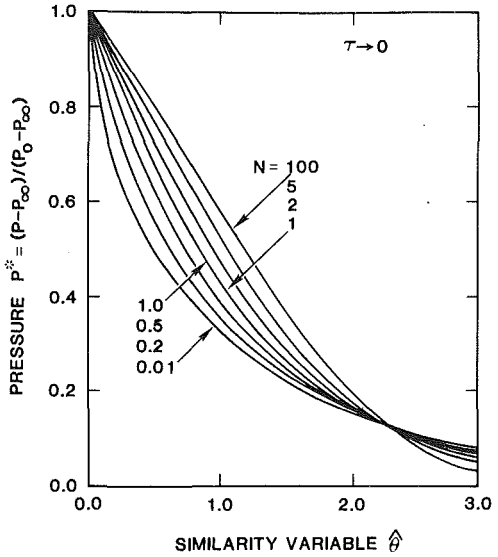

Fig. 1 Self-similar pressure profiles of the early inertia-dominated flow for various pressure ratios $N = P_0/P_\infty$

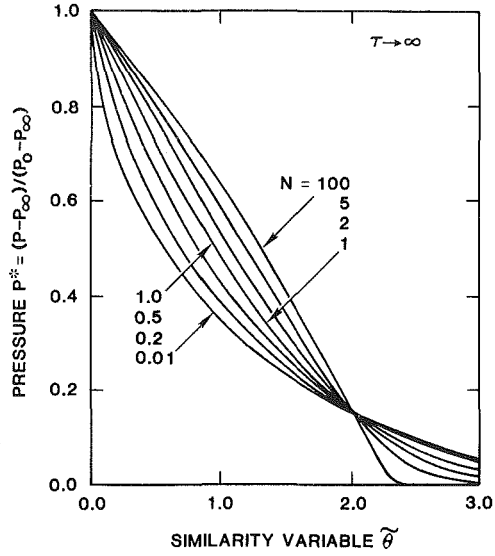

Fig. 2 Self-similar pressure profiles of the late viscous-dominated flow for various pressure ratios $N = P_0/P_\infty$

$$-\frac{\partial P^*}{\partial \hat{\theta}} = \rho^* u^* \mid u^* \mid + \tau^{1/3} u^* \tag{17}$$

In the limit $\tau \to 0$, (17) becomes independent of τ, thus admitting the possibility of a τ-independent asymptotic solution for which $\tau \partial P^*/\partial \tau \to 0$ in (16), and hence P^* satisfies the following ordinary differential equations (ODE's)

$$-\frac{2}{3}\hat{\theta} P_0^{*\prime} + (\rho_0^* u_0^*)' = 0; \quad -P_0^{*\prime} = \rho_0^* u_0^* \mid u_0^* \mid \tag{18}$$

in which primes are derivatives with respect to $\hat{\theta}$ and $P_0^*(\hat{\theta}) = P^*(\hat{\theta}, 0; N)$.

The solutions to (18) illustrated in Fig. 1 are calculated by standard shooting method ($u_0^*(0)$ is the shooting parameter) and are checked against Morrison's results [2] for $N \geq 2$. The inflow velocity $u_0^*(0)$ is listed in Table 1 for various N. Note that $u_0^*(0)$ approaches a constant (and finite) value in the limits as $N \to \infty$ and as $N \to 1$, but that $u_0^*(0) \to \infty$ as $N \to 0$. The inlet velocity and pressure gradient must become increasingly large as $N \to 0$, because in that limit $\rho_0^*(0) \to 0$ in accordance with (13). In spite of the increasingly steep pressure gradient near $x = 0$, the far field approaches a stationary limit as $N \to 0$, suggesting that there are two different length scales, as in the inner/outer structure of boundary-layer problems.

V Late Viscous-Dominated Flow

The late-time viscous-dominated flow is captured by the scale functions (which are chosen such that $f'/g = 1/2$ and $fg = 1$ in (10,11))

$$\tilde{f} = \tau^{1/2}, \quad \tilde{g} = \tau^{-1/2} \tag{19}$$

in which case the similarity variable is

$$\tilde{\theta} = \frac{x}{l_r \tau^{1/2}} = \frac{x}{t^{1/2}} \sqrt{\frac{\mu \alpha_0 \epsilon}{\kappa}} \left(\frac{2N}{1+N} \right) \tag{20}$$

and the PDE's (10, 11) become

$$\tau \frac{\partial P^*}{\partial \tau} - \frac{1}{2}\tilde{\theta} \frac{\partial P^*}{\partial \tilde{\theta}} + \frac{\partial}{\partial \tilde{\theta}} (\rho^* u^*) = 0 \tag{21}$$

$$-\frac{\partial P^*}{\partial \tilde{\theta}} = u^* + \frac{1}{\sqrt{\tau}} \rho^* u^* \mid u^* \mid \tag{22}$$

In the limit $\tau \to \infty$, (22) becomes independent of τ, thus admitting the possibility of a τ-independent asymptotic solution

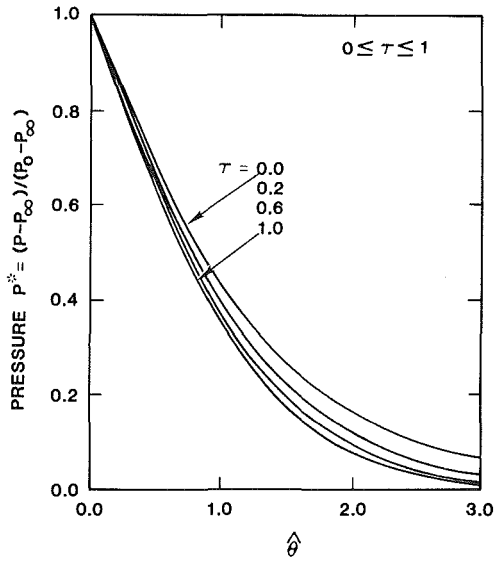

Fig. 3 Pressure profiles at various early/intermediate times τ (for $N \to 1$)

for which $\tau \partial P^*/\partial \tau \to 0$ in (21), and hence P^* satisfies the following ODE

$$-\frac{1}{2}\tilde{\theta} P_\infty^{*\prime} + (\rho_\infty^* u_\infty^*)' = 0; \quad -P_\infty^{*\prime} = u_\infty^* \tag{23}$$

in which the primes are derivatives with respect to $\tilde{\theta}$ and $P_\infty^*(\tilde{\theta}) = P^*(\tilde{\theta}, \infty; N)$. The solutions to (23) which are illustrated in Fig. 2 are calculated by a standard shooting method ($u_\infty^*(0)$ is the shooting parameter) and are checked against Morrison's results [1] for $N \geq 5$. The inflow velocity is given in Table 1.

The limiting cases are all interesting. As $N \to 1$, the ODE reduces to the heat equation and the solution is simply the complementary error function. As $N \to \infty$, $\rho_\infty^* \to 0$ at the leading edge, resulting in a type-change singularity with discontinuous slope [9]. As $N \to 0$, $\rho_\infty^* \to 0$ at $x = 0$, resulting in an increasing large pressure gradient at the inlet. In particular it appears, both in the ODE's and in the results, that for $N \to 0$ (and hence $\rho^* \to 2(1 - P^*)$)

$$\lim_{\theta \to 0} (1 - P^*) P^{*\prime} = \text{Constant independent of } N$$

Table 1 Inflow velocity at early, intermediate, and late times for various pressure ratios

		$\tau \to 0$	$\tau = 1$	$\tau \to \infty$
	$N = \frac{P_0}{P_\infty}$	$u^*(0,0) = \frac{u}{u_r}\sqrt[3]{\tau}$	$u^*(0,1) = \frac{u}{u_r}$	$u^*(0,\infty) = \frac{u}{u_r}\sqrt{\tau}$
COMPRESSION	100.	.433		.316.
	10.	.470	.308	.340
	5.	.510	.328	.366
	2.	.627	.402	.441
	1.0[a]	.816	.512	.564
RAREFACTION	0.5	1.189	.699	.805
	0.2	2.293	1.11	1.517
	0.1	4.120	1.47	2.695
	0.01	36.933		23.83

[a] Entry for N = 1 describes both a gas flow in the limit as $N \to 1$ and a liquid flow under any pressure ratio

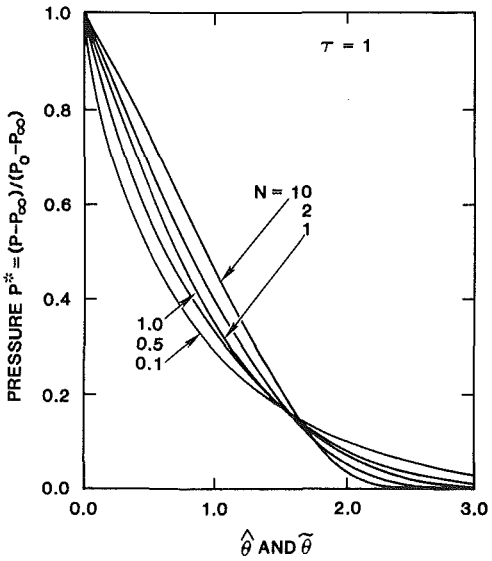

Fig. 4 Pressure profiles in the intermediate transition period for various pressure ratios $N = P_0/P_\infty$

and hence that the pressure comes away from the origin like $P^* = 1 - C\sqrt{\theta}$. An analogous observation holds for the early self-similar asymptotic of the previous section, which explains the similarity between the small-N behavior of the two cases. It should be kept in mind, however, that there is always an inner boundary-layer region near the origin where P^* is sufficiently close to unity that the approximation, $\rho \sim 2(1 - P^*)$, is not adequate. Although it is only the outer solution which approachs a stationary limit as $N \to 0$, the limiting condition noted immediately above suggests that the inlet mass flow ($\rho^* u^*$) approaches a finite limit as $N \to 0$, both in the early similarity flow and in the late similarity flow. It follows that $u^*(0) \to$ constant$/N$ as $N \to 0$, in agreement with the early and late columns of the table.

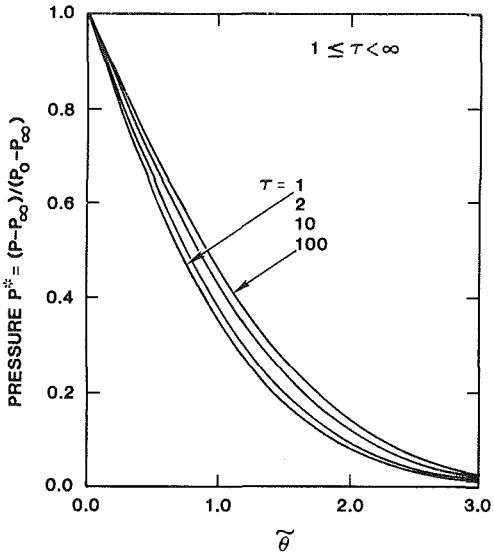

Fig. 5 Pressure profiles at various intermediate/late times τ (for $N \to 1$)

VI Inertia-Dominated to Viscous-Dominated Transition

The intermediate-time transition flow is calculated by a method-of-lines integration of the parabolic PDE's (either 16, 17 or 21, 22), marching forward in time along 100 lines of constant θ. The computation is executed by the well documented MOL1D code [10], exercising the options in which θ-derivatives are approximated by second-order centered-difference operators and the τ-derivatives are approximated by a variable step, Gear-type integrator.

The initial data for the PDE solver is the early self-similar solution $P^*(\hat{\theta},0;N)$ from Fig. 1. Integration is begun from a small, but nonzero, initial time τ_0 in order to avoid the singularity at $\tau = 0$. The accuracy of this starting procedure was verified by checking the convergence of the numerical solution for successively smaller choices of τ_0. The early solution does have a series expansion in powers of $\sqrt[3]{\tau}$, but it can only be developed through the application of matched asymptotic expansions (inner and outer in θ), because the early self-similar solution suffers from a nonuniformity for small τ as $\theta \to \infty$. The early expansion is not pursued in view of the considerable analytical and computational effort which would be required and because the more direct numerical approach is quite adequate.

The early-time PDE's (16,17) are integrated forward in time from $\tau = \tau_0$ to $\tau = 1$. Figure 3 displays the pressure profiles at various early-intermediate times for the particular case of $N \to 1$. Figure 4 illustrates the pressure profiles at $\tau = 1$ for all values of N.

A smooth transition in the numerics is undertaken at $\tau = 1$. Integration of the early PDE's (16,17) is halted, and integration of the late PDE's (21,22) is begun. The transfer between systems requires no interpolation because at $\tau = 1$ it happens that: $\tilde{\theta}$ and $\hat{\theta}$ are identical, $P^*(\hat{\theta}) = P^*(\tilde{\theta})$, and $u^*(\hat{\theta}) = u^*(\tilde{\theta})$ (since $\hat{g}(\tau) = \tilde{g}(\tau)$ and $\hat{f}(\tau) = \tilde{f}(\tau)$ at $\tau = 1$). For this same reason, the abcissa in Fig. 4 can be read as either $\hat{\theta}$ or $\tilde{\theta}$.

The late-time PDE's are integrated forward in time from $\tau = 1$ to $\tau = 100$. Figure 5 displays the pressure profiles at various intermediate-late times for the particular case $N \to 1$. As time increases, the solution approaches the late self-similar asymptotic solution given previously in Fig. 2.

It is remarkable to find that the solution for all times can be tightly bounded by simply knowing the pressure profiles for

the three extreme cases: $\tau \to 0$ (Fig. 1), $\tau = 1$ (Fig. 4), and $\tau \to \infty$ (Fig. 2). For $0 < \tau < 1$, the solution lies between the results for $\tau = 0$ and $\tau = 1$ (as in Fig. 3). For $1 < \tau < \infty$, the solution lies between the results for $\tau = 1$ and $\tau = \infty$ (as in Fig. 5). Regardless of the pressure ratio, N, the pressure profiles for $\tau = 0$ and $\tau = 1$ are not far apart when plotted versus $\hat{\theta}$, and the profiles for $\tau = 1$ and $\tau \to \infty$ are equally close together when plotted versus $\tilde{\theta}$. In view of these observations, the stated information is an adequate characterization of the solution for all times, for all pressure ratios, for ideal gasses and for liquids.

VII Summary

Transient one-dimensional flow through a porous medium is analyzed, based on the well-established Forchheimer model, which includes both the viscous and the inertial contributions to the flow resistance. The problem is formulated such that the pressure ratio N is the only parameter,

$N > 1$ ideal gas compression

$N \to 1$ constant compressibility (liquid)

$N < 1$ ideal gas rarefaction,

and the solution curves become asymptotically stationary in the limits of strong compression ($N \to \infty$) and of strong rarefaction ($N \to 0$). The analysis spans the full range of time:

(*a*) early self-similar inertia-dominated flow; $P^*(\hat{\theta},0;N)$ in Fig. 1

(*b*) early/intermediate departure from the similarity flow; $P^*(\hat{\theta},\tau;N)$ in Fig. 3

(*c*) intermediate balance between viscous and inertial effects; $P^*(\hat{\theta},1;N) = P^*(\tilde{\theta},1;N)$ in Fig. 4

(*d*) intermediate/late approach to the similarity flow; $P^*(\tilde{\theta},\tau;N)$ in Fig. 5

(*e*) late self-similar viscous-dominated flow; $P^*(\tilde{\theta},\infty;N)$ in Fig. 2

Prior to the numerical solution, a generalized separation-of-variables transforms the problem to parabolic PDE's (in θ and τ) which collapse into the appropriate ODE's (in θ) under the limits as $\tau \to 0$ and as $\tau \to \infty$. The same methodology can be applied, using general ODE and PDE software, to a rather broad class of problems which possess self-similar asymptotic solutions [11].

References

1 Morrison, F. A., Jr., "Transient Gas Flow in a Porous Column," *I/EC Fundamentals,* Vol. 11, No. 2, 1972, pp. 191–197.

2 Morrison, F. A., Jr., "Similarity in Transient High Speed Gas Flow Through Porous Media," ASME JOURNAL OF FLUIDS ENGINEERING, Vol. 98, 1976, pp. 567–568.

3 Morrison, F. A., Jr., "Transient Non-Darcy Gas Flow in a Finite Porous Bed," ASME JOURNAL OF FLUIDS ENGINEEING, Vol. 99, 1977, pp. 779–781.

4 Matthews, C. S., and Russell, D. G., *Pressure Buildup and Flow Tests in Wells,* Society of Petroleum Engineers of AIME, Dallas, 1967.

5 Scheidegger, A. H., *The Physics of Flow Through Porous Media,* University of Toronto Press, 1974.

6 Firoozabadi, A., and Katz, D. L., "An Analysis of High-Velocity Gas Flow Through Porous Media," *J. Pet. Tech.,* Feb. 1979, pp. 211–216.

7 Philip, J. R., "Transient Fluid Motions in Saturated Porous Media," *Australian J. Physics,* Vol. 10, No. 43, 1957, pp. 43–53.

8 Ergun, S., "Fluid Flow Through Packed Column," *Chemical Engineering Progress,* Vol. 48, 1952, pp. 89–94.

9 Pimbley, G. H., Jr., "Wave Solutions Traveling Along Quadratric Paths for the Equation $u_t - (k(u)u_x)_x = 0$," *Quarterly of Applied Mathematics,* Vol. XXXV, Apr. 1977, pp. 129–138.

10 Hyman, J. M., "A Method of Lines Approach to the Numerical Solution of Conservation Laws," Third IMACS Intl. Symp. on Computer Methods for PDE's, Lehigh University, June 20–22, 1979.

11 Barenblatt, G. I., and Zel'dovich, Ya B., "Self-Similar Solutions as Intermediate Asymptotics," *Annual Review of Fluid Mechanics,* Vol. 4, 1972, pp. 285–312.

Turbulent Shear Flows Over a Step Change in Surface Roughness

W. H. Schofield
Senior Research Scientist,
Aeronautical Research Laboratories,
Department of Defense,
Fishermen's Bend,
Victoria, Australia
Mem. ASME

A large body of data now exists on the response of turbulent shear flows to sudden or step changes in surface roughness. Authors have used a variety of methods to reduce and present the data; thus a consistent description of these flows has not yet been presented. This paper presents all available data reduced in a uniform way. As there are extremely few Reynolds stress measurements within this large body of data, the analyses presented here are necessarily based on mean velocity profiles. It is shown that the growth rate of the new internal layer for all types of flow both with and without pressure gradient can be described in terms of a single length scale associated with the new wall condition. It is also shown that all mean velocity profiles after a step change in roughness display semi-logarithmic distributions. However, in the region immediately downstream of a step the constant of proportionality (the von Karman constant) has values different from the usual equilibrium value of 0.41. The differences appear to be large with values for the constant ranging between about 0.2 to 0.8.

Introduction

The response of turbulent shear flows to a discontinuous or step change in surface roughness[1] is of both theoretical and practical interest. Theoretical interest lies in the proposal, advanced by Clauser [1], that such flows are promising cases to study the complicated nonlinear exchange mechanisms that determine the development of turbulent shear flows. Practical interest lies in the need to predict flow development and turbulent exchange rates over surfaces that have unavoidable changes in surface roughness (e.g. wind over different crops) or have been intentionally roughened (e.g. for increased heat transfer). These interests have led to many studies and hence a considerable body of data now exists covering a wide range of flows. In nearly all these studies no turbulence measurements were recorded and hence any analysis of the data must of necessity be based on mean flow data.

The major feature of turbulent flows over a step is the generation of a new internal layer. This layer starts at the step and grows outwards from the wall with distance downstream. Outside this layer, turbulence quantities are determined by conditions before the step. A different turbulence structure is generated inside the new internal layer where the flow is adjusting to the new wall condition.

There have been several theoretical analyses (notably by Townsend [2,3,4]) for the case of deep atmospheric layers over a step where there is no pressure gradient in the direction of flow. However, most flows of engineering interest occur with pressure gradients and there is no theoretical analysis comparable to Townsend's work for these flows.

In spite of the large amount of data collected for engineering flows, a coherent description of their response to a step has not as yet emerged. An important reason for this is that the various authors have reduced and presented their data using a variety of methods and nondimensionalizing parameters. Schofield [5], guided by Townsend's theory for zero pressure gradient flow, has suggested for all cases of flow over a step, either with or without a pressure gradient, that the growth rate of the new internal layer can be related solely to the local roughness scale of the new wall condition (Z, defined later) by

$$\frac{\delta_i}{Z_n}\left\{\log_e \frac{\delta_i}{Z_n} - 1\right\} = 2\,\kappa^2\{X_s/Z_n\} \qquad (1)$$

The experimental support for equation (1) presented by Schofield was thin and did not cover a wide range of flows. The present work starts by reducing, in a uniform way, all available data and comparing it with equation (1).

It has been theoretically postulated by Townsend [2,3,4] and Mulhearn [6] that the usual logarithmic wall similarity will be invalid for flow immediately after a step. Experimental results of some authors (Bradley [7] and Antonia and Luxton [8,9]) appear to confirm that the usual law of the wall gives a poor description of mean velocity profiles in the region immediately downstream of the step. The data are analyzed here with the aims of determining (*a*) the nature, magnitude and extent of the failure of wall similarity after a step, (*b*) values of wall shear stress in the region where the usual wall similarity relations are invalid.

Data Reduction

The published data considered here are drawn from sixteen

Contributed by the Fluids Engineering Division for publication in the JOURNAL OF FLUIDS ENGINEERING. Manuscript received by the Fluids Engineering Division, March 26, 1979.

[1] *"Step change in roughness" is abbreviated to "step" throughout this paper.*

papers and are quite diverse. Data came from atmospheric layers, conduit flows, and laboratory boundary layers with and without pressure gradient. These flows contained several types of step; smooth to rough, rough to smooth, and rough to less rough. Usually the roughness geometry at the step was arranged so that the crests of the elements were level with the height of the smooth wall on the other side of the step. However in a few studies the roughness at the step was not flush but was upstanding. In all the work considered, mean velocity profile development over the step was measured. In most studies some estimate or measurement of wall shear stress distribution after the step was made by the authors.

Internal Layer Thickness. The height of the new internal layer has been determined and defined in several ways by various authors. The definition used here is "the height of the new internal layer (δ_i) is that distance above the wall where the mean velocity profile (u/U) merges with a corresponding profile of a reference layer that has developed under identical conditions but without the change in wall roughness." In most studies, measurements in such a reference layer were not taken, but in many cases such measurements are not really necessary. For instance in undisturbed conduit or zero pressure gradient boundary layer flows at high Reynolds number, velocity profiles change slowly, and hence a velocity profile taken just before the step can be used as a reference for profiles downstream of the step. Such methods introduce errors into the determination of δ_i that could have been avoided if a reference layer were used. However, as δ_i is defined in terms of a merge point between experimental profiles its value cannot be determined precisely and the additional inaccuracy introduced by these methods would be marginal. In boundary layer flows with pressure gradient, mean profiles change rapidly and a reference layer is essential to determine the height of the new internal layer.

The atmospheric data considered here have been deduced from Jackson [10] where similar methods were used to determine δ_i. Jackson, however, distinguishes two values of δ_i; one being the height at which modified and reference flows agree exactly and the other where they differ by 1 percent. This distinction implies an accuracy in the experimental data not found in the data analyzed by the present author.

Wall Shear. Authors have used a variety of methods to estimate values of wall shear after a step. A common approach has been to simply assume that the usual wall similarity applies within flow after a step, i.e., for smooth walls

$$\frac{u}{u_\tau} = \frac{1}{\kappa}\log_e\frac{yu_\tau}{\nu} + A \tag{2a}$$

$$= \frac{1}{\kappa}\log_e y/Z \tag{2b}$$

which defines the wall length scale (Z) appearing in equation (1). For flow over a rough wall, the wall similarity relation can be expressed

$$\frac{u}{u_\tau} = \frac{1}{\kappa}\log_e\left(\frac{y_T+\epsilon}{\nu}\right)u_\tau + A - \frac{\Delta u}{u_\tau} \tag{3a}$$

$$= \frac{1}{\kappa}\log_e\left(\frac{y_T+\epsilon}{Z}\right) \tag{3b}$$

where[2] Z is here the length scale for rough wall flow and $\Delta u/u_\tau$ is the roughness function which is related to the roughness height k, (see Hama [13]) by

$$\frac{\Delta u}{u_\tau} = \frac{1}{\kappa}\log_e\frac{ku_\tau}{\nu} + D \tag{4}$$

It is shown in this paper that after a step, wall similarity breaks down and these equations do not provide a good description of the mean velocity near the wall. The data do, however, consistently show that the mean velocity profiles after a step have semi-logarithmic distributions near the wall. Thus the mean velocity can be described by an equation in the form of equations (2) or (3) but with the constants having different values from their usual equilibrium values. As shown later the similarity laws are gradually reestablished downstream of the step and hence these "constants" must change with distance from the step eventually regaining their equilibrium values. They are thus functions of X_s and are written here as $\kappa(X_s)$, $A(X_s)$. The variations of $\kappa(X_s)$ and $A(X_s)$ are discussed in detail below and this discussion involves estimates of the correct skin friction coefficient of the flow. Some limited conclusions are drawn but the exact values of c_f', $\kappa(X_s)$, $A(X_s)$ immediately after a step remain uncertain. As values for the wall length scale Z are determined from equations (2) or (3) and (4) it follows that the values of Z_n will also be inaccurate immediately after a step. However at moderate distances downstream of a step, departures from the standard wall similarity are not large and thus calculated values of Z_n will have reasonable accuracy. The expressions for Z_n are;

$$Z_n = \left(\frac{2}{c_f'}\right)^{1/2}\frac{\nu}{U}\exp(-\kappa A) \tag{5}$$

from equations (2) for a smooth wall after the step and

[2] ϵ is defined as the distance below the crests of the roughness elements where the effective origin of the mean profile is located; see Moore [11] or Perry, Schofield and Joubert [12].

Nomenclature

A = constant in logarithmic law of the wall (= 5.0)
b = regression line intercept
c_f' = local skin friction coefficient = $\tau_w/\frac{1}{2}\rho U^2$
D = empirical roughness constant
k = typical dimension of wall roughness (usually height)
l = mixing length
m = regression line slope
u = mean velocity in the principal flow direction
U = mean velocity in the free stream
u_τ = friction velocity = $(\tau_w/\rho)^{1/2}$
X_s = distance downstream of the step
y = coordinate normal to the wall
Z = wall length scale
δ_i = height of new internal layer
δ_u = total layer thickness immediately before a step
ϵ = error in origin of boundary layer on a rough wall
θ = boundary layer momentun thickness
κ = von Karman's constant (= 0.41)
$\kappa(X_s)$ = variable replacing von Karman's constant in flow field downstream of a step
ν = kinematic viscosity of fluid
ρ = density of fluid
τ = shear stress
τ_w = wall shear stress
$\Delta u/u_\tau$ = roughness function
$-\overline{\rho u' v'}$ = Reynolds stress

Subscripts

1 = calculated using assumption 1
2 = calculated using assumption 2
n = on the new wall
T = measured from the crest of the element

$$Z_n = k \exp(\kappa(D-A)) \tag{6}$$

from equations (3) and (4) for a rough wall after a step.

A problem here is that many authors do not give values for D (the empirical roughness constant for a particular roughness geometry). Values for D were evaluated here as follows. Equation (3) may be rewritten as

$$\frac{u}{U} = \frac{1}{\kappa}\left(\frac{c_f'}{2}\right)^{1/2} \log_e(y_T+\epsilon) + \left(\frac{c_f'}{2}\right)^{1/2}\left\{\frac{1}{\kappa}\log_e\frac{U}{\nu}\left(\frac{c_f'}{2}\right)^{1/2} + A - \frac{\Delta u}{u_\tau}\right\} \tag{7}$$

$$= \frac{1}{\kappa}\left(\frac{c_f'}{2}\right)^{1/2}\log_e(y_T+\epsilon) + N$$

where

$$N = \left(\frac{c_f'}{2}\right)^{1/2}\left\{\frac{1}{\kappa}\log_e\frac{U}{\nu}\left(\frac{c_f'}{2}\right)^{1/2} + A - \frac{\Delta u}{u_\tau}\right\} \tag{8}$$

Thus $\log_e(y_T + \epsilon)$ plotted against u/U [3] will give a straight line that intercepts the u/U axis at N, which by equation (8) gives $\Delta u/u_\tau$ and then D by equation (4). As wall similarity is assumed throughout, values of D will be in error for those regions of flow immediately downstream of steps. The error will again be greatest immediately after the step and decrease as wall similarity is reestablished.

Growth Rate of Internal Layer

The height of the new internal layer nondimensionalized with the local wall length scale (Z_n) is plotted against nondimensional distance from the step in Fig. 1. Results for 179 profiles are presented representing data for rough to smooth, smooth to rough, and rough to less rough steps. Fig. 1(*a*) shows data for flows without pressure gradient, Fig. 1(*b*) presents data for flows in favorable pressure gradient, and Fig. 1(*c*) shows the adverse pressure gradient data. In all three cases the data show reasonable agreement with equation (1). Other authors have presented their results nondimensionalized with the total flow thickness (e.g. pipe diameter, channel height, boundary layer total thickness), wall length scale upstream of the step, combinations of length scales before and after the step. The present data were nondimensionalized with all these parameters but in every case the correlation produced was inferior to that shown in Fig. 1(*d*).

Figure 1(*d*) combines all the data and shows that the correlation extends over slightly more than five orders of magnitude variation. A good description of the data and one more amenable to engineering calculations is the linear least squares fit,

$$\log_{10}\{\delta_i/Z_n\} = 0.92\log_{10}\left\{\frac{X_s}{Z_n}\right\} - 0.75$$

$$\text{or}\quad \frac{\delta_i}{Z_n} = 0.18\left(\frac{X_s}{Z_n}\right)^{0.92} \tag{9}$$

which has a correlation with the data of 0.98. Equation (9) is shown in Fig. 1(*d*).

Wall Similarity

A general examination of wall similarity after a step would be greatly helped if direct measurements of wall shearing stress profiles were available. Unfortunately in the large volume of data analyzed here only a few Reynolds stress profiles exist. These have been used where possible but the analyses presented here are mainly based on mean velocity profiles and the resulting conclusions are therefore limited.

[3] Using the equilibrium of unperturbed value of ϵ if it is known or some reasonable estimate of it, if it is not.

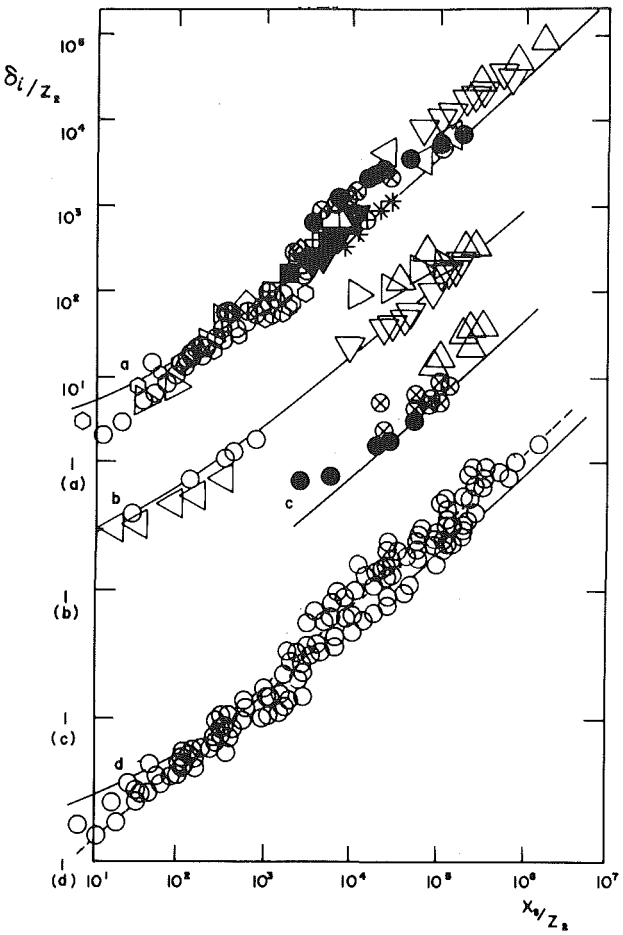

Fig. 1 Growth of internal layer. *a*) Flows without pressure gradient. □, Angle [14]; ◇, Blackador et. al. [15]; ▼, Bradley [7], smooth to rough; ▷, Bradley [7] rough to smooth; △, Bradley [7], rough to smooth; ■, Kutzbach [16]; ∗, Plate and Hidy [17]; ⊖, Yeh and Nickerson [18] smooth to upstanding rough; ⊕, Yeh and Nickerson [18] smooth to rough; ○, Antonia and Luxton [8] smooth to rough, low Reynolds number; ▷, Antonia and Luxton [8] smooth to rough, high Reynolds number; ○, Antonia and Luxton [19] smooth to upstanding rough; ⊗, Antonia and Luxton [9] rough to smooth, low Reynolds number; ●, Antonia and Luxton [9] rough to smooth, high Reynolds number; ◁, Narayana [20]; ⊕, Islam and Logan [21]. *b*) Flows with favorable pressure gradient ▽, Logan and Jones [22]; △, Narayana [20]; ○, Siuru and Logan [23]; ▷, Tani and Makita [24] rough to smooth; ◁, Tani and Makita [24] smooth to rough. *c*) Flows with adverse pressure gradient ⊗, Narayana [20] rough to smooth; ●, Narayana [20] rough to less rough; △, Schofield [5]. *d*) All data. ——, equation (1); — — —, equation (9).

Smooth Wall After the Step. Clauser's [1] method of determining skin friction is based on rewriting equation (2(*a*)) in the form,

$$\frac{u}{U} = \left(\frac{c_f'}{2}\right)^{1/2}\left\{\frac{2.303}{\kappa}\log_{10}\left(\frac{yU}{\nu}\right)\right\} + \left(\frac{c_f'}{2}\right)^{1/2}\left\{\frac{2.303}{\kappa}\log_{10}\left(\frac{c_f'}{2}\right)^{1/2} + A\right\} \tag{10}$$

This equation relates two measurable variables u/U, yU/ν by a family of straight lines that vary in both slope and intercept with skin friction coefficient. A local skin friction coefficient is therefore determined by plotting the mean velocity profile on axes u/U versus $\log_{10}(yU/\nu)$ and comparing it with the Clauser family of lines. If the usual wall similarity exists, then the inner profile shows a linear distribution that agrees in both slope and intercept with a particular line of the family and this

agreement determines the skin friction coefficient for that profile.

Figure 2 shows the wall regions of a typical set of mean velocity profiles after a rough to smooth step. All profiles exhibit semi-logarithmic distributions. Immediately after the step these distributions do not agree with local Clauser lines and are better correlated by the linear regression lines shown. The linear regression line has in each case been fitted to all points in the wall region provided that they are, outside the viscous and buffer sublayers ($yu_\tau/\nu > 70$), within the new internal layer ($y < \delta_i$) and are unaffected by the wake component of the boundary layer (i.e. $yu_\tau/\nu \leq 300$). Thus the linear regression lines shown in the figures are based on the experimental points around the center of the range shown. Disagreement between the regression lines and the local Clauser lines (indicating breakdown in wall similarity) is greatest just after the step but decreases with distance downstream. In general departures from wall similarity are small after $X_s/\delta_u \simeq 20$.

The regression line

$$u/U = m \log_{10}\left(\frac{yU}{\nu}\right) + b$$

models the generalized similarity relation based on equation (10), viz.,

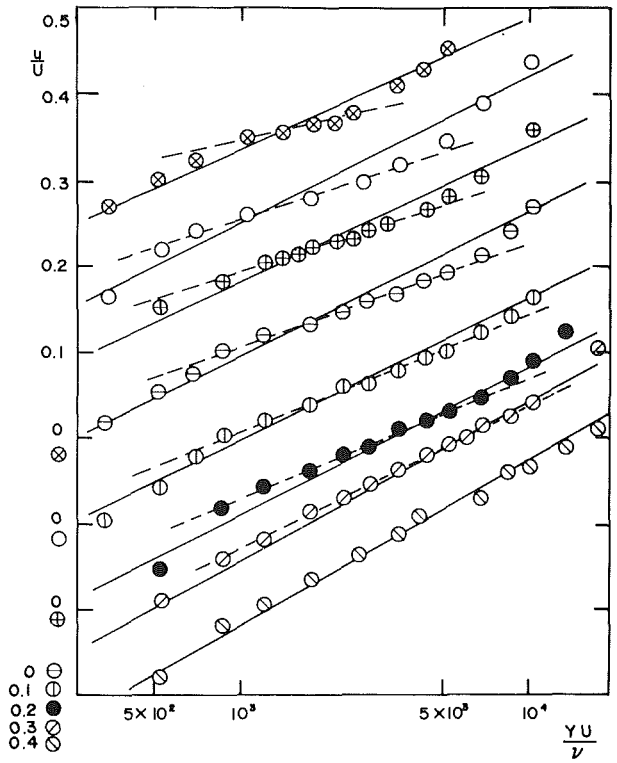

Fig. 2 Smooth wall clauser chart. Results of Antonia and Luxton [9] high Reynolds number. ⊗, X_s/δ_u = 0.36; ○, 0.72; ⊕, 1.43; ⊖, 1.79; Φ, 2.14; ●, 4.21; ∅, 8.93; ⊘, 16.46. ———, equation (10) with κ = 0.41, A = 5.0; — — —, linear regression lines.

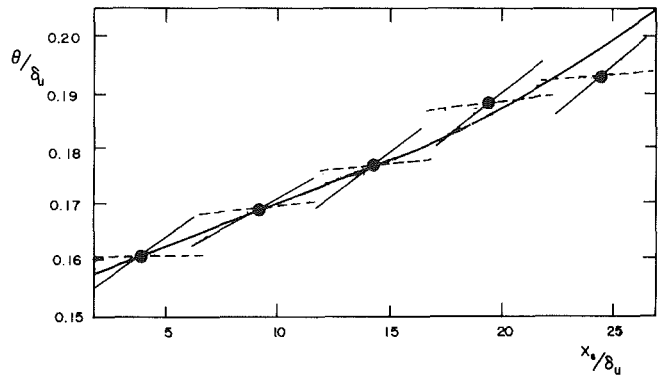

Fig. 3 Momentum thickness growth after a rough to smooth step. Results of Narayana [20]. ———, curve fitted to results; ———, local slope based on c_{f_1}'; — —, local slope based on c_{f_2}'.

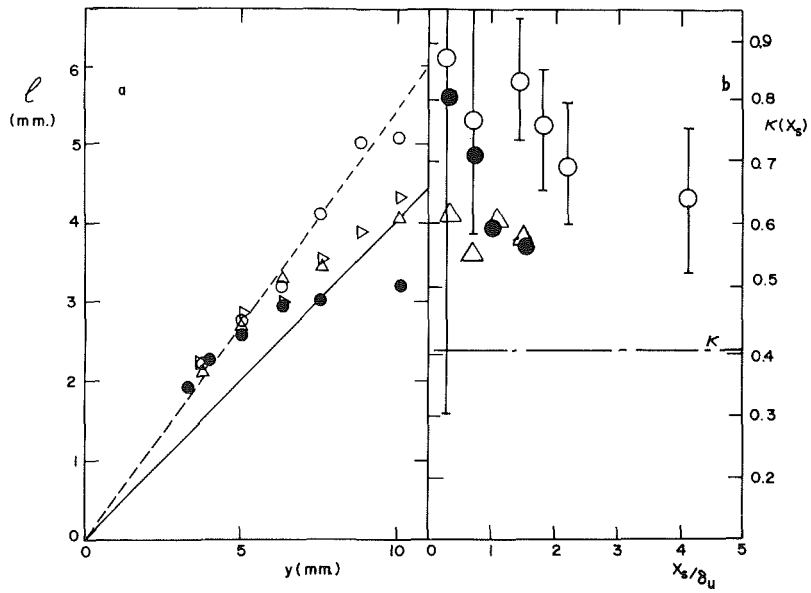

Fig. 4 Mixing length variation after a rough to smooth step. *a*) Results of Antonia and Luxton [9] high Reynolds number. ———, similarity distribution ($l = \kappa y$); — — —, distribution for X_s/δ_u = 1.1. *b*) Variation of κ (X_s). Results of Antonia and Luxton [9] high Reynolds number. ○, values derived from equation 11; using assumption 1. △, values derived from Fig. 4(*a*); ●, average values derived from assumption $\kappa(X_s) = \kappa[\tau(y)/\tau_w]^{1/2}$. Vertical bars show 95 percent uncertainty bands.

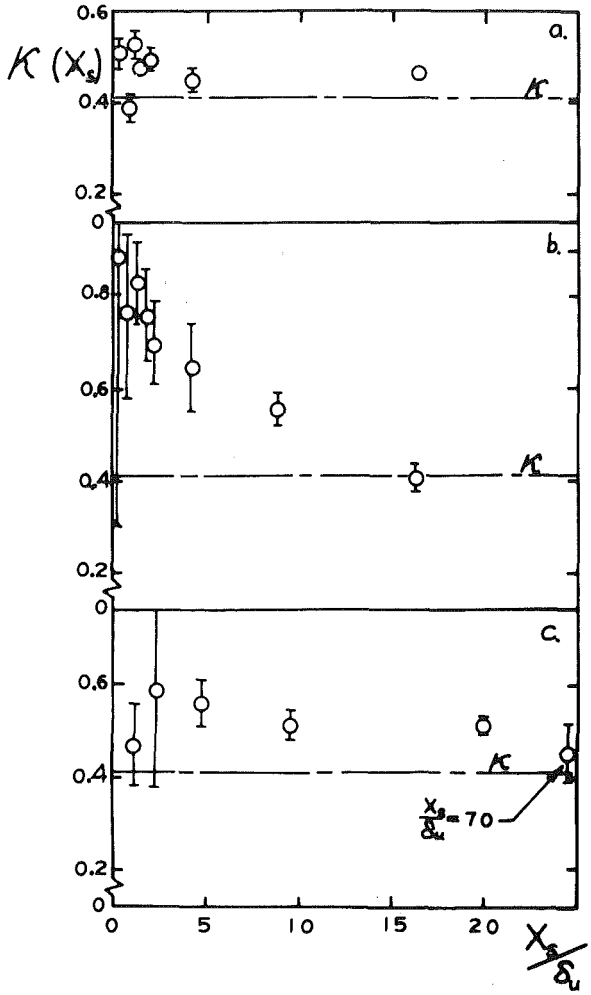

Fig. 5 Variation of $\kappa(X_s)$ downstream of a rough to smooth step. (*a*) Antonia and Luxton [9] low Reynolds number; (*b*) Antonia and Luxton [9] high Reynolds number; (*c*) Tani and Makita [24]. Vertical bars show 95 percent uncertainty bands.

$$\frac{u}{U}=\left(\frac{c_f'}{2}\right)^{1/2}\left\{\frac{2.303}{\kappa(X_s)}\log_{10}\left(\frac{yU}{\nu}\right)\right\}$$

$$+\left(\frac{c_f'}{2}\right)^{1/2}\left\{\frac{1}{\kappa(X_s)}\log_e\left(\frac{c_f'}{2}\right)^{1/2}+A(X_s)\right\}$$

A comparison of these two forms gives

$$m=\left(\frac{c_f'}{2}\right)^{1/2}\left[\frac{2.303}{\kappa(X_s)}\right] \qquad (11(a))$$

$$b=\left(\frac{c_f'}{2}\right)_{1/2}\left[\frac{1}{\kappa(X_s)}\log_e\left(\frac{c_f'}{2}\right)^{1/2}+A(X_s)\right] \qquad (11(b))$$

Thus we have two equations and three unknowns $\kappa(X_s)$, $A(X_s)$, and c_f'. If we had independent accurate values for c_f' immediately after the steps (measured by say a force balance set in the wall) we could determine $\kappa(X_s)$ and $A(X_s)$. As we do not have such independent accurate values for c_f' we proceed by comparing two extreme propositions or assumptions viz.; (1) $A(X_s) = A = 5.0$ for all X_s, (2) $\kappa(X_s) = \kappa = 0.41$ for all X_s. Each assumption will give a different value of c_f' which we denote as c_{f_1}' and c_{f_2}', respectively. Independent evidence tends to support the first proposition but is not definitive.

The first piece of evidence involves comparisons between the two estimates of c_f' and the estimate given by the boundary layer momentum balance. In nonzero pressure gradient layers the momentum balance gives c_f' as the small difference between two large numbers and thus is extremely inaccurate. Even in zero pressure gradient flow where $c_f'/2 = d\theta/dx$, estimation of c_f' depends on drawing a smooth curve through plotted values of θ and must therefore smooth out sharp discontinuities in c_f' that occur near a step. A comparison between c_{f_1}', c_{f_2}' and θ versus X_s, such as that shown in Fig. 3 is therefore rather uncertain even for this zero pressure gradient flow. The slope of the line drawn through the experimental points lies between the slopes given by the two sets of values for c_f'. Away from the step where $d\theta/dx$ would be more accurate, the slope $d\theta/dx$ agrees best with c_{f_1}'. Comparisons with other data also tend to favor the first proposition that $\kappa(X_s)$ is a function of X_s and $A(X_s)$ is a constant (5.0). The possibility, of course, exists that neither extreme assumption is correct and that both $\kappa(X_s)$ and $A(X_s)$ vary downstream of the step. The data in Fig. 3 would certainly support this possibility.

The second piece of evidence involves the few available Reynolds stress measurements in flow after a step. Antonia and Luxton [8] measured some $\rho\overline{u'v'}$ profiles near the wall at the same stations as their mean velocity profile measurements. They could therefore calculate the Prandtl mixing length from $l = -(\overline{u'v'})^{1/2}/\partial u/\partial y$ and typical values for one of their layers are shown in Fig. 4(*a*). Near the wall $l = \kappa y$ in an equilibrium flow and this is shown in the figure by a continuous line. As the experimental points near the wall fall above this line it follows that $\kappa(X_s) > \kappa\ (= 0.41)$ for these profiles. Data points near the wall are unfortunately sparse and values of $\kappa(X_s)$ estimated by drawing lines through the first few points (as illustrated by the broken line in Fig. 4(*a*)) will have very poor accuracy. Such estimates are shown in Fig. 4(*b*) and while their precise values may be unknown Fig. 4(*a*) shows that they must be greater than κ. As this evidence also supports the first proposition, values of $\kappa(X_s)$ were calculated from equation (11) using assumption (1) and these are also shown in Fig. 4(*b*). For each profile an uncertainty analysis was performed on the slope and intercept of the regression line (m,b) using the method described by Draper and Smith [25]. The uncertainty in values of $\kappa(X_s)$ were then determined using the method of Kline and McClintock [26]. The bands of uncertainty thus vary considerably as they depend on the number of experimental points fitted to the regression line and the closeness of the fit. Although the uncertainty bands are wide, the results show these values of $\kappa(X_s)$ to be consistently greater than $\kappa(= 0.41)$. This result is further supported by similar analyses of other layers that give results of which those shown in Fig. 5 are typical.

The final piece of evidence comes from a group of authors (Galbraith and Head [27], Reeves [28], Galbraith, Sjolander and Head [29], Glowacki and Chi [30]) who present a good case for the law of the wall (equation 2(*a*)) to be rewritten as

$$\frac{u}{u_\tau}=\frac{1}{\kappa(\tau(y)/\tau_w)^{1/2}}\log_e\frac{yu_\tau}{\nu}+A \qquad (12)$$

where $\tau(y)$ is the shear stress at distance y from the wall. The authors contend that the usual law of the wall (equation 2(*a*)) breaks down in layers with strong adverse pressure gradients because $\tau(y)$ differs significantly from τ_w in the wall layer and hence $\kappa(\tau(y)/\tau_w)^{1/2}$ differs significantly from κ. Analyses, both theoretical and of a wide selection of experimental data, (all in strong adverse pressure gradient) are presented to support their propositions.

The layers considered in this paper also have shear stress profiles in which $\tau(y)$ differs significantly from τ_w, but in this case the difference is caused by the change in roughness.[4]

[4] Wholly for zero pressure gradient flow but only partially for flows with pressure gradient.

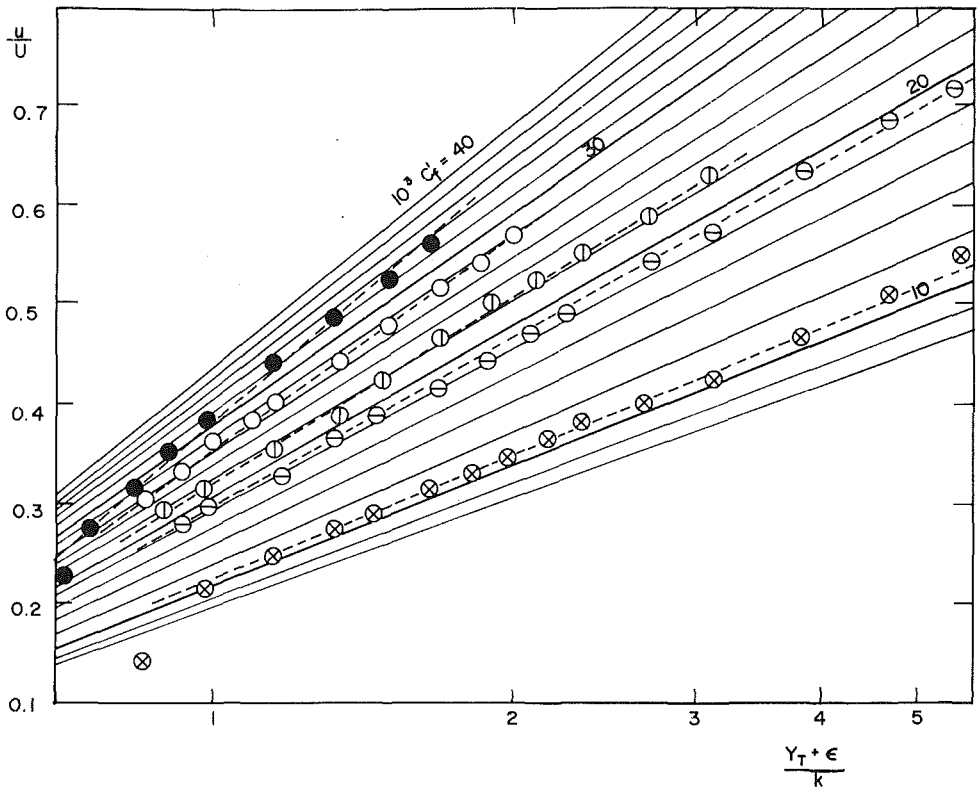

Fig. 6 Rough wall clauser chart. Results of Antonia and Luxton [8] low Reynolds number. ●, X_s/δ_u = 0.53; ○, 1.05; ○, 2.11; ⊖, 3.16; ⊗, 23.68. _____, equation (14) with κ = 0.41, A = 5.0, ϵ/k = 0.67, D = 1.8; — —, linear regression lines.

Within the new internal layer the shear stress is determined by the new wall conditions and it is reasonable to expect $\tau(y) = \tau_{wn}$. Outside the internal layer, the flow is unaware of the new wall condition and the shear stress is determined by the shear stress upstream of the step. Shear stress profiles for zero pressure gradient flow (see Antonia and Luxton [8]) do not, however, show a sudden change in stress at $y = \delta_i$ but rather an approximately linear variation in stress from the wall out to the edge of the new internal layer. Hence, the value of $\kappa(\tau(y)/\tau_{wn})^{1/2}$ varies with y. Values of $\kappa(X_s)$, evaluated previously, have been average values across the logarithmic region and therefore for comparison purposes values of $\kappa[\tau(y)/\tau_{wn}]^{1/2}$ at the edge of the logarithmic region have been averaged with the wall value (κ = 0.41). These values are also shown in Fig. 4(*b*) and although again they have poor accuracy they are in broad agreement with previous results.

Rough Wall After the Step. Well downstream of a smooth to rough step, the wall flow will be described by the usual wall similarity relation for fully rough wall flow, which by combining equations (3) and (4) can be written

$$\frac{u}{u_\tau} = \frac{1}{\kappa}\log_e\left(\frac{y_T+\epsilon}{k}\right) + (A-D) \tag{13}$$

As in the rough to smooth step case, results show that although equation (13) does not hold in the region immediately downstream of the step the profiles still display semi-logarithmic distributions.[5] Therefore deviations from wall similarity have to be explained once again by variations of one or more of the "constants" in equation (13) and in this case there are two new constants associated with the roughness geometry, ϵ/k and D. To evaluate deviations from equilibrium wall similarity, a chart for rough wall flow similar to a Clauser chart for smooth wall flow is necessary. Such a chart must be based on the equilibrium similarity relation, equation (13), rewritten as

$$\frac{u}{U} = \frac{2.303}{\kappa}\left(\frac{c_f'}{2}\right)^{1/2}\log_{10}\left(\frac{y_T+\epsilon}{k}\right) + \left(\frac{c_f'}{2}\right)^{1/2}(A-D) \tag{14}$$

A "rough wall Clauser chart" can now be constructed using u/U versus $\log_{10}\{(y_T+\epsilon)/k\}$ as variables and c_f' as a parameter determining both slope and intercept of the family of straight lines. Such a chart is shown in Fig. 6. Equation (14) depends on ϵ/k and D, the values of which vary between different roughness geometries and therefore each particular roughness geometry will have a different rough wall Clauser chart. This also means that, unless equilibrium values of ϵ/k and D are known, a rough wall Clauser chart cannot be constructed.

The chart shown in Fig. 6 is for the roughness geometry used by Antonia and Luxton and plotted on the chart are their profiles after a smooth to rough step. As before, all profiles display logarithmic distributions of mean velocity but profiles immediately after the step do not agree with local chart lines, indicating a breakdown in the usual wall similarity. The deviation from equilibrium conditions decreases with distance downstream and wall similarity is reestablished downstream of the step. In general after $X_s/\delta_u = 20$, departures from wall similarity were small for all smooth to rough step layers analyzed here.

[5] The evidence in this case is equivocal. The existence of a logarithmic distribution of velocity depends in some degree on the value chosen for ϵ. However it appears to be a general result that any plausible value of ϵ results in a logarithmic velocity distribution. This point is discussed and illustrated in Antonia and Luxton [8] and Perry and Joubert [31].

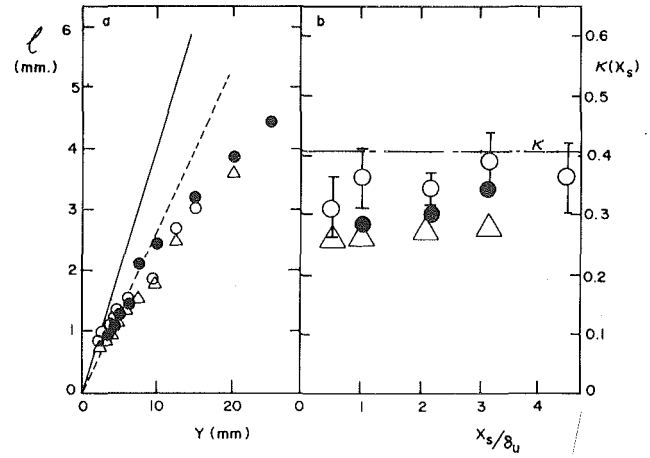

Fig. 7 Mixing length variation after a smooth to rough step. *a*) Results of Antonia and Luxton [8] low Reynolds number flow.___, similarity distribution ($l = \kappa y$), ___ ___ _, distribution for $X_s/\delta_u = 1.0$. *b*) Variation of $\kappa(X_s)$ Results of Antonia and Luxton [8] low Reynolds number flow. ○, values derived from equation 15 using assumption 1; ●, values derived from Fig. 7(*a*); △, average values derived from assumption $\kappa(X_s) = \kappa[\tau(y)/\tau_w]^{1/2}$

As before, a comparison of the regression line and the similarity relation with variable constants is made. However in this case the additional assumption is made that ϵ/k and D, the roughness geometry constants, retain their equilibrium values after a step.[6] The comparison gives

$$m = \frac{2.303}{\kappa(X_s)}\left(\frac{c_f'}{2}\right)^{1/2} \qquad (15(a))$$

$$b = \left(\frac{c_f'}{2}\right)^{1/2}(A(X_s) - D) \qquad (15b))$$

and this set of equations is again solved by using one of two extreme assumptions; (1) $A(X_s) = A$, (2) $\kappa(X_s) = \kappa$ which again gives two estimates for c_f'. As before, comparisons between the two estimates of the value of c_f' and the growth rate of the boundary layer momentum thickness favor the first assumption [$A(X_s) = A$] but again these comparisons are not decisive and can only be regarded as (consistent) indications. The evidence using the Reynolds stress measurements of Antonia and Luxton [8] shown in Fig. 7 is more definite. As shown in Fig. 7(*a*) the experimental points near the wall fall consistently below the line $l = \kappa y$ thus supporting the first proposition that $\kappa(X_s) < \kappa$ (= 0.41) which is an inequality in the opposite direction to that after a rough to smooth step. Crude estimates of $\kappa(X_s)$ from the sparse experimental points shown in Fig. 7(*a*) are shown in Fig. 7(*b*). They are in broad agreement with values of $\kappa(X_s)$ calculated from equations (15) using assumption (1). The results of similar calculations applying equation (15) and assumption (1) to other layers are shown in Fig. 8. For all these calculated values the 95 percent uncertainty intervals are shown and these again vary from point to point. The majority of the results support the conclusion that $\kappa(X_s) \leq \kappa$ after a smooth to rough step. However as several uncertainty bands extend outside this range and one is completely outside the range this conclusion must be tentative. Third estimates of $\kappa(X_s)$ from

$$\kappa(X_s) = \kappa[\tau(y)/\tau_w]^{1/2}$$

are shown in Figs. 7(*b*) and 8(*c*) and these also support the conclusion. As before, the possibility of the other "constants" (A, D, ϵ/k) varying after a smooth to rough step has not been eliminated and small variations in them are quite possible.

Wall Shear Distribution

Figure 9 shows typical results for the skin friction coefficient variation over a step. Values for the skin friction coefficient using both extreme assumptions are shown but the curve faired through the points is biased towards those derived using assumption (1). The form of the curve is typical with the skin friction after a step undershooting the

[6] Although this may seem a reasonable assumption no substantive evidence for it can be presented. It is made here as it is the least controversial assumption that allows the analysis to proceed.

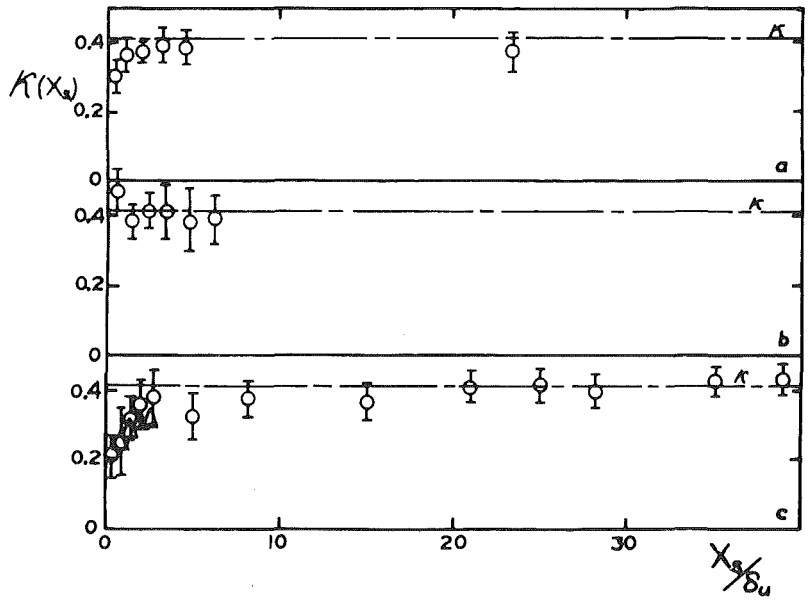

Fig. 8 Variation of $\kappa(X_s)$ downstream of a smooth to rough step. (*a*) Antonia and Luxton [8] low Reynolds number. (*b*) Antonia and Luxton [8], high Reynolds number flow. (*c*) Antonia and Luxton [19], △, ibid-values derived from the assumption $\kappa(X_s) = \kappa[\tau(y)/\tau_w]^{1/2}$

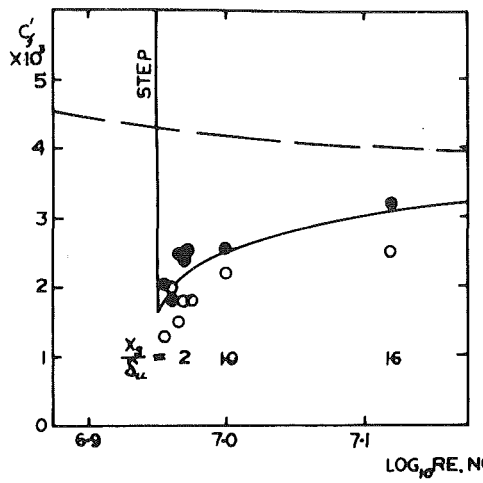

Fig. 9 Wall shear distribution. Results of Antonia and Luxton [8], low Reynolds number flow. ●, c_{f_1}'; ○, c_{f_2}'; _____, curve faired through results for flow over a step; ___ ___, skin friction for flow without a step.

equilibrium value and then slowly returning to equilibrium. For a smooth to rough step the skin friction variation is similar but reversed as the skin friction overshoots the equilibrium distribution before asymptotically returning to it. Comparisons of wall shear stress adjustment with the corresponding reestablishment of wall similarity suggest that for all the layers analyzed here the wall shear adjustment requires the larger distance. Full results for all 179 profiles analyzed in this paper are available from the author.

Conclusions

1. The growth of the new internal layer after a step depends solely on the local length scale of the new wall that is producing the new internal layer. The result applies to all turbulent flows of engineering interest over five orders of magnitude variation in parameters and is unaffected by pressure gradients of either sign in the flow.

2. In turbulent flows over a step the usual wall similarity relations do not describe the mean velocity after the step. This is due at least in part to a variation of von Karman's constant (κ) after the step. After a rough to smooth step it increases above its equilibrium value but conversely decreases below its equilibrium value after a smooth to rough step. It is possible that other constants in the similarity relations also vary after a step but this cannot be determined with the present data. The flows reapproach equilibrium conditions downstream of the step with departures from equilibrium generally being small after $X_s/\delta_u \simeq 20$.

3. The wall shear stress after a step initially overshoots the equilibrium stress for the new surface and this is followed by a slow asymptotic approach to the equilibrium distribution. The distance required to attain the equilibrium shear stress is larger then that required for reestablishment of wall similarity.

References

1 Clauser, F.H., "Turbulent Boundary Layers in Adverse Pressure Gradients," *Journal of the Aeronautical Sciences*, Vol. 21, 1954, pp. 91–108.

2 Townsend, A.A., *The Structure of Turbulent Shear Flow*, 2nd edition, Cambridge University Press, 1976.

3 Townsend, A.A., "Self-Preserving Flow Inside a Turbulent Boundary Layer," *Journal of Fluid Mechanics*, Vol. 22, 1965, pp. 773–798.

4 Townsend, A.A., "The Flow in a Turbulent Boundary Layer After a Change in Surface Roughness," *Journal of Fluid Mechanics*, Vol. 26, 1966, pp. 255–266.

5 Schofield, W.H., "Measurements in Adverse-Pressure-Gradient Turbulent Boundary Layers with a Step Change in Surface Roughness," *Journal of Fluid Mechanics*, Vol. 70, 1975, pp. 721–761.

6 Mulhearn, P.J., "Relations between Surface Fluxes and Mean Profiles of Velocity, Temperature and Concentration, Downwind of a Change in Surface Roughness," *Quarterly Journal of the Royal Meteorological Society*, Vol. 103, 1977, pp. 785–802.

7 Bradley, E.F., "A Micrometerological Study of Velocity Profiles and Surface Drag in the Region Modified by a Change in Surface Roughness," *Quarterly Journal of the Royal Meteorological Society*, Vol. 94, 1968, pp. 361–379.

8 Antonia, R.A., and Luxton, R.E., "The Response of a Step Change in Surface Roughness. Part 1: Smooth to Rough," *Journal of Fluid Mechanics*, Vol. 48, 1971, pp. 721–761.

9 Antonia, R.A., and Luxton, R.E., "The Response of a Step Change in Surface Roughness. Part 2: Rough to Smooth," *Journal of Fluid Mechanics*, Vol. 53, 1972, pp. 737–757.

10 Jackson, N.A., "The Propagation of Modified Flow Downstream of a Change in Roughness," *Quarterly Journal of the Royal Meteorological Society*, Vol. 102, 1976, pp. 924–933.

11 Moore, W.L., Ph.D. thesis, State University of Iowa, 1951.

12 Perry, A.E., Schofield, W.H., and Joubert, P.N., "Rough Wall Turbulent Boundary Layers," *Journal of Fluid Mechanics*, Vol. 37, 1969, pp. 383–413.

13 Hama, F.R., "Boundary Layer Characteristics for Smooth and Rough Surfaces," *Transactions of the Society of Naval Architects and Marine Engineers*, Vol. 62, 1954, pp. 333–351.

14 Angle, R.P., M.Sc. thesis, Dept. of Geography, University of Alberta, Edmonton, 1973.

15 Blackador, A.K., Panofsky, H.A., Glass, P.E., and Boogaard, J.F., "Determination of the Effect of Roughness Change on the Wind Profile," *Physics of Fluids Supplement* on "Boundary Layers and Turbulence," 1967, pp. S209–S211.

16 Kutzbach, J.E., "Investigations of the Modification of Wind Profiles by Artificially Controlled Surface Roughness," University of Wisconsin, Dept. of Meteorology Annual Report, 1961, pp. 71–113.

17 Plate, E.J., and Hidy, G.M., "Laboratory Study of Air Flowing Over a Smooth Surface onto Small Water Waves," *Journal of Geophysical Research*, Vol. 72, 1967, pp. 4626–4641.

18 Yeh, F.F., and Nickerson, E.C., "Air Flow over Roughness Discontinuity," Project Themis Tech. Rept. No. 8, Colorado State University, 1970.

19 Antonia, R.A., and Luxton, R.E., "The Response of a Turbulent Boundary Layer to an Upstanding Change in Surface Roughness," ASME *Journal of Basic Engineering*, Vol. 93, 1971, pp. 22–34.

20 Narayana, P.A.A., "An Experimental Investigation of Turbulent Boundary Layers Over Smooth and Rough Surfaces," Delft University of Tech., Rept. LR-235, 1977.

21 Islam, O., and Logan, E., "Channel Flow Over a Smooth-to-Rough Surface Discontinuity with Zero Pressure Gradient," ASME JOURNAL OF FLUIDS ENGINEERING, Vol. 98, 1976, pp. 626–635.

22 Logan, E., and Jones, J.B., "Flow in a Pipe Following an Abrupt Increase in Surface Roughness," ASME *Journal of Basic Engineering*, Vol. 85, 1963, pp. 35–40.

23 Siuru, W.D., and Logan, E., "Response of a Turbulent Pipe Flow to a Change in Roughness," ASME JOURNAL OF FLUIDS ENGINEERING, Vol. 99, 1977, pp. 546–555.

24 Tani, I., and Makita, H., "Response of a Turbulent Shear Flow to a Stepwise Change in Wall Roughness," *Zietschrift für Flugwissenshaften*, Vol. 19, 1971, pp. 335–339.

25 Draper, N.R., and Smith, H., "Fitting a Straight Line by Least Squares," *Applied Regression Analysis*, Wiley, New York, 1966, pp. 1–33.

26 Kline, S.J., and McClintock, F.A., "Describing Uncertainties in Single-Sample Experiments," *Mechanical Engineering*, Vol. 75, No. 1, Jan. 1953, pp. 3–9.

27 Galbraith, R.A.McD., and Head, M.R., "Eddy Viscosity and Mixing Length from Measured Boundary-Layer Developments," *Aeronautical Quarterly*, Vol. 26, 1975, pp. 133–154.

28 Reeves, B.L., "Two-Layer Model of Turbulent Boundary Layers," *A.I.A.A. Journal*, Vol. 12, 1974, pp. 932–939.

29 Galbraith, R.A. McD., Sjolander, S., and Head, M.R., "Mixing Length in the Wall Region of Turbulent Boundary Layers," *Aeronautical Quarterly*, Vol. 28, 1977, pp. 97–110.

30 Glowacki, W.J., and Chi, S.W., "Effect of Pressure Gradient on Mixing Length for Equilibrium Turbulent Boundary Layers," *A.I.A.A. Journal*, paper 72–213, 1972.

31 Perry, A.E., and Joubert, P.N., "Rough-Wall Boundary Layers in Adverse Pressure Gradients," *Journal of Fluid Mechanics*, Vol. 17, 1963, pp. 193–211.

Calculation of Annular and Twin Parallel Jets Using Various Discretization Schemes and Turbulence-Model Variations

M.A. Leschziner
Research Engineer,
University of Karlsruhe,
Kaiserstrasse 12,
D-7500 Karlsruhe,
FRG; Present Address:
Department of Mechanical Engineering,
University of Manchester
Institute of Science and Technology,
Manchester, UK.

W. Rodi
Research Engineer,
University of Karlsruhe,
Kaiserstrasse 12,
D-7500 Karlsruhe, FRG

The paper examines the performance of three discretization schemes for convection and three turbulence-model variations when used to simulate the recirculating flow in an annular and a plane twin-parallel jet in still air. The discretization schemes considered are:

(i) the hybrid central/upwind differencing scheme (CUDS),
(ii) the hybrid central/skew-upwind differencing scheme (CSUDS) and
(iii) the quadratic, upstream-weighted differencing scheme (QUDS).

Of these, the second and third were proposed recently as superior alternatives to the first in respect of numerical diffusion. The turbulence models examined are the standard k-ϵ model and two variants of this. The first accounts for effects of streamline curvature on turbulence and the second for the preferential influence of normal stresses on the dissipation of turbulence energy. It is shown that numerical scheme (i) results, particularly in conjunction with the turbulence-model modifications, in severe solution errors and in a generally anomalous response to changes in the modelled viscosity field. In contrast, schemes (ii) and (iii) yield, in all cases, similar results and respond in an expected manner to the modifications. The modifications, particularly that accounting for streamline curvature, reduce, in some cases drastically, the discrepancies between computed and experimental data and yield for both jets examined generally satisfactory results.

1 Introduction

It has been the experience of several authors [1-6] that numerical procedures for turbulent recirculating flows often yield bad agreement with experimental data. In particular, the dimensions of the recirculation region are found to be underpredicted by up to 30 percent, depending on the flow considered and the grid and turbulence model used. Turbulence-model defects were usually blamed for the discrepancies, but since the numerical schemes employed were mostly based on upwind discretization, which may introduce significant numerical diffusion, the results are far from conclusive.

It is well known that curvature strongly influences turbulent transport in shear layers. Moreover, the size of a recirculation zone (that in cavities, of course, excepted) is affected by details in the curved shear layer bordering the zone. It can therefore be expected that failure to account for curvature effects will lead to significant errors. In most calculations, such effects have in fact been neglected in the turbulence models employed. The marked response of solutions to grid refinement and the lack of response to changes in the turbulence model reported by some authors suggests, however, that numerical diffusion at least significantly contributes to the discrepancies by obscuring physical transport processes. This conclusion is lent support by four studies [7-10] which examine the performance of upwind differencing in simple model problems. The studies show that numerical diffusion can have strongly damaging effects on solution accuracy if the flow is skewed relative to the numerical mesh and the streamwise Peclet number $Pe = |V|\Delta/\Gamma$ exceeds the value 2. This observation bears great importance for recirculating flows since, as stated before, the size of the recirculation zone depends on diffusive transport in the bordering shear layer and this is skewed due to curvature.

In order to identify and correct turbulence-model defects it is thus necessary to first minimize numerical diffusion. The only way of doing this in algorithms using hybrid central/upwind differencing for convection is to refine the grid until all important flow regions can be handled with non-diffusive central differences. This is obviously an expensive way if not barred by computer-time and storage limitations. The alternative is to use more complex and sophisticated discretization methods for convection. Two such methods, one by Raithby [11] termed "skew-upwind differencing" and

Contributed by the Fluids Engineering Division for publication in the JOURNAL OF FLUIDS ENGINEERING. Manuscript received by the Fluids Engineering Division, June 19, 1980.

the other by Leonard [12] called "quadratic upstream-weighted differencing," were recently examined for idealized flow cases by the first author of this paper [10]. The schemes were found to be far superior to the conventional upwind formulation; they also form the basis for the present study which is mainly concerned with the simulation of turbulence in recirculating flows.

With very few exceptions [6,13] this simulation has been carried out with variations of the so-called k-ϵ turbulence model described by Launder and Spalding [14]. The model in its standard form does not account for important secondary strain effects such as resulting from curvature, and one objective of the present study has been to isolate and quantify the errors arising from this deficiency in the case of an annular jet and a plane twin-parallel jet sketched in Fig. 1. For this purpose, it was essential to use discretization schemes having little numerical diffusion. A second objective has been to develop and to evaluate, also for the annular and the twin jet, two novel modifications to the basic model. One modification accounts for effects of streamline curvature on turbulence and has been derived by simplification of an algebraic Reynolds-stress model, as described by Gibson [15]. The model itself originates from simplifying the Reynolds-stress transport equations. The second modification proposed and tested here is based on one by Hanjalić and Launder [18] for strongly accelerated one-dimensional flows. The modification accounts for the preferential influence of normal stresses on the dissipation of turbulent energy.

Curvature modifications to the k-ϵ model for recirculating flow were previously used by Militzer, et al. [1] and Durst and Rastogi [4]. Militzer's correction is essentially a curvature-dependent attenuation of the production of turbulence energy. Conceptually, this is unsatisfactory as the production term does not require modelling in the standard k-ϵ model and should, therefore, remain unaltered. In addition, it can be shown that the curvature parameter was incorrectly evaluated. Durst and Rastogi used a Richardson-number-dependent correction to the dissipation equation, originally proposed by Launder [16] for boundary-layer flows on rotating bodies. The correction is essentially equivalent to a reduction in the turbulent length scale (or mixing length) proposed by Bradshaw [17]. It is wholly empirical and its width of applicability as well as its physical basis are open to doubt. Through its derivation from the Reynolds-stress equations, the curvature correction proposed here has a sounder basis. It should be emphasized, however, that the modifications to the k-ϵ model suggested here are of a rather preliminary nature and that further research is needed on the development and testing of turbulence models for recirculating flows.

2 Calculation Procedure

2.1 Basic Equations. With the turbulent stresses substituted by eddy-viscosity relations, the equations governing the flows considered are as follows:

$$\frac{\partial U}{\partial x} + \frac{1}{y^j}\frac{\partial y^j V}{\partial y} = 0 \tag{1}$$

$$U\frac{\partial U}{\partial x} + V\frac{\partial U}{\partial y} = -\frac{1}{\rho}\frac{\partial P}{\partial x} + 2\frac{\partial}{\partial x}\left[\nu_{\text{eff}}\frac{\partial U}{\partial x}\right] + \frac{1}{y^j}\frac{\partial}{\partial y}\left[y^j \nu_{\text{eff}}\left(\frac{\partial U}{\partial y} + \frac{\partial V}{\partial x}\right)\right] \tag{2}$$

Nomenclature

b = width of plane jet
B = distance between twin plane jets
$C_1, C_1', C_1'', C_2, C_\mu$ = turbulence-model constants
C_{ij} = directional cosine of angle between directions i and j
CSUDS = abbreviation for "(hybrid) central/skew-upwind differencing scheme"
CUDS = abbreviation for "(hybrid)central/upwind differencing scheme"
d = small diameter of pipe expansion
D = large diameter of pipe expansion
k = turbulent kinetic energy
K_1, K_2 = constants in C_μ relation
l_m = mixing length
L = macro eddy-length scale
n = coordinate normal to streamline
P = static pressure
Pe = grid Peclet number
P_{ij} = production of turbulent stress $\overline{u_i u_j}$
P_k = production of turbulent kinetic energy
P_ϵ = production of dissipation rate of k
QUDS = abbreviation for "quadratic upstream-weighted differencing scheme"
r = radial coordinate
R_c = radius of curvature
Re_j = jet Reynolds number $\left(\frac{\bar{U}(D-d)}{\nu} \text{ or } \frac{\bar{U}b}{\nu}\right)$
s = coordinate parallel to streamline
S_{ij} = rate of strain tensor
$\overline{u_i u_j}$ = Reynolds stress tensor
U = velocity in x-direction
$\bar{U}$ = average velocity in x-direction
U_ℓ = centerline velocity in x-direction
$\hat{U}$ = maximum velocity in x-direction
U_0 = jet-exit velocity
V = velocity in y-direction
$\mathbf{V}$ = velocity vector
x, y = cartesian coordinates
α, β = turbulence-model constants
Γ = effective diffusivity
δ = mixing layer thickness
δ_{ij} = Kronecker delta
$\Delta x, \Delta y$ = control-volume dimensions or internodal distances in numerical mesh
Δ = control volume dimension in direction of velocity vector
ϵ = rate of dissipation of turbulent kinetic energy
ϵ_{ijk} = alternating third-order tensor
θ = angle between streamline and x-direction
κ = von Kármán constant
ν = kinematic fluid viscosity
ν_t = kinematic eddy viscosity
ν_{eff} = kinematic effective viscosity
ν_{ad} = kinematic artificial viscosity
ρ = fluid density
$\sigma_k, \sigma_\epsilon$ = Prandtl/Schmidt numbers for k and ϵ, respectively
τ_w = wall shear stress
ϕ = any scalar property
ψ = stream function

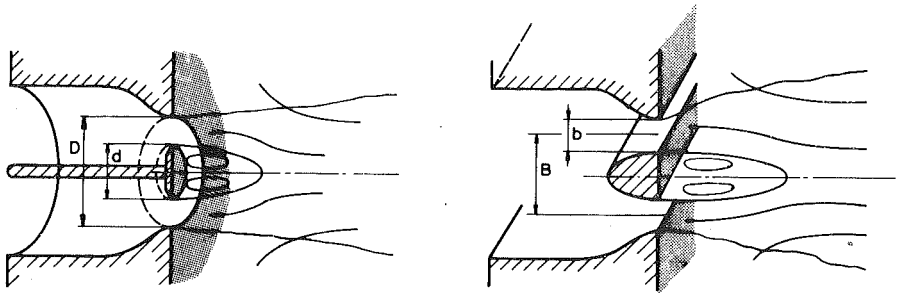

Fig. 1 Flow geometries considered

$$U\frac{\partial V}{\partial x}+V\frac{\partial V}{\partial y}=-\frac{1}{\rho}\frac{\partial P}{\partial y}+\frac{\partial}{\partial x}\left[\nu_{\text{eff}}\left(\frac{\partial U}{\partial y}+\frac{\partial V}{\partial x}\right)\right]$$
$$+\frac{2}{y^j}\frac{\partial}{\partial y}\left[y^j\nu_{\text{eff}}\frac{\partial V}{\partial y}\right]-2j\frac{\nu_{\text{eff}}}{y^{2j}}V \tag{3}$$

where

$j = 0$ applies to plane cases,
$j = 1$ applies to axisymmetric cases.

In the above, U and V are the x and y-directed velocities, respectively, P is the pressure, ν_{eff} the sum of the kinematic fluid and eddy viscosities and ρ is the density.

2.2 The Turbulence Models. The standard k-ϵ model and its two variations examined in this study employ the eddy viscosity concept and calculate the eddy viscosity ν_t from:

$$\nu_t = C_\mu\frac{k^2}{\epsilon} \tag{4}$$

In (4) the turbulence energy k characterizes the intensity of the turbulent fluctuations and the dissipation rate ϵ the length scale of the energy-containing eddies through the relation $\epsilon\alpha k^{3/2}/L$. The distribution of k and ϵ is determined from the solution of semiempirical transport equations which, in the standard k-ϵ model, are as follows:

$$U\frac{\partial k}{\partial x}+V\frac{\partial k}{\partial y}=\frac{\partial}{\partial x}\left(\frac{\nu_{\text{eff}}}{\sigma_k}\frac{\partial k}{\partial x}\right)$$
$$+\frac{1}{y^j}\frac{\partial}{\partial y}\left(y^j\frac{\nu_{\text{eff}}}{\sigma_k}\frac{\partial k}{\partial y}\right)+P_k-\epsilon \tag{5}$$

$$U\frac{\partial \epsilon}{\partial x}+V\frac{\partial \epsilon}{\partial y}=\frac{\partial}{\partial x}\left(\frac{\nu_{\text{eff}}}{\sigma_\epsilon}\frac{\partial \epsilon}{\partial x}\right)$$
$$+\frac{1}{y^j}\frac{\partial}{\partial y}\left(y^j\frac{\nu_{\text{eff}}}{\sigma_\epsilon}\frac{\partial \epsilon}{\partial y}\right)+\frac{C_1\epsilon}{k}P_k-\frac{C_2\epsilon^2}{k} \tag{6}$$

where

$$P_k\equiv\nu_{\text{eff}}\left\{2\left[\left(\frac{\partial U}{\partial x}\right)^2+\left(\frac{\partial V}{\partial y}\right)^2+j\left(\frac{V}{y^j}\right)^2\right]+\left(\frac{\partial U}{\partial y}+\frac{\partial V}{\partial x}\right)^2\right\}$$

represents the generation of turbulence energy by the interaction of mean velocity gradients and turbulent stresses. The constants appearing in (4) to (6) take the values $C_\mu = 0.09$; $C_1 = 1.44$; $C_2 = 1.92$; $\sigma_k = 1.0$; $\sigma_\epsilon = 1.3$, as given in [14].

Differences between the standard model and the two modified versions are described in the following two subsections.

(*i*) *Streamline Curvature Modification.* Experimental studies reviewed in [17] show that the turbulent shear stress and the degree of anisotropy between the normal stresses are very sensitive to curvature. Several theoretical studies show [1, 16, 19] that this sensitivity is not reflected by "standard" mixing-length and k-ϵ models, and that empirical ad-hoc modifications need to be introduced to achieve a proper response. In contrast, Reynolds-stress models, whether of the algebraic or of the transport type, need no such modifications [20,21]. The curvature modification detailed below is based on one of these models, namely the algebraic stress model of Gibson [15]. The model consists, in essence, of a set of algebraic equations resulting from the omission of all transport terms (i.e. convection and diffusion) from related differential equations governing the transport of the Reynolds stresses [22]. This omission reflects the assumption of local stress equilibrium. The algebraic equations may collectively be written, in a general form, as:

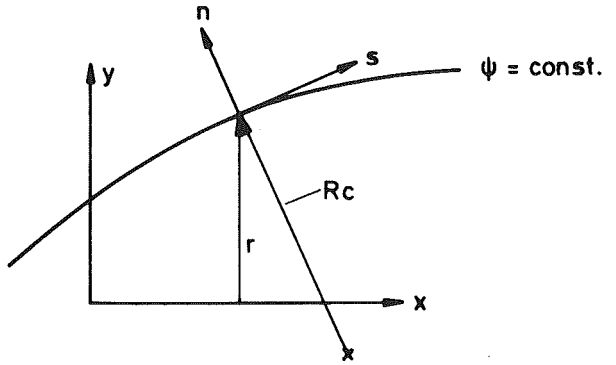

Fig. 2 Streamline coordinate system

$$P_{ij}=\alpha\frac{\epsilon}{k}\left(\overline{u_iu_j}-\frac{2}{3}\delta_{ij}k\right)+\beta\left(P_{ij}-\frac{2}{3}\delta_{ij}P_k\right)+\frac{2}{3}\epsilon\delta_{ij} \tag{7}$$

As indicated, equation (7) represents the balance between the rate of production P_{ij} of the stress $\overline{u_iu_j}$, pressure-strain (first and second term on the R.H.S) and dissipation, where α and β are constants having the values 1.5 and 0.6, respectively, as in [22].

On the assumption of local equilibrium of turbulence energy, expressed by $P_k = \epsilon$, equations (7) simplify to:

$$\frac{\overline{u_iu_j}}{k}=\frac{1-\beta}{\alpha\epsilon}P_{ij}-\frac{2}{3}\frac{\delta_{ij}}{\alpha}(1-\alpha-\beta) \tag{8}$$

The effect of curvature on the stresses can be identified from equation (8) if (i,j) are taken as the streamline coordinates (s, n), as shown in Fig. 2. With R_c denoting the local radius of curvature and r the distance from the axis of symmetry (for axially symmetric flow), P_{ij} can be expressed as follows:

$$P_{ss}=-2\overline{u_s^2}\frac{\partial Us}{\partial s}-2\overline{u_su_n}\left(\frac{\partial U_s}{\partial n}+\frac{U_s}{R_c}\right) \tag{9}$$

$$P_{nn}=-2\overline{u_n^2}\frac{\partial U_n}{\partial n}+4\overline{u_nu_s}\frac{U_s}{R_c} \tag{10}$$

$$P_{ns} = -\overline{u_n^2}\frac{\partial U_s}{\partial n} + \left(2\overline{u_s^2} - \overline{u_n^2}\right)\frac{U_s}{R_c} + \overline{u_n u_s}\frac{U_r}{r} \qquad (11)$$

Equations (8) to (11) suffice for the evaluation of the stresses $\overline{u_n^2}$, $\overline{u_s^2}$, and $\overline{u_n u_s}$ provided the mean flow and k as well as ϵ are known or determinable. However, it is only the shear stress $\overline{u_n u_s}$ on which attention is focused, for this is the only important stress in the momentum equations in a curved shear layer such as that bordering the recirculation zone. The objective, therefore, is to obtain, by combining (8) to (11), an expression which relates $\overline{u_n u_s}$ to the respective rate of strain $(\partial U_s/\partial n + U_s/R_c)$ and, in this way, to extract a curvature dependence of the coefficient C_μ (see equation (4)). This objective is readily achieved by introducing the simplifications:

$$\frac{U_r}{r} = \frac{\partial U_n}{\partial n} = \frac{\partial U_s}{\partial s} = 0 \qquad (12)$$

These may seem bold assumptions on first sight, but it should be recognized that the aim here is to isolate the effect of the extra curvature-strain rate U_s/R_c on C_μ and nothing more. Combination of equations (8) to (11) results in:

$$-\overline{u_s u_n} = \frac{-K_1 K_2}{\left[1 + 8K_1^2\frac{k^2}{\epsilon^2}\left(\frac{\partial U_s}{\partial n} + \frac{U_s}{R_c}\right)\frac{U_s}{R_c}\right]}\frac{k^2}{\epsilon}\left(\frac{\partial U_s}{\partial n} - \frac{U_s}{R_c}\right) \qquad (13)$$

where

$$K_1 \equiv \frac{1-\beta}{\alpha}$$

$$K_2 \equiv \frac{2}{3}\frac{(1-\alpha-\beta)}{\alpha}$$

Comparison of (13) with (4) shows that the above implies:

$$C_\mu \equiv \frac{-K_1 K_2}{\left[1 + 8K_1^2\frac{k^2}{\epsilon^2}\left(\frac{\partial U_s}{\partial n} + \frac{U_s}{R_c}\right)\frac{U_s}{R_c}\right]} \qquad (14)$$

There are two features of equation (14) which require further consideration. First, C_μ may assume negative values if $(\partial U_s/\partial n)/(U_s/R_c)$ is negative and sufficiently large in magnitude. Therefore, an arbitrary positive limit must be imposed for physical realism, as will be discussed later. Second, a slight inconsistency would arise when (14) is used directly in conjunction with the k-ϵ model in that C_μ reduces to $-K_1K_2 = 0.13$; this compares to the "standard" value 0.09. In the actual calculations K_1K_2 was therefore replaced by 0.09.

What remains to be evaluated are the terms $\partial U_s/\partial n$ and U_s/R_c from U, V and their x and y-directed derivatives which are supplied by the solution algorithm. This is the subject of Appendix A.

(ii) Preferential Dissipation Modification. The modification dealt with in this subsection was originally proposed by Hanjalić and Launder [18] for strongly accelerated flows, with the intention to also improve the k-ϵ model when applied to recirculating flows. It reflects the observation that the decay by dissipation of grid turbulence passed through a strong contraction is far higher than without the contraction. As there are only normal stresses acting in this flow (if one excludes the near-wall regions), and as this phenomenon has not been observed when the turbulence was subjected to shear, Hanjalić and Launder concluded that normal stresses are more effective than shear stresses in promoting the transfer of turbulence energy from large to small eddies and thus the rate of dissipation. The modification involves a replacement of the "production-of-dissipation" term $P_\epsilon \equiv \epsilon/k\, C_1 P_k$ in equation (6) by the general expression:

$$P_\epsilon = \frac{\epsilon}{k}\left(C_1' P_k - C_1'' \nu_t\, \epsilon_{ijk}\epsilon_{lmk}\frac{\partial U_i}{\partial x_j}\frac{\partial U_l}{\partial x_m}\right) \qquad (15)$$

where $C_1' = 2.1$, $C_1'' = 0.8$ and ϵ_{ijk} is the alternating third-order tensor. For two-dimensional situations this yields:

$$P_\epsilon = \frac{\epsilon}{k}\left[C_1' P_k - C_1'' \nu_t\left(\frac{\partial U}{\partial y} - \frac{\partial V}{\partial x}\right)^2\right] \qquad (16)$$

in which the inner bracketed term is the vorticity, i.e. a coordinate invariant quantity. In thin shear flows this is also close to the shear strain (since $\partial V/\partial x << \partial U/\partial y$). With $P_{k,n}$ and $P_{k,s}$ respectively denoting the production by normal and shear stresses, relation (16) may be written as:

$$P_\epsilon = \frac{\epsilon}{k}\left[C_1' P_{k,n} + (C_1' - C_1'')P_{k,s}\right] \qquad (17)$$

which clearly demonstrates the preferential treatment of normal stresses.

A problem arises when the above modification is to be applied to recirculating flows. In such a case, the vorticity bears no relation to the shear strain and the modification loses its intended purpose. A case in point is a free-vortex motion in which the vorticity is zero yet the shear stress is finite and large. In order to overcome this problem, it is suggested to retain the basic idea of preferential-normal-stress treatment suggested by equation (17) also for recirculating flows, with the stresses defined in a streamline coordinate system. This is not a tensor-invariant correction, but, similar to the C_μ-correction discussed earlier, it is meant to have its main effect in the important shear-layer regions of the flow. For the actual calculations, (17) is cast in the form of:

$$P_\epsilon = \frac{\epsilon}{k}\left[C_1' P_k - C_1'' \nu_t S_{ns}^2\right] \qquad (18)$$

where S_{ns} is the shear strain in the direction of the streamline and is given by equation (22) in Appendix A. $C_1' = 2.24$ was adopted instead of Hanjalić and Launder's value of 2.1 to insure that the shear production will be identical to that in the standard k-ϵ model (i.e. $C_1 - C_1'' = C_1 = 1.44$).

2.3 The Numerical Schemes. In order to solve the system of partial differential equations governing the mean flow and turbulent quantities, the solution algorithm of Gosman and Pun [23] was appropriately modified. The code, in its original form, embodied a hybrid central/upwind difference scheme for the convection terms. In this, the upwind-difference part is used if the cell or grid-Peclet number in a given direction exceeds 2 and the central-difference part otherwise.

Because of the problem of numerical diffusion posed by the upwind formulation, two alternative schemes, one proposed by Raithby [11] and the other by Leonard [12], were incorporated into the basic code. It would go beyond the scope of this paper to discuss the schemes and their performance in detail; such a discussion is provided in reference [10] so that it may suffice here to provide a brief description of the salient features of the schemes.

Both schemes, as well as the conventional upwind scheme are used in conjunction with the fully conservative control-volume approach. With this approach, discretization of the convection terms requires the evaluation of control-volume face values from surrounding nodal values. The schemes

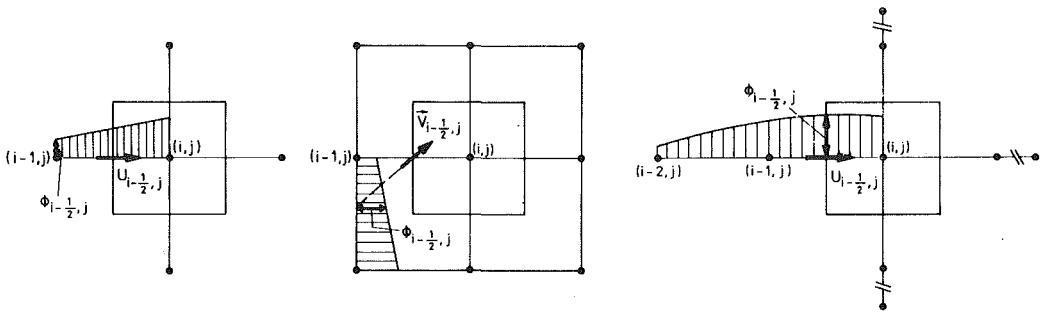

(a) upwind scheme *(b)* skew-upwind scheme *(c)* quadratic scheme

Fig. 3 Methods of obtaining control-volume-face values

differ in respect of the method by which the face values are obtained, as shown in Fig. 3. The "skew-upwind differencing" scheme of Raithby, although like the conventional upwind scheme formally only first-order accurate, yields a significant reduction in numerical diffusion by taking the direction of the velocity vector into account, as illustrated in Fig. 3(*b*). In this way, the so-called "skewness error" – by far the most damaging part of numerical diffusion in two-dimensional flows – is drastically reduced. The method of Leonard, termed "quadratic upstream-weighted differencing," is entirely free from numerical diffusion. As shown in Fig. 3(*c*), it is based on the use of upstream-shifted parabolic interpolation for every control-volume face.

It should finally be mentioned that Raithby's and Leonard's schemes were only used in the solution of the momentum equations. Test computations have shown the solutions for k and ϵ to be on the whole insensitive to the discretization method, particularly in the high shear regions bordering the recirculation zone. This reflects the fact that in the influential high shear zones the source terms dominate over convective transport in both the k and ϵ equation.

3 Application

In the following, selected computational results are presented and compared with experimental data for two recirculating free flows, one axially symmetric, the other plane. The geometries are sketched in Fig. 1. The first configuration is a jet issuing from an annulus of diameter ratio $d/D = 0.72$ at a Reynolds number $\mathrm{Re}_j \equiv \bar{U}(\mathrm{D}-\mathrm{d})/\nu = 9.7 \times 10^3$ into still air. Related experimental data were obtained by Durão [25] with the aid of a laser-Doppler velocimeter. The second configuration consists of two plane jets issuing from two slots of equal width b separated by $B = 6b$ from each other. This flow was investigated experimentally by Militzer [24] for $\mathrm{Re}_j \equiv \bar{U}b/\nu = 5.56 \times 10^4$ with a three-hole probe and a hot-wire probe.

3.1 Computational Details and Boundary Conditions. The domain of solution considered in both cases extended to a downstream distance of approximately 2.7 times the experimental recirculation length and to a lateral distance of 3.5 $\times D/2$ for the annular jet and 3.5 $\times (B + b)/2$ for the plane jet.

All computations reported here were performed with a mesh consisting of 38 $\times$ 37 nonuniformly distributed grid lines with ca. 21 $\times$ 16 uniformly distributed nodes located within the recirculation zone. Significantly finer grids could not be used because of computer-storage and time limitations. The maximum mesh-expansion ratio was 1.2 in either direction.

The boundary conditions used for the present computations are summarized in Table 1.

In the table, L is a macro length scale related to the mixing length l_m which is assumed to obey $l_m = 0.09\delta$ (δ = jet half width). At the plug wall, V was not prescribed; instead the logarithmic law of the wall was used to determine the wall-shear stress τ_w. From this, k and ϵ were evaluated at the near-wall nodes, as given in Table 1, on the assumption that local equilibrium of turbulence energy prevails up to a distance Δx from the wall. The inlet-velocity profile in the plane jet was taken as uniform. In the annular jet it was found that a uniform velocity based on the reported Reynolds number yielded a flow rate 40 percent in excess of that obtained by integrating the measured profiles $U(y)$ at $x/D = 0.1$, 0.3, 0.65 and extrapolating to $x/D = 0$. For this reason a nonuniform inlet profile, obtained by extrapolation from $x/D = 0.1$ and 0.3, was prescribed.

3.2 Results and Discussion. A selection of results for the two jets examined are shown in Figs. 4 to 13.

Presented first in Figs. 4 to 6 are distributions of centerline velocity for the annular and plane jets and lateral profiles of axial velocity at two positions of the plane jet, all obtained

Table 1 Boundary conditions

Boundary	U	V	P	k	ϵ
Jet inlet	from experiment (see text)	0	–	from experiment	$k^{3/2}/L$ $L = 0.56\delta$
Symmetry axis	$\partial U/\partial y = 0$	0	–	$\partial k/\partial y = 0$	$\partial \epsilon/\partial y = 0$
Exit	$\partial U/\partial x = 0$	$\partial V/\partial x = 0$		$\partial k/\partial x = 0$	$\partial \epsilon/\partial x = 0$
Entrainment boundary	0	– (calculated)[a]	0	0	0
Plug wall	0	τ_w (wall law)	–	$\tau_w/\rho C_\mu^{1/2}$	$\left(\frac{\tau_w}{\rho}\right)^{3/2} \Big/ k\Delta x$

[a] This was done by solving Equation (3) with the assumption $P = 0$, $U = 0$ just outside the domain of solution.

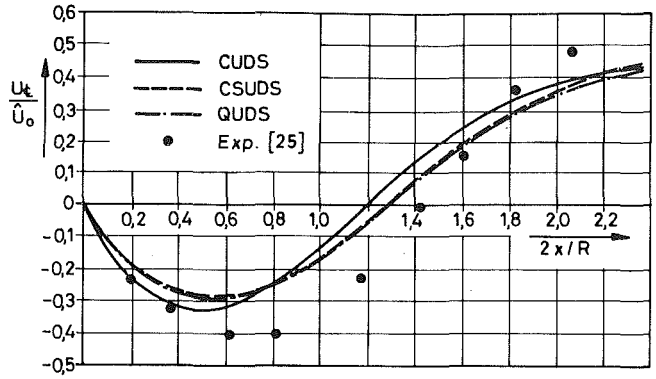

Fig. 4 Centerline velocity, annular jet, $k-\epsilon$ model

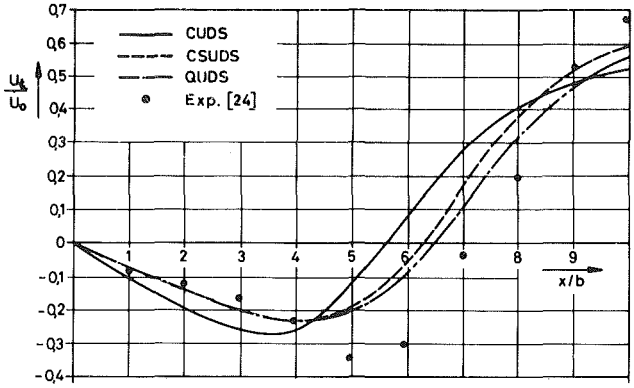

Fig. 5 Centerplane velocity, plane jet, $k-\epsilon$ model

with the standard k-ϵ model. The figures show consistent differences between hybrid central/upwind scheme (CUDS) solutions on the one hand and hybrid-central/skew-upwind (CSUDS) and quadratic scheme (QUDS) solutions on the other, particularly in respect of the stagnation-point position and the minimum velocity value. The fact that two such different schemes as the CSUDS and QUDS yield solutions close to each other already suggests that these must be nearly grid independent and, therefore, numerically accurate. Test computations performed for the annular jet with grids as coarse as 27 × 25 nodes confirmed this notion. It was found that CSUDS and QUDS solutions, in contrast to those of the CUDS, hardly responded to changes in grid density. In addition, CUDS solutions were found to progressively approach those predicted by the CSUDS and QUDS as the grid was refined. This last observation, in particular, suggests that it is artificial diffusion which affected the CUDS results. The fact that significant artificial diffusion is present event when the 38 × 37 mesh is used, is illustrated in Fig. 7. This shows contours of the ratio ν_{ad}/ν_{eff} evaluated with the aid of de-Vahl Davis's relation [7]

$$\nu_{ad} = \frac{|\mathbf{V}|\Delta x \Delta y \sin 2\theta}{4(\Delta y \sin^3\theta + \Delta x \cos^3\theta)}$$

where

ν_{ad} is the artificial viscosity,
$\mathbf{V}$ is the velocity vector
and θ is the skewness angle.

Within the area bounded by $\nu_{ad}/\nu_{eff} = 1$, the axial as well as the lateral grid-Peclet numbers ($\mathrm{Pe}_x = U\Delta x/\nu_t$, $\mathrm{Pe}_y = V\Delta y/\nu_t$) exceed the value 2, in which case upwind differencing is used throughout and physical viscosity is ignored. It is seen that the above area borders the streamline $\psi = 0$ and thus includes parts of the shear layer in which diffusive transport is important. It is the excessive viscosity in these parts which adversely affects the performance of the CUDS. It may thus be concluded that only the differences between CSUDS/QUDS solutions and the corresponding experimental results, which are by no means minor, can be attributed to defects in the standard k-ϵ model.

The effect of including the curvature correction is shown in Figs. 8 to 11. First, Fig. 8 shows contours of C_μ, as evaluated from relation (14), in the vicinity of the recirculation zone in the annular jet. As expected, the correction leads to a significant reduction in C_μ around the separation streamline, i.e. in the curved shear layer bordering the recirculation zone. Within this zone C_μ would tend to zero or even reverse sign if a lower limit were not placed. This limit was chosen as 0.025. This value is of course somewhat arbitrary, but in regions where C_μ is below it, the concept of local equilibrium of turbulent stresses and energy, on which the curvature correction is based, can certainly not be expected to hold. It can be seen from Figs. 9 to 11 that the modification results in a substantial improvement in the predictions, particularly in respect of the centerline velocity, when the CSUDS and the QUDS are used. Here again, the above schemes yield similar results though the QUDS appears to suffer increasingly from over-and undershoots which are just discernible when the k-ϵ model is used (Fig. 6). In contrast, use of the CUDS actually results in a slight shortening of the recirculation region and a general overall deterioration in predictive accuracy. The anomalous response of the CUDS to the modification, in particular the insensitivity of the stagnation-point location, can again be explained by artificial diffusion. This is particularly damaging here since the reduction in viscosity

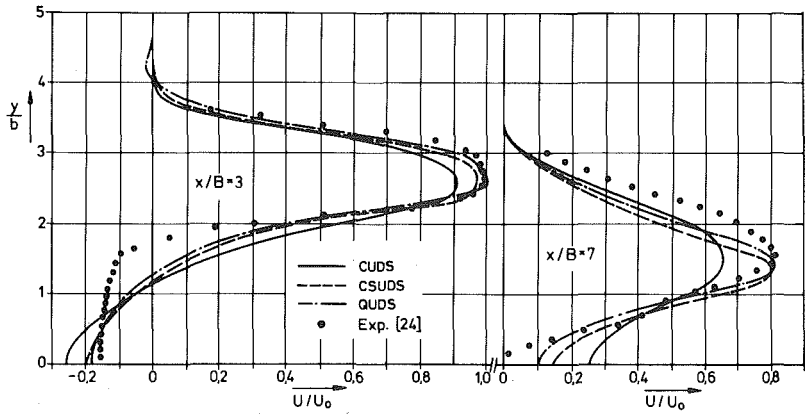

Fig. 6 Lateral profiles of axial velocity, plane jet, $k-\epsilon$ model

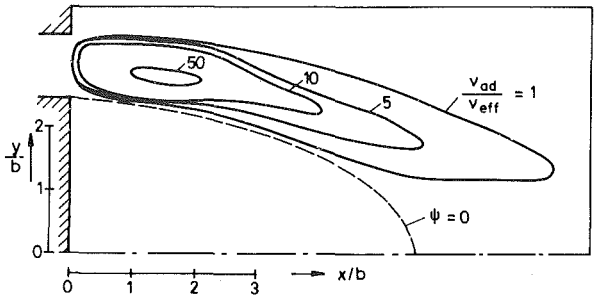

Fig. 7 Contours of ν_{ad}/ν_{eff} plane jet, $k-\epsilon$ model, CUDS

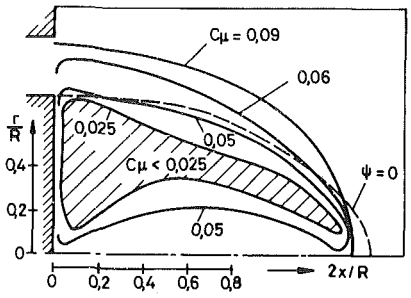

Fig. 8 Contours of C_μ, annular jet, $k-\epsilon$ model and curvature modification CSUDS

resulting from the turbulence-model modification leads to a significant extension of the region bounded by $\nu_{ad}/\nu_{eff} = 1$.

Finally, the response of the center-line velocity to the normal-stress modification is shown in Figs. 12 and 13. Like the curvature correction, the present one was found to yield a marked reduction of the modelled viscosity, this time however, by an increase in the rate of dissipation. It can be seen that the effect of the correction is qualitatively quite similar to that of the curvature modification, which also applies to the radial profiles not included here. The agreement with the experimental data is, however, not quite as good as that achieved with the curvature modification. It may be concluded that the preferential treatment of normal-stress production in the ϵ-equation yields a correction in the right direction, which supports the basic idea of this treatment. It is, unfortunately, not possible to deduce from the experiments whether it is C_μ that should be reduced or ϵ that should be increased in order to yield the lower eddy-viscosity values necessary for a correct prediction of free recirculating flows. Therefore, it is difficult to say which of the corrections has more physical realism. It seems likely that both effects on ν_t are present in reality, but attempts to combine the two modifications proved unfruitful, possibly because of the strong non-linear nature of the problem. The strong reduction in the modelled viscosity led to instabilities or severe under- and overshoots in QUDS computations, while the performance of the CUDS just deteriorated further. The CSUDS did respond to the combined modification, but the excessive length of the recirculation zone predicted in combination with an inappropriate depression of the minimum centerline velocity indicated that the viscosity level was underestimated by the combined correction.

4 Conclusions

Three numerical schemes have been applied, in combination with three turbulence-model variations to two unconfined recirculating flows, and their performance has been examined. The study allows the following conclusions to be drawn:

(i) The hybrid central/upwind differencing scheme must be considered a highly deficient tool for simulating unconfined recirculating flows and is, unless exceedingly fine grids are used, entirely unusable if the validity of turbulence-model modifications is to be investigated.

(ii) The hybrid central/skew-upwind and the quadratic upstream-weighted differencing schemes appear to perform well for the applications considered, yield similar solutions and respond in a similar manner to changes in the modelled viscosity, provided the viscosity level is not unrealistically low. The quadratic scheme has, however, been found to suffer, albeit to a limited extent, from boundedness problems manifesting themselves by slight over-and undershoots.

(iii) The standard k-ϵ model fails to represent accurately the effects of turbulence in the recirculating flows examined.

(iv) Of the turbulence-model modifications proposed, the one acounting for effects of streamline curvature is the most effective, leading to greatly improved agreement with experimental data.

Acknowledgments

The work documented in this paper was sponsored by the Sonderforschungsbereich 80, University of Karlsruhe. The calculations were performed on the UNIVAC 1106/1108 computer of the University of Karlsruhe.

References

1 Militzer, J., Nicoll, W.B. and Alpay, J.A. "Some Observations on the Numerical Calculation of the Recirculation Region of Twin Parallel Symmetric Jet Flow," *Proc. Symp. on Turbulent Shear Flows,* Pennsylvania State University, 1977, pp. 18.11-18.18.

2 Castro, I.P., "The Numerical Prediction of Recirculating Flows," *Proc.*

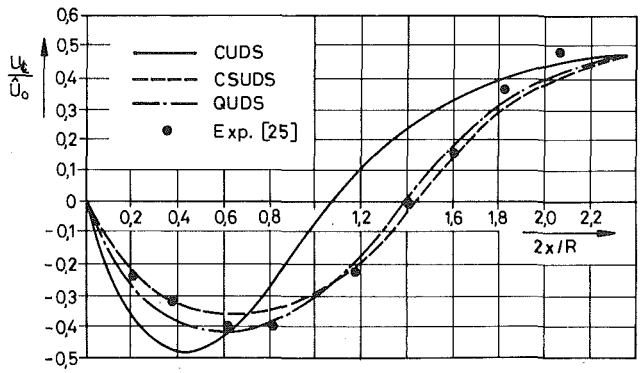

Fig. 9 Centerline velocity, annular jet, $k-\epsilon$ model and curvature modification

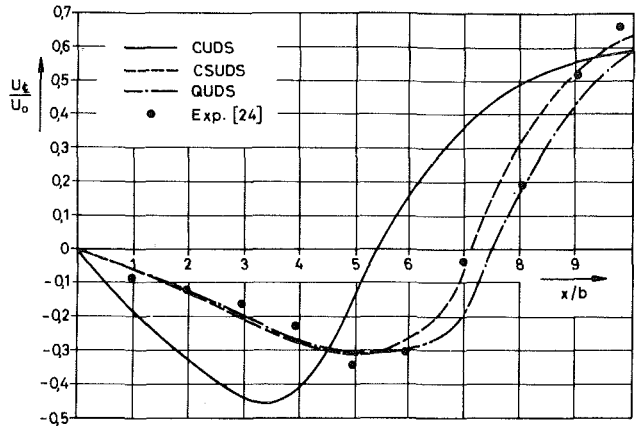

Fig. 10 Centerplane velocity, plane jet, $k-\epsilon$ model and curvature modification

1st Int. Conf. on Numerical Methods in Laminar and Turbulent Flow, University College Swansea, 1978, pp. 329-339.

3 Gosman, A.D., Khalil, E.E., and Whitelaw, J.H., "The Calculation of Two-Dimensional Turbulent Recirculating Flow," *Turbulent Shear Flows,* Vol. 1, Springer, 1979.

4 Durst, F., and Rastogi, A.K., "Turbulent Flow over 2D-Fences," *Turbulent Shear Flows,* Vol. 2, Springer Verlag, 1980.

5 Vasilic-Melling, D., "Three-Dimensional Turbulent Flow past Rectangular Bluff Bodies," Ph.D. thesis, University of London, 1976.

6 Pope, S.B., and Whitelaw, J.H., "The Calculation of Near-Wake Flows," *Journal of Fluid Mechanics,* Vol. 73, 1976, pp. 9-32.

7 de Vahl Davis, G., and Mallinson, G.D., "An Evaluation of Upwind and Central Difference Approximations by a Study of Recirculating Flow," *Computers and Fluids,* Vol. 4, 1976, pp. 29-43.

8 Raithby, G.D., "A Critical Evaluation of Upstream Differencing Applied to Problems Involving Fluid Flow," *Computer Methods in Applied Mechanics and Engineering,* Vol. 9, 1976, pp. 75-103.

9 Raithby, G.D., and Torrance, K.E., "Upstream-Weighted Differencing Schemes and their Application to Elliptic Problems Involving Fluid Flow," *Computers and Fluids,* Vol. 2, 1974, pp. 191-206.

10 Leschziner, M.A., "Practical Evaluation of Three Finite-Difference Schemes for the Computation of Steady-State Recirculating Flows," *Computer Methods in Applied Mechanics and Engineering,* Vol. 23, 1980, pp. 293-312.

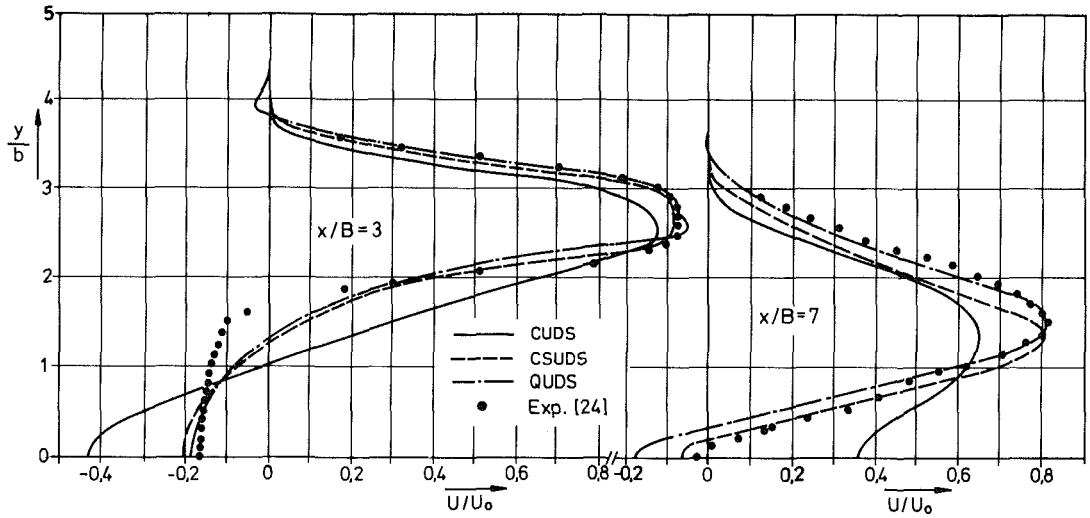

Fig. 11 Lateral profiles of axial velocity, plane jet, $k-\epsilon$ model and curvature modification

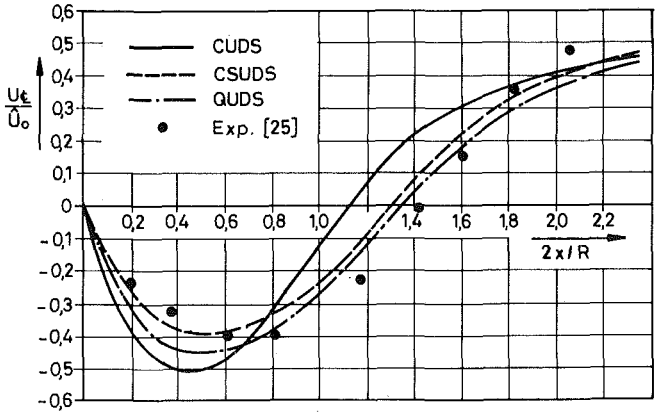

Fig. 12 Centerline velocity, annular jet, $k-\epsilon$ model and normal-stress modification

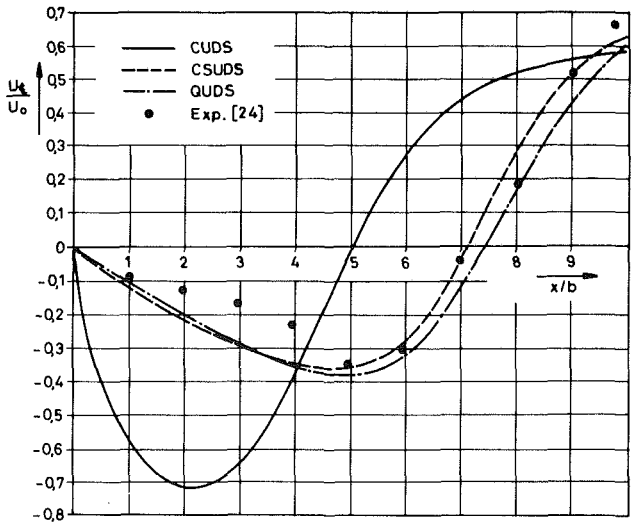

Fig. 13 Centerplane velocity, plane jet, $k-\epsilon$ model and normal-stress modification

11 Raithby, G.D., "Skew-Upwind Differencing Schemes for Problems Involving Fluid Flow," *Computer Methods in Applied Mechanics and Engineering,* Vol. 9, 1976, pp. 153–164.

12 Leonard, B.P., "A Stable and Accurate Convective Modelling Procedure Based on Quadratic Upstream Interpolation," *Computer Methods in Applied Mechanics and Engineering,* Vol. 19, 1979, pp. 59–98.

13 Briggs, M., Mellor, G., and Yamada, T., "A Second Moment Turbulence Model Applied to Fully Separated Flows," *Turbulence in Internal Flow,* ed. S.N. Murthy, Hemisphere Publishing Corporation, 1977, pp. 249–281.

14 Launder, B.E., and Spalding, D.B., "The Numerical Calculation of Turbulent Flows," *Computer Methods in Applied Mechanics and Engineering,* Vol. 3, 1974, p. 267.

15 Gibson, M.M., "An Algebraic Stress and Heat-Flux Model for Turbulent Shear Flow with Streamline Curvature," *International Journal of Heat and Mass Transfer,* Vol. 21, 1978, pp. 1609–1617.

16 Launder, B.E., Priddin, C.H., and Sharma, B.S., "The Calculation of Turbulent Boundary Layers on Spinning and Curved Surfaces," ASME JOURNAL OF FLUIDS ENGINEERING, Vol. 99, 1977, pp. 231–239.

17 Bradshaw, P., "Effects of Streamwise Curvature on Turbulent Flows," *AGARDograph,* No. 169, 1973.

18 Hanjalić, K., and Launder, B.E., "Preferential Spectral Transport by Irrotational Staining," *Turbulent Boundary Layers,* ASME, 1979, pp. 101–110.

19 Rodi, W., "Influence of Buoyancy and Rotation on Equations for the Turbulent Length Scale," *Proc. 2nd Symp. on Turbulent Shear Flows,* Imperial College London, 1979, pp. 10.37–10.42.

20 Gibson, M.M., and Rodi, W., "A Reynolds Stress Closure Model of Turbulence Applied to the Calculation of a Highly-Curved Mixing Layer," *Journal of Fluid Mechanics,* Vol. 103, 1981.

21 Irwin, H.P.A.H., and Arnot Smith, P., "Prediction of the Effect of Streamline Curvature on Turbulence," *The Physics of Fluids,* Vol. 18, 1975, pp. 624–630.

22 Launder, B.E., Reece, G.J., and Rodi, W., "Progress in the Development of a Reynolds-Stress Turbulence Closure," *Journal of Fluid Mechanics,* Vol. 68, 1975, pp. 537–566.

23 Gosman, A.D., and Pun, W.M., "Calculation of Recirculating Flows," (Lecture notes), Dept. of Mech. Eng., Imperial College London, Rep. No. HTS/74/2, 1974.

24 Militzer, J., "Dual Plane Parallel Turbulent Jets: The Measurement and Prediction of the Mean Velocity Field," Ph.D. thesis, University of Waterloo, Canada, 1977.

25 Durao, D.F.G., "The Application of Laser Anemometry to Free Jets and Flames with and without Recirculation," Ph.D. thesis, University of London, 1976.

APPENDIX A

Calculation of Curvature-Dependent $C\mu$

The following outlines how the terms $\partial U_s/\partial n$ and U_s/R_c, which appear in equation (14) Section 2.2 (i), are obtained from the velocity field (U, V).

The radius of curvature R_c is evaluated from:

$$\frac{1}{R_c} = \frac{d^2y/dx^2}{[1+(dy/dx)^2]^{3/2}}\Bigg|_{\psi=\text{const.}} \tag{19}$$

which is a well known formula from differential calculus. With $dy/dx|_{\psi=\text{const}} = V/U$, Equation (19) yields:

$$\frac{1}{R_c} = \frac{UV\left(\frac{\partial V}{\partial y} - \frac{\partial U}{\partial x}\right) + U^2\frac{\partial V}{\partial x} - V^2\frac{\partial U}{\partial y}}{(U^2+V^2)^{3/2}} \tag{20}$$

The magnitude of U_s is simply obtained from a vectorial summation of U and V, but care has to be taken in respect of the sign. This is, in principle, determined by examining the signs of U and V in relation to the sign of R_c. The gradient $\partial U_s/\partial n$ is evaluated as follows. Given a rate-of-strain tensor $S_{ij}^{(1)}$ in an orthogonal coordinate system '(1)', the corresponding tensor $S_{kl}^{(2)}$ in a rotated system '(2)' is related S_{ij} by:

$$S_{kl}^{(2)} = S_{ij}^{(1)} C_{ik} C_{jl} \tag{21}$$

where C_{ik} are the directional cosines between the unit vectors $\hat{i}^{(1)}$ and $\hat{k}^{(2)}$. For an angle of rotation θ, equation (21) yields for S_{ns}, the shear strain along the stream line:

$$S_{ns} = 0.5(S_{yy} - S_{xx})\sin 2\theta + S_{xy}\cos 2\theta \tag{22}$$

Since the strains in equation (22) are given by:

$$\begin{aligned} S_{ns} &\cong \frac{\partial U_s}{\partial n} - \frac{U_s}{R_c} \\ S_{xx} &= 2\frac{\partial U}{\partial x} \\ S_{yy} &= 2\frac{\partial V}{\partial y} \\ S_{xy} &= \frac{\partial U}{\partial y} + \frac{\partial V}{\partial x} \end{aligned} \tag{23}$$

the gradient $\partial U_s/\partial n$ can be determined given the angle θ between the velocity vector (i.e. the tangent to the streamline) and the x-axis.

I. Sud
Research Assistant Professor,
Department of Mechanical Engineering
and Materials Science,
Duke University,
Durham, N.C. 27706
Mem. ASME

J. B. Chaddock
Professor and Chairman,
Department of Mechanical Engineering
and Materials Science,
Duke University,
Durham, N.C. 27706
Mem. ASME

Drag Calculations for Vehicles in Very Long Tubes From Turbulent Flow Theory

Fundamental turbulent flow techniques are used to examine the annular fluid flow occurring in an idealized model of a high speed ground transportation system. The model consists of a smooth cylindrical train moving in an infinitely long tunnel, creating an annular gap with one wall in motion. The developing, and the fully developed, flow regions are separately analyzed by using fundamental relations of turbulent flow and Von Karman's similarity hypothesis. The relevant equations are developed and numerical solution procedures presented. Limited sample calculations show good agreement with existing empirical and experimental results.

Introduction

A proposed configuration for high-speed ground transportation has been a vehicle, or train of vehicles, moving in a completely enclosing tube. In an idealized case, the train could be cylindrical, creating a concentric annulus flow with one moving wall. Choosing a coordinate system fixed to the vehicle, the annulus will have an outer wall moving at a constant velocity and a stationary inner wall.

Numerous experimental and empirical studies have been conducted on models of vehicles travelling in tubes. Some of the well known investigators in this field are Gouse and Hoppe [1], Magnus and Panunzio [2], and Strom [3]. Davidson [4] gives an extenisve bibliography of the published papers on drag of vehicles travelling in tubes.

Earnshaw [5] has proposed a model using the logarithmic law of the wall for the flow in the annular gap between the vehicle and the tunnel. This model is for long vehicles and assumes fully-developed flow to be existing over the majority of the length of the vehicle. Experiments conducted by Nayak, Gralewski, and Stevens [6] indicate that this model is sufficiently accurate for most engineering purposes. However, the assumption of a fully developed flow existing over the majority of the length of the vehicle may not be valid. The sample calculation performed here shows that the developing flow region can extend for more than 15m at the leading part of the train. The pressure drop at the leading edge of the train was found to be more than four times the pressure drop in the fully developed flow region. Considering the annular flow to be fully developed for the entire length of the train could result in significant underestimating of the drag for a short train.

Brighton and Jones [7] have shown that the logarithmic law of the wall is inadequate for describing the flow in a stationary annulus, particularly for large radius ratios. Although most train-tunnel combinations have small radius ratios, the extension of a concept not generally valid in stationary annulus to an annulus with one wall in motion can be questioned. It was our purpose to conduct a fundamental turbulent flow analysis to study the flow in the annular gap between the train and the tunnel and to calculate the drag on such trains. Such an analysis would also be a useful tool for studying the flow mechanism in the vehicle-tunnel annular gap.

Two regions of flow were considered, the entrance or developing flow region at the leading part of the vehicle, and a fully developed velocity profile established some distance downstream. The analysis and numerical solution procedures were separately developed for these two regions, in each case using the fundamental equations of turbulent flow and Von Karman's similarity hypothesis. Limited sample calculations, performed with the aid of a computer, show good agreement with existing empirical and experimental results.

Literature Survey on Annular Flow

Among the early studies on turbulent annular flow, two often cited are those of Heidiger [8] and Mikrjukov [9]. Both have reported that the ratio of the radius of maximum velocity in turbulent flow to that in laminar flow (r_{mt}/r_{ml}) is greater than unity. More recent results of Brighton and Jones [7], of Kays, Leung, and Reynolds [10], and of Quarmby [11] report that the ratio, r_{mt}/r_{ml}, is less than unity. This result is also confirmed by Lawn and Elliot [12]. None of these experimental investigations have been successful in presenting a general correlation for the turbulent velocity profile in an annulus.

Of the several analytical studies that have been reported on fully developed flow in an annulus, that of Quarmby [13] has used the more fundamental approach, and yields results in good agreement with his experimental results [11]. Barrow, Lee, and Roberts [14] applied Von Karman's similarity hypothesis, and set $r_{mt}/r_{ml} = 1$. Their results were in poor agreement with experimental velocity profiles on the inner wall. Levy [15] used a modified version of Reichardt's expression for eddy diffusivity. His results for the inner velocity

Contributed by the Fluids Engineering Division for publication in the JOURNAL OF FLUIDS ENGINEERING. Manuscript received by the Fluids Engineering Division, October 9, 1979.

profile were also in poor agreement with experiments. Michiyoshi and Nakajima [16] used the correlation of Kays, Leung, and Reynolds [10] for the radius of maximum velocity. This procedure can be questioned as it makes r_{mt} dependent only on the radius ratio, independent of Reynolds number.

Based on a study of the literature cited above, it was our judgment to use the more fundamental analysis approach of Quarmby [13] for the fully developed flow region.

A good analysis of the annular entry length flow problem is not available in the literature. Okiishi and Serovy [17] obtained some experimental results, and in a later paper Okiishi and Bathie [18] present an approximate method for predicting inlet turbulent flow development characteristics for an annular region. Wilson and Medwell [19] have presented integral solutions for the boundary layer flow in an annulus. They used a modified Reichardt's expression for the eddy viscosity. Levy [15] had earlier used a similar procedure for fully developed annular flow, but his results for the inner velocity profile were in poor agreement with experiments. The calculations of Wilson and Medwell could, therefore, be subject to the same inaccuracies. Quarmby's success in applying Von Karman's equations for the fully developed flow region, were the basis for our selecting this approach for the developing flow region. We were also influenced by the fact that his annular flow experiments were in good agreement with the theory.

Fully Developed Flow Region

Development of Equations. At any location in a one-dimensional turbulent flow field, the shear stress can be represented by

$$\tau=\rho(\nu+\epsilon_m)\frac{du}{dy} \tag{1}$$

This can be nondimensionalized in the usual way, to give

$$\frac{\tau}{\tau_w}=\left(1+\frac{\epsilon_m}{\nu}\right)\frac{du^+}{dy^+} \tag{2}$$

For the viscous sublayer (and buffer layer) Deissler's empirical equation for eddy diffusivity in nondimensional form is written as

$$\frac{\epsilon_m}{\nu}=n^2u_1{}^+y^+[1-\exp(-n^2u_1{}^+y^+)] \tag{3}$$

For the turbulent region, the similarity hypothesis of Von Karman [20] yields

$$\epsilon_m=l^2\left|\frac{du_2}{dy}\right| \tag{4}$$

where

$$l=K\left|\frac{du_2/dy}{d^2u_2/dy^2}\right| \tag{5}$$

It was convenient to divide the flow into two regions of $r < r_{mt}$, and $r > r_{mt}$ as illustrated in Fig. 1. The velocity profile at the annular entrance was assumed to be uniform. Using subscripts 1 and 2 for the viscous sublayer and turbulent zones of flow, respectively, equations (1) through (5) yield the following differential relationships for the annulus velocity profile.

1. In the outer region, $r_m < r < r_0$:

(a.) Viscous sublayer; $0 < y_0 < y_{l0}$

$$\frac{du_{10}^{+\prime}}{dy_0^+}=\frac{\tau/\tau_0}{1+n_0{}^2u_{10}^{+\prime}y_0^+[1-\exp(-n_0{}^2u_{10}^{+\prime}y_0^+)]} \tag{6}$$

with $u_{10}^{+\prime}=0$ at $y_0^+=0$

(b.) Turbulent region, $y_{l0} < y_0 < y_{m0}$

$$\frac{d^2u_{20}^{+\prime}}{dy_0^{+2}}=\frac{-K(du_{20}^{+\prime}/dy_0^+)^2}{(\tau/\tau_0-du_{20}^{+\prime}/dy_0^+)^{1/2}} \tag{7}$$

with $u_{20}^{+\prime}=u_{10}^{+\prime}$, and, $\dfrac{du_{20}^{+\prime}}{dy_0{}^+}=\dfrac{du_{10}^{+\prime}}{dy_0^+}$ at $y_0^+=y_{l0}^+$

The superscript $'$ represents velocity with respect to the outer wall. To obtain true velocities it is necessary to add V^+, e.g. $u_{10}^+=u_{10}^{+\prime}+V^+$, etc.

2. In the inner region, $r_i < r < r_m$:

(a.) Viscous sublayer, $0 < y_i < y_{li}$:

Nomenclature

a = r_{mt}/r_i
b = r_0/r_i
f = friction factor
D_H = hydraulic diameter
D_l = drag per linear foot of vehicle
D_T = total drag
K = constant in Von Karman's similarity hypothesis
n = Deissler's damping factor
p = undisturbed tunnel pressure level
ΔP_w = pressure loss in the wake region
r = radius
r_{ml} = radius of maximum velocity in viscous flow
r_{mt} = radius of maximum velocity in turbulent flow
r^+ = ru^*/ν
Re_N = Reynolds number, D_Hu_b/ν
$r_{\delta i}$ = $r_i+\delta_i$
$r_{\delta i}^+$ = $r_{\delta i}u_i{}^*/\nu$
$r_{\delta 0}$ = $r_0-\delta_0$
s = radius ratio, r_i/r_0
u = time averaged axial fluid velocity
u_b = bulk velocity
u^+ = nondimensionalized velocity, u/u^*
u^* = $(\tau_w/\rho)^{1/2}$
u_δ = velocity in the core region
V = vehicle velocity
V^+ = U/u_0^*
x = axial distance
y = distance from wall
y_l = distance from wall to edge of viscous sublayer
y^+ = yu^*/ν
z = distance from inner wall
δ = thickness of fluid boundary layer
ϵ_m = eddy diffusivity of momentum
μ = viscosity
ν = kinematic viscosity
ρ = density
τ = shear stress

Subscripts

b = bulk value
i = refers to the inner region of the flow
l = at boundary between viscous and turbulent flow zones
m = at point where velocity in annulus is a maximum
0 = refers to the outer region of the flow
t = turbulent
w = at wall
δ = core region or outer edge of boundary layer
1 = in viscous sublayer
2 = turbulent region

Superscripts

$'$ = denotes velocities with respect to outer wall
$*$ = friction velocity
$+$ = nondimensionalized distance or velocity

$$\frac{du_{1i}^+}{dy_i^+} = \frac{\tau/\tau_i}{1+n_i^2 u_{1i}^+ y_i^+ [1-\exp(-n_i^2 u_{1i}^+ y_i^+)]} \tag{8}$$

with $u_{1i}^+ = 0$ at $y_i^+ = 0$

(*b.*) Turbulent region, $y_{li} < y_i < y_{mi}$:

$$\frac{d^2 u_{2i}^+}{dy_i^{+2}} = \frac{-K(du_{2i}^+/dy_i^+)^2}{(\tau/\tau_i - du_{2i}^+/dy_i^+)^{1/2}} \tag{9}$$

with $u_{2i}^+ = u_{1i}^+$, and, $\frac{du_{2i}^+}{dy_i^+} = \frac{du_{1i}^+}{dy_i^+}$ at $y_i^+ = y_{li}^+$

The boundary conditions imposed on the above four equations are that the values of the velocities and their slopes be matched at the edge of the viscous sublayers. To integrate these equations, additional relationships had to be developed. These relationships, developed by Sud [21], are given below.

$$\frac{\tau}{\tau_i} = \frac{r_i^+ [(r_i^+ + y_{mi}^+)^2 - (y_i^+ + r_i^+)^2]}{(y_i^+ + r_i^+)[(r_i^+ + y_{mi}^+)^2 - r_i^{+2}]} \tag{10}$$

$$\frac{\tau}{\tau_0} = \frac{r_0^+ [(r_0^+ - y_0^+)^2 - (r_0^+ - y_{m0}^+)^2]}{(r_0^+ - y_0^+)[r_0^{+2} - (r_0^+ - y_{m0}^+)^2]} \tag{11}$$

$$\frac{\tau_0}{\tau_i} = \frac{(b^2-a^2)}{b(a^2-1)} \tag{12}$$

$$y_{m0}^+ = \left(1 - \frac{a}{b}\right) r_0^+ \tag{13}$$

$$y_{mi}^+ = \frac{(a-1)}{b}\left[\frac{b(a^2-1)}{b^2-a^2}\right]^{1/2} r_0^+ \tag{14}$$

$$r_i^+ = \frac{1}{b}\left[\frac{b(a^2-1)}{b^2-a^2}\right]^{1/2} r_0^+ \tag{15}$$

$$u_{m0}^+ = u_{mi}^+ \left[\frac{b(a^2-1)}{b^2-a^2}\right]^{1/2} \tag{16}$$

The Reynolds number for annulus flow is expressed in terms of the equivalent diameter, $D_H = 2(r_0 - r_i)$, and the bulk velocity, thus, $\mathrm{Re}_N = D_H u_b/\nu$. In terms of the variables for the inner and outer regions this becomes,

$$\mathrm{Re}_N = \frac{4}{b+1}\left[\frac{1}{r_i^+}\int_0^{y_{mi}^+} u_i^+ (y_i^+ + r_i^+) dy_i^+ + \frac{b}{r_0^+}\int_0^{y_{mo}^+} u_0^+ (r_0^+ - y_0^+) dy_0^+\right] \tag{17}$$

The friction factor can be expressed as

$$f = \frac{2r_0\tau_0 + 2r_i\tau_i}{(r_0+r_i)\rho u_b^2} = \frac{8(b-1)^3}{b(b^2-a^2)}\left(\frac{r_0^+}{\mathrm{Re}_N}\right)^2 \tag{18}$$

Quarmby [13] obtained good agreement with experimental results letting

$$n_i^2 = n_0^2 = n^2,\ y_{li}^+ = y_{l0}^+ = y_l^+,\ K = 0.36$$

Quarmby [13], gives the relationship between y_l^+ and Re_N, and between n^2 and y_0^+. Reynolds numbers for our problem have values, such that $y_m^+ > 5 \times 10^3$. Then, from Quarmby [13], $n^2 = 0.0154$ and $y_l^+ = 15$.

Solution of the Differential Equations. The preceding development of equations and relationships has closely followed that of Quarmby [13]. The differences were due to the motion of the outside wall. Quarmby obtained his solutions using as independent variables $b(= r_0/r_i)$ and r_0^+. In the solutions sought here, it seemed more practical to start from the following known quantities: r_0, b, fluid properties, and Re_N. Starting from these quantities the following iterative procedure was used to obtain numerical integrations of the velocity profile.

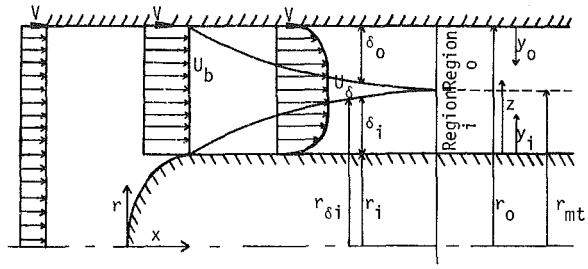

Fig. 1 Developing and fully developed flow in an annulus with outer wall moving at velocity *V*

1. Assume, $r_0^+ = r_0(\tau_0/\rho)^{1/2}/\nu$ and calculate τ_0
2. Assume, $a = r_{mt}/r_i$
3. Calculate, y_{m0}^+ [equation (13)]
   y_{mi}^+ [equation (14)]
   r_i^+ [equation (15)]
4. Calculate, τ/τ_i [equation (10)]
   τ/τ_0 [equation (11)]
5. Integrate equation's (6), (7), (8), and (9) to obtain the velocity profile in the inner and outer region, and obtain u_{m0}^+ and u_{mi}^+
6. Calculate, a [equation (16)]. Compare with assumed value, step 2, and repeat to convergence criterion
7. Calculate, Re_N [equation (17)]
8. Calculate, r_0^+ [equation (18)]. Compare with assumed value, step 1, and repeat to convergence criterion.
9. Calculate, f [equation (18)]

$$dp/dx = fu_b^2/(r_0 - r_i)$$

Hamming's modified predictor-corrector method [22], for the solution of general initial-value problems, was used in the integration for the velocity profiles. The above procedure was programmed for execution on an IBM 370/165 computer system. The program yields values of τ_0, τ_i, r_{mt}, f, and dp/dx. It was of interest also to determine the ratio, r_{mt}/r_{ml}. To this end a solution of the Navier-Stokes equations for fully-developed, viscous flow in a concentric annulus, with the outer wall moving at a constant velocity, V, was obtained. The radius of the maximum velocity, from this solution was:

$$r_{ml} = \left[\frac{(g_c/4\mu)(dp/dx)(b^2-1)r_i^2 - V}{(g_c/2\mu)(dp/dx)\ln b}\right]^{1/2} \tag{19}$$

Validation of Formulation and Numerical Procedure. As a check on the proper formulation and accuracy of the numerical method used, solutions were obtained for the degenerate case of zero wall velocity ($V = 0$). These results were compared with the solutions of Quarmby [13] and found to be in excellent agreement by Sud [21].

Developing Flow Region

Development of Equations. The integral equations for developing turbulent flow in an annulus have been presented by Okiishi and Serovy [17] and by Wilson and Medwell [19].

Figure 1 illustrates the conditions for the developing velocity profile with the coordinate system fixed to the vehicle, or inner wall, and with the outer wall of the annulus moving at a constant velocity, V. Detailed developments of the momentum integral equations are given in Wilson and Medwell [19] and Sud [21]. The resulting equations are:

$$\frac{x}{r_i} = \int_0^{\{\}} \frac{1}{(r_i^+)^2} d\left[\int_{r_i^+}^{r_{\delta i}^+} (u_{\delta i}^+ - u^+) u^+ r^+ dr^+\right] + \int_{\frac{Re_N}{2}\frac{s}{1-s}}^{u_{\delta i}^+ r_i^+} \left\{\frac{u_{\delta i}^+ [(r_{\delta i}^+)^2 - (r_i^+)^2]}{2(r_i^+)^3} - \frac{1}{(r_i^+)^3}\int_{r_i^+}^{r_{\delta i}^+} u^+ r^+ dr^+\right\} d(u_{\delta i}^+ r_i^+) \quad (20)$$

and

$$\frac{x}{r_0} = \int_0^{\{\}} \frac{1}{(r_0^+)^2} d\left[\int_{r_{\delta 0}^+}^{r_0^+} (u_{\delta 0}^+ - u^+) u^+ r^+ dr^+\right] + \int_{\frac{Re_N}{2}\frac{1}{1-s}}^{u_{\delta 0}^+ r_0^+} \left\{\frac{u_{\delta 0}^+ [(r_0^+)^2 - (r_{\delta 0}^+)^2]}{2(r_0^+)^3} - \frac{1}{(r_0^+)^3}\int_{r_{\delta 0}^+}^{r_0^+} u^+ r^+ dr^+\right\} d(r_{\delta 0}^+ r_0^+) \quad (21)$$

The upper limits of the first integrals in equations (20) and (21) are the variables of the differentials inside those integrals.

The Reynolds number, obtained from the equation of continuity, can be expressed as

$$Re_N = 2\left\{\frac{r_{\delta 0}^{+2} u_{\delta 0}^+}{r_0^+(1+s)} - \frac{s r_{\delta i}^{+2} u_{\delta i}^+}{r_i^+(1+s)}\right\} + \frac{4}{1+s}\left\{\frac{s}{r_i^+}\int_{r_i^+}^{r_{\delta i}^+} u^+ r^+ dr^+ + \frac{1}{r_0^+}\int_{r_{\delta 0}^+}^{r_0^+} u^+ r^+ dr^+\right\} \quad (22)$$

To perform the integration of equation (20) and equation (21) the Von Karman similarity hypothesis is assumed for representing the velocity distribution. The shear stress and eddy viscosity are again represented by equations (2), (3), and (4).

As illustrated in Fig. 1, the flow field has two boundary layers, one at the inner wall of thickness δ_i (and radius $r_{\delta i}$) and one at the wall of thickness δ_0. Equations (6), (7), and (8), and (9) are still valid, provided the application ranges for these equations are redefined as follows.

1. Outer Region, $r_{\delta 0} < r < r_0$:
   a. Viscous sublayer; $0 < y_0 < y_{l0}$
   b. Turbulent Region; $y_{l0} < y_0 < y_{\delta 0}$
2. Inner Region, $r_i < r < r_{\delta i}$:
   a. Viscous sublayer; $0 < y_i < y_{li}$
   b. Turbulent Region; $y_{li} < y_i < y_{\delta i}$

To obtain the velocity distribution, an assumption on the variation of τ/τ_w must be made. Following Wilson and Medwell [19], a linear variation of τ/τ_w was used. As in the case of the fully developed flow, the authors have assigned the following values to the constants in the expressions for eddy diffusivity:

$$n_i^2 = n_0^2 = n^2 = 0.0154, y_{li}^+ = y_{l0}^+ = y_l^+ = 15, K = 0.36$$

Solution of the Differential Equations. Again, Hamming's modified predictor-corrector method [22] was used to integrate the velocity profile. The solution procedure, as finally evolved, is outlined in Table 1. Two looping interpolations are performed on the variables δ_0^+ and r_i^+. The integration of equations (20) and (21) were performed by the trapezoidal rule.

Sample Calculations

The above procedures were used to perform sample calculations on a vehicle-tunnel system. The principal criteria for the parameter selection was that the resulting model be practically feasible and consistent with the analysis developed above. The parameter selection is discussed by Sud [21]. The vehicle tunnel dimensions were chosen as:

Tunnel Diameter	4.88m	(16 ft)
Vehicle Diameter	3.66m	(12 ft)
Vehicle Length	122m	(400 ft)

Table 1 Outline of procedure used in the numerical solution of the turbulent boundary layer equations

1. Select a value δ_i^+ and integrate Equations (8) and (9), with the redefined regions, to obtain the velocity profile in the inner region.
2. Choose values of δ_0^+ over a sufficiently wide range (eight values of δ_0^+ from 70 to 16,000 were chosen)

   For each value of δ_0^+:
3. Integrate Equations (6) and (7), with the redefined regions, to obtain the relative outside velocity profile (in terms of u_0^+).
4. Choose values of r_i^+ over a sufficiently wide range (eight values of r_i^+ from 90,000 to 205,000 were chosen)

   For each value of r_i^+:
5. Obtain τ_{wi} and τ_{wo} and thus u_i^* and u_0^* noting that $u_{\delta 1} = u_{\delta 2}$. Determine V^+ and using the results of step 3, obtain u_0^+.
6. Calculate the Reynolds number from (22) for each value of r_i^+. From the actual value of Re_N, interpolate for the value of r_i^+. Repeat step 5 with this value of r_i^+.

   Interpolation
7. Calculate x/r_i and x/r_0 from Equations (20) and (21).
8. Determine a calculated value of s for each value of δ_0^+.
9. From the real value of s, interpolate to get the actual value of δ_0^+. Repeat calculations for this value.
10. Knowing the core velocity for two subsequent points, obtain $dp/dx = -\rho u_\delta (du_\delta/dx)$
11. Obtain friction factors using these dp/dx.

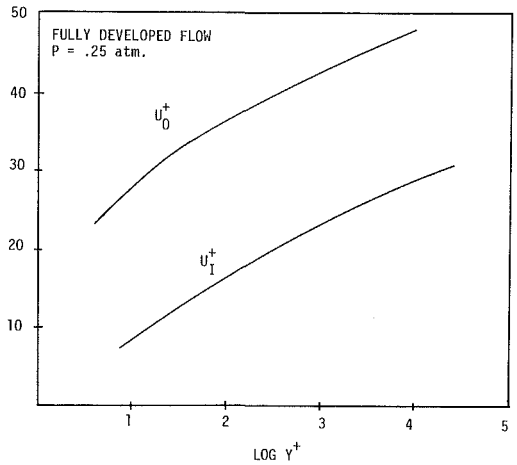

Fig. 2 Fully developed flow profile on the outer and inner surfaces, p = 0.25 atm.

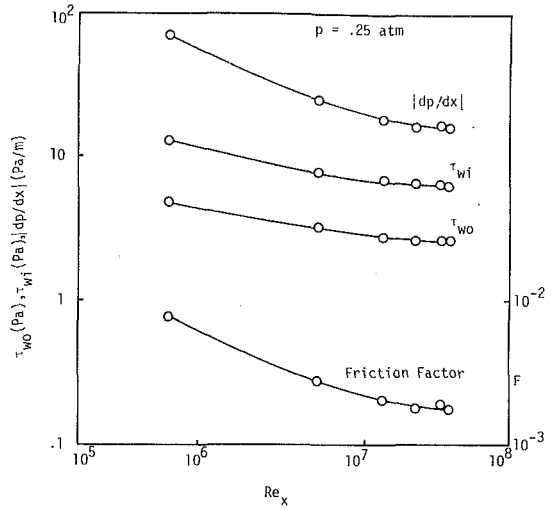

Fig. 3 Wall shear stresses, pressure gradient and friction factor for developing flow. p = 0.25 atm.

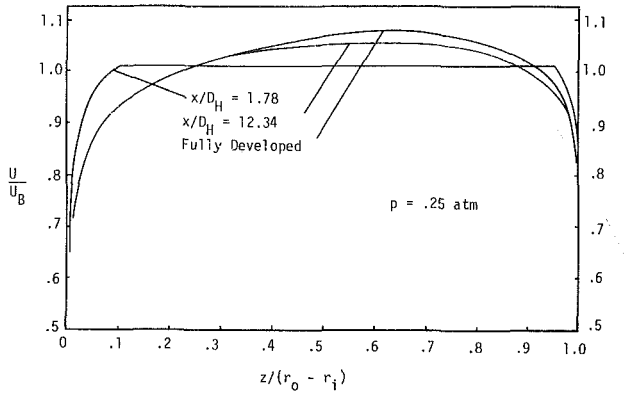

Fig. 4 Developing velocity profile in the entrance region. p = 0.25 atm.

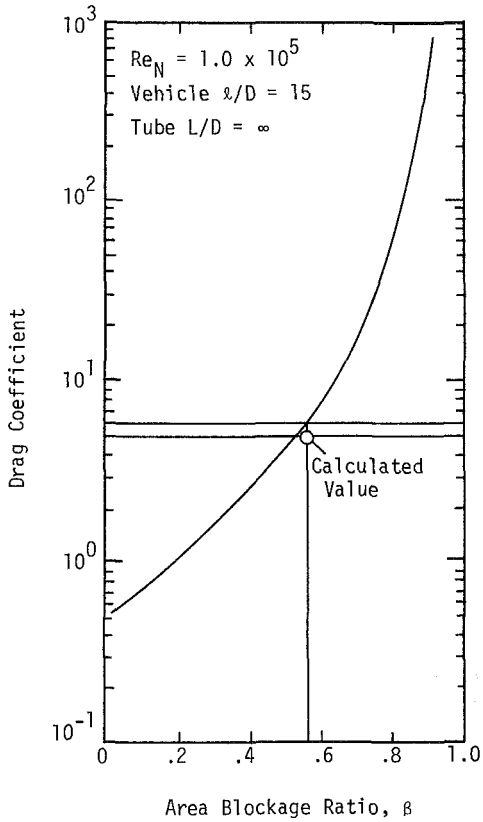

Fig. 5 Comparison of experimental drag coefficients of principal investigators (reproduced from Davidson [4]).

Two tunnel pressure levels of 0.1 and 0.25 atmospheres were used, and a single train speed of 61m/s(200 ft/s)

Fully Developed Flow Region. The dimensionless fully developed velocity profiles for the tunnel pressure level of 0.25 atm is given in Fig. 2. Sud [21] gives various other plots, including the velocity distribution for the pressure level of 0.1 atm, and the variation of ϵ_m/ν over the annular section.

Developing Flow Region. Sud [21] gives the detailed results obtained for the two tunnel pressure levels considered. The values of δ_i^+ were increased in increments of 5000, until a further increment of 5000 would overlap the fully developed region. At this point, further increments of δ_i^+ were reduced to 2000, and the solution carried forward until the fully developed region was reached.

A comparison of the results for the developing region with those for fully developed flow showed good agreement [21]. Since the solutions for the developing and the fully developed regions were obtained independently it lends confidence to the results.

Figure 3 shows the variation of the wall shear stresses, pressure gradient, and friction factor in the developing flow region for a pressure level of 0.25 atm. As expected, these parameters decrease with distance from the inlet to the annular section, to asymptotically merge to the fully developed values. Figure 4 compares the velocity profile in the developing region with the fully developed velocity profile. It can be seen that for large values of x/D_H, the developing profile compares well with the solution for fully developed flow. Plots for the tunnel pressure level of 0.1 atm are also available [21].

Drag Calculations. The total drag on the vehicle will be a sum of the skin friction drag and the pressure or form drag, i.e.,

$$D_T = D_{sf} + D_f \tag{23}$$

The pressure drag is the means by which the shear stress on the tunnel wall is coupled to the vehicle drag.

The two factors contributing to the pressure drag are the flow around the vehicle and the pressure loss in the wake due to the sudden expansion in that area. It was assumed that the form drag is given by the product of the frontal area and the total pressure drop across the length of the tunnel.

Substituting the expressions for the skin friction and pressure drag into equation (23), the total drag becomes

$$D_T = \pi r_i \int_0^L \left(2\tau_i - r_i \frac{dp}{dx}\right) dx + \pi r_i^2 \Delta P_w \tag{24}$$

Hammit [23] gives an expression for the pressure loss in the wake region as:

$$\frac{\Delta P_w}{\frac{1}{2}\rho V^2} = \alpha_w \left(\frac{\beta}{1-\beta}\right)^2 \tag{25}$$

where β is the vehicle blockage ratio and α_w has a value between 0 and 1. A very low value of α_w indicates a well streamlined body and a high value of α_w indicates a blunt body. Except for practical limitations, the vehicle in our model will be well streamlined. Thus the value of α_w was chosen as 0.25 for this analysis.

Using Equation (24), the drag on the vehicle is

$$\begin{aligned} p &= 0.10 \text{ atm} \quad D_T = 14{,}310 \text{ N} \\ p &= 0.25 \text{ atm} \quad D_T = 30{,}684 \text{ N} \end{aligned} \tag{26}$$

of which 912 N and 2277 N, respectively, are due to the wake losses.

Comparison With Empirical and Experimental Results. Several investigators [1], [24], [25], [26], [27], have reported experimental results from models simulating vehicles travelling in tubes. Davidson [4] has reduced and correlated the results of all these investigators to a common plot of drag coefficient based on vehicle speed and area versus the area blockage ratio. This plot is reproduced as Fig. 5 and is for a vehicle l/d of 15 and a Reynolds number of 10^5 based on vehicle speed and diameter. To obtain analytical results from our model corresponding to these conditions, equation (24) was used to recalculate the drag with a vehicle length of 54.9m (180 ft). The drag coefficient so calculated, was adjusted by the 1/6 rule suggested in reference [28], to get a value corresponding to a Reynolds number of 10^5. The resulting value for the drag coefficient is 5.0, as indicated on Fig. 5, for both the pressure levels of 0.1 and 0.25 atm. The corresponding correlated experimental value from Fig. 5 is 6.0. The calculations performed yield results considered to be in reasonable agreement with established experimental values. It should be noted that our analytical results were 16 percent lower than the experimental values. The analytical results have not accounted for losses occurring at the preentrance to the annular flow region, or for other losses inherent in an experimental study of this problem. Proper accounting of these losses could improve the agreement between the analytical and the experimental results.

Discussion

A high speed ground transportation vehicle, travelling in a totally enclosing tube has been modelled as a concentric annulus with one wall in motion. The analysis yielded a system of differential equations which can be solved by numerical procedures which are outlined. Calculations have been performed for a single condition. The result obtained has been compared with established empirical and analytical results and found to be in reasonable agreement. The results show that a comprehensive model, based on the use of turbulent flow theory, can be used to predict the drag on idealized models of vehicles in tubes. Additional comparisons with experimental results would be desirable for a definitive validation of the theoretical model. The limited scope and funding for this research study precluded additional comparisons from being made.

References

1 Hoppe, R. G., and Gouse, S. W., Jr., "Fluid Dynamic Drag on Vehicles Traveling Through Tubes," Carnegie-Mellon University Report No. 1-59076-1, Aug. 1969, NTIS No. PB 188 451.

2 Magnus, D., and Panunzio, S., "Aerodynamics of High Speed Ground Vehicles in Tubes," GASL, Presented at CASE/AIAA Meeting in Ottawa, Canada, July 1969. AIAA Paper No. 69-140.

3 Strom, C., "Aerodynamic Analysis of Vehicles in Tunnels," Paper presented at International Symposium on Aerodynamics and Ventilation of Vehicle Tunnels, University of Kent, Canterbury, England, Apr. 1973.

4 Davidson, J. V., "Aerodynamic Drag of Tube Vehicles," Masters thesis, Duke University, Durham, 1974.

5 Earnshaw, P. B., "On the Aerodynamic Resistance to Long Trains Passing Through Long Close-Fitting Tunnels," RAE, Tech. Rept. 70199, Nov. 1970.

6 Nayak, U. S. L., Gralewski, Z. A., and Stevens, S. J., "The Aerodynamic Drag of Tube Vehicles Travelling at Low Subsonic Speeds," Paper presented at the Second International Symposium on the Aerodynamics and Ventilation of Vehicle Tunnels, Cambridge, England, Mar. 1976.

7 Brighton, J. A., and Jones, J. B., "Fully Developed Turbulent Flow in Annuli," ASME *Journal of Basic Engineering*, Vol. 86, Dec. 1964, pp. 835–844.

8 Rothfus, R. R., Monrad, C. C., Sikchi, K. G., and Heidiger, W. J., "Isothermal Skin Friction in Flow through Annular Sections," *Industrial and Engineering Chemistry*, Vol. 47, May 1955, pp. 913–918.

9 Mikrjukov, V., "Turbulent Flow of a Fluid in a Straight Pipe of Annular Cross-Section," *Technical Physics of the USSR*, State Technical Theoretical Press, Leningrad, Vol. 4, 1937, pp. 961–977.

10 Kays, W. M., Leung, E. Y., and Reynolds, W. C., "Heat Transfer with Turbulent Flow in Concentric and Eccentric Annuli with Constant and Variable Heat Flux," Stanford University Report AHT 4, Stanford 1962.

11 Quarmby, Alan, "An Experimental Study of Turbulent Flow Through Concentric Annuli," *International Journal of Mechanical Sciences*, Vol. 9, Apr. 1967, pp. 205–221.

12 Lawn, C. J., and Elliot, C. J., "Fully Developed Turbulent Flow through Concentric Annuli," *Journal of Mechanical Engineering Science*, Vol. 14, June 1972, pp. 195–204.

13 Quarmby, Alan, "An Analysis of Turbulent Flow in Concentric Annuli," *Applied Scientific Research*, Vol. 19, July 1968, pp. 250–293.

14 Barrow, H., Lee, Y., and Roberts, A., "The Similarity Hypothesis Applied to Turbulent Flow in an Annulus," *International Journal of Heat and Mass Transfer*, Vol. 8, Dec. 1965, pp. 1499–1505.

15 Levy, S., "Turbulent Flow in an Annulus," ASME *Journal of Heat Transfer*, Vol. 89, Feb. 1967, pp. 25–31.

16 Michiyoshi, Itaru, and Nakajima, Tsuyoshi, "Fully Developed Turbulent Flow in a Concentric Annulus," *Journal of Nuclear Science and Technology*, Vol. 5, July 1968, pp. 354–359.

17 Okiishi, T. H., and Serovy, C. K., "An Experimental Study of the Turbulent-Flow Boundary-Layer Development in Smooth Annuli," ASME *Journal of Basic Engineering*, Vol. 89, Dec. 1967, pp. 823–836.

18 Okiishi, T. H., and Bathie, W. W., "An Approximate Method for Predicting Annulus Inlet Turbulent Flow Development Characteristics," ASME *Journal of Basic Engineering*, Vol. 92, Sept. 1970, pp. 667–669.

19 Wilson, N. W., and Medwell, J. O., "An Analysis of the Developing Turbulent Hydrodynamic and Thermal Boundary Layers in an Internally Heated Annulus," ASME *Journal of Heat Transfer*, Vol. 64, Feb. 1971, pp. 25–32.

20 Schlichting, Hermann, *Boundary Layer Theory*, Sixth Edition, McGraw-Hill New York, 1968.

21 Sud, Ish, "An Analysis of Turbulent Flow and Heat Transfer for Vehicles Travelling in Tubes," Ph.D. dissertation, Duke University, Durham, 1974.

22 Carnahan, B., Luther, H. A. and Wilkes, J. O., *Applied Numerical Methods*, Wiley, New York, 1969.

23 Hammit, Andrew G., *The Aerodynamics of High Speed Ground Transportation*, Western Periodicals Company, 1973.

24 Grittner, S. F., "Aerodynamic Characteristics of Vehicles Travelling in Perforated Tubes," Master's thesis, Duke University, Durham, N.C., Aug. 1972.

25 Smith, L. D., "Experimental Investigation of Tube Vehicle Aerodynamic Characteristics," Master's thesis, Duke University, Durham, N.C., Aug. 1972.

26 Caltech, "Experimental Aerodynamic Characteristics of Vehicles in Confined Spaces," Technical Report No. IRT-UMTA-DC-MTD-7-72-13, Caltech, Pasadena, Calif., Dec. 1972.

27 Gregorek, G. M., and Engle, J. H., "An Experimental Study of Aerodynamics of Vehicles Travelling at High Speeds through Long Tubes," The Ohio State University, Columbus, Ohio. Presented at the International Conference on Vehicle Mechanics at Wayne State University, July 1968.

28 Gouse, S. W., Noyes, B. S., and Swarden, M., "Aerodynamic Drag on a Body Travelling in a Tube," PB 177 211, Oct. 1967.

Journal of Fluids Engineering

Book Reviews

Computational Fluid Dynamics, edited by Wolfgang Kollman, 1980, Hemisphere Publishing Corp., 612 pp., $55.00. **Computational Fluid Dynamics, Vol. 2,** edited by Wolfgang Kollman, 1980, Hemisphere Publishing Corp., 265 pp., $55.00

REVIEWED BY PHILIP T. HARSHA

As progress in the modeling of the physical aspects of fluid dynamics continues, the need for more general and more capable numerical solution techniques continues to grow: for many applications of current interest the computational problems are more severe than those involved in modeling the physical phenomena. For some problems in fluid dynamics, the selection of a computational approach can affect the solution in unexpected ways. Thus a working knowledge of the techniques available is essential to the fluid dynamicist who is concerned with flowfields in complicated geometries or flows with strongly coupled heat and mass transfer effects. At the same time, the literature available on computational techniques continues to burgeon, so that volumes such as the two reviewed here, which incorporate survey articles on a variety of subjects in the area of computational fluid dynamics, fill a continuing need.

Both of these volumes represent collections of notes from lecture series held at the von Karman Institute for Fluid Dynamics. The first volume incorporates notes from lectures given in March 1978. These lectures include discussions of body-fitted coordinate systems, panel methods for subsonic aerodynamics, hydrodynamic stability problems, finite element methods applied to transonic aerodynamics, inviscid internal flows (of both mixed transonic and rotational subsonic character), fast elliptic solvers, the use of multi-grid systems to enhance the rate of convergence of numerical solutions, the computation of vortex flows by panel methods, and the application of a technique called perturbed functional iterations for the numerical solution of nonlinear implicit finite difference equations. Volume 2 represents lectures given in March 1979; here the subjects covered include compressible high Reynolds number flows, three-dimensional viscous flows, free-surface problems, and an overview of numerical methods for time-dependent partial differential equations.

Since the coverage of subjects in these two volumes is quite broad, different articles will be of more immediate interest to different readers. Thus, this reviewer found the article on body-fitted coordinates in the first volume and the survey of compressible high-Reynolds number flows in the second volume to be of immediate interest. These two articles also serve to illustrate the overall character of both of the volumes. The first-mentioned, by Joe F. Thompson of Mississippi State University, is primarily a summary of the results of an extensive program of research into coordinate system formulations carried out by Prof. Thompson and his colleagues. It thus provides extensive documentation of this work, with numerous examples, and a lengthy bibliography of reports, papers, and theses and dissertations written at MSU on various aspects of coordinate transformation techniques and their application. The second paper, by Hollanders and Viviand of ONERA, is a survey of a variety of techniques for the solution of compressible high Reynolds number flow problems, covering both physical aspects such as turbulence modeling and the numerical frameworks which have been used to obtain solutions of these problems, as well as a useful discussion of the appropriate definition of boundary conditions for the applications considered. It is thus a more general survey than the paper by Prof. Thompson. Both types of article are valuable, and other examples of each type can be found in these volumes. Thus they represent a very useful reference compilation, and their reference value is enhanced by the incorporation of a detailed index for all of the papers in each volume.

Although these collections are a useful reference compilation, this reviewer found the omission of introductory overview papers to be a major flaw. Both of these books were produced from author-prepared typescripts, presumably to reduce the publication time required, since the field of computational fluid dynamics is rapidly evolving. An effort to reduce publication time may also account for the lack of introductory overviews, but such an overview should have been included in each volume. None of the papers in these volumes include an abstract, so that an introductory summary would have been extremely valuable to the reader in assessing the applicability of the material discussed in each paper to his particular problem.

Journal of Fluids Engineering

Discussion

A Photographic Study of Cavitation in Jet Flow[1]

J. Raabe.[2] With and without polymer additives at different air contents in underwater jet flow by "transillumination" in high contrast enlargers combines the detection and observation of many high interesting phenomena with an intricate and refined, up-to-date measuring technique.

The authors may be congratulated on their effective experimental work.

Some questions may arise from the description of the experimental apparatuses, some others about the phenomena observed and some about supposed errors concerning time intervals.

On the one hand on page 132 it is mentioned that the inlet pressure to the nozzle was measured by a calibrated pressure gage. On the other hand the only varying pressure in the test according to the denotation and σ-formula used on page 133 seems to be the pressure p, which is defined as that around the jet and taken as atmospheric. Shall this mean that the atmospheric pressure was measured by pressure gage?

On page 132 it is mentioned that the camera used a rotating mirror to provide image-motion compensation of a predominantly axially-moving jet stream.

In this context the duration of an illumination period of one flash would be of interest. Obviously one aim of the snap shots was also the observation of the cavity growth, which simultaneously happens with the axial motion of the whole cavity. Since only the latter was compensated, the bubble growth indicated by the sequence of figures could be obscured by a too long duration of an individual flash. One example for this: The first cavity downstream from the nozzle in Fig. 7 shows (taken as a radial bubble) within the time interval mentioned of $\Delta t = 20\,s$ and by accounting for the length scale of approximately 10:1 a radial increment of

$$\Delta R = 0.803.10^{-3}\text{m}$$

This yields a "radial" growth rate of the bubble

$$R = \frac{\Delta R}{\Delta t} = \frac{0.803\ 10^{-3}}{20\ 10^{-6}} = 40\ \text{m/s}$$

Under the assumption that the tests were carried out in an altitude of sea level and with a water temperature of $T = 293$ K (20°C) the differential pressure $p-p_v$ can be approximated by

$$p-p_v = 98963\ \text{Pa}$$

and the density of water by

$$\rho = 10^3\text{kg/m}^3$$

From this yields the average jet velocity as

$$v = 14.08\ \sqrt{1/\sigma} \qquad (1)$$

Introducing into (1) $\sigma = 0.13$ from Fig. 7 $\sigma = 0.13$ one obtains

$$v = 39.1\ \text{m/s}$$

That means: Axial and radial velocity components of the phenomena to be observed are of the same order of magnitude.

This is obviously contrary to the authors expectation when they compensated by a rotating mirror *only* the axial component.

Moreover, the last results reveal some doubts about a too long duration of one flash period in relation to the period between subsequent figures. Assuming a bubble growth rate according to

$$v = \sqrt{\frac{2}{3\rho}(p_v - p_\infty)} \qquad (2)$$

in which p_∞ means the pressure outside the bubble (usually a tensile stress) and approximated by $p_\infty = 0$ it yields from (2) with $p_v\ (T = 20°) = 2383$ Pa and $\rho = 10^3\text{kg/m}^3$

$$v = \frac{2.2830}{3.10^3}\quad 1{,}4\ \text{m/s}$$

The discrepancy between the measured growth rate of bubble $v = 40$ m/s and this last reasonably expected value is in my opinion partly due to too a long duration of the flash. This deforms the cavities during light exposure time in connection with a supposed turbulence-induced cross-motion of these cavities.

Otherwise the very fundamental question would arise for the physical reason of a bubble growth rate of $v = 40$ m/s as shown e.g. in Fig. 7. I cannot imagine the pressure p_∞ around the bubble to be strongly negative in a free jet.

In connection with turbulence as one of the origins of this phenomenon it would be of interest to measure in such tests, simultaneously, the turbulence level.

The pressure of turbulence is indicated by the rippling of the jet boundary.

From drag reduction by polymere addition one knows also the influence of polymere additives on velocity profile and a turbulence level distribution.

Therefore it seems advizable and would be of high interest to measure during such observations the structure and intensity of the turbulence, which obviously here originates from instabilities of the vortex layer on the jet boundary. This measurement could be eventually realized by Laser-Doppler techniques.

An indication that the cavity formation has something to

1 By J. W. Hoyt and J. Taylor, published in the March, 1981, issue of the ASME JOURNAL OF FLUIDS ENGINEERING, Vol. 103, No. 1, pp. 14-18.

2 Professor, Head of Chair and Laboratory for Hydraulic Machinery & Equip. der Technischen, Universitat Munchen, Federal Republic of Germany.

do with the ripple on the jet boundary may be recognized from Fig. 2, in which cavities are only situated on stations, where the jet boundary is convexly-outwardly curved.

It would be of interest to know the authors opinion about turbulence influence on cavity formation and its measurement.

Turbulence may also cause a slippage of the cavities in direction and across the main flow.

If one neglects the effects of bubble cross-motion, slippage, bubble growth rate, to a long light exposure time and assuming the bubble motion to correspond that of the jet velocity according to equation (1) and the latter to be constant over one cross section and the length scale of the figure mentioned to be correct, some obvious errors are contained in the figures with respect to the time interval indicated.

Fig. 2 Δt should be 30 μs instead of 10 μs
Fig. 3 Δt should be 19 μs instead of 10 μs
Fig. 5 Δt should be 60 μs instead of 80 μs
Fig. 8 Δt should be 9.4 μs instead of 28 μs
Fig. 9 Δt should be 17 μs instead of 28 μs
Fig.10 Δt should be 31 μs instead of 42 μs

The "should be-values" were calculated by myself in tracking e.g. the front part of a definite cavity in two subsequent figures. By this a cavity path Δx is fixed. By the jet velocity v according to eq. 1) the time interval is obtained as

$$\Delta t = \frac{\Delta x}{v}$$

On the one hand the discrepancy between these calculated and mentioned time intervals may be due to the neglected effects of cross and lengthwise bubble slippage and bubble growth rate. On the other hand it may be caused by the impossibility to coordinate corresponding cavities in subsequent figures.

Also the coordination of wrong figures may be the cause for it and at last the mention of wrong time-intervals in the text may be an error.

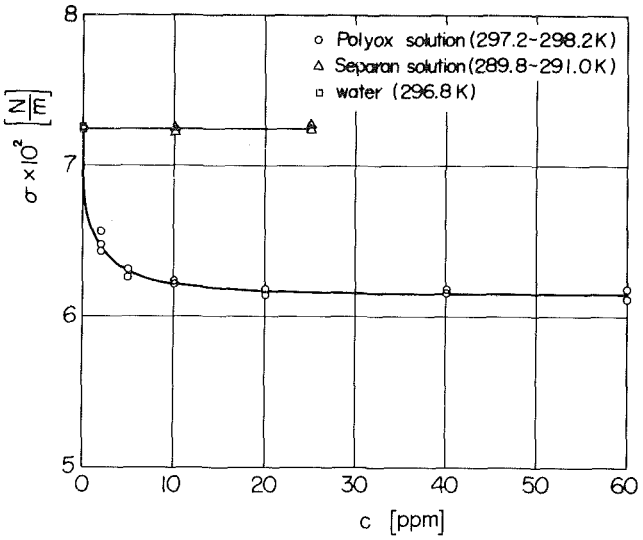

Fig. 1 Relation between surface tension σ and polymer concentration C

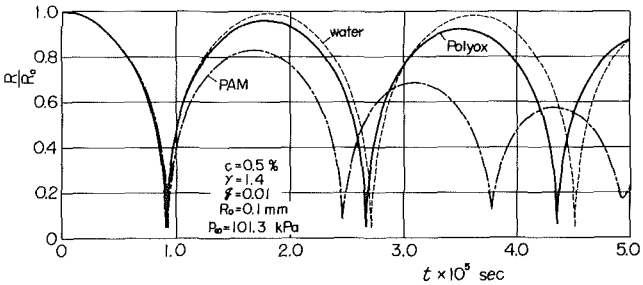

Fig. 2 Comparison of bubble radius-time history in a polyox solution with a PAM solution

(γ: ratio of specific heats of gas in a bubble, R_0: initial bubble radius, q: pressure ratio inside and outside of a bubble R: bubble radius, t: time, p_∞: liquid pressure far from a bubble)

A. Shima[3] and T. Tsujino[3]. This work found experimentally in jet cavitation that an addition of drag reducing polymers (polyethylene oxide and polyacrylamide) occurred the cavitation inhibition. As pointed out, a lowering of surface tension implies decreased cavitation resistance, but the authors should pay attention that the surface tensions of drag reducing polymer solutions are not always less than that of pure water. That is, as shown in Fig. 1,[4] an addition of polyethylene oxide into water makes small the surface tension, as well as the result of author,[5] while the value of surface tension for a polyacrylamide solution is almost similar to that of water. Hence the surface tension is not an essential factor as the suppression of cavitation inception due to polymer additives is discussed. We think that it is important to examine non-Newtonian characteristic of the flow field and the bubble behavior in polymer solutions. According to our theoretical investigation[4] on the bubble dynamics, the damping of the bubble oscillation in a PAM solution appears more strongly than the cases of polyox solution and water (see Fig. 2). We will expect further consideration on their points from the photographs of great interest conducted in this paper.

[3] Institute of High Speed Mechanics, Tohoku University, Sendai, Japan.
[4] Shima, A. and Tsujino, T., Unpublished.
[5] Hoyt, J. W., "Effect of Polymer Additives on Jet Cavitation," ASME JOURNAL OF FLUIDS ENGINEERING, Vol. 98, 1976, pp. 106–112.

Authors' Closure

The comments by Professors Shima and Tsujino are most welcome, since they introduce new experimental data regarding the properties of polymer solutions. In view of their data showing large differences in the surface tension of the two polymers used in our study, it appears that surface-tension modification may not be an important parameter in the cavitation characteristics of polymer solutions. Both poly (ethylene oxide) and polyacrylamide solutions show major cavitation appearance changes compared with pure water, even in concentrations of 25 ppm. Other non-Newtonian characteristics of these polymer solutions may have important influences on bubble oscillations, as shown in the discusser's second figure. We await with great interest the publication of the details of the calculations shown in the figure.

Professor Raabe asks as to the value of atmospheric pressure used in our calculations; since the computed cavitation number is more sensitive to velocity than local atmospheric pressure for these jet experiments, we used a standard value (101.3 kPa) for the atmospheric pressure.

Professor Raabe also questions the usefulness of the image-motion compensation technique as applied to cavitation photography, since he computes the bubble growth rate to be of the same order of velocity as the jet itself. Accepting his calculations as to bubble-radius velocity for the moment, it is still apparent that stopping the axial motion of the jet by the camera mechanism reduces the amount of axial bubble motion to be stopped by the flash. Experiments have shown that we consistently achieve sharper photographs when using the motion-compensation technique.

We have gone over our equipment, electronics, and test records carefully, and are convinced that the flash duration was very close to 1.5 μs, well within the 1 to 4 μs specified in the text. Since the bubbles in the pairs of photographs can be expanding, contracting, rotating, and nonspherical as well as translating, we have no faith in calculations which purport to show bubble growth rate or bubble axial velocity, based on scaling these photographs over the rather long time range involved. Our timing-interval electronics were not very sophisticated (being constructed by the authors themselves) but nevertheless, based on our calibrations, we feel that they yield much more accurate time intervals than one could estimate by scaling bubble movement from the photographs. In going over our results again, we did find a caption error regarding time intervals which we have corrected in the final text, so we are grateful to Professor Raabe for drawing our attention to this area. We agree with Professor Raabe that details of the turbulent flow in the cavitating region of the jet would add grately to our understanding of the physics involved.

We especially thank the discussors for their comments and additional information, all of which combine to make the study of the effect of polymer solutions on cavitation even more intriguing.

Turbulent Boundary Layer Flow Through a Gap in a Wall Mounted Roughness Element[1]

I. P. Castro.[2] My only major criticism of this work is the author's use of ideas developed to describe the growth of an internal layer after a step change in roughness (for which the final equilibrium flow differs from the initial one) for their case, which is essentially one of a wake flow relaxing back to the same initial equilibrium flow. I believe this has led to some confusion in their thinking. They state, quite correctly, that "the mechanism of flow readjustment downstream of the distortion proceeeds by a flow modification that works outwards from the wall" but confuse this internal layer, whose characteristics are determined mainly by the wall conditions (as in the roughness change case) with the "wake" behind the gap; the "edge" of the former is mistakenly taken as δ_i. The latter is simply the outer edge of the wake which does, of course, also move outwards but at a rate which is certainly not determined by wall parameters. The authors do not state to what distance from the wall their Clauser-plots for determining C_f had the usual log-law behaviour, but I surmise that it was always substantially less than δ_i. Indeed, despite the author's claim that equation (4) gives 'a useful description of the internal layer growth', Fig. 4 does, in fact, show that δ_i is always larger than that given by equation 4 by a factor of 3 or 4 in the early stages of relaxation of the wake. With their definition of δ_i I do not believe that z is a relevant length scale at all.

The final comment concerns the author's remarks regarding Fig 4. It would have been interesting to plot profiles measured at the same $x_{/D}$, rather than $x_{/H}$. Far downstream the flow will (to first order) only know about the change in the drag of the block (or, perhaps the change in *moment* of momentum - Counihan, Hunt and Jackson, 1974) which is presumably determined solely by changes in $D_{/H}$. It is therefore more likely that the proper scaling necessary for any possible downstream similarity should be based on $x_{/D}$. In fact, the mean flow profiles demonstrate that the thickness of the inner region is considerably greater for $D_{/H} = 0.5$ ($x_{/D} = 448$) than it is for $D_{/H} = 10$ ($x_{/D} = 22$), in line with the preceding argument.

Authors' Closure

The authors do not believe that the flows studied can be described as "essentially a relaxing wake flow;" in fact two of the flows ($D/H = 5,10$) have their wake component *reduced* by the notch. The readjustment of the flows is initiated and driven by the wall flow because it is the wall flow which quickly adjusts to the new conditons. The outer (wake) flow is driven back to equilibrium conditions on its inner boundary by the wall flow. This is illustrated in figure 2 where the outer wake flow is invarient (rather than "relaxing") from $X_{/H} \simeq 8$ onwards and is not changed until the inner readjusting flow works its way upwards through the wake. The growth in the height of this inner flow (for which δ_i is a standard notation) is a central feature of the flow as it is a measure of the flow's readjustment after the perturbation. It is difficult to see how the growth in the outer edge of the wake, which would be governed primarily by the entrainment of inviscid fluid by the outer flow, could be of the same importance.

The use of Z as a nondimensionalizing parameter does give a collapse of the results which is substantially better than that given by any other parameter. The results shown in Fig. 3 show a fairly high degree of correlation with each other even though they come from widely differing flows, $D/H = 0$ to $D/H = 10$. The use of Z is offered simply as the best procedure known to the authors.

The use of X/D as the scaling parameter does not result in downstream similarity either in the mean velocity or the longitudinal turbulence field. This can be appreciated by converting the X/H values on the profiles in Fig. 4 into X/D values and then comparing profiles with approximately corresponding values of X/D for the two gap sizes ($D/H = 1$ and 5). The authors hold to their view that far downstream of the gap the flows have forgotten the details of their distortions and are reapproaching equilibrium in a similar manner and that Fig. 4 supports this view.

[1] By W. H. Schofield, D. S. Barber, and E. Hogan, published in the March, 1981, issue of the JOURNAL OF FLUIDS ENGINEERING, Vol. 103, No. 1, pp. 97-103.

[2] Department of Mechanical Engineering, University of Surrey, Guildford, Surrey GU2 5XH, United Kingdom.

Professor Raabe also questions the usefulness of the image-motion compensation technique as applied to cavitation photography, since he computes the bubble growth rate to be of the same order of velocity as the jet itself. Accepting his calculations as to bubble-radius velocity for the moment, it is still apparent that stopping the axial motion of the jet by the camera mechanism reduces the amount of axial bubble motion to be stopped by the flash. Experiments have shown that we consistently achieve sharper photographs when using the motion-compensation technique.

We have gone over our equipment, electronics, and test records carefully, and are convinced that the flash duration was very close to 1.5 μs, well within the 1 to 4 μs specified in the text. Since the bubbles in the pairs of photographs can be expanding, contracting, rotating, and nonspherical as well as translating, we have no faith in calculations which purport to show bubble growth rate or bubble axial velocity, based on scaling these photographs over the rather long time range involved. Our timing-interval electronics were not very sophisticated (being constructed by the authors themselves) but nevertheless, based on our calibrations, we feel that they yield much more accurate time intervals than one could estimate by scaling bubble movement from the photographs. In going over our results again, we did find a caption error regarding time intervals which we have corrected in the final text, so we are grateful to Professor Raabe for drawing our attention to this area. We agree with Professor Raabe that details of the turbulent flow in the cavitating region of the jet would add grately to our understanding of the physics involved.

We especially thank the discussors for their comments and additional information, all of which combine to make the study of the effect of polymer solutions on cavitation even more intriguing.

Turbulent Boundary Layer Flow Through a Gap in a Wall Mounted Roughness Element[1]

I. P. Castro.[2] My only major criticism of this work is the author's use of ideas developed to describe the growth of an internal layer after a step change in roughness (for which the final equilibrium flow differs from the initial one) for their case, which is essentially one of a wake flow relaxing back to the same initial equilibrium flow. I believe this has led to some confusion in their thinking. They state, quite correctly, that "the mechanism of flow readjustment downstream of the distortion proceeeds by a flow modification that works outwards from the wall" but confuse this internal layer, whose characteristics are determined mainly by the wall conditions (as in the roughness change case) with the "wake" behind the gap; the "edge" of the former is mistakenly taken as δ_i. The latter is simply the outer edge of the wake which does, of course, also move outwards but at a rate which is certainly not determined by wall parameters. The authors do not state to what distance from the wall their Clauser-plots for determining C_f had the usual log-law behaviour, but I surmise that it was always substantially less than δ_i. Indeed, despite the author's claim that equation (4) gives 'a useful description of the internal layer growth', Fig. 4 does, in fact, show that δ_i is always larger than that given by equation 4 by a factor of 3 or 4 in the early stages of relaxation of the wake. With their definition of δ_i I do not believe that z is a relevant length scale at all.

The final comment concerns the author's remarks regarding Fig 4. It would have been interesting to plot profiles measured at the same $x_{/D}$, rather than $x_{/H}$. Far downstream the flow will (to first order) only know about the change in the drag of the block (or, perhaps the change in *moment* of momentum - Counihan, Hunt and Jackson, 1974) which is presumably determined solely by changes in $D_{/H}$. It is therefore more likely that the proper scaling necessary for any possible downstream similarity should be based on $x_{/D}$. In fact, the mean flow profiles demonstrate that the thickness of the inner region is considerably greater for $D_{/H} = 0.5$ ($x_{/D} = 448$) than it is for $D_{/H} = 10$ ($x_{/D} = 22$), in line with the preceding argument.

Authors' Closure

The authors do not believe that the flows studied can be described as "essentially a relaxing wake flow;" in fact two of the flows ($D/H = 5,10$) have their wake component *reduced* by the notch. The readjustment of the flows is initiated and driven by the wall flow because it is the wall flow which quickly adjusts to the new conditons. The outer (wake) flow is driven back to equilibrium conditions on its inner boundary by the wall flow. This is illustrated in figure 2 where the outer wake flow is invarient (rather than "relaxing") from $X_{/H} \simeq 8$ onwards and is not changed until the inner readjusting flow works its way upwards through the wake. The growth in the height of this inner flow (for which δ_i is a standard notation) is a central feature of the flow as it is a measure of the flow's readjustment after the perturbation. It is difficult to see how the growth in the outer edge of the wake, which would be governed primarily by the entrainment of inviscid fluid by the outer flow, could be of the same importance.

The use of Z as a nondimensionalizing parameter does give a collapse of the results which is substantially better than that given by any other parameter. The results shown in Fig. 3 show a fairly high degree of correlation with each other even though they come from widely differing flows, $D/H = 0$ to $D/H = 10$. The use of Z is offered simply as the best procedure known to the authors.

The use of X/D as the scaling parameter does not result in downstream similarity either in the mean velocity or the longitudinal turbulence field. This can be appreciated by converting the X/H values on the profiles in Fig. 4 into X/D values and then comparing profiles with approximately corresponding values of X/D for the two gap sizes ($D/H = 1$ and 5). The authors hold to their view that far downstream of the gap the flows have forgotten the details of their distortions and are reapproaching equilibrium in a similar manner and that Fig. 4 supports this view.

[1] By W. H. Schofield, D. S. Barber, and E. Hogan, published in the March, 1981, issue of the JOURNAL OF FLUIDS ENGINEERING, Vol. 103, No. 1, pp. 97-103.

[2] Department of Mechanical Engineering, University of Surrey, Guildford, Surrey GU2 5XH, United Kingdom.

Pressure and Vortex Shedding Patterns Around a Low Aspect Ratio Cylinder in a Sheared Flow at Transcritical Reynolds Numbers[1]

P. K. Stansby.[2] The main result of this paper is that the cellular wake structure of a circular cylinder of aspect ratio 9⅓ in a shear flow is similar at subcritical and transcritical Reynolds numbers. Reference is made to the experiments made by the writer (reference [14]), published in references [5 and 6]. This work emphasises the influence of end effects in uniform as well as shear flows and, for the former, end plate dimensions were optimised to remove end effects and so make the flow as two-dimensional as possible. The considerable spanwise variation of base pressure or the completely misleading uniform base pressure which can occur without end plates has also been reported in reference [15].

Certain complex three-dimensional end effects are thus virtually eliminated by suitable end plates although it became apparent from the shear flow work that they produce extra stabilising effects. These are discussed below. Rooney and Peltzer use very small end plates which will probably leave marked end effects in uniform flow (according to our experience). A more direct comparison between the influence of shear at subcritical and transcritical Reynolds numbers would perhaps have been made with larger end plates and we are pleased to note their proposed use for further studies.

The following misinterpretations should be noted. In the Introduction the statement that " . . . . the number and length of cells were insensitive to variations in shear and aspect ratio . . . . " is mistakenly accredited to reference [5] and is obviously incorrect. Reference [6] is later reported to have said that " . . . . for most cases only two end cells were produced . . . . " This was reported for an aspect ratio of 8; at the higher aspect ratio investigated, 16, cells other than the end cells occur. (Note that values up to 32 were investigated in reference [5].)

This latter point is vital to the actual application under consideration where the aspect ratio is around 100. The end cells are a special case and unlike the cells inbetween. They are stabilised by end plates as they are forced to approach the end plates normally. For aspect ratios of 8 or 9 end cells cover virtually all the span. At a value of 16 cells occur in between which may be fixed in position or moving and are of uncertain length, these properties being dependent upon all the incident flow parameters, including end plate dimensions. For OTECs with aspect ratios of around 100 these cells will occur over most of the span. (In our experiments the end cell at the high velocity end was usually about 5 diameters long and the end cell at the low velocity end about 3 diameters long.)

Reference is now made to the Conclusions, "following investigation 1.," where shear is to be varied to determine its influence on the two-cell structure. Figure 12 in reference [5] shows how the shear parameter β influences the end cells (at subcritical Reynolds numbers) and it appears that the two end cells approach in frequency as $\beta \rightarrow 0$. In uniform flow it seems likely that there will be two end cells of the same frequency. The observation in Conclusion 1, that it was impossible to determine a correlation between shear and cell length, was made because only end cells were present (dependent upon the ends rather than shear).

Conclusion 4 states that fluctuating pressures in uniform flow were significantly lower than in shear flow. The former are, however, very much influenced by the degree of three-dimensionality of the flow. The well-correlated shedding in nearly two-dimensional flow produces higher fluctuating pressures than less coherent wakes. In these experiments three-dimensionality will result from the very small end plates. The conclusion that shear increases fluctuating pressures is thus qualified. There are two conflicting effects here: shear will decorrelate vortex shedding causing a less coherent wake and reduce fluctuating pressures, while at the same time the unsteady behaviour of the streamwise vorticity from the incident shear flow will produce additional fluctuating pressures. At this point it is pertinent to mention that 'real' incident flows have a turbulence intensity of around 10 percent further complicating matters.

Since a good deal has been said about the stabilising influence of the ends, it is appropriate to mention a further stabilising influence described in the Introduction. Cylinder vibration can produce "locking-on" in shear flows as well as uniform flows (reference [6]). In shear flow the locked-on cell is stable in position and frequency and appears to stabilise unlocked-on cells above and below. In uniform flow varying the cylinder frequency n_c produces a range of values of n_c/n_{sc} (n_{so} being the shedding frequency from a fixed cylinder) for locking-on, dependent on vibration amplitude. In shear flow this variation can be produced along the span with a fixed n_c since n_{so} varies along the span and the range for locking-on is similar. However, the flow is in other ways rather different and a quasi-two-dimensional prediction for shear flows could well give misleading predictions of flow-induced vibrations. This is because the phase between lift and cylinder displacement is crucial to the latter. The phase varies along the span in shear flow but clearly not in a way which corresponds to the variation with n_c/n_{so} in uniform flow. For example, a jump of around 180° occurs in the middle of the locked-on range in uniform flow whilst a continuous spanwise variation occurs in shear flow (inferred from reference [6]). The ideas inherent in the formula in reference [6] for the spanwise extent of locking-on will have to be extended to accommodate phase variations for reliable predictions of flow-induced vibrations. (It does not even follow that, because forced cylinder oscillation produces locking-on in shear flow, flow-induced vibrations will also occur, although it is of course likely.)

It is suggested that prediction methods should be established at subcritical Reynolds numbers with high aspect ratio cylinders (greater than at least 30) in the controlled environment of the laboratory. Tests at these Reynolds numbers should be made with turbulent shear flows with realistic length scales and intensities. Once the method has been established, it should be calibrated by spot checks at transcritical Reynolds numbers through full or half scale experiments. (If this is the only way that very high aspect ratios may also be achieved.) The spanwise distribution of the unsteady force is the vital measurement.

1 By D. M. Rooney and R. D. Peltzer, published in the March, 1981 issue of the JOURNAL OF FLUIDS ENGINEERING, Vol. 103, No. 1, pp. 88-96

2 Simon Engineering Laboratories, University of Manchester, Manchester M13 9PL England.

Additional References

14. Stansby, P. K., "Vortex Wakes of Cylinders Oscillating in Uniform and Sheared Flows," Ph.D. dissertation, University of Cambridge, 1974.

15. Stansby, P. K., "The Effects of End Plates on the Base Pressure Coefficient of a Circular Cylinder," *Aeronautical Journal*, Vol. 78, 1974, p.36.

Authors' Closure

The authors welcome Dr. Stansby's comments and criticisms of their paper. A few closing comments will now be made.

Our apparent misinterpretation of the results in reference [5] was an unfortunate misprint, for which the authors are grateful to Dr. Stansby for pointing out. The statement should have ended "for an aspect ratio $L/D = 8$" instead of "and aspect ratio."

We are acutely aware of the limitations imposed by small aspect ratio cylinders, but saw no alternative which would permit an admittedly incomplete investigation of transcritical shedding patterns. The significant finding that transcritical flow patterns closely parallel subcritical flow patterns (even granted that only two forced end cells were observed) remains valid. To attribute the division of the shedding frequencies into a cellular pattern solely to the endplate effect would require further demonstration. Our tests clearly indicated a single spanwise shedding frequency at St = 0.165 in subcritical uniform flow and at St = 0.215 in transcritical uniform flow. No measurements were made near the center of the span to determine whether the shedding occurred in phase on both sides of the cylinder. Yet the evidence adduced by Dr. Stansby to infer that as β approaches zero, two end cells of the same frequency persist (as opposed to a single cell) does not seem compelling. If that were the case, the cell lengths should become equal as the limit is reached. However, Fig. 12 in reference [5] shows no change in the relative cell lengths of 5D and 3D with decreasing β. The implication is that there is either a discontinuity for very low values of β, when one spanwise cell suddenly appears (our contention), or the gradual transition to two cells of length 4D occurs at values of β smaller than examined in any investigation yet undertaken. In any case, the data on endplate cells versus shear flow cells remains inconclusive.

Subsequent tests employing the optimum endplate design for cylinders with an aspect ratio of 17 have been reported by the authors [16] and should help resolve some of the remaining questions about the relationship between roughness, shear parameter, and vortex shedding cell lengths for subcritical and critical Reynolds number flows. In addition, the authors have now examined results of tests on cylinders with aspect ratios of 27 and 48 in sheared flow and have determined that the strong cellular structure so evident at aspect ratios of 16 to 20 appears to break down, at least for subcritical flows in the range $2 \times 10^4 \leq Re \leq 1 \times 10^5$, for a given value of the shear parameter. Corroborating evidence for this phenomenon can be seen in similar tests performed elsewhere [(17)].

Additional References

16 Peltzer, R. D., and Rooney, D. M., "The Effect of Upstream Shear and Surface Roughness on the Vortex Shedding Patterns and Pressure Distributions Around a Circular Cylinder in Transitional Re Flows," VPI & SU Report VPI-Aero-110, Apr. 1980.

17 Peterka, J. A., Cermak, J. E., and Woo, H. G. C., "Experiments on the Behavior of Cables in a Linear Shear Flow," Colorado State University Progress Report, 19 May, 1980.

A Theoretical Model for the Transverse Impingement of Free Jets at Low Reynolds Number[1]

S. B. Friedman.[2] An engineering research should have, as a minimum, the objective of either explaining the underlying cause of some physical effect, or providing a model by which design can be reasonably performed.

The subject paper falls into the first of the above categories. The phenomena of the "backward-bending" jet is complex and, as well demonstrated in this paper, can be attributed to many causes. If there is any weakness in the conclusions it is that the relative importance of the various causes is not considered or discussed.

In the original work by Dr. Martin and myself, a very simple and workable design model was established, which accounted for better than 90 percent of the previously unexplained variation. A quick analysis and comparison of our work and this one shows little significant improvement in the predictive value using the newer model.

In conclusion, this work should be a valuable addition to the literature, considering both its content and methodology.

Authors' Closure

We would like to acknowledge the comments of Dr. Friedman and his interest in this research; a continuation of his initial experimental work.

The purpose of the theoretical study was to develop a more detailed understanding of the mechanism describing the phenomena of the "backward-bending" jet. That greater insight was achieved and greatly compliments the original intuitive modelling proposed by Dr. Friedman. It is therefore very satisfactory that the original empirical relationships can still be used effectively for design.

[1] By R. Winton and H. R. Martin, published in the December, 1980, issue of the JOURNAL OF FLUIDS ENGINEERING, Vol. 102, No. 4, pp. 510-518.

[2] Department of Manufacturing Engineering, Miami University, Oxford, Ohio 45056.

Authors' Closure

The authors welcome Dr. Stansby's comments and criticisms of their paper. A few closing comments will now be made.

Our apparent misinterpretation of the results in reference [5] was an unfortunate misprint, for which the authors are grateful to Dr. Stansby for pointing out. The statement should have ended "for an aspect ratio $L/D = 8''$ instead of "and aspect ratio."

We are acutely aware of the limitations imposed by small aspect ratio cylinders, but saw no alternative which would permit an admittedly incomplete investigation of transcritical shedding patterns. The significant finding that transcritical flow patterns closely parallel subcritical flow patterns (even granted that only two forced end cells were observed) remains valid. To attribute the division of the shedding frequencies into a cellular pattern solely to the endplate effect would require further demonstration. Our tests clearly indicated a single spanwise shedding frequency at St = 0.165 in subcritical uniform flow and at St = 0.215 in transcritical uniform flow. No measurements were made near the center of the span to determine whether the shedding occurred in phase on both sides of the cylinder. Yet the evidence adduced by Dr. Stansby to infer that as β approaches zero, two end cells of the same frequency persist (as opposed to a single cell) does not seem compelling. If that were the case, the cell lengths should become equal as the limit is reached. However, Fig. 12 in reference [5] shows no change in the relative cell lengths of 5D and 3D with decreasing β. The implication is that there is either a discontinuity for very low values of β, when one spanwise cell suddenly appears (our contention), or the gradual transition to two cells of length 4D occurs at values of β smaller than examined in any investigation yet undertaken. In any case, the data on endplate cells versus shear flow cells remains inconclusive.

Subsequent tests employing the optimum endplate design for cylinders with an aspect ratio of 17 have been reported by the authors [16] and should help resolve some of the remaining questions about the relationship between roughness, shear parameter, and vortex shedding cell lengths for subcritical and critical Reynolds number flows. In addition, the authors have now examined results of tests on cylinders with aspect ratios of 27 and 48 in sheared flow and have determined that the strong cellular structure so evident at aspect ratios of 16 to 20 appears to break down, at least for subcritical flows in the range $2 \times 10^4 \leq Re \leq 1 \times 10^5$, for a given value of the shear parameter. Corroborating evidence for this phenomenon can be seen in similar tests performed elsewhere [(17)].

Additional References

16 Peltzer, R. D., and Rooney, D. M., "The Effect of Upstream Shear and Surface Roughness on the Vortex Shedding Patterns and Pressure Distributions Around a Circular Cylinder in Transitional Re Flows," VPI & SU Report VPI-Aero-110, Apr. 1980.

17 Peterka, J. A., Cermak, J. E., and Woo, H. G. C., "Experiments on the Behavior of Cables in a Linear Shear Flow," Colorado State University Progress Report, 19 May, 1980.

A Theoretical Model for the Transverse Impingement of Free Jets at Low Reynolds Number[1]

S. B. Friedman.[2] An engineering research should have, as a minimum, the objective of either explaining the underlying cause of some physical effect, or providing a model by which design can be reasonably performed.

The subject paper falls into the first of the above categories. The phenomena of the "backward-bending" jet is complex and, as well demonstrated in this paper, can be attributed to many causes. If there is any weakness in the conclusions it is that the relative importance of the various causes is not considered or discussed.

In the original work by Dr. Martin and myself, a very simple and workable design model was established, which accounted for better than 90 percent of the previously unexplained variation. A quick analysis and comparison of our work and this one shows little significant improvement in the predictive value using the newer model.

In conclusion, this work should be a valuable addition to the literature, considering both its content and methodology.

Authors' Closure

We would like to acknowledge the comments of Dr. Friedman and his interest in this research; a continuation of his initial experimental work.

The purpose of the theoretical study was to develop a more detailed understanding of the mechanism describing the phenomena of the "backward-bending" jet. That greater insight was achieved and greatly compliments the original intuitive modelling proposed by Dr. Friedman. It is therefore very satisfactory that the original empirical relationships can still be used effectively for design.

[1] By R. Winton and H. R. Martin, published in the December, 1980, issue of the JOURNAL OF FLUIDS ENGINEERING, Vol. 102, No. 4, pp. 510-518.

[2] Department of Manufacturing Engineering, Miami University, Oxford, Ohio 45056.